LBNL-52189

ERNEST ORLANDO LAWRENCE
BERKELEY NATIONAL LABORATORY

Particle Deposition in Ventilation Ducts

Mark R. Sippola

Environmental Energy Technologies Division

September 2002

Ph.D. Thesis

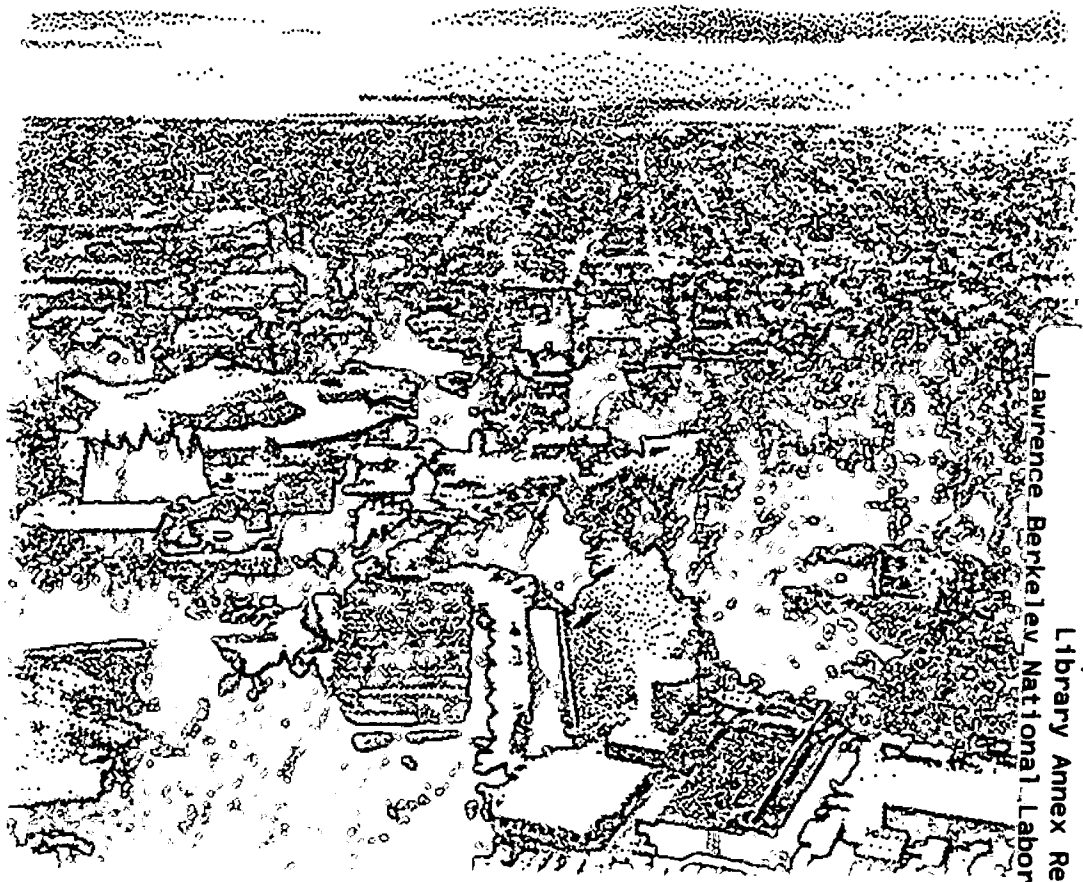

DISCLAIMER

LBNL – 52189

Particle Deposition in Ventilation Ducts

Mark R. Sippola

Environmental Energy Technologies Division
Indoor Environment Department
Lawrence Berkeley National Laboratory
University of California
Berkeley, CA 94720

September 2002

This work was supported by the Office of Nonproliferation Research and Engineering, Chemical and Biological National Security Program, of the National Nuclear Security Administration , U.S. Department of Energy under Contract No. DE-AC03-76SF00098.

Particle Deposition in Ventilation Ducts

by

Mark Raymond Sippola

B.S. (The Ohio State University) 1996
M.S. (University of California, Berkeley) 1997

A dissertation submitted in partial satisfaction of the

requirements for the degree of

Doctor of Philosophy

in

Engineering - Civil and Environmental Engineering

in the

GRADUATE DIVISION

of the

UNIVERSITY OF CALIFORNIA, BERKELEY

Committee in charge:

Professor William W. Nazaroff, Chair
Professor Robert A. Harley
Professor Dorian Liepmann

Fall 2002

ABSTRACT

Particle Deposition in Ventilation Ducts

by

Mark Raymond Sippola

Doctor of Philosophy in Civil and Environmental Engineering

University of California, Berkeley

Professor William W. Nazaroff, Chair

Exposure to airborne particles is detrimental to human health and indoor exposures dominate total exposures for most people. The accidental or intentional release of aerosolized chemical and biological agents within or near a building can lead to exposures of building occupants to hazardous agents and costly building remediation. Particle deposition in heating, ventilation and air-conditioning (HVAC) systems may significantly influence exposures to particles indoors, diminish HVAC performance and lead to secondary pollutant release within buildings. This dissertation advances the understanding of particle behavior in HVAC systems and the fates of indoor particles by means of experiments and modeling.

Laboratory experiments were conducted to quantify particle deposition rates in horizontal ventilation ducts using real HVAC materials. Particle deposition experiments were conducted in steel and internally insulated ducts at air speeds typically found in ventilation ducts, 2-9 m/s. Behaviors of monodisperse particles with diameters in the size range 1-16 μm were investigated. Deposition rates were measured in straight ducts with

a fully developed turbulent flow profile, straight ducts with a developing turbulent flow profile, in duct bends and at S-connector pieces located at duct junctions. In straight ducts with fully developed turbulence, experiments showed deposition rates to be highest at duct floors, intermediate at duct walls, and lowest at duct ceilings. Deposition rates to a given surface increased with an increase in particle size or air speed. Deposition was much higher in internally insulated ducts than in uninsulated steel ducts. In most cases, deposition in straight ducts with developing turbulence, in duct bends and at S-connectors at duct junctions was higher than in straight ducts with fully developed turbulence.

Measured deposition rates were generally higher than predicted by published models. A model incorporating empirical equations based on the experimental measurements was applied to evaluate particle losses in supply and return duct runs. Model results suggest that duct losses are negligible for particle sizes less than 1 μm and complete for particle sizes greater than 50 μm. Deposition to insulated ducts, horizontal duct floors and bends are predicted to control losses in duct systems. When combined with models for HVAC filtration and deposition to indoor surfaces to predict the ultimate fates of particles within buildings, these results suggest that ventilation ducts play only a small role in determining indoor particle concentrations, especially when HVAC filtration is present. However, the measured and modeled particle deposition rates are expected to be important for ventilation system contamination.

TABLE OF CONTENTS

LIST OF FIGURES

LIST OF TABLES

NOMENCLATURE

a, b, c, d	parameters in equations (2.122)-(2.126)
A	cross sectional area of a duct, m^2
A_{bend}	internal surface area of a duct bend, m^2
A_d	apparent surface area of a duct surface sample or S-connector, m^2
A_H	material-dependent Hamaker constant, kg m^2 s^{-2}
a_o, b_o	parameters in equations (2.107)-(2.109)
a_1, a_2, a_3	constants in equation (2.68)
a_4, a_5, a_6	constants in equation (2.68)
A_1, B_1, C_1	parameters in Nikuradse's (1936) empirical equation for the Fanning friction factor in Table 2.1
a_x, b_x, c_x	general experimental parameters in an error analysis
C	instantaneous local airborne particle concentration, # m^{-3}
C'	fluctuating airborne particle concentration, # m^{-3}
C^+	dimensionless airborne particle concentration, equation (2.84)
C_o	projected time-averaged concentration at the shrouded nozzle, # m^{-3}
C_1	time-averaged concentration at test duct 1, equation (3.8), # m^{-3}
C_2	time-averaged concentration at test duct 2, equation (3.10), # m^{-3}
$C_{1,up}$	time-averaged concentration upstream of test duct 1, # m^{-3}
$C_{1,down}$	time-averaged concentration downstream of test duct 1, # m^{-3}
$C_{2,up}$	time-averaged concentration upstream of test duct 2, # m^{-3}
$C_{2,down}$	time-averaged concentration downstream of test duct 2, # m^{-3}

C_3	projected time-averaged concentration at test duct 3, equation (4.6), # m^{-3}
C_4	projected time-averaged concentration at test duct 4, equation (4.7), # m^{-3}
$C_{5,out}$	projected time-averaged concentration at the outlet of bend 5, equation (4.9), # m^{-3}
$C_{6,in}$	projected time-averaged concentration at the inlet of bend 6, equation (4.8), # m^{-3}
C_{ave}, $\overline{C}$	time-averaged airborne particle concentration, # m^{-3}
C_{bulk}	time-averaged particle concentration in the turbulent core of a duct, # m^{-3}
C_c	Cunningham slip correction factor, equation (2.14)
C_d	drag coefficient of a spherical particle, equations (2.32)-(2.33)
C_f	fluorescein concentration in rinsing solution in a fluorometric analysis, ng mL^{-1}
$C_{f,b}$	background fluorescein concentration in a fluorometric analysis, ng mL^{-1}
C_{in}	flow-weighted average concentration at a duct inlet, # m^{-3}
C_{indoor}	indoor particle concentration, kg m^{-3}
C_{inlet}	concentration entering a sampling nozzle inlet, # m^{-3}
C_{out}	flow-weighted average concentration at a duct outlet, # m^{-3}
$C_{outdoor}$	outdoor particle concentration, kg m^{-3}
C_{outlet}	concentration at the outlet of a sampling transport line, # m^{-3}
C_{shroud}	concentration in a shroud upstream of a sampling nozzle inlet, # m^{-3}
$C_{shroud,c}$	concentration in a shroud upstream of a sampling nozzle inlet and near the shroud centerline, # m^{-3}
$C^+_{\Delta^+}$	dimensionless particle concentration at the dimensionless capture distance

CL_{rel}	relative 95% confidence interval of an experimental variable, equation (D.10), %
CL_{x_o}	95% confidence limits for an experimental variable, equation (D.9)
d_a	aerodynamic particle diameter, m
D_B	Brownian diffusion coefficient of a particle, equation (2.30), $m^2 s^{-1}$
D_h	hydraulic duct diameter, equation (2.4), m
d_{inlet}	inlet diameter of a sampling nozzle, m
d_{mm}	mass-mean particle diameter, m
d_p	particle diameter, m
d_{shroud}	inner diameter of a shroud on a shrouded nozzle, m
d_t	inner diameter of a transport line, m
D_T	temperature gradient dependent diffusion constant of a particle, $m^2 s^{-1}$
De	Dean number for flow through a bend, equation (2.28)
e	offset in the origin of the air velocity profile at a rough surface, m
e^+	dimensionless offset in the origin of the air velocity profile at a rough surface, $= eu^*/\nu$
e_o	the charge of a single electron, -1.6×10^{-19} C
E	strength of an electric field, V m^{-1}
E_o	potential energy of a surface, equation (2.120), kg $m^2 s^{-2}$
$E_{indoor}(t)$	arbitrary indoor particle emissions profile, kg h^{-1}
E_r	relative error, equation (D.7), %
EF	deposition velocity enhancement factor, as in example equation (4.19)
EF_{4c2}	enhancement factor in test duct 4 to ceiling panel 2, equation (4.19)

f	Fanning friction factor, equation (2.7)
f_e	fraction of particles exhausted from a building, equations (6.31) and (6.40)
f_f	fraction of particles filteres, equations (6.27) and (6.36)
f_i	fraction of particles depositing to indoor surfaces, equations (6.29) and (6.38)
f_r	fraction of particles depositing in return ducts, equations (6.30) and (6.39)
f_s	fraction of particles depositing in supply ducts, equations (6.28) and (6.37)
F	parameter used for predicting the total aspiration efficiency of a shrouded nozzle, equation (B.20)
F_b	fraction of supplied air that bypasses HVAC filters
F_C	Coulomb force on a charged particle, equation (2.43), kg m s^{-2}
F_d	drag force on a particle, equation (2.31), kg m s^{-2}
F_e	electrostatic force on a particle, equation (2.45), kg m s^{-2}
F_e^+	dimensionless electrostatic force on a particle, $= F_e \nu / m_p u^{*3}$
F_g	gravitational force on a particle, equation (2.36), kg m s^{-2}
F_l	shear induced lift force on a particle, equation (2.38), kg m s^{-2}
F_l^+	dimensionless shear induced lift force on a particle, $= F_l \nu / m_p u^{*3}$
F_t	turbophoretic force on a particle, equation (2.51), kg m s^{-2}
F_{th}	thermophoretic force on a particle, equation (2.40), kg m s^{-2}
g	gravitational acceleration at Earth's surface, 9.81 m s^{-2}
g^+	dimensionless gravitational acceleration, equation (2.74)
h	vertical height measured by a profilometer, m
H	height of a duct with rectangular cross-section, m

H_{th}	thermophoretic force coefficient, equation (2.41)
h_{ave}	average height of a profilometer scan, m
h_{max}	maximum height measured in a profilometer scan, m
h_S	vertical height that an S-connector projects into the airflow, m
J	particle flux, # m^{-2} s^{-1}
J_{1f1}	particle flux in test duct 1 to floor panel 1, # m^{-2} s^{-1}
J_{1f2}	particle flux in test duct 1 to floor panel 2, # m^{-2} s^{-1}
J_{1f3}	particle flux in test duct 1 to floor panel 3, # m^{-2} s^{-1}
J_{1f4}	particle flux in test duct 1 to floor panel 4, # m^{-2} s^{-1}
J_{4c2}	particle flux in test duct 4 to ceiling panel 2, # m^{-2} s^{-1}
J_B	particle flux due to Brownian diffusion, equation (2.29), # m^{-2} s^{-1}
J_{diff}	particle diffusive flux due to Brownian and turbulent diffusion, equation (2.47), # m^{-2} s^{-1}
k	roughness scale of a surface, m
k^+	dimensionless roughness of a surface, equation (2.11)
k_1, k_2, k_3	constants in equations (2.52)-(2.54)
k_4, k_5	constants in equations (5.4)-(5.5)
k_6	constant in equation (5.10)
k_a	thermal conductivity of air, W m^{-1} K^{-1}
k_B	Boltzman constant, 1.38×10^{-23} J/K
k_d	overall indoor particle decay constant, equation (6.33), h^{-1}
k_p	thermal conductivity of particulate material, W m^{-1} K^{-1}
Kn	particle Knudsen number, equation (2.15)

L, ΔL	length of a segment of duct, m
l_{bend}	fraction of particles entering a duct run lost in a bend, equation (6.21)
$l_{ceiling}$	fraction of particles entering a duct run lost to the ceiling of a single duct generation, equation (6.9)
l_{duct}	fraction of particles entering a duct run lost in a single duct generation, equation (6.17)
l_{floor}	fraction of particles entering a duct run lost to the floot of a single duct generation, equation (6.19)
L_{inlet}	length of the inlet piece of the shrouded nozzle, m
L_{offset}	distance between the shroud inlet and nozzle inlet in a shrouded nozzle, m
L_p	length of a duct panel analyzed for particle deposition, m
l_r	total fraction of particles lost in a return duct run
l_s	total fraction of particles lost in a supply duct run
l_S	fraction of particles entering a duct run lost to the S-connectors of a single duct generation, equation (6.20)
L_S	transverse length of an S-connector, m
L_{shroud}	length of a shroud on a shrouded nozzle, m
$L_{t,nv}$	length of a nonvertical segment of a sampling transport line, m
$L_{t,total}$	total length of a sampling transport line, m
l_{total}	total fraction of particles lost in a duct run, equation (6.22)
l_{wall}	fraction of particles entering a duct run lost to the wall of a single duct generation, equation (6.18)
m	fluorescein mass measured by fluorometric analysis, ng

M	total particle mass associated with an indoor particle release, equation (6.35), kg
$m_{5,in}$	total airborne fluorescein mass entering bend 5, ng
$m_{6,in}$	total airborne fluorescein mass entering bend 6, ng
m_{bend}	fluorescein mass deposited inside a duct bend, ng
$m_{bend,5}$	fluorescein mass deposited inside bend 5, ng
m_d	fluorescein mass on a duct surface or S-connector surface, ng
m_{elbow}	fluorescein mass inside the elbow piece of the shrouded nozzle, ng
m_f	fluorescein mass on a filter, ng
m_{fh}	fluorescein mass on a filter holder, ng
$m_{f/p}$	mass of fluorescein in a single particle, ng
m_{in}	total airborne fluorescein mass entering a bend, ng
m_{inlet}	fluorescein mass inside the inlet piece of the shrouded nozzle, ng
m_n	fluorescein mass inside a sampling nozzle, ng
m_p	mass of a particle, kg
$m_{presented}$	total airborne fluorescein mass presented to the leading edge of an S-connector, ng
m_S	fluorescein mass deposited on an S-connector, ng
m_{shaft}	fluorescein mass inside the shaft piece of the shrouded nozzle, ng
n	net excess of electrons on a particle (electrons minus protons)
n_d	number of distinct duct generations in a duct run
n_b	number of bend in a duct run
N	particle number count in an APS size bin

N_m	number of repeated measurement of an experimental variable
N_p	number of vertical displacements measured in a single profilometer scan
N_S	number of S-connectors in a duct generation
od_{inlet}	outer diameter of the inlet piece at the waist of the shrouded probe, m
$\Delta P/\Delta L$	pressure drop per unit length of duct, kg m^{-2} s^{-2}
P	perimeter of a section through a duct normal to the direction of flow, m
P_A	static pressure at location A, Pa
P_{bend}	particle penetration fraction through a duct bend
P_{bend5}	particle penetration through bend 5
P_{bend6}	particle penetration through bend 6
P_C	static pressure at location C, Pa
$P_{ceiling}$	particle penetration through a duct generation owing to deposition only at the duct ceiling, equations (6.3) and (6.7)
P_{duct}	particle penetration fraction through a duct, equations (2.2)-(2.3)
P_{floor}	particle penetration through a duct generation owing to deposition only at the duct floor, equations (6.5) and (6.7)
P_S	particle penetration through a duct generation owing to deposition only at S-connectors at duct junctions, equations (6.6)
P_t	particle penetration through a portion of a duct run, equation (6.1)
P_{total}	particle penetration through an entire duct run, equation (6.1)
P_v	velocity pressure measured by a pitot tube, Pa
P_{wall}	particle penetration through a duct generation owing to deposition only at the duct wall, equations (6.4) and (6.8)

Pr	Prandtl number of air, ~ 0.7
q	electric charge on a particle, equation (2.44), C
Q_i	sampling pump flow rate to achieve isokinetic sampling, equation (3.2), $m^3 s^{-1}$
Q_{pump}	sampling pump flow rate, $m^3 s^{-1}$
Q_s	building supply air flow rate, $m^3 s^{-1}$
r	restitution coefficient of a surface
R	fraction of return air recirculated to a building
R_o	bend ratio, equation (2.18)
R_{ave}	arithmetic average roughness of a surface from a profilometer scan, m
R_{bend}	radius of a duct bend, m
$r_{ceiling}$	rate of particle loss to the ceiling of a duct generation, equations (6.10) and (6.14)
r_{duct}	total rate of particle loss in a duct generation, equation (6.16)
r_{floor}	rate of particle loss to the floor of a duct generation, equation (6.12) and (6.14)
r_{indoor}	rate of particle loss to indoor surfaces, equation (6.25), kg h^{-1}
r_p	particle radius, m
r_p^+	dimensionless particle radius, $= r_p u^* / \nu$
r_S	rate of particle loss to the S-connectors of a duct generation, equation (6.13)

r_{wall}	rate of particle loss to the wall of a duct generation, equations (6.11) and (6.15)
Re	flow Reynolds number in a duct, equation (2.10)
Re_p	particle Reynolds number, equation (2.34)
S	stopping distance of a particle, equation (2.80), m
S^+	dimensionless stopping distance of a particle, equation (2.81)
$s_{a_x}, s_{b_x}, s_{c_x}$	random errors associated with the experimental parameters a_x, b_x, and c_x
s_{d_p}	random error in particle diameter measurement, equation (D.11), m
s_{x_o}	random error associated with calculated experimental variable x_o
Sc	particle Schmidt number, equation (2.55)
St	particle Stokes number, equation (2.19)
St_{inlet}	Stokes number defined at a sampling nozzle inlet, equation (B.5)
St_S	Stokes number defined at an S-connector, equation (4.15)
St_{shroud}	Stokes number defined at a shroud inlet, equation (B.21)
St_t	Stokes number defined in a sampling transport tube, equation (B.13)
t	experimental time, min
T	temperature, °C or K
T_o	air temperature at the duct centerline, °C or K
T_{total}	total transmission through a sampling system, equation (B.3)
T_w	surface temperature of a duct wall, °C or K
ΔT	temperature difference between the air at $y^+ = 200$ and a duct surface, °C or K

ΔT_{200}^{+}	dimensionless temperature gradient parameter, equation (C.4)
u	instantaneous streamwise air velocity, m s^{-1}
$\overline{u}$	time averaged mean streamwise air velocity, m s^{-1}
u'	fluctuating streamwise air velocity, m s^{-1}
u^*	friction velocity, equations (2.5)-(2.6), m s^{-1}
u_1^*	lowest nominal experimental friction velocity in steel or insulated ducts
u_2^*	middle nominal experimental friction velocity in steel or insulated ducts
u_3^*	highest nominal experimental friction velocity in steel or insulated ducts
$\overline{u'v'}$	the time average of the product of the streamwise and wall normal fluctuating air velocity components, m^2 s^{-2}
u_o	local air velocity immediately upstream of a sampling nozzle, m s^{-1}
u_a	local air velocity, m s^{-1}
U_{ave}	bulk average air velocity in a duct, m s^{-1}
u_c	air velocity at the duct centerline, m s^{-1}
u_i	local streamwise air velocity, m s^{-1}
u_{inlet}	air velocity at a sampling nozzle inlet, m s^{-1}
u_S	air velocity integrated over the height of an S-connector, m s^{-1}
u_{shroud}	average air velocity in a shroud upstream of a sampling nozzle inlet, m s^{-1}
u_t	air velocity through a sampling transport line, m s^{-1}
v	instantaneous wall normal air velocity, m s^{-1}
V	volume of indoor space, m^{-3}
$\overline{v}$	time averaged mean wall normal air velocity, m s^{-1}

v'	fluctuating wall normal air velocity, m s^{-1}
$\overline{v'C'}$	the time average of the product of the wall normal fluctuating air velocity and the fluctuating airborne particle concentration, kg m^{-2} s^{-1}
V_d	particle deposition velocity, equation (2.1), m s^{-1}
$V_{d,c}$	average deposition velocity to the ceiling of test ducts 1 and 2, equation (4.3), m s^{-1}
$V_{d,comp}$	composite deposition velocity in a square horizontal duct, equation (4.4), m s^{-1}
$V_{d,f}$	average deposition velocity to the floor of test ducts 1 and 2, equation (4.1), m s^{-1}
$V_{d,w}$	average deposition velocity to the wall of test ducts 1 and 2, equation (4.2), m s^{-1}
$V_{d,1c}$	average deposition velocity to the ceiling of test duct 1, m s^{-1}
$V_{d,1f}$	average deposition velocity to the floor of test duct 1, m s^{-1}
$V_{d,1w}$	average deposition velocity to the wall of test duct 1, m s^{-1}
$V_{d,4c2}$	deposition velocity in test duct 4 to ceiling panel 2, equation (4.20), m s^{-1}
V_d^+	dimensionless deposition velocity, equation (2.12)
$V_{d,c}^+$	dimensionless deposition velocity to a horizontal ceiling
$V_{d,c,S}^+$	dimensionless deposition velocity to a ceiling S-connector
$V_{d,diff}^+$	dimensionless deposition velocity due to particle diffusion
$V_{d,f}^+$	dimensionless deposition velocity to a horizontal floor
$V_{d,f,S}^+$	dimensionless deposition velocity to a floor S-connector

$V^+_{d,inertial}$	dimensionless deposition velocity due to particle inertia
$V^+_{d,S}$	dimensionless deposition velocity to an S-connector
$V^+_{d,w}$	dimensionless deposition velocity to a vertical wall
$V^+_{d,w,S}$	dimensionless deposition velocity to a wall S-connector
v_g	gravitational settling velocity of a particle, equation (2.37), m s^{-1}
v_p	particle velocity, m s^{-1}
$v_{p,o}$	initial particle velocity, m s^{-1}
$v_{p,crit}$	critical particle impact velocity for determining the likelihood of particle bounce upon impact with a wall, equation (2.119), m s^{-1}
v_{pcy}	particle convective velocity in the wall-normal direction, m s^{-1}
v^+_{pcy}	dimensionless particle convective velocity in the wall-normal direction, $= v_{pcy}/u^*$
v_{px}	particle velocity in the axial direction, m s^{-1}
v^+_{px}	dimensionless particle velocity in the axial direction, $= v_{px}/u^*$
v_{py}	particle velocity normal to the wall, m s^{-1}
v^+_{py}	dimensionless particle velocity normal to the wall, $= v_{py}/u^*$
v'_{py}	fluctuating particle velocity normal to the wall, m s^{-1}
$v_{py,o}$	initial particle velocity towards the wall in a sublayer model, m s^{-1}
$v^+_{py,o}$	dimensionless initial particle velocity towards the wall in a sublayer model, $= v_{py,o}/u^*$

v^+_{py,Δ^+}	dimensionless wall-normal particle velocity at the dimensionless capture distance in a free flight model
V_r	volume of rinsing solution in a fluorometric analysis, mL
v'_{rms}	root-mean-square of the fluctuating wall-normal air velocity, m s^{-1}
v'^+_{rms}	dimensionless root-mean-square of the fluctuating wall-normal air velocity, equation (2.23)
v_t	turbophoretic velocity of a particle, equation (2.50), m s^{-1}
v_{th}	thermophoretic velocity of a particle, equation (2.42), m s^{-1}
v^+_{th}	dimensionless thermophoretic velocity of a particle, equation (C.8)
w	instantaneous spanwise air velocity, m s^{-1}
W	width of a duct with rectangular cross-section, m
$\overline{w}$	time averaged mean spanwise air velocity, m s^{-1}
w'	fluctuating spanwise air velocity, m s^{-1}
W_p	width of a duct panel analyzed for particle deposition, m
x	streamwise distance in a duct, m
x^+	dimensionless streamwise distance in a duct, $= xu^*/\nu$
x_o	a calculated experimental variable in an error analysis
$\overline{x}_o$	average value of a repeatedly measured experimental variable
y	wall-normal distance in a duct, m
y^+	dimensionless wall-normal distance in a duct, equation (2.24)
y_b	thickness of the buffer layer in equation (2.97), m
y_e	equilibrium separation between a particle and a surface, m

y_o^+ dimensionless lower boundary for integration of the mass conservation equation in a turbophoretic model

z spanwise distance in a duct, m

z^+ dimensionless spanwise distance in a duct, $= zu^*/\nu$

z_{lim} initial spanwise particle location in a sublayer model, m

z_{lim}^+ dimensionless initial spanwise particle location in a sublayer model, $= z_{lim}u^*/\nu$

Greek symbols

β indoor loss coefficient, h^{-1}

β_t angle of a transport line measured from the horizontal plane, radians

Δ particle capture distance in free-flight deposition models, m

Δ^+ dimensionless particle capture distance in free-flight deposition models

ε_o permittivity of air, 8.86×10^{-12} C^2 N^{-1} m^{-2}

ϕ angle of a bend in a sampling transport line, radians

ϕ_k roughness parameter in equations (2.75)-(2.77)

η_a aspiration efficiency at a sampling nozzle inlet, equation (B.1)

$\eta_{a,inlet}$ aspiration efficiency at the nozzle inlet of a shrouded nozzle, equation (B.18)

$\eta_{a,shroud}$ aspiration efficiency at the shroud of a shrouded nozzle, equation (B.17)

$\eta_{a,total}$ total aspiration efficiency at a shrouded nozzle, equation (B.19)

η_B transport efficiency through a transport line owing to Brownian diffusion

η_{bend}	transport efficiency through a bend in a transport line
η_g	transport efficiency through a transport line owing to gravitational settling
η_{inlet}	transport efficiency through a short length inside a sampling nozzle inlet owing to particle inertia and anisokinetic sampling
η_S	S-connector deposition fraction, equation (4.10)
η_t	transport efficiency of sampling transport lines
κ	gravitational deposition parameter, equation (B.8)
λ	mean free path of gas molecules, m
λ_o	outdoor air exchange rate for an indoor space, equation (6.24) h^{-1}
λ_s	total air exchange rate for an indoor space, equation (6.23) h^{-1}
λ_x	streamwise length of near-wall low-speed streaks, m
λ_x^+	dimensionless streamwise length of near-wall low-speed streaks, $= \lambda_x u^* / \nu$
λ_y	wall-normal depth of near-wall low-speed streaks, m
λ_y^+	dimensionless wall-normal depth of near-wall low-speed streaks, $= \lambda_y u^* / \nu$
λ_z	spanwise width of near-wall low-speed streaks, m
λ_z^+	dimensionless spanwise width of near-wall low-speed streaks, $= \lambda_z u^* / \nu$
μ	dynamic viscosity of air, kg m^{-1} s^{-1}
ν	kinematic viscosity of air, m^2 s^{-1}
θ	angle of a duct bend, radians
ρ_a	air density, kg m^{-3}
ρ_p	particle density, kg m^{-3}

$\sigma_{d_{mm}}$	standard deviation of the mass-mean particle diameter measurement, equation (D.11), m
σ_k	standard deviation of the roughness height of a surface, m
σ_k^+	dimensionless standard deviation of the roughness height of a surface, $= \sigma_k u^* / \nu$
σ_{x_o}	standard deviation of an experimental variable, equation (D.8)
τ^+	dimensionless particle relaxation time, equation (2.17)
τ_a	air shear stress, equation (2.25), kg m^{-1} s^{-2}
τ_e	time scale of near-wall turbulent air eddies, equation (2.16), s
τ_f	integral timescale of turbulence, equation (2.13), s
τ_p	particle relaxation time, equation (2.13), s
τ_w	shear stress at a duct wall, kg m^{-1} s^{-2}
ξ_a	eddy viscosity of air, m^2 s^{-1}
ξ_p	eddy diffusivity of a particle, m^2 s^{-1}
ζ	diffusional deposition parameter in equation (B.11)

ACKNOWLEDGEMENTS

This work was supported by the Office of Nonprofileration Research and Engineering, Chemical and Biological National Security Program, of the National Nuclear Security Administration, U.S. Department of Energy under Contract No. DE-AC03-76SF00098.

CHAPTER 1

Introduction to Particles and HVAC Systems

1.1 Issues Regarding Particles and HVAC Systems

1.1.1 Particles and human health

Particulate matter in air with aerodynamic diameter less then 10 μm (PM_{10}) is a criteria pollutant regulated by the United States Environmental Protection Agency to protect human health. In the US, the National Ambient Air Quality Standard (NAAQS) for PM_{10} is 150 $\mu g/m^3$ averaged over a 24-hour period and 50 $\mu g/m^3$ averaged over a one-year period. A new standard for particles of aerodynamic diameter less than 2.5 μm ($PM_{2.5}$) has been promulgated. It would limit $PM_{2.5}$ concentrations to 65 $\mu g/m^3$ over a 24-hour average and 15 $\mu g/m^3$ over a yearly average (http://www.epa.gov/airs/criteria.html). Whether there is any perfectly safe level for human exposure to particulate matter is unknown.

By the start of the 1900's, it was widely acknowledged that air pollution was linked to poor human health. Public attention was more keenly focused on the health impacts of air pollution after episodes of very high particulate matter levels in Meuse Valley, Belgium (December, 1930), Donora, Pennsylvania (October, 1948) and London, England (December, 1952) were observed to be associated with increases in human illness and death. More recent epidemiological studies have demonstrated positive correlations between ambient PM_{10} concentrations and human morbidity and mortality (Pope & Dockery, 1999; and Pope, 2000). There is also strong epidemiological evidence

indicating that ambient $PM_{2.5}$ contributes to adverse human health effects (Schwartz *et al.*, 1996). Both acute and chronic health effects have been observed to occur at particle concentrations common in US cities and at levels below the NAAQS. Subpopulations most likely to be at greatest risk from PM_{10} exposure include the elderly, young children, asthmatics and those with preexisting impairment of respiratory and pulmonary systems. While opinions are not unanimous, most epidemiologists and reviewers believe that the body of evidence strongly suggests that exposure to particulate air pollution, and especially $PM_{2.5}$, is an important risk factor for mortality, respiratory symptoms and diseases, and exacerbation of existing pulmonary and cardiovascular diseases.

The link between ambient particulate concentrations and the concentration to which individuals are exposed has not been fully elucidated. Behavioral studies document that people spend most of their time indoors. Particle concentrations and sources indoors are not the same as outdoors. Most of the air breathed by individuals is indoor air, which raises some questions about the epidemiological link between ambient PM_{10} concentrations and human health problems. Personal exposure concentrations have often been observed to be greater than indoor or outdoor concentrations, possibly due to a 'personal cloud' effect. Personal PM_{10} exposure concentrations do not correlate well with ambient PM_{10} levels in cross-sectional studies, but the two measures show a better correlation in longitudinal studies that account for personal variability (Wallace, 2000).

Exposure to airborne particles has significant associated costs. Total annual cost due to death and morbidity has been estimated at $28 billion in the UK (Pearce & Crowards,

1996) and the benefit in health care savings of achieving new the $PM_{2.5}$ standards in the US has been estimated at $32 billion (Ostro & Chestnut, 1998).

1.1.2 HVAC systems and indoor air quality

To understand the contribution of ambient particulate matter to human exposure, it is important to know how the particle size distribution is modified as outdoor air travels into a building. Particle deposition in supply ventilation ducts reduces the indoor concentration of particles of outdoor origin. Heating, ventilating and air conditioning (HVAC) systems also continuously modify indoor particle concentrations as air is recirculated. Air travels from outdoors into a building via three main routes: mechanical ventilation through a ducted HVAC system, natural ventilation through open doors and windows, and infiltration through gaps and cracks in the building envelope. Most intermediate and large commercial buildings are mechanically ventilated and, for these buildings, mechanical ventilation is usually the dominant entry path of outdoor air to the indoor environment. Consequently, particle deposition in HVAC systems influences particle concentrations within buildings.

HVAC systems play a central role in maintaining indoor air quality in large buildings and their improper functioning may lead to a variety of problems. Numerous studies have found higher rates of occupant complaints about indoor air quality and health symptoms in mechanically ventilated buildings compared to those that are naturally ventilated (Wargocki *et al.*, 2000). A NIOSH survey found that HVAC deficiencies accounted for more than half of the indoor air quality problems in nonindustrial buildings (Crandall &

Sieber, 1996). Ventilation ducts can act as sinks, and in some cases as sources, for a variety of pollutants including particulate matter, microorganisms and volatile organic compounds (VOCs). Particles may deposit to and resuspend from duct surfaces. Particle deposits sorb and desorb VOCs in the passing air stream. Bacteria and fungi deposit on HVAC surfaces and grow if sufficient water is present. Such growth produces microbial VOCs (MVOCs) and may amplify the concentration of bioaerosols in the air stream. Chemical interactions can occur between pollutants and HVAC surfaces, and particle deposits may alter the nature of these surface interactions (Morrison *et al.*, 1998). For example, particles of biological origin often contain unsaturated fatty acids. If these deposit in ducts, they will be exposed to ozone, which can oxidize the unsaturated acids, producing aldehydes that can be released into the air stream (Pasanen *et al.*, 2000). Deposited materials may also become nutrient sources for microorganisms that release MVOCs. These sorts of transformations might be of great importance in overall HVAC hygiene. In addition to these pollutant interactions, ventilation duct materials like sealants, fibrous insulation and residual manufacturing oils may directly pollute the ventilation air (Batterman & Burge, 1995). In summary, particle deposition in HVAC systems alters the exposure of building occupants to particles of outdoor origin and is linked to a host of indoor air quality concerns.

1.1.3 Chemical and biological agents

The accidental or intentional airborne release of aerosolized chemical or biological agents within or near a building may lead to exposure of the building occupants to these harmful substances. Agents released outdoors may be drawn into a building by the HVAC

system; those released within a building may be spread to other parts of the building by the HVAC system. In either case, deposition in the supply and return ductwork may significantly influence exposures. An understanding of particle deposition in HVAC ducts can also help in planning responses in terms of HVAC system operation in the event of a detected release. Deposition may also be important for post-release remediation since the HVAC system may require decontamination to minimize exposure owing to the resuspension of contaminants.

1.2 Types of HVAC Systems

All equipment that helps to provide and condition indoor air constitutes HVAC systems. This includes louvers, fans, air cleaners, heating and cooling equipment, ducts, humidifiers and dehumidifiers, terminal devices and control equipment. Such systems are widely variable in terms of complexity, quality, operation and maintenance. These systems serve the multiple purposes of providing fresh air to the indoor space, controlling indoor air temperature and controlling indoor pollutants by ventilation. Standards for acceptable building ventilation and thermal conditions have been established and are maintained by the American Society of Heating, Refrigeration and Air-Conditioning Engineers, as are guidelines for HVAC commissioning and maintenance (ASHRAE, 1989a, 1989b, 1992).

One may broadly divide HVAC systems into small unitary systems and large central units. Unitary systems provide air to a single building zone, while central units are capable of delivering air to multiple zones with different heating and cooling

requirements. Interior portions of large buildings filled with people, lighting and equipment often require cooling even during the coldest months of the year. Perimeter portions of buildings that share walls with the outdoors typically require more flexible temperature control because they are more directly influenced by outdoor temperature, wind and direct sunlight.

Unitary systems handle a small flow of air (0.2-2 m^3/s), serve small floor areas (~150 m^2) and have a relatively low initial cost. Multiple unitary systems, each with an independent fan, thermal control and ductwork, may be used to ventilate larger spaces. On average, unitary systems have shorter duct runs than central units because of their decentralized locations. Ducts associated with these systems usually have a hydraulic diameter less than 70 cm and tend to be constructed of galvanized steel, duct board and flexible duct. Unitary systems are often operated intermittently, under thermostatic control, cycling on and off several times per hour when the building is occupied. Ventilation of commercial retail strip malls, offices, restaurants and professional buildings are the most common applications of these systems. Such buildings are estimated to make up about half of the of the non-residential building stock in the United States (Delp *et al.*, 1997).

Central HVAC units serve large building areas (greater than 1000 m^2) and handle large airflow rates (5-50 m^3/s). Central systems are designed to operate as either constant air volume (CAV) or variable air volume (VAV) systems. Constant air volume systems provide a time invariant flow rate of air to each space, and room temperature is controlled by means of heating or cooling the supplied air. Variable air volume systems achieve

temperature control by regulating the amount of cooled air provided to each space. Most central systems feature continuous operation and have galvanized steel ducts of rectangular cross section to distribute the air. Fiberglass insulation is commonly used on the interior surface of large ducts near fans to absorb acoustic vibrations and to provide thermal insulation. The plenums and largest ducts in these systems may have a hydraulic diameter of several meters and the smallest ducts, those leading to the room supply registers, have a typical hydraulic diameter of 0.15-0.3 m. Duct air speeds range from a maximum of 10-15 m/s near the fans to a minimum of 1-2 m/s at supply registers. Central systems are sometimes turned off overnight when a building is unoccupied and then operated at higher than normal flow rates in the morning to flush accumulated pollutants from the building before it is reoccupied. Central systems are common in mid-sized to large office buildings and retail centers, as well as university buildings, theaters and multiple use buildings. Often, several large central systems are required to ventilate very large buildings.

1.3 HVAC System Components and Particle Deposition

Particle deposition in HVAC systems reduces airborne concentrations within buildings but may lead to other indoor air quality concerns. Deposition rates from turbulent flows are influenced by a variety of factors including particle size, degree of air turbulence and the roughness and orientation of the deposition surface. Because of the complexity of flows and variety of surfaces in even the simplest ventilation system, particle deposition rates are likely to vary widely along the length of a single duct run.

Figure 1.1 shows a typical air flow configuration in an HVAC mechanical room. Outside air is brought through louvers into the supply plenum and mixed with a fraction of the return air from the building. This air mixture is filtered, thermally conditioned, and then drawn into a supply fan that distributes the air through a branched duct system to various parts of the building. Return air intakes are located throughout the building. These intakes direct air through return ducts or plenum spaces back to the HVAC mechanical room where a fraction is recirculated and the rest is exhausted outside the building.

1.3.1 Outside air louvers, filters, cooling and heating

The fraction of outside air in the supply air is controlled by louvers at the air intake and is commonly varied by means of a control system that depends on the outdoor air temperature. Supply air may consist of only outside air if it is at or near the desired temperature. This operation is termed the 'economizer mode' due to the energy savings realized by reducing the need to heat or cool ventilation air. When the outside air temperature deviates from the desired supply temperature, outside air louvers partially close and a larger fraction of return air is directed to the supply. Ventilation standards require that a minimum amount of outside air be brought into any occupied building (ASHRAE, 1989a). Because indoor and outdoor air usually carry different types and concentrations of particulate matter, air louvers influence particle deposition in the rest of the HVAC system by altering the type and amounts of air contaminants introduced into the system.

Filtration in HVAC systems has traditionally been designed to protect mechanical equipment and not human health. Many common HVAC filters are inefficient for particle sizes less than 10 μm (Hanley *et al.*, 1994). Bypass of air around filters has been observed, but rarely quantified. It has been estimated that 15% of the provided air does not pass through filters in a typical building (Ottney, 1993). Such filter bypass flow, which could transmit particles of all sizes, is expected to increase as the pressure drop across the filter increases from usage. Return air ducts usually carry unfiltered indoor air. Thus, a broad distribution of particle sizes is expected to be present in both supply and return ducts.

Heating or cooling of supply air is usually accomplished by passing air through a fin-and-tube type heat exchanger. Such heat exchangers are potentially important sites for particle deposition (Siegel, 2002). They are designed to promote efficient heat exchange, and mass transfer tends to be high in systems with high heat transfer. Fouling induced by particle deposition on heat exchanger surfaces can decrease the effectiveness of heat transfer, degrading temperature control and increasing operating costs through the need for a lower temperature coolant (or warmer heating fluid). In addition, when the supply air is cooled below its dew point, water condenses from the air stream. Condensed water can reduce the size of airflow channels in the heat exchanger and alter particle deposition. If not properly drained, condensed water and the wetted surfaces in the HVAC system can become sites for microbial growth. Subsequent release of bioaerosols, such as mold spores, can constitute another source of particles in the ducts.

1.3.2 Supply fan and ventilation ducts

After being heated or cooled, air is distributed through the supply ducts by the supply fan. Particles can deposit on the fan housing and fan blades and, in the case of severe fouling, impede its performance. As particles deposit on filters, heat exchangers and ducts, the resistance to airflow through these systems may increase. For a constant air supply rate, increasing the airflow resistance increases the pressure drop along the duct, causing the fan to consume more energy; the magnitude of this increased energy consumption depends on the specific performance conditions of the fan.

Increasing the flow resistance can also reduce the rate at which air is delivered to the indoor space. Such a reduction in flow rate commonly leads to decreased fan energy use (Parker *et al.*, 1997). Particle deposits that alter the airflow and pressure drop in a duct system will also influence the duct leakage rate and the overall rate of energy use by the HVAC system through the rate at which energy is lost by conduction through duct walls. Thus, the effect of particle deposits on overall HVAC system energy consumption is uncertain in both sign and magnitude and is likely to be HVAC system dependent.

Ventilation duct systems usually consist of a very large duct after the supply fan that branches several times into successively smaller diameter ducts to deliver air to a variety of locations within the building. Duct branches, bends and reducing sections are required to achieve proper air distribution and maintain air velocities. Most ducts are fabricated from sheet metal, but the smallest ducts that lead to supply registers are often made of flexible aluminum or Mylar to allow for easier installation. A length of duct is made up

of several short sections connected in series by various fittings. These fittings can serve as sites for local particle deposition. Air may leak through the joints between duct sections and through seams resulting from duct fabrication. Studies of duct leakage in California buildings have found average leakage rates in supply ducts as a percentage of the system flow rate at the inlet to be 25% in light commercial buildings (Levinson *et al.*, 1997) and 10-20% in large commercial buildings (Fisk *et al.*, 1999). Particles will exit ducts with leakage air in positively pressured (supply) ducts and enter ducts through leaks in negatively pressured (return) ducts.

Ideally, duct surfaces should be kept clean and dry; however, even new ducts may be soiled from storage prior to installation and debris from the building's construction phase. In addition, new steel ducts have been identified as sources of VOCs in indoor air from residual oils left from the original machining and fabrication (Pasanen *et al.*, 1995).

Airflow through ventilation ducts is turbulent, and particles can deposit on ducts owing to interactions with this turbulence, by gravitational settling, and by other mechanisms. With usage, ducts have been observed to accumulate particulate deposits on their interior surfaces. Wallin (1994) observed that such deposits could reduce the amount of air flowing through ducts, especially small diameter ducts, and thus could degrade the performance of the ventilation system. Previous measurements of the density of dust deposits on the floors of ventilation ducts in office buildings and schools and the inferred dust accumulation rates are presented in Table 1.1. General consistency among studies is observed for the mean and range of both the deposit density and accumulation rates,

despite variability in the methods used and in the building location and age. The size distributions of such deposited dusts have not been measured, but the total mass of the deposits in all cited studies is likely to have been dominated by very large particles, debris and fibers. Measurement of deposit density has been shown to vary depending on the method used for quantification (Holopainen *et al.*, 1999).

Duct cleaning is an increasingly common practice in both residential and commercial buildings. It can help maintain proper duct flow rates and provide a potential preventive and corrective benefit for indoor air quality. Duct cleaning businesses in the US are certified by the National Air Duct Cleaners Association (NADCA), which has developed standards and methods for duct cleaning and cleanliness measurement. The maximum deposit density for a duct to be considered clean is 0.1 g/m^2 based on a vacuum-and-filter-cassette method (NADCA, 1992).

1.3.3. Duct components and terminal devices

Ventilation systems include duct components that locally modify airflow and offer surface area for particle deposition. Fin-and-tube heating and cooling coils are often installed at the end of the ducted distribution system to enable local thermostatic control of air temperature. Turning vanes, dampers, variable air volume boxes and registers help direct the air stream, control flow rates and distribute air properly. The presence of such components and devices can alter the fate of particles that enter HVAC systems.

1.4 Overview of the Research

The main objectives of this research were to determine particle deposition rates in ventilation ducts and to determine the best methods for predicting these rates. Knowledge of particle deposition rates in ventilation ducts is useful for modeling exposures to particles within buildings and for more completely understanding particle fates. To meet these objectives, laboratory experiments measuring particle deposition rates were conducted in galvanized steel and insulated ducts for a variety of particle sizes and air speeds. For both steel and insulated ducts, deposition rates were measured in ducts where the turbulent flow profile was fully developed and in ducts where the turbulent flow profile was developing, immediately after an inlet and immediately after a bend. Deposition within duct bends and to duct connectors at joints between duct sections was also measured. Published particle deposition models were compared to the deposition rates measured in the experiments. Because mechanistic models systematically and substantially underpredict deposition rates, an empirical model was developed for simulating deposition to various locations in ventilation ducts based on the experimental results. The empirical model was applied to predict particle losses from air traveling through several supply and return duct runs. Factors that dominate particle deposition in ducts were explored with the empirical model.

1.5 Outline of the Dissertation Contents

A significant body of literature exists on the topic of particle deposition from turbulent flow. Chapter 2 provides an extensive review of both experimental and theoretical investigations into the topic and considers the relevance of the published literature to the

case of deposition in ventilation systems. Chapter 2 is long. If the reader is interested in learning about the new experimental and modeling work, they are encouraged to read only sections 2.1 and 2.2 to become familiar with parameters and terminology that are used throughout the dissertation and then to skip to Chapter 3.

To better understand particle behavior in ventilation ducts, two sets of laboratory experiments were conducted, one in a galvanized steel duct system and one in an internally insulated duct system. In both sets of experiments, deposition rates of fluorescent monodisperse particles to duct surfaces were directly measured at several locations along the experimental duct system. Ducts where deposition was measured were horizontal and had a square cross section measuring 15.2 cm on a side. Deposition rates were measured in straight ducts with a fully developed turbulent flow profile, in straight ducts with a developing turbulent flow profile, in 90° duct bends and to duct connectors at duct junctions. In straight ducts, deposition was measured separately to the duct floor, wall and ceiling. Deposition at duct connectors was only measured in the steel system and duct bends in the insulated system were not internally insulated. In the steel system, experiments were performed with 1, 3, 5, 9 and 16 μm diameter particles at nominal air speeds of 2.2, 5.3 and 9.0 m/s. In the insulated system, experiments with nominal particle sizes of 1, 3, 5, 8 and 13 μm were conducted at nominal air speeds of 2.2, 5.3 and 8.8 m/s. In Chapter 3, the experimental apparatus and methods for studying deposition in both duct systems are described in detail. Results are presented for measurements made in straight ducts with fully developed turbulence in both the steel and insulated systems. The influence of particle size, air speed, surface orientation and

surface type on measured deposition rates is discussed. In Chapter 4, results of measurements made in the straight duct sections with developing turbulence, in 90° duct bends and at duct connectors are presented. Variations in deposition rate with location within the duct system for a given particle size and air speed are discussed.

In Chapter 5, the experimental results are compared to deposition predictions from published models. Factors that could explain differences between measured deposition rates and model predictions are explored. Empirical equations for predicting particle deposition in ventilation ducts based on the experimental results are developed. In Chapter 6, these empirical equations are applied to several supply and return duct runs whose characteristics are based on sampling real buildings to determine the range of expected particle losses expected when air travels through ventilation ducts. These empirical equations are coupled with indoor particle deposition model and information about filter efficiencies to predict the ultimate fates of particles drawn into an archetypal mechanically ventilated building at its outdoor air intake. The ultimate fates of particles released indoors are also considered for cases with different duct losses and HVAC filtration status. The implications of this modeling effort to HVAC operation and maintenance and to human exposure to particulate material are discussed.

A summary of the research findings is given in Chapter 7 and opportunities for further research in this field are discussed. Appendix A describes methods used to estimate the surface roughness of the experimental ducts used in these studies. Appendix B presents data regarding the performance of isokinetic nozzles and a specially designed shrouded

anisokinetic nozzle when sampling from ventilation duct flows. Temperature, pressure drop and relative humidity measurements made during experiments are presented in Appendix C, and thermophoretic effects in the experiments are discussed. Methods for calculating measurement variability and experimental uncertainty are documented in Appendix D.

Table 1.1 Measured densities of dust on duct floors in office buildings and schools.

Investigator	Number of samples	Mean (range) ($g\ m^{-2}$)	Accumulation rate ($g\ m^{-2}y^{-1}$)
Valbjørn *et al.* (1990)	NR	6.8 (1.1-51)	0.7
Laatikainen *et al.* (1991)	27	18 (3.6-140)	2.3 (0.5-13)
Pasanen *et al.* (1992)	44	11 (1.2-58)	3.5 (1.2-8.3)
Pasanen (1994)	44	13 (1.2-160)	1.0
Fransson (1996)	15	4.0 (1.7-12)	0.2-0.3
Ishikawa *et al.* (1996)	6	10 (2.0-19)	NR
Björkroth (1999)	15	4.1 (0.04-11)	NR
Collet *et al.* (1999)	21	12 (0.1-59)	NR
Luoma *et al.* (1999)	17	6.5 (0.7-47)	0.6 (0.1-5.9)

NR = Not reported

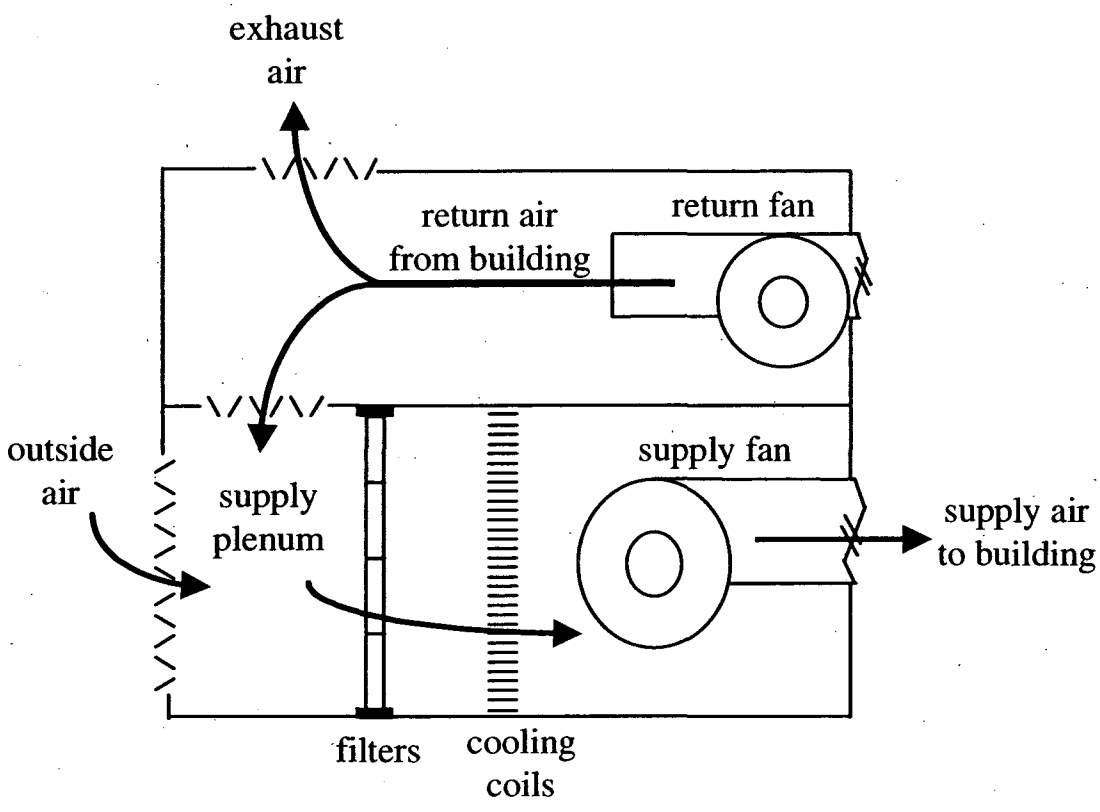

Figure 1.1 Schematic diagram of airflow through the mechanical room for a typical HVAC system.

CHAPTER 2

Literature Review of Particle Deposition from Turbulent Flows

2.0 Abstract

This chapter reviews published experimental and theoretical investigations of particle deposition from turbulent flows and considers the applicability of this body of work to the specific case of particle deposition from flows in the ducts of heating, ventilating and air conditioning (HVAC) systems. Particle deposition can detrimentally affect the performance of HVAC systems and it can influence the exposure of building occupants to a variety of air pollutants.

Following a brief introduction (section 2.1) and the definition of key parameters (section 2.2), section 2.3 reviews published experimental investigations of particle deposition rates from turbulent flows and considers the ramifications of the experimental evidence with respect to HVAC ducts. Section 2.4 considers the structure of turbulent airflows in ventilation ducts with a particular emphasis on turbulence investigations that have been used as a basis for particle deposition models. Published literature on predicting particle deposition rates from turbulent flows is reviewed in section 2.5.

A large quantity of experimental data regarding particle deposition from turbulent flows has been collected using a range of techniques of varying quality. Nearly all of these data have been collected from straight tubes or ducts with a fully developed turbulent flow

profile and the data are widely scattered. Most of the data of acceptable quality have been collected from tubes or ducts with hydraulic diameters much smaller than ducts in typical HVAC systems. Particle deposition from turbulent flow with a developing flow profile has not been systematically investigated and only two investigations of deposition from turbulent flow through bends have been published. Developing turbulent flow profiles and bends are common in HVAC ducts.

Owing to the large number of investigations into particle deposition from turbulent flow, much is known; however, the direct applicability to the case of particles in HVAC ducts is limited. Particle size, turbulence intensity and the roughness and orientation (horizontal or vertical) of the deposition surface are parameters that control deposition rates and all of these factors are likely to be pertinent in HVAC ducts. Particle diameters of concern in HVAC ducts range from about 0.003 to 30 μm and deposition rates are known to vary strongly in this range. Friction velocities in HVAC ducts are likely to be in the range 0.1-1 m/s and variations of turbulence intensities in this range are likely to influence deposition rates. Both microscale surface roughness (from less than 1 micron up to hundreds of microns) and macroscale roughness (about 1 mm and larger) have been demonstrated to enhance deposition relative to the case of a smooth deposition surface. Microscale roughness intrinsic to the duct material, or due to corrosion or previous deposition of particles, and macroscale roughness from thermal insulation, joints between duct sections and debris are all potentially important in HVAC ducts. The floors of horizontal ducts are likely to experience higher rates of deposition than vertical duct walls or horizontal duct ceilings owing to the influence of gravity on large particles.

With respect to deposition in HVAC ducts, the overall experimental data set is most lacking in information regarding the influence of developing turbulent flow profiles, microscale roughness and duct bends on particle deposition.

Particle deposition from turbulent flow depends on the nature of the turbulent flow field. Interactions between particles and air turbulence frequently determine deposition rates. Properties of turbulent flow that have been incorporated into particle deposition models include the fluctuating velocity component normal to the wall and the eddy viscosity. Coherent structures in near-wall turbulence such as low-speed axial streaks, near-wall streamwise vortices, bursts and downsweeps have been theorized to be important for the deposition of certain sized particles. A representative fraction of experiments and numerical simulations investigating these turbulent properties and structures are described. Turbulence near both smooth and rough walls is addressed; however, investigations into turbulence near smooth walls are more substantial and consistent in their findings. These descriptions of turbulent flow provide a foundation for understanding particle deposition models and the results of numerical simulations of particle deposition from turbulent flows.

Four broad methods of predicting particle deposition rates are found in the literature: empirical equations, Eulerian models, sublayer models and Lagrangian simulations. These methods usually require information about the particle size and density, as well as the air speed and dimensions of the duct containing the flow. Deposition rates are most

commonly reported in the form of the dimensionless deposition velocity, V_d^+, versus the dimensionless relaxation time, τ^+, a measure of particle inertia.

Empirical equations are simple best fits to experimental data and are easy to apply. They can be combined and applied to a broad range of particle sizes and they can be applied to both vertical and horizontal deposition surfaces. They are of limited value for rough deposition surfaces because of sparse experimental data. Empirical equations are the only predictive method that has been developed for deposition from turbulent flow in bends. While offering little fundamental understanding, certain empirical equations can be applied to aspects of particle deposition in HVAC ducts with reasonable confidence.

Eulerian models include gradient diffusion models, free-flight models and turbophoretic models, all of which are quickly solvable with current computing power. Gradient diffusion models, when applied with reasonable assumptions, are unlikely to perform well over the full range of particle sizes for deposition in HVAC ducts. Some free-flight models achieve success in predicting particle deposition rates through a combination of theory and empiricism. Free-flight models as presented in the literature are solely applicable to vertical deposition surfaces, though they could be adapted to horizontal surfaces. Some free-flight models have achieved moderate success predicting deposition to rough surfaces by a very simple method. Recommended free-flight models may yield reasonable predictions in HVAC ducts, but there is little advantage to these models over the recommended empirical equations. Turbophoretic models are a significant improvement over gradient diffusion and free-flight models and are the models that are

most appropriate for application to HVAC ducts. These models are applicable to vertical and horizontal surfaces over the entire range of particle sizes. Turbophoretic models are able to account for a broader range of particle transport mechanisms than other Eulerian models. They achieve good agreement with the trends and magnitudes of experimental data with only a small amount of empiricism. The same simple method of accounting for surface roughness is used in turbophoretic models as in free-flight models.

Sublayer models are semi-Lagrangian models that can be solved rapidly with current computing power to give reasonable predictions of particle deposition to vertical and horizontal surfaces. To account for surface roughness, some sublayer models apply a similar method as the simple method used in free-flight models. Some of these models achieve reasonable agreement with the magnitudes of experimentally observed deposition rates and recommended sublayer models may be applied to the case of deposition in HVAC ducts with reasonable expectations about their performance.

Lagrangian simulations of particle deposition have included those conducted in simple modeled turbulent flows to highly detailed flows generated by large eddy simulation (LES) and direct numerical simulation (DNS). Lagrangian simulations are often considered 'numerical experiments' because the results are for discrete particle sizes and specific to the numerically simulated flow conditions, much like physical experiments. The results of Lagrangian simulations are valuable for informing expectations about deposition in HVAC ducts; however, the high level of computational power required by these simulations makes them unsuitable at present for predicting deposition rates under

the variety of conditions found in buildings. These simulations provide vast amounts of information on the forces acting on particles, particle velocities and particle deposition rates and offer insight into the factors that contribute to experimental uncertainty. Results from Lagrangian simulations of particle deposition generally agree with the trends and magnitudes observed in experiments. The single reported Lagrangian simulation to consider deposition surface roughness resulted in the same trends as observed in experiments and in Eulerian models using similar methods.

Turbophoretic models are the best means of predicting particle deposition rates in HVAC ducts. They offer accuracy similar to other models; however, they offer greater versatility in application and are based on physically realistic assumptions. Turbophoretic models have two main limitations when being applied to HVAC ducts that are common to other models as well. First, the models assume a fully developed turbulent flow profile which not appropriate throughout HVAC systems. Second, the method of accounting for surface roughness is somewhat simplistic and corroborated by only a single data set. While models do capture the broad trends seen in experiments, they can deviate markedly from observations. In general, existing modeling approaches and empirical data are not sufficient to reliably predict particle deposition in HVAC ducts. Overall, obtaining accurate input information for predicting particle deposition rates is a concern regardless of the type of predictive method used.

2.1 Introduction

There is widespread interest in the deposition of particles from turbulent airflows due to its applicability in such diverse fields as aerosol sampling, inhalation toxicology, atmospheric transport and fate of pollutants, air cleaning and semiconductor microcontamination. The focus of this dissertation is on one important application of particle deposition from turbulent airflows, evaluating particle losses in ventilation ducts. Numerous reviews of turbulent particle deposition experiments and theories exist (Kneen & Strauss, 1969; Owen, 1969; Sehmel, 1980; Papavergos & Hedley, 1984); however, several advances have been made since the most recent summary. Investigations into this topic in the literature have utilized three main methods: physical experiments, Eulerian modeling, and Lagrangian simulations.

Section 2.2 defines several parameters useful for discussing particle deposition from turbulent flows. Section 2.3 reviews published experimental investigations of particle deposition rates from turbulent flows. Studies conducted in straight tubes and ducts are discussed, then experiments performed in tube bends are considered. The relevance of the overall data set to HVAC ducts is discussed in the last part of this section. Turbulent duct flows are discussed in section 2.4. Empirical equations, Eulerian models and Lagrangian simulations predicting particle deposition rates from turbulent flows are discussed in section 2.5.

2.2 Definition of Parameters

The deposition velocity, V_d, of a particle to a duct surface is defined as

$$V_d = \frac{J}{C_{ave}} \tag{2.1}$$

where J is the time-averaged particle flux to the surface (mass or number per area per time) and C_{ave} is the time-averaged airborne particle concentration in the duct (mass or number per volume), usually evaluated at the centerline of the flow. Among other factors, the deposition velocity is a function of particle size.

Penetration through a duct is defined by

$$P_{duct} = \frac{C_{out}}{C_{in}} \tag{2.2}$$

where C_{out} and C_{in} are the flow-weighted average particle concentrations at the outlet and inlet of the duct, respectively. If the deposition velocity is known for a given particle size, and deposition to the duct interior is uniform (or the deposition velocity is interpreted as the area-weighted average over all surfaces), then the penetration of that particle size through a straight duct section is related to the deposition velocity as follows:

$$P_{duct} = \exp\left(\frac{-4LV_d}{D_h U_{ave}}\right) \tag{2.3}$$

where L is the duct length, U_{ave} is the average air speed and D_h is the hydraulic diameter of the duct defined as

$$D_h = \frac{4A}{P} \tag{2.4}$$

Here, A is the cross sectional area of the duct and P is the perimeter of a section through the duct, normal to the direction of flow.

Turbulent duct flows can be characterized in part by their turbulence intensity as measured by the friction velocity, u^*, which is defined as

$$u^* = \sqrt{\tau_w / \rho_a} \tag{2.5}$$

where τ_w is the shear stress at the duct wall and ρ_a is the air density. Assuming that the wall shear stress is uniform inside the duct, a balance of pressure forces and shear stress forces in the duct leads to this relationship:

$$u^* = U_{ave}\sqrt{f/2} \tag{2.6}$$

where f is the Fanning friction factor. For a fully developed turbulent flow, f is given by

$$f = \frac{\Delta P}{\Delta L}\frac{D_h}{2\rho_a U_{ave}^2} \tag{2.7}$$

where $\Delta P/\Delta L$ the pressure drop per unit duct length. The friction velocity may be determined experimentally for a known air velocity and hydraulic duct diameter by means of measuring the pressure drop and by applying equations (2.6) and (2.7). Alternatively, empirical expressions may be used to calculate the friction factor. For a smooth-walled flow, the Blasius equation or the von Karman correlation may be used to estimate the friction factor.

Blasius: $f = 0.0791 \cdot \mathrm{Re}^{-0.25}$ $(2800 < \mathrm{Re} < 10^5)$ (2.8)

von Karman: $1/\sqrt{f} = 4.0\log\left(\mathrm{Re}\sqrt{f}\right) - 0.4$ $(2800 < \mathrm{Re} < 3.2\times10^6)$ (2.9)

Here, Re is the Reynolds number of the duct flow calculated by

$$\mathrm{Re} = \frac{D_h U_{ave}}{\nu} \tag{2.10}$$

where ν is the kinematic viscosity of the air. For turbulent flow past smooth walls, the friction at the surface results from viscous drag. For rough walls, form drag on the roughness elements may be an important contributor to the total friction. If the mean microscale roughness height is k, the dimensionless roughness height, k^+, is defined by

$$k^+ = \frac{ku^*}{\nu} \tag{2.11}$$

Schlichting (1979) defined three regimes of flow resistance for turbulent flow in rough pipes:

hydraulically smooth regime:	$k^+ \leq 5$
transition regime:	$5 \leq k^+ \leq 70$
completely rough regime:	$k^+ > 70$

In the hydraulically smooth regime, roughness elements are submerged in the nearly laminar layer near the wall and roughness does not significantly influence the friction of the flow. In this case, the friction factor depends only on viscosity (through Re) as seen in equations (2.8) and (2.9). As k^+ grows to greater than 5, a portion of the roughness elements protrude into more turbulent flow and form drag on these elements increases the flow resistance relative to a smooth wall. In this case, the friction factor is observed to depend on both the air viscosity and on the relative roughness height, k/D_H. In the completely rough regime, roughness elements protrude far into the turbulent flow and dominate the flow resistance so that the friction factor no longer depends significantly on

viscosity, rather it depends on the relative roughness height alone. Equations for computing the friction factor of flows through ducts with rough walls are provided in Table 2.1. These equations strictly hold only for closely-packed, sand-grain type roughness elements. For differently shaped or more widely spaced roughness, an equivalent sand-grain roughness can be defined, but it must be determined experimentally. For very large roughness elements like grasses, friction velocities are usually determined based on measurements of the velocity profile far from the wall, in the logarithmically varying region of the flow.

The friction velocity in a smooth-walled duct is typically about 5% of the average velocity; in rough walled ducts, the friction velocity is a slightly greater proportion of the mean flow. The range of friction velocities expected in ventilation ducts is about 0.1-1.0 m/s. In terms of flow resistance, most clean steel ducts are expected to be in the hydraulically smooth regime. Ducts with roughness caused by deposits, corrosion or insulation are likely to be either in the hydraulically smooth regime or the transition regime, although the completely rough regime may be approached in some cases with large roughness elements and high friction velocities. The equivalent hydraulic roughness of fiberglass duct insulation has been estimated to be 3.0 mm, meaning most flows through insulated ducts are expected to be in the transitional or completely rough regime (ASHRAE, 1995).

The dimensionless particle deposition velocity is defined by normalizing the deposition velocity with the friction velocity:

$$V_d^+ = \frac{V_d}{u^*} = \frac{J}{C_{ave}u^*} \tag{2.12}$$

In studies of particle deposition from turbulent flow, it is common to investigate the relationship between the dimensionless particle deposition velocity and the dimensionless particle relaxation time. The dimensional relaxation time of a particle, τ_p, is the characteristic time for a particle velocity to respond to a change in air velocity. It may be calculated for spherical particles in the Stokes flow regime as follows:

$$\tau_p = \frac{C_c \rho_p d_p^2}{18\mu} \tag{2.13}$$

where C_c is the Cunningham slip correction factor, ρ_p is the particle density, d_p is the particle diameter and μ is the dynamic viscosity of air. The slip correction factor can be estimated by the expression

$$C_c = 1 + \mathrm{Kn}\left[1.257 + 0.4\exp\left(-\frac{1.1}{\mathrm{Kn}}\right)\right] \tag{2.14}$$

where the Knudsen number, Kn, is

$$\mathrm{Kn} = \frac{2\lambda}{d_p} \tag{2.15}$$

and λ is the mean free path of gas molecules, equal to 0.065 μm at a temperature of 25 °C and atmospheric pressure.

Turbulent eddies in duct flows display a wide range of length scales, with the largest eddies limited by the duct dimensions and the smallest limited by the dissipative action of molecular viscosity. Smaller eddies tend to be shorter lived while larger eddies persist

for a longer time before disappearing. The smallest eddies in a flow are those near the walls and their average lifetime may be estimated by

$$\tau_e = \nu / u^{*2} \tag{2.16}$$

Because deposition happens at walls, particle interactions with near-wall eddies are potentially important in determining deposition rates. A dimensionless particle relaxation time, τ^+, can be defined by comparing the particle relaxation time to the timescale associated with the near-wall turbulent eddies

$$\tau^+ = \frac{\tau_p}{\tau_e} = \frac{C_c \rho_p d_p^2 u^{*2}}{18 \mu \nu} \tag{2.17}$$

In general, particle motion is only affected by eddies with durations at least as long (in a magnitude sense) as the particle relaxation time. Particles do not have sufficient time to respond to the shorter lived eddies. A value of $\tau^+ < 0.1$, indicates that a particle is able to fully respond to even the smallest turbulent eddies. In this case, the particle is expected to closely follow all turbulent air fluctuations. A particle with $\tau^+ > 10$ will be relatively unaffected by the small near-wall eddies and will only be significantly affected by larger eddies further from the wall. The motion of particles with relaxation times close to the lifetime of the near-wall eddies, $0.1 < \tau^+ < 10$, is expected to be heavily influenced by these eddies, with instantaneous particle velocities equilibrating with, but then disengaging from, the local air velocity. Consequently, such particles frequently shoot ahead of or lag behind the near-wall eddies.

Considering particles in the diameter range 0.003-30 μm, expected values of τ^+ span from about 10^{-6} for a 0.003 μm particle in a flow with low turbulence, up to about 100 for a 30 μm particle in a highly turbulent flow.

For particle deposition to smooth, vertical walls, the dimensionless deposition velocity is expected to be a nearly unique function of the dimensionless relaxation time. In the case of rough deposition surfaces, the dimensionless deposition velocity can also be strongly influenced by the shape and magnitude of the roughness elements. Electrical and thermal forces can also significantly influence the dimensionless deposition velocity, as can gravitational forces in the case of a non-vertical deposition surface.

2.3 Review of Experimental Data

2.3.1 Straight tubes and ducts

Many experimental investigations have been conducted that pertain to particle deposition from turbulent airflow through ducts. Major factors that have been observed experimentally to influence depositions rates include particle size, degree of air turbulence, surface orientation with respect to gravity and roughness of the deposition surface. The best experimental investigations are those that employ a monodisperse aerosol, have a well characterized air flow and deposition surface, and directly measure deposited particles at surfaces. These conditions are satisfied by only a small fraction of the studies. This review is limited to papers reported in English. It is further limited to investigations in which sufficient information was reported so that deposition rates could be associated with specific particle sizes for a given deposition surface.

Experimentally measured particle deposition velocities from turbulent flows have historically been presented as plots of V_d^+ versus τ^+. Figure 2.1 is such a plot showing most of the published data for particles depositing from flow through vertically oriented tubes of small diameter. This figure illustrates the importance of particle size, as measured by τ^+, in determining particle deposition. The data of Shimada *et al.* (1993) for deposition from a horizontal tube is included so as to extend the lower range of τ^+ and to illustrate the trends in deposition as τ^+ becomes very small. (The effect of gravity on deposition from this horizontal flow is expected to be negligible owing to the very small particle sizes, d_p = 0.01-0.04 μm, used in these experiments.)

Following the terminology of Wood (1981b), the data in Figure 2.1 are divided into three regimes: the *diffusion* regime, the *diffusion-impaction* regime, and the *inertia-moderated* regime. Although the data are broadly scattered in this plot, trends are still clearly visible. Very small particles, those in the diffusion regime, have small inertia and follow all turbulent eddies. Their transport to surfaces depends mostly on Brownian and turbulent diffusion. In a typical HVAC duct flow, turbulent diffusion is much stronger than Brownian diffusion, except extremely close to the duct wall where turbulent fluctuations decay to zero. The dimensionless deposition velocity decreases as τ^+ increases in the diffusion regime because of the decrease in Brownian diffusivity as particle size increases. In the diffusion-impaction regime, particles follow turbulent air fluctuations less faithfully and may shoot ahead of or lag behind eddies near the wall. Hence, through this interaction between particle inertia and turbulent eddies, particles

may deposit without relying on Brownian diffusion to make the final step to the surface, and V_d^+ increases substantially, even for relatively small increases in τ^+. For the largest particles, those in the inertia-moderated regime, the dimensionless deposition velocity is observed to level off and become nearly independent of τ^+. In this case, particles are too large to respond to the rapid fluctuations of near-wall eddies and transport to the wall by turbulent diffusion is weak. These particles reach the wall through momentum imparted by large eddies in the core of the turbulent flow.

The wide scatter among the data in Figure 2.1 is in part a testament to the difficulty of obtaining accurate experimental data in even the simplest turbulent flow. In the diffusion-impaction regime particle deposition scales in rough proportion to d_p^4. Thus, small errors in particle sizing or small amounts of polydispersity in the aerosol can lead to large errors in properly interpreting the experimental results. In addition, the character of the deposition surface and its roughness, even on the scale of a few microns, may strongly influence deposition. Unfortunately, the roughness of deposition surfaces has rarely been measured and reported in experimental studies. Other factors that may contribute to the data scatter are differences in particle density, differences in method and data quality from different investigators and differences in the magnitude of the lift force between vertical upward flow and downward flow (Fan & Ahmadi, 1993). Thermophoretic and electrophoretic forces may also influence particle behavior unbeknownst to the investigator. Furthermore, particle bounce or resuspension have occasionally been observed in some investigations and accounting for these processes is difficult.

2.3.2 Details about experiments in straight tubes and ducts

Tables 2.2-2.6 summarize the characteristics of the ducts, particles and methods used in most of the published experimental studies on aerosol deposition from turbulent duct flows. Tables 2.2 and 2.3 respectively summarize experiments conducted in *horizontal* and *vertical* tubes with hydraulic diameters *less* than 2.7 cm. Tables 2.4 and 2.5 respectively summarize studies in *horizontal* and *vertical* tubes with hydraulic diameters *greater* than 2.7 cm. Table 2.6 explains the codes used to describe the experimental methods in the columns labeled 'Methods & comments' in Tables 2.2-2.5.

Methods for experimentally determining particle deposition velocities vary widely, but two broad schemes are available. The first method involves direct measurement of the airborne concentration and the particle flux to the surface followed by calculation of the deposition velocity according to equation (2.1). Methods *a*, *b* and *c* in the column entitled 'Methods & comments' in Tables 2.2-2.5 are variations of this technique. The principal alternative method is to measure airborne particle concentrations in the duct at upstream and downstream locations and infer the deposition velocity by equations (2.2) and (2.3). This is method *d* in Tables 2.2-2.5. The fluorometric, radioactive and microscopic techniques of methods *a-c* are much more sensitive and reliable for determination of deposition velocities than method *d*. When using method *d*, small errors in measuring penetration can lead to large errors in calculating the deposition velocity, especially for particle penetrations near zero or one. Also, particle loss mechanisms other than deposition to duct walls may influence the interpretation of data collected by method

d. Those methods in which deposition flux is measured directly are far less susceptible to these types of errors. Data collected by method *d* often exhibit low reproducibility (e.g., Lee & Gieseke, 1994) and are rarely of high quality.

Measurement of airborne concentrations in duct flows usually involves filter sampling or quantification by a particle counting device, though alternative techniques (methods *w, x* and *z* in Tables 2.2-2.5) have been implemented. As a rule, isokinetic sampling should be used to deliver a sample to the filter or particle counter, especially for particles larger than 2 μm. Often in these experiments, the ducts were too small to accommodate a sampling probe and the entire air stream was sampled to determine the concentration. Uncertainties in concentration measurements may arise from anisokinetic sampling, deposition losses in transport lines, intrinsic uncertainties of particle monitoring equipment and laboratory analytical errors. Isokinetic sampling or absolute filtration coupled with fluorometric or radioactive techniques (methods *t* and *u*) are likely to yield the most reliable results. Microscopic counting of filter samples may yield high quality results as well, but is likely to be more susceptible to errors by the investigator. Where fluorometric, radioactive or microscopic techniques were used for surface flux determination, the same technique was used for filter sample analysis. Concentrations measured by particle counters generally have a larger uncertainty than filter samples owing to variations in device performance, the increased potential for transport line losses and the difficulty of achieving isokinetic sampling with a constant flow pump.

Accurate determination of particle size is important. The dimensionless relaxation time is proportional to d_p^2, and V_d^+ is observed to be approximately proportional to d_p^4 in the diffusion-impaction regime. Thus, small errors in sizing can translate into large errors in measured deposition rates. Comments labeled *f-m* in the tables refer to the method of particle sizing used in an experiment.

The duct material, duct diameter, roughness and flow orientation all play a role in determining particle deposition from a duct flow. A horizontal rectangular duct has three distinct internal surfaces: the floor (upward facing), the wall (vertically oriented) and the ceiling (downward facing). For particles larger than about 0.1 μm, deposition velocities to these surfaces are expected to differ owing to the influence of gravity. Particles in horizontal ducts of round cross section are expected to deposit in a similarly nonuniform manner as in rectangular ducts. In a vertical round duct, all surfaces are the same and deposition is expected to be uniform over the entire internal perimeter. Nearly all investigations in horizontal flows have examined deposition only to the duct floor; only Sehmel (1973) looked at differences in deposition to the duct floor and ceiling. In cases where deposition velocities are inferred from concentration measurements (Adam *et al.*, 1996; Cheong, 1997), the deposition surface must be considered to include the entire internal perimeter of the duct and information on differences in deposition to distinct surfaces is inaccessible. Deposition surface materials have included a variety of metals and plastics, as well as glass. Electrostatic effects may influence deposition when the surface is nonmetallic, especially when steps have not been taken to neutralize the test aerosol (comment *n* in Tables 2.2-2.5).

Surface roughness may be divided into microscale roughness, with average roughness heights much less than a millimeter, and macroscale roughness, referring to roughness elements on the order of a millimeter or larger. Theoretical (Browne, 1974; Wood, 1981a; Fan & Ahmadi, 1993; Li *et al.*, 1994) and experimental (El-Shobokshy, 1983; Wells & Chamberlain, 1967; Lai, 1997) evidence suggests that both roughness scales influence particle deposition. All real materials possess microscale roughness, and this has rarely been quantified in deposition experiments. Ducts with significant microscale roughness are often hydraulically smooth. Because Brownian diffusivities of particles are much smaller than the molecular viscosity of air, the particle boundary layer is much thinner than the aerodynamic boundary layer. Therefore, microscale roughness elements can influence particle deposition even in hydraulically smooth flows. When particle deposition is the concern, quantification of surface roughness is needed rather than simple classification of the surface as hydraulically smooth. Macroscale roughness, in the form of fibers or grasses (Chamberlain, 1967; Wells & Chamberlain, 1967; Sehmel, 1970a), repeated ribs (Chamberlain *et al.*, 1984; Hahn *et al.*, 1985; Lai, 1997) and uniform three-dimensional elements (Lai, 1997), has been more frequently characterized and its influence on deposition more systematically investigated. Roughnesses reported in Tables 2.2-2.5 include both microscale and macroscale conditions.

On occasion, researchers have seen fit to apply a coating of petroleum jelly, viscous oil or similar tacky substance to the deposition surface to prevent particles from bouncing upon impact or from becoming reentrained into the flow after depositing. These surface

treatments have allowed some researchers to assess the role of particle bounce or reentrainment in their experiments. The way such coatings may influence deposition from the standpoint of microscale roughness is not apparent. Evidence of particle bounce or reentrainment has been observed in some experiments (Friedlander & Johnstone, 1957; Postma & Schwendiman, 1960; Chamberlain, 1967; Sehmel, 1968; Rouhiainen & Stachiewicz, 1970). When observed, these phenomena have usually been greater for larger particle sizes and higher air speeds.

Deposition of liquid droplets in annular flow has been frequently considered experimentally. Annular flow consists of a thin liquid layer on the walls of a conduit flowing concurrently with the air stream. Disturbances at the liquid-air interface cause polydisperse droplets to be released into the air and it is the deposition of these droplets back into the liquid layer that is studied. A review of experiments of droplet deposition from annular flow is available (McCoy & Hanratty, 1977). Investigations of this type were not included in this review because of the polydisperse aerosols and the poorly characterized wave-like surface condition at the liquid-air interface.

2.3.3 Historical development of experiments in straight tubes and ducts

2.3.3.a Particle size and air velocity

The seminal experimental investigation into understanding particle deposition from turbulent flows was conducted by Friedlander & Johnstone (1957). Their data showed increased particle deposition with increases in air velocity and particle diameter for particles in the diffusion-impaction regime. Subsequent measurements of deposition

from small diameter tubes have confirmed these findings (Postma & Schwendiman, 1960; Sehmel, 1968; Liu & Agarwal, 1974).

Using glass tubes, Liu & Agarwal (1974) conducted experiments that are widely considered the benchmark for particle deposition from turbulent flow because of the high quality of their methods and the reproducibility of the data. The data are shown in Figure 2.2 along with those of El-Shobokshy (1983) and are observed to cover both the diffusion-impaction and inertia-moderated regimes. The data of Liu & Agarwal clearly show the large increase in deposition velocity with particle size in the diffusion-impaction regime and a subtle decrease in deposition velocity as particle size increases in the inertia-moderated regime. This leveling of dimensionless deposition velocities for large values of τ^+ has been corroborated experimentally by Forney & Spielman (1974).

Wells & Chamberlain (1967) were the first to investigate deposition in the diffusion regime. Their data confirmed the expected decrease in deposition with increases in particle size within the diffusion regime until Brownian diffusion becomes negligible. Chamberlain *et al.* (1984) made a single observation of deposition in the diffusion regime. Shimada *et al.* (1993) provided a larger data set of reasonable quality for deposition in the diffusion regime, showing increasing deposition for decreasing particle size. The data of Wells & Chamberlain and Shimada *et al.* are displayed in Figure 2.1.

2.3.3.b Microscale roughness

El-Shobokshy (1983) explored deposition to surfaces with three different levels of microscale roughness: smooth glass and brass machined to microscale roughnesses of 7 and 20 μm ($k^+ = 0.5$ and 1.5). As shown in Figure 2.2, his data agree well with those of Liu & Agarwal (1974) for the case of the smooth surface. Deposition to the roughened surfaces was enhanced up to two orders of magnitude above the smooth case. The deposition enhancement was greatest for the smallest particles studied. To date, this is the only experimental investigation to systematically investigate the connection between increases in microscale roughness and increases in particle deposition.

It should also be noted that Postma & Schwendiman (1960) saw either no difference in deposition or slightly less deposition to 'as fabricated' and 'grit roughened' surfaces as compared to polished tubes in the diffusion-impaction regime. Sehmel (1968) classified some pipes in his study as smooth or rough based on a visual inspection. In the two reported experimental runs comparing smooth and rough pipes, the deposition rate to the rough pipe was larger than to the smooth pipe in one case, and the deposition rates were equal in the other case. Ilori (1971) estimated the size of roughness elements in his experimental tubes by examining the surfaces under a microscope. The glass tube was determined to be optically smooth, while the plastic and aluminum tubes were found to have maximum roughness heights of about 5 μm. Particles in the diffusion-impaction regime had measured deposition rates to the rough surfaces that were equal to or up to two times greater than those to the glass surface. It seems likely that microscale roughness enhances deposition for some particle sizes, and the systematic inquiry by El-

Shobokshy supports this viewpoint; however, investigations with more qualitative assessments of surface roughness have found it to have much less of an impact on deposition than indicated by the measurements of El-Shobokshy.

2.3.3.c Fibrous and macroscale roughness

Wells & Chamberlain (1967) studied particles in the diffusion and diffusion-impaction regimes depositing to a hydraulically smooth brass surface and a surface with fibrous roughness elements with an average length of about 100 μm (k^+ ~ 3-10). From Figure 2.3, it can be seen that deposition to the fibrous roughness was up to three orders of magnitude greater than deposition to the smooth brass surface.

Sehmel (1970a) investigated deposition of 6-14 μm particles to 7 mm tall artificial grass on the floor of a square duct (k^+ ~ 90-700). The results of this study are presented in Figure 2.4, along with later results (Sehmel, 1973) for deposition to a smooth surface on the floor of the same duct. Lines predicting particle deposition by gravitational settling to a smooth floor at the three friction velocities of Sehmel's 1973 experiments are also included in the figure. Dimensionless deposition velocities are approximately equal for both surfaces for larger particles. On the other hand, deposition to the artificial grass surface is enhanced by about an order of magnitude over the smooth surface as particle diameter decreases. This is similar to the trend observed by El-Shobokshy (1983) for deposition to microscale roughness.

Lai (1997) measured deposition of 0.7-7.1 μm particles to surfaces with repeated rib roughness and three-dimensional blocks on the floor of a duct and compared these values to those for deposition onto the smooth floor of the same duct. Compared to smooth surfaces, deposition velocities to surfaces with ribs were 2-3 times higher and those to surfaces with three-dimensional blocks higher by a factor of 5-19. In addition, the distribution of three-dimensional roughness blocks on the surface slightly influenced deposition. Chamberlain *et al.* (1984) studied the effects of repeated rib roughness on the deposition of large particles and Hahn *et al.* (1985) performed similar experiments for small, diffusive particles. Effects of spacing between the ribs were unclear in both cases and neither work compared deposition rates to a similar smooth surface.

2.3.4 Tube bends

Deposition in bend sections is potentially important, but it has rarely been investigated experimentally under turbulent flow conditions. Only two experimental inquiries have been conducted on aerosol deposition in bends with turbulent flow and these were both conducted in very small diameter tubes. The conditions of these experiments are summarized in Table 2.7. The interior surface roughness of the deposition tube was not reported in either experiment. The bend ratio, R_o, presented in the table is defined by

$$R_o = \frac{2R_{bend}}{D_h} \tag{2.18}$$

where R_{bend} is the radius of the bend measured at the centerline.

Pui *et al.* (1987) investigated particle penetration through 90° bends in both laminar and turbulent flow conditions, but only the turbulent flow results are discussed here. McFarland *et al.* (1997) conducted experiments similar to those of Pui *et al.* in 90° bends with a variety of bend ratios. These investigators found it most appropriate to present their data as plots of bend penetration versus particle Stokes number as shown in Figure 2.5. The Stokes number is defined by

$$\mathrm{St} = \frac{C_c \rho_p d_p^2 U_{ave}}{9\mu D_h} = \frac{2\tau_p U_{ave}}{D_H} \tag{2.19}$$

The data show a sharp decrease in bend penetration as the Stokes number increases from near zero to one. The data of McFarland *et al.* in Figure 2.5 show that increasing the bend ratio tends to increase particle penetration through the bend for a given Stokes number, especially for bend ratios in the range 1-4. The data collected by Pui *et al.* at a bend ratio of 5.7 show good agreement with the trends in the data of McFarland *et al.*, but the data of Pui *et al.* suggest greater penetration at the higher Stokes numbers.

Figure 2.6 shows the data of Pui *et al.* (1987) and McFarland *et al.* (1997) in a plot of V_d^+ versus τ^+ along with the experimental data of Liu & Agarwal (1974) for particle deposition in a straight tube collected under comparable conditions. Dimensionless deposition velocities in these bends are observed to be greater than those in the straight tube sections, in some cases by one to two orders of magnitude. Deposition velocities in these experiments in tube bends are quite high and are potentially important in terms of particle penetration through ducts. However, the tubes in which these experiments were

conducted were of very small diameter and their relevance to the much larger diameter duct bends in ventilation systems is uncertain.

2.3.5 Relevance of current data to deposition in ventilation ducts

Most of the experimental work conducted to date is not directly applicable to the case of particle deposition from flow through HVAC ducts. Several studies have focused on particle losses in aerosol sampling lines and have been performed in small diameter tubes with air speeds and friction velocities much higher than those found in ventilation ducts. Experiments in ducts with hydraulic diameters of 15 cm or larger, similar to those in HVAC systems, have often focused on very large roughness elements not commonly found in ventilation ducts. Few investigations have considered differences in deposition to the distinct surfaces in horizontal rectangular ducts and no consideration has been given to complex developing turbulent flows. Experiments using real HVAC materials for the deposition surface are rare. However, the experimental information does provide a mostly consistent picture that can lead to informed expectations of particle behavior in HVAC systems. The overall data set places bounds on the expected deposition behavior of particles in ventilation ducts and provides a foundation for understanding upon which more detailed questions about particle behavior in turbulent flows may be investigated.

The data of Liu & Agarwal (1974) collected in vertical tubes have proven valuable for evaluating the predictive capabilities of theoretical models and the data provide estimates for expected particle deposition rates to vertical surfaces in HVAC systems. The finding by Wells & Chamberlain (1967) of an increase in particle deposition to fibrous filter

paper by orders of magnitude as compared to smooth brass leads to questions regarding the analogous situation of deposition to fiberglass liners on duct interiors compared to galvanized steel. The increases in deposition velocities with increases in microscale roughness in the experiments of El-Shobokshy (1983) indicate that deposition in ducts may be enhanced as duct surfaces corrode or as particles deposit to surfaces and thereby contribute to microscale surface roughness. The deposition enhancement on two-dimensional rib roughness compared to a smooth surface measured by Lai (1997) informs expectations about particle deposition at joints between duct sections, where an internal ridge is commonly present.

Experimental data with direct relevance to HVAC ducts are those that were collected in ducts with hydraulic diameters greater than or equal to 15 cm without extremely large roughness elements. All such data are presented in Figure 2.7. The deposition surface in all of these experiments was the floor of a horizontal duct, except in the case of Montgomery & Corn (1970) where the internal perimeter of a round horizontal duct was the deposition surface. The data collected by Kvasnak *et al.* (1993) for irregularly shaped particles flowing through a 15 cm wide and 2.5 cm high duct are included even though the hydraulic diameter of this duct is somewhat smaller than the others.

The data in Figure 2.7 are not expected to follow the same deposition regimes illustrated in Figure 2.1 because of the influence of gravity when deposition is to a floor surface. Gravitational settling establishes a minimum deposition rate to floor surfaces. The data in Figure 2.7 scattered; however, some of the scatter arises from the use of dimensionless

parameters. When scaled by the friction velocity, equal deposition velocities have different values of V_d^+ for different turbulence intensities. In cases where the turbulence intensity is low, particles deposit to floors at approximately the gravitational settling velocity. Thus, the lower limit for deposition rates shifts in plots of V_d^+ versus τ^+ as can be seen by the gravitational settling lines in Figure 2.4. As the turbulence intensity increases, particles may deposit at rates higher than the gravitational settling velocity as a result of interactions with turbulent eddies.

The only work in the literature to investigate deposition in a horizontal duct to a surface other than the floor is Sehmel (1973), who measured deposition rates to duct floors and ceilings. No data are presented in the literature for deposition to the wall of a horizontal duct. Muyshondt *et al.* (1996) report data for 20 μm particles depositing to the walls of a 10.2 cm diameter vertical pipe, but their experimental techniques were not sensitive. Notably, deposition rates measured by Muyshondt *et al.* were about an order of magnitude higher than the data from Liu & Agarwal (1974). The data for deposition to the floor and ceiling of a 61 cm square duct as measured by Sehmel (1973) are shown in Figure 2.8. The measured deposition velocities to the ceiling were one to two orders of magnitude lower than those to the floors. This figure also shows the variation in dimensionless deposition velocities to floor surfaces with changes in the friction velocity described in reference to Figure 2.4.

The investigations of Adam *et al.* (1996) and Cheong (1997) are both directly concerned with particle deposition in HVAC ducts, but are of questionable value owing to the poor

quality of the experimental methods and the unclear data reporting. Adam *et al.* measured particle penetration through a horizontal square duct of 30 cm width by monitoring upstream and downstream locations with infrared particle monitors. In addition to studying a straight duct, particle penetration through a flow reducer, a single 90° duct bend, a double 90° bend and a flow damper positioned at four different angles were measured. A polydisperse test aerosol was used and most data were presented as least-squares fits of the percentage of particles penetrating the duct versus the flow rate. The data of Adam *et al.* for the straight duct section is presented in the traditional method of τ^+ versus V_d^+ in Figure 2.9. A particle diameter of 1.5 μm was used to calculate representative values of τ^+ for the 0.5-2.0 μm polydisperse aerosol. A comparison with Figures 2.7 and 2.8 shows that hese data are clearly inconsistent with other data for deposition to nominally smooth surfaces. Cheong used experimental techniques and data reporting similar to Adam *et al.* when investigating the effect of the aspect ratio in rectangular ducts on deposition of a polydisperse aerosol of unreported size distribution. The data from Cheong for deposition in a 30 cm square duct are also shown in Figure 2.9 where, again, an average particle diameter of 1.5 μm was assumed to enable presentation of the data in this form. These data also seem inconsistent with previously observed trends and the inconsistencies are likely to be a consequence of the unreliable methods used. Other than Adam *et al.*, no data on particle deposition to ventilation duct components are reported in the literature.

Most experimental determinations of particle deposition from turbulent flow have been limited to deposition from fully developed flow in straight ducts, but a fully developed

flow profile is frequently not the case in ventilation ducts. Deposition from turbulent flow in bends and at duct branches has rarely been reported in the literature, and there are no reports of such measurements in large-diameter ducts. Differences in deposition rates from developing turbulent flow and flow with a fully developed turbulent flow profile have been mentioned by some researchers, but have not been the subject of systematic investigation. In most cases, deposition from the developing flow downstream of a duct inlet has been observed to be greater than that in fully developed flow (Chamberlain, 1967; Sehmel, 1968; Ilori, 1971). Occasionally the opposite trend has been observed (Friedlander & Johnstone, 1957; Liu & Agarwal, 1974). The effect has not often been reported quantitatively.

The overall data set in the literature for particle deposition from turbulent flow has addressed a broad range of experimental conditions. While results are often not directly comparable, and measured particle deposition rates, even within individual data sets, are frequently widely scattered, clear trends and broad consistency in the data can be observed. Direct relevance of the data set to ventilation ducts is limited. Of all data of reliable quality, only Sehmel (1973) and Lai (1997) have performed experiments in ducts similar to those found in HVAC systems. Only Sehmel (1973) has reported differences in particle deposition to the distinct surfaces in horizontal ducts. Air traveling through an HVAC system typically traverses several bends and branches that alter flow conditions from the fully developed state. No investigations have been reported regarding deposition at these sites from ducts with sizes relevant to building ventilation systems. There are no quantitative data on particle deposition from incompletely developed flows

associated with inlet sections or flow after bends in large ducts. Complexities of air flow through HVAC ducts and the surface character of insulated or used and soiled ducts are two primary factors that set the real situation of particle deposition in ventilation ducts apart from all previous experimental investigations.

2.4 Turbulent Airflow in Ventilation Ducts

Most models of particle deposition from turbulent flows have focused on particle interactions with turbulent eddies in the near-wall region of the flow. The description of near-wall turbulence in this section provides a basis for understanding the assumptions and limitations of the deposition models discussed in section 2.5. The near-wall turbulence phenomena described are the fluctuating wall-normal velocity component, the eddy viscosity and organized vortices, bursts and downsweeps. Some key experiments and numerical investigations regarding these phenomena are discussed for turbulent flows near both smooth walls (section 2.4.1) and rough walls (section 2.4.2). A brief discussion of secondary flows in rectangular ducts and in duct bends is provided in section 2.4.3.

2.4.1 Description of turbulent flow near *smooth* walls

For particles in the diffusion and diffusion-impaction regimes, deposition is dominated by particle behavior in a very thin region near the wall. An understanding of the structure of turbulent duct flow very near the duct wall illuminates particle deposition behavior observed both in experiments and in Lagrangian simulations. Very close to boundaries, flow variables are expected to be independent of Reynolds number when

nondimensionalized by the near-wall scaling variables, the friction velocity (u^*) and the kinematic viscosity (ν). Dimensionless quantities, sometimes called wall variables and signified by the + superscript, are formed by multiplying velocities by $1/u^*$, lengths by u^*/ν and times by u^{*2}/ν.

2.4.1.a Fluctuating velocity component normal to a smooth wall

Fluid velocities in turbulent flows are unsteady and appear to fluctuate randomly. Instantaneous velocity components in a turbulent flow can be expressed as a sum of the mean velocity component and a fluctuating velocity component as follows

$$u = \bar{u} + u' \tag{2.20}$$

$$v = \bar{v} + v' \tag{2.21}$$

$$w = \bar{w} + w' \tag{2.22}$$

where $\bar{u}$, $\bar{v}$ and $\bar{w}$ are the time-averaged mean velocity components in the x, y and z (streamwise, wall-normal and spanwise for ducts) directions defined in Figure 2.10 and u', v' and w' are the fluctuating velocity components in the corresponding directions. These fluctuating velocity components play a significant role in the transport of heat, mass and momentum in turbulent flows. In particular, interactions between particles and the fluctuating air velocity component normal to the wall, v' in equation (2.21), were suspected to control deposition to vertical surfaces in the earliest theories. A gradient in the wall-normal fluctuating air velocity component leads to a turbophoretic drift of particles toward a wall, as described later. The quantification of the wall-normal

fluctuating velocity component was a point of disagreement amongst early particle deposition theories.

Investigations into near-wall turbulence have been frequently conducted in four distinct types of flows: turbulent boundary layers over a flat plate, channel flow, duct flow and pipe flow. Channel flow is flow between two infinite parallel plates and can be approximated experimentally in a duct with an aspect ratio (width:height) greater than 5:1. Duct flow refers to flow in a duct of rectangular cross-section that, for this discussion, has an aspect ratio of less than 5:1. Pipe flow is defined as flow through a tube of circular cross section. While each of these flows is distinct and may differ far from the boundaries, the near-wall turbulence is expected to be similar in each case because the flow in this region is dominated by the presence of a single proximate wall. Flow in HVAC ducts can usually be classified as duct flow or pipe flow.

Techniques for experimental measurement of turbulent fluctuating velocity components include hot wire anemometry (HWA), laser Doppler anemometry/velocimetry (LDA/LDV) and particle image velocimetry (PIV). The different methods yield similar results. All have the limitation that velocities very close to a wall are difficult to measure and are less accurate than velocities measured far from the wall as a consequence of wall interferences. Laufer (1954) was one of the first to report experimental data regarding the near-wall normal fluctuating velocity component, v'. This investigation considered airflow through a 25.4 cm diameter pipe at Reynolds numbers of 50,000 and 500,000. Figure 2.11 shows the data collected by Laufer plotted as the dimensionless root-mean-

square (rms) wall-normal velocity, v'^{+}_{rms}, versus the dimensionless distance from the wall, y^{+}, where y is the distance from the wall and

$$v'^{+}_{rms} = \frac{\sqrt{\overline{(v')^2}}}{u^*} \tag{2.23}$$

$$y^{+} = \frac{yu^*}{\nu} \tag{2.24}$$

Included in Figure 2.11 are the data collected by Durst *et al.* (1995) by LDA in oil flow through a 5 cm diameter pipe at Reynolds numbers from 7440 to 20,800. Durst *et al.* were able to make high quality measurements very close to the pipe wall by taking great care to minimize wall effects. The two data sets agree well over a range of flow Reynolds numbers due to the scaling of the fluctuating velocity components and the distance from the wall by the friction velocity and air viscosity. The values of v'^{+}_{rms} measured by Laufer are generally higher than those of Durst *et al.*, probably because of larger wall interferences in the former case.

In recent years, much has been learned about turbulent flows by conducting numerical simulations on computers. Direct numerical simulation (DNS) provides the most accurate means of simulating turbulence. In DNS, the Navier-Stokes equations are solved numerically with resolution in time and space fine enough to capture even the smallest turbulent eddies. DNS is computationally intensive, and the need for computational power increases dramatically as the Reynolds number increases. Thus, DNS is limited to relatively low Reynolds numbers and short simulation times. Large eddy simulation (LES) is a method of generating a turbulent flow field that is not as

severely restricted to low Reynolds number as DNS. In LES, only the large scale turbulent eddies are simulated directly, and the small scale eddies are modeled by a subgrid scale model. Information about the small-scale eddies is lost, but reasonably accurate modeling of the subgrid eddies is possible because the behavior of these eddies is more universal. These computational methods have proven to be very reliable and have the advantage over physical experiments of providing information on flows very close to boundaries.

Profiles of v'^{+}_{rms} versus y^{+} in channel flow at two different Reynolds numbers as calculated from the DNS of Moser *et al.* (1999) are shown in Figure 2.11 along with experimental pipe flow data. Equation (2.90) is discussed later, in section 2.5.4.a. The bottom panel of this figure shows the same data as the top panel with the axes scaled to focus attention on data near the wall. The profiles from the DNS at the two different Reynolds numbers diverge away from the wall, but converge for values of y^{+} less than 20. Reasonable agreement between the DNS data and the physical experiments is observed. However, values of v'^{+}_{rms} immediately adjacent to the wall are lower in DNS than in experiments, possibly owing to wall interference in the physical experiments. The profiles calculated by DNS follow the quadratic relationship expected from theory (Chapman & Kuhn, 1986).

DNS has been performed in square ducts (Gavrilakis, 1992; Huser & Biringen, 1993). Profiles of v'^{+}_{rms} versus y^{+} near the center of the duct walls agree with the results from

channel DNS. In the square duct flows, values of v'^{+}_{rms} were lower near the corners relative to those near the center of the duct walls.

2.4.1.b Eddy viscosity

The similarity between the mechanisms of mass and momentum transport in fluid flows gives rise to the analogy between the eddy viscosity inducing momentum transport and the eddy diffusivity inducing mass transport. In most theories of particle deposition from turbulent flow, the eddy diffusivity of particles has been assumed to be equal to the eddy diffusivity of the air, and specification of this parameter and its dependence on y^+ has been a primary concern. The assumption of the equivalence of the eddy diffusivity to the eddy viscosity is valid for particles in homogeneous isotropic turbulence and for very small particles (i.e., those in the diffusion regime) near a wall. However, the assumption breaks down for larger particles, which possess significant inertia, especially in the vicinity of a wall where the turbulence is anisotropic.

It can be shown that substitution of equations (2.20)-(2.22) into the fluid momentum conservation equation and subsequent time averaging can lead to the following expression for the fluid shear stress (Kay & Nedderman, 1990):

$$\tau_a = \rho_a \left(\nu \frac{\partial \bar{u}}{\partial y} - \overline{u'v'} \right) \tag{2.25}$$

where τ_a is the time-averaged local shear stress in the air, $\partial \bar{u}/\partial y$ is the mean velocity gradient normal to the duct wall and $\overline{u'v'}$ is the time average of the product of the streamwise (u') and wall-normal (v') fluctuating velocity components. The first term on

the right side of (2.25) is the contribution to shear owing to viscous forces and the second term is the shear stress induced by turbulent fluctuations.

In analogy with the viscous transport of momentum by gradient diffusion through random interactions of molecules, turbulent momentum transport is often modeled as gradient diffusion by random interactions of turbulent eddies. The term representing the turbulent transport of momentum, $-\overline{u'v'}$, is often modeled by this expression:

$$-\overline{u'v'} = \xi_a \frac{\partial \bar{u}}{\partial y} \tag{2.26}$$

where ξ_a is the eddy viscosity of the turbulent airflow. This eddy viscosity is not a property of the air, but a property of the turbulent flow. Also, contrary to molecular viscosity, the eddy viscosity is not constant. It varies strongly with distance from a wall because the size of the largest eddies increases with distance from a boundary. Combining (2.25) and (2.26), the shear stress per unit fluid density may be expressed as

$$\frac{\tau_a}{\rho_a} = (\nu + \xi_a)\frac{\partial \bar{u}}{\partial y} \tag{2.27}$$

In this model, the molecular and eddy viscosities are assumed to additively and independently contribute to momentum transport.

Several correlations from the literature for the variation of eddy viscosity with distance from the wall are reproduced in Table 2.8. Based on continuity arguments, it is now well accepted that ξ_a is proportional to $(y^+)^3$ in the close vicinity of a wall (Chapman & Kuhn, 1986). The correlation from Davies (1966a) is the only one from Table 2.8 that does not

follow this relationship. The eddy viscosity correlations of Lin *et al.* (1953), Davies (1966a) (with $Re = 10^4$) and Lai & Nazaroff (2000) are plotted in Figure 2.12 and general agreement among the expressions is observed.

Figure 2.12 also clearly illustrates the very large change in eddy viscosity with distance from the wall. This variation in eddy viscosity gives rise to three distinct regions of the turbulent flow: the viscous sublayer where momentum transport is dominated molecular viscosity, the turbulent core where momentum transport is dominated by eddy viscosity, and the intermediate buffer layer where both molecular and eddy viscosities contribute significantly to momentum transport. These regions have historically been defined by

viscous sublayer:	$y^+ \leq 5$	$\xi_a << \nu$
buffer layer:	$5 \leq y^+ \leq 30$	$\xi_a \approx \nu$
turbulent core:	$y^+ \geq 30$	$\xi_a >> \nu$

The concept of eddy viscosity has proven useful for explaining momentum and gaseous mass transport phenomena in turbulent flows. The analogous concept of particle eddy diffusivity has achieved only limited success in explaining particle behavior in turbulent flows as will be discussed in more detail in sections 2.5.1.g, 2.5.4.a and 2.5.4.c.

2.4.1.c Organized structures in turbulence near a smooth wall

Early studies of turbulence were framed around the assumption that turbulent motions were completely random and without structure. The flow visualization experiments of Kline *et al.* (1967) and Corino & Brodkey (1969) were among the first to indicate a

regular structure in the near-wall region, dominated by coherent vortical structures and intermittent downsweeping and bursting phenomena. It is now well recognized that these coherent structures are responsible for generating most of the turbulent fluctuation energy and for transporting most of the momentum associated with turbulence. There is also strong evidence from Lagrangian simulations that they contribute profoundly to particle deposition from turbulent flows. Because of their potential importance in influencing particle deposition, a brief description near-wall turbulent structures is merited. While ordered structures have been observed in near-wall turbulence, the region may still be rightfully characterized as having a high degree of disorder.

Cantwell (1981) provides a review of the early visualization and correlation studies and presents a detailed description of the near-wall turbulence structure and the associated bursting and downsweeping phenomena as it was understood at the time. Subsequent experimental studies and DNS investigations have partially modified this earlier understanding, but a consensus on the shape, strength, spatial orientation and dynamic role of most of the observed near-wall structures has yet to be reached. The presence of short-lived alternating streaks of high axial speed and low axial speed fluid immediately adjacent to the wall resulting from associated longitudinal streamwise vortices is well accepted. Observed dimensions of low speed streaks have varied widely, but central estimates of nondimensional lengths in the streamwise, wall normal, and spanwise directions are $\lambda_x^+ \sim 1000$, $\lambda_y^+ \sim 30$, and $\lambda_z^+ \sim 50$, respectively. An approximation of the instantaneous alternating arrangement of high speed and low speed streaks is shown in Figure 2.13. Individual streaks are temporal in nature, but the overall streaky structure is

maintained because new streaks are formed as others subside. Low speed streaks have been observed to terminate with a 'burst' of the fluid away from the wall and into the turbulent core as suggested by Figure 2.14. Bursts of low speed fluid away from the wall have been associated with a corresponding downward sweep towards the wall of relatively high velocity fluid to fill the void left by the bursting fluid. The frequency and intensity of bursts and downsweeps were found to increase with increasing Reynolds number. The duration of the events has been estimated to be 20-25% of the mean time period between bursts (Chapman & Kuhn, 1986).

Figure 2.14 also illustrates the association of low speed streaks in the viscous sublayer with pairs of coherent counter-rotating streamwise vortices in the buffer region as observed in early visualization studies. The streamwise vortices have similar dimensions as low speed streaks and are the primary producers of turbulent shear stress. It is these eddies that have been implicated in Lagrangian simulations in depositing particles in the diffusion-impaction regime to surfaces (Zhang & Ahmadi, 2000).

Moin & Mahesh (1998) chronicle the advances made by DNS to the understanding of the near-wall turbulence structure. The existence and extent of alternating streaks of high-speed and low-speed fluid and associated vortices have been confirmed by DNS. However, DNS data suggest that near-wall vortices are usually not paired with a counter-rotating vortex, but commonly exist independently. DNS also suggests that the length of near-wall vortices is somewhat less than the length of low speed fluid streaks. The

importance of experimentally observed bursts and downsweeps of fluid that terminate low speed streaks has been questioned based on DNS results.

While the current understanding of near-wall turbulence is far from complete, the basic structures of streaks and vortices near walls have been repeatedly observed in experiments and simulations. Interactions between these structures and particles may strongly influence particle deposition. The discovery of these near-wall structures provided the starting point for sublayer theories of particle deposition to walls from turbulent flows (Fichman *et al.*, 1988; Fan & Ahmadi, 1993).

2.4.2 Description of turbulent flow near *rough* walls

Investigations into the near-wall turbulence structure in flows past rough walls are far more limited than smooth-walled studies. Roughness elements on walls can increase flow resistance compared to smooth walls because of form drag on the elements. In a similar way, roughness elements can enhance particle deposition by offering sites for particle impaction and by reducing the thickness of the viscous sublayer near the wall. The extent to which particle deposition may be enhanced is likely to depend on the size, shape and spacing of the roughness elements. Several key differences have been observed between the near-wall turbulence structure of smooth and rough walls. Thus, it is conceivable that surface roughness may also influence particle deposition by altering the turbulence structures that are expected to be responsible for deposition.

2.4.2.a Turbulence in rough wall boundary layers: Experiments

Certain features of turbulence over rough walls have been observed to be different than features of turbulence near smooth walls. Grass (1971) studied the impact of sand-grain type roughness on turbulent flow characteristics by performing visualization experiments in an open water-channel flow with hydraulically smooth, transitionally rough ($k^+ = 20.7$) and fully rough ($k^+ = 84.7$) boundaries. This study confirmed the existence of low-speed streaks, sweeps and bursts in flows over rough walls, but noted that streamwise vortices were less apparent in rough-wall flows compared to smooth-wall flows. The spanwise extent of low-speed streaks was observed to be the same near smooth and rough walls. Notable differences between the smooth- and rough-wall cases were the location of the origin of the mean velocity profile and the difference in the profile of v'^+_{rms} versus y^+. The mean velocity profile in the cases with rough surfaces was offset from the smooth-surface case to a location between the flat surface and the mean roughness height of the sand grains. The measured profile of v'^+_{rms} versus y^+ agreed with the data of Laufer (1954) for the smooth wall; however, measured values of v'^+_{rms} near the rough walls were larger, and the measured increase was greater for larger roughness elements.

Krogstad *et al.* (1992) used HWA to measure mean and fluctuating velocities in a turbulent air boundary layer over a completely rough surface roughened by means of a wire mesh with a thickness of 1.55 mm. They made comparisons to measurements over a smooth surface. Similar to the observations of Grass (1971), an offset in the mean velocity profile was noted as was a nearly twofold increase in v'^+_{rms} near the mesh-roughened surface as compared to the smooth boundary. Only small differences for

profiles of $-\overline{u'v'}$ between smooth and rough walls were observed, suggesting that the eddy viscosity does not vary appreciably with changes in surface condition. Bursts and downsweeps at the mesh-roughened surface occurred with a greater frequency and intensity than in the smooth-wall boundary layer. A key contribution of this work was the recognition that the impact of a rough wall on a flow may be felt not only in the immediate vicinity of the wall, but also well outside the buffer layer.

Grass *et al.* (1993) were the first to experimentally verify the existence of coherent streamwise vortical structures in rough-walled turbulent flows. Visualization experiments were performed in an open channel water flow with the surface roughened by closely packed glass beads with diameters in the range 1.15-12 mm. In contrast to the relatively constant dimensions observed in the smooth-wall case, the spanwise extent of the vortical structures was seen to be proportional to the size of the roughness elements.

The work of Krogstad & Antonia (1999) highlighted the deficiencies of characterizing surface roughness by only the mean height. In this study, HWA measurements were made in a turbulent air boundary layer over repeated rib roughness and wire mesh roughness. Both cases were in the fully rough regime with an equivalent dimensionless sand grain roughness of 340. For these two flows with identical mean velocity profiles, the profiles of v'^{+}_{rms} versus y^{+} differed dramatically near the wall with v'^{+}_{rms} values over the mesh being much greater than those over the ribs. Wall-normal velocity profiles were larger than smooth-wall profiles for both roughness cases. Labraga *et al.* (1997) also demonstrated the need to characterize roughness by more than just the mean height.

These investigators made HWA measurements in a fully rough air channel roughened by elements with different aspect ratios and the frequency of bursts and downsweeps were found to depend on the aspect ratio of the roughness elements.

2.4.2.b Turbulence in rough walled channels and pipes: Experiments

Surface roughness has been observed to have the opposite effect on profiles of v'^{+}_{rms} versus y^{+} in the bulk flow of channel and pipe flow as compared with a turbulent boundary layer adjacent to a single bounding surface. Mazouz *et al.* (1998) present HWA measurements in an air channel flow with smooth and completely rough ($k^{+} = 335$) walls that were roughened by repeated ribs. Measurements suggested that values of v'^{+}_{rms} were suppressed in the case of fully rough walls compared to smooth walls throughout the entire channel. Measurements very close to the wall were not presented. These measured profiles compare favorably to the measurements of Sabot *et al.* (1977) in smooth and rough pipe flows. The experiments by Mazouz *et al.* and Sabot *et al.* dealt solely with the bulk airflow and did not address near-wall turbulence. Consequently, it is not clear whether such differences between boundary layer flows and pipe and channel flows exist in the near-wall region. Using the same experimental facility as Mazouz *et al.*, Demare *et al.* (1999) studied the impact of fully roughened walls on bursting and downsweeping frequency. They found that frequencies decreased by about a factor of two in the rough-wall case compared to the smooth wall. Differences in the structures of the near-wall layers of channel and pipe flows as compared to boundary layer flows were attributed to interchanges of vortices between the different wall layers, which cannot happen in a turbulent boundary layer with a single wall.

2.4.2.c Turbulence in rough walled channels and pipes: Simulations

As compared to smooth-wall investigations, DNS has played a less dominant role in the understanding of turbulence near rough walls because of the difficulty and computational expense of applying boundary conditions at the rough surfaces. Choi *et al.* (1993) successfully implemented DNS in a channel with walls roughened by longitudinal ribs in the transitionally rough regime ($k^+ = 20$ and 40). Longitudinal ribs are oriented in the direction of flow, an arrangement that has been observed to reduce drag relative to a smooth wall for some configurations. Profiles of v'^+_{rms} versus y^+ near the wall depended on the position above the tip or valley of the rib and interactions between the rib peaks and streamwise vortices were hypothesized to determine whether the rib configuration would increase or decrease the drag of the flow. A novel idea put forth in this work was the definition of the offset in the velocity profile based on the fluctuating streamwise velocity component, u', rather than on the mean velocity.

Miyake *et al.* (2000) present DNS results for channel flow with one smooth wall and the other wall roughened by conical roughness elements to give a sand-grain type roughness with $k^+ \sim 25$. In this simulation, very little difference was observed between profiles of v'^+_{rms} versus y^+ over the smooth wall and the transitionally rough wall.

Friedrich *et al.* (2001) point out that a boundary condition of partial wall permeability accurately models wall roughness in DNS. They present results of DNS in a smooth pipe as well as in pipes with five different wall permeabilities. Values of v'^+_{rms} near the wall

(presented in Wagner & Friedrich, 1998) were found to be much higher near the permeable 'rough' walls than near the smooth wall. This observation is in qualitative agreement with measurements in turbulent boundary layers (Krogstad & Antonia, 1999).

In summary, roughness has been observed to have a dramatic, though sometimes uncertain, effect on the structure of near-wall turbulence. Surface roughness has been accounted for in some particle deposition theories from the standpoint of reducing the particle transport distance across the viscous sublayer. The effect of changes in the structure of the near-wall turbulence owing to surface roughness on particle deposition processes has not been explored theoretically. Changes in turbulence structure caused by changes in surface roughness have an unknown impact on the deposition of particles entrained in flows near roughened walls.

2.4.3 Secondary flows

Turbulent flow in ducts of rectangular cross section is different than flow in pipes or channels because the average wall normal and spanwise velocities have nonzero values in duct flows. At the corners of a duct, the interaction of the vertical and horizontal boundary layers establishes corner vortices, as shown in Figure 2.15, with flow toward the duct corners along the corner bisectors and flow toward the center of the duct along wall bisectors. Up to eight large-scale vortices in the plane normal to the mean flow direction may comprise the secondary flow in a square duct, and more vortices may be present as the duct aspect ratio increases. The intensity of this secondary flow is approximately 2-3% of the bulk velocity (Kay & Nedderman, 1990).

Another secondary flow of importance in ventilation ducts is that established in a bend. An example of the secondary flow in the plane normal to the mean flow that may be established at the outlet of a bend is shown in Figure 2.16. Two large, counter rotating vortices are established with flow along the horizontal centerline of the duct towards the outside of the bend and flow returning to the inside of the bend along the floor and ceiling of the duct. Experimental evidence indicates that from one to three secondary vortices may be established in a bend and that the shape and intensity of the secondary flow resulting from a bend depends on the Dean number

$$\mathrm{De} = \mathrm{Re}\left(\frac{D_h}{2R_{bend}}\right)^{0.5} \tag{2.28}$$

The magnitude of these types of secondary flows is usually less than 10% of the axial velocity (Boersma & Nieuwstadt, 1996). Bends skew the mean velocity profile toward the outer duct wall. Also, the LES results of Boersma & Nieuwstadt of turbulent flow in a pipe bend indicate that v'^{+}_{rms} achieves higher values near the inner wall and lower values near the outer wall when compared to a straight pipe. As best I can determine, the influence of secondary flows on particle deposition has not been addressed theoretically in the literature.

2.4.4 Turbulent airflow summary

Most models of particle deposition from turbulent flows require some representation of the near-wall turbulence. Advances in understanding near-wall turbulence have supported advances in predictive models of particle deposition. The structure of fully

developed turbulence near smooth walls has been well studied; profiles of v'^{+}_{rms} and ξ_a are predictable and near-wall vortices, low axial speed streaks, bursts and downsweeps have been well characterized. Turbulence near rough walls has been studied less frequently, but studies have shown the structure of turbulence near rough walls to be different than near smooth walls and dependent on the size and shape of the roughness elements. When modeling particle deposition to rough surfaces, no effort has yet been made to account for changes in the structure of turbulence owing to roughness; only the offset in the velocity profile due to the roughness elements has been considered. Likewise, secondary flow structures in rectangular ducts and in bends have not yet been incorporated into deposition models.

2.5 Review of Literature on Predicting Particle Deposition Rates

Particle deposition models provide estimates of deposition rates given information about the particles, the airflow in which the particles are suspended and the airflow conduit. Particle deposition rates predicted by models are most commonly expressed in terms of the dimensionless deposition velocity, V_d^+. Common input information for most models includes the particle size and density, the air velocity, and the duct dimensions. Some models are able to predict the influence of surface roughness, thermal gradients or electrical fields on deposition rates and require additional input information. The orientation of the deposition surface influences particle deposition, but only a small fraction of published models have considered deposition rates to both horizontal and vertical surfaces.

No models presented in the literature have attempted to account for all forces that may act on a particle. Frequently, models have focused on predicting deposition rates of particles in a single deposition regime (diffusion, diffusion-impaction or inertia-moderated) because of the presumed unique deposition mechanisms in each regime. Model evaluation by comparison to experimental data has been limited. Owing to the wide scatter in experimental data, it is difficult to make fine distinctions among models based on such comparisons under most circumstances.

This section first discusses the mechanisms that can cause particles to move relative to an air stream. Then the four main methods for predicting particle deposition rates are discussed: empirical equations, Eulerian models, sublayer models and Lagrangian simulations. The discussion follows a mostly chronological development of models within each method of prediction.

2.5.1 Particle transport mechanisms

Forces and mechanisms influencing particle motion that are potentially present in turbulent ventilation duct flow are discussed in this section. All of the mechanisms are applicable to turbulent flow, but only turbulent diffusion and turbophoresis are unique to turbulent flow. All equations developed in this section are strictly applicable for rigid, spherical particles only; however, they are commonly applied in environmental aerosol dynamics models even when these conditions are not strictly met.

2.5.1.a Brownian diffusion

Brownian motion is always present as a result of the random interactions between particles and air molecules. The flux of particles owing to Brownian diffusion is calculated by applying Fick's law of diffusion, written here for flux in one dimension:

$$J_B = -D_B \frac{\partial C}{\partial y} \tag{2.29}$$

where J_B is the Brownian diffusive particle flux in the y-direction, $\partial C/\partial y$ is the y-component of the particle concentration gradient and D_B is the particle Brownian diffusivity. The Brownian diffusivity of a particle in air can be calculated by the Stokes-Einstein relation, corrected for slip:

$$D_B = \frac{C_C k_B T}{3\pi d_p \mu} \tag{2.30}$$

where $k_B = 1.38\times10^{-23}$ J/K is Boltzmann's constant and T is the absolute temperature. A net flux of particles generated by Brownian diffusion only exists in the presence of a nonzero concentration gradient. Brownian diffusion can be the dominant transport mechanism of very small particles over very small distanes, but is weak for particles larger than about 0.1 μm.

2.5.1.b Drag force

Whenever there is relative motion between a particle and the surrounding air, the particle experiences a drag force from the air that tends to reduce that relative motion. In the general case, the drag force on a particle is calculated by

$$F_d = \frac{\pi d_p^2 \rho_a |u_a - v_p|(u_a - v_p) C_d}{8 C_c} \tag{2.31}$$

where u_a is the local air velocity, v_p is the particle velocity, C_d is the drag coefficient and the sign of the force is determined by the difference in the air and particle velocities. The drag coefficient of a sphere can be calculated by the following equations:

$$C_d = \frac{24}{\mathrm{Re_p}} \qquad \mathrm{Re_p} < 0.3 \tag{2.32}$$

$$C_d = \frac{24}{\mathrm{Re_p}}\left(1 + 0.15\mathrm{Re_p}^{0.687}\right) \qquad 0.3 < \mathrm{Re_p} < 800 \tag{2.33}$$

where $\mathrm{Re_p}$ is the particle Reynolds number

$$\mathrm{Re_p} = \frac{d_p |v_p - u_a|}{\nu} \tag{2.34}$$

Equation (2.32) is the drag coefficient for particles obeying Stokes law, while (2.33) is an empirical fit to experimental observations. The derivation of Stokes law assumes that the fluid flow far from the particle is uniform and that the particle is not accelerating relative to the fluid. These assumptions are frequently violated for particles in HVAC duct flow, but the errors introduced by these violations are likely to be small. For particles that do not obey Stokes law because $\mathrm{Re_p} > 0.3$, the particle relaxation time could be calculated by

$$\tau_p = \frac{C_c \rho_p d_p^2}{18 \rho_a \nu (1 + 0.15\mathrm{Re_p}^{0.687})} \tag{2.35}$$

instead of by equation (2.13), where, in this case, $\mathrm{Re_p}$ is evaluated at the initial velocity difference $|v_{p,o} - u_a|$. However, this expression assumes that $\mathrm{Re_p} > 0.3$ for the entire

relaxation period. In reality, as a particle relaxes towards the fluid velocity, the particle Reynolds number decreases towards zero. Even if the Reynolds number has a high initial value, some fraction of the relaxation period will occur with the particle obeying Stokes law. In most of the literature and in the results presented in this review, equation (2.13) is used to relate relaxation time to particle size.

2.5.1.c Gravitational force

Particles more dense than air settle owing to the effects of gravitational acceleration. Neglecting buoyancy (appropriate for $\rho_a << \rho_p$) the net gravitational force on a particle is

$$F_g = \frac{\pi}{6} d_p^3 \rho_p g \tag{2.36}$$

where g is the gravitational acceleration, which at the surface of Earth is approximately equal to 9.81 m/s^2. A balance of the drag force with the gravitational force on a particle leads to a simple expression for the particle gravitational settling velocity

$$v_g = \tau_p g \tag{2.37}$$

The importance of gravitational settling increases with particle size. It is generally an unimportant mechanism for particles smaller than 0.1 μm in diameter.

2.5.1.d Shear-induced lift force

A particle entrained in a shear flow field may experience a lift force perpendicular to the main flow direction. The magnitude of this shear-induced lift force for particles in a constant shear flow far from any walls was first calculated by Saffman (1965, 1968) to be

$$F_l = \frac{1.62\mu d_p^2 (du/dy)}{\sqrt{\nu |du/dy|}} (u - v_{px}) \tag{2.38}$$

where du/dy is the air velocity gradient normal to the duct wall and v_{px} is the particle velocity in the axial direction. The direction of the lift force depends on the relative velocity between the particle and air in the x-direction (streamwise). A particle in a velocity gradient near a wall (where du/dy is positive) with a streamwise velocity higher than the air velocity will experience a negative lift force, i.e., towards the wall. A particle that lags the air stream in the x-direction will have a lift force away from the wall.

Equation (2.38) as derived by Saffman has the constraints that

$$\frac{d_p^2 |du/dy|}{\nu} < 1 \qquad \text{and} \qquad \mathrm{Re}_p < \frac{d_p^2 |du/dy|}{\nu} \tag{2.39}$$

McLaughlin (1991) performed a theoretical analysis in which the second constraint was relaxed and found the magnitude of the lift force to be less than or equal to that expressed by equation (2.38). Subsequent analyses by McLaughlin (1993) and Cherukat & McLaughlin (1994) modified Saffman's expression to account for the presence of a wall and the near-wall expressions suggested a lessening of the lift force magnitude as the wall is approached. Wang *et al.* (1997) used the term 'optimum lift force' for the lift force modified to relax the Reynolds number constraints and to account for the presence of a wall and this convention is adopted in this report. The lift force arises due to particle inertia and is most important for large particles. Lagrangian simulations suggest that the lift force is most important very close to the wall ($y^+ < 20$), where the velocity gradient is largest and the differences between particle and fluid velocities are greatest.

2.5.1.e Thermophoresis

If a temperature gradient exists in an air volume, a particle in that volume tends to migrate towards the cooler region. The motion is the result of gas molecules on the warm side striking the particle with a greater average momentum than those on the cooler side. For larger particles, the establishment of a temperature gradient within the particle alters the gas temperature field near the particle and complicates the analysis. This motion can be evaluated by balancing the drag force with the thermophoretic force, which acts in the direction of decreasing temperature. This expression for thermophoretic force is given by Talbot *et al.* (1980):

$$F_{th} = -\frac{3\pi\mu^2 d_p H_{th}}{\rho_a T}\frac{dT}{dy} \tag{2.40}$$

where dT/dy is the y-component of the temperature gradient and H_{th} is the thermophoretic force coefficient

$$H_{th} = \left(\frac{2.34}{1+3.42\text{Kn}}\right)\left(\frac{k_a/k_p + 2.18\text{Kn}}{1+2k_a/k_p + 4.36\text{Kn}}\right) \tag{2.41}$$

Here, k_a and k_p are the thermal conductivities of the air and the particle material, respectively. The thermophoretic velocity, obtained when the thermophoretic force is balanced by drag is

$$v_{th} = \frac{-C_c \nu H}{T}\frac{dT}{dy} \tag{2.42}$$

The thermophoretic velocity in a given temperature gradient is at a maximum and nearly independent of particle size for particles smaller than 1 μm. For larger particles, the

thermophoretic velocity decreases with increasing particle size, provided that $k_a/k_p < \sim 0.2$. Thermal gradients are common in HVAC ducts because the delivered air is often heated or cooled and ducts are often outside of the thermal envelope of buildings.

2.5.1.f Electrostatic drift

A charged particle in an electric field experiences an electrostatic force. The Coulomb force on a particle due to the electric field is calculated by

$$F_C = qE \tag{2.43}$$

where q is the charge on the particle and E is the electric field strength. The particle charge is calculated from its net excess or deficit of electrons

$$q = ne_o \tag{2.44}$$

where n is the number of electrons of deviation (including sign) from the electrically neutral state and e_o is the charge of a single electron, -1.6×10^{-19} C.

Li & Ahmadi (1993c) present an equation that predicts the electrostatic force on a charged particle near a conducting surface as

$$F_e = qE - \frac{q^2}{16\pi\varepsilon_o y^2} + \frac{qEd_p^3}{16y^3} - \frac{3\pi\varepsilon_o d_p^6 E}{128y^4} \tag{2.45}$$

where ε_o is the permittivity of air, equal to 8.86×10^{-12} C^2 N^{-1} m^{-2}. The terms on the right side of equation (2.45) respectively account for the Coulomb force, image force, dielectric force and dipole-dipole force. Li & Ahmadi's analysis suggested that the dielectric force and the dipole-dipole force are negligible and that the Coulomb force

dominates when an electric field is present. Because of the use of electrically conducting materials, significant electric fields are not expected in HVAC ducts. In the absence of an electric field, the only component of the electrostatic force that can influence particle motion is the image force. The image force is always directed towards a wall and is only appreciable extremely close to a wall. It only occurs near a conducting surface. Charges accumulated on electrically insulating materials may give rise to electric fields and influence the motion and deposition of charged particles.

2.5.1.g Turbulent diffusion

In the same way that fluctuating turbulent velocity components contribute to momentum transport in turbulent flows, turbulent fluctuations contribute to the diffusive flux of particles. The instantaneous particle concentration in a turbulent flow can be expressed as the sum of an average and a fluctuating concentration, just as the instantaneous turbulent velocity components are expressed in equations (2.20)-(2.22):

$$C = \overline{C} + C' \tag{2.46}$$

where C is the instantaneous concentration, $\overline{C}$ is the time averaged concentration and C' is the fluctuating concentration. Substitution of equation (2.46) into the particle mass conservation equation for duct flow and Reynolds averaging leads to a total particle diffusive flux (averaged over turbulent fluctuations) in the direction normal to the wall of

$$J_{diff} = -D_B \frac{d\overline{C}}{dy} - \overline{v'C'} \tag{2.47}$$

where J_{diff} is the total diffusive flux and $\overline{v'C'}$ is the contribution to the total diffusive flux from turbulent fluctuations. Continuing the analogy with turbulent momentum transport, the term $\overline{v'C'}$ is commonly modeled for homogeneous turbulence by

$$\overline{v'C'} = \xi_p \frac{d\overline{C}}{dy} \tag{2.48}$$

so that the total diffusive flux can be represented by

$$J_{diff} = -\left(D_B + \xi_p\right)\frac{d\overline{C}}{dy} \tag{2.49}$$

Here, ξ_p is the eddy diffusivity of the particle, which is often assumed to be equal to the eddy viscosity of air, ξ_a. This assumption implies that there is no slip velocity between the particle and the air, which is untrue in many circumstances. However, the equality of ξ_p to ξ_a has been shown to be true for larger particles in homogeneous turbulence, where ξ_a is constant (Hinze, 1975). As with Brownian diffusion, there is no net particle flux owing to turbulent diffusion in the absence of a concentration gradient.

2.5.1.h Turbophoresis

In turbulence that is inhomogeneous, the gradient in turbulent fluctuating velocity components gives rise to turbophoresis, a particle transport mechanism that is distinct from turbulent diffusion. Because turbulent velocity fluctuations decay to zero at surfaces, near-wall turbulence is highly inhomogeneous with a gradient in turbulence intensity as a function of near-wall distance. The velocity of a particle with sufficient inertia can be decoupled from the local air velocity because of the lag in particle response, as measured by its relaxation time. Where there is a gradient in turbulence

intensity, the likelihood that an inertial particle is thrown to a region of lower turbulence intensity near a wall is greater than the likelihood that it will make the return journey away from the wall. This asymmetry leads to a net migration of particles in turbulent flows down a gradient in turbulence intensity and towards walls. Caporaloni *et al.* (1975) were the first to recognize this phenomenon and they calculated the turbophoretic velocity to be

$$v_t = -\tau_p \frac{d\left(\overline{v'^2_{py}}\right)}{dy} \tag{2.50}$$

The same expression was derived somewhat more rigorously by Reeks (1983). Caporaloni *et al.* provided an expression relating the particle rms wall-normal velocity to that of the fluid. Subsequent investigators (Guha, 1997; Young & Leeming, 1997) have proposed similar expressions for this relationship. Combining equations (2.13), (2.31), (2.32) and (2.50), and assuming that the drag force balances turbophoresis, the net turbophoretic force applied to a particle can be expressed as

$$F_t = \frac{\pi}{6}\rho_p d_p^3 \frac{d\left(\overline{v'^2_{py}}\right)}{dy} \tag{2.51}$$

Turbophoresis has rarely been explicitly recognized in the literature, even though it proves to be a dominant transport mechanism in turbulent flows for some inertial particles near walls. In contrast to turbulent diffusion, turbophoresis gives rise to a flux of particles even in the absence of a concentration gradient.

2.5.1.i Combining transport mechanisms

In Eulerian particle deposition models, particle transport mechanisms are usually assumed to be additive. This assumption appears valid for most practical purposes; however, there are cases when mechanisms do not act independently, but influence one another. An example is the effect of crossing trajectories identified by Yudine (1959) in which turbulent diffusion is reduced owing to the influence of gravitational settling. Small particles are able to follow fluid streamlines, but large particles influenced by gravitational settling may lose contact with eddies before the eddies decay. The heavy particles thus undergo a less intense turbulent diffusion owing to a lower velocity correlation with the surrounding fluid.

2.5.1.j Other transport mechanisms

The previously discussed transport mechanisms have all been included in at least one form of particle deposition model. Other forces to transport particles exist but have been shown to be negligible for particle-air systems. The Basset history force, the Magnus force due to particle spin, the buoyancy force, the hydrodynamic force due to the pressure gradient in the flow and the Faxen correction for unsteady Stokes flow are all routinely ignored (Maxey & Riley, 1983).

2.5.2 Methods: Empiricism, Eulerian models and Lagrangian simulations

There are four basic approaches to predicting particle deposition rates in turbulent flows: empirical equations, Eulerian modeling, sublayer modeling and Lagrangian simulation. Empirical equations are simple best fits to collected experimental data, while Eulerian

models and Lagrangian simulations are theoretically based approaches. In the Lagrangian approach, the air is considered a continuous phase and the trajectory of a single particle through the airflow is predicted from the sum of all forces acting on the particle. By solving particle trajectories for particles from several different initial locations, airflow with particles can be simulated and information about particle deposition can be obtained. The Eulerian approach treats both the particles and the air as separate continuous phases. Individual trajectories of particles are not calculated, rather the overall behavior of an ensemble of particles is predicted through the introduction of the volume-averaged concentration and the solution of the conservation equations for the particle phase. Both Eulerian and Lagrangian methods require knowledge of the turbulent flow field and are suitable for solid or liquid particles depositing from airflow in a duct. Comparisons of Eulerian and Lagrangian methods are available in the literature (Durst *et al.*, 1984; Gouesbet & Berlemont, 1999). In general, Lagrangian simulations require less conceptual modeling and capture more of the fundamental physics involved in particle motion, but at a much greater computational cost. Sublayer models are also discussed in this section. These models use a Lagrangian scheme to locate a single limiting particle trajectory in the near-wall region upon which deposition velocity predictions are based. Sublayer models are not fully Lagrangian simulations that find deposition rates from large numbers of calculated particle trajectories. They are classified separately from Eulerian models and Lagrangian simulations.

Most models and simulation approaches share some common limitations. Most predict the deposition of rigid spherical particles to a vertical wall so that gravity is not a direct

factor in determining deposition. Thermal gradients and electrical fields are usually ignored. All models address deposition from fully developed turbulent flow only. Particle concentrations are assumed to be low enough to ignore particle-particle interactions. (Such interactions are unlikely to be a concern when applied to the case of particles in HVAC ducts.) The presence of particles is also assumed not to affect the structure of air turbulence. The duct is assumed to be a perfect sink for particles so that once a particle contacts a wall, it does not bounce or detach and become reentrained. In the following sections, when models are applied to simulate experiments, the conditions in the model applications are set to be as close as possible to the physical conditions of the experiments.

2.5.3 Empirical equations

Due to the historical lack of a physically satisfying and well performing model of particle deposition from turbulent flow, empirical equations have frequently been proposed as the best means to predict particle deposition. The equations are generally successful in representing experimental data because they are adjusted to fit these data, but they offer little in the way of understanding particle behavior or predicting deposition from flows that have not been the subject of particle deposition experiments. The most common form of empirical equations for deposition to vertical surfaces in the three deposition regimes are as follows (Papavergos & Hedley, 1984):

diffusion regime ($\tau^+ < \sim 0.1$): $$V_d^+ = k_1 \mathrm{Sc}^{-2/3} \qquad (2.52)$$

diffusion-impaction regime ($\sim 0.1 < \tau^+ < \sim 10$): $$V_d^+ = k_2 \tau^{+2} \qquad (2.53)$$

inertia-moderated regime ($\sim 10 < \tau^+$): $V_d^+ = k_3$ (2.54)

where k_1, k_2 and k_3 are empirical constants and the particle Schmidt number, important in the diffusion regime, is defined as

$$\mathrm{Sc} = \frac{\nu}{D_B} \tag{2.55}$$

Published empirical equations for predicting particle deposition to smooth surfaces in the three different deposition regimes are presented in sections 2.5.3.a-2.5.3.c The application of these empirical equations to nonvertical surfaces is discussed in section 2.5.3.d and published empirical equations for deposition to rough surfaces are considered in section 2.5.3.e.

2.5.3.a Empirical equations in the diffusion regime

In the diffusion regime where particles are very small and Brownian motion is an important particle transport mechanism, particle deposition is similar to deposition of gaseous species because of the extremely small particle inertia. The film model of mass transfer of a diffusive species to a wall theorizes a turbulent core perfectly mixed by eddies and a thin laminar film near the wall where only molecular processes occur. A sharp boundary is assumed to divide the turbulent core and the laminar layer leading to the concentration profile of a diffusive species shown in Figure 2.17. Based on the analogy between momentum transfer and mass transfer, the film model predicts the dimensionless deposition velocity of a species to be

$$V_d^+ = \sqrt{\frac{f}{2}}\mathrm{Sc}^{-1} \tag{2.56}$$

and substitution of the Blasius formula, equation (2.8), for f yields

$$V_d^+ = 0.1989 \mathrm{Re}^{-1/8} \mathrm{Sc}^{-1} \tag{2.57}$$

The film model is a rudimentary theory that neglects the contribution of turbulent diffusion in the near-wall region. A key limitation is the implicit assumption that the particle boundary layer thickness is independent of the particle diameter. Smaller particles diffuse faster and have thicker boundary layers than larger particles; thus the true dependence of deposition velocity on the Brownian diffusivity is less than the proportional dependence predicted by equations (2.56) and (2.57). A more rigorous consideration of the development of the particle concentration boundary layer and its dependence on Brownian diffusivity suggests that the Schmidt number exponent should be –2/3 instead of –1. Colburn's j-factor approach, based on an analogy to these analyses predicts (Kay & Nedderman, 1990)

$$V_d^+ = \sqrt{\frac{f}{2}} \mathrm{Sc}^{-2/3} \tag{2.58}$$

or

$$V_d^+ = 0.1989 \mathrm{Re}^{-1/8} \mathrm{Sc}^{-2/3} \tag{2.59}$$

after substitution of equation (2.8). This result is in agreement with the relationship suggested by equation (2.52) and the –2/3 exponent can be considered to have strong theoretical, as well as empirical justification. It should be pointed out that equations (2.56)-(2.59) were developed for smooth surfaces only, as the analogy between momentum and mass transfer only holds when there is no contribution to the overall drag from form drag on roughness elements.

The main difference between equations (2.52) and (2.59) is the Reynolds number dependence in equation (2.59), but this dependence is very weak. Values of k_1 for equation (2.52) calculated by equation (2.59) range from 0.073 when $Re = 10^3$ down to 0.035 when $Re = 10^6$. Values of k_1 recommended by various authors are summarized in Table 2.9 and these values are near the range predicted by Colburn's j-factor analogy. In the cases of Cleaver & Yates (1975) and Wood (1981b), these constants are not the result of fits to experimental data, rather they come from theoretical analyses coupled with simplifying mathematical approximations. While equation (2.52) is often treated as a simple empirical expression, it is more correctly a mathematical approximation to a more rigorous theoretical analysis, supported by experimental evidence.

Empirical equations slightly different in form from equation (2.52) have also been proposed. Shaw & Hanratty (1977) found the best fit to turbulent diffusional deposition data collected in a liquid flow system to be

$$V_d^+ = 0.0889 \mathrm{Sc}^{-0.704} \tag{2.60}$$

with the difference between the –0.704 and –2/3 exponents being statistically significant. Shimada *et al.* (1993) correlated the results of several numerical calculations of diffusional deposition by the equation

$$V_d^+ = \frac{2.4\times10^{-4}\,\mathrm{Re}^{0.92}\,D_B^{0.67}}{D_h u^*} \tag{2.61}$$

where all variables are in SI units (i.e. length in m, time in s). The purpose of casting the expression in this form was to compare it with the analysis of Friedlander (1977) who

derived a theoretical expression for diffusional deposition from pipe flow assuming the particle eddy diffusivity, ξ_p, to be equal to Lin *et al.*'s (1953) expression for eddy viscosity near the wall. The expression from Friedlander was

$$\frac{V_d D_h}{D_B} = 0.042 \mathrm{Re} \mathrm{Sc}^{1/3} \sqrt{f} \tag{2.62}$$

which was recast by Shimada *et al.* as

$$V_d^+ = \frac{3.0 \times 10^{-4} \mathrm{Re}^{0.88} D_B^{0.67}}{D_h u^*} \tag{2.63}$$

However, for clarity in the context of this discussion, equation (2.63) can be more simply rewritten by substitution of equations (2.6), (2.8) and (2.10) giving

$$V_d^+ = 0.061 \mathrm{Sc}^{-2/3} \tag{2.64}$$

using a value of 1.55×10^{-5} $m^2 s^{-1}$ for the kinematic viscosity of air. Thus, although they appear significantly different, equations (2.61) and (2.62) reduce to the same form as equation (2.52) and are in agreement with other expressions for diffusional deposition derived from mathematical approximations.

A comparison of equation (2.52) with $k_1 = 0.063$ to the empirical expressions of equations (2.60) and (2.61) is presented graphically in Figure 2.18. Experimental data collected by Shimada *et al.* in a very small (6 mm diameter) tube are included in the figure for comparison. To eliminate the confounding influence of Reynolds number (e.g., equation (2.59)), only data collected at a Reynolds number of approximately 10^4 are included on the figure. Setting k_1 equal to 0.063 in equation (2.52) is the same as applying Colburn's

j-factor analogy at a Reynolds number of 10^4. From Figure 2.18, it is easy to see that there is little difference between the expressions, especially for $\tau^+ < 0.1$ where the equations are most applicable. In addition, these equations demonstrate good agreement with the experimental data. Because particles that are strongly influenced by Brownian motion are insignificantly affected by gravity, these equations for the diffusion regime may be applied equally to horizontal and vertical surfaces.

2.5.3.b Empirical equations in the diffusion-impaction regime

Proposed empirical equations to predict deposition velocities for particles in the diffusion-impaction regime to vertical surfaces have largely been of the form expressed by equation (2.53). These equations represent simple best fits to experimental data and a summary of values for k_2 reported in the literature is given in Table 2.10. All of the proposed constants agree to within a factor of 2.

Papavergos & Hedley (1984) also proposed correlations of the form of equation (2.53) for horizontal floor and ceiling surfaces based on the data collected by Sehmel (1973). These equations are

$$\textit{horizontal floor:} \qquad V_d^+ = 2\times10^{-3}\tau^{+2} \tag{2.65}$$

$$\textit{horizontal ceiling:} \qquad V_d^+ = 4\times10^{-5}\tau^{+2} \tag{2.66}$$

They suggest that deposition to a floor is greater by a factor of 3-6 than deposition to a vertical wall and that deposition to a ceiling is diminished by a factor of 9-15 compared to wall deposition.

Erhart (1986) found that a form of equation (2.53), modified by a factor proposed by Gieseke *et al.* (1980) to account for variations in Reynolds number, fit his data better than the unmodified equation. The modified equation is

$$V_d^+ = 6.2\times10^{-4}\tau^{+2} + 2.0\times10^{-8}\,\mathrm{Re} \qquad (2.67)$$

The term with the Reynolds number represents an *ad hoc* modification that is unlikely to be useful over a wide range of Reynolds numbers.

Muyshondt *et al.* (1996) assumed the deposition velocity could be correlated to both τ^+ and Re and fit the experimental data they collected in the diffusion-impaction regime to a sigmoid curve. The best fit was found to be

$$V_d^+ = a_1 \exp\left[-0.5\left(\frac{\mathrm{Re}-a_2}{a_3}\right)^2\right] + a_4 \exp\left[-0.5\left(\frac{\ln(\tau^+)-\ln(a_5)}{a_6}\right)^2\right] \qquad (2.68)$$

$a_1 = 0.0226$ $\qquad$ $a_4 = 0.1394$

$a_2 = 4.03\times10^4$ $\qquad$ $a_5 = 49.0$

$a_3 = 1.533\times10^4$ $\qquad$ $a_6 = 1.136$

with the limitations that $0.1 < \tau^+ < 100$ and $2500 < \mathrm{Re} < 50{,}000$. While it is generally true that increasing the number of fitting variables can improve the quality of a model-measurement comparison, it does so at the cost of losing the causal connections between the model equation and the underlying physical process. Thus, while the form of equations (2.52) and (2.53) reveal some mechanistic underpinnings, equation (2.68) reflects pure empiricism.

Dimensionless deposition velocities predicted by equation (2.53), with $k_2 = 4.5\times10^{-4}$, and by equations (2.67) and (2.68) are compared to the experimental data of Liu & Agarwal (1974) in Figure 2.19. The data were collected for 1-21 μm particles depositing to the walls of a 1.27 cm diameter tube at a Reynolds number of 10,000. Equation (2.53), which is an empirical fit to the data, agrees well with the data in the diffusion-impaction regime as expected. Equations (2.67) and (2.68) both seem to overpredict deposition velocities for low values of τ^+. This overprediction is likely the result of making the original empirical fit to data that were collected by techniques that were insufficiently sensitive to distinguish among low values of V_d^+ in the range of 10^{-3}-10^{-6}.

2.5.3.c Empirical equations in the inertia-moderated regime

For relatively large particles depositing to vertical surfaces, deposition has been observed to be nearly independent of particle size. The Reynolds analogy for mass transfer to pipe walls in a turbulent flow assumes that there is no viscous layer resistance to mass transfer near the wall and that mass transfer rates are set by resistance in the turbulent core. This assumption is approximately true for large particles and the result of the Reynolds analogy for mass transfer is

$$V_d^+ = \sqrt{\frac{f}{2}} \tag{2.69}$$

This result predicts deposition to be independent of particle size and to be slightly dependent on the Reynolds number via the friction factor (equations (2.8) and (2.9)).

Several investigators have suggested that deposition velocities to vertical surfaces for particles in the inertia-moderated regime are constant and have recommended specific values for k_3 to be used in equation (2.54). These recommended values are given in Table 2.11 and there is little variation in the reported constants.

Several investigators have noted a decrease in experimentally observed deposition velocity as particle size increases through the inertia-moderated regime. Some have suggested that this phenomenon is best explained as the result of large particles bouncing upon impact with the wall or resuspending into the flow after deposition. Most theoretical treatments agree that, even in the absence of bounce or resuspension, the decreased response to turbulent velocity fluctuations of the very large particles should lead to a reduction in deposition rate with an increase in particle size in the inertia-moderated regime. Reeks & Skyrme (1976) provide a theoretical expression to calculate particle deposition in the inertia-moderated regime that predicts decreased deposition with increased particle size. Wood (1981b) developed a simple mathematical approximation to this result and adjusted the constants to fit Liu & Agarwal's (1974) data for large particle deposition. The result from Wood is

$$V_d^+ = \frac{2.6}{\sqrt{\tau^+}}\left(1-\frac{50}{\tau^+}\right) \qquad \text{if} \quad \tau^+ \geq 270 \tag{2.70}$$

$$V_d^+ = 0.13 \qquad \text{if} \quad 17 \leq \tau^+ < 270$$

For $\tau^+ \geq 270$, these equations predict a moderately decreasing deposition velocity with increasing particle relaxation time.

A comparison is made between equation (2.54) with $k_3 = 0.18$ recommended by Papavergos & Hedley (1984), the Reynolds analogy of equation (2.69) and equation (2.70) from Wood (1981b) in Figure 2.20. The experimental data in the figure were collected by Liu & Agarwal (1974) in a 1.27 cm tube at a Reynolds number of 50,000. The equations recommended by Wood show excellent correlation with the data as expected because they were fit to these data. The constant deposition velocities suggested by other researchers and by the Reynolds analogy all show reasonable agreement (in magnitude if not in exact value) with the data.

2.5.3.d Synthesis of empirical equations

Although most empirical equations are valid for only one deposition regime, deposition across the entire range of particle sizes is easily predicted by a simple combination of equations. Empirical equations in the form of equations (2.52)-(2.54) can be applied to vertical surfaces across all deposition regimes when configured in the following manner:

$$V_d^+ = k_1 \mathrm{Sc}^{-2/3} + k_2 {\tau^+}^2 \qquad \text{if} \quad k_1 \mathrm{Sc}^{-2/3} + k_2 {\tau^+}^2 \le k_3 \tag{2.71}$$

$$V_d^+ = k_3 \qquad \text{if} \quad k_1 \mathrm{Sc}^{-2/3} + k_2 {\tau^+}^2 > k_3 \tag{2.72}$$

To apply empirical equations of this type to horizontal surfaces, Kvasnak & Ahmadi (1996) added a simple modification to account for the effect of gravitational settling on particle deposition. The result is

$$V_d^+ = k_1 \mathrm{Sc}^{-2/3} + k_2 {\tau^+}^2 + g^+ \tau^+ \tag{2.73}$$

where g^+ is the dimensionless gravitational acceleration defined by

$$g^+ = \frac{g\nu}{u^{*3}} \tag{2.74}$$

and g is positive for a floor and negative for a ceiling surface. In equation (2.73) the first term on the right side accounts for Brownian diffusion, the second term accounts for interactions between particle inertia and turbulent eddies and the final term accounts for gravitational settling. Equation (2.73) can be applied to horizontal surfaces for all particle sizes. The leveling of deposition velocities for particles in the inertia-moderated regime is not expected to be observed when considering deposition to ventilation duct floors. At friction velocities typically found in ducts, the transport of particles with dimensionless relaxation times larger than 10 is strongly influenced by gravity. As particle size increases in the inertia-moderated regime, deposition rates are expected to increase owing to increases in the gravitational settling rate.

Equation (2.73), with representative values of $k_1 = 0.057$ and $k_2 = 4.5\times10^{-4}$, is compared to the data collected by Sehmel (1973) for particle deposition to the floor and ceiling of a horizontal square duct in Figure 2.21. Also included on this figure are equations (2.65) and (2.66), the empirical fits to the data of Sehmel (1973) for the floor and ceiling, respectively. Equation (2.73) compares favorably to the experimental data for the floor. Also, the slope of equation (2.73) follows the slope of the experimental data more closely than equation (2.65), implying that deposition in this case is dominated by gravity as expressed in (2.73) and not by inertial interactions with turbulence as expressed by (2.65). Equation (2.73) is less successful in predicting the experimental data at the

ceiling. The excellent agreement between equation (2.66) and the experimental data for the ceiling derives from the fact that (2.66) was developed as a correlation to these data.

Following the same technique of linear summation of deposition mechanisms as in equation (2.73), successes have been reported for estimating deposition velocities of particles under the influence of thermal gradients (He & Ahmadi, 1998) and electrical fields (Fan & Ahmadi, 1994) by rather simple equations.

2.5.3.e Empirical equations for rough surfaces

All of the preceding empirical equations are recommended only for smooth walls. Wood (1981b) modified the theoretical results of Davies (1966b) for deposition of particles in the diffusion regime to account for surface roughness. Wood recommended the following mathematical approximations for deposition of particles in the diffusion regime to walls with roughness in the hydraulically smooth or transitionally rough regime

hydraulically smooth ($0.45k^+ \leq 5$):

$$\phi_k = \frac{k^+ \mathrm{Sc}^{1/3}}{32.2} \tag{2.75}$$

$$V_d^+ = \left[24.2 + 14.5 \mathrm{Sc}^{2/3} \left(\frac{2\pi}{3\sqrt{3}} - \frac{k^+ Sc^{1/3}}{27.6} \right) \right]^{-1} \quad \text{if} \quad \phi_k << 1 \tag{2.76}$$

$$V_d^+ = \left[\frac{1524}{0.45k^+ (0.9k^+ - 5/\phi_k)} - 6.3 \right]^{-1} \quad \text{if} \quad \phi_k >> 1 \tag{2.77}$$

transitionally rough ($5 \leq 0.45k^+ \leq 70$):

$$V_d^+ = \frac{0.2}{\ln\left(\frac{25.2}{0.45k^+ - 4.8}\right)} \tag{2.78}$$

A correlation for the deposition velocity of particles in the diffusion regime to completely rough surfaces based on a theoretical analysis is (Davies, 1983)

$$V_d^+ = 0.080\mathrm{Sc}^{-1/2} \tag{2.79}$$

This equation has a form similar to equation (2.52), but the dependence on Sc differs.

Fan & Ahmadi (1993) present a perturbation solution to the equations of particle motion used in their sublayer model to predict deposition rates of particles in the diffusion-impaction regime to vertical surfaces with small amounts of roughness. The resulting empirical equation is in a complex form with many variables that need to be calculated, but the calculations are straightforward. The empirical equation gave predictions similar to their sublayer model for both smooth and rough surfaces. Other than the perturbation solution of Fan & Ahmadi (1993), I am unaware of any empirical expressions for predicting deposition of particles outside the diffusion regime to rough surfaces. I am also unaware of any data in the diffusion regime investigating deposition to rough surfaces with values of $k^+ < 140$, with which to compare equations (2.75)-(2.78).

2.5.4. Eulerian models

There are three main classes of Eulerian models for predicting particle deposition rates: gradient diffusion models, free-flight models and turbophoretic models. Gradient diffusion and free-flight models entail solving the particle mass conservation equation.

Turbophoretic models solve the particle mass and particle momentum conservation equations. Gradient diffusion models consider turbulent and Brownian diffusion to be the only mechanisms of particle transport that induce deposition. Free-flight models explain particle deposition as a combination of diffusion towards a wall followed by a final step to the wall in 'free-flight' at a velocity much higher than that of the air near the wall. Turbophoretic models consider particle transport by both diffusion and turbophoresis and offer a more physically satisfying explanation of particle deposition compared to free-flight models. Through the inclusion of the particle momentum equation, turbophoretic models are also more readily able to include forces like shear-induced lift than are other Eulerian models.

The development of free-flight models for smooth and rough surfaces are respectively discussed in sections 2.5.4.a and 2.5.4.b. Gradient diffusion models and turbophoretic models are reviewed in sections 2.5.4.c and 2.5.4.d, respectively.

2.5.4.a Free-flight models for smooth surfaces

The first major theory of particle deposition from turbulent flow was the free-flight theory proposed by Friedlander & Johnstone (1957). The theory aimed to explain the extremely rapid increase in deposition velocity to a vertical surface with small increases in particle size in the diffusion-impaction regime observed in their own experiments. Many subsequent authors have added modifications to this original theory and good reviews of the evolution of the free-flight theory are available (Papavergos & Hedley, 1984; Wallin, 1994). This section first describes the general ideas of the free-flight

theory then discusses the assumptions made by various investigators to implement the theory. All of these free-flight models predict deposition to vertical surfaces only.

The free-flight deposition theory is based on the idea that particles are able to deposit onto a wall by traversing the laminar region near the wall in free flight instead of diffusing through a near-wall concentration boundary layer. Particles entrained in turbulent eddies are assumed to travel towards the wall by a combination of turbulent and Brownian diffusion to the relatively quiescent region adjacent to the wall. At this point the turbulent eddies dissipate, but particles continue moving toward the wall in free flight. Particles impact on the surface where they deposit owing to their inertia. Particles are assumed to stop diffusing towards the wall and begin free flight to the wall at a distance about equal to their stopping distance away from the wall. The stopping distance is the characteristic distance that the particle, given an initial velocity, will travel through stagnant air before coming to rest. The stopping distance is calculated by

$$S = \tau_p v_{p,o} \tag{2.80}$$

where S is the stopping distance and $v_{p,o}$ is the initial velocity of the particle. The stopping distance is made dimensionless by this expression:

$$S^+ = \frac{Su^*}{\nu} \tag{2.81}$$

Mathematically, the free-flight theory is a solution of the particle mass conservation equation in the direction normal to a wall. Writing this equation for turbulent flow and subsequently applying Reynolds averaging leads to Fick's law of diffusion, modified to include the effects of turbulent diffusion:

$$J_{diff} = (D_B + \xi_p)\frac{d\overline{C}}{dy} \tag{2.82}$$

This is a restatement of equation (2.49), although here the negative sign is dropped and flux toward the wall is defined to be positive. In dimensionless form, equation (2.82) is

$$V_d^+ = \left(\frac{D_B}{\nu} + \frac{\xi_p}{\nu}\right)\frac{dC^+}{dy^+} \tag{2.83}$$

where

$$C^+ = \frac{\overline{C}}{C_{bulk}} \tag{2.84}$$

and C_{bulk} is the particle concentration in the turbulent core of the duct, which is assumed to be constant.

The capture distance, Δ, is defined as the distance from the wall at which the depositing particle begins its free flight to the wall. The particle is assumed to undergo Brownian and turbulent diffusion from the core region to the capture distance. Equation (2.83) is integrated from the turbulent core, where $C^+ = 1$, to the particle capture distance to yield

$$\frac{1 - C^+_{\Delta^+}}{V_d^+} = \int_{\Delta^+}^{y^+(C^+=1)} \frac{dy^+}{\left(\frac{D_B}{\nu} + \frac{\xi_p}{\nu}\right)} \tag{2.85}$$

where $y^+(C^+ = 1)$ is the dimensionless distance from the duct wall to the turbulent core, Δ^+ is the dimensionless particle capture distance, and $C^+_{\Delta^+}$ is the dimensionless particle concentration at the dimensionless capture distance. The parameter $C^+_{\Delta^+}$ is unknown and

is not easily measured. This variable may be eliminated from the analysis by substituting for the flux of particles at the capture distance, which is defined as follows:

$$J = \left(v_{py} \cdot \overline{C}\right)_{\Delta^+} \tag{2.86}$$

where v_{py} is the particle velocity normal to the wall. The dimensionless deposition velocity can be written

$$V_d^+ = \frac{J}{C_{bulk} u^*} \tag{2.87}$$

Substitution of equation (2.86) into (2.87) gives

$$V_d^+ = \left[\left(\frac{v_{py}}{u^*}\right)\left(\frac{\overline{C}}{C_{bulk}}\right)\right]_{\Delta^+} = v^+_{py,\Delta^+} C^+_{\Delta^+} \tag{2.88}$$

where v^+_{py,Δ^+} is the dimensionless y-component of particle velocity at Δ^+. Equation (2.88) can then be substituted into (2.85) to eliminate $C^+_{\Delta^+}$ and give a general form of the free-flight model:

$$\frac{1}{V_d^+} = \frac{1}{v^+_{py,\Delta^+}} + \int_{\Delta^+}^{y^+(C^+=1)} \frac{dy^+}{\left(\frac{D_B}{\nu} + \frac{\xi_p}{\nu}\right)} \tag{2.89}$$

The dimensionless deposition velocity may be evaluated given information or appropriate assumptions about ξ_p, Δ^+ and v^+_{py,Δ^+}. Not all free-flight models conform exactly to equation (2.89), but this form provides a useful framework for looking at the influence of different assumptions on the predictions of free-flight models. Often, investigators have

focused on integrating equation (2.89) and expressing it in the form of an analytical equation to allow for easier evaluation of deposition velocities.

In their original model, Friedlander & Johnstone (1957) ignored Brownian diffusion and assumed the particle eddy diffusivity, ξ_p, to be equal to Lin *et al.*'s (1953) correlations for the eddy viscosity, ξ_a. The dimensionless capture distance, Δ^+, was assumed to be equal to the dimensionless stopping distance of the particle, S^+. The initial dimensionless velocity of the particle before making the free flight to the wall, v^+_{py,Δ^+}, was assigned a constant value of 0.9 regardless of particle size. This value for v^+_{py,Δ^+} was chosen to match the wall-normal, root-mean-square fluctuating velocity of the air in the turbulent core as measured by Laufer (1954) (see Figure 2.11). Resistance to particle transport through the turbulent core to a distance of $y^+ = 30$ was calculated by the Reynolds analogy. This resistance was added in series with the resistance represented by the integral in equation (2.89), which was integrated from $y^+ = \Delta^+$ to $y^+ = 30$ (with $D_B = 0$) to determine V_d^+. The first term on the right side of equation (2.89) was ignored. This is equivalent to assuming that the normalized particle concentration at Δ^+ is very much smaller than one. A summary of the assumptions made by Friedlander & Johnstone and by several other investigators that have proposed variations on this free-flight model is given in Table 2.12. Friedlander & Johnstone summed the resistances to transport in the turbulent core, buffer layer and viscous sublayer. The resistance in the turbulent core was derived from the Reynolds analogy and the resistance in the buffer layer and viscous sublayer was calculated by integration of equation (2.89). The result was three expressions for the dimensionless deposition velocity that depend only on the stopping

distance; the proper equation to apply is determined by the magnitude of S^+. A comparison of the theory of Friedlander & Johnstone with the data collected by Liu & Agarwal (1974) is presented in Figure 2.22. The model-measurement agreement is favorable, but the discontinuities in the model are physically unrealistic.

Davies (1966b) suggested many modifications to the free-flight theory of Friedlander & Johnstone (1957). Davies noted that the capture distance should include the particle radius to account for the interception effect. Also, he suggested that the initial free-flight velocity, v^+_{py,Δ^+}, be equated to the local root-mean-square of the wall-normal fluctuating air velocity component instead of a constant value as recommended by Friedlander & Johnstone. Davies approximated the measurements of Laufer (1954) for the rms wall-normal fluctuating air velocity by this expression:

$$v'^+_{rms} = \frac{y^+}{y^+ + 10} \tag{2.90}$$

This profile is compared to data from experiments and DNS in Figure 2.11. Far from the wall, equation (2.90) approximately follows the trends in the data. Near the wall, in the bottom panel of the figure, equation (2.90) predicts values of v'^+_{rms} that are higher than the data. This profile does not predict the near-wall dependence of v'^+_{rms} on y^{+2} that is expected from theory (Chapman & Kuhn, 1986).

Davies included the effects of Brownian diffusion in his analysis for cases when $\Delta^+ < 20(D_B/\nu)^{1/3}$. In addition, a continuous correlation for the eddy viscosity was used instead

of the correlation proposed by Lin *et al.* (1953). The assumptions in this free-flight model are more physically satisfying than those in Friedlander & Johnstone's work because the initial free-flight velocity is not assigned arbitrarily, but is equal to the local fluid velocity fluctuations at the point at which free flight begins. Despite these apparent improvements, the theory of Davies is observed to considerably underpredict the experimental data in Figure 2.22. The effect of Brownian diffusion in this model is apparent at small relaxation times where the deposition velocity is predicted to increase as particle size decreases.

Liu & Ilori (1974) sought to explain the discrepancy between the model of Davies (1966b) and the experimental data by suggesting that the particle eddy diffusivity was not equal to the eddy viscosity of air as had previously been assumed. Liu & Ilori proposed that the particle eddy diffusivity was greater than the eddy viscosity, especially for large particles, and argued that the particle eddy diffusivity should be calculated by

$$\xi_p = \xi_a + v'^2_{rms}\tau_p \tag{2.91}$$

In the work of Liu & Ilori (1974), this equation for the particle eddy diffusivity, along with Davies' (1966b) expression for v'^+_{rms} (equation 2.90) and Owen's (1960) expression for the eddy viscosity of air (see Table 2.8), was substituted into a variant of equation (2.89). The limits of the integration were chosen to be the dimensionless duct centerline and Δ^+. Because the resulting integral expression was improper at the duct centerline, the equation was solved by analogy to the similar case of diffusion of a vapor from turbulent flow to a pipe wall. The model of Liu & Ilori is shown in Figure 2.22, and very good agreement with the data is observed. However, the form of the expression for the particle

eddy diffusivity given in (2.91) lacks a strong theoretical foundation. The eddy diffusivity of particles has been shown to be equal to the eddy viscosity of air over a long period of time and this modification really amounts to a clever semiempirical tuning of the free-flight model to better fit the data. Brownian diffusion was neglected in the development of this theory, as is evident by the extremely low deposition velocities predicted for $\tau^+ < 0.1$.

The free-flight theories of Davies (1966b) and Liu & Ilori (1974) were significantly different in terms of basic assumptions from the original theory of Friedlander & Johnstone (1957). Numerous other free-flight theories have been proposed that differ from one of these theories in only subtle ways. Independent of Friedlander & Johnstone, Owen (1960) proposed a free-flight theory of particle in which Δ^+ was assumed to be 1.6 regardless of particle size. This highly questionable assumption leads to a theory that predicts no variation in deposition with particle size, a prediction clearly at odds with experimental findings. The work of Owen, while being based on unrealistic assumptions, was the only free-flight model to consider particle deposition to floors and ceilings. Beal (1970) proposed a theory similar in most ways to Friedlander & Johnstone's, but with an even higher initial free-flight velocity based on the local axial fluid velocity. Most subsequent investigators have found this free-flight velocity to be unrealistically high. The theory of Beal introduced the concept of a particle sticking probability as a means of accounting for particle bounce, but only sticking probabilities equal to unity were used in his analysis. A free-flight theory incorporating a different correlation for the eddy viscosity of air was proposed by Wasan *et al.* (1973). Forney & Spielman (1974)

modified Friedlander & Johnstone's theory to eliminate the discontinuities in the predicted relationship between deposition velocity and relaxation time.

In conclusion, although some free-flight theories give predictions of deposition that compare favorably to the best available experimental data, these theories are often based on questionable assumptions. The free-flight theory based on the most realistic assumptions, that of Davies (1966b), predicts deposition velocities one to two orders of magnitude lower than those observed experimentally in portions of the diffusion-impaction regime.

2.5.4.b Free-flight models for rough surfaces

The first modeling work to attempt to account for the effect of deposition surface roughness was that of Browne (1974) who followed a suggestion made by Davies (1966a). Browne used all the same assumptions as Davies (1966b) except that the dimensionless capture distance was modified to account for surface roughness. The dimensionless capture distance was defined as

$$\Delta^+ = S^+ + r_p^+ + k^+ + \sigma_k^+ - e^+ \tag{2.92}$$

where r_p^+ is the dimensionless particle radius, σ_k^+ is the dimensionless standard deviation of the roughness height and e^+ is the dimensionless offset in the axial air velocity profile owing to the roughness elements. These dimensionless parameters are made nondimensional by multiplying the dimensional parameters by the factor u^*/ν. The dimensional forms of these parameters are defined graphically in Figure 2.23. The definition of the capture distance in this manner implies that particles deposit above the

mean roughness height by a distance equal to one roughness height standard deviation. Browne recommends direct measurement of k and σ_k. For cases in which the standard deviation in roughness height is not measurable, he suggests the following correlation:

$$\sigma_k^+ = 0.17k^+ \tag{2.93}$$

The point where the axial air velocity profile decays to zero is located somewhere between the peaks and the troughs of the roughness elements. The dimensionless height of this origin in the velocity profile relative to the lowest valleys in the roughness elements was estimated by Browne to be

$$e^+ = 0.53k^+ + 0.0034k^{+2} \tag{2.94}$$

This correlation is based on three measurements made by Grass (1971) in a water channel flow with sand-grain type roughness elements.

With the simple modification of the particle capture distance represented by equations (2.92)-(2.94), Browne modified the model of Davies (1966b) to account for the effect of surface roughness. The predictions of this model are compared in Figure 2.24 to the experimental data collected by El-Shobokshy (1983) in vertical tubes with 0, 7 and 20 μm roughness elements, corresponding to values of k^+ of 0, 0.5 and 1.5. This model consistently predicts less deposition than observed in the experiments, but it does capture similar trends as the experiments. Large increases in deposition with increases in surface roughness are seen in the model and in the experiments. Furthermore, the importance of surface roughness in determining deposition velocity diminishes as the particle size

increases. This is especially clear in the model, where the lines for the three different roughness values converge for values of τ^+ greater than 20.

El-Shobokshy & Ismail (1980) modified the model of Liu & Ilori (1974) to account for surface roughness by changing Δ^+ using equations (2.92)-(2.94). They also included Brownian diffusion in their analysis. El-Shobokshy & Ismail used the Lin *et al.* (1953) correlation for the eddy viscosity. By setting the upper integration limit at the edge of the turbulent core instead of the duct centerline, they were able to solve for deposition velocity without resorting to an analogy to vapor diffusion as in Liu & Ilori. The model of El-Shobokshy & Ismail is displayed in Figure 2.24 at the three different roughness heights of the experiments. This model exhibits better agreement with the experimental data at all roughness levels than the model of Browne (1974). As with the previous model, this model follows the trends observed in the experimental data set.

Wood (1981a) presents a free-flight model that includes Brownian diffusion and is suitable for calculating deposition to rough surfaces. For the initial free-flight velocity, Wood correlated his model output with Liu & Agarwal's (1974) experimental data to arrive at a constant value of 0.69 for v^+_{py,Δ^+}, applicable for all particle sizes. To account for rough surfaces, Wood used a similar approach as Browne (1974), where the capture distance was defined as

$$\Delta^+ = S^+ + r_p^+ + k^+ - e^+ \tag{2.95}$$

and the offset in the velocity profile was chosen to be

$$e^+ = 0.55k^+ \tag{2.96}$$

Equation (2.95) is the same as (2.92) except that the standard deviation of the roughness height is neglected. Equation (2.96) is a simpler version of (2.94) based on the same three velocity profile offsets measured by Grass (1971). Considering the sparse data, equations (2.95) and (2.96) are probably more appropriate estimates of a particle capture distance than (2.92)-(2.94).

The proposed model of Wood (1981a) applied to the three roughness conditions in the experiments of El-Shobokshy (1983) is presented in Figure 2.25. Similar results as observed in Browne's (1974) modes accounting for roughness are observed. The model follows similar trends as the experimental data, but model predictions are somewhat lower than the measurements.

Im & Ahluwalia (1989) present a free-flight model that accounts for surface roughness and is mostly independent of the previously discussed models. The particle eddy diffusivity was not assumed to equal the eddy viscosity; rather, a relationship between the two depending on the ratio of the turbulent integral time scale to the particle relaxation time was proposed. The turbulent integral time scale was defined as

$$\tau_f = \frac{2y_b}{3u^*} \tag{2.97}$$

where y_b is the thickness of the buffer layer, taken to occur at $y^+ = 80$. The initial free-flight velocity of the particle was assumed to depend on the ratio τ_f/τ_p as well. The particle capture distance was taken to be

$$\Delta^+ = S^+ + e^+ \tag{2.98}$$

This formulation neglects particle interception and assumes that particles deposit at the same height as the origin of the velocity profile. This is the same as assuming that the particle concentration profile is offset to the same point as the velocity profile. Experimental data compiled by Cebeci & Smith (1974) for the offset in the velocity profile versus roughness height were used to develop the following correlation

$$e^+ = 0.7\sqrt{k^+} + 0.014k^+ \tag{2.99}$$

This correlation yields a somewhat larger velocity profile offset than equations (2.94) or (2.96) for values of k^+ less than about 2 and a smaller offset in the velocity profile for larger values of k^+.

Model results from Im & Ahluwalia (1989) are shown in Figure 2.25. The model predicts extremely low deposition for small particles because it neglects Brownian diffusion. It shows reasonable agreement with the experimental data depositing to the smooth surface and predicts less deposition than observed experimentally for the rough surfaces. As a consequence of the scaling of the free-flight velocity and eddy diffusivity with the turbulent integral time scale, this model also predicts decreasing deposition velocity with increasing particle size in the inertia-moderated regime. This feature is not observed in any other free-flight model.

Overall, the model of El-Shobokshy & Ismail (1980) appears to be the free-flight model that compares most favorably to the limited experimental data on deposition to rough

surfaces, at least in the diffusion-impaction regime. It also displays good agreement with experimental data to smooth surfaces and includes Brownian diffusion in its analysis. However, this model arbitrarily assigns particle diffusivities greater than the eddy viscosity as represented by equation (2.91). Another weakness is that the method of accounting for roughness in this model is based on intuition and the correlation for the offset in velocity profile used to calculate the capture distance is based on only three data points, with only one of those being in the hydraulically smooth region of interest here. It is uncertain whether the model-measurement agreement is the result of the model capturing the physics of the deposition process or a mere coincidence. The model for rough surfaces presented by Browne (1974), based on the model for smooth walls proposed by Davies (1966b), seems to be the free-flight model based on the most physically sound assumptions, but it underpredicts measured deposition velocities by an order of magnitude or more. In general, free-flight theories can compare favorably to experimental measurements when they assume either seemingly unreasonably large initial free-flight velocities or large particle eddy diffusivities. When the assumptions are most realistic, the theories tend to predict deposition velocities that are much lower than observed in experiments.

2.5.4.c Gradient diffusion models

Gradient diffusion models are similar to free-flight models in that they are solutions to the particle mass conservation equation. In fact, gradient diffusion models can be considered a conceptual simplification of free-flight models where the only deposition mechanisms included are Brownian and turbulent diffusion. Particles are assumed to

diffuse from the turbulent core all the way to the wall, with no allowance made for jumping across the near-wall region of the flow by inertial coasting as in free-flight models. Thus, gradient diffusion models are free of the somewhat questionable assumption made in free-flight models that a depositing particle stops diffusing precisely at the capture distance and instantly begins its free flight to the wall.

Equation (2.82), Fick's law of diffusion in one dimension, is the starting point for gradient diffusion models. Nondimensionalizing this equation and solving for the dimensionless deposition velocity in the case of a smooth surface yields

$$\frac{1}{V_d^+} = \int_{r_p^+}^{y^+(C^+=1)} \frac{dy^+}{\left(\frac{D_B}{\nu} + \frac{\xi_p}{\nu}\right)} \tag{2.100}$$

The lower limit of the integral is the dimensionless particle radius, r_p^+, because the center of a particle deposited on a smooth wall lies at a distance of the particle radius from the surface. Because diffusion is assumed to be the only deposition mechanism, no assumptions about initial free-flight velocity or particle capture distance are required as in free-flight models. One only needs to assume a correlation for the particle eddy diffusivity and a distance from the wall where the particle concentration is constant ($y^+(C^+ = 1)$) to solve equation (2.100).

Sehmel (1970b) used experimental deposition data in the framework of the free-flight theory to back calculate the initial free-flight velocities of depositing particles. He found that initial free-flight velocities decreased as particle size increased which is the opposite

of what one would expect if free flight were indeed the means by which particles arrive at the surface. He also concluded that free-flight theories did not acceptably predict deposition velocities and he abandoned the concept of free-flight deposition in favor of deposition by gradient diffusion only. Sehmel (1970b) represents the first published non free-flight model. In this model, he proposed that the particle eddy diffusivity is greater than the eddy viscosity. By correlating the available experimental deposition data (Stavropolous, 1954; Friedlander & Johnstone, 1957; Postma & Schwendiman, 1960; Sehmel, 1968), he arrived at an expression for the particle eddy diffusivity for a particle depositing to a smooth vertical wall of

$$\frac{\xi_p}{\nu} = 0.011 y^{+1.1} \tau^{+1.1} \tag{2.101}$$

In applying the model, equation (2.101) is considered to be bounded by two limits. On the high side, the particle eddy diffusivity cannot exceed this value:

$$\frac{\xi_p}{\nu} = 0.4 y^{+} \tag{2.102}$$

On the low side, the particle eddy diffusivity is limited by this expression:

$$\frac{\xi_p}{\nu} = 0.001 y^{+3} \tag{2.103}$$

With these equations for the particle eddy diffusivity, Sehmel (1970b) recommends integrating equation (2.100) from the duct centerline. This model is compared to the data collected by Liu & Agarwal (1974) in Figure 2.26. The model agrees with the magnitude and functional shape of the measurements. Discontinuities in the model are visible and result from the abrupt changes in particle eddy diffusivity when the bounds expressed by

equations (2.102) and (2.103) are reached and equation (2.101) is no longer applied. The proposed equations for ξ_p have no sound theoretical support. Instead, they represent empirical fits to the data that were then available.

Gradient diffusion models for deposition to horizontal floor and ceiling surfaces were presented by Sehmel (1973). Similar to Sehmel (1970b), particle eddy diffusivity correlations were back calculated from experimental data. Correlations with functional forms similar to equation (2.101) were proposed for the eddy diffusivity of particles depositing to both floor and ceiling surfaces. Bounds of applicability similar to equations (2.102) and (2.103) were also provided. Because these correlations were based smaller data sets than that for the vertical surface, they are potentially less universally applicable.

Another gradient diffusion model that has been proposed is that of Lai & Nazaroff (2000). This model was developed for predicting particle deposition to indoor surfaces where turbulence intensities are much smaller than in most turbulent flows considered here. In indoor environments, particle inertia is not expected to be important for determining particle transport; thus, inertia was excluded from consideration in this model. For particle deposition to a vertical surface, this work recommends integrating equation (2.100) from an upper bound of $y^+ = 30$ using a correlation for the eddy viscosity based on a fit to data from DNS applied to channel flow (see Table 2.8). For deposition to floors and ceilings, a term for the flux due gravitational settling is included in the original flux equation. Thus, equation (2.82) becomes

$$J = \left(D_B + \xi_p\right)\frac{d\overline{C}}{dy} \pm v_g \overline{C} \tag{2.104}$$

In this work, the eddy viscosity and particle eddy diffusivity were assumed to be equal. This model, when applied to the experimental conditions of Liu & Agarwal (1974), drastically underpredicts particle deposition in the diffusion-impaction and inertia-moderated regimes, as seen in Figure 2.26. The eddy viscosity correlation is accurate and the model is based on sound assumptions if turbulent and Brownian diffusion are the only mechanisms leading to deposition. That this model so seriously underpredicts deposition velocities to vertical surfaces in the diffusion-impaction and inertia-moderated regimes strongly demonstrates the importance of particle inertia in influencing deposition in these domains.

Gradient diffusion models are probably inappropriate for predicting deposition velocities in sampling tubes and ventilation ducts where air velocities are high and particles may not faithfully follow fluid streamlines. The gradient diffusion model with the best physical basis, that of Lai & Nazaroff (2000), does not incorporate effects owing to particle inertia and consequently predicts deposition velocities far lower than are observed experimentally. The gradient diffusion model of Sehmel (1970b) shows better agreement with the experimental data, but the correlation for the particle eddy diffusivity was chosen to make the model fit the available experimental data and it is not supported by theory. The particle eddy diffusivity used in this model needs to be orders of magnitude greater than the eddy viscosity for the model to perform well. As noted earlier, several researchers have advanced strong arguments that, over long time periods, the particle eddy diffusivity should be equal to the eddy viscosity.

2.5.4.d Turbophoretic models

Caporaloni *et al.* (1975) were the first investigators to recognize turbophoresis as a mechanism of particle transport. Turbophoresis was expected to be most important for transporting particles in regions very close to boundaries where turbulence is highly inhomogeneous. Caporaloni *et al.* suggest that the exclusion of turbophoresis from previous models is the reason that assumptions about free flight to the wall, allowing the particle to jump over the highly inhomogeneous but low intensity turbulence near the wall, were necessary to achieve agreement with the experimental data. They proposed a model accounting for turbophoresis, as well as Brownian and turbulent diffusion, which was based on a solution of the particle mass conservation equation:

$$J = -\left(D_B + \xi_p\right)\frac{d\overline{C}}{dy} + v_t\overline{C} \tag{2.105}$$

This equation is simply a restatement of equation (2.82) modified to account for particle flux due to a turbophoretic velocity. A simple method for calculating the turbophoretic velocity as a function of distance from the wall was provided and is repeated here

$$v_t = -\tau_p \frac{d\overline{v_{py}'^2}}{dy} \tag{2.106}$$

$$\overline{v_{py}'^2} = \left(\frac{a_o\tau_f + b_o^2}{a_o\tau_f + 1}\right)v'^2 \tag{2.107}$$

$$a_o = \frac{9\mu}{\left(2\rho_p + \rho_a\right)r_p^2} \tag{2.108}$$

$$b_o = \frac{3\rho_a}{2\rho_p + \rho_a} \tag{2.109}$$

$$\tau_f = \frac{\xi_a}{v'^2} \tag{2.110}$$

No specific correlation was suggested for the eddy viscosity, ξ_a, or for the fluid wall-normal velocity fluctuations, v', as a function of the distance from the wall; however, any of those presented in this review could reasonably be used. This model also ignored the particle radius in the boundary condition, thus neglecting the interception effect.

Guha (1997) and Young & Leeming (1997) both began with the particle mass *and* momentum conservation equations, performed Reynolds averaging and, through modest simplifying assumptions, arrived at a set of equations that could be simultaneously solved for particle deposition velocity. The two models are essentially the same, both building on ideas first put forth by Johansen (1991), but Guha developed the equations in Cartesian coordinates and Young & Leeming developed the equations in radial coordinates. The model published by Guha is described here and is representative of both models. The derivation of the equations lends more insight into the origin of the turbophoretic term than provided in Caporaloni *et al.* (1975). The dimensionless form of the particle mass conservation equation that Guha presents is

$$V_d^+ = -\left(\frac{D_B + \xi_p}{\nu}\right)\frac{\partial C^+}{\partial y^+} + v_{pcy}^+ C^+ - C^+ \frac{D_T}{\nu}\frac{\partial(\ln T)}{\partial y^+} \tag{2.111}$$

where v_{pcy}^+ is the dimensionless particle convective velocity in the y-direction (normal to the wall) and D_T is the temperature-gradient-dependent diffusion constant. The particle convective velocity in the second term on the right-hand-side (RHS) of equation (2.111) allows for differences between the particle velocity and the local fluid velocity. This

convective velocity may result from a turbophoretic force, but it may also arise from a lift force or an electrical force, and is thus more general than the second term on the RHS of equation (2.105), which is due solely to turbophoresis. The third term on the RHS of equation (2.111) allows for particle transport by thermophoresis.

A key advance made by Guha (1997) was the inclusion of the particle momentum equation to provide a rigorous means of calculating the particle convective velocity. The dimensionless forms of the x- and y-momentum equations, as presented in that work, are

$$x\text{-momentum:} \qquad v_{pcy}^{+}\frac{\partial v_{px}^{+}}{\partial y^{+}} = \frac{1}{\tau^{+}}\left(u^{+} - v_{px}^{+}\right) + g^{+} \tag{2.112}$$

$$y\text{-momentum:} \qquad v_{pcy}^{+}\frac{\partial v_{pcy}^{+}}{\partial y^{+}} + \frac{v_{pcy}^{+}}{\tau^{+}} = -\frac{\partial v_{py}^{+2}}{\partial y^{+}} + F_{l}^{+} + F_{e}^{+} \tag{2.113}$$

Here, u^{+} is the dimensionless axial fluid velocity, v_{px}^{+} is the dimensionless axial particle velocity and v_{py}^{+} is the dimensionless wall-normal particle velocity (equal to the sum of the dimensionless diffusive and convective velocities). The y-momentum equation allows for the inclusion of the lift force and an electrical force. The gravitational force is included as a positive term in the x-momentum equation here, indicating a vertically downward airflow. Depending on the orientation of the flow and the deposition surface, the term for gravity may have the opposite sign or be included in the y-momentum equation for accurate accounting of the force. The first term on the RHS of equation (2.113) has the same form as the turbophoretic term from Caporaloni *et al.* (1975) in equation (2.106). Guha presents a similar model as expressed in (2.107) to relate the fluctuating particle velocity to the local fluctuating velocity of the fluid

$$v_{py}'^2 = \left(\frac{1}{1+0.7(\tau_p/\tau_f)} \right) v'^2 \tag{2.114}$$

where τ_f is calculated by equation (2.110). This is a difficult quantity to represent because the particle velocity often may not directly relate to the local air velocity.

Guha adopted the simple relationship proposed by Wood (1981a) to account for both interception and surface roughness, thus the wall boundary condition for the particle mass conservation equation is evaluated at

$$y_o^+ = r_p^+ + k^+ - e^+ = r_p^+ + 0.45k^+ \tag{2.115}$$

This model assumes that the particle eddy diffusivity is equal to the eddy viscosity.

Application of this model requires simultaneous numerical solution of equations (2.111)-(2.113). This is a more difficult task than solution of the previously presented free-flight or gradient diffusion models, but current computing power allows for solution in just a few seconds of CPU time. Neglecting the lift force decouples equation (2.113) from equations (2.111) and (2.112) and allows for a somewhat easier solution of deposition velocities. This model is attractive because it is applicable in all deposition regimes and it offers the capability of including a variety of forces, including the turbophoretic force, which had not been rigorously applied in any previous Eulerian model. It also has flexibility regarding deposition to floor and ceiling surfaces.

To illustrate the importance of turbophoresis in determining the particle deposition rates, predictions from the model of Guha (1997) are plotted in Figure 2.27 while retaining and

excluding the particle convective velocity term in equation (2.111). In this model application, the deposition surface was vertical and smooth, and thermal, electrical and lift forces were ignored so that the only phenomenon contributing to the particle convective velocity was turbophoresis. The data of Liu & Agarwal (1974) are also shown in the figure. In the case when turbophoresis is ignored, equation (2.111) becomes nearly identical to the gradient diffusion model of Lai & Nazaroff (2000) and the model predicts low deposition velocities in the diffusion-impaction and inertia-moderated regimes. The inclusion of the turbophoretic term leads to the prediction of a dramatic increase in deposition velocity in the diffusion-impaction regime. A plateau and decrease in deposition as particle size increases through the inertia-moderated regime is also predicted. These trends are in much better agreement with the observed data than predictions from most other theoretically based models, but the agreement with the data is not perfect.

Figure 2.28 again compares the model of Guha (1997) to the experimental data of Liu & Agarwal (1974). In this case, the model was applied with three different deposition surface roughnesses of 0, 5 and 20 μm, corresponding to dimensionless roughness values of 0, 0.25 and 1.0. The model line for $k^+ = 0.25$ agrees well with the data across the entire range of particle sizes. More than one investigator has suggested that small amounts of surface roughness in the experiments of Liu & Agarwal led to measured deposition velocities that were slightly enhanced compared to those that would have occurred if the surface had been truly smooth (Wood, 1981a; Guha, 1997). However, a roughness of 5 μm is probably larger than the level that was present in these experiments.

Other modeling efforts with this type of model (Johansen, 1991) suggest that relatively small temperature gradients or the presence of an electric charge on the particles during the experiments of Liu & Agarwal could account for the discrepancy in deposition velocities between model and measurement at the smallest particle sizes studied.

Young & Leeming (1997) used their model to analyze predicted airborne particle concentration profiles near a vertical deposition surface. They found that particles in the diffusion-impaction regime were predicted to have a maximum in the concentration profile very near the wall. This finding is consistent with the accumulation of particles in the near-wall region predicted by many Lagrangian simulations (i.e. Brooke *et al.*, 1994). Turbophoretic models are the only Eulerian models that predict this near-wall accumulation of particles.

Turbophoretic models of the form presented in Guha (1997) and Young & Leeming (1997) are probably the Eulerian models that are best suited to predicting particle deposition in ventilation ducts. These models faithfully reproduce trends observed in experimental data and give reasonably good predictions of absolute deposition. Furthermore, these models are applicable across the entire size range of particles and they are physically satisfying, with only a small amount of empiricism. Such models can account for a wide variety of forces that may act on particles. They may be applied to both horizontal and vertical surfaces. They also show good agreement with deposition velocities and concentration profiles predicted by the best Lagrangian simulations, but at a much lower computational cost. These models are limited to application in fully

developed turbulent flow. Changes in deposition rates owing to the presence of flow disturbances and surface irregularities are not predicted by these models.

2.5.5 Sublayer models

Sublayer models use a Lagrangian scheme to calculate particle trajectories in the near-wall region of a flow and thereby predict particle deposition velocities. However, these models are different than fully Lagrangian simulations that calculate trajectories for large numbers of particles. In sublayer models, a single limiting trajectory in the near-wall region is determined for a particle that just impacts the surface. Predicted deposition velocities are based on the percentage of trajectories that would bring particles into closer contact with the wall than the limiting trajectory. These models are termed sublayer models because limiting particle trajectories are calculated only for the near-wall flow region, sometimes called the sublayer. Owen (1969) commented on the weaknesses of free-flight models and proposed '...that particles are convected to the wall from the region of energetic turbulent motion outside the viscous sublayer by the occasional large eddy that encroaches on it...'. This proposition was based on the then recent discovery of turbulent bursts, downsweeps and coherent structures in near-wall turbulence described by Kline *et al.* (1967).

Three groups of researchers have proposed sublayer models and all follow the same general scheme. The coherent near-wall turbulence described by Kline *et al.* (1967) and others is modeled as a two-dimensional, stagnation-point flow as described in Schlichting (1979). Figure 2.29 provides a schematic description of such flow in the y-z plane,

normal to the main flow direction. Flow is directed towards the wall near a centerline that passes through a stagnation point and is deflected away from the wall further from the stagnation point. As described earlier, these structures repeat at regular intervals with a typical spacing of approximately $\lambda_z^+ = 100$. The region outside that shown in the figure is assumed to have a uniform particle concentration. A particle entering the near-wall region from the well-mixed region is assumed to deposit to the wall if its initial spanwise location is closer to the centerline than the initial location of the limiting trajectory. Conversely, it is swept back up into the well-mixed core if the starting position is further from the centerline than the limiting trajectory. Trajectories are calculated by assuming an initial position and solving the particle equations of motion with the goal of determining the limiting particle trajectory. The limiting particle trajectory is defined as that trajectory which leads to the deposition of the particle at a distance of $\lambda_z/4$ from the centerline. A particle following the limiting trajectory and depositing on a smooth wall is shown in Figure 2.29. Once the limiting trajectory is determined, the dimensionless deposition velocity for inertial particles can be calculated from the initial spanwise particle location of this trajectory, z_{lim}, and the initial particle velocity towards the wall at this location, $v_{py,o}$, via

$$V_{d,inertial}^+ = \frac{2 z_{\lim}^+ v_{py,o}^+}{\lambda_z^+} \tag{2.116}$$

This approach of determining a critical trajectory to predict particle deposition rates is common in other applications, such as sedimentation basins for water and waste-water treatment, particle impactors and laminar flow electrostatic precipitators. For particles

where Brownian diffusion is significant, this method is invalid and a different approach that includes Brownian diffusion is necessary.

Cleaver & Yates (1975) were the first investigators to propose a mathematical form of a sublayer model for smooth surfaces. Their model assumed that the boundary between the turbulent core and the sublayer occurred at $y^+ = 10$ and particles were assumed to enter the sublayer with an initial dimensionless velocity, $v^+_{py,o}$, of 0.5. In the particle momentum equations used to calculate the limiting trajectory, the drag force was assumed to be the only force acting on the particle. Cleaver & Yates applied their model with two different sublayer flow models, the two-dimensional stagnation flow model described above and a flow model based on the experimental data of Laufer (1954). They found little difference between the model predictions. The model was found to predict deposition velocities lower than measured in experiments and it was modified to account for axial convection into regions with flow towards the wall. The manifestation of this modification was an *ad hoc* factor to improve the model-measurement agreement and it has weak theoretical support. Cleaver & Yates performed a separate analysis for deposition of particles when Brownian diffusion is important. They solved the diffusion equation for stagnation point flow and, through some simplifying assumptions, arrived at this expression for diffusional deposition velocity:

$$V^+_{d,diff} = 0.084 \mathrm{Sc}^{-2/3} \tag{2.117}$$

This expression has the same form as the empirical equation (2.52) for the diffusive deposition regime. Cleaver & Yates suggested that the deposition velocity of all particles could be predicted by adding the inertial and diffusive components of deposition:

$$V_d^+ = V_{d,inertial}^+ + V_{d,diff}^+ \qquad (2.118)$$

One of the results reported by this modeling effort was the influence of the particle to fluid density ratio on deposition velocities when plotted in the form of V_d^+ versus τ^+. This has repeatedly been proven in subsequent investigations, and it is believed that Cleaver & Yates were the first to recognize the importance of this density ratio.

Fichman *et al.* (1988) proposed a sublayer model with particle momentum equations that included both drag and the shear-induced lift force. The sublayer-turbulent core boundary was assumed to be at y^+=30 and the initial dimensionless particle velocity was taken as 0.8. Correlations were developed to model the two-dimensional stagnation flow. Fichman *et al.* found good agreement between their model and experimental data and they attributed the improvement over previous models to the inclusion of the lift force. The lift force was noted to be especially important for particles in the diffusion-impaction regime very close to the wall ($y^+ < 10$). Application of the model in this review is made impractical owing to what seem to be errors in the reporting of constants used in the solution of the particle momentum equations. The same difficulty with this model has been reported by Fan & Ahmadi (1993).

The most well-developed sublayer model in the literature is that of Fan & Ahmadi (1993), which includes drag, shear-induced lift and gravitational forces in the particle momentum equations. The boundary condition for a deposited particle was modified to account for surface roughness following the method of Browne (1974) (equations (2.92-2.94)). In this model, the interface between the turbulent core and the sublayer was

assumed to occur at $y^+ = 12$ and the initial dimensionless particle velocity upon entering the sublayer was assumed to be 0.7. This value of $v^+_{py,o}$ is somewhat higher than experimentally measured values at this distance from the wall (0.3-0.5), and the higher value was rationalized by the fact that particles near the centerline of a downsweep will tend to have a higher wall-normal velocity than the time-averaged value over all locations. The sublayer flow was approximated using the model presented in Schlichting (1979). Fan & Ahmadi adopted the method of Cleaver & Yates (1975) for particles with significant rates of Brownian diffusion; accordingly, the total deposition velocity was calculated using equations (2.116)-(2.118).

The model of Fan & Ahmadi (1993) is compared to the experiments of Liu & Agarwal (1974) in Figure 2.30. The model for deposition to a vertical wall is applied assuming three different values for the surface roughness, 0, 5 and 20 μm, corresponding to values of k^+ of 0, 0.25 and 1.0. The model predicts the general shape of the data reasonably well, although for deposition to the smooth surface in the range of $1 < \tau^+ < 10$, it predicts an increase in deposition velocity that is sharper than observed experimentally. In the diffusion-impaction regime the model for the smooth surface underpredicts deposition for $\tau^+ < 4$ and overpredicts for $\tau^+ > 4$. The inaccurate sharpness of the model may derive from representing the turbulence structure as uniform based on its mean properties, rather than variable with a distribution of properties. If deposition is more strongly influenced by turbulence events that are more intense than the average, models that are based on mean turbulence properties will give unreliable predictions. Deposition velocities are predicted to increase dramatically in the diffusion and diffusion-impaction regimes with

increases in surface roughness. Again, as observed in previous models, small amounts of roughness buried in the laminar sublayer are predicted to strongly enhance deposition rates. This consistent modeling outcome for different types of models could be anticipated since the method of accounting for the surface roughness in all the models is nearly identical.

Fan & Ahmadi (1993) also provide an empirical expression based on a perturbation solution that closely reproduces the deposition predictions of the full sublayer model, including the effects of surface roughness and shear-induced lift. Fan & Ahmadi (1994) and Fan & Ahmadi (1995), respectively, extended their sublayer model to account for electrical fields and nonspherical particles.

Sublayer models are not fully Lagrangian models; a small number of trajectories of a given sized particle are calculated until the limiting particle trajectory is found. Because deposition velocities are calculated based on the limiting particle trajectory and not on statistics of a large ensemble of particles, the computational requirements are significantly lower than fully Lagrangian models and sublayer models may be solved in just a few seconds of CPU time with current computational power. These models attempt to capture the interaction between particles and near-wall turbulent eddies that impinge on the deposition surface. From investigations of the near-wall turbulence structure and Lagrangian simulations of particle deposition, these eddies are believed to play a key role in the deposition of particles, especially those in the diffusion-impaction regime. Sublayer models reasonably predict deposition trends and magnitude observed in

experiments with physically satisfying assumptions. The sublayer model of Fan & Ahmadi (1993) is the most appropriate model of this type for application to the case of particle deposition in ventilation ducts.

2.5.6 Lagrangian simulations

The general approach to investigating particle deposition in turbulent flow by Lagrangian simulation involves two steps. First, the flow field is mathematically described, and second, particles are released into the simulated flow and trajectories are tracked based on the prescribed equations of particle motion. It is usually assumed that the presence of particles in the fluid does not affect the structure of the turbulent flow. This assumption is termed the one-way coupling assumption, referring to the fact that the fluid affects the particle momentum, but the particles do not influence the momentum of the fluid. This assumption is reasonable when the mass concentration of suspended particles is very much smaller than the air density, as would be true in ventilation ducts. Lagrangian models discussed here are grouped by the method used for generating the turbulent flow field. Those using simple stochastic turbulence models are discussed first, followed by simulations that use LES and DNS to generate the turbulent flow.

2.5.6.a Lagrangian simulations with stochastically modeled turbulent flow

A summary of the flow conditions and assumptions used in the Lagrangian simulations discussed in this section is given in Table 2.13. The earliest works in this area (those of Hutchinson *et al.*, 1971 and Reeks & Skyrme, 1976) are not included in Table 2.13. These early works were developed as predictive models to be applied to a variety of

conditions. They comprised composites of Lagrangian simulations and Eulerian models and were not 'numerical experiments' of the type represented by more recent Lagrangian simulations.

It should be noted that turbulent diffusion and turbophoresis do not appear in the 'Forces' column of Table 2.13. These phenomena must be included in Eulerian models to capture the interactions between particles and turbulent eddies; in Lagrangian simulations, these particle-eddy interactions are directly calculated. Thus, particle drift owing to turbulent diffusion and turbophoresis are captured to some degree in all Lagrangian simulations.

The first particle deposition model to incorporate a Lagrangian framework (Hutchinson *et al.*, 1971) was crude relative to current Lagrangian simulations. This model was divided into two sections: a Lagrangian random walk trajectory in the plane normal to the main flow was calculated to determine the fraction of particles that approach a stagnant wall layer and then an Eulerian calculation, similar in concept to the free-flight models, was used to calculate the fraction of those particles approaching the wall layer that actually traverse the layer and deposit. When multiplied together, these two fractions yield the fraction of the total particles in the system that deposit. The stagnant wall layer was assumed to have a thickness of $y^+ = 1.25$ to best fit the experimental data.

Hutchinson *et al.* (1971) assumed that steps taken in the random walk were the result of interactions with large, energy-containing turbulent eddies and only the drag force was taken into account. Relationships for the length and time scales associated with these

eddies were taken from the work of Townsend (1956) and Laufer (1954). The direction of each step was randomly assigned; thus, the likely correlation between successive steps in time was ignored. The fraction of particles approaching the stagnant wall layer that actually deposit was determined by integrating the particle velocity density distribution function over all possible initial particle velocities and approach angles to determine the fraction of particles of that size with sufficient inertia to reach the wall by free flight. Reasonable agreement with the available data was reported in this work; however, the wall-layer thickness was empirically adjusted to achieve the best fit to the data.

Reeks & Skyrme (1976) followed the same procedure outlined in Hutchinson *et al.* (1971). However, instead of solving for a random-walk trajectory to determine the fraction of particles approaching the stagnant wall region, the particle flux toward the wall region was obtained through integration of the particle velocity distribution function that was assumed to be jointly normal. Calculation of the fraction of these particles approaching the wall that actually deposit was carried out as in Hutchinson *et al.*, except that the stagnant wall layer was assumed to begin at a distance from the wall of $y^+ = 5$, instead of $y^+ = 1.25$. The model of Reeks & Skyrme was developed for large particles in the inertia-moderated regime and at the high end of the diffusion-impaction regime. It predicts an extremely rapid increase in deposition velocity as particle size increases through the diffusion-impaction regime, one that is much larger than observed experimentally or predicted by any other model. The model does successfully predict deposition velocity magnitudes and trends in the inertia-moderated regime, but this

agreement with the experimental data was facilitated by the empirical adjustment of two model parameters.

The first fully Lagrangian simulation of particle deposition from turbulent flow is presented by Kallio & Reeks (1989). In this study, and in those that have followed, the deposition velocity of a given sized particle is determined from the calculated trajectories of thousands of particles. The turbulent flow in this work was modeled as a two-dimensional random velocity field. Profiles of mean and fluctuating air velocities were fit to the experimental results of Laufer (1954) and others. Particle trajectories were determined from repeated interactions with discrete turbulent eddies. Each turbulent eddy was assumed to have a random wall-normal velocity component drawn from a Gaussian distribution and a random time scale drawn from an exponential distribution. Particles were assumed to interact with eddies for a length of time equal to the eddy time scale. The particle momentum equations included the lift force. The lift force was not included in some simulations so that its influence on deposition could be evaluated.

The results of the simulation of Kallio & Reeks (1989) are plotted along with the data of Liu & Agarwal (1974) in Figure 2.31. Details such as the air velocity and the duct diameter for the simulated flow were not reported by Kallio & Reeks. This relatively simple simulation agrees well with the experimental data on several points. The magnitudes of deposition velocities and the slopes of the deposition curve in the diffusion-impaction regime are similar in both cases. The decrease in deposition at high values of τ^+ observed in experiments is also observed in the simulation. This simulation

also suggests that the lift force is most important for particles with dimensionless relaxation times in the range $1 < \tau^+ < 20$. However, the authors caution that the effect of the lift force is only approximate, because the restrictions on the equation for lift force derived by Saffman (1965, 1968) were frequently violated and because the equation is not strictly applicable near a wall. Another observation in this simulation was the accumulation of particles in the diffusion-impaction regime near the vertical wall, in the region $0.1 < y^+ < 3$. This increase in the particle concentration profile near the wall is similar to that predicted by means of the turbophoretic model of Young & Leeming (1997).

Li & Ahmadi (1993a) performed a particle deposition simulation where, using the method of Ounis *et al.* (1991), Brownian diffusion was simulated as a Gaussian white-noise process. The particle momentum equations also included the effects of drag, lift and gravity. The turbulent velocity field was generated from a Gaussian random field that was modified to account for the anisotropic nature of the turbulence near the wall. This simulation allowed particles striking the wall to either deposit or to bounce depending on the energy of the particle-surface collision. Particles striking the surface with a velocity greater than a critical velocity bounced, while those with a lesser velocity deposited. The critical velocity was defined by

$$v_{p,crit} = \sqrt{\frac{2E_o}{m_p}\left(\frac{1-r^2}{r^2}\right)} \tag{2.119}$$

where m_p is the particle mass, r is the restitution coefficient and E_o is the potential energy of the surface. The restitution coefficient ranges from zero to one, with a value of one indicating a perfectly reflecting surface. The surface potential energy was calculated by

$$E_o = \frac{A_H d_p}{12 y_e} \tag{2.120}$$

where y_e is the equilibrium separation between a particle and a surface (recommended to be 0.4 nm) and A_H is the material dependent Hamaker constant for the particle-surface interaction (on the order of 10^{-19} J).

Li & Ahmadi (1993a) performed simulations in 2 cm wide vertical and horizontal channels with an air velocity of 5 m/s and a friction velocity of 30 cm/s. Results for particles of two different densities depositing to a vertical wall are displayed in Figure 2.32 along with Liu & Agarwal's (1974) data. The results from the simulation lie somewhat below the experimental data for both particle densities. This simulation does capture the shape of the deposition curve seen in experiments across the entire range of particle sizes, even in the diffusion regime. Only a small difference is observed for particles of different densities.

Figure 2.33 shows the results of Li & Ahmadi's (1993a) simulation of deposition to a horizontal floor. Simulated deposition rates to the floor are much greater than those to the vertical wall owing to the effects of gravitational settling. The results compare favorably with the experimental findings of Sehmel (1973) who collected experimental data at a similar friction velocity of 34.1 cm/s. The simulation results for all but the

smallest particles lie just above the line representing the expected deposition velocity if gravitational settling were the only particle transport mechanism. As observed in other Lagrangian simulations and as predicted by turbophoretic models, an accumulation of particles in the diffusion-impaction regime very close to the vertical wall was observed in this simulation. Such a concentration profile was not observed in the case of the horizontal floor surface owing to the influence of gravity.

Li & Ahmadi (1993a) also simulated deposition in cases where particles were allowed to bounce after impact depending on the energy of the collision. The results of these investigations, shown in Figure 2.34, suggest that particle bouncing upon wall impact was only important for $\tau^+ > 10$, (i.e., for particles in the inertia-moderated regime). Particles where bounce was important had diameters of 30 μm or larger.

Li & Ahmadi (1993b) used the same procedure as Li & Ahmadi (1993a) to investigate the role of surface roughness in particle deposition to vertical walls and horizontal floors. In this case, the condition for particle deposition was modified for rough surfaces by the method described in Wood (1981a) (equation (2.95)) and particle bounce was ignored. To my knowledge, this is the only Lagrangian simulation of particle deposition to include surface roughness. Results of simulations considering deposition to a vertical wall with four different surface roughness values are shown along with the experimental data of El-Shobokshy (1983) in Figure 2.35. In this simulation, increasing surface roughness dramatically increased deposition for smaller particles, and the effect decreases as particle size increased. These are the same trends seen in the data of El-Shobokshy and

predicted by all Eulerian models that account for roughness. This simulation yields lower values of deposition velocity than the experimental data, similar to most Eulerian models. As in previous simulations with smooth vertical walls, an accumulation of particles in the diffusion-impaction regime was observed in the near-wall region of the rough vertical walls, although the effect was less dramatic in the rough wall case. Simulation results for deposition to rough horizontal floors are shown in Figure 2.36. The impact of roughness on deposition velocity is much less here than in the vertical wall simulation. No difference in deposition velocity is seen for particles with $\tau^+ > 0.1$ because gravitational settling is the dominant deposition mechanism in this case and it is relatively unaffected by changes in surface roughness.

Li *et al.* (1994) used a similar method as in Li & Ahmadi (1993a) to examine deposition in a channel at a 12.5 mm wide (streamwise) by 6.1 mm tall rectangular obstruction and for a more streamlined trapezoidal obstruction of similar dimensions. Deposition to the three exposed faces of the obstructions was evaluated and the presence of the obstructions was found to significantly enhance particle deposition, especially for larger particles, owing to impaction. The upstream face of the obstructions experienced the greatest amount of deposition and the enhancement in deposition compared to that on the flat channel surface was less for the more streamlined trapezoidal obstruction. While the results of this work are not directly comparable to other experiments or models, they are an indication of the importance of flow obstructions in enhancing deposition.

Chen & Ahmadi (1997) performed Lagrangian simulations following a procedure similar to Li & Ahmadi (1993a). Transport from turbulence interactions, Brownian diffusion, gravitational settling and lift were all included. In this case, however, the flow configuration was a pipe instead of a channel and the optimum lift force recommended by McLaughlin (1993) was implemented. Because the lift force depends on the difference between the particle and fluid axial velocities, it has been argued (Fan & Ahmadi, 1993) that the direction of flow in a vertical system could affect particle deposition velocities through the lift force. An upward flow scheme should cause the particle to lag the fluid in the axial direction, leading to a lift force away from the wall and reducing deposition, while a downward flow scheme should have the opposite effect. A goal of these simulations was to evaluate the magnitude of this effect. Figure 2.37 shows the results of the simulations of Chen & Ahmadi for two cases of downward flow, one in the absence of gravity and one including gravity, which should increase the magnitude of the lift force. The difference between the two cases is largest for $1 < \tau^+ < 10$, but the difference is less than other models and simulations have predicted. The authors attribute the lesser effect observed in their simulation to the use of optimum lift force, which is smaller than the lift force applied in most other models calculated by equation (2.38).

2.5.6.b Lagrangian simulations with turbulent flow from LES and DNS

Table 2.14 summarizes the conditions and assumptions made in the Lagrangian particle simulations discussed in this section. Lagrangian simulations provide details of particle trajectories that allow for the extraction of a wealth of information on their behavior in turbulent flows. Not all the simulations included in Table 2.14 are directly concerned

with particle deposition, but all provide information on the behavior of particles in air turbulence that gives insight into the particle deposition process. Values in the table are both as presented in the cited articles and as I have calculated. In cases of a channel flow configuration, D_h refers to the full height of the channel. Frequently, authors of these studies report channel heights in dimensionless units without reference to a friction velocity for converting to a height with dimensions. As a final introductory note, in studies that allowed for the lift force and gravity, these forces were not included in every simulation; commonly, the authors would run identical simulations with and without one of these forces to illustrate the effect of that force on particle deposition.

The first Lagrangian simulation of particle deposition using a flow field generated by DNS was that of McLaughlin (1989) who studied the deposition of particles with values of τ^+ in the range 2-6 in a simulated vertical channel flow with Re = 4000. This pioneering work yielded deposition velocities similar to those measured by experiment, as illustrated in Figure 2.38. McLaughlin introduced several new ideas that were expanded upon by subsequent investigators. In particular, McLaughlin concluded that particles were brought to the wall by strong, well-organized fluid motions. An accumulation of particles in the diffusion-impaction regime near the wall ($y^+ < 5$) was identified such that the concentration near the wall was about twice the core concentration. Particle velocities were observed to lag the fluid velocities in both the streamwise and wall-normal directions in the turbulent core, but to lead the fluid in both directions very near the wall. Depositing particles impacted the wall with normal velocities on the order of $0.5u^*$, suggesting an inertial deposition mechanism rather than a

diffusive one. Also noted was the potential importance of the lift force on the particle trajectory in the near-wall region. McLaughlin suggested that the main limitations of this simulation were associated with the particle momentum equation. The particle Reynolds number conditions for both the Stokes drag force and the lift force were violated by the particles in the simulations. Deposition velocities from this simulation agreed well with the experimental data over the limited range of dimensionless relaxation times studied; furthermore, this work provided information on particle Reynolds numbers, particle velocities and near wall particle concentrations that were unattainable by experiment or previous Eulerian modeling.

Ounis *et al.* (1991) made a significant advance in Lagrangian simulations when they included a method to account for particle transport by Brownian diffusion. Ounis *et al.* (1991) and Ounis *et al.* (1993) simulated the motion of 0.01–0.1 μm particles in the near-wall region of a DNS-generated flow by implementing a Gaussian white-noise process for the Brownian force. These simulations indicate that Brownian motion significantly affects behavior near the wall for particle with diameters less than 0.05 μm and that turbulence significantly affects deposition rates of particles with diameters larger than 0.03 μm. Of particular note in this simulation was that the initial locations of depositing particles that were not affected by Brownian motion were concentrated in bands where coherent vortices form strong streams toward the wall. These bands in initial particle location were separated by 100–150 wall units and corresponded to locations where near-wall vortices caused strong flows towards the wall. This is strong evidence that these vortices are responsible for the deposition of inertial particles. For particles strongly

influenced by Brownian diffusion, no such patterns in initial location were observed for depositing particles. The resulting deposition velocities of these 0.01–0.1 μm particles from Ounis *et al.* (1993) are compared to the empirical equation (2.52) with $k_1 = 0.084$ for particles in the diffusion regime in Figure 2.39. Note that limits of the relaxation time in this figure are different than in most others in this chapter, the low relaxation times in this study are the result of the small particle sizes and the low friction velocity, 3.7 cm/s. The simulation results are in close agreement with the empirical equation.

Brooke *et al.* (1992) and Brooke *et al.* (1994) conducted Lagrangian particle tracking in a DNS-generated vertical channel flow with particles in the diffusion-impaction regime considering only the drag force. The paper by Brooke *et al.* (1992) contains observations similar to those reported in other simulation work. These include the accumulation of particles in the diffusion-impaction regime near the vertical wall and their segregation into the low-speed streaks, the violation of the particle Reynolds number criteria for drag calculation, the importance of near-wall vortices in causing particle deposition and impact velocities of depositing particles on the same order as the friction velocity. While these high impact velocities were consistent with the high initial free-flight velocities required in free-flight theories, turbophoresis, and not turbulent diffusion, was suggested as the mechanism by which particle arrive at their capture distance. Brooke *et al.* (1994) took a detailed look at particle velocities in the near-wall region and found that a small fraction, defined as free-flight particles, had a velocity much greater than, and disengaged from, the local fluid velocity. Particles with velocities similar to the local fluid velocity were defined as entrained particles. Free flight was determined to be significant only

near the wall ($y^+ < 20$) and these free-flight particles were much more likely to deposit than entrained particles. The most likely distance from which a depositing particle would begin free flight to the wall was found to be $y^+ \sim$ 7-9, regardless of the relaxation time. This location corresponded to an inflection point in the profile of the root-mean-square of the wall-normal air velocity fluctuations in this simulation. The turbophoretic force would be expected to be appreciable at this location owing to the steep gradient in turbulence intensity. Brooke *et al.* (1994) also analyzed trajectories of particles released very near the wall, at $y^+ < 3$. These particles rarely deposited and, when they did, they usually first escaped the near-wall region and initiated a free flight to the wall from a greater distance.

Chen & McLaughlin (1995) performed a simulation in a DNS-generated vertical-channel flow using a particle equation of motion with the wall-corrected drag force and the optimum lift force. Extremely large accumulations of particles in the diffusion-impaction regime were observed for $y^+ < 1$; a value of $C^+ = 250$ was observed for particles with $\tau^+ =$ 10 in this near-wall region. Deposition velocities from this simulation are less than those from the experiments of Liu & Agarwal (1974) as seen in Figure 2.40. Deposition rates in this simulation are lower than observed in other numerical simulations, possibly due to the decreased lift force and increased drag force near the wall. Chen & McLaughlin developed an empirical fit to their simulation results to study the effects of particle polydispersity on deposition rates. They suggested that very small amounts of polydispersity can lead to large changes in measured deposition rates in experiments. Polydispersity of aerosols is cited as a likely cause of the wide scatter in experiments.

Wang & Squires (1996a) and Wang & Squires (1996b) demonstrated the feasibility of particle simulations in LES-generated channel flows. Because of the enormous computational intensity required, DNS is limited to low flow Reynolds numbers and short simulation times. The LES method was used to increase the Reynolds numbers in simulations and to simulate particles with long relaxation times that are currently not amenable to analysis by DNS. These advantages in LES are achieved by the less accurate accounting of small-scale near-wall turbulent eddies. Wang & Squires (1996a) observed similar particle velocity statistics and particle concentration profiles in simulations in flows generated by LES and DNS. As seen in simulations using DNS, particles in the diffusion-impaction regime accumulating near the wall were found to segregate preferentially in the low-speed, low-vorticity streaks. Wang & Squires (1996b) compared particle simulations in an LES-generated vertical-channel flow at Reynolds numbers of 11,160 and 79,400 to the DNS results of McLaughlin (1989). The comparison of LES and DNS was favorable and features of particle behavior commonly observed in simulations with DNS were also observed in this LES. The LES results deviated most from the DNS results for smaller particles that are most sensitive to the smallest eddies, which are modeled approximately in LES but are completely resolved in DNS. The deposition profile from the simulation of Wang & Squires (1996b) at Re = 11,160 is shown in Figure 2.41 for cases where the lift force was either included or excluded. The results of this simulation agree well with the experimental data, and with previous DNS results (Figure 2.38). Both simulations predicted a steeper increase in V_d^+ with τ^+ in the diffusion-impaction regime than has been observed experimentally, but the

magnitude of deposition in the simulations is in accord with experiments. Almost no difference was seen in this deposition profile when the Reynolds number was increased from 11,160 to 79,400. In general, these works showed LES to be a useful tool in analyzing particle deposition in larger Reynolds number flows and for larger values of τ^+ than currently can be simulated by DNS.

Uijttewaal & Oliemans (1996) performed simulations of particles in the inertia-moderated regime in vertical cylindrical-tube flows generated by both DNS and LES. DNS was used to generate a flow with Re = 5300, and LES was used to generate flows with Reynolds numbers of 18,300 and 42,000. Due to the large particle sizes in these simulations, the Stokes drag force was modified to account for large particle Reynolds numbers. Many of the results commonly reported in DNS particle transport simulations were observed in these LES simulations: an accumulation of particles in the near-wall region in the diffusion-impaction regime; and large particle Reynolds numbers and large impact velocities when depositing to a wall, suggesting a nondiffusive deposition mechanism. Deposition velocities of particles in these simulations are compared to the experiments of Liu & Agarwal (1974) in Figure 2.42. Note that Figure 2.42 extends further into the inertia-moderated regime than most figures presented in this review. The simulation results match those of the experiments in absolute magnitude and in the trend of decreasing deposition velocity with increasing particle size in the inertia-moderated regime. Simulated deposition velocities increased with increasing Reynolds number at the highest relaxation times. Because these particles are so large, their motion is not significantly influenced by flows in the near-wall region. Instead it is dominated by

larger eddies in the turbulent core that scale with the Reynolds number. While concentration profiles of particles in the diffusion-impaction regime showed a near-wall accumulation of particles, no such accumulation was observed for particles in the inertia-moderated regime.

Wang *et al.* (1997) calculated trajectories incorporating the optimum lift force in the particle equations of motion in the same LES channel flows described in Wang & Squires (1996b). Figure 2.43 displays the results. Deposition velocities when including optimum lift were higher than when lift was ignored, and this effect was greatest for $2 < \tau^+ < 20$. As noted in other simulations, the influence of the lift force was less when calculated as the optimum lift force (Wang & Squires, 1996b). Very little difference was observed for the deposition velocities at two different Reynolds numbers (11,160 and 79,400). The deposition velocities in these simulations are less than measurements of Liu & Agarwal (1974). The slope of the V_d^+ versus τ^+ curve is in better agreement with the experimentally observed slope in simulations with the optimum lift than in simulations using the unmodified lift force equations (Wang & Squires, 1996b).

Zhang & Ahmadi (2000) analyzed particle deposition to vertical walls and horizontal floors in a DNS-generated channel flow. This investigation mainly focused on differences in deposition between upward vertical flow and downward vertical flow owing to changes in the lift force; however, the study is unique in that it is the only DNS-Lagrangian simulation that includes deposition to a floor. By noting that the initial locations of depositing particles are concentrated in bands, this work also clearly

reemphasized that particle deposition to vertical surfaces in the diffusion-impaction regime is associated with high speed downsweeps of fluid periodically spaced in the spanwise direction by about 100 dimensionless units. The same effect was not observed for very small particles where Brownian diffusion is important or for particles depositing to the horizontal floor surface because of the effect of gravity. Deposition velocities from the simulations of Zhang & Ahmadi are presented in Figures 2.44-2.46. Figure 2.44 dramatically demonstrates the effect of the lift force in flows with low friction velocities of 3 and 10 cm/s. In this figure, deposition rates to the vertical wall in the horizontal flow are much lower than those in the vertical downward flow. In the vertical downward flow, the lift force is directed towards the wall. In the horizontal flow, the lift force was neglected. Furthermore, the increase in deposition in the downward flow is much greater for the smaller friction velocity. This reason for this is that gravitational settling leads to a larger slip velocity and, thus, larger lift force in the lower air velocity case. The simulation results from the vertical flows exhibit much higher deposition velocities than the experimental data. At least in part, this difference can be attributed to the experiments being conducted at far greater friction velocities.

Figure 2.45 shows simulation results from Zhang & Ahmadi (2000) comparing vertical upward flow to vertical downward flow at a higher friction velocity of 30 cm/s. Deposition velocities in these two cases are nearly identical and the flow direction has little impact on the magnitude of the lift force or the deposition velocity at this higher friction velocity. This simulation suggests that the direction of flow is only important for very small friction velocities, less than about 10 cm/s. This result should be taken with

caution considering that the equation used for lift in this simulation has been shown to overpredict the magnitude of the force (Wang *et al.*, 1997).

Simulated deposition rates to the horizontal floor at two friction velocities from Zhang & Ahmadi (2000) are presented with the comparable experimental data of Sehmel (1973) in Figure 2.46. The primary deposition mechanism in this case is gravitational settling and excellent agreement between the simulations and the experiments is observed. As observed in experiments, dimensionless deposition velocities to floors are much higher than those to vertical surfaces in these simulations and they are highly dependent on the magnitude of the friction velocity.

Lagrangian simulations of particles in turbulent airflows have provided much information regarding particle deposition to surfaces and particle-turbulence interactions. Because individual particle trajectories are calculated in Lagrangian simulations, details of particle motion are accessible that are unattainable by experiment. For particles in the diffusion-impaction regime depositing to vertical walls, temporal deposition patterns and high wall-impact velocities illustrate the importance of near-wall turbulent vortices in influencing particle deposition. Accumulation of particles in the diffusion-impaction regime near vertical walls has also been frequently observed in Lagrangian simulations.

Figure 2.47 displays deposition velocities from several Lagrangian simulations for particles depositing to smooth vertical surfaces in cases where the lift force was both neglected and included. The diffusion, diffusion-impaction and inertia-moderated

particle deposition regimes seen in the experimental data in Figure 2.1 are evident in Figure 2.47. The data from Lagrangian simulations are less scattered than the experimental data, but significant scatter is present in the simulation results. In the simulations, there are no errors involved in determining particle size or deposition fluxes and this undoubtedly helps to reduce the scatter compared to physical experiments. Changes in factors like particle density, friction velocity (especially at low values of friction velocity) and the method of accounting for forces acting on the particles are most likely to contribute to the spread in the results observed in Figure 2.47.

Lagrangian simulations of particle deposition to floors have also demonstrated good agreement with experiments; however, no simulations have been performed analyzing deposition to a ceiling. Investigations of particle deposition to rough surfaces by Lagrangian simulations have been limited. The work that has been done suggests similar trends as observed in Eulerian models and experiments in the case of vertical walls. Roughness had a lesser effect in simulations on deposition to a floor. In sum, Lagrangian simulations have proven extremely useful for investigating the behavior of particles in turbulent airflows, but their usefulness as tools for predicting particle deposition from a given flow is constrained by high computational cost and time.

2.5.7 Empirical equations for particle deposition in duct bends

Most studies of particle deposition in bends have been conducted in laminar flow. Only two models to predict deposition from turbulent flow in bends have been published. Both report empirical equations to calculate particle penetration through a bend. The model of

Pui *et al.* (1987) is a fit to experimental data and the model of McFarland *et al.* (1997) is a fit to the results of simple Lagrangian simulations.

Pui *et al.* (1987) measured particle penetration through 90° bends in 0.50-0.85 cm diameter tubes and found that the best correlation to their experimental data was given by

$$P_{bend} = \frac{C_{outlet}}{C_{inlet}} = 10^{-0.963\mathrm{St}} \tag{2.121}$$

The form of this equation was supported by arguments from turbulent mixing theory.

McFarland *et al.* (1997) performed experiments and Lagrangian simulations to investigate particle penetration through 45-180° bends in 1.6 cm diameter tubes. Only the results of the Lagrangian simulations were used to develop the following empirical equation for predicting particle penetration through bends:

$$\ln P_{bend} = \frac{4.61 + a\theta\mathrm{St}}{1 + b\theta\mathrm{St} + c\theta\mathrm{St}^2 + d\theta^2\mathrm{St}} - 4.61 \tag{2.122}$$

$$a = -0.9526 - 0.05686R_o \tag{2.123}$$

$$b = \frac{-0.297 - 0.0174R_o}{1 - 0.07R_o + 0.0171R_o^2} \tag{2.124}$$

$$c = -0.306 + \frac{1.895}{\sqrt{R_o}} - \frac{2.0}{R_o} \tag{2.125}$$

$$d = \frac{0.131 - 0.0132R_o + 0.000383R_o^2}{1 - 0.129R_o + 0.0136R_o^2} \tag{2.126}$$

Here, θ is the bend angle in radians and R_o is the bend ratio defined in equation (2.18). Note also that the equation for parameter d presented in McFarland *et al.* has a minor

error that is corrected in equation (2.126). Because the model proposed by McFarland *et al.* is able to account for a variety of bend angles and bend ratios, it is somewhat more flexible than the equation of Pui *et al.* which was validated only for 90° bends with a single bend radius of 5.7. Neither of these bend-penetration models account for changes in the bend orientation with respect to the direction of gravitational acceleration.

A comparison of the two bend-penetration models is given in Figure 2.48. The models are applied to the case of a 90° bend in a 15-cm diameter duct with an average air speed of 5 m/s. Both models predict nearly complete penetration of the smallest particles and nearly complete deposition in the bend for the largest particles. For intermediate sized particles, the model of Pui *et al.* predicts lower values of particle penetration than the model of McFarland *et al.* There are no experimental data to evaluate these models when the bends have diameters similar to those in HVAC systems.

Duct bends in HVAC systems may be oriented in a variety of ways and these different orientations are likely to influence the deposition of some particles within the bends. For example, owing to the influence of gravity, a bend that directs a horizontal flow vertically upwards will likely have different particle deposition characteristics than a bend that directs a horizontal flow to flow vertically downwards. Such effects have not been investigated by theory or experiment. We are also unaware of any reports investigating the influence of surface roughness on particle deposition within bends.

2.5.8 Summary of methods for predicting particle deposition rates

Airflows through ventilation ducts of commercial buildings are turbulent and span a range of air velocities and flow types. Ventilation ducts vary widely in terms of material, size, cleanliness and internal roughness. Models to predict particle deposition in ventilation ducts should be applicable to the broad range of flow conditions and surface characteristics in HVAC systems and should be able to account for variations in particle size and density.

A variety of techniques for predicting particle deposition from turbulent flows have been presented, ranging in complexity from empirical equations to DNS-based Lagrangian simulations. Empirical equations are based on fits to experimental data using equation forms that may or may not have a theoretical foundation. Theoretically based models and simulations have generally been found to underpredict deposition rates compared to experimental measurements.

Empirical equations are simple to use and show good agreement with data from physical experiments and Lagrangian simulations. The main drawbacks of empirical equations are that they offer little insight into particle deposition mechanisms and that their applicability to flows different from those for which they were developed is uncertain. In addition, it is not possible to account for surface roughness in most cases when using empirical equations. Despite these limitations, empirical equations can provide quick estimates of particle deposition velocities, even in cases where thermal gradients or electric fields exist. Among the methods, equations (2.52)-(2.54) along with equations

(2.71)-(2.74) are likely to yield reasonable predictions for particle deposition to smooth vertical and horizontal surfaces across all deposition regimes.

Eulerian models include gradient diffusion models, free-flight models and turbophoretic models. Gradient diffusion models have been determined to be inappropriate for the high air velocities and friction velocities typical in HVAC ducts. Experiments and Lagrangian simulations suggest that mechanisms other than Brownian and turbulent diffusion are responsible for the deposition of particles outside of the diffusion regime. These other mechanisms are not taken into account in gradient diffusion models. Free-flight models allow for a free-flight deposition mechanism similar to what is observed in Lagrangian simulations. However, the method of accounting for free flight is crude and free-flight models are based on somewhat unsatisfying and sometimes contradictory assumptions. Most free-flight models rely on empiricism to achieve agreement with experimental data, and those that do not (e.g., Davies, 1966b) substantially underpredict most experimental data. The model of El-Shobokshy & Ismail (1980) is the recommended free-flight model for application in HVAC ducts. This model is highly empirical, but it achieves good agreement with experiments and simulations for both smooth and rough vertical surfaces. A limitation of all free-flight models is that they are not applicable to horizontal surfaces. The turbophoretic models of Guha (1997) and Young & Leeming (1997) are the most appropriate Eulerian models for predicting particle deposition in HVAC ducts. These models are more difficult to apply than other Eulerian models, but they are based on more physically sound assumptions. These are the only Eulerian models with the ability to give an accurate accounting of all particle transport mechanisms, including turbophoresis.

Turbophoretic models predict deposition rates similar to those observed in experiments and simulations. They also predict the accumulation of particles in the diffusion-impaction regime near vertical walls, as is observed in Lagrangian simulations. These models exhibit good performance when applied to both vertical and horizontal surfaces and to both smooth and rough surfaces.

Sublayer models simulate near-wall turbulence as a two-dimensional stagnation-point flow and use a Lagrangian scheme in this near-wall layer to estimate deposition rates. The modeled flow is meant to represent the near-wall eddies observed to be responsible for depositing certain particles to vertical surfaces in Lagrangian simulations. These models are not fully Lagrangian and the resulting equations can be solved quickly (~ a few seconds) with current computing power. The sublayer model of Fan & Ahmadi (1993) is the most well-developed in the literature and the best sublayer model for application to HVAC ducts. This sublayer model had been extended to account for surface roughness, electrical charge and nonspherical particles. It can also be applied to horizontal surfaces.

Fully Lagrangian simulations have yielded much information that is applicable to particle deposition in HVAC ducts, but such simulations are impractical as predictive tools owing to their current high computational cost. Lagrangian particle simulations with flow fields generated by DNS are currently limited to flow Reynolds numbers less than about 10,000. Flows generated by LES have allowed particle simulations in flows with Reynolds numbers approaching 80,000. These techniques reach into the lower end of the

range of flow Reynolds numbers of interest for HVAC ducts, i.e. 10^4 to 3×10^6. The information generated by these simulations can be viewed as the results of numerical experiments, analogous to physical experiments. Deposition velocities from most Lagrangian simulations are within the range observed in experiments. Provided that Lagrangian simulations accurately account for all forces acting on particles, they can be an excellent source of information for comparison to Eulerian models. As computational power increases, Lagrangian simulations will be able to investigate higher flow Reynolds numbers and more complex flow geometries. But for the near future, these techniques should be viewed as high-end research tools, rather than as tools for engineering analyses of particle deposition in real HVAC systems.

Even the most sophisticated particle deposition models have only limited direct applicability to the case of particle deposition in HVAC systems. Except for those few efforts that have dealt explicitly with bends, all equations, models and simulations discussed in this review are concerned exclusively with deposition from flows in straight ducts with fully developed turbulent flow profiles. Such flows occur in real ventilation ducts, but the frequent occurrence of bends, junctions and obstructions makes developing turbulent flow profiles a common aspect of HVAC duct flow. No models or simulations have been advanced to help understand particle deposition from turbulent flows with undeveloped velocity profiles. In addition, no theoretical consideration has been given to the influence of secondary flows in rectangular ducts on particle deposition.

Roughness elements on the interior of duct surfaces are likely to vary in terms of shape, height and surface density. Surface roughness is typically accounted for in models by changing the criteria for particle deposition by using the method proposed by Browne (1974). This model adjustment was developed specifically for the case of closely packed sand-grain type roughness and considers only the average height of the roughness elements. Most models that account for surface roughness exhibit a similar response, probably because the method of accounting for roughness is fundamentally the same. No models consider other geometrical aspects of roughness elements like width or orientation, and roughness element densities other than closely packed sand-grain type have not been thoroughly addressed. Roughness has also been observed to change the structure of turbulence near walls. How deposition rates may change as a result of these changes in the near-wall turbulence has not been addressed by any models or simulations.

In summary, predicting particle behavior in turbulent flows with developing velocity profiles and accounting for different types of roughness elements are the main difficulties when modeling particle deposition from flows in ventilation ducts. Further research addressed toward improving these aspects of models, augmented by well-designed laboratory experiments will improve our ability to model particle deposition from turbulent flow in HVAC systems.

Table 2.1 Equations for the Fanning friction factor in ducts with rough walls.

Reference	Correlation
Nikuradse[a] (1936)	$\frac{1}{\sqrt{f}} = A_1 + B_1 \log\left(\mathrm{Re}\sqrt{f}\right) + C_1 \log\left(k/D_h\right)$
Colebrook (1939)	$\frac{1}{\sqrt{f}} = 4.0 \log\left(\frac{2.51}{\mathrm{Re}\sqrt{f}} + \frac{k}{3.7 D_h}\right)$
Bennet & Meyers (1962)	$\frac{1}{\sqrt{f}} = 2.14 - 4.06 \log\left(\frac{4.73}{\mathrm{Re}\sqrt{f}} + \frac{k}{D_h}\right)$
Altshul (1970)	$f = 0.0275\left(\frac{68}{\mathrm{Re}} + \frac{k}{D_h}\right)^{0.25}$
White (1986)	$\frac{1}{\sqrt{f}} = -3.6 \log\left[\frac{6.9}{\mathrm{Re}} + \left(\frac{k}{3.7 D_h}\right)^{1.11}\right]$

[a] As reported in Ch. 2 of Idelchik (1986), the constants A_1, B_1 & C_1 depend on the value of the quantity $\mathrm{Re}k\sqrt{f}/D_h$ as follows:

Value of $\mathrm{Re}k\sqrt{f}/D_h$	A_1	B_1	C_1
3.6-10	-0.8	2.0	0
10-20	0.068	1.13	-0.87
20-40	1.538	0	-2.0
40-191.2	2.471	-0.588	-2.588
> 191.2	1.138	0	-2.0

Table 2.2 Particle deposition experiments in horizontal tubes with hydraulic diameter less than 2.7 cm.

Investigator	Duct				Particles			Methods & comments[b]
	Deposition surface	D_h (cm)	k (μm)[a]	Re ($\times 10^3$)	Material (density) (g/cm^3)	d_p (μm)	τ^+ (-)	
Yoder & Silverman (1967)	round copper tube	2.62	NR	5-85	Polystyrene (1.05)	0.26 & 0.8	0.00093-0.91	d, m, v
Ström (1972)	round steel tube with bends	1.68	2	0.45-5	Di-octyl phthalate (0.97)	2.1-15	0.19-1.3	c, d, l, u
Wasan *et al.* (1973)	round stainless steel tube	0.635	NR	5-17	Saccharin (0.83)	0.6-5.8	0.051-31	d, k, y
Erhart (1986)	round glass tube	1.1	HS	4-56	Oleic acid (0.72)	1.0-7.3	0.029-14	d, l, v
Shimada *et al.* (1993)	round copper tube	0.6	NR	0.12-18	Sodium chloride (2.16)	0.01-0.04	0.0005-0.031	d, h, y

[a] NR = not reported; HS = surface reported as hydraulically smooth, but no direct roughness measurement was made

[b] See Table 2.6 for explanation of these comments.

Table 2.3 Particle deposition experiments in vertical tubes with hydraulic diameter less than 2.7 cm.

Investigator	Duct				Particles			Methods & comments[b]
	Deposition surface	D_h (cm)	k (μm)[a]	Re ($\times 10^3$)	Material (density) (g/cm^3)	d_p (μm)	τ^+ (-)	
Stavropoulos (1957)	round glass tubes[c]	2.54	NR	3.5-67	Lycopodium spores (0.75)	30	3-500	b, m, n, w
Friedlander & Johnstone (1957)	round glass and brass tubes[c]	glass, 0.54-2.5 brass, 1.38–2.5	NR	2.8-44	Iron (7.86) Aluminum flakes (2.7) Lycopodium spores (0.75)	0.8–2.63 1.81 30	0.31-23	b, m, n, t
Postma & Schwendiman (1960)	round steel and aluminum tubes[c]	steel, 1.9 aluminum, 2.54	HS HS	3-22	Zinc sulfide (4.09) Glass (2.2)	2.0 & 4.0 30	0.063-190	b, m, n, t
Wells & Chamberlain (1967)	brass rod placed axially in a copper pipe, sometimes with inner rod covered with fibrous filter paper	2.54	HS & 100	1-51	Aitken nuclei (NR) Tricresyl phosphate (1.18) Polystyrene (1.05)	0.17 0.65-2.1 5.0	0.0026-11	c, i, n, t
Liu & Agarwal (1974)	round glass tube	1.27	HS	10 & 50	Olive oil (0.92)	1.4-21	0.21-770	a, m, u
El–Shobokshy (1983)	round glass and brass tubes	glass, 0.8 brass, 0.8	HS 7 & 20	10	Fluorescein (1.5)	1.0–6.2	0.4-15	a, l, u
Lee & Gieseke (1994)	round copper tube with bends	0.62-0.77	HS	1.8-56	Di-octyl phthalate (0.97)	0.035-1.3	0.00086–1.8	a, d, l, u, y

[a] NR = not reported; HS = surface reported as hydraulically smooth, but no direct roughness measurement was made

[b] See Table 2.6 for explanation of these comments.

[c] For some or all experiments, the deposition surface was coated with adhesive or oil to minimize particle bounce and reentrainment.

Table 2.4 Particle deposition experiments in horizontal tubes with hydraulic diameter greater than 2.7 cm.

Investigator	Duct				Particles			Methods & comments[b]
	Deposition surface	D_h (cm)	k (μm)[a]	Re ($\times 10^3$)	Material (density) (g/cm^3)	d_p (μm)	τ^+ (-)	
Alexander & Coldren (1951)	interior perimeter of a round steel pipe	4.72	NR	77-283	Water (1.0)	27	210-2200	e, j, n, p, z
Chamberlain (1967)	various large roughness elements (grass, toweling, glass) on the floor of a square copper duct[c]	30	450-80,000	22-370	Aitken nuclei (NR) Tricresyl phosphate (1.18) Polystyrene (1.05) Ragweed pollen (1.0) Lycopodium spores (1.19)	0.08 1.0 5.0 19.0 32.4	0.00054-850	c, m, n, t, x
Sehmel (1970a)	artificial grass on floor of a square duct	61	7000	91-563	Uranine (1.5)	6.0-14	0.38-130	a, l, n, x
Montgomery & Corn (1970)	interior perimeter of a round aluminum tube	15.4	HS	48-366	Uranine-methyl blue (1.33)	0.44-2.16	0.03-2.9	a, b, m, t
Sehmel (1973)	brass shim stock on floor or ceiling of a square duct	61	NR	89-545	Uranine (1.5)	0.10-28	0.0027-75	a, l, n, t, x
Chamberlain *et al.* (1984)	copper sheet on floor of a square duct with repeated rib roughness elements[c]	30	HS, 150, & 2200	42-1220	Aitken nuclei (NR) Tricresyl phosphate (1.18) Polystyrene (1.05) Iron oxide (1.0) Lycopodium spores (1.19)	0.08 1.1 0.6-5.0 2.0-5.0 32	0.00012-360	c, l, m n, t
Hahn *et al.* (1985)	round steel pipe with repeated rib roughness	8.83	6350	93-98	Uranine (1.5)	0.04-0.20	0.0075-0.063	a, h, t
Kvasnak *et al.* (1993)	gold plate on floor of a rectangular duct[c]	4.35	0.1	15	Glass (2.2) Irregular rust (4.2) Irregular dust (2.4)	5-45 1.0-10 5.1-10	0.06-80	b, m, n, t
Adam *et al.* (1996)	interior perimeter of a square steel duct	30	NR	53-131	Oil smoke (NR)	0.5-2.0	0.0038-0.019	d, f, n, p, v
Cheong (1997)	interior perimeter of a square and rectangular steel duct	30, 40 & 48	NR	65-371	Oil smoke (NR)	NR	0.0021-0.12	d, f, n, p, v
Lai (1997)	smooth and rough machined plastic on floor of a square duct[c]	15	HS, 2000 & 6000	44	Indium acetylacetonate (0.91) Porous silica (1.18)	0.7 2.5-7.1	0.0058-0.53	c, g, t

[a] NR = not reported; HS = surface reported as hydraulically smooth, but no direct roughness measurement was made

[b] See Table 2.6 for explanation of these comments.

[c] For some or all experiments, the deposition surface was coated with adhesive or oil to minimize particle bounce and reentrainment.

Table 2.5 Particle deposition experiments in vertical tubes with hydraulic diameter greater than 2.7 cm.

Investigator	Duct				Particles			Methods & comments[b]
	Deposition surface	D_h (cm)	k (μm)[a]	Re ($\times 10^3$)	Material (density) (g/cm^3)	d_p (μm)	τ^+ (-)	
Sehmel (1968)	round aluminum tubes[c]	0.53, 1.57, 2.93 & 7.14	NR	4.2-61	Uranine-methyl blue (1.5)	1.0-28	0.04-86	a, l, n, u
Ilori (1971)	round glass, aluminum and plastic tubes	glass, 2.79 aluminum, 3.00 plastic, 2.97	HS 5.0 5.0	5-50	Uranine-methyl blue (1.42)	6.0 & 9.0	0.37-45	a, m, u
Forney & Spielman (1974)	round glass tubes[c]	1.3, 1.78, 2.54, 3.12, 3.65 & 4.4	NR	4-51	Ragweed pollen (0.48) Lycopodium spores (0.65) Polystyrene (1.05) Pecan pollen (0.94)	19.5 30.9 32 48.5	3.6-780	b, k, n, t
Muyshondt *et al.* (1996)	round tubes	1.3, 2.6, 5.2 & 10.2	NR	2.6-54	Oleic acid (0.93)	5-20	0.3-70	d, m, u

[a] NR = not reported; HS = surface reported as hydraulically smooth, but no direct roughness measurement was made

[b] See Table 2.6 for explanation of these comments.

[c] For some or all experiments, the deposition surface was coated with adhesive or oil to minimize particle bounce and reentrainment.

Table 2.6 Explanation of comments in Tables 2.2-2.5 and Table 2.7.

Methods for determining particle surface flux	
Code	**Description of method**
a	direct measurement by fluorescence of deposition surface extract
b	direct measurement by microscopic count on small part of deposition surface
c	direct measurement by radioactivity or neutron activation of deposition surface
d	inferred from difference in upstream and downstream air concentrations
e	inferred from airborne concentration gradient
Methods for determining particle size	
Code	**Description of method**
f	particle sizing by optical particle counter
g	particle size as given by manufacturer
h	particle sizing by electrostatic classification
i	particle sizing by sedimentation velocity in a Schaefer cell
j	particle sizing by empirical equation
k	particle sizing not discussed
l	particle sizing by theory of vibrating orifice, spinning disc generator or evaporation/condensation generator
m	particle sizing by microscopy
Miscellaneous comments	
Code	**Comment**
n	no steps taken to neutralize test aerosol
p	polydisperse aerosol
Methods for determining particle airborne concentration	
Code	**Description of method**
t	isokinetic filter sampling with microscopic counting, fluorescent or radioactive methods
u	filtration of entire air stream after the test section with fluorescent or radioactive methods
v	anisokinetic sampling with particle counter or cloud chamber and photographic counting
w	mass difference of particle source
x	mass impacted on wires/rods in the duct with fluorescent or radioactive methods
y	intermittent sampling of entire air stream with particle counter
z	anisokinetic sampling with gravimetric determination of collection on impaction plates

Table 2.7 Particle deposition experiments in tube bends with turbulent flow.

Investigator	Duct				Particles			Methods & comments[a]
	Deposition surface	D_h (cm)	R_o (-)	Re ($\times 10^3$)	Material (density) (g/cm^3)	d_p (μm)	τ^+ (-)	
Pui *et al.* (1987)	round stainless steel and glass tube bends	0.503-0.851	5.7	6-10	Oleic acid (0.89)	1.0-7.0	0.4-27	a, l, u
McFarland *et al.* (1997)	round wax tube bends	1.6	1-20	3-20	Oleic acid (0.89)	10	0.4-23	d, l, u

[a] See Table 2.6 for explanation of these comments.

Table 2.8 Correlations for the eddy viscosity of air.

Investigator	Correlation for the eddy viscosity of air, ξ_a	Comments
Lin *et al.* (1953)	$\frac{\xi_a}{\nu}=\left(\frac{y^+}{14.5}\right)^3$ $y^+ \le 5$ $\frac{\xi_a}{\nu}=\frac{y^+}{5}-0.959$ $5 < y^+ \le 30$	Best fit to previously measured velocity distributions. Discontinuous at $y^+ = 5$.
Owen (1960)	$\frac{\xi_a}{\nu}=\left(\frac{y^+}{10}\right)^3$ $y^+ \le 5$ $\frac{\xi_a}{\nu}=0.012\left(y^+-1.6\right)^2$ $5 < y^+ \le 20$ $\frac{\xi_a}{\nu}=0.4\left(y^+-10\right)$ $y^+ > 20$	Best fit to previously measured velocity distributions. Smoother correlation than that of Lin *et al.* (1953).
Wasan & Wilke (1964)	$\frac{\xi_a}{\nu}=\frac{4.16\times10^{-4}\,y^{+3}-1.515\times10^{-5}\,y^{+4}}{1-4.16\times10^{-4}\,y^{+3}+1.515\times10^{-5}\,y^{+4}}$ $y^+ \le 20$	Expression based on empirical logarithmic velocity distribution
Davies (1966a)	$\frac{\xi_a}{\nu}=\frac{y^{+\left(4-y^{+0.08}\right)}}{10^3\left(\frac{2.5\times10^7}{\mathrm{Re}}\right)^{\left(\frac{y^+}{y^++400}\right)}}$ $0.05 \le y^+ \le 500$	Only correlation with a dependence on Re. ξ_a is not proportional to y^{+3} as the wall is approached.
Cebeci & Smith (1974)	$\frac{\xi_a}{\nu}=0.41y^+\left[1-\exp\left(\frac{y^+}{26.0}\right)\right]^2$	No comment.
Lai & Nazaroff (2000)	$\frac{\xi_a}{\nu}=7.669\times10^{-4}\,y^{+3}$ $0 \le y^+ \le 4.3$ $\frac{\xi_a}{\nu}=0.001y^{+2.8214}$ $4.3 \le y^+ \le 12.5$ $\frac{\xi_a}{\nu}=0.0107y^{+1.8895}$ $12.5 \le y^+ \le 30$	Best fit to velocity statistics from DNS of channel flow by Kim *et al.* (1987).

Table 2.9 Recommended values of k_1 for equation (2.52).

Investigator	k_1
Cleaver & Yates (1975)	0.084
Friedlander (1977)	0.059
Wood (1981b)	0.045
Davies (1983)	0.075
Papavergos & Hedley (1984)	0.07

Table 2.10 Recommended values of k_2 for equation (2.53).

Investigator	k_2
Kneen & Strauss (1969)	3.79×10^{-4}
Liu & Agarwal (1974)	6×10^{-4}
Wood (1981b)	4.5×10^{-4}
Papavergos & Hedley (1984)	3.5×10^{-4}

Table 2.11 Recommended values of k_3 for equation (2.54).

Investigator	k_3
Wood (1981b)	0.13
Davies (1983)	0.30
Papavergos & Hedley (1984)	0.18
Fan & Ahmadi (1993)	0.14

Table 2.12 Summary of assumptions for free-flight model by different investigators.

Investigators	Particle eddy diffusivity, ξ_p	Eddy viscosity (Table 2.8), ξ_a	Dimensionless capture distance, Δ^+	Dimensionless particle velocity at Δ^+, $v^+_{py,\Delta+}$
Friedlander & Johnstone (1957)	$\xi_p = \xi_a$	Lin *et al.* (1953)	S^+	0.9
Davies (1966b)	$\xi_p = \xi_a$	Davies (1966a)	$S^+ + r_p^+$	$\Delta^+/(\Delta^+ + 10)$
Liu & Ilori (1974)	$\xi_p = \xi_a + v\tau^+ v'^{+2}_{rms}$	Owen (1960)	$S^+ + r_p^+$	$\Delta^+/(\Delta^+ + 10)$
Browne (1974)	$\xi_p = \xi_a$	Davies (1966a)	$S^+ + r_p^+ + k^+ + \sigma_k^+ - e^+$	$\Delta^+/(\Delta^+ + 10)$
El-Shobokshy & Ismail (1980)	$\xi_p = \xi_a + v\tau^+ v'^{+2}_{rms}$	Lin *et al.* (1953)	$S^+ + r_p^+ + k^+ + \sigma_k^+ - e^+$	$\Delta^+/(\Delta^+ + 10)$
Wood (1981a)	$\xi_p = \xi_a$	Lin *et al.* (1953)	$S^+ + r_p^+ + k^+ - e^+$	0.69
Im & Ahluwalia (1989)	$\xi_p = \xi_a\left[1 + \frac{\exp(-\tau_f/\tau_p + 1) - 1}{1.72[(\tau_f/\tau_p)^2 - 1]}\right]$	Cebeci & Smith (1974)	$S^+ + e^+$	$0.8\left[\frac{\tau_f}{\tau_f + \tau_p}\right]^{1/2}$

Table 2.13 Summary of conditions in Lagrangian particle deposition simulations with stochastically modeled turbulent flow[a].

Investigator	Duct				Particles			
	Deposition surface	D_h (cm)	k (μm)	Re (-)	ρ_p (g/cm^3)	d_p (μm)	τ^+ (-)	**Forces in particle momentum equation**
Kallio & Reeks (1989)	Vertical duct wall	NR	0	NR	0.6, 0.924 & 6.0	NR	0.3-1000	drag, lift
Li & Ahmadi (1993a)	Vertical wall and horizontal floor in channel flow	2	0	6657	0.92 & 2.45	0.01-50	1.4×10^{-4}-110	drag, gravity, lift, Brownian diffusion
Li & Ahmadi (1993b)	Vertical wall and horizontal floor in channel flow	2	0, 10, 40 & 100	6657	2.45	0.01-10	1.6×10^{-4}-9.2	drag, gravity, lift, Brownian diffusion
Li *et al.* (1994)	Rectangular and trapezoidal blocks on wall in vertical channel flow	2	6100	6657	2.45	0.01-30	1.2×10^{-4}-40	drag, gravity, lift, Brownian diffusion
Chen & Ahmadi (1997)	Vertical pipe wall	24.7	0	50,000	1.225 & 2.45	0.01-100	1.3×10^{-5}-110	drag, gravity, optimum lift, Brownian diffusion

[a] NR = not reported

Table 2.14 Summary of conditions in Lagrangian particle deposition simulations with turbulent flow from LES and DNS[a].

Investigator	Duct			Particles			
	Deposition surface	D_h (cm)	Re (-)	ρ_p (g/cm^3)	d_p (μm)	τ^+ (-)	Forces in particle momentum equation
McLaughlin (1989)	Vertical channel wall	2	4000	0.86 & 1.8	17.2-29.6	2-6	Stokes drag, lift
Ounis *et al.* (1991)	Vertical channel wall	10	6500	0.80	0.01-0.1	5×10^{-7}-7×10^{-6}	Stokes drag, Brownian diffusion
Brooke *et al.* (1992)	Vertical channel wall	NR	9040	0.80	NR	3-10	Stokes drag
Ounis *et al.* (1993)	Vertical channel wall	10	6500	0.80	0.01-0.1	5×10^{-7}-7×10^{-6}	Stokes drag, Brownian diffusion
Brooke *et al.* (1994)	Vertical channel wall	NR	9040	0.80	NR	3-10	Stokes drag
Chen & McLaughlin (1995)	Vertical channel wall	0.625	7050	1.14	1.0-24.3	0.1-50	wall-corrected drag, optimum lift, Brownian diffusion
Wang & Squires (1996a)	Vertical channel wall	4	6400 & 27,600	0.75, 2.2 & 8.9	7-90	2-2000	Stokes drag corrected for high Re_p, gravity
Wang & Squires (1996b)	Vertical channel wall	NR	11,160 & 79,400	0.86 & 1.8	NR	0.5-200	Stokes drag corrected for high Re_p, lift
Uijttewaal & Oliemans (1996)	Vertical pipe wall	5	5300-42,000	1.2	3.6-940	5-10,000	Stokes drag corrected for high Re_p, gravity, lift
Wang *et al.* (1997)	Vertical channel wall	NR	11,160 & 79,400	0.80	NR	0.5-200	Stokes drag corrected for high Re_p, optimum lift
Zhang & Ahmadi (2000)	Vertical channel wall and horizontal channel floor	NR	8000	1.12 & 2.24	0.01-50	1×10^{-5}-100	Stokes drag corrected for high Re_p, gravity, lift, Brownian diffusion

[a] NR = not reported; all simulations assumed smooth surfaces ($k = 0$)

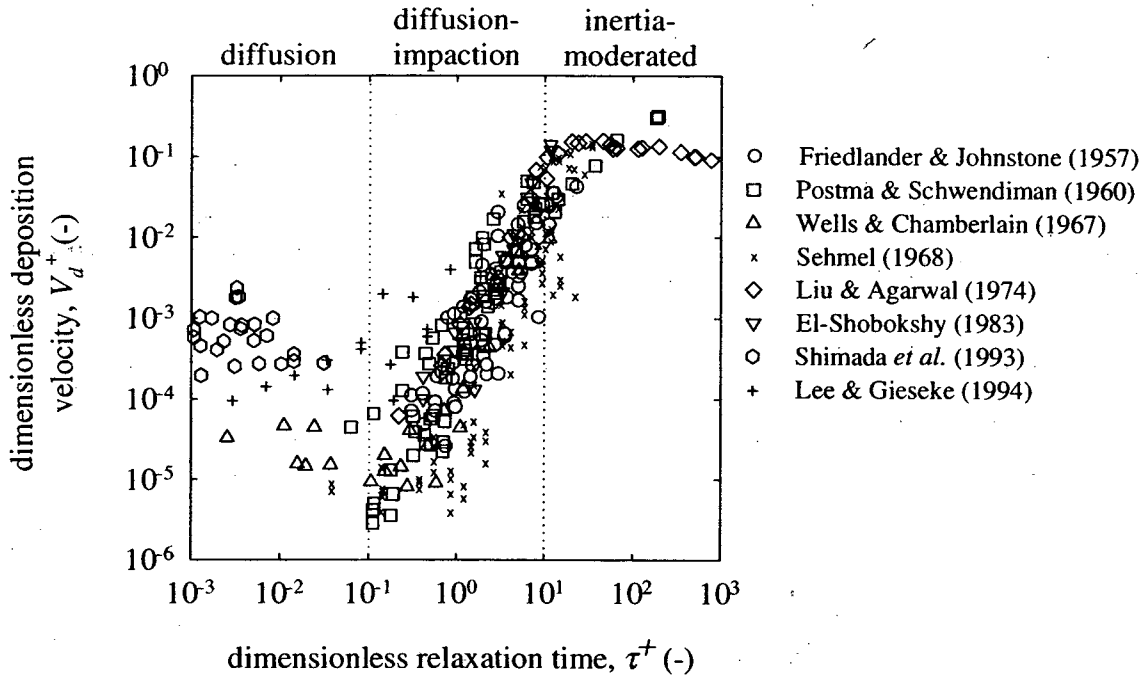

Figure 2.1 Experimental data for particle deposition from turbulent flow through small vertical tubes.

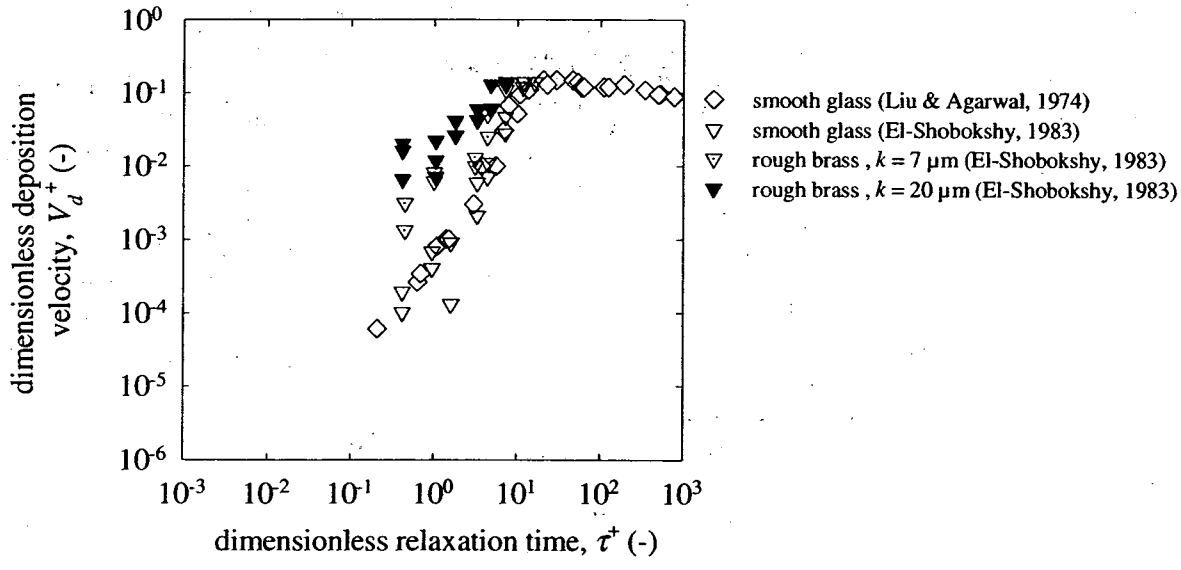

Figure 2.2 Experimental data for deposition to smooth and rough vertical walls.

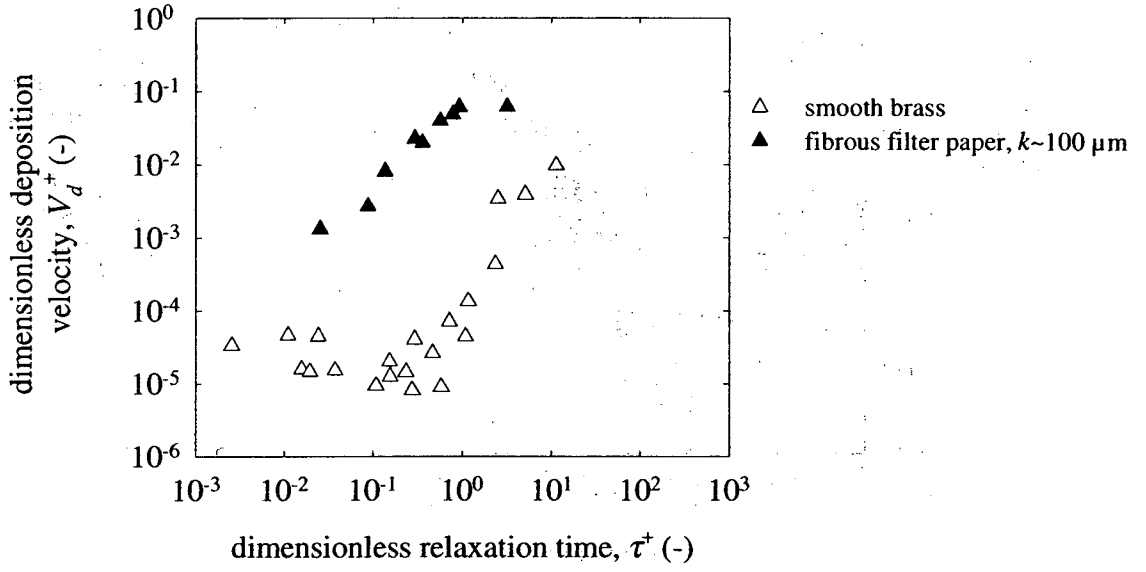

Figure 2.3 Experimental data collected by Wells & Chamberlain (1967) for deposition to vertically oriented smooth brass and fibrous filter paper (with roughness length scale, k, of about 100 μm).

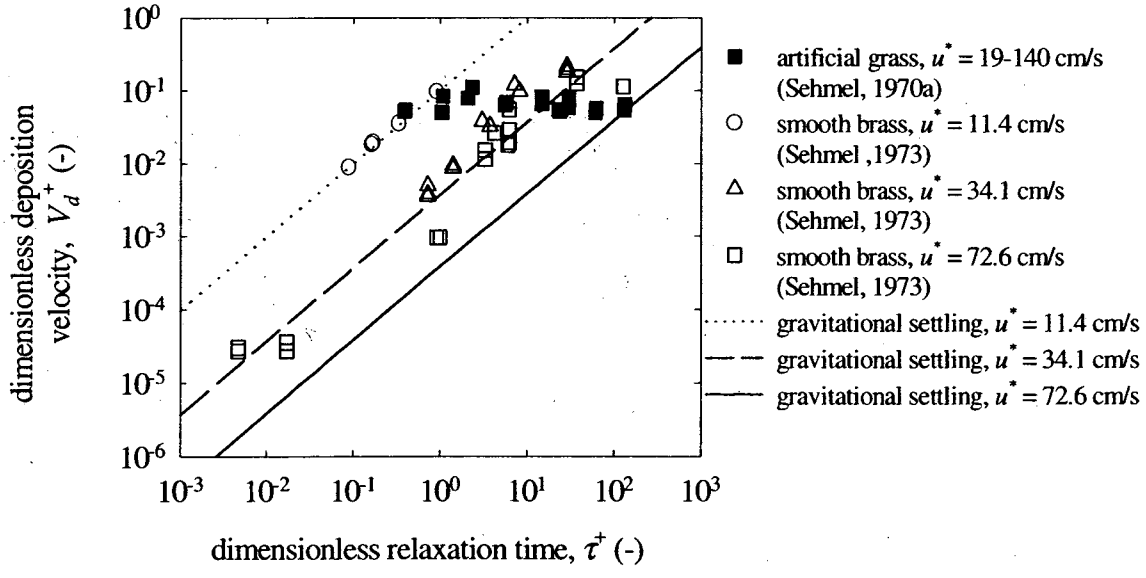

Figure 2.4 Experimental data for deposition to a smooth duct floor and a duct floor covered with artificial grass at different values of the friction velocity, u^*.

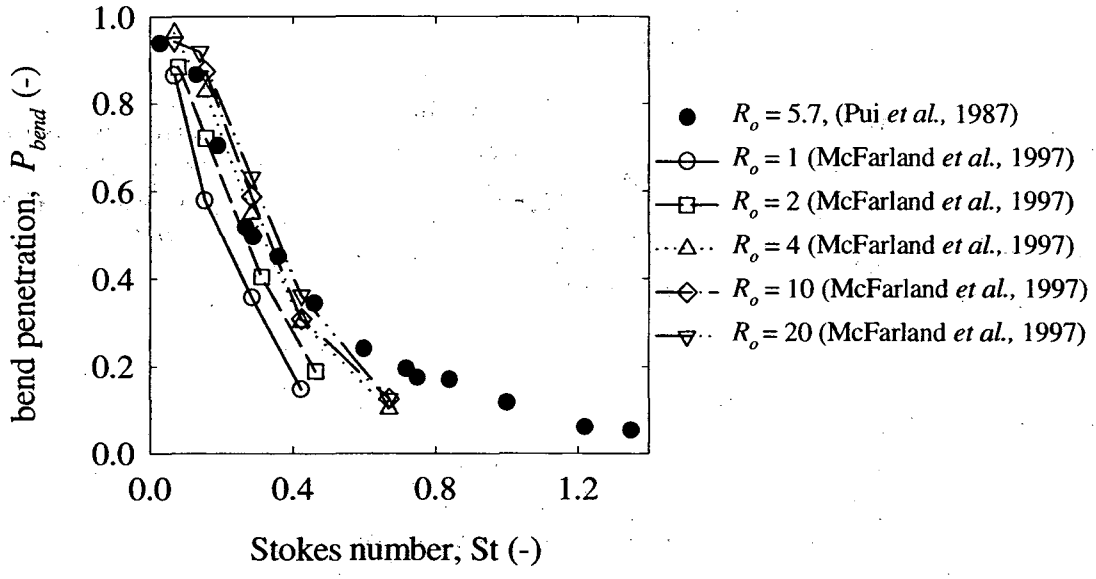

Figure 2.5 Experimental data for particle penetration through 90° bends with turbulent flow and small tube diameters.

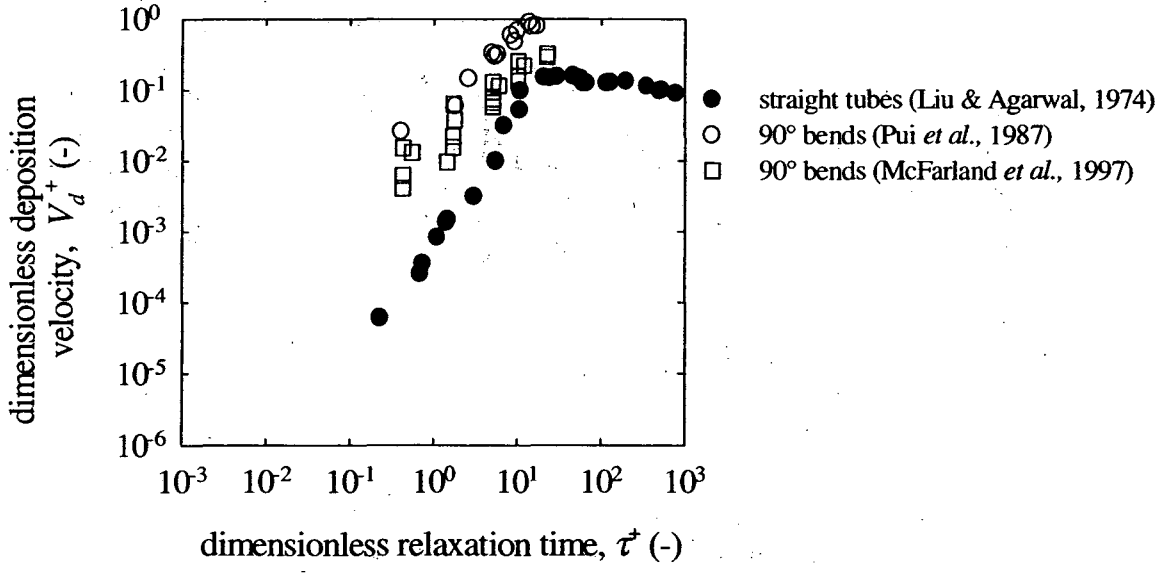

Figure 2.6 Experimental data for deposition in 90° bends with turbulent flow and small tube diameters compared to similar data collected in straight tubes.

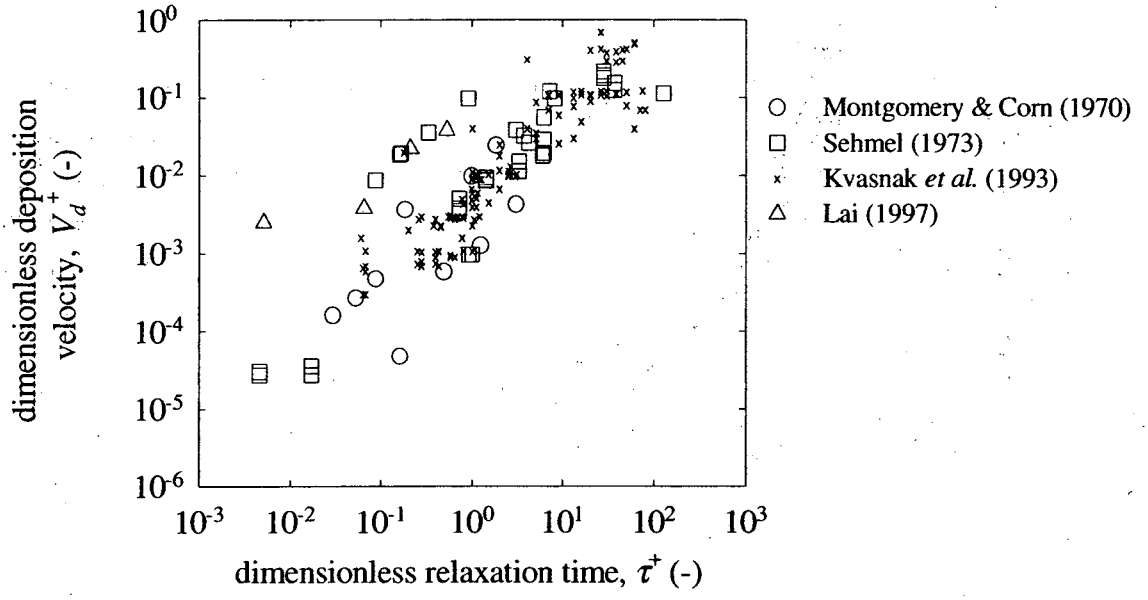

Figure 2.7 Experimental data for deposition to the smooth floors of large ducts.

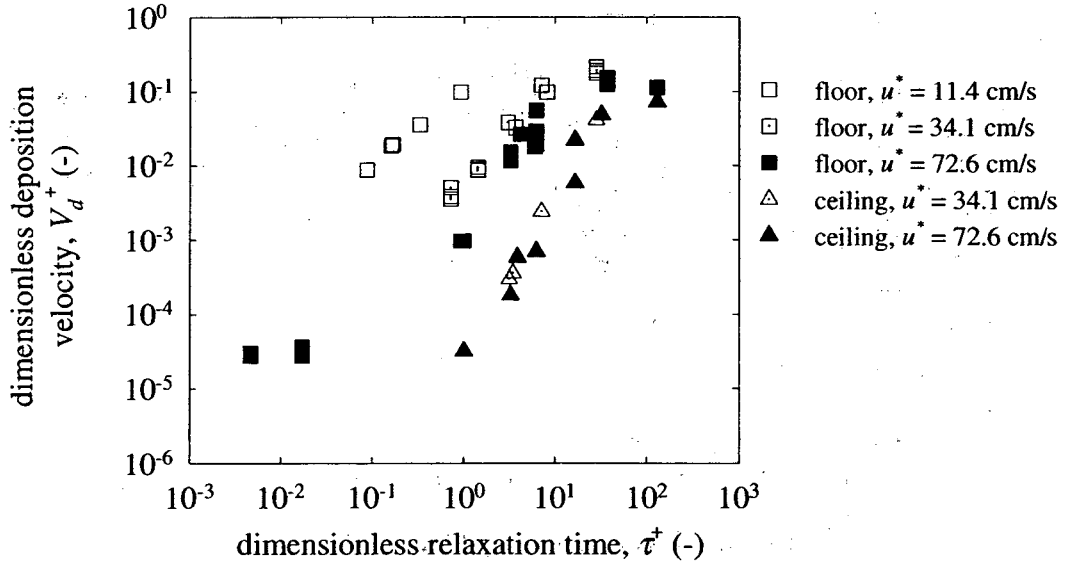

Figure 2.8 Experimental data collected by Sehmel (1973) for deposition to the smooth floor and ceiling of a horizontal duct at three different values of the friction velocity, u^*.

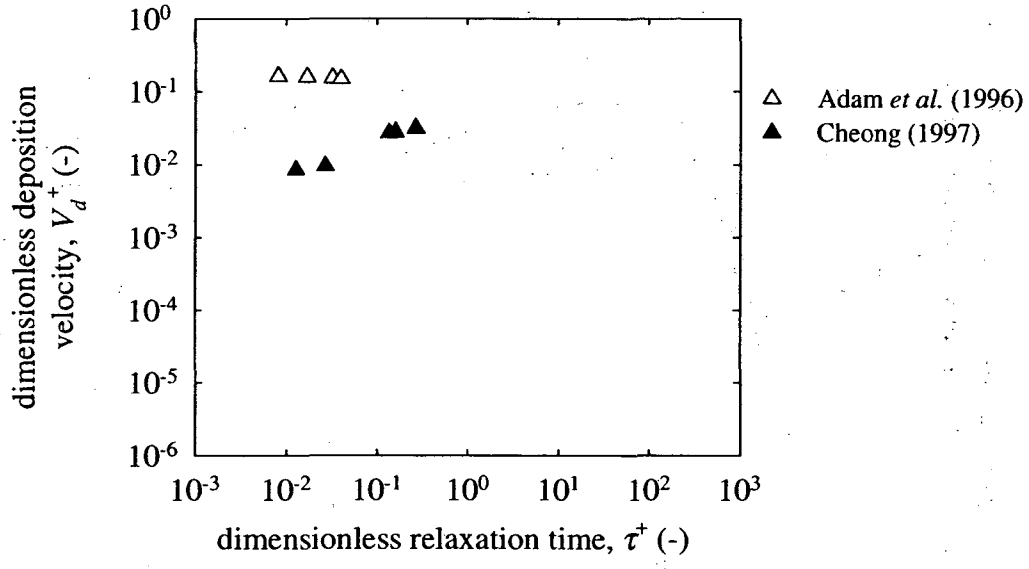

Figure 2.9 Experimental data for polydisperse aerosols depositing in large horizontal ducts measured by inferring deposition from differences in concentration measurements.

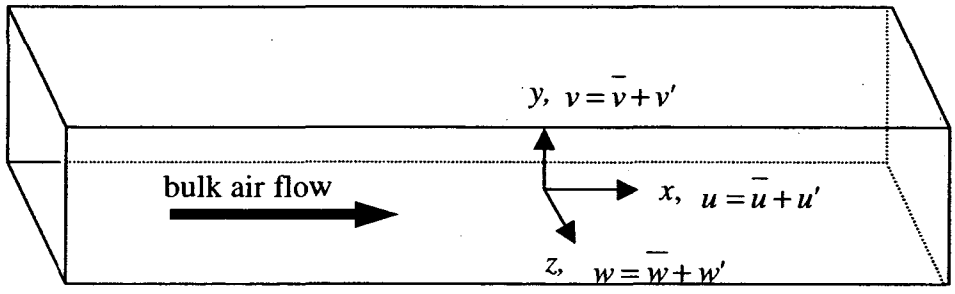

Figure 2.10 Definition of coordinate directions and velocity components in turbulent duct flow.

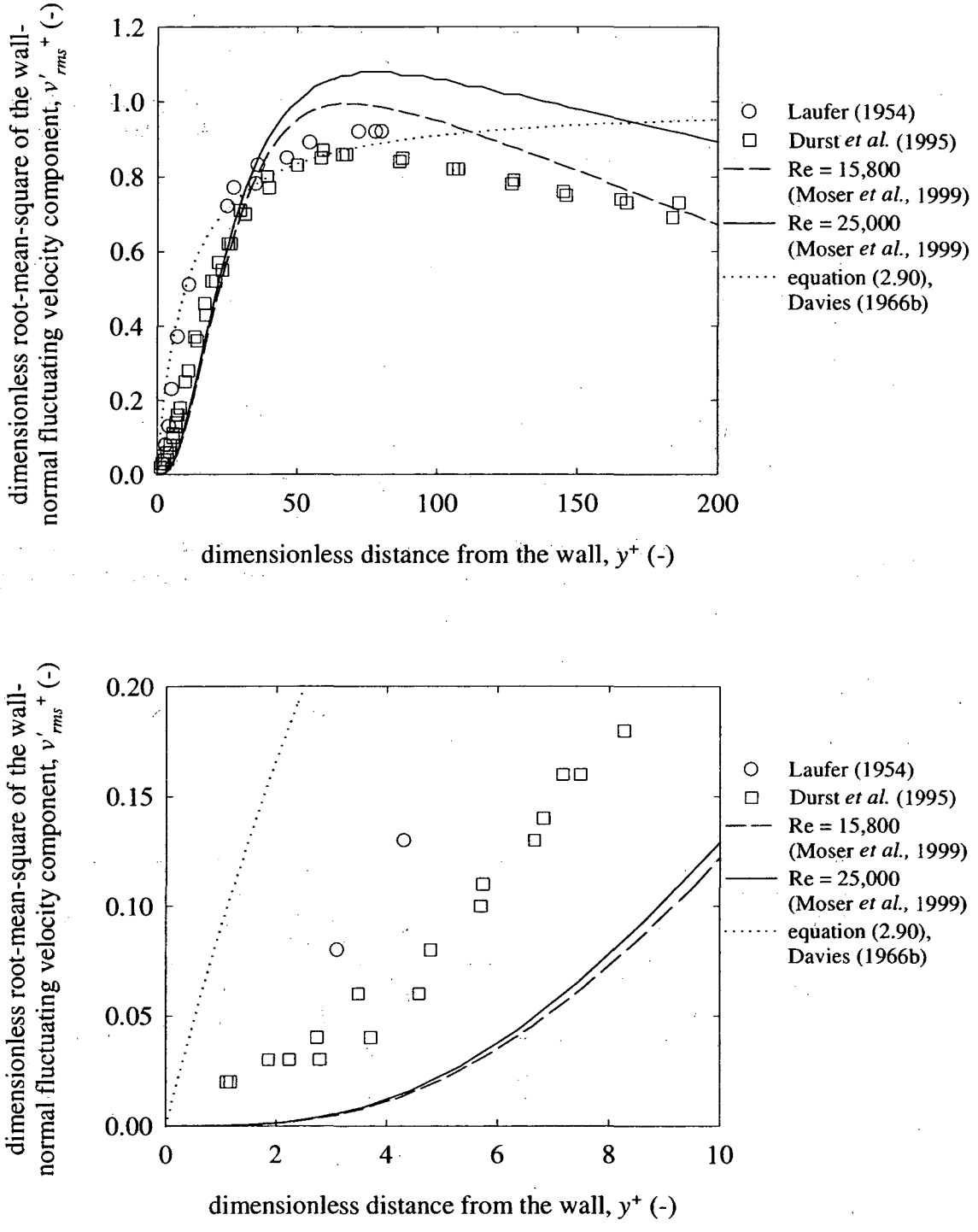

Figure 2.11 Profiles of v'^{+}_{rms} versus y^{+} derived from measurements in pipe flow and DNS of channel flow. The bottom panel shows the same data as the top panel with the axes scaled to focus attention near the wall.

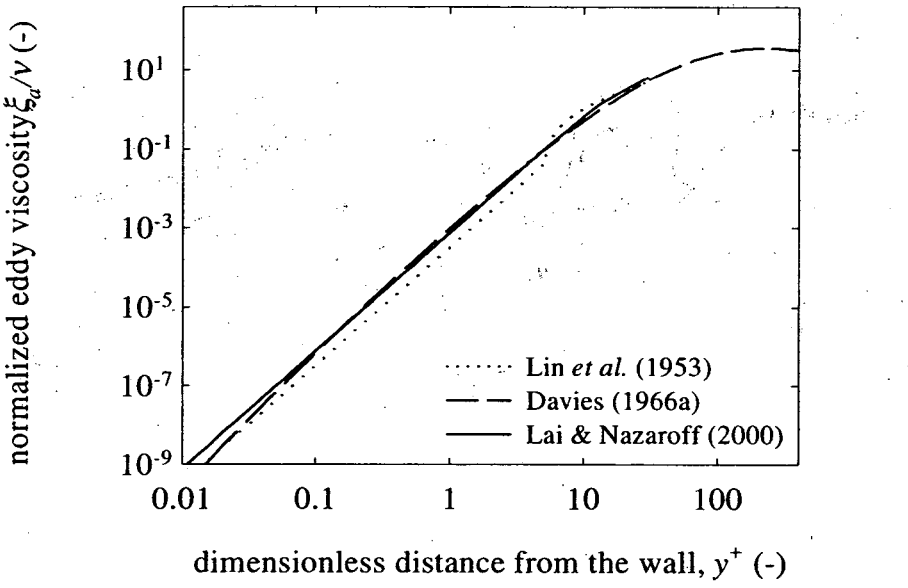

Figure 2.12 Comparison of correlations for eddy diffusivity versus dimensionless distance from a wall.

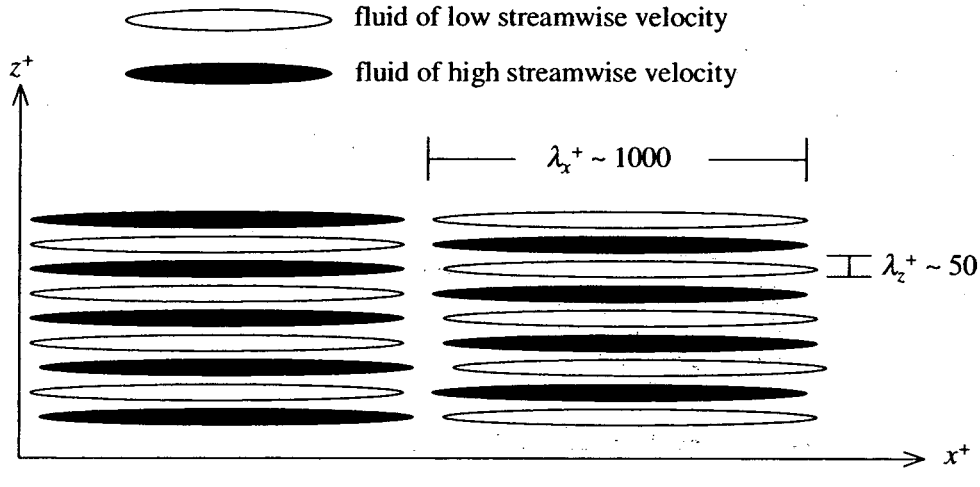

Figure 2.13 Approximate instantaneous arrangement of alternating low-speed and high-speed streaks of fluid near a wall in turbulent flow.

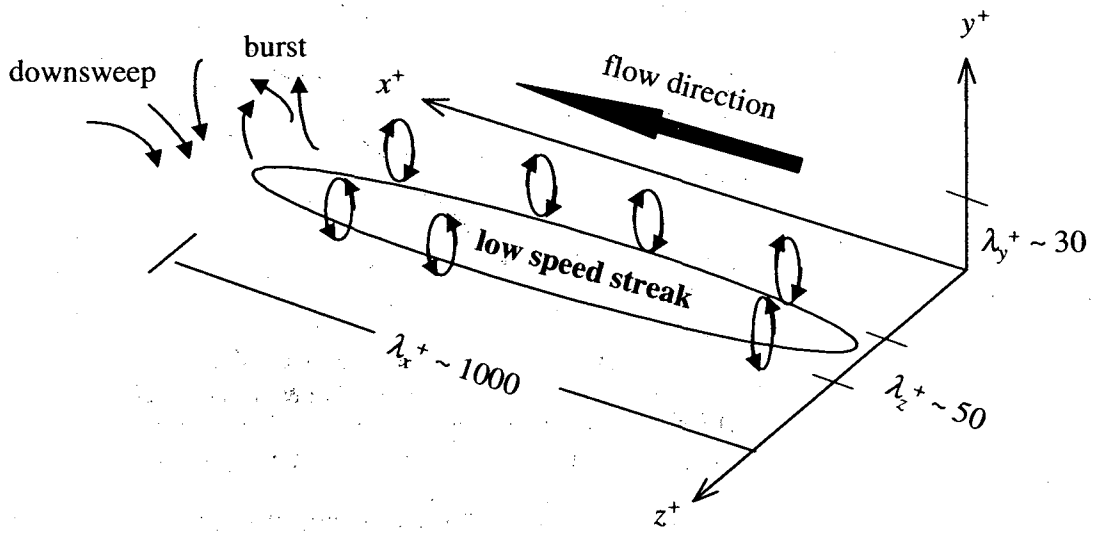

Figure 2.14 Schematic of near-wall turbulence illustrating the association between low-speed streaks, streamwise vortices, bursts and downsweeps.

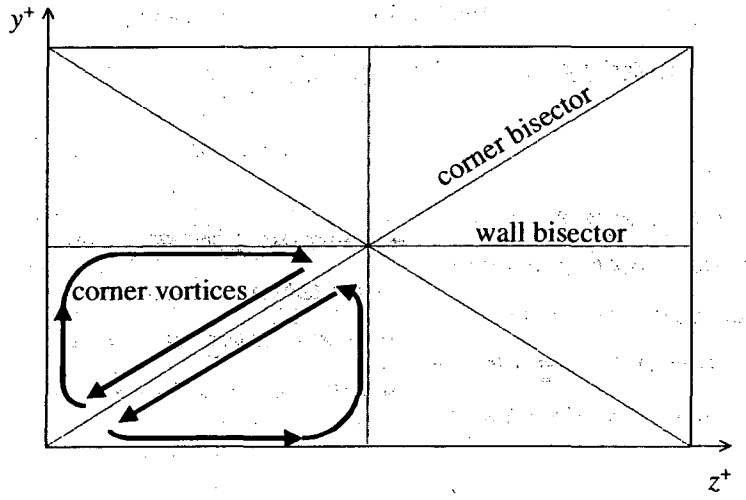

Figure 2.15 Secondary flow in the y-z plane of a straight rectangular duct with fully developed turbulent flow.

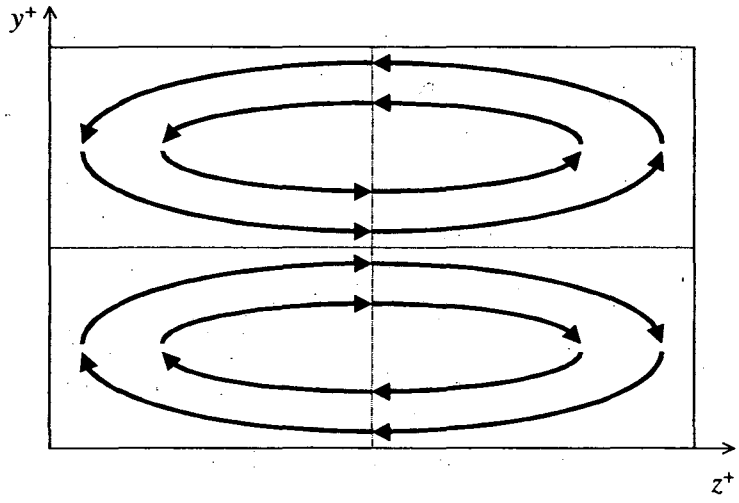

Figure 2.16 Secondary flow established in the y-z plane in a leftward turning bend with the outside of the bend to the right.

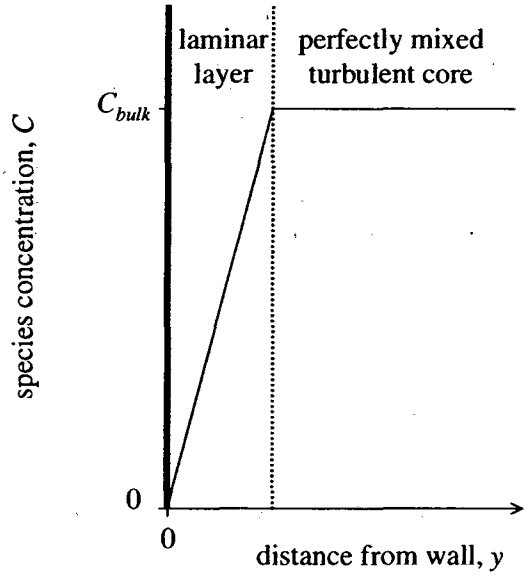

Figure 2.17 Concentration profile of a diffusive species based on the assumptions of the film model.

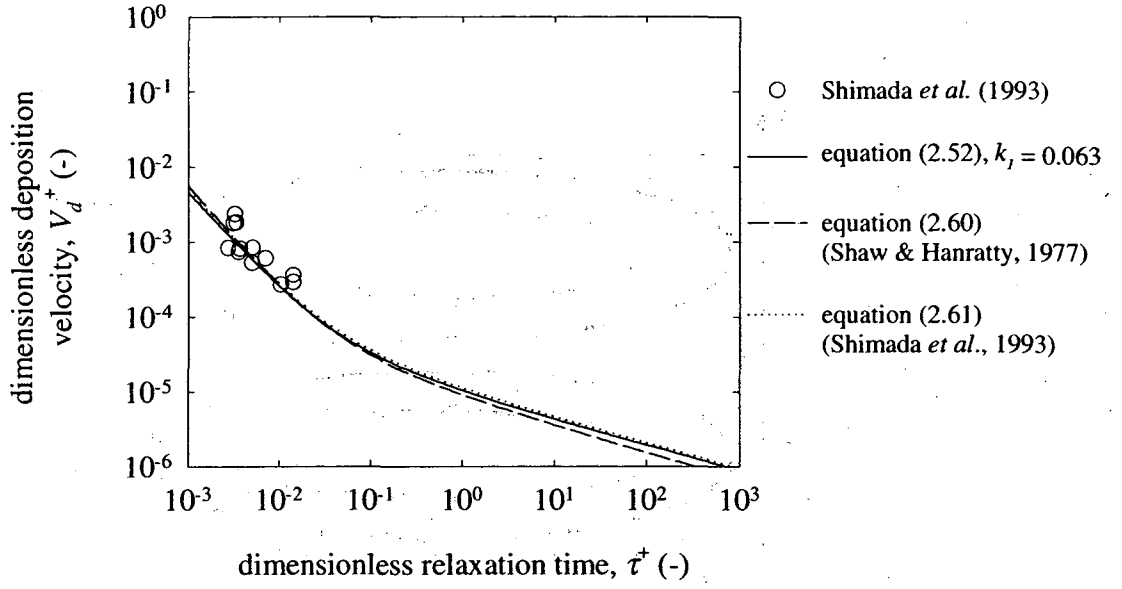

Figure 2.18 Comparison of empirical expressions for deposition to smooth surfaces in the diffusion regime.

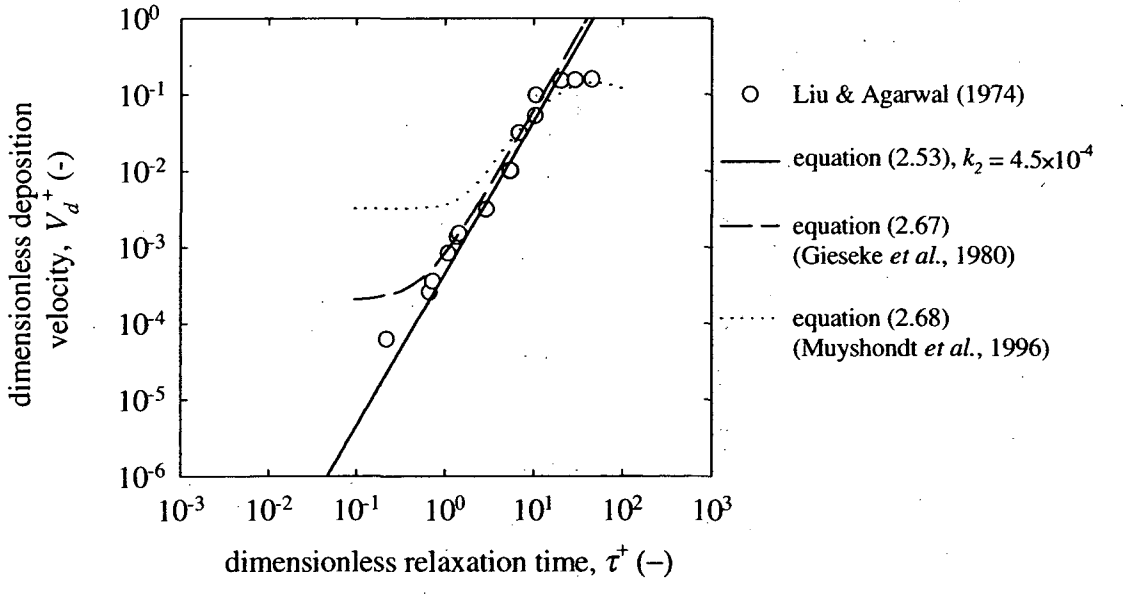

Figure 2.19 Comparison of empirical expressions for deposition to smooth vertical walls in the diffusion-impaction regime.

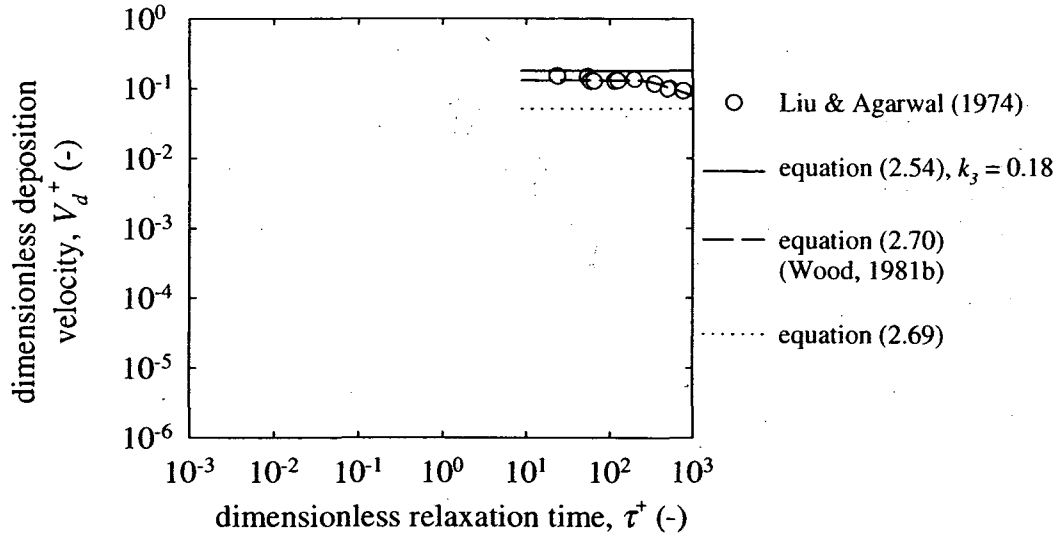

Figure 2.20 Comparison of empirical expressions for deposition to smooth vertical walls in the inertia-moderated regime.

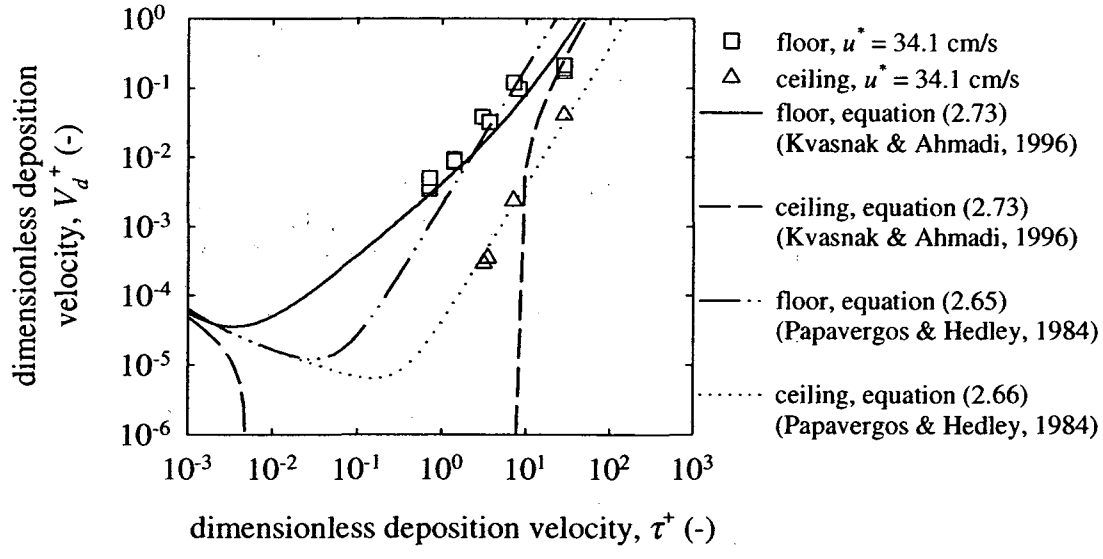

Figure 2.21 Comparison of empirical expressions for deposition to smooth horizontal floors and ceilings. Sehmel (1973) collected data at a friction velocity of 34.1 cm/s.

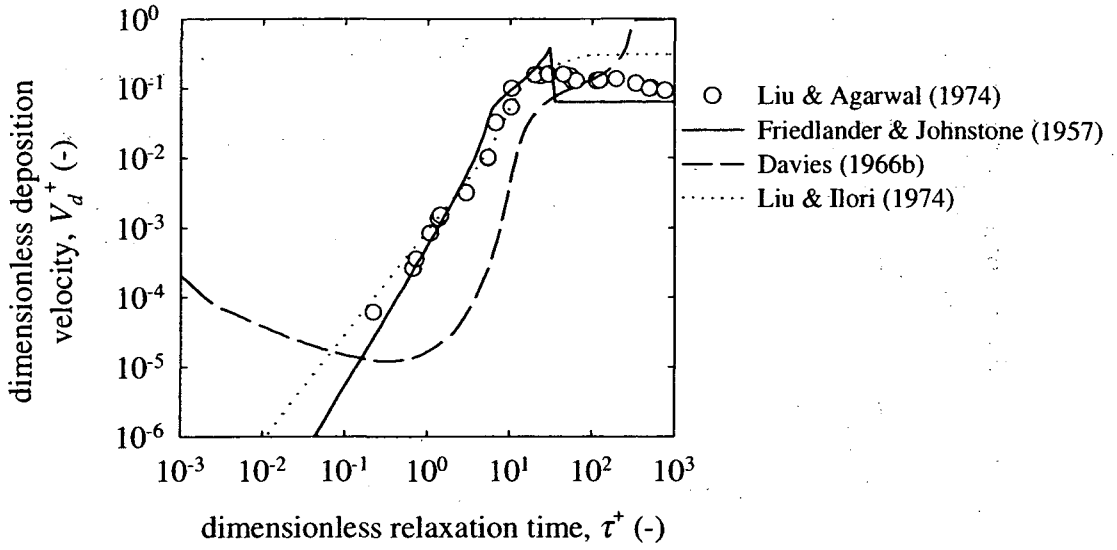

Figure 2.22 Comparison of free-flight models with experimental data in the case of deposition to a smooth vertical wall.

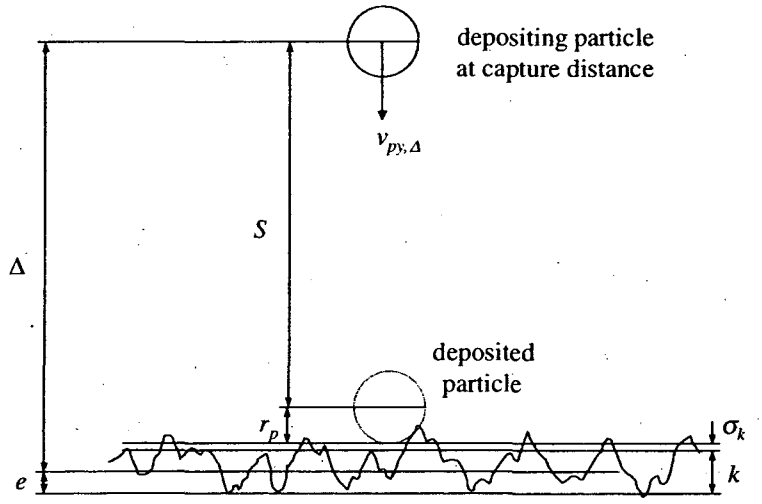

Figure 2.23 Description of parameters to determine the particle capture distance to a rough surface by the method recommended by Browne (1974).

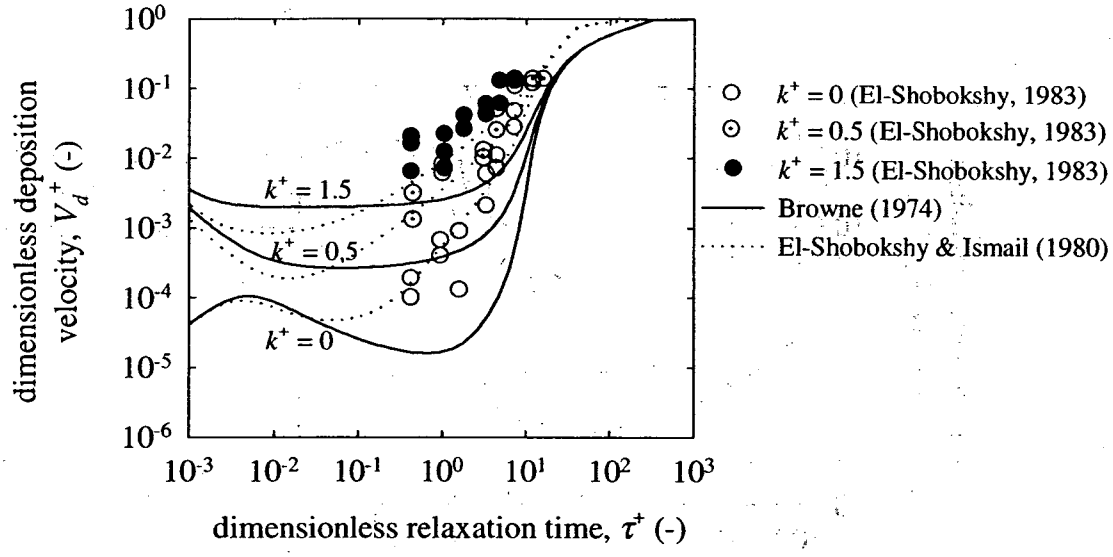

Figure 2.24 Comparison of free-flight models with experimental data in the case of deposition to smooth and rough vertical walls.

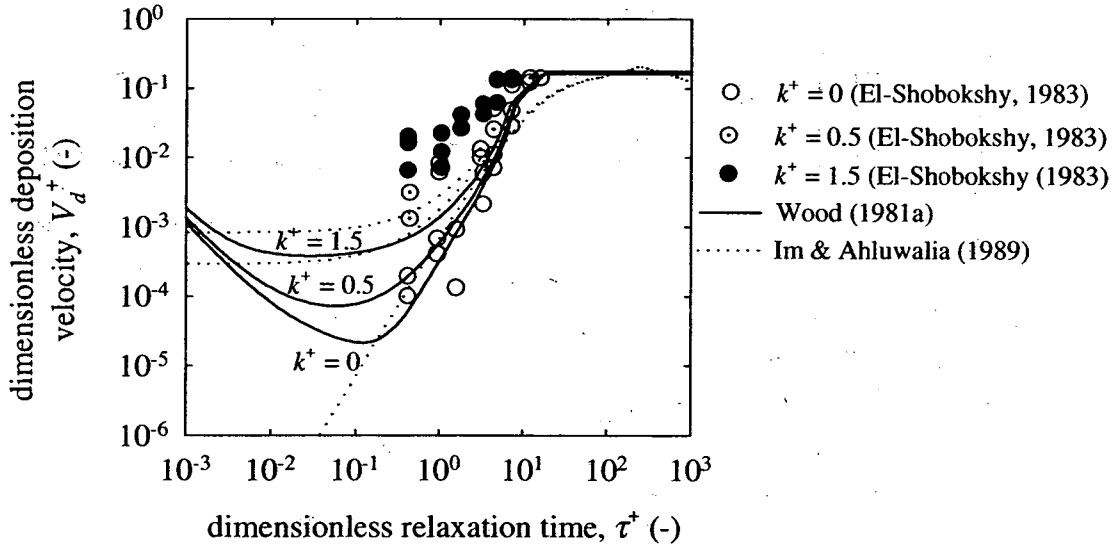

Figure 2.25 Comparison of free-flight models with experimental data in the case of deposition to smooth and rough vertical walls.

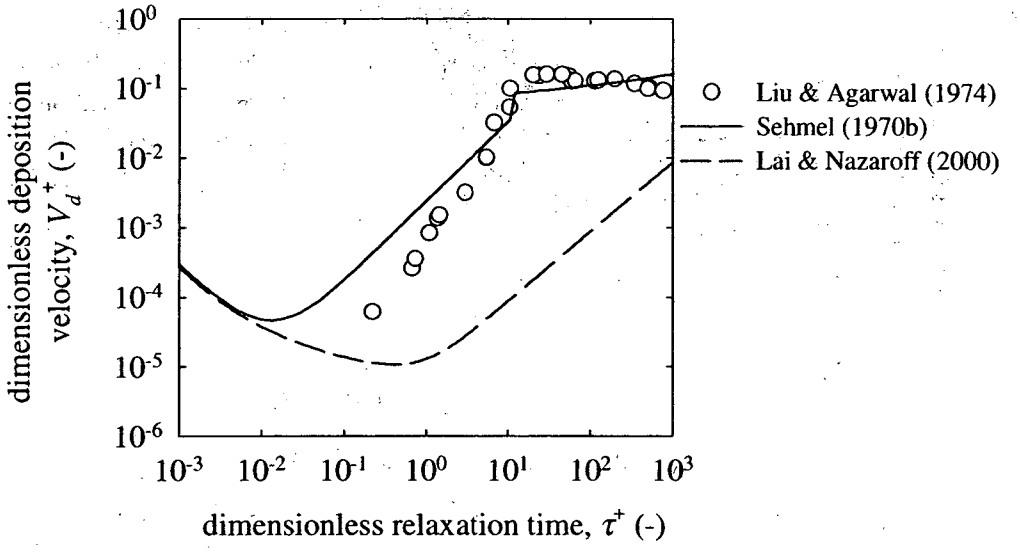

Figure 2.26 Comparison of gradient diffusion models with experimental data in the case of deposition to a smooth vertical wall.

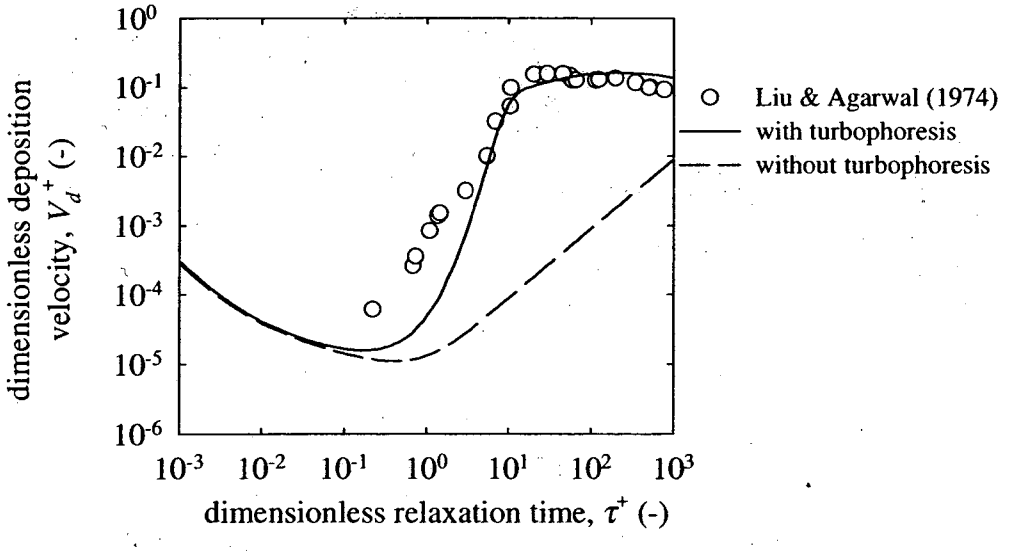

Figure 2.27 Comparison of the turbophoretic model of Guha (1997) with and without turbophoresis in the case of deposition to a smooth vertical wall.

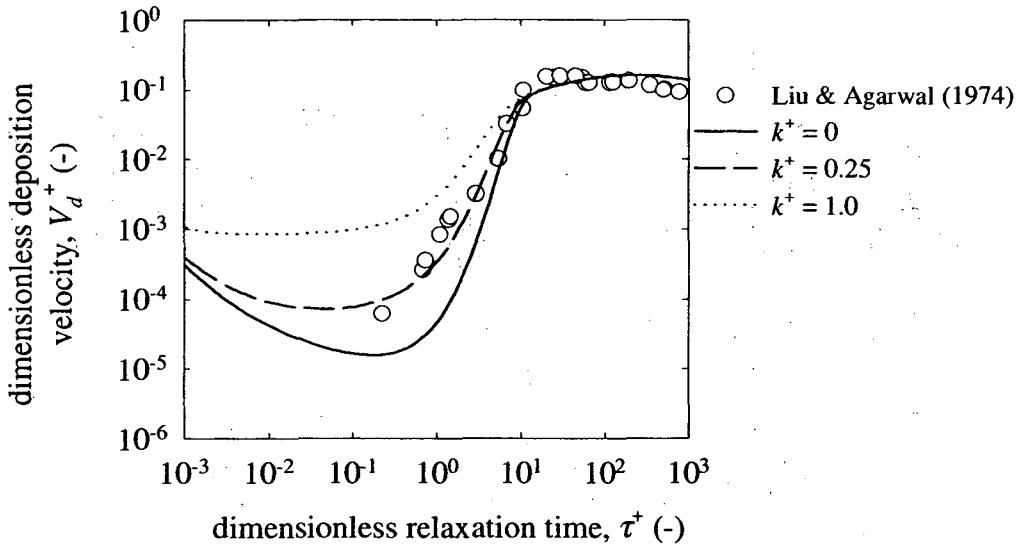

Figure 2.28 Comparison of the turbophoretic model of Guha (1997) for deposition to vertical walls with different roughness values to the experiments of Liu & Agarwal (1974).

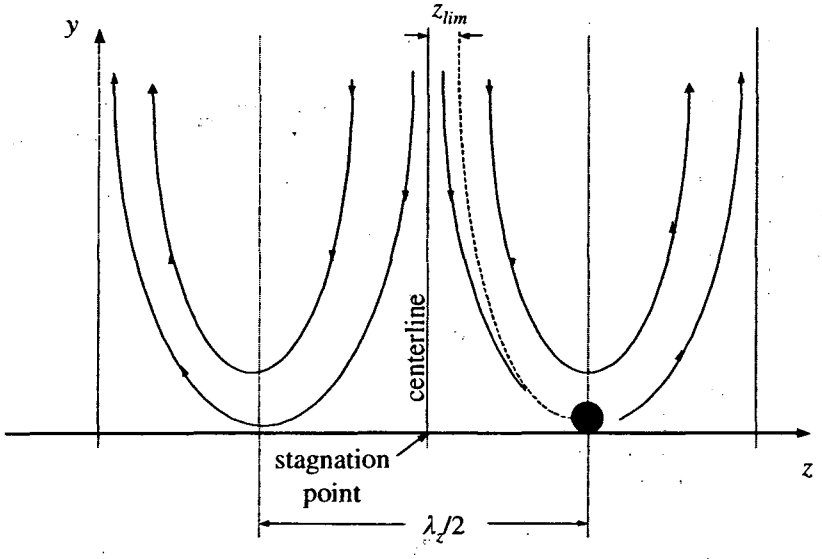

Figure 2.29 Schematic of two-dimensional stagnation point flow used to model near-wall turbulence in sublayer models. A particle depositing at the limiting trajectory is shown.

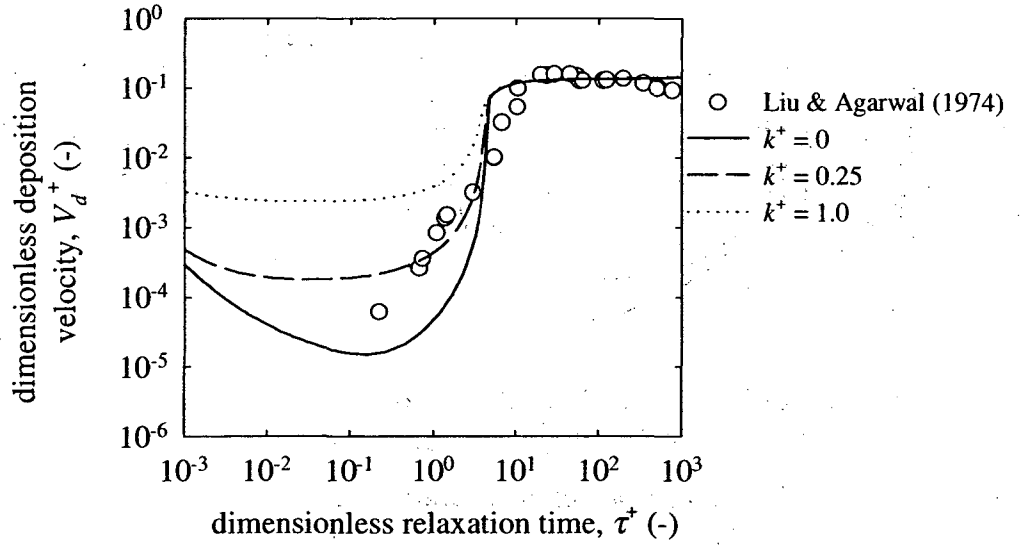

Figure 2.30 Comparison of the sublayer model of Fan & Ahmadi (1993) for deposition to vertical walls with different roughness values to the experiments of Liu & Agarwal (1974).

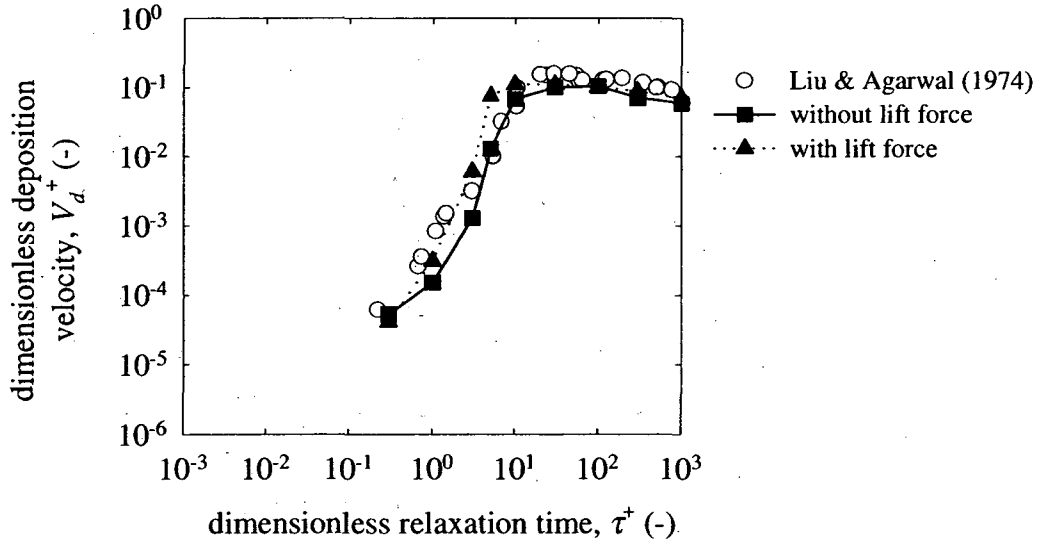

Figure 2.31 Deposition to a smooth vertical wall in the Lagrangian simulation of Kallio & Reeks (1989) with and without the lift force.

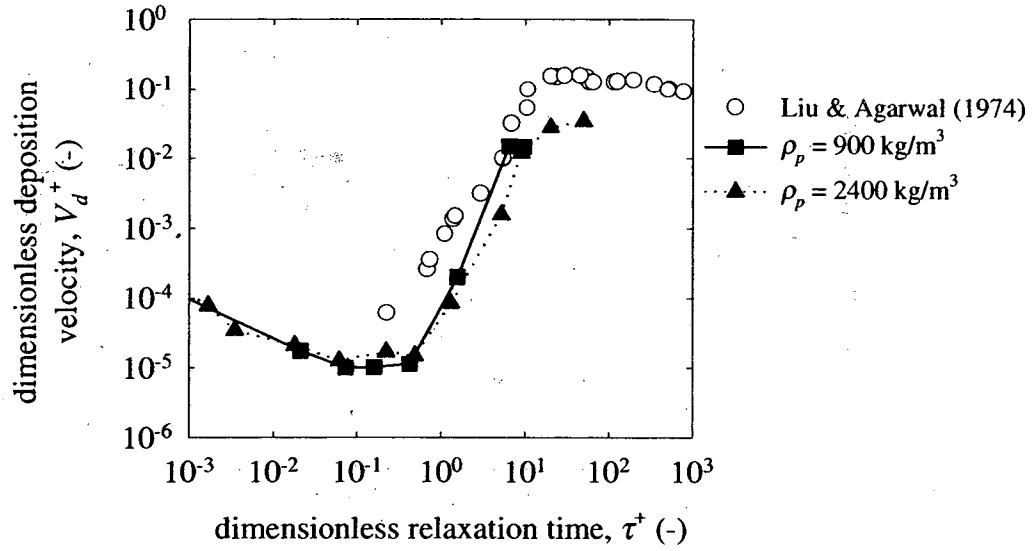

Figure 2.32 Deposition to a smooth vertical wall in the Lagrangian simulation of Li & Ahmadi (1993a) for particle densities of 900 and 2400 kg/m^3.

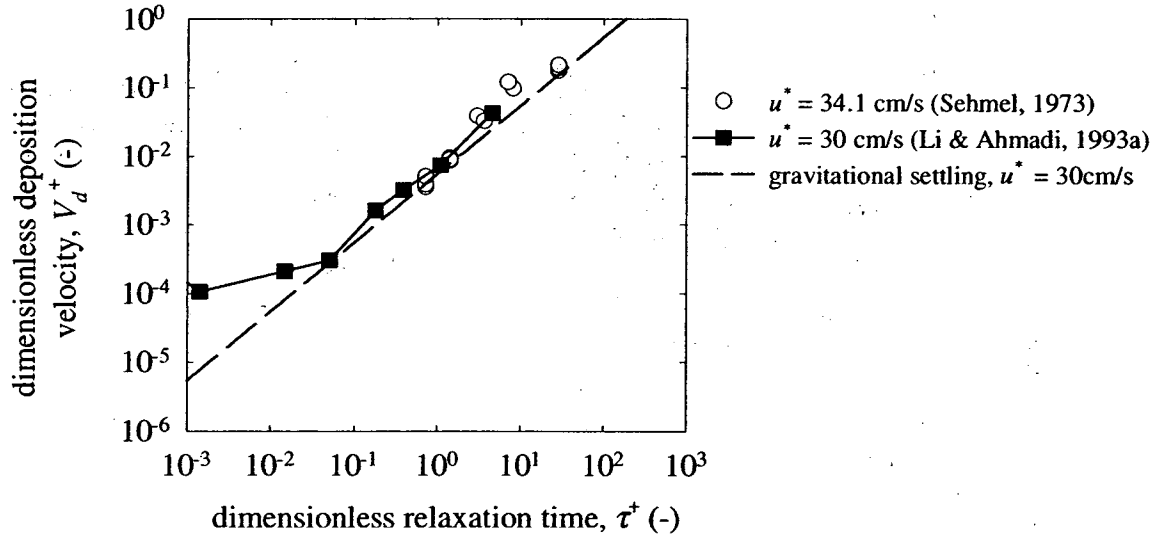

Figure 2.33 Deposition to a smooth horizontal floor in the Lagrangian simulation of Li & Ahmadi (1993a) compared to the similar experiments of Sehmel (1973).

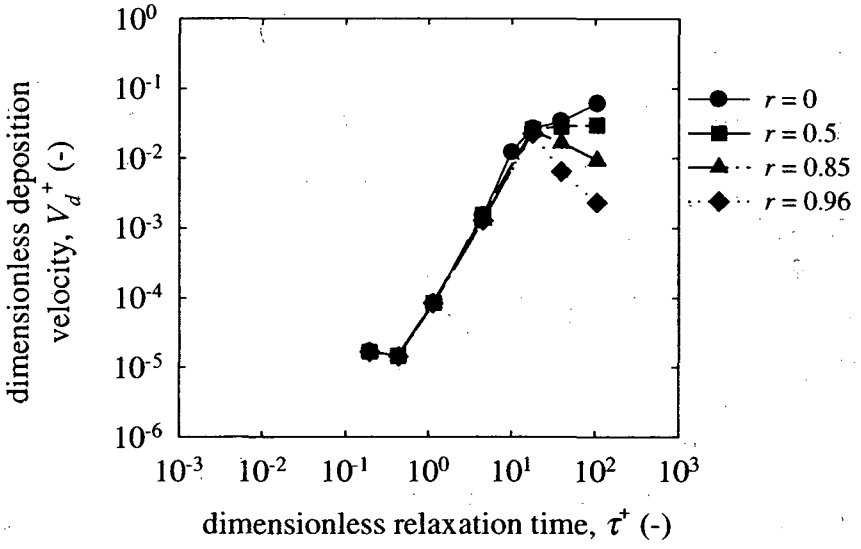

Figure 2.34 Deposition to a smooth vertical wall in the Lagrangian simulation of Li & Ahmadi (1993a) allowing for particle bounce with different restitution coefficients, r.

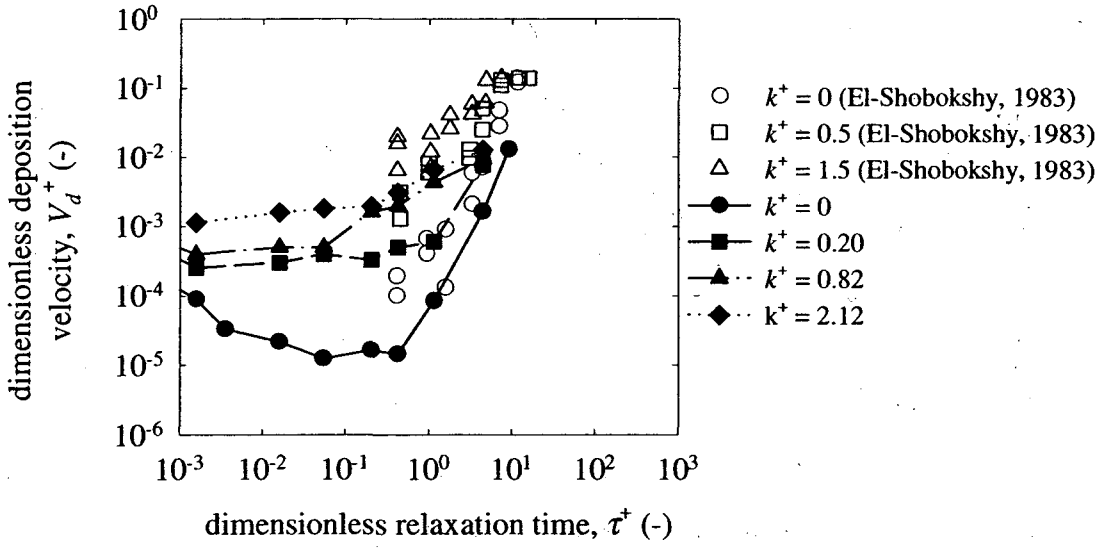

Figure 2.35 Deposition to smooth and rough vertical walls in the Lagrangian simulation of Li & Ahmadi (1993b) with four different dimensionless roughness values, k^+.

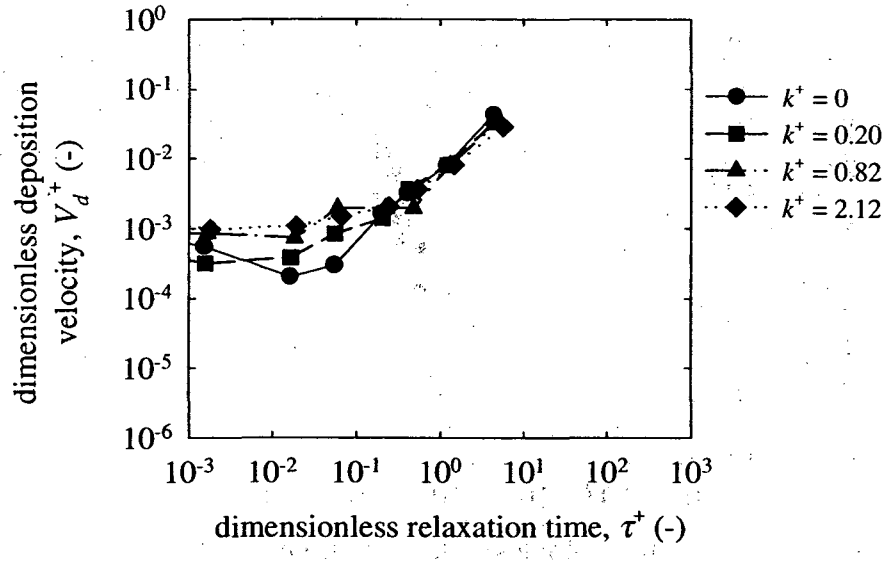

Figure 2.36 Deposition to rough horizontal floors in the Lagrangian simulation of Li and Ahmadi (1993b) with four different dimensionless roughness values, k^+.

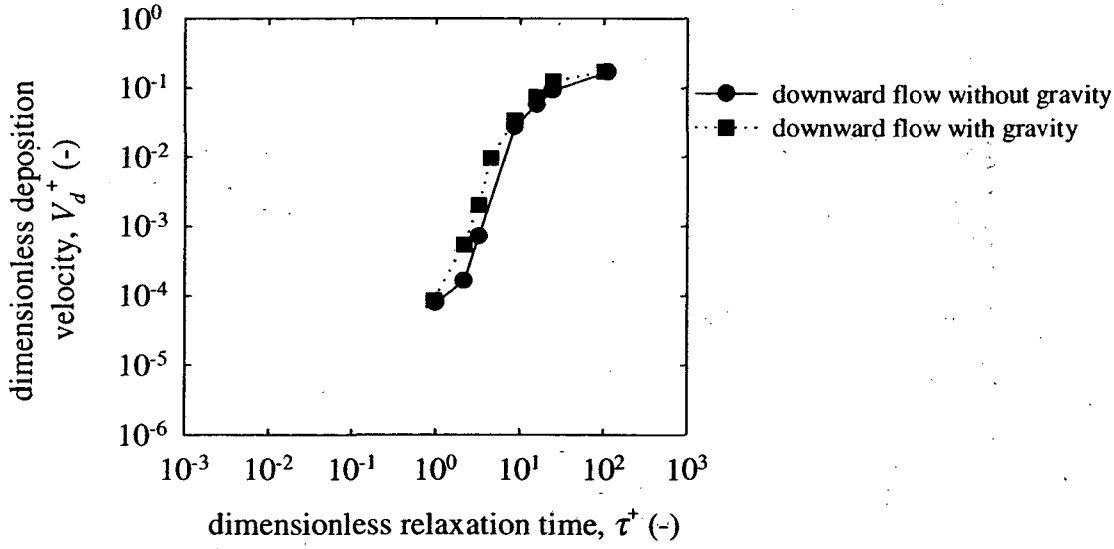

Figure 2.37 Results of deposition to a smooth vertical wall in the Lagrangian simulation of Chen & Ahmadi (1997) showing the influence of gravity in a vertical flow through the lift force.

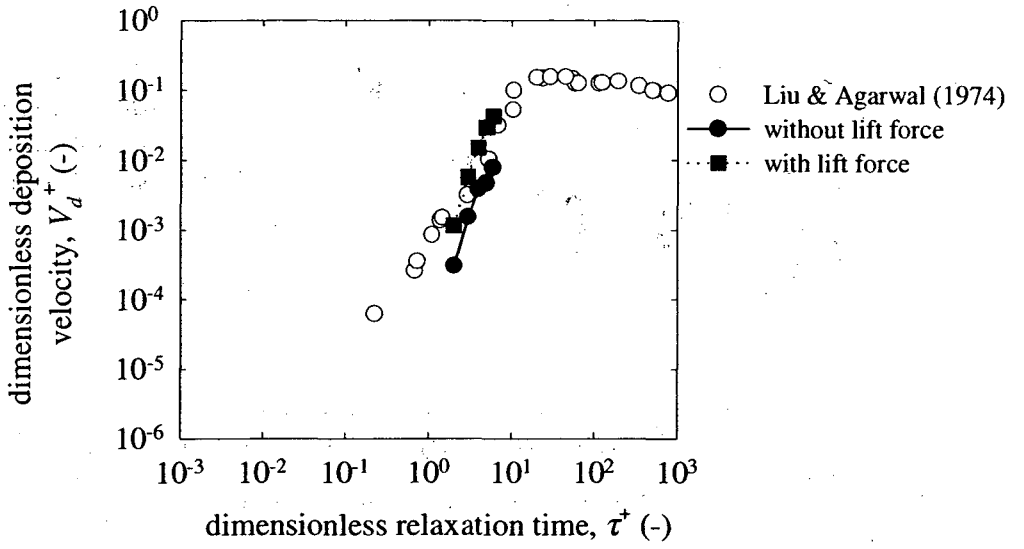

Figure 2.38 Deposition to a smooth vertical wall in the DNS-Lagrangian simulation of McLaughlin (1989) with and without the lift force compared to the experiments of Liu & Agarwal (1974).

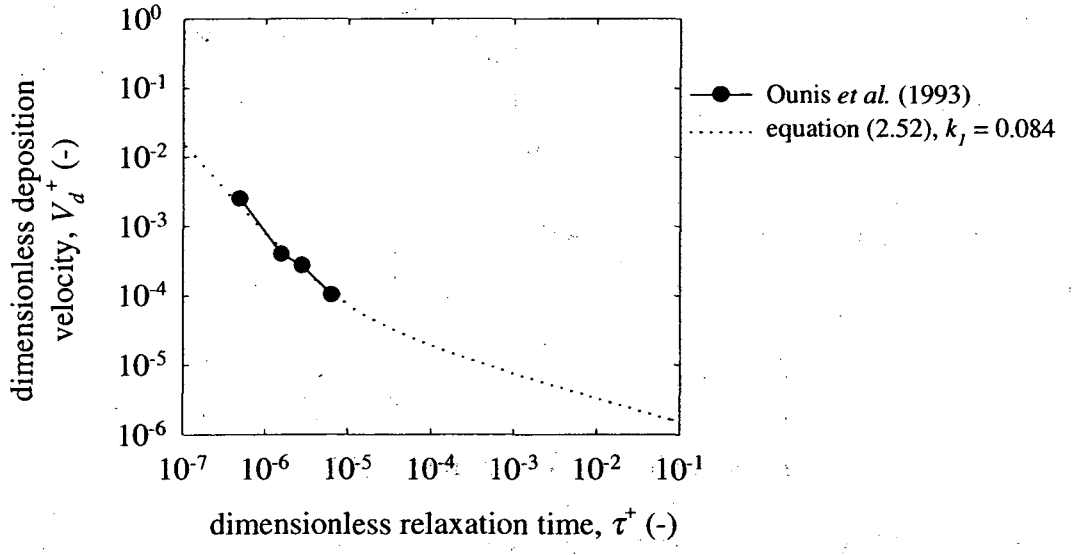

Figure 2.39 Deposition to smooth walls in the DNS-Lagrangian simulation of Ounis *et al.* (1993) for particles in the diffusive regime compared to equation (2.52).

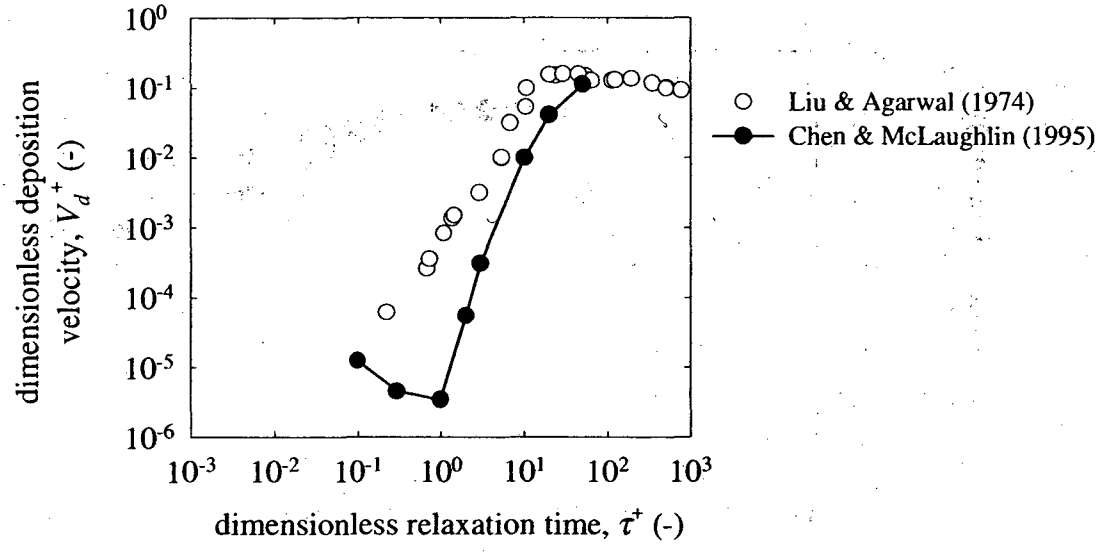

Figure 2.40 Deposition to a smooth vertical wall in the DNS-Lagrangian simulation of Chen & McLaughlin (1995) with wall-corrected drag and optimum lift forces compared to the experiments of Liu & Agarwal (1974).

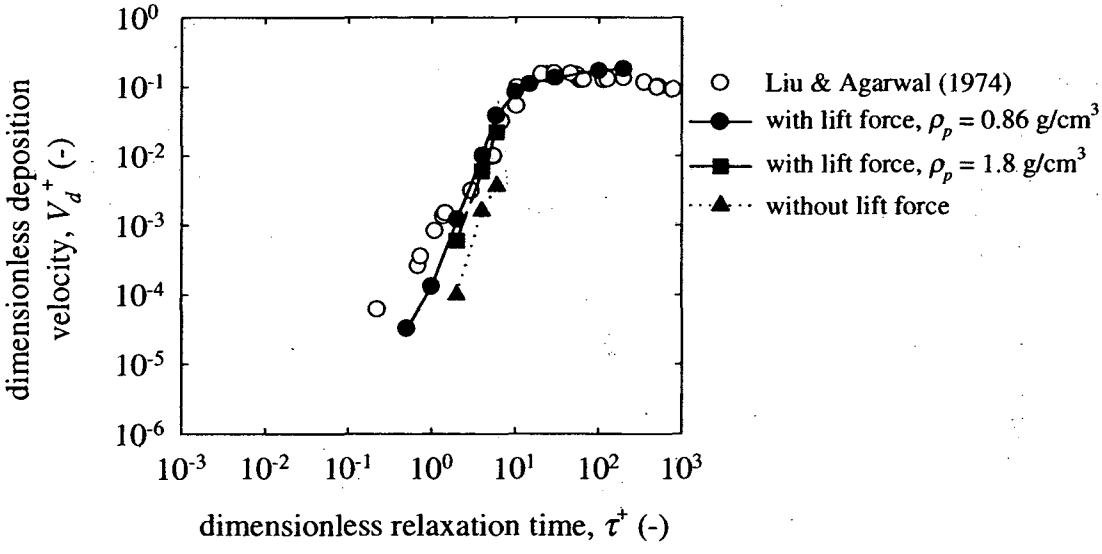

Figure 2.41 Deposition to a smooth vertical wall in the LES-Lagrangian simulation of Wang & Squires (1996b) with and without the lift force compared to the experiments of Liu & Agarwal (1974).

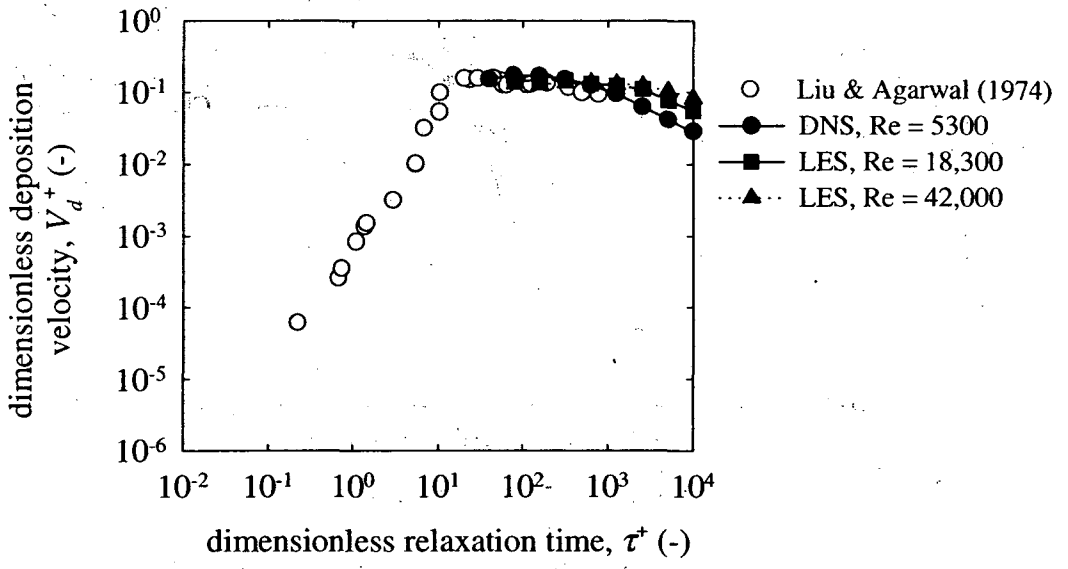

Figure 2.42 Deposition to smooth vertical walls in the DNS- and LES-Lagrangian simulations of Uijttewaal & Oliemans (1996) compared to the experiments of Liu & Agarwal (1974).

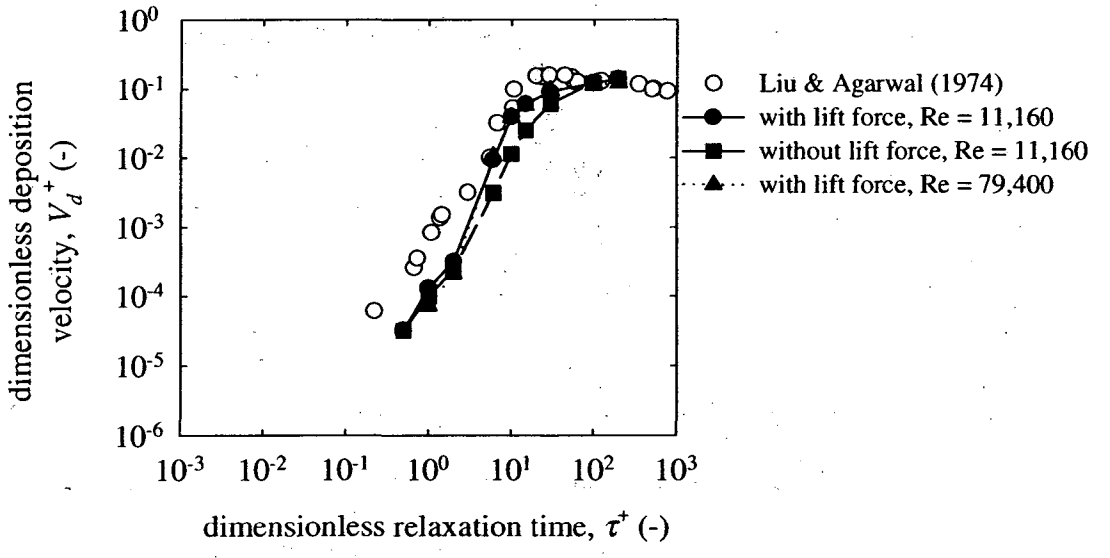

Figure 2.43 Deposition to a smooth vertical wall in the LES-Lagrangian simulation of Wang *et al.* (1997) with and without the optimum lift force compared to the experiments of Liu & Agarwal (1974).

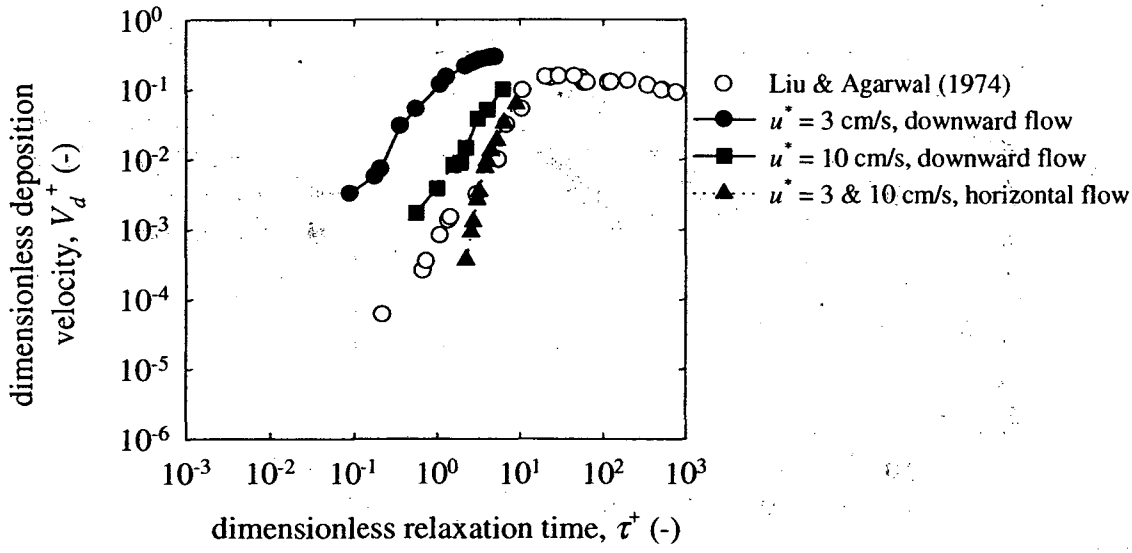

Figure 2.44 Deposition to a smooth vertical wall in the DNS-Lagrangian simulation of Zhang & Ahmadi (2000) with downward and horizontal flow at low friction velocities compared to the experiments of Liu & Agarwal (1974).

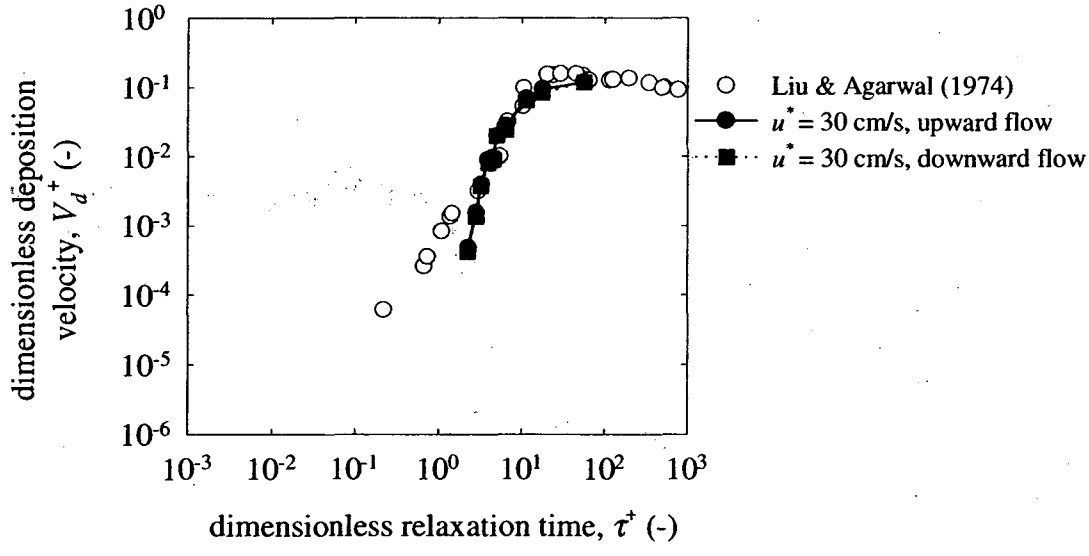

Figure 2.45 Deposition to a smooth vertical wall in the DNS-Lagrangian simulation of Zhang & Ahmadi (2000) from upward and downward flow at high friction velocities compared to the experiments of Liu & Agarwal (1974).

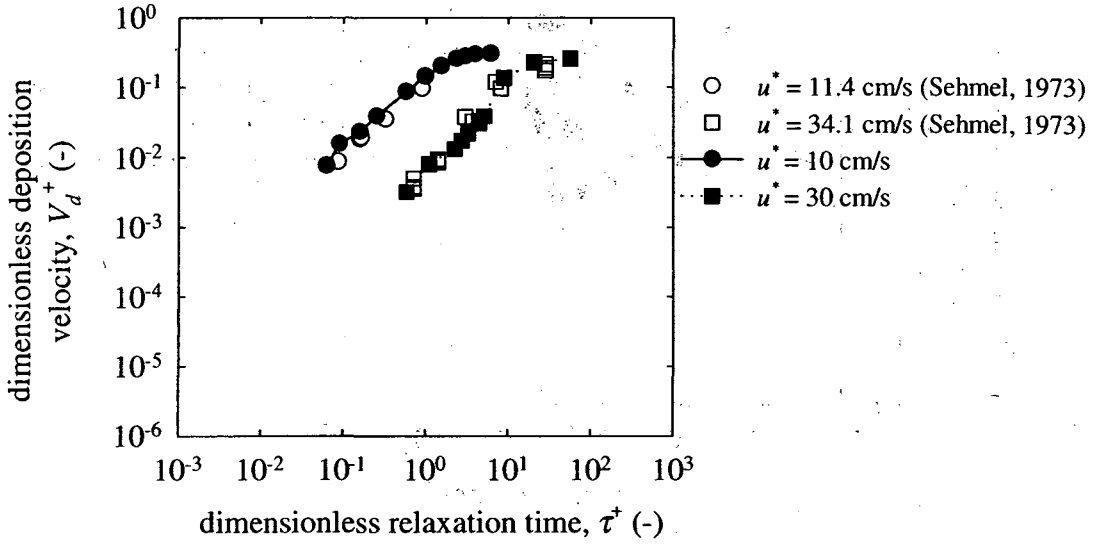

Figure 2.46 Deposition to a smooth horizontal floor in the DNS-Lagrangian simulation of Zhang and Ahmadi (2000) at two friction velocities compared to the similar experiments of Sehmel (1973).

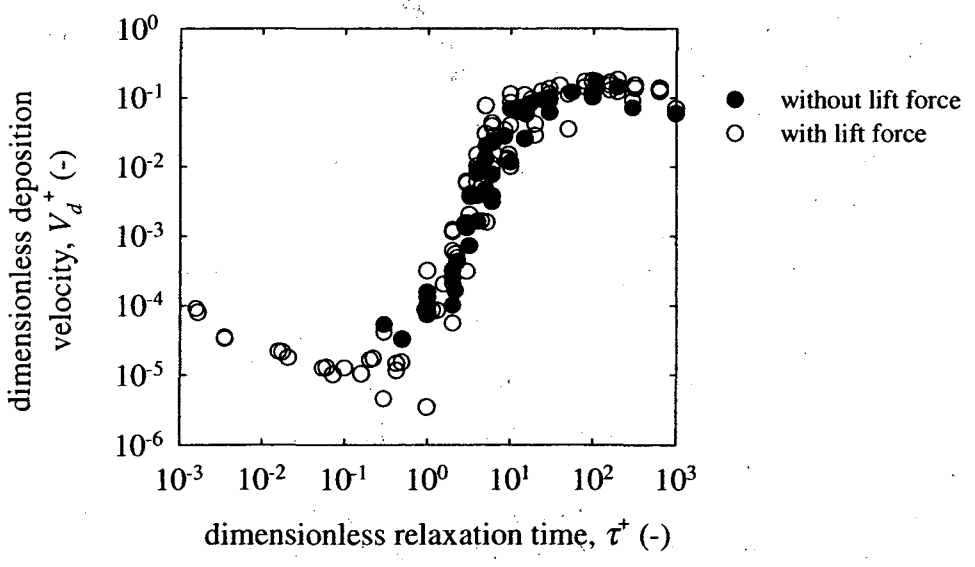

Figure 2.47 Deposition to smooth vertical walls in several Lagrangian simulations.

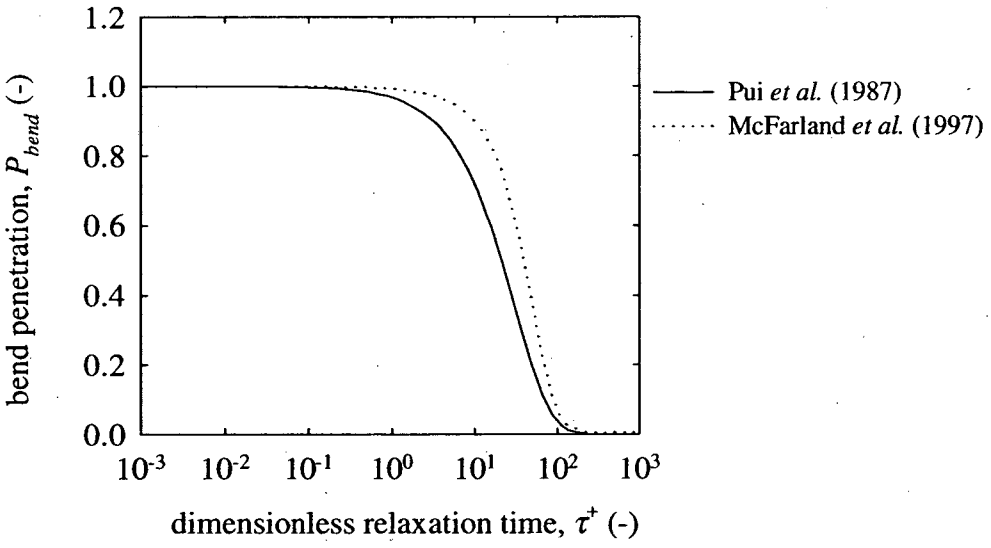

Figure 2.48 Comparison of empirical model predictions for particle penetration through a 90° bend in a 15 cm diameter duct at a velocity of 5 m/s.

CHAPTER 3

Experiments Measuring Particle Deposition from Fully Developed Turbulent Flow in HVAC Ducts

3.0 Abstract

Particle deposition in ventilation ducts influences particle exposures of building occupants and may lead to a variety of indoor air quality concerns. Experiments have been performed in a laboratory to study the effects of particle size, air speed and surface character on deposition rates of particles from turbulent air flows in galvanized steel and internally insulated ducts with hydraulic diameters of 15.2 cm. The duct systems were constructed of materials typically found in commercial HVAC systems. In the steel duct system, experiments with nominal particle sizes of 1, 3, 5, 9 and 16 μm were conducted at each of three nominal air speeds: 2.2, 5.3 and 9.0 m/s. In the insulated duct system, deposition rates of particles with nominal sizes of 1, 3, 5, 8 and 13 μm were measured at nominal air speeds of 2.2, 5.3 and 8.8 m/s. Fluorescent techniques were used to directly measure the deposition velocities of monodisperse fluorescent particles to duct surfaces (floor, wall and ceiling) at two straight duct sections where the turbulent flow profile was fully developed.

In steel ducts, particle deposition rates were higher to the floor than to the wall, which, in turn, were greater than to the duct ceiling. In insulated ducts, deposition was nearly the same to the duct floor, wall and ceiling for a given particle size and air speed. Deposition

to duct walls and ceilings was dramatically enhanced in insulated ducts compared to steel ducts. Deposition velocities to all three duct surfaces in both systems were found to increase with increases in particle size or air velocity over the ranges studied. Deposition rates measured in the current experiments were in general agreement with the limited observations of similar systems by previous researchers.

3.1 Introduction

Airborne particles adversely affect human health. Ventilation ducts are usually the dominant entry path of outdoor air into large buildings and indoor air is often circulated through ventilation ducts to be mixed with outdoor air, thermally conditioned, and returned to the indoor space. Most indoor air in large buildings passed through a ventilation duct at least once, and some air has passed through several times.

Airborne particles deposit to surfaces from turbulent flows by a variety of mechanisms. When such deposition occurs in ventilation ducts, it influences exposures of building occupants to particles. If bioaerosols deposit, subsequent growth or chemical interactions can lead to the release of a variety of indoor air pollutants such as mold spores and microbial volatile organic compounds. A better understanding of particle behavior in ventilation ducts is needed to evaluate pollutant exposures within buildings and contamination of HVAC systems.

Because of its importance to numerous systems, particle deposition from turbulent flow has been widely studied experimentally and theoretically. Factors known to be important

for determining deposition rates include particle size, degree of air turbulence, deposition surface roughness and the orientation of the deposition surface with respect to gravity. Particle deposition experiments were thoroughly reviewed in section 2.3 and models of deposition from turbulent flows were reviewed in section 2.5.

While there is a large body of experimental literature on particle deposition from turbulent flows, the specific case of deposition in ventilation ducts has not been substantially addressed. Most deposition experiments have been conducted in small diameter round tubes at high air speeds and friction velocities. Deposition within the horizontal ducts is expected to be nonuniform owing to the influence of gravity, but differences in deposition rates to different surface orientations have rarely been investigated. Particle deposition in ventilation systems is also likely to be strongly influenced by turbulent flow conditions and the roughness associated with real duct materials. Thus, one can not reliably generalize results from experiments in small diameter tubes to deposition in ventilation ducts.

Horizontal floors, vertical walls and horizontal ceilings are common in nearly all runs with rectangular ducts. Most experiments conducted in ducts with diameters and air speeds similar to those found in HVAC systems have only measured deposition rates to floors (Chamberlain *et al.*, 1984; Kvasnak *et al.*, 1993; Lai (1997)). Sehmel (1973) is the only investigator to report deposition rates to the ceiling of a horizontal duct. He measured deposition rates to a duct ceiling that were one to two orders of magnitude less than to a floor. Deposition to walls from vertical flows have been reported, but several

authors have suggested that particle deposition to vertical walls from vertical flows is likely to be different than from horizontal flows owing to the shear-induced lift force (Fan & Ahmadi, 1993; Wang & Squires, 1997). There are no measurements of particle deposition to a vertical wall from a horizontal flow. While most particle deposition in ducts is likely to occur at duct floors, information regarding deposition to duct walls and ceilings is necessary for achieving a more complete understanding of deposition from turbulent flows.

The microscale roughness character of the deposition surface is likely to influence particle deposition rates. Several theoretical analyses suggest that roughness elements of a few microns in size could dramatically increase deposition (Browne, 1974; Fan & Ahmadi, 1993). The experiments of El-Shobokshy (1983) showed orders of magnitude increases in deposition when the deposition surface roughness was increased from smooth to 7 and 20 μm. The experimental work of Wells & Chamberlain (1967) and Sehmel (1970a) showed very high deposition rates to fibrous surfaces compared to metallic surfaces. Theoretical treatments of deposition to fibrous surfaces have yielded similar results (Gutfinger & Friedlander, 1985; Oron & Gutfinger, 1986).

Ducts in large commercial buildings are usually constructed of galvanized steel. Commonly, some ducts are internally lined with fiberglass insulation to reduce noise transmission and to provide a thermal barrier. The fiberglass insulation generally has a fibrous composite layer on the airstream side to prevent glass fibers from being entrained into the airflow. Other materials used for duct construction are fiberglass duct board,

corrugated aluminum and flexible spiral-wound Mylar. Particle deposition rates are likely to be strongly influenced by the type of internal duct surface. The microscale roughness of duct materials and the fibrous character of the internal insulation may both play a role in determining deposition rates in real ventilation ducts, but the magnitude of the effect is uncertain. Experiments using materials common to real HVAC systems are rare and none have explored how roughness levels of real duct surfaces influence particle deposition.

In this chapter, experiments that have been conducted to investigate the influence of particle size, air speed, deposition surface character and turbulent flow character on particle deposition rates in HVAC ducts are described. The experiments were conducted in two experimental systems with the same layout: a galvanized steel duct system and an internally insulated duct system. Duct materials and air speeds investigated are common to commercial building HVAC systems and particle deposition was directly measured on the floors, walls and ceilings of the experimental duct surfaces.

In section 3.2, the experimental apparatus and equipment are described and the procedure for conducting an entire experiment and for performing the subsequent wet-chemistry analysis is described for the steel system. Methods for calculating reported data are detailed in section 3.3. Blank experiments to evaluate detection limits are reported in section 3.4. Section 3.5 describes differences between experiments in the steel and insulated systems. Each experiment yielded a large amount of data; section 3.6 reports results for deposition rates in straight duct sections where the turbulent flow profile was

fully developed in both the steel and insulated systems. These results are discussed in section 3.7 and conclusions are summarized in section 3.8. Deposition rates measured at other locations in the steel and insulated duct systems, such as at bends or locations where the turbulent flow profile was not fully developed, are reported in Chapter 4.

3.2 Experimental Methods in the Steel Duct System

This section describes the apparatus, equipment and methods used to conduct experiments in the steel duct system. Most details regarding the apparatus, equipment and methods in the steel system are the same as in the insulated system; differences between experiments performed in the two systems are described in section 3.5.

In the steel system, experiments were performed at three nominal air speeds of 2.2, 5.3 and 9.0 m/s for each of five nominal particle diameters: 1, 3, 5, 9 and 16 μm. One replicate experiment was performed with 1 μm particles at an air speed of 5.3 m/s, thus a total of sixteen experiments were conducted in the steel system. Nominal air speeds of 2.2, 5.3 and 9.0 m/s in the steel system corresponded to nominal friction velocities of 12, 28 and 45 cm/s.

3.2.1 Experimental apparatus

A schematic of the experimental apparatus for measuring particle deposition rates in ventilation ducts is shown in Figure 3.1. When experiments were performed, the two louvers were in the closed position as shown in Figure 3.1 so that the airflow followed a recirculating path in the clockwise direction. Air flowed out of the mixing box into the

lower duct and returned to the fan inlet via the upper duct. High efficiency particle in air (HEPA) filters were located on the non flow sides of the closed flow louvers and were not directly in use when the flow arrangement was in a recirculating path. Airflow was induced by means of a fan with an adjustable speed motor. Monodisperse experimental particles tagged with a fluorescent tracer (sodium fluorescein) were injected into the duct system at the mixing box. Because of the small rate of output of particles from the particle generator, the recirculating flow path was implemented to allow airborne particle concentrations in the duct to increase above levels that could be realized in a single-pass flow arrangement.

For each experiment, particle deposition fluxes to duct surfaces were measured at six general locations, labeled 1-6 in Figure 3.1. Test ducts 1 and 2 were sections in long, straight segments of duct where the turbulent flow had a fully developed flow profile. Test duct 3, immediately after the mixing box outlet, and test duct 4, immediately after a 90° bend, were duct sections where the turbulent flow profile was developing. The remaining two locations were 90° duct bends termed bend 5 and bend 6. Bend 5 change the flow direction from vertical to horizontal and was immediately preceded by another 90° bend associated with a branched section of duct. Bend 6 was a right turn in the horizontal plane and was at the end of the long, straight upper duct.

Time-averaged airborne particle concentrations were measured immediately upstream and downstream of test ducts 1 and 2 by isokinetic sampling to filters for the duration of an experiment. Concentrations measured upstream and downstream of test duct 1 were

respectively labeled $C_{1,up}$ and $C_{1,down}$; those measured near test duct 2 were labeled $C_{2,up}$ and $C_{2,down}$.

Air temperature, relative humidity, air velocity and static pressures in the duct were measured during experiments. Air temperature was continuously measured at locations A and B, labeled in Figure 3.1; relative humidity was continuously monitored at location A. Static pressure in the duct was continuously measured at locations A and C and these measurements were used to determine the pressure drop along the duct. The bulk air velocity was measured immediately upstream of test ducts 1 and 2 at the beginning of each experiment.

3.2.2 Experimental equipment

The adjustable speed fan consisted of a 27 cm diameter direct-drive high-pressure blower (Dayton Mfg., Model 4C108) with a 1 hp 3-phase motor (Dayton Mfg.) and an AC inverter (General Electric, Model AF-300) to provide adjustable speed control. The fan blew air directly into a galvanized steel mixing box measuring 0.61×0.91×1.02 m (Walter Mork Inc.). The experimental particles were produced by means of a vibrating orifice aerosol generator (VOAG) (TSI Inc., Model 3450) and a Boltzmann charge distribution was imparted on the experimental aerosol by passing it through a particle neutralizer (TSI Inc., Model 3054) with a Kr-85 radioactive source. Air flowed out of the mixing box and into the lower duct through a 15.2 cm (6.0 in) diameter round opening. The lower duct was attached to the mixing box outlet via a short section of flexible Mylar duct and a galvanized steel transition element to convert the flow from a round to a square cross

section. Figure 3.2 is a photograph of the portion of the experimental apparatus including the VOAG, particle neutralizer, fan and mixing box. Also visible in this photograph is bend 6 at the end of the upper duct.

The lower and upper ducts were horizontally oriented and consisted of several 1.5 m (5.0 ft) long galvanized steel sections with 15.2×15.2 cm (6.0×6.0 in) square cross sections (Allied Mechanical HVAC). Each duct section was constructed from 24 gauge galvanized steel and had four beading ridges spaced at intervals of 30.5 cm (12 in). These ridges ran transverse to the flow direction around the entire perimeter of the duct. When viewed from inside the duct, the beading was recessed into the wall and had a depth of 1.0 mm and a width of 8.0 mm. Beading is common in HVAC ducts and serves to increase the structural strength of large ducts. A discussion of the internal surface roughness of both the steel and insulated ducts is given in Appendix A. Duct bends 5 and 6 were 90° bends with a bend radius of 22.9 cm (9.0 in), giving a bend ratio of $R_o = 3.0$.

Individual sections of duct were connected in series by an S-and-drive connection system. Each junction was fastened by two S-connectors and two drive connectors. Figure 3.3 is a close-up photograph of the junction between two duct sections prior to being connected. An S-connector is attached to the duct on the right in the photograph. To complete the connection, the leading edge of the left-hand duct must be inserted into the exposed slot of the S-connector. In this manner, the two ducts are aligned and slightly overlap. The S-connector name is derived from its flattened S-shape when viewed from the side. Also visible in Figure 3.3 are the leading edges on the sidewalls of

the ducts. These leading edges are folded back to create grooves down which C-shaped drive-connectors are slid on the outside of the joint to prevent the duct sections from being pulled apart. An S-connector may influence particle deposition because a portion of it is exposed to the internal flow. S-connectors projected a height of 2.0 mm into the flow. Drive connectors do not directly influence particle deposition because they are located on the duct exterior.

Duct sections in the lower duct were connected with S-connectors at the duct floor and ceiling and drive connectors on the exterior sidewall; duct sections in the upper duct had S-connectors on the sidewalls and had drive connectors on the exterior of the duct ceiling and floor. This arrangement was used to evaluate potential differences in particle deposition rates to duct surfaces resulting from the presence or absence of S-connectors on that surface. Particle deposition fluxes were measured to the two S-connectors on the floor of test duct 1, the two on the ceiling of test duct 1 and the four on the sidewalls of test duct 2 for all experiments in the steel system. All duct sections, even bends and transition elements, were connected via the S-and-drive system.

At the end of the lower duct, the flow encountered a branched duct with louvers to control the flow direction. In the experimental configuration the flow was directed through the upward branch, through a 90° bend (bend 5) and into the upper duct heading back towards the fan inlet. A photograph of this transition from the lower duct to the upper duct is shown in Figure 3.4. Bend 5 and test duct 4, immediately after bend 5, can be seen. Also visible in this photograph are the transverse beading ridges on test duct 4.

The lower duct was made up of eleven duct sections, including the final branched section, for a total length of 16.8 m (55.0 ft). The inlet to test duct 1 was located 12.2 m (40.0 ft) downstream of the mixing box outlet; this provided a length of 80 hydraulic diameters for the turbulent flow profile to develop. The upper duct consisted of twelve straight duct sections and had a total length of 18.3 m (60.0 ft). Test duct 2 was 13.7 m (45.0 ft) downstream of bend 5, giving a length of 90 hydraulic diameters for the flow profile to develop. The lower duct and the upper ducts were immediately adjacent to the wall upon which they were mounted. At the end of the upper duct, a 90° bend, bend 6, directed the flow away from the wall and into a downward turning bend and a branched duct that directed air back to the fan inlet via a short section of flexible Mylar duct.

The entire system was sealed with foil duct tape to minimize air leakage into and out of the duct. Duct junctions, longitudinal duct seams and mixing box connections were all carefully sealed with foil duct tape. The junctions of test ducts were sealed with masking tape that allowed for easier removal after an experiment than the foil duct tape.

An Aerodynamic Particle Sizer (APS) (TSI Inc, Model 3320) was used to continuously sample the test aerosol at the centerline of the lower duct through a specially designed shrouded sampling nozzle. The high capacity HEPA filters (Farr, Model 1XT-232312) were 0.59×0.59 m with a depth of 0.29 m and were connected to the system via galvanized steel transition components that were 1.0 m in length.

3.2.3 Experimental protocol with steel duct system

A well defined protocol was followed during all experiments. The experimental procedure is first described generally, then details of certain steps are provided. The steps involved in conducting a single experiment were as follows.

1. On the day preceding the start of an experiment, test duct sections, eight S-connectors, sampling nozzles, and filter holder assemblies were cleaned and dried.
2. To begin an experiment, isokinetic sampling pumps were turned on to warm up and the data acquisition board that controlled air temperature, relative humidity and pressure sensors was turned on.
3. Duct sections adjacent to test duct sections in the apparatus were cleaned and dried.
4. Isokinetic sampling nozzles and the shrouded nozzle for the APS were installed; then the test duct sections were installed and the joints and seams of the test sections were sealed with masking tape.
5. The duct was straightened and secured to its mounting brackets with bungee cords.
6. The fan was turned on and set to the proper speed, flow louvers were properly positioned, and air leaks in the system were diagnosed and sealed with tape.
7. Measurements of centerline air velocity pressures were made at the sampling nozzle locations and the sampling pump flow rates were adjusted to achieve isokinetic sampling.
8. The bulk air velocities in the upper and lower duct were measured.
9. Filters were inserted into the filter holders and these were attached to the isokinetic sampling nozzles.

10. Sampling pump flow rates were measured and readjusted to the isokinetic rate if necessary. The pumps were attached to the sampling nozzles and filter holders.
11. Fluorescent experimental particles were generated and injected into the system.
12. The APS was attached to the shrouded aerosol probe and programmed to collect aerodynamic particle size data for the duration of the experiment.
13. The experiment was allowed to run for several hours.
14. After sufficient time had elapsed, the particle generator was turned off.
15. Centerline air velocity pressures were measured at the sampling nozzle locations and the isokinetic sampling pump flow rates were measured.
16. The fan, APS and sampling pumps were turned off and all test ducts, sampling nozzles, filter holders and filters were removed for fluorescence analysis.
17. The data acquisition system was turned off.
18. Fluorescent techniques were used to measure the particle mass deposited on filters, inside the filter holders and inside the sampling nozzles to determine time-averaged airborne particle concentrations during the experiment.
19. Fluorescent techniques were used to measure the particle mass deposited on duct surfaces and S-connectors to help determine particle deposition fluxes.

3.2.3.a Cleaning in steps 1 and 3

Prior to starting an experiment, the six test duct sections (four straight ducts and two bends) and the eight S-connectors associated with test ducts 1 and 2 were cleaned by rinsing with tap water. Test ducts were rinsed in a large steel tub filled with water to completely submerge all duct sections. Tap water continuously flowed into the tub and

out the bottom at a rate of about 9 L/min for an average residence time of about one hour. Test ducts were rinsed for about 5 hours, removed and manually towel-dried both internally and externally. The test ducts were then rinsed for an additional 5 hours before being set out to air-dry overnight. S-connectors for test ducts 1 and 2, isokinetic sampling nozzles and filter holder assemblies, all of which were analyzed for fluorescent particle mass at the end of each experiment, were rinsed in a laboratory sink using the same basic method.

When not in use, the experimental apparatus was missing the six test duct sections. With the apparatus in this state, the connecting edges of ducts adjacent to the test duct locations were scrubbed with a wet towel and then dried. This was done to reduce the transfer of residual fluorescent material from these ducts to the cleaned S-connectors that were to be installed. Throughout the entire experimental set-up, operation, shut-down and subsequent wet-chemical analysis, latex gloves were worn by the experimentalist. These gloves were frequently changed to reduce the transfer of fluorescent material from hands to the test duct sections or other items to be analyzed.

3.2.3.b Installation of test ducts and sampling nozzles in step 4

Stainless steel sampling nozzles (Apex Instruments Inc.) were installed through the floor of the duct immediately upstream and immediately downstream of test ducts 1 and 2 to collect filter samples for quantification of the airborne particle concentration. The nozzles were positioned along the flow axis with inlets at the duct centerline. Figure 3.5 shows photographs of an isokinetic sampling nozzle installed in the duct downstream of

test duct 1. In these photographs, test duct 1 has been removed. Also visible in the photographs are the 47 mm filter holder assembly and the associated isokinetic sampling pump. Depending on the experimental air velocity, nozzles with nominal inlet diameters of either 3.05 mm (0.120 in) or 4.57 mm (0.180 in) were installed so isokinetic sampling velocities could be achieved with the range of flow rates available from the pumps. The actual inlet diameters of all nozzles were measured using calipers.

Once the sampling nozzles were installed, the cleaned test ducts were installed. Test ducts 1 and 2 were installed using the cleaned S-connectors. Care was taken to not touch any duct surfaces that were to be analyzed later for particle deposition fluxes. The joints and seams of test ducts were sealed with strongly adhering masking tape. This masking tape was in direct contact with the portion of the S-connectors on the exterior of the ducts; however, it was determined by previous experimentation to have no effect on the fluorescence determination when measuring particle fluxes to the S-connectors.

3.2.3.c Air velocity measurements and determination of isokinetic pump rates in steps 7, 8 and 15

All air velocity determinations were made by means of a pitot tube (Dwyer Instruments Inc., Model H-11) with an outside diameter of 3.2 mm (0.125 in) attached to a digital handheld manometer (Energy Conservatory, Model DG-3) to measure the air velocity pressure. This manometer measured pressure differences with a resolution of 0.1 Pa with an expected accuracy of ±0.1 Pa. The pitot tube was inserted into the duct through sampling holes drilled into the duct walls that were sealed by tape when not in use.

Positioning of the pitot tube was achieved manually by aligning etchings on the pitot tube exterior with the duct wall. The manometer yielded time-averaged values for the velocity pressure every five seconds. The velocity pressure, P_v, was used to calculate the local air velocity via the following expression:

$$u = \sqrt{\frac{2P_v}{\rho_a}} \tag{3.1}$$

Two types of air velocities were measured during experiments: centerline air velocities and bulk air velocities. Centerline air velocities were needed at each sampling nozzle to determine the proper flow rate to achieve isokinetic sampling. Determination of centerline air velocities was accomplished by a single measurement immediately upstream of each sampling nozzle. The isokinetic sampling rate, Q_i, was calculated by

$$Q_i = \frac{\pi}{4} d_{inlet}^2 u_c \tag{3.2}$$

where d_{inlet} is the inlet diameter of the sampling nozzle and u_c is the local centerline air velocity. Continuously adjustable sampling pumps and a mass flow controller (Sierra, Model Sidetrack III) were used to draw air through the sampling nozzles at the isokinetic flow rate. The flow rates were measured using an electronic bubble flow meter (Gilian Instruments, Gilibrator). Sampling nozzles delivered the aerosol to nitrocellulose filters (Osmonics) that were 47 mm in diameter with a 0.8 μm pore size and were inserted into 47 mm Teflon filter holders (Apex Instruments).

Average air velocities were measured using the equal area method in which the average velocity was calculated as the average of 16 local air velocity measurements. The

positioning of the pitot tube for these 16 measurement was in a 4×4 grid in the *y-z* plane of the duct as shown in Figure 3.6. Thus, the average air velocity was calculated by

$$U_{ave} = \frac{\sum_{i=1}^{16} u_i}{16} \tag{3.3}$$

where u_i is the local streamwise air velocity at each of the 16 points in Figure 3.6. The accuracy of this equal area method for calculating the average air velocity is expected to be ± 2%. The average air velocity was measured in the lower duct immediately upstream of test duct 1 and in the upper duct immediately upstream of test duct 2. The average velocities in these two locations always agreed to within 2% for a given experiment. The value of U_{ave} reported for an experiment is the average of these two realizations.

3.2.3.d Temperature, relative humidity and static pressure measurements in steps 2 and 17

The air temperature, relative humidity and pressure drop in the duct were monitored with appropriate sensors controlled by an automatic data acquisition board (Adac, Series 5000). This data board recorded voltage outputs from the temperature, relative humidity and pressure sensors once every 1-10 minutes. The time interval between measurements was smaller for shorter experiments than for longer experiments. Each data point recorded was the average of ten measurements taken over a ten second span. The logged voltages are expected to be accurate to within ±0.007 V. Reported temperatures, relative humidities and pressure drops are the averages of the hundreds of measurements made during the time that particles were injected into the system.

The air temperature within the duct was measured in the lower duct immediately downstream of test duct 3, location A in Figure 3.1, and in the upper duct immediately downstream of test duct 2, location B. Thermistors (Omega, Series 2252) were mounted so that the sensor tips were located along the duct centerline. These thermistors are expected to be accurate to within ±0.1 °C. The ambient air temperature in the room was monitored with a thermistor and the data acquisition board.

Relative humidity was measured at the duct centerline at location A. The relative humidity sensor (Vaisala, HMD60) was expected to be accurate to within ±2% for relative humidities in the range 0-90% and temperatures in the range 10-40 °C. Duct air temperatures and relative humidities were always within these specified ranges during experiments.

The static pressure was monitored in the lower duct at two locations: an upstream location 1.8 m (6.0 ft) after the mixing box outlet, location A, and a downstream location 14.9 m (49.0 ft) after the mixing box outlet, location C in Figure 3.1. The pressure sensors (Setra, Model 264) measured the pressure in the duct relative to the atmosphere through wall-mounted pressure taps. These pressure sensors were internally recalibrated after every ten measurements and expected to be accurate to within ±5 Pa.

The static pressures at the upstream and downstream locations, respectively P_A and P_C, were used to calculate the axial pressure gradient in the straight duct by

$$\frac{\Delta P}{\Delta L} = \frac{P_A - P_C}{\Delta L} \tag{3.4}$$

where ΔL is the distance between the two measurement locations. The friction factor and friction velocity were then calculated using equations (2.6) and (2.7). Friction velocities calculated from static pressure measurements in both the upper and lower ducts using the pitot tube and digital manometer agreed with these reported values to within ±3%.

3.2.3.e Particle generation and collection of particle size data in steps 11 and 12

Monodisperse particles were generated by means of a vibrating orifice aerosol generator (VOAG). This device generates particles by forcing a liquid stream through a small orifice that vibrates at a known frequency. The liquid stream, referred to as the aerosol solution, is a mixture of nonvolatile solutes in a volatile solvent. As the aerosol solution passes through the vibrating orifice, it breaks up into liquid droplets, which are of uniform size because the orifice is vibrated at a controlled frequency. The volatile component of the liquid droplets rapidly evaporates, leaving the nonvolatile solutes, which are the experimental particles. Being liquid, these particles are spherical and they are highly monodisperse. The final diameter of the generated particles can be controlled and depends on the vibration frequency of the orifice, the aerosol solution feed rate and the concentration of nonvolatile solutes in the aerosol solution.

In these experiments, the aerosol solution was a mixture of three components: isopropyl alcohol (IPA), oleic acid, and a solution of solid fluorescein in 0.1 M aqueous ammonium hydroxide. The fluorescein-ammonium hydroxide solution was made by mixing 5.0 g of fluorescein into one liter on 0.1 M aqueous ammonium hydroxide. The IPA and the water served as the volatile solvents and the nonvolatile solutes were oleic acid and

fluorescein. Fluorescein was the fluorescent tracer that allowed the quantification of particle airborne concentrations and surface fluxes. In the experiments conducted in the galvanized steel duct system, particles with nominal diameters of 1, 3, 5, 9 and 16 μm were investigated. The components of the aerosol solution, the VOAG settings and the resulting particle density for these nominal particle sizes are reported in Table 3.1. Table 3.2 gives the same information for the nominally 1, 3, 5, 8 and 13 μm diameter particles investigated in the insulated duct system. Note that the aerosol solutions for 1 μm particles contained no oleic acid; thus, these particles were solid ammonium fluorescein. Particle larger than 1 μm consisted of oleic acid droplets with ammonium fluorescein suspended in this liquid.

Before injecting the generated particles into the mixing box, particle size and monodispersity were monitored with an APS. Once particles were input to the system, experimental run times varied in the range 4-144 hours depending on the particle size and air speed. Smaller particles have lower deposition rates and less fluorescent tracer mass per particle; thus, experiments with small particles require longer times to accumulate a detectable mass on duct surfaces than those using large particles.

During experimental operation, particles in the ventilation duct were continuously monitored using an APS. The aerosol was delivered to the APS via a specially designed shrouded sampling anisokinetic nozzle located in the lower duct 9.0 m (29.5 ft) downstream of the mixing box outlet. A shrouded nozzle was used in this case to deliver the maximum number of particles to the APS. A description of the shrouded nozzle and

an evaluation its performance based on experiments in the insulated duct system can be found in Appendix B. Aerodynamic particle size data collected by the APS were used to calculate the mean physical diameter of experimental particles during the experiment.

3.2.3.f Wet-chemistry analysis in steps 18 and 19

Airborne particle concentrations and particle surface fluxes were quantified by fluorescent techniques in a wet-chemistry lab. Filters, duct surface panels, S-connectors and interior portions of nozzles and filter holders were each rinsed with a known amount of rinsing solution in a glass tray or Pyrex beaker. The fluorescence of the resulting wash solution was measured by means of a fluorometer (Turner Designs, Model TD-700). The flourometer was calibrated with five samples of known fluorescein concentration in the range 0-125 ng/mL. The rinse was a buffer solution of sodium phosphate dibasic heptahydrate in water at a concentration of 13.4 g/L with a pH of 9.2.

To begin the wet-chemistry analysis, a known volume of rinsing solution was delivered to a tray or beaker. The tray or beaker was then rinsed thoroughly with the rinsing solution and the fluorescence of the resulting solution was measured in the fluorometer to determine the background fluorescence. This background was usually zero. Then the piece to be analyzed was added to the tray or beaker and manually rinsed. A minimum of three fluorescence measurements were performed for each piece and rinsing was repeated multiple times between each measurement. Further rinsing and measurement was performed if the measured fluorescence had not stabilized by the third measurement. All

liquid measurements of 100 mL or less were made by means of a pipette; volumetric flasks were used to measure larger volumes.

In general the mass of fluorescein on a filter, on a duct surface, on an S-connector or inside a sampling nozzle or filter holder was be determined by

$$m = V_r\left(C_f - C_{f,b}\right) \tag{3.5}$$

where m is the fluorescein mass, V_r is the volume of rinsing solution, C_f is the concentration of fluorescein in the resulting rinse solution and $C_{f,b}$ is the background fluorescein concentration.

3.2.3.g Determination of particle concentrations in step 18

Not all particles entering the isokinetic sampling nozzle reach the filter, some deposit on the interior of the nozzle walls or in the filter holder. To get an accurate determination of the airborne concentration, the particle mass at these locations must be measured and included in the concentration determination. Filters were rinsed by soaking in a known amount of rinsing solution. Filter holders and nozzles were rinsed by repeatedly passing a small amount of buffer solution from a measured quantity through the piece by means of small-volume disposable transfer pipettes. The mass of fluorescein on a filter, m_f, the mass deposited inside a sampling nozzle, m_n, and the mass of fluorescein on the interior of a filter holder, m_{fh}, were each determined by equation (3.5). Appendix B presents particle transport efficiencies through the isokinetic nozzles evaluated from these mass determinations.

Airborne particle concentrations at the four measurement locations were calculated by

$$C_{ave} = \frac{m_f + m_n + m_{fh}}{m_{f/p} Q_{pump} t} \tag{3.6}$$

where t is the total experimental time, Q_{pump} is the flow rate of the sampling pump and $m_{f/p}$ is the mass of fluorescein in a single particle. Values for Q_{pump} were taken to be the average of the bubble flow meter measurements taken at the beginning and end of the experiment. The value for $m_{f/p}$ was expected to be constant for any given experiment and was calculated from the theory of VOAG operation. A value for $m_{f/p}$ does not need to be known to calculate a particle deposition velocity because it cancels from equation (2.1) when one substitutes for the particle concentration and the deposition flux.

3.2.3.h Determination of particle deposition fluxes in step 19

For the straight test ducts 1-4, panels to be analyzed for particle deposition were cut from the galvanized steel duct using electric sheet metal shears (Kett Tools, Model K200). For each straight duct, twelve panels were cut out and rinsed: four panels each from the duct floor, sidewall and ceiling. The four panels from each duct surface were centered at locations that were 0.30, 0.61, 0.91 and 1.22 m (1.0, 2.0, 3.0 and 4.0 ft) from the test duct inlet and were labeled as shown in Figure 3.7. Cut panels were rectangular and typically measured about 0.1×0.2 m. Panels were individually rinsed in glass trays with a known volume of buffer solution and the fluorescence of the resulting rinse was measured in the fluorometer. Disposable small-volume transfer pipettes were used to ensure thorough coverage of the entire duct panel by the rinsing solution in cases where the solution volume was too small to completely submerge a duct panel. After flourescence analysis,

panels were measured to determine their lengths and widths. This same method of analysis was used for the S-connectors associated with test duct 1 and 2.

To measure particle deposition fluxes to bends 5 and 6, the interiors of the bends were rinsed with a measured quantity of rinsing solution. The bends were not cut into panels as were the straight test ducts. Instead, deposition to the entire interior surface of the bend was measured. Thus, no distinction between deposition to the floor, wall and ceiling surfaces within the bends was made. The fluorescence of the resulting wash solution was then quantified by the fluorometer as with all other samples.

The mass of fluorescein on a duct surface, m_d, was calculated by equation (3.5). The particle mass flux to a duct surface or S-connector was calculated by

$$J = \frac{m_d}{m_{f/p} A_d t} \tag{3.7}$$

where A_d is the apparent surface area of the rinsed surface. This surface area was measured for each S-connector and individual duct panel. For duct bends, the interior surface area was 0.22 m^2.

3.3 Calculation Procedures

3.3.1 Deposition velocities

Deposition velocities in test ducts 1 and 2, where the turbulent flow profile was fully developed, were the most straightforward to calculate by equation (2.1). The concentration for deposition velocity calculations in test duct 1, C_1, was

$$C_1 = \frac{C_{1,up} + C_{1,down}}{2} \tag{3.8}$$

Particle deposition fluxes to four panels at each of the floor, wall and ceiling surfaces of both test ducts 1and 2 were measured in each experiment. Deposition to the floor of test duct 1 is taken as an example here. The reported deposition velocity to the floor of duct 1, $V_{d,1f}$, was calculated by

$$V_{d,1f} = \frac{J_{1f1} + J_{1f2} + J_{1f3} + J_{1f4}}{4C_1} \tag{3.9}$$

where J_{1f1}, J_{1f2}, J_{1f3} and J_{1f4} are the measured particle fluxes in test duct 1 to floor panels 1, 2, 3 and 4, respectively. This same scheme was used to calculate the reported deposition velocities for the wall, $V_{d,1w}$, and ceiling, $V_{d,1c}$, surfaces of test duct 1. The same calculation procedure was followed for each surface of test duct 2. The appropriate concentration in test duct 2 for calculating deposition velocities, C_2, was

$$C_1 = \frac{C_{2,up} + C_{2,down}}{2} \tag{3.10}$$

3.3.2 Particle diameters and relaxation times

The APS sampled the experimental aerosol in the ventilation duct continuously for the duration of an experiment through a shrouded aerosol sampling probe mounted at the centerline of the lower duct. The APS collected data for number counts of particles in 51 aerodynamic size bins in the range 0.54-19.8 μm. A particle's aerodynamic diameter is the diameter that a particle of unit density would have if it had the same gravitational settling velocity as the actual particle. Reference diameters for APS size bins are

determined as the mass-mean aerodynamic diameter of particles integrated over the bin width and assuming a uniform size distribution. The APS size bins referenced to aerodynamic diameters, d_a, were converted to size bins referenced to physical particle diameters, d_p, by

$$d_p = \frac{d_a}{\sqrt{\rho_p}} \tag{3.11}$$

The density of the experimental particles was calculated from the volume-weighted average of oleic acid (891 kg m^{-3}) and fluorescein (1350 kg m^{-3}) in the particle. The amounts of oleic acid and fluorescein in the final particles were known from the original aerosol solution mixture. The mass-mean diameter of the experimental particles, d_{mm}, was calculated from the number counts, N, in each size bin from the APS by

$$d_{mm} = \left[\frac{\sum_{i=1}^{51} N_i d_{p,i}^3}{\sum_{i=1}^{51} N_i} \right]^{1/3} \tag{3.12}$$

where the index variable, i, refers to the particle size bin. The reported diameters of all experimental particles were measured and calculated in this manner. Particle relaxation times were then calculated by substituting d_{mm} for d_p in equation (2.13).

3.4 Blank Experiments: Detection Limits and Particle Resuspension

Blank experiments were conducted following the procedures outlined in section 3.2.3 with the exception that fluorescent particles were not generated or injected into the experimental duct in step 11. These blank experiments were used to determine the limits of detection of the experimental methods. In these blank experiments, the measured

masses of fluorescein on the air filters, isokinetic sampling nozzles and filter holders were all typically 0.0 ng. The measured masses of fluorescein on the duct panels during blank experiments were typically in the range 0-2 ng. The minimum fluorescein mass that could reliably be measured above background on a duct panel was taken to be 4 ng. When experiments with particles were conducted, the measured fluorescein mass on duct panels typically ranged from hundreds to tens of thousands of nanograms. The minimum amount of fluorescent material that was collected on a surface during any of the particle experiments was about 10 ng (on ceiling panels of ducts during experiments with 1 μm particles).

Blank experiments were conducted at average air velocities of 2.2, 5.3 and 9.0 m/s. In the process of conducting blank experiments, it was discovered that certain fluorescent experimental particles generated in previous experiments had the potential to resuspend into the airstream and subsequently re-deposit onto the cleaned test duct surfaces. Specifically, resuspension was observed at average duct air speeds of 5.3 and 9.0 m/s for experimental particles that were 5 μm in diameter and larger. Resuspension of 1 or 3 μm particles was not detected, nor was resuspension of any particles at air speeds of 2.2 m/s. Resuspension was not quantified or systematically investigated.

Because of the observed resuspension of particles, experiments were conducted in a pattern to reduce the possibility that resuspension of particles with diameters different from those being generated for an experiment could influence the experimental results. Thus, experiments using particles of the same nominal size were conducted in succession

at the three air speeds, from low to high. After three experiments with the same particle size, the entire duct system was dismantled, rinsed with tap water, dried and reassembled. Straight duct sections, short flexible duct sections, duct bends, branched ducts and transition components were all cleaned using the same methods described in section 3.2.3.a. The mixing box was rinsed and dried by hand. The adjustable speed fan was dismantled and the fan blades and fan housing were rinsed and dried by hand. Blank experiments conducted after cleaning the entire duct system in this manner showed no signs of resuspension of residual fluorescent particles. Number count versus particle size data collected by the APS showed no signs of resuspension of previously generated experimental particles. After cleaning, three more experiments were conducted for the next largest particle size, and then the entire system was cleaned again.

3.5 Differences between the Internally Insulated and Steel Duct Systems

In the insulated system, experiments were performed at three nominal air speeds of 2.2, 5.3 and 8.8 m/s for each of five nominal particle diameters: 1, 3, 5, 8 and 13 μm. Air speeds of 2.2, 5.3 and 8.8 m/s corresponded to nominal friction velocities of 16, 37 and 63 cm/s. Fifteen distinct experiments were conducted in the insulated system.

The internally insulated duct system had the same configuration shown in Figure 3.1 for the steel system and all equipment except for the ductwork was the same as described in sections 3.2.1-3.2.2. The straight duct sections of the insulated system were steel with 20.3×20.3 cm (8.0×8.0 in) square cross sections and 2.5 cm (1.0 in) thick acoustic fiberglass insulation on all interior surfaces. Thus, the flow area in the insulated ducts

was 15.2×15.2 cm (6.0×6.0 in), the same as in the steel system. The internal insulation (Certainteed, ToughGard R) was fiberglass overlaid with a fire-resistant, black composite surface on the airstream side. Photographs of the insulation surface presented to the internal flow and a discussion of the roughness of this material are in Appendix A. The insulation was installed by spot welding to the steel duct surfaces.

The 90° bends (bends 5 and 6) and the branched duct sections were not internally insulated. These bends were the same pieces used in the steel duct system. Transition elements were used to connect the larger insulated ducts with the bends and branched duct section. Flow contraction elements were located before the branched duct at the end of the lower duct and before bend 6; a flow expansion was located after bend 5.

3.5.1 Experimental protocol with insulated system

All air velocity, temperature, relative humidity, static pressure, particle size, airborne concentration and deposition flux measurements made during experiments in the steel duct system described in sections 3.2.3.c-3.2.3.h were made during experiments in the insulated duct system except deposition flux measurements to S-connectors, which were buried under the insulation and not expected to influence particle deposition.

An additional airborne concentration measurement was made during experiments in the insulated system to evaluate the performance of a shrouded nozzle. This shrouded nozzle was installed in the lower duct 10.5 m (34.5 ft) downstream of the mixing box outlet. Sample air was drawn through the shrouded nozzle by a constant-flow pump and

delivered to a 47 mm nitrocellulose filter in a filter holder assembly similar to those used with the isokinetic nozzles. The filter holder used with the shrouded nozzle was modified to accommodate the larger outlet diameter of the shrouded nozzle compared to those associated with the isokinetic nozzles. This shrouded nozzle was identical to that used to deliver aerosol samples to the APS. A description of the shrouded nozzle and the results of its performance in these experiments can be found in Appendix B.

Experiments in the insulated duct system followed the same experimental protocol as outlined for the steel duct system in section 3.2.3 with some minor modifications. In step 1 of the protocol, only sampling nozzles, the shrouded nozzle and filter holder assemblies were pre-cleaned. Test ducts were not soaked due to the presence of the insulation and S-connectors were not cleaned because they were not analyzed. Insulated test ducts were stored away from any potential fluorescein contamination with their ends sealed. Measurements showed that the background fluorescein mass on insulation panels from ducts stored in this manner were in the range 0-4 ng; this level was sufficiently low for use in experiments where the fluorescein mass on insulation panels was typically thousands of nanograms.

In step 3 of the protocol, duct sections adjacent to test ducts in the apparatus were not cleaned and dried. This was done in the steel duct system to reduce contamination of the S-connectors that were analyzed; because S-connectors were not analyzed in the insulated system, this cleaning step was not performed.

In step 4, a second shrouded nozzle was installed in the lower duct. A filter holder with a filter was attached to this shrouded nozzle in step 9 and this was attached to a constant-flow sampling pump in step 10. This shrouded nozzle was removed for fluorescence analysis in step 16. In step 18, the internal surfaces of the shrouded nozzle and its filter holder assembly, along with its filter were analyzed using fluorescent techniques.

When particle masses on the duct surfaces of the straight test duct sections were determined in step 19, the panels that were analyzed were the black composite top layer of the insulation that was exposed to the duct flow, not the steel part of the duct. These panels were obtained by cutting open the test duct to gain access to the interior, and then slicing out panels with a handheld razor blade. An effort was made to cut panels that were centered on the same locations as described in Figure 3.7; however, this was not always possible owing to the presence of spot welds that held the insulation in place.

All other details of the experimental procedure when using the insulated system were the same as when using the steel system. The same overall order of experiments, where three experiments with particles of the same size were conducted before proceeding to experiments with the next largest particle size, was followed for both the steel and insulated systems.

The entire insulated system could not be disassembled and cleaned between experiments with different particle sizes because of the presence of interior insulation in the straight ducts. Thus, only the short flexible duct sections, duct bends, branched ducts, transition

components, mixing box and adjustable speed fan were cleaned. Blank experiments conducted after this cleaning suggested that residual fluorescent particles deposited in the straight insulated ducts would not significantly influence experimental results. The minimum mass that could be reliably detected above background on an insulation panel was taken to be 10 ng. The minimum mass detected on an insulation panel in an experiment in the insulated system was about 200 ng. As in the steel system, data collected by the APS during experimental runs showed no signs of resuspension of previously deposited experimental particles.

3.6 Experimental Results in Ducts with Fully Developed Turbulent Flow Profiles

3.6.1 Particle and airflow data

A summary of measured particle and airflow data from each experiment is given for the steel duct system in Table 3.3 and for the insulated duct system in Table 3.4. Experiments in these tables are grouped by air speed and then listed in order of increasing particle size within each air speed grouping. Experimental run 7 was performed with the same particle size and air speed as run 6 to evaluate the repeatability of the experiments; all other experiments are unique combinations of particle size and air speed.

Examples of temperature, relative humidity and pressure drop profiles versus time for experiments conducted at the three air speeds in both the steel and the insulated systems are provided in Appendix C. This appendix also presents duct surface temperature measurements in the steel system and a brief analysis of deposition rates attributable to thermophoresis in these experiments.

3.6.2 Results in straight steel ducts

Particle deposition rates were measured in test ducts 1 and 2, where the turbulent flow profile was fully developed, in each experiment. Table 3.5 is a summary of measured dimensionless deposition velocities to the duct floor, sidewall and ceiling in the steel system at test ducts 1 and 2. The data in Table 3.5 for the steel system are presented graphically in Figures 3.8-3.17.

Figures 3.8-3.10 respectively show measured deposition velocities to the duct ceiling, wall and floor versus air speed for the steel system. Deposition velocities presented in these figures are the average of those measured in test ducts 1 and 2. Measured floor deposition velocities at the three air speeds are plotted versus particle diameter in Figure 3.11 and compared to the gravitational settling velocity, v_g. A particle density of 1200 kg/m^3 was assumed for the gravitational settling velocity calculation. Deposition data at air speeds of 2.2, 5.3 and 9.0 m/s are respectively presented as plots of V_d^+ versus τ^+ in Figures 3.12-3.14. In these figures, measured deposition velocities from test ducts 1 and 2 are shown as independent data points. Vertical error bars on these data points indicate the measurement variability among deposition velocities quantified on the four duct panels for the given surface. These error bars are only shown in cases where they are significantly larger than the size of the data point. Appendix D discusses the calculation procedures for determining measurement variability. Assumptions and calculation procedures for determining uncertainty levels of other reported data based on propagation of experimental errors are also discussed in Appendix D.

Figure 3.15 compares measured dimensionless ceiling deposition velocities at all three air speeds to the only other known data for particle deposition to a duct ceiling, where deposition was measured to a smooth brass surface by Sehmel (1973). Sehmel collected data at three air speeds corresponding to friction velocities of 11.4, 34.1 and 72.6 cm/s. Measured dimensionless wall deposition velocities at all three air speeds are compared to the vertical-wall deposition data collected by Liu & Agarwal (1974) in Figure 3.16. Figure 3.17 compares measured dimensionless floor deposition velocities at all three air speeds to floor deposition data from the literature.

3.6.3 Results in straight insulated ducts

Table 3.6 is a summary of measured dimensionless deposition velocities to the duct floor, wall and ceiling in the insulated system at test ducts 1 and 2. The data in Table 3.6 are presented graphically in Figures 3.18-3.25.

Figures 3.18-3.20 respectively show measured deposition velocities to the duct ceiling, wall and floor versus air speed for the insulated system. Deposition velocities reported in these figures are the average of those measured in test ducts 1 and 2. Figure 3.21 compares measured floor deposition velocities in the insulated system at the three air speeds with the gravitational settling velocity. Deposition data at air speeds of 2.2, 5.3 and 8.8 m/s in the insulated system are respectively presented as plots of V_d^+ versus τ^+ in Figures 3.22-3.24. In these plots, measured deposition velocities from test ducts 1 and 2

are shown independently, as in Figures 3.12-3.14. Vertical error bars, when present, are an indication of the measurement variability for different panels at the same duct surface.

There are no data available in the literature for particle deposition to a fibrous rough surface at the floor or ceiling of a duct. Data were collected by Wells & Chamberlain (1967) for particles depositing to a vertical surface covered with fibrous filter paper with a fiber length of 100 μm. The data from Wells & Chamberlain are compared to the dimensionless wall deposition velocities measured at the three air speeds in Figure 3.25.

3.7 Discussion

3.7.1 Particle deposition in steel ducts

Figures 3.8-3.10 clearly show that deposition velocities to duct ceiling, wall and floor surfaces increase with increases in both particle size and air speed. For a given air speed, increases in particle diameter from 1 to 16 μm increased deposition velocities to duct ceilings by factors in the range 37-180. For duct walls and floors, the same factors were in the ranges 160-920 and 200-420, respectively. The influence of particle size on deposition rates was weakest for deposition to the duct ceiling surface (Figure 3.8) and strongest for deposition to the duct wall (Figure 3.9). For a given particle size, increasing the air speed from 2.2 to 9.0 m/s increased deposition velocities to the duct ceiling by factors in the range 4.7-120. The same factors were in the ranges 5.9-50 and 1.5-4.1 for duct walls and floors, respectively. The influence of air speed on deposition rates was strongest for deposition to the duct ceiling (Figure 3.8) and weakest for the duct floor

(Figure 3.10). Good agreement was observed between data collected in run 6 with 1 μm particles at an air speed of 5.3 m/s and the data collected in run 7 at the same conditions.

In Figure 3.11, it can be seen that deposition velocities to the duct floor for all particle sizes were approximately equal to the corresponding gravitational settling velocity at the lowest air speed. At air speeds of 5.3 and 9.0 m/s, deposition velocities of the larger particles were enhanced compared to the gravitational settling velocity. A rough dividing line can be drawn at a dimensionless particle relation time of one. Particles with τ^+ values less than one (except for 5 μm particles at the 5.3 m/s air speed, where $\tau^+ = 0.48$) deposited nearly at the gravitational settling velocity, those with τ^+ values greater than one deposited at rates greater than the gravitational settling velocity. This suggests that at lowest air speed, particle deposition to duct floors was controlled by gravitational settling, but at the higher air speeds, where turbulent air fluctuations were greater, one or more turbulence related transport mechanism significantly contributed to deposition.

The importance of the orientation of the deposition surface for determining particle deposition rates is apparent from Figures 3.12-3.14. For a given particle size and air speed, the deposition rate to the duct floor was always greater than the deposition rate to the duct wall, which, in turn, was always greater than the deposition rate to the duct ceiling. Data at the lowest air speed, shown in Figure 3.12, show deposition rates to the duct floor that were 2-3 orders of magnitude greater than deposition rates to the ceiling and 1-2 orders of magnitude greater than deposition rates to the wall. The differences in deposition rates to the duct floor, wall and ceiling decreased with increasing air speed, as

can be seen by the tighter grouping of the data for the different surfaces in Figures 3.13 and 3.14 as compared to Figure 3.12.

Regarding changes in deposition rates resulting from the different locations of S-connectors in test ducts 1 and 2, no clear trends are discernable in the data. Good agreement is observed between most measurements made in test duct 1 and test duct 2.

In Figure 3.15 comparing measured deposition rates to the ceiling of ducts 1 and 2 to the data of Sehmel (1973), reasonable agreement at common friction velocities is observed in the region where the two data sets overlap. Sehmel observed no deposition to the duct ceiling at his lowest friction velocity of 11.4 cm/s. This contrasts the data collected in the current experiments at the lowest air speed, with a friction velocity of 12 cm/s, where ceiling deposition was indeed observed. In fact, for similar values of τ^+ in the current experiments, dimensionless deposition velocities to the ceiling were usually greatest at the lowest air speed studied.

Measured values of $V_{d,w}^+$ at the two higher air speeds show good agreement with values from Liu & Agarwal (1974) in Figure 3.16, but the data collected at 2.2 m/s lie above the other data. When plotted as $V_{d,w}^+$ versus τ^+, data for deposition to vertical walls collected at different air speeds are expected to fall on a single curve. The data of Liu & Agarwal were collected at a friction velocity of about 74 cm/s. The lack of agreement of the low-air-speed data with the other data is possibly attributable to the low friction velocity in those experiments relative to the others. A similar increase in values of $V_{d,w}^+$ with a

decrease in friction velocity was observed in the DNS-Lagrangian simulations of Zhang & Ahmadi (2000) (described in section 2.5.6) at low friction velocities. The effect was caused by a higher lift force at lower friction velocities in those simulations, but the effect was only observed in vertical flows where gravity influenced the particle axial velocity.

In Figure 3.17 comparing measured floor deposition rates to other floor deposition data from the literature, good agreement among the data is observed for common friction velocities. Data collected at air speeds with nominal friction velocities of 12 and 28 compare favorably with data collected by Sehmel (1973) at friction velocities of 11.4 and 34.1 cm/s, respectively. Data collected at the highest air speed with a nominal friction velocity of 45 cm/s fall mostly between the data from Sehmel collected at friction velocities of 34.1 and 72.6 cm/s, as expected. Data collected by Lai (1997) at a friction velocity of 21 cm/s are also in agreement with trends observed in the current data set.

3.7.2 Particle deposition in insulated ducts

From Figures 3.18-3.20, it can be seen that measured deposition velocities to all three duct surfaces in the insulated system increase with increases in both particle size and air speed. These same trends are observed in Figures 3.8-3.10 for the steel system, but the trends are weaker in the insulated system. For a given air speed, increases in particle diameter from 1 to 16 μm increase deposition rates to duct ceilings by factors in the range 13-33. These same factors for the duct wall and floor are in the ranges 27-39 and 29-96, respectively. For a given particle size, increasing the air speed from 2.2 to 8.8 m/s increased deposition rates to duct ceilings by factors in the range 22-46. The same

factors were in the ranges 15-54 and 5.3-24 for duct walls and floors, respectively. The weaker influence of particle size and air speed on deposition rates in the insulated system as compared to the steel system probably reflects the importance of insulation roughness elements in determining particle deposition rates. This observation is in accord with most deposition model predictions that account for surface roughness.

Deposition velocities to duct ceilings and walls were greatly enhanced in the insulated ducts as compared to the steel ducts. Deposition rates to the duct floor increased only slightly from steel ducts to insulated ducts. This enhancement can be observed by comparing Figures 3.18-3.20 for the insulated system to the analogous Figures 3.8-3.10 for the steel system. For 1-5 μm particles, deposition velocities to ceilings of insulated ducts were 79-760 times higher than deposition velocities to ceilings of steel ducts at the same air speed. For duct walls and floors, the same factors were in the ranges 15-190 and 0.8-21, respectively. Quantitative comparisons between the two systems are confounded at large particle sizes because of the different sizes used in each system.

Figure 3.21 shows that at the lowest air speed, measured floor deposition velocities were approximately equal to gravitational settling velocities, but at the higher air speeds, floor deposition velocities were significantly greater than gravitational settling velocities. The observed enhancement above the gravitational settling velocities is more dramatic and clear in the insulated system than in the steel system (Figure 3.11) for all particle sizes.

Data at the lowest air speed in the insulated ducts, presented in Figure 3.22, show deposition rates to the duct ceiling, wall and floor to be nearly equal for the smallest particle size. For larger particles, differences in deposition rates to the different surfaces are apparent. Owing to the influence of gravity, deposition rates to the floor are greater than to the wall or ceiling for 3-13 μm particles. At the lowest air speed, differences in deposition velocities to the duct ceiling, wall and floor are much smaller in the insulated system than in the steel system. Data in insulated ducts at the two higher air speeds in Figures 3.23-3.24 show nearly equal deposition rates to the ceiling, wall and floor surfaces for all particle sizes. Measured dimensionless deposition velocities to the floor surface are usually slightly higher than to the wall or ceiling, but differences are far smaller than observed in the steel system. Particles were observed to deposit in a nearly uniform manner within the insulated ducts at the two higher air speeds. This suggests that roughness elements associated with the insulation play a dominant role in controlling deposition at these air velocities.

In Figure 3.25, comparing the measured wall deposition rates to similar data from the literature, Wells & Chamberlain's (1967) data lie above the data measured in the insulated system, but similar trends were observed in both data sets. Both sets of data exhibit a similar slope for data with $\tau^+ < 1$ and a leveling of the data for values of $\tau^+ > 1$. Wells and Chamberlain (1967) observed a marked increase in deposition rates to a fibrous surface compared to a smooth metallic surface; a similar deposition enhancement was observed in the current experiments in insulated ducts compared to steel ducts.

3.8 Conclusions

Particle deposition rates to the ceiling, walls and floor of steel and insulated horizontal ducts have been measured for a range of particle sizes and air speeds. These deposition rates, measured in ducts where the turbulent flow profile was fully developed, are summarized in Table 3.5 for steel ducts and in Table 3.6 for insulated ducts. The experiments were performed with real HVAC materials and deposition to duct surfaces was directly measured. The measured deposition rates are expected to be representative of rates in real HVAC ducts.

In steel ducts, deposition rates were much greater to the floor than to the walls or ceiling for all particle sizes and air speeds. Increasing air speed within the range 2.2-9.0 m/s led to increased deposition rates to steel surfaces of all orientations, as did increasing particle size within the range 1-16 μm. Deposition velocities to the duct floor were approximately equal to the gravitational settling velocity for particles with dimensionless relaxation times less than one, and these deposition rates were enhanced compared to the gravitational settling rate for particles with relaxation times greater than one.

The presence or absence of S-connectors on the internal surface of a duct had no observable effect on measured deposition rates to downstream surfaces. Measured deposition rates in the steel ducts were in general agreement with similar experiments from the literature.

For a given particle size, air speed and duct surface, deposition rates were higher, often much higher, in insulated ducts than in steel ducts; this was especially true for wall and ceiling surfaces. Deposition to duct floors at an air speed of 2.2 m/s was the only case in which deposition rates in insulated ducts were not significantly enhanced compared to rates in steel ducts. Deposition in the insulated ducts was nearly uniform to floor, wall and ceiling surfaces, especially at air speeds of 5.3 and 8.8 m/s. Increasing air speed and particle size led to increases in deposition rates to insulated duct surfaces, but the effect was less dramatic than observed in steel systems. The rough and fibrous character of the exposed insulation inside an insulated duct appears to be a strong factor influencing particle deposition.

Table 3.1 Aerosol solution mixtures, VOAG settings and particle densities for particles in the steel system.

Nominal particle size (μm)	IPA volume in aerosol solution (mL)	Oleic acid volume in aerosol solution (mL)	Fluorescein solution volume in aerosol solution (mL)	VOAG frequency (Hz)	Aerosol solution feed rate (mL/min)	Particle density, ρ_p (g/cm^3)
1	1000	0	2.0	45,000	0.14	1.35
3	1000	0.1	40	45,000	0.14	1.17
5	1000	0.5	300	45,000	0.14	1.21
9	1000	0.9	100	30,000	0.41	1.03
16	1000	10.0	400	30,000	0.41	0.95

Table 3.2 Aerosol solution mixtures, VOAG settings and particle densities for particles in the insulated system.

Nominal particle size (μm)	IPA volume in aerosol solution (mL)	Oleic acid volume in aerosol solution (mL)	Fluorescein solution volume in aerosol solution (mL)	VOAG frequency (Hz)	Aerosol solution feed rate (mL/min)	Particle density, ρ_p (g/cm^3)
1	1000	0	2.0	45,000	0.16	1.35
3	1000	0.1	40	45,000	0.16	1.17
5	1000	0.5	250	45,000	0.16	1.19
8	1000	1.0	200	30,000	0.44	1.09
13	1500	8.0	400	30,000	0.44	0.96

Table 3.3 Particle and airflow data for experiments in the steel system.

Run # (-)	Air speed, U_{ave} (m s^{-1})	Particle diameter, d_{mm} (μm)	Particle density, ρ_p (g cm^{-3})	Friction velocity, u^* (m s^{-1})	Air temperature, T (°C)	Relative humidity (%)
1	2.2	1.0	1.4	0.12	22.0	45
2	2.2	2.8	1.2	0.12	22.0	45
3	2.1	5.2	1.2	0.12	21.8	38
4	2.2	9.1	1.0	0.13	22.2	46
5	2.2	16	1.0	0.12	22.4	46
6	5.3	1.0	1.4	0.28	24.1	43
7	5.2	1.0	1.4	0.26	23.0	44
8	5.2	3.1	1.2	0.26	23.0	43
9	5.4	5.2	1.2	0.27	22.9	42
10	5.3	9.8	1.0	0.28	23.0	46
11	5.3	16	1.0	0.28	23.1	44
12	9.0	1.0	1.4	0.45	26.9	27
13	9.0	3.1	1.2	0.42	25.4	40
14	8.8	5.4	1.2	0.44	25.6	35
15	9.2	8.7	1.0	0.46	25.9	26
16	9.1	15	1.0	0.45	25.9	41

Table 3.4 Particle and airflow data for experiments in the insulated system.

Run # (-)	Air speed, U_{ave} (m s^{-1})	Particle diameter, d_{mm} (μm)	Particle density, ρ_p (g cm^{-3})	Friction velocity, u^* (m s^{-1})	Air temperature, T (°C)	Relative humidity (%)
17	2.2	1.0	1.4	0.16	22.0	26
18	2.2	3.0	1.2	0.16	22.0	26
19	2.2	5.3	1.2	0.16	22.6	38
20	2.2	8.4	1.1	0.16	22.8	43
21	2.2	13	1.0	0.16	23.2	28
22	5.3	1.0	1.4	0.37	24.8	32
23	5.2	2.9	1.2	0.37	23.4	31
24	5.2	4.9	1.2	0.37	23.9	38
25	5.3	8.2	1.1	0.38	24.7	44
26	5.3	13	1.0	0.38	24.3	33
27	8.9	1.0	1.4	0.62	26.1	28
28	8.7	2.8	1.2	0.62	26.8	27
29	8.9	5.0	1.2	0.62	27.0	32
30	8.9	8.4	1.1	0.64	27.6	22
31	8.9	13	1.0	0.64	27.2	28

Table 3.5 Dimensionless deposition velocities in steel system in test ducts 1 and 2.

Run # (-)	U_{ave} (m s^{-1})	d_{mm} (μm)	τ^+ (-)	Test duct (-)	$V^+_{d,c}$ (-)	$V^+_{d,w}$ (-)	$V^+_{d,f}$ (-)
1	2.2	1.0	4.6×10^{-3}	1	2.8×10^{-6}	9.6×10^{-6}	3.5×10^{-4}
				2	2.0×10^{-6}	1.3×10^{-5}	3.6×10^{-4}
2	2.2	2.8	0.028	1	2.5×10^{-5}	6.2×10^{-5}	2.7×10^{-3}
				2	1.9×10^{-5}	7.5×10^{-5}	2.7×10^{-3}
3	2.1	5.2	0.098	1	3.0×10^{-5}	1.6×10^{-4}	0.011
				2	5.5×10^{-5}	4.5×10^{-4}	0.011
4	2.2	9.1	0.27	1	1.3×10^{-5}	7.7×10^{-4}	0.025
				2	1.5×10^{-4}	7.4×10^{-4}	0.031
5	2.2	16	0.72	1	3.9×10^{-5}	2.0×10^{-3}	0.073
				2	1.4×10^{-4}	1.5×10^{-3}	0.070
6	5.3	1.0	0.023	1	4.2×10^{-6}	2.2×10^{-5}	2.2×10^{-4}
				2	4.7×10^{-6}	2.3×10^{-5}	2.0×10^{-4}
7	5.2	1.0	0.022	1	5.4×10^{-6}	2.3×10^{-5}	2.0×10^{-4}
				2	5.6×10^{-6}	2.7×10^{-5}	2.0×10^{-4}
8	5.2	3.1	0.16	1	1.3×10^{-5}	4.9×10^{-5}	1.5×10^{-3}
				2	2.7×10^{-5}	5.1×10^{-5}	1.5×10^{-3}
9	5.4	5.2	0.48	1	4.9×10^{-5}	2.5×10^{-4}	8.5×10^{-3}
				2	4.6×10^{-5}	4.5×10^{-4}	7.9×10^{-3}
10	5.3	9.8	1.5	1	3.1×10^{-5}	1.1×10^{-3}	0.021
				2	9.7×10^{-5}	8.9×10^{-4}	0.017
11	5.3	16	3.6	1	1.6×10^{-4}	0.012	0.074
				2	7.4×10^{-4}	0.018	0.069
12	9.0	1.0	0.062	1	2.1×10^{-5}	2.6×10^{-5}	1.8×10^{-4}
				2	1.3×10^{-5}	2.7×10^{-5}	2.0×10^{-4}
13	9.0	3.1	0.42	1	2.1×10^{-5}	1.1×10^{-4}	1.2×10^{-3}
				2	3.7×10^{-5}	1.2×10^{-4}	1.1×10^{-3}
14	8.8	5.4	1.4	1	1.3×10^{-4}	1.4×10^{-3}	0.013
				2	1.7×10^{-4}	1.4×10^{-3}	0.012
15	9.2	8.7	3.2	1	6.7×10^{-4}	3.8×10^{-3}	0.027
				2	1.2×10^{-3}	3.3×10^{-3}	0.025
16	9.1	15	8.8	1	2.2×10^{-3}	0.021	0.083
				2	3.6×10^{-3}	0.027	0.077

Table 3.6 Dimensionless deposition velocities in insulated system in test ducts 1 and 2.

Run # (-)	U_{ave} (m s^{-1})	d_{mm} (μm)	τ^+ (-)	**Test duct** (-)	$V^+_{d,c}$ (-)	$V^+_{d,w}$ (-)	$V^+_{d,f}$ (-)
17	2.2	1.0	7.8×10^{-3}	1	4.5×10^{-4}	4.2×10^{-4}	5.7×10^{-4}
				2	3.8×10^{-4}	3.2×10^{-4}	5.0×10^{-4}
18	2.2	3.0	0.054	1	1.4×10^{-3}	1.2×10^{-3}	2.2×10^{-3}
				2	1.2×10^{-3}	1.0×10^{-3}	2.9×10^{-3}
19	2.2	5.3	0.17	1	2.5×10^{-3}	3.5×10^{-3}	7.3×10^{-3}
				2	2.9×10^{-3}	3.3×10^{-3}	7.1×10^{-3}
20	2.2	8.4	0.39	1	4.4×10^{-3}	6.7×10^{-3}	0.018
				2	3.6×10^{-3}	4.0×10^{-3}	0.015
21	2.2	13	0.81	1	5.7×10^{-3}	0.015	0.056
				2	5.2×10^{-3}	0.013	0.047
22	5.3	1.0	0.043	1	1.2×10^{-3}	1.0×10^{-3}	1.4×10^{-3}
				2	1.0×10^{-3}	1.3×10^{-3}	1.1×10^{-3}
23	5.2	2.9	0.28	1	6.6×10^{-3}	6.0×10^{-3}	7.8×10^{-3}
				2	7.9×10^{-3}	6.2×10^{-3}	7.4×10^{-3}
24	5.2	4.9	0.80	1	0.023	0.017	0.024
				2	0.022	0.021	0.022
25	5.3	8.2	2.1	1	0.034	0.040	0.051
				2	0.033	0.036	0.042
26	5.3	13	4.5	1	0.045	0.050	0.070
				2	0.026	0.032	0.044
27	8.9	1.0	0.12	1	2.4×10^{-3}	1.8×10^{-3}	2.5×10^{-3}
				2	2.2×10^{-3}	2.5×10^{-3}	2.3×10^{-3}
28	8.7	2.8	0.72	1	0.014	0.014	0.015
				2	0.015	0.016	0.017
29	8.9	5.0	2.3	1	0.032	0.031	0.037
				2	0.029	0.029	0.031
30	8.9	8.4	6.0	1	0.047	0.051	0.062
				2	0.047	0.052	0.058
31	8.9	13	12	1	0.054	0.057	0.075
				2	0.047	0.054	0.064

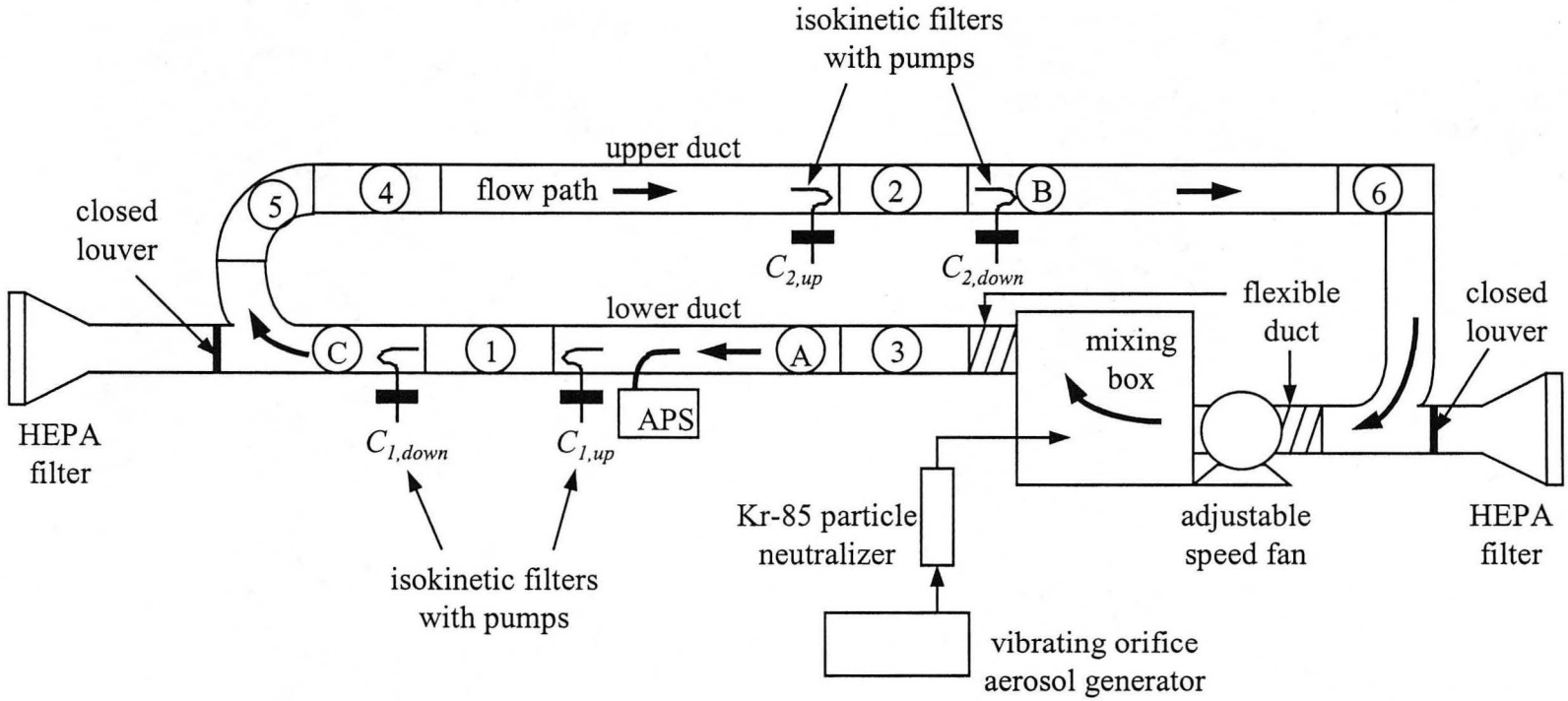

Figure 3.1 Schematic diagram of the experimental apparatus. This figure is not drawn to scale.

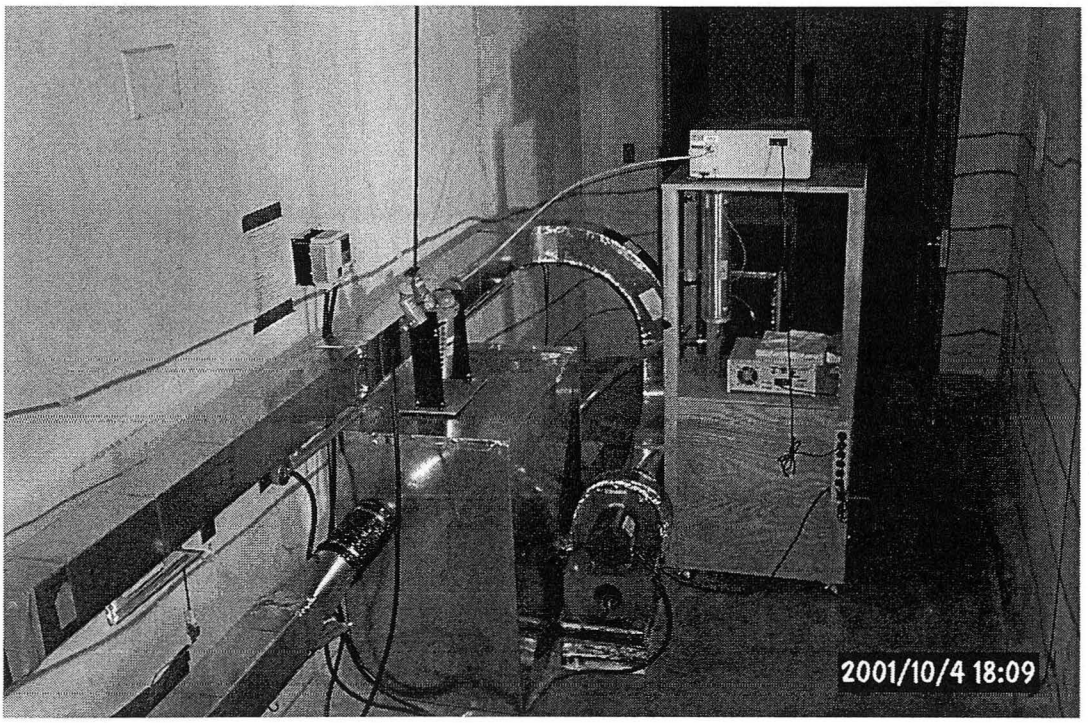

Figure 3.2. A photograph of a portion of the experimental apparatus.

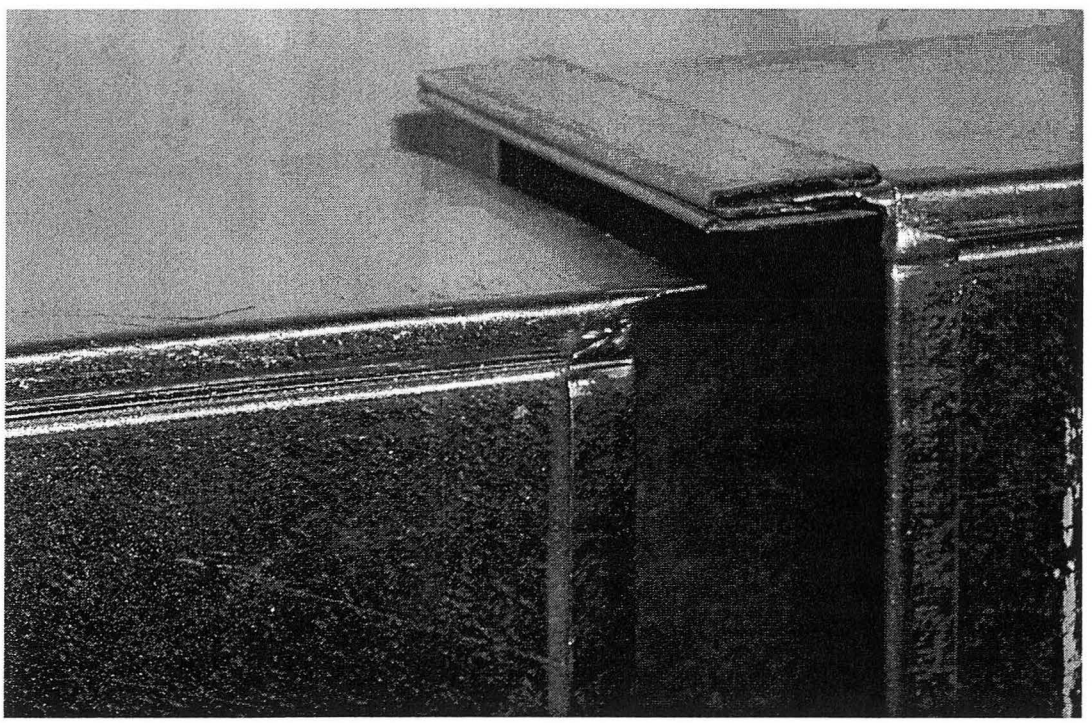

Figure 3.3 A close-up photograph showing the junction between two disconnected duct sections. An S-connector is visible on the leading edge of the duct on the right.

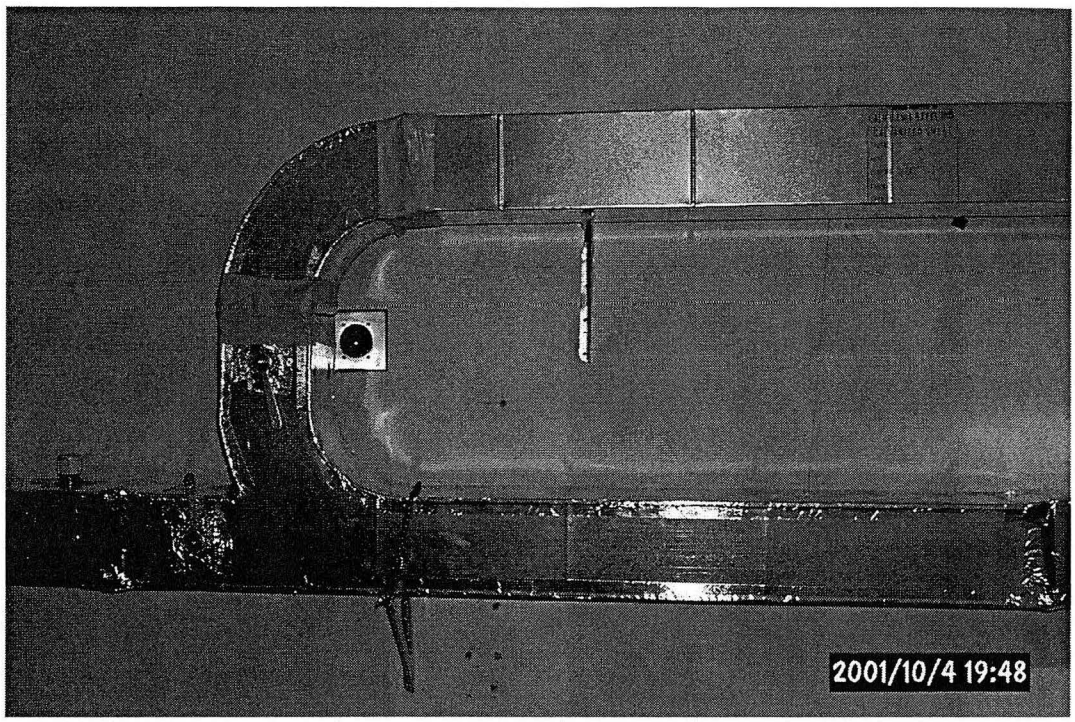

Figure 3.4 A photograph of the transition to the upper duct at the end of the lower duct. Bend 5 and test duct 4 are visible.

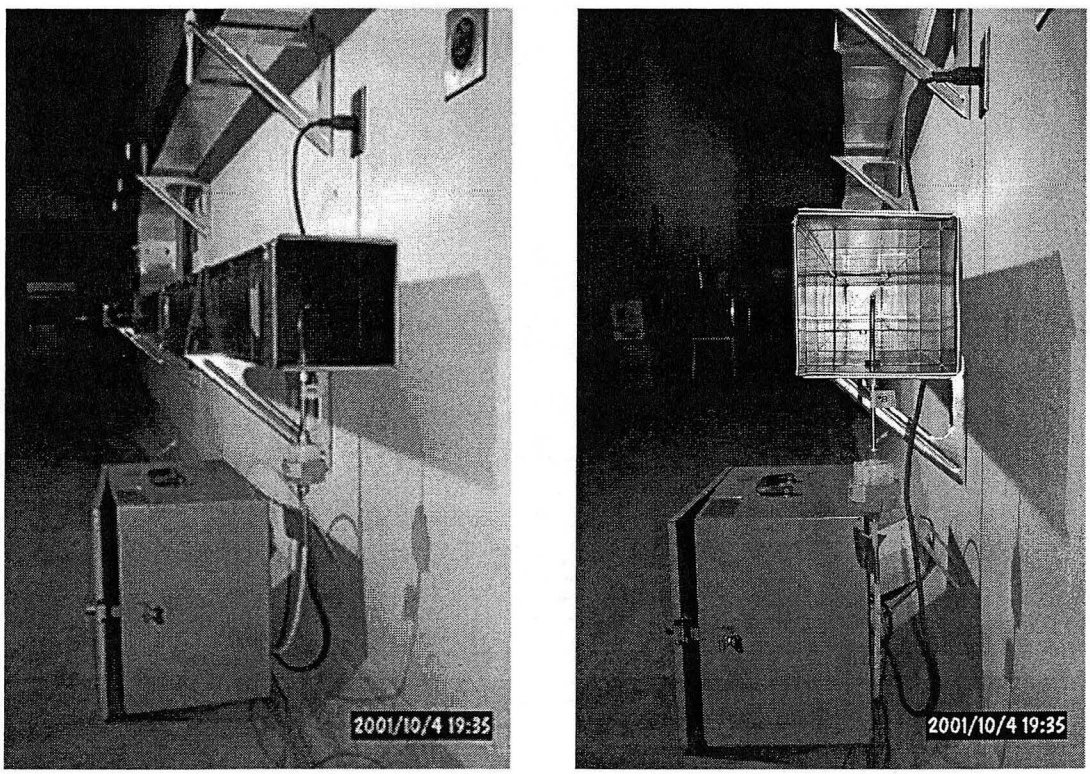

Figure 3.5 Isokinetic nozzle installed at the duct centerline downstream of test duct 1. Air is drawn through the nozzle and filter holder by the sampling pump.

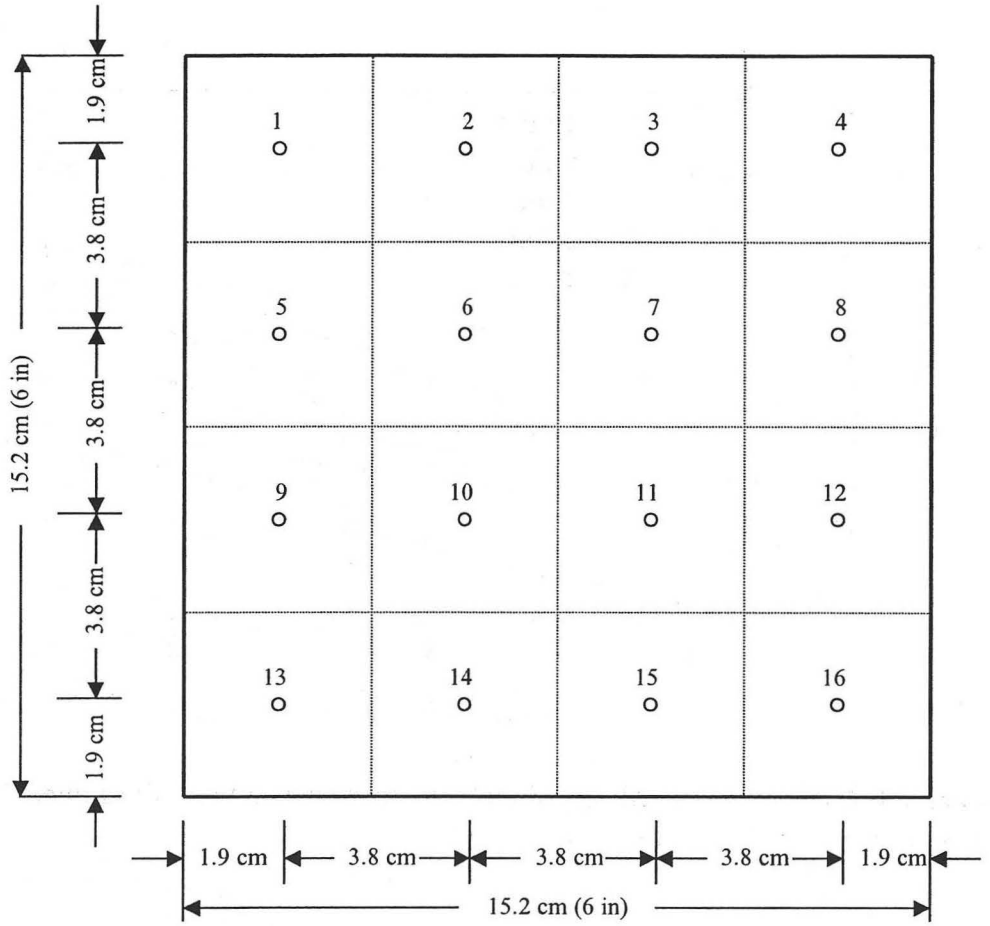

Figure 3.6 Locations of local area velocity measurements made in the *y-z* plane of the duct for determination of the average air speed.

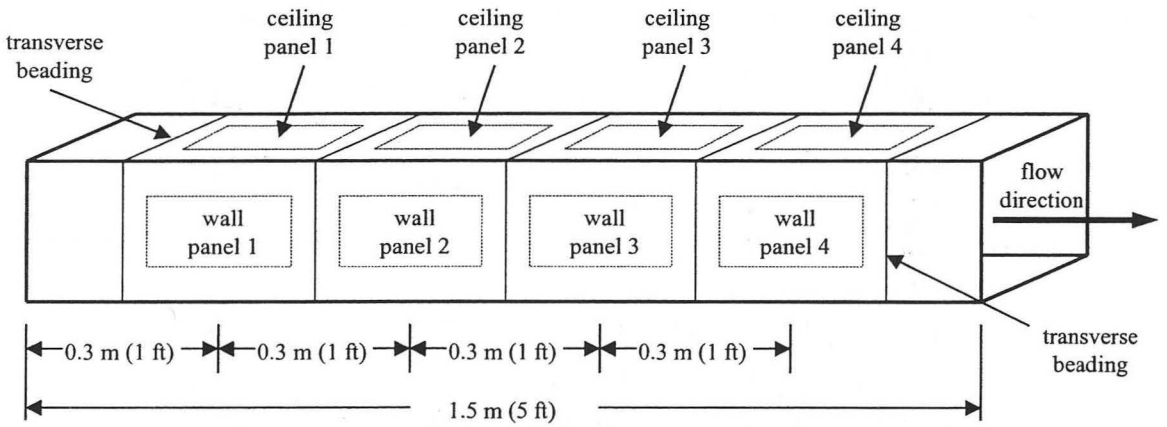

Figure 3.7 Schematic diagram showing the locations of panels cut out of a straight test duct for determination of the particle flux. Panels on the ceiling and wall are shown. Panels were similarly spaced and labeled on the duct floor.

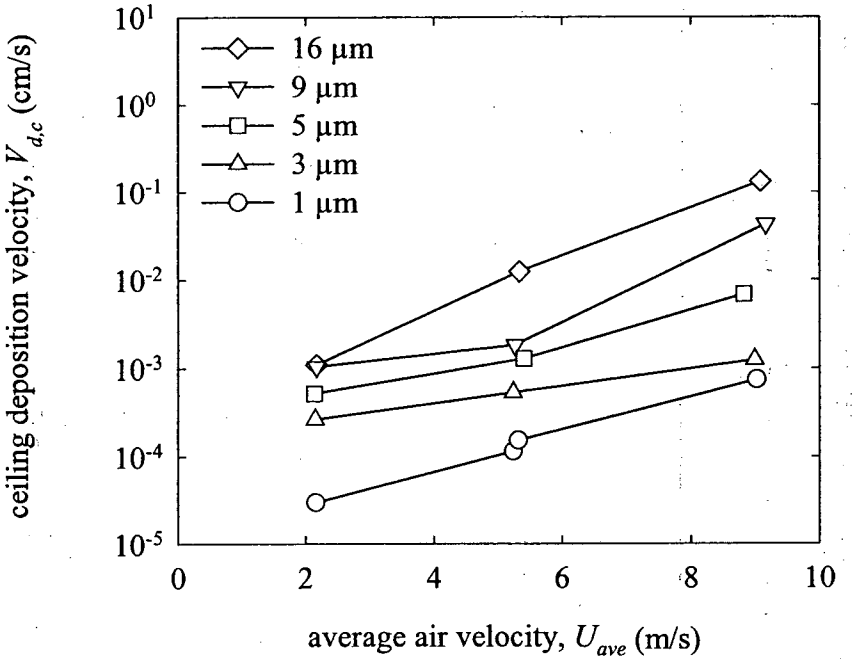

Figure 3.8 Average measured deposition velocity to the ceiling of test ducts 1 and 2 versus air speed in the steel system.

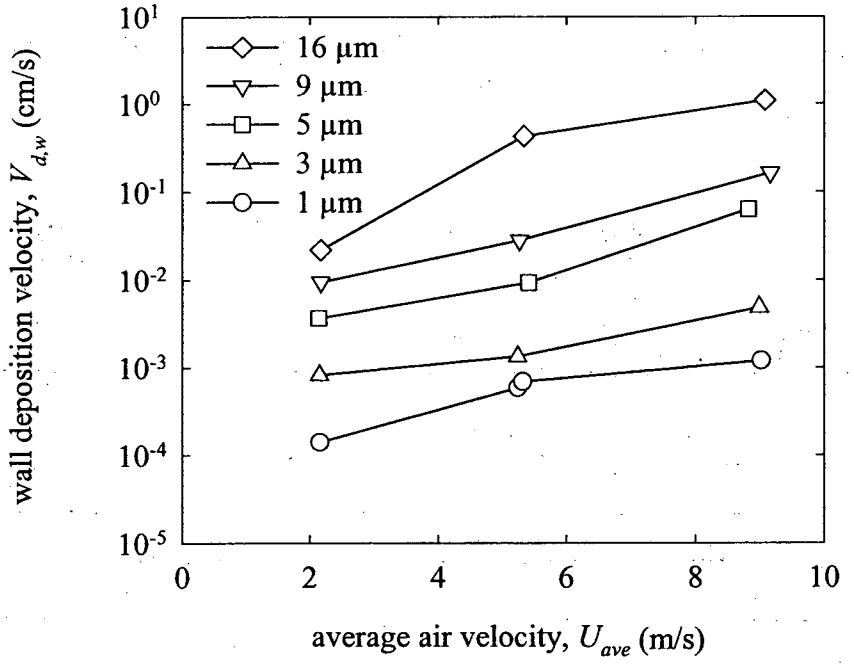

Figure 3.9 Average measured deposition velocity to the wall of test ducts 1 and 2 versus air speed in the steel system.

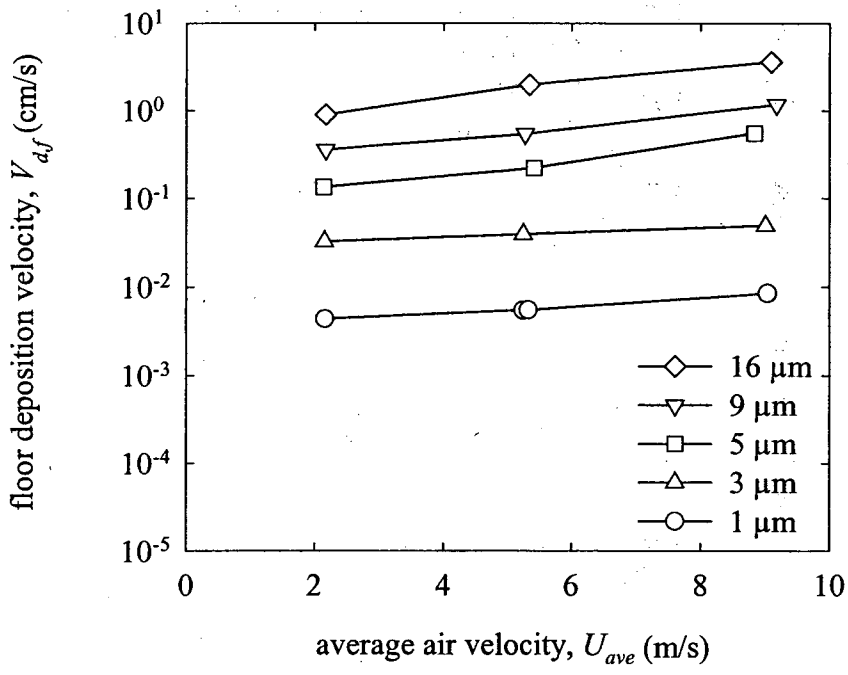

Figure 3.10 Average measured deposition velocity to the floor of test ducts 1 and 2 versus air speed in the steel system.

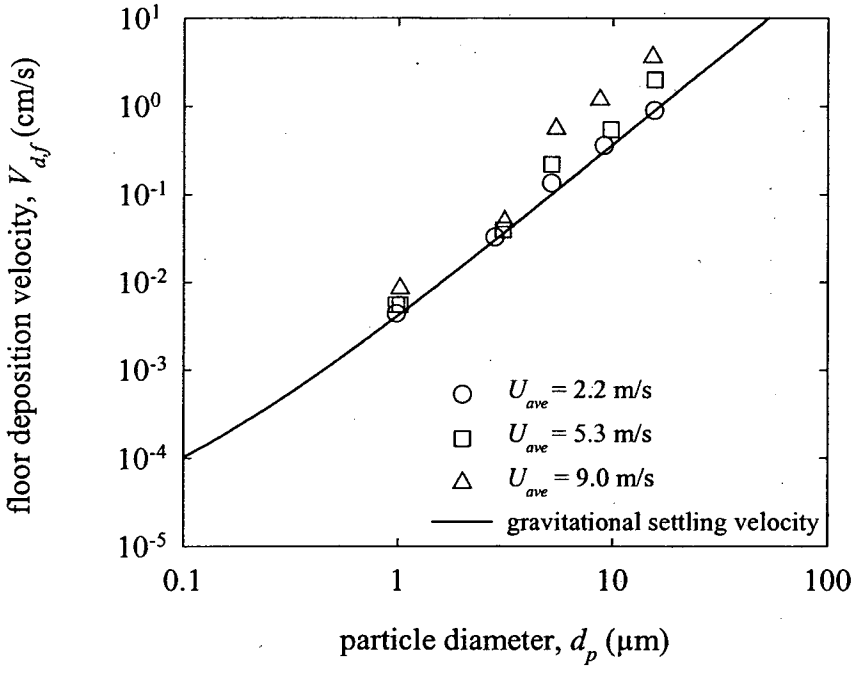

Figure 3.11 Comparison of the average measured deposition velocities to the floor of test ducts 1 and 2 in the steel system to the gravitational settling velocity.

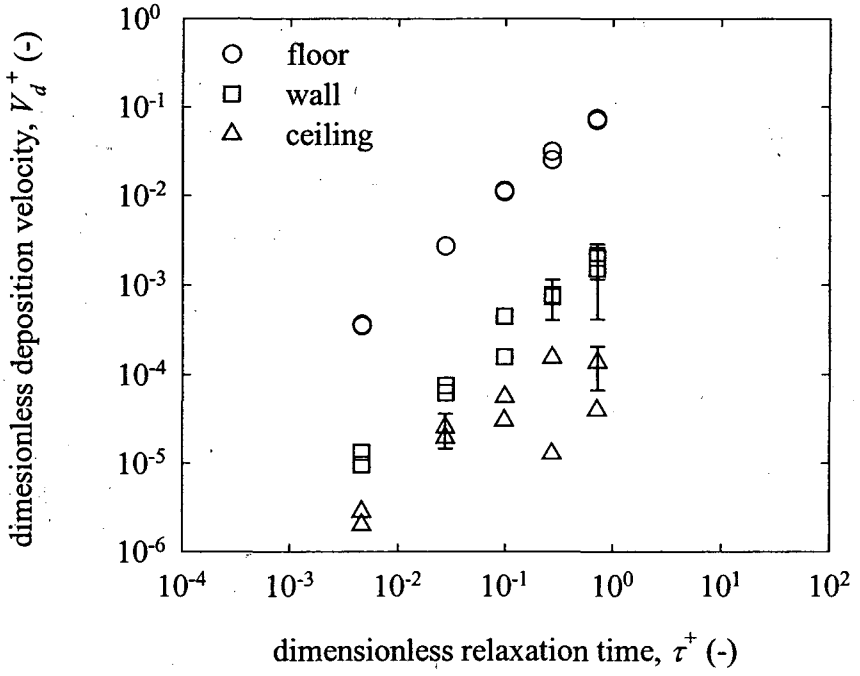

Figure 3.12 Measured dimensionless deposition velocities for particles depositing to the floor, wall and ceiling of test ducts 1 and 2 in the steel system at 2.2 m/s.

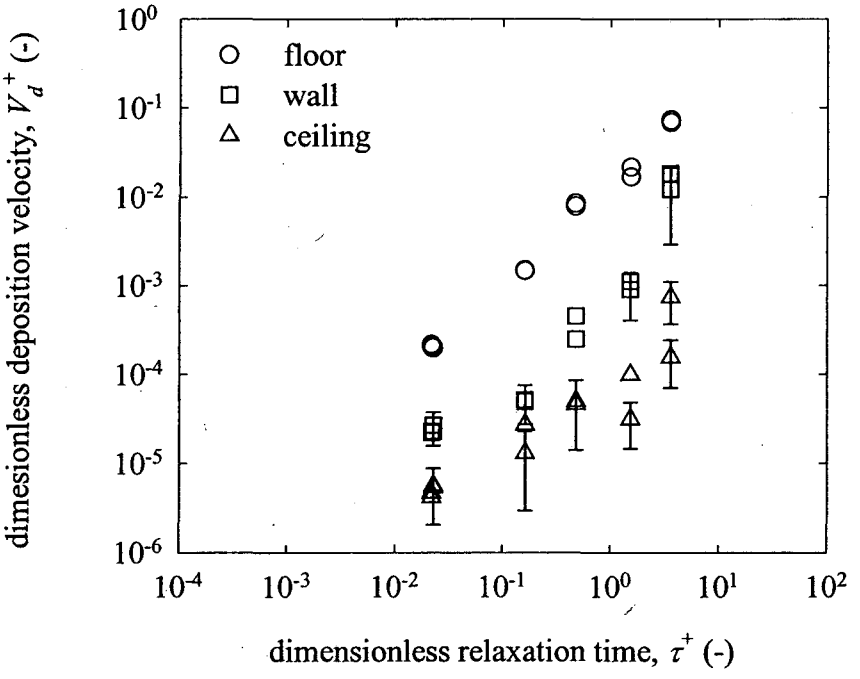

Figure 3.13 Measured dimensionless deposition velocities for particles depositing to the floor, wall and ceiling of test ducts 1 and 2 in the steel system at 5.3 m/s.

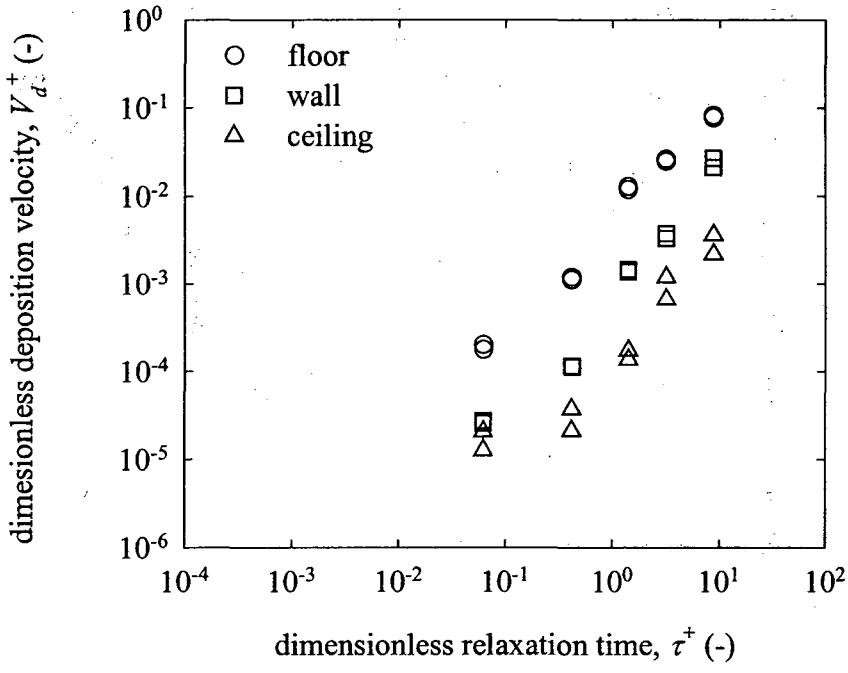

Figure 3.14 Measured dimensionless deposition velocities for particles depositing to the floor, wall and ceiling of test ducts 1 and 2 in the steel system at 9.0 m/s.

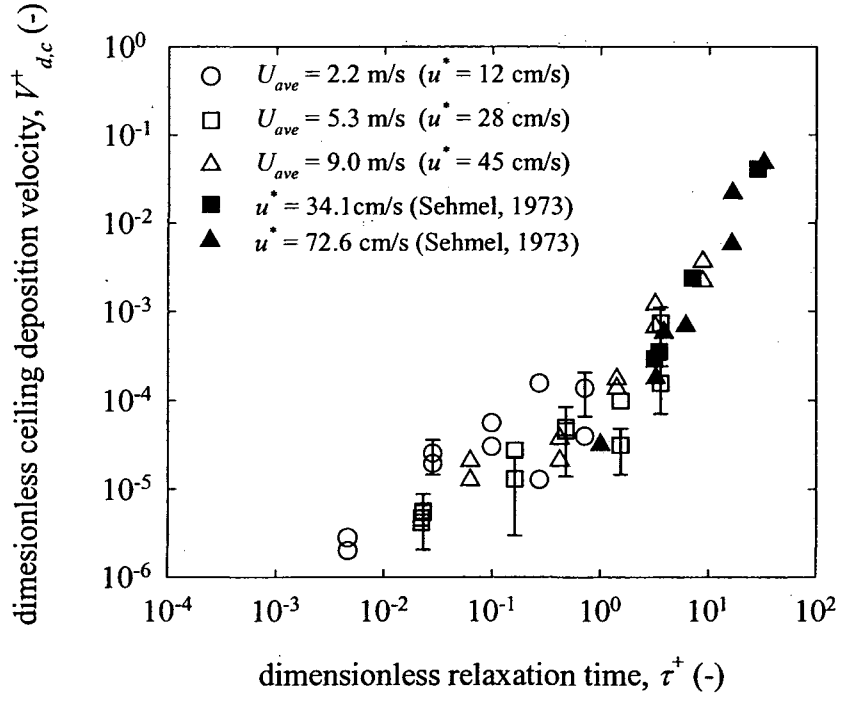

Figure 3.15 Comparison of dimensionless ceiling deposition velocities measured at three air speeds in the steel system with the data of Sehmel (1973).

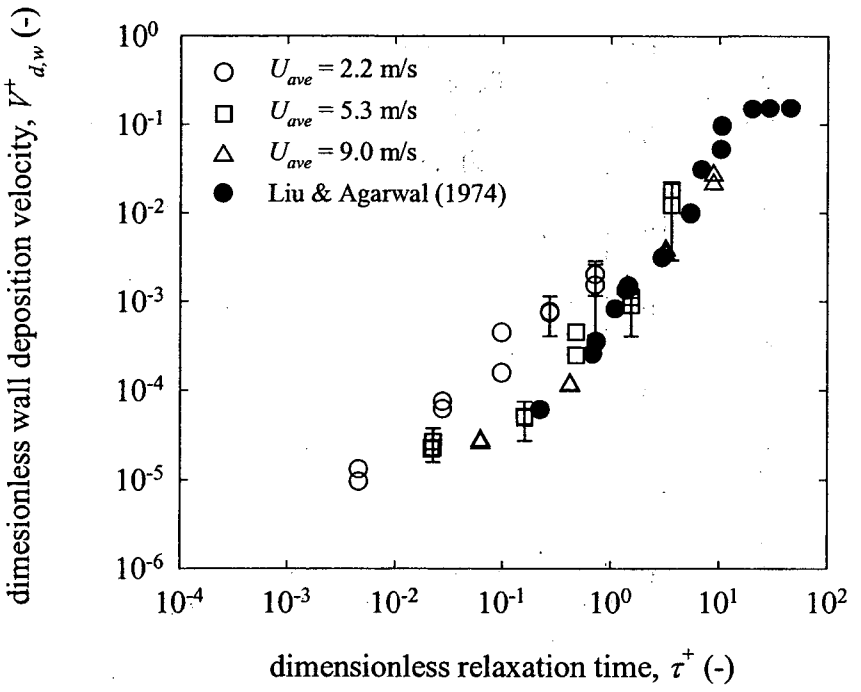

Figure 3.16 Comparison of dimensionless wall deposition velocities measured at three air speeds in the steel system with the data of Liu & Agarwal (1974).

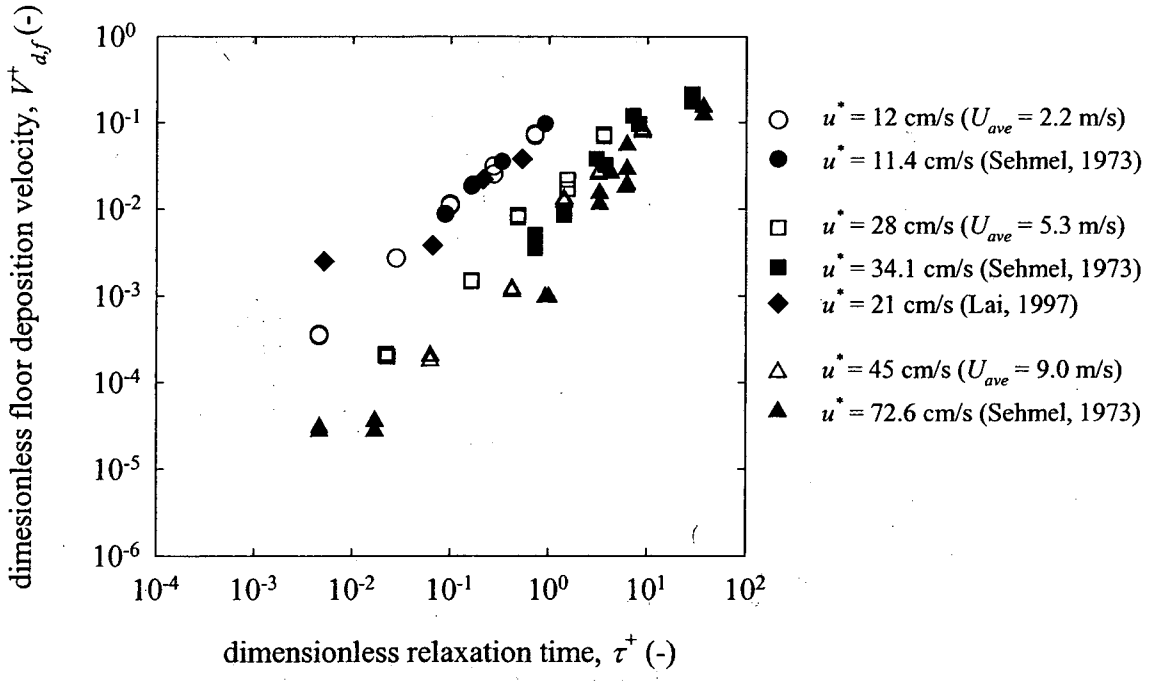

Figure 3.17 Comparison of dimensionless floor deposition velocities measured at three air speeds in the steel system with the data of Sehmel (1973) and Lai (1997).

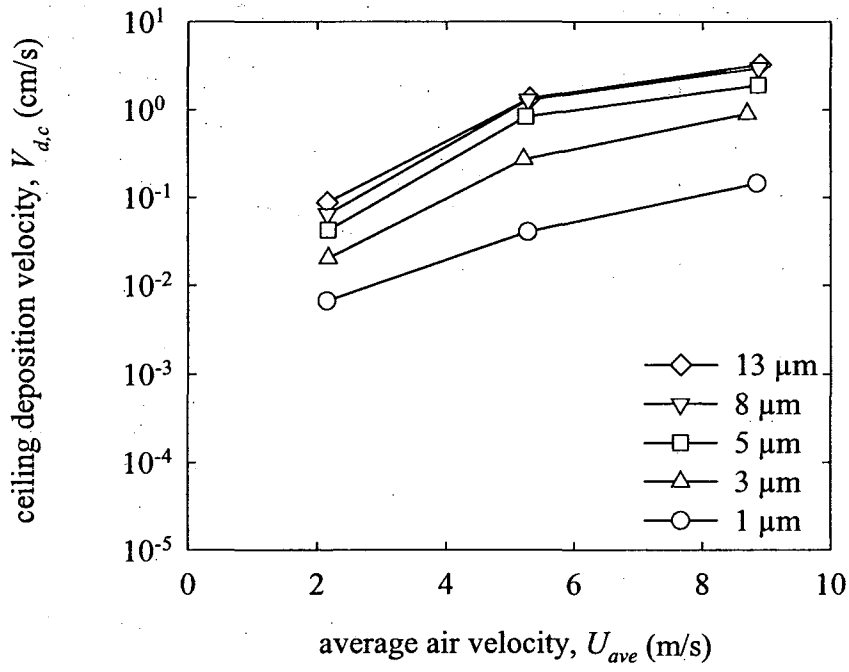

Figure 3.18 Average measured deposition velocity to the ceiling of test ducts 1 and 2 versus air speed in the insulated system.

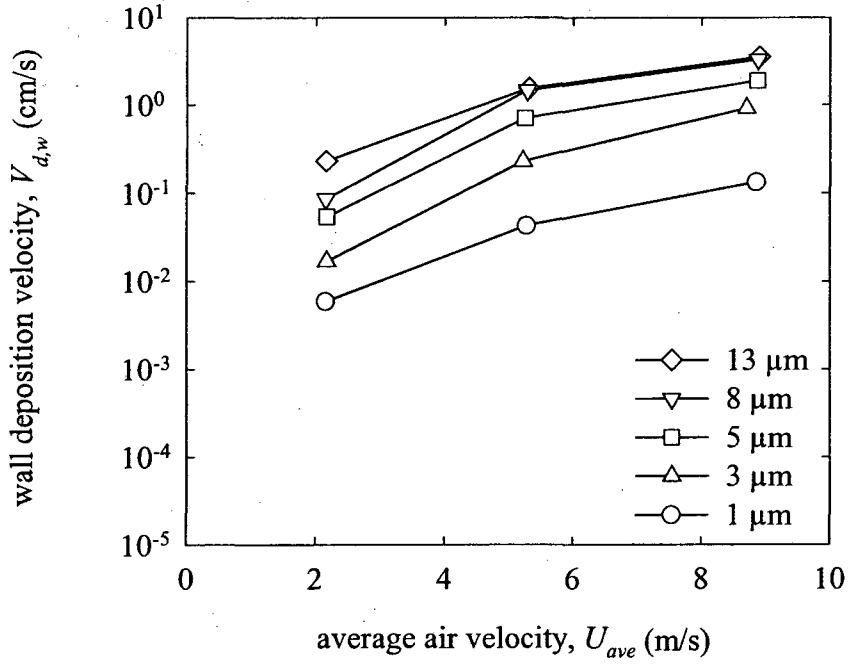

Figure 3.19 Average measured deposition velocities to the wall of test ducts 1 and 2 versus air speed in the insulated system.

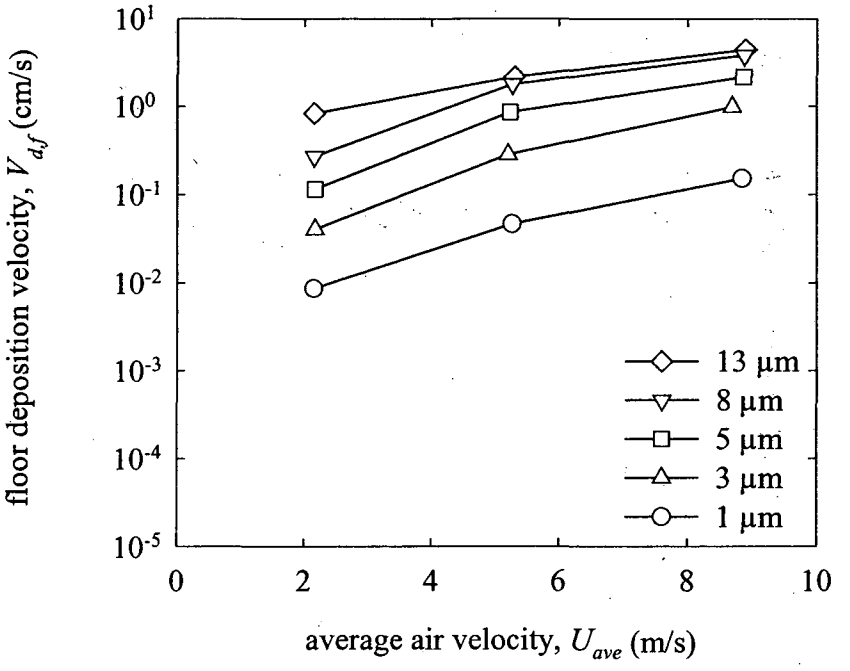

Figure 3.20 Average measured deposition velocities to the floor of test ducts 1 and 2 versus air speed in the insulated system.

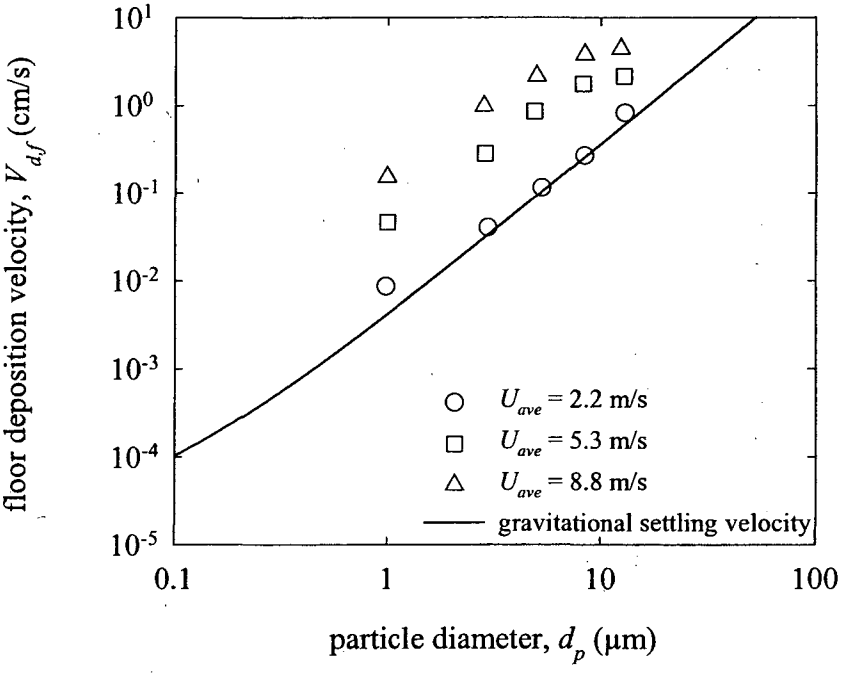

Figure 3.21 Comparison of the average measured deposition velocities to the floor of ducts 1 and 2 in the insulated system to the gravitational settling velocity.

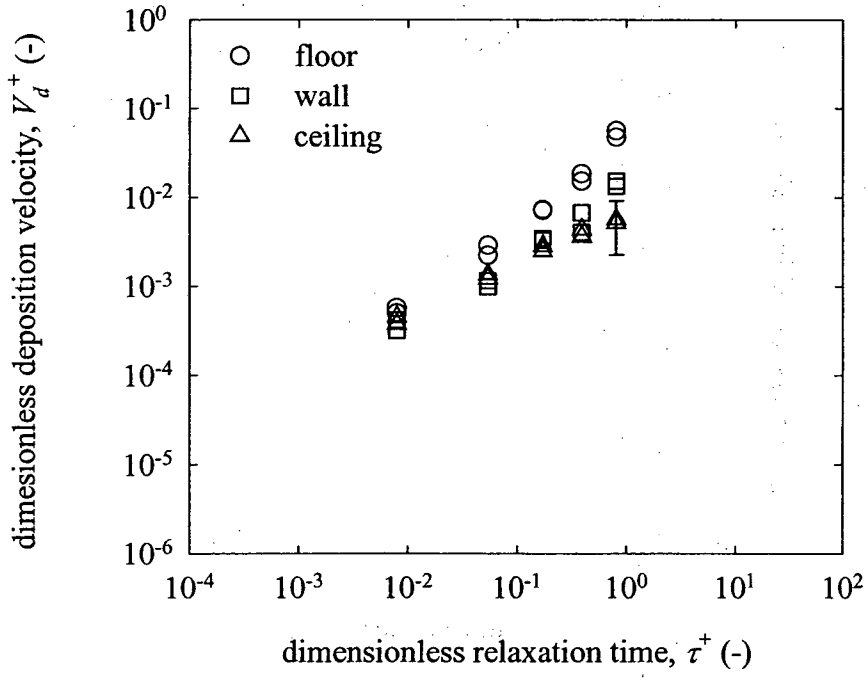

Figure 3.22 Measured dimensionless deposition velocities for particles depositing to the floor, wall and ceiling of test ducts 1 and 2 in the insulated system at 2.2 m/s.

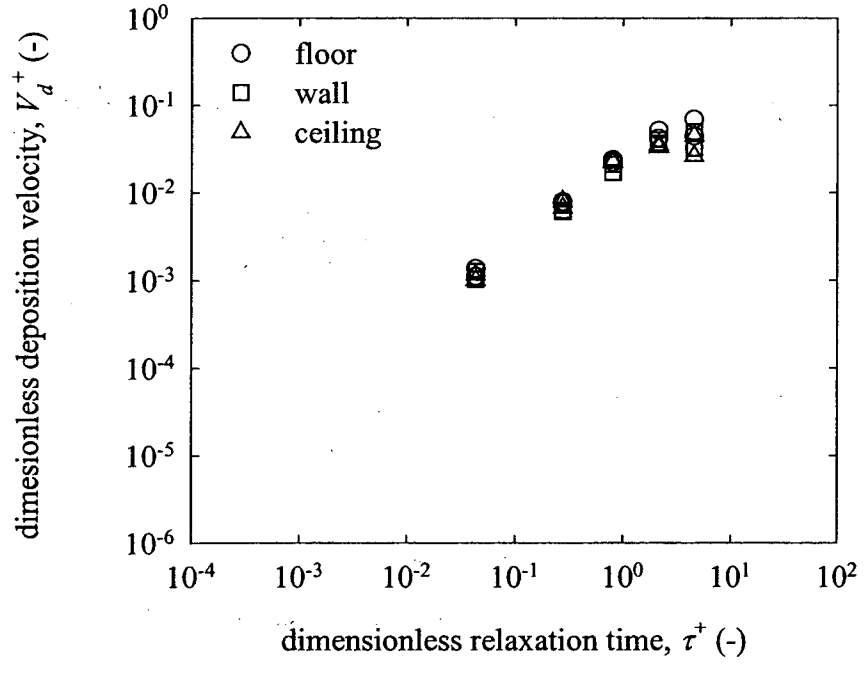

Figure 3.23 Measured dimensionless deposition velocities for particles depositing to the floor, wall and ceiling of test ducts 1 and 2 in the insulated system at 5.3 m/s.

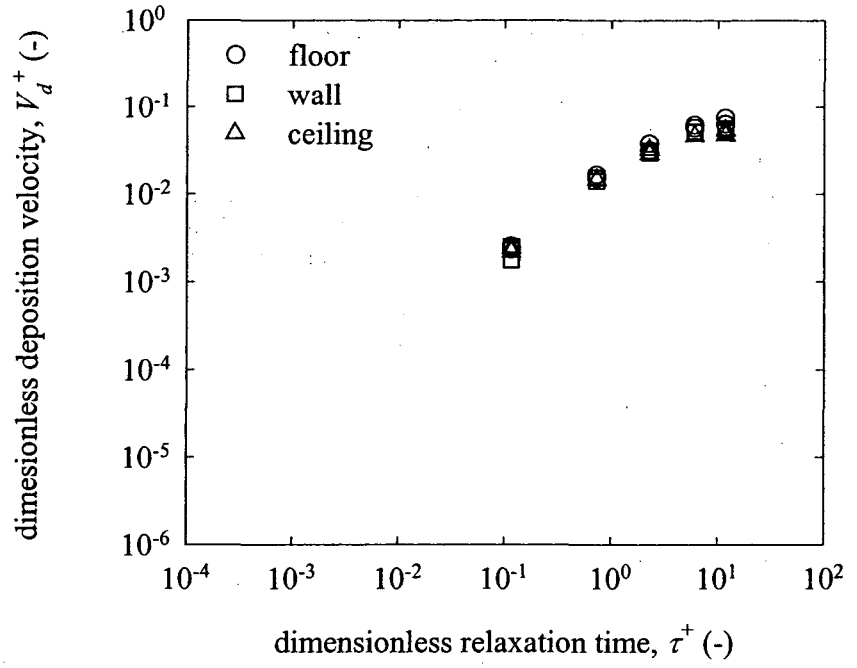

Figure 3.24 Measured dimensionless deposition velocities for particles depositing to the floor, wall and ceiling of test ducts 1 and 2 in the insulated system at 8.8 m/s.

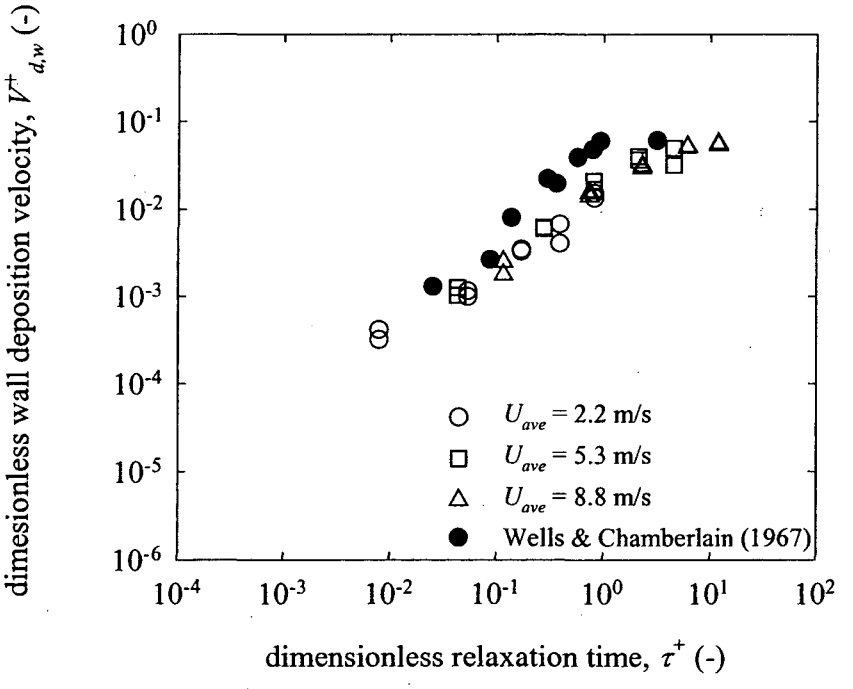

Figure 3.25 Comparison of $V_{d,w}^+$ measured at three air speeds in the insulated system with the data of Wells & Chamberlain (1967) for deposition to fibrous filter paper.

CHAPTER 4

Measurements of Particle Deposition at S-connectors, in Duct Bends, and in Ducts with Developing Turbulent Flow Profiles

4.0 Abstract

There are many circumstances in ventilation duct flow where the turbulent flow profile is disturbed or not fully developed and these conditions are likely to influence particle deposition to duct surfaces. Particle deposition rates at eight S-connectors, in two 90° duct bends and in two ducts where the turbulent flow profile was not fully developed were measured in a laboratory duct system with both galvanized steel and internally insulated ducts with hydraulic diameters of 15.2 cm. In the steel duct system, experiments with nominal particle diameters of 1, 3, 5, 9 and 16 μm were conducted at each of three nominal air speeds: 2.2, 5.3 and 9.0 m/s. In the insulated duct system, deposition of particles with nominal diameters of 1, 3, 5, 8 and 13 μm was measured at nominal air speeds of 2.2, 5.3 and 8.8 m/s. Fluorescent techniques were used to directly measure the deposition velocities of monodisperse fluorescent particles to duct surfaces.

Deposition at S-connectors, in bends and in ducts with developing turbulence was often greater than deposition in ducts with fully developed turbulence for equal particle sizes, air speeds and duct surface orientations. Deposition rates at all locations were found to increase with an increase in particle size or air speed. High particle deposition rates at S-connectors resulted from impaction and these deposition rates were nearly independent of

the orientation of the S-connector. Deposition rates in the two 90° bends differed by over an order of magnitude in some cases, probably because of the difference in turbulence conditions at the bend inlets. Deposition in the bend with an undisturbed inlet was lower than in the bend immediately downstream of a branched duct that was likely to disturb the turbulent flow profile. In steel ducts where the turbulent flow profile was not fully developed, the deposition enhancement relative to fully developed turbulence generally increased with air speed and decreased with downstream distance from the duct inlet. This enhancement was greater at the duct ceiling and wall than at the duct floor. In insulated ducts, this deposition was less pronounced overall than in the steel ducts and trends observed in steel ducts were generally weaker in the insulated ducts.

4.1 Introduction

Particle deposition to duct surfaces occurs at several locations within a ventilation system, but deposition has only been well studied from fully developed turbulent flows. Flow paths through ventilation ducts are commonly complex. A typical flow path from outdoors to an indoor space includes several branches and bends. The turbulent flow profile in a straight duct section after a bend is asymmetrical and changes with distance downstream of the bend until it is once again fully developed. Transition elements, temperature control coils, dampers and other components disturb flow profiles and further complicate most ventilation duct flows. Duct components and ridges at joints between duct sections are sites where particles may deposit by impaction. A large percentage of the total deposition in ventilation systems is likely to occur at locations other than to the walls of straight ducts where turbulent flow profiles are fully developed.

Most ventilation duct runs consist of several short sections connected in series. Mechanical connectors at joints between these sections can cause internal ridges that project a few millimeters into the duct flow and provide surface area for particles to deposit by impaction. Deposition at ridges resulting from duct connections has not been investigated experimentally, but the similar case of deposition to repeated transverse ribs on duct floors have been studied. Chamberlain *et al.* (1984) measured deposition rates of 0.6-5 μm particles to ribs with a height of 22 mm and a spacing of 326 mm in a large duct and found high deposition to the upstream face of the ribs and low deposition to the horizontal top of the rib. Lai (1997) measured deposition to 6 mm ribs spaced by 60 mm for 0.7-7.1 μm particles and reported higher local deposition at the transverse ribs than between the ribs. He also reported an increase in overall deposition by a factor of 2-3 to the ribbed floor surface versus a smooth duct floor. Both of these studies used ribs that were larger and more closely spaced than the ridges that result from duct connectors, but they indicate that connectors may significantly influence particle deposition rates.

Because of the different flow conditions and the potential for particle deposition by inertial impaction, deposition rates in bends are likely to be different than those in straight duct sections. However, experimental reports of deposition from turbulent flow within bends are limited to investigations in tubes of very small diameter (Pui *et al.*, 1987; McFarland *et al.*, 1997). High deposition rates of 1-10 μm particles were measured in these small tube bends compared to most measured deposition rates in straight tubes. There are no reports of particle deposition in bends with duct diameters similar to those

found in HVAC ducts, but ventilation duct bends may be important site for particle deposition in buildings.

Particle deposition from a turbulent flow is sensitive to the character of the flow and the degree of turbulence. Much of the turbulent flow in ventilation ducts does not have a fully developed flow profile because of the frequent occurrence of branches, bends and transitions in these systems. The distance for a turbulent flow profile to become fully developed after a disturbance is typically 40-100 hydraulic duct diameters (Hinze, 1975). EPA Method 1 gives guidelines for selecting sampling locations when measuring particle concentrations from airstreams in stacks (U.S. EPA, 1993). Method 1 recommends sampling at locations that are a minimum of 8 diameters downstream and 2 diameters upstream from any flow disturbance in order to obtain a representative aerosol sample from the stack. Particle deposition downstream of a flow disturbance is likely to be nonuniform if the airborne concentrations are nonuniform. Because particle deposition from turbulent flows is dependent on the nature of the turbulence, deposition rates in HVAC systems are likely to vary with location along the length of a duct run.

Particle deposition from disturbed or undeveloped turbulent flows has not been the subject of systematic experimental investigation. Several researchers have noted differences between deposition rates from fully developed and developing turbulent flows, but reports are inconsistent. Friedlander & Johnstone (1957) noted significantly less deposition at the inlet of their small tube for a distance of about 20 tube diameters than at locations where the turbulence was fully developed. A similar reduction in

deposition rates were observed at small tube inlets by Liu & Agarwal (1974). Chamberlain (1966) reported vapor deposition rates for the first six diameters of length in a large duct that were up to twice the rates in fully developed flow. Sehmel (1968) reported deposition rates of 16 μm particles that were dramatically enhanced near the inlet of a small tube compared to the rest of the tube. A numerical analysis by Zhang *et al.* (2001) in a laminar flow modeled after the human lung suggested that high local particle deposition is likely in straight airway sections immediately downstream of a bend. Experimental measurement of deposition rates in straight duct sections after bends has not been reported. Bends and other flow disturbances are common to ventilation ducts and are likely to influence particle deposition in a large fraction of duct runs. Basic experimental evidence of how deposition rates change with particle size and air speed at locations where turbulent flow is disturbed would be useful for evaluating losses of airborne particles as they travel through ventilation ducts.

In this chapter, measurements of particle deposition in a laboratory duct system to S-connectors at duct junctions, in duct bends and in straight ducts where the turbulent flow profile was not fully developed are presented and discussed. These straight duct sections with developing turbulence are located immediately downstream of the duct inlet after a mixing plenum and immediately after a 90° duct bend. These measurements were made in the duct system described in Chapter 3.

4.2 Experimental Methods

Particle deposition in steel and insulated duct systems was measured at a variety of locations within a laboratory duct system for particle sizes in the range 1-16 μm and air speeds in the range 2.2-9.0 m/s. Locations where particle deposition was measured were at two duct sections where the turbulent flow profile was fully developed (test ducts 1 and 2), at eight S-connectors (associated with test ducts 1 and 2), two 90° duct bends (bends 5 and 6) and two straight duct sections where the turbulent flow profile was not fully developed (test ducts 3 and 4). A schematic of the experimental apparatus is given in Figure 3.1; detailed descriptions of the apparatus and experimental methods, as well as results of particle deposition measurements made in ducts with a fully developed turbulent flow profile, are given in Chapter 3. This chapter reports on particle deposition measured to S-connectors in the steel system, and on particle deposition in duct bends and in straight duct sections where the turbulent flow profile was not fully developed in both the steel and insulated duct systems. The measurements reported in this chapter were made during the same experimental runs 1-31 for which physical data are reported in Tables 3.3 and 3.4.

Eight S-connectors were analyzed for particle deposition after each experiment for runs 1-16: four associated with test duct 1 and four associated with test duct 2. Test duct 1 had two S-connectors horizontally oriented on the duct floor (one each at the upstream and downstream ends) and two oriented horizontally on the ceiling. All four S-connectors associated with test duct 2 were vertically oriented on the walls. A

comprehensive description of the S-connectors use in these experiments is provided in section 3.2.2.

Bends 5 and 6 were not internally insulated in any experiments; the same galvanized steel bends were used in both the steel and insulated systems. They were rinsed after each experiment and reused. The bends turned 90° and had a radius of 22.9 cm (9.0 in) measured at the centerline, giving a bend ratio of 3.0. Bend 5 was located immediately after another 90° bend associated with the branched section in the lower duct. Bend 5 was oriented vertically and changed the flow direction from vertical and upwards to horizontal. Bend 6 was located at the end of the long, straight upper duct and directed the flow to make a right turn in the horizontal plane. When installed, bend 5 had less horizontally oriented surface area than bend 6, which had equal amount of floor and ceiling surface area. When bends were analyzed, deposition to the entire internal surface was measured and no distinctions were made among deposition rates to ceiling, wall or floor surfaces.

Test duct 3 was located immediately after the outlet from the mixing box in the lower duct. Test duct 4 was located immediately after bend 5 in the upper duct. As a consequence of upstream flow perturbations, the turbulent flow profile was not fully developed in these ducts. There is a greater uncertainty in deposition velocities measured in test ducts 3 and 4 than in test ducts 1 and 2 because airborne concentrations were not measured directly at test ducts 3 and 4. Among the different experiments, sarger uncertainties are expected for larger particle sizes where concentration projections were

more sensitive to experimental errors. As for all other straight ducts where deposition was measured, twelve total panels from each of test ducts 3 and 4 were analyzed for particle deposition, four panels each on the duct ceiling, wall and floor. The panel numbering convention is described in Figure 3.7.

4.3 Calculation Procedures

4.3.1 Estimation of particle concentrations

Airborne concentrations and deposition velocities measured at test ducts 1 and 2 were used to estimate particle concentrations throughout the straight duct sections of the experimental apparatus. Airborne concentrations at test ducts 3 and 4 were needed to calculate particle deposition velocities at these locations. Airborne concentrations at the inlet or outlet of bends 5 and 6 were needed to evaluate particle penetrations through these bends.

Deposition velocities measured to each surface in test ducts 1 and 2 for a given particle size and air speed were averaged:

$$V_{d,f} = \frac{V_{d,1f} + V_{d,2f}}{2} \tag{4.1}$$

$$V_{d,w} = \frac{V_{d,1w} + V_{d,2w}}{2} \tag{4.2}$$

$$V_{d,c} = \frac{V_{d,1c} + V_{d,2c}}{2} \tag{4.3}$$

These are the average deposition velocity values reported in Figures 3.8-3.10 for steel ducts and in Figures 3.18-3.20 for insulated ducts. These values were subjected to

surface-area-weighted averaging to yield a composite deposition velocity for a horizontal duct, $V_{d,comp}$, by

$$V_{d,comp} = \frac{V_{d,f} + 2V_{d,w} + V_{d,c}}{4} \tag{4.4}$$

The relative weights of the deposition velocities in equation (4.4) derive from the fact that in a square horizontal duct, there are equal areas of floor and ceiling surface and twice that area of wall surface. Particle penetration through straight horizontal sections of the experimental duct could then be estimated by the following equation:

$$P_{duct} = \frac{C_{out}}{C_{in}} = exp\left(\frac{-4LV_{d,comp}}{D_h U_{ave}}\right) \tag{4.5}$$

Thus, concentrations at test duct 3, C_3, and test duct 4, C_4, were estimated by:

$$C_3 = \frac{C_1}{exp\left(\frac{-4LV_{d,comp}}{D_h U_{ave}}\right)} \tag{4.6}$$

$$C_4 = \frac{C_2}{exp\left(\frac{-4LV_{d,comp}}{D_h U_{ave}}\right)} \tag{4.7}$$

Here, L was length between the midpoints of the two ducts between which the concentration was being projected, 12.2 m (40.0 ft) in equation (4.6) and 13.7 m (45.0 ft) in equation (4.7). The magnitude of the concentration decrease along the duct length depended on the particle size and air speed. Table 4.1 shows projected values of C_4 as multiples of the measured concentrations, C_2, for selected experimental runs in both the steel and insulated system. The experimental runs in Table 4.1 were chosen to illustrate the full range concentration changes between test ducts 4 and 2. The change in

concentration along the duct was at a minimum for the smallest particles at the lowest air speed (runs 1 and 17) and at a maximum for the largest particles at the highest air speed (runs 16 and 31). Runs 9 and 24 represent typical intermediate cases for the steel and insulated systems, respectively. Concentration projections between test ducts 1 and 3 were of a similar magnitude to those between test ducts 2 and 4. Deposition velocities in test ducts 3 and 4 were calculated from these estimated concentrations and the surface fluxes measured to duct panels.

The concentration at the inlet of bend 6, $C_{6,in}$, was estimated by

$$C_{6,in} = C_2 \exp\left(\frac{-4LV_{d,comp}}{D_h U_{ave}}\right) \tag{4.8}$$

where L was 3.8 m (12.5 ft). Because of uncertain particle deposition in the branched duct section preceding bend 5, particle concentrations at the inlet to bend 5 could not be projected from measurements made at test duct 1. Instead, concentrations at the outlet of bend 5, $C_{5,out}$, were projected from measurements at test duct 2 by

$$C_{5,out} = \frac{C_2}{exp\left(\frac{-4LV_{d,comp}}{D_h U_{ave}}\right)} \tag{4.9}$$

where L was 14.5 m (47.5 ft).

4.3.2 Deposition velocities and deposition fractions at S-connectors

The deposition flux of particles to an S-connector was determined by fluorescent techniques and equation (3.7). Deposition velocities were calculated by equation (2.1)

using C_1 and C_2 for the airborne concentrations in the calculation for S-connectors on test ducts 1 and 2, respectively. Dimensionless deposition velocities to S-connectors on the duct ceiling, wall and floor were respectively termed $V_{d,c,S}^{+}$, $V_{d,w,S}^{+}$ and $V_{d,f,S}^{+}$.

Observations during the rinsing analysis of S-connectors suggested that for most particle sizes, the majority of particle mass on S-connectors was deposited at the leading edge that was presented to the airstream. Thus, S-connector deposition fractions were also calculated. The S-connector deposition fraction, η_S, was defined by

$$\eta_S = \frac{m_S}{m_{presented}} \tag{4.10}$$

where m_S is the fluorescein mass deposited on the S-connector and $m_{presented}$ is the total fluorescein mass in the airstream presented to the leading edge of the connector during an experiment. This presented mass was calculated by

$$m_{presented} = C_{ave} h_S L_S u_S t m_{f/p} \tag{4.11}$$

where L_S was the transverse length of the S-connector, h_S is the height that the S-connector projects into the flow and u_S is the streamwise air velocity integrated over this height. C_{ave} is the appropriate time-averaged airborne concentration, either C_1 or C_2. Because the particle boundary layer is very thin, the particle concentration is expected to be nearly uniform from the duct centerline to distances from the wall that are much less than one millimeter. Therefore, the particle concentration presented to S-connectors is expected to be approximately equal to the concentration in the core of the duct. All S-connectors were uniform with L_S = 14.7 cm and h_S = 2.0 mm. The universal velocity

distribution was used for the air velocity integration; this distribution is (Brodkey & Hershey, 1988):

$$u^+ = y^+ \qquad y^+ \le 5 \tag{4.12}$$

$$u^+ = 5\ln y^+ - 3.05 \qquad 5 < y^+ \le 30 \tag{4.13}$$

$$u^+ = 2.5\ln y^+ + 5.5 \qquad y^+ > 30 \tag{4.14}$$

Data for S-connector deposition fractions were plotted versus particle S-connector Stokes numbers, St_S, defined by the following expression:

$$St_S = \frac{2\tau_p u_S}{h_S} \tag{4.15}$$

4.3.3 Bend penetrations

Penetration through bends was calculated by the following equation:

$$P_{bend} = 1 - \frac{m_{bend}}{m_{in}} \tag{4.16}$$

where m_{bend} is the fluorescein mass deposited in the bend calculated by equation (3.5), and m_{in} is the total mass of airborne fluorescein entering the bend inlet.

The total fluorescein mass entering bend 6 was calculated by

$$m_{6,in} = C_{6,in} D_h^2 U_{ave} t m_{f/p} \tag{4.17}$$

By mass balance, the total fluorescein mass entering bend 5 is equal to the sum of the mass exiting the bend in the airstream plus the mass deposited inside the bend:

$$m_{5,in} = C_{5,out} D_h^2 U_{ave} t m_{f/p} + m_{bend5} \tag{4.18}$$

where m_{bend5} is the fluorescein mass deposited in bend 5 calculated by equation (3.5).

4.3.4 Deposition velocities and enhancement factors in ducts with developing turbulent flow profiles

In test ducts 1 or 2, where the turbulent flow profile was fully developed, the measured particle deposition fluxes to each panel of a given duct surface were approximately equal. In contrast, measured deposition rates to the four panels of a given surface in test duct 3 or 4 usually showed a trend of decreasing deposition flux with increasing panel number. Thus, it was deemed useful to report deposition rates in these ducts in terms of an enhancement factor rather than as an average of the deposition velocities measured to each panel of a given surface as in equation (3.9) for test ducts 1 and 2.

The enhancement factor, *EF*, is the ratio of the measured deposition velocity to a panel in a duct with a developing turbulent flow profile (test duct 3 or 4) to the average deposition velocity in ducts with fully developed turbulent flow profiles (test ducts 1 and 2) for the same particle size and air speed. For example, the enhancement factor in test duct 4 for the second ceiling panel is

$$EF_{4c2} = \frac{V_{d,4c2}}{V_{d,c}} \tag{4.19}$$

Here, $V_{d,4c2}$ is the deposition velocity in test duct 4 to ceiling panel 2, calculated by

$$V_{d,4c2} = \frac{J_{4c2}}{C_4} \tag{4.20}$$

J_{4c2} is the particle flux in test duct 4 to ceiling panel 2 and $V_{d,c}$ is the average of the measured deposition velocities to the ceilings of test ducts 1 and 2 expressed by equation (4.3). This same calculation procedure was used to determine enhancement factors for all panels on the three surfaces of test ducts 3 and 4.

4.4 Experimental Results

4.4.1 Particle deposition at S-connectors

Measured dimensionless deposition velocities to S-connectors in the steel system are presented in Table 4.2. Reported values for $V_{d,c,S}^{+}$ and $V_{d,f,S}^{+}$ are for individual measurements, whereas those for $V_{d,w,S}^{+}$ are the average of four measurements. Figures 4.1-4.3 present these dimensionless deposition velocities to S-connectors at air speeds of 2.2, 5.3 and 9.0 m/s, respectively. In these figures, each measurement of deposition to an S-connector on the duct floor or ceiling is shown as a single data point. Data points representing deposition to wall S-connectors are the average of four measurements with error bars representing measurement variability. Error bars are only included when they are significantly larger than the size of the data point. Figure 4.4 displays measured S-connector deposition fractions versus S-connector Stokes numbers.

4.4.2 Particle deposition in duct bends

Tables 4.3 and 4.4 respectively summarize measured bend penetrations for experiments in the steel and insulated systems. Figure 4.5 shows measured penetrations through bend 5 versus particle diameter at different air speeds in both the steel and insulated systems.

Figure 4.6 is the same plot for bend 6. Penetrations through bends 5 and 6 versus the bend Stokes number are respectively plotted in Figures 4.7 and 4.8.

To enable comparison to deposition in straight ducts, particle deposition data in bends are shown as plots of the composite dimensionless deposition velocity versus dimensionless relaxation time in Figures 4.9-4.14. The average dimensionless deposition velocities for bends are averaged over the entire internal surface area of the bend; those reported for straight ducts are surface-area-weighted averages of deposition velocities measured to the floor, wall and ceiling of straight ducts in the steel system. The surface-area-weighted averaging was performed to make the data in the straight ducts directly comparable to the data in the bends. Figures 4.9-4.11 display data for bend 5 at air speeds of 2.2, 5.3 and 9.0 m/s, respectively. The same data collected in bend 6 are shown in Figures 4.12-4.14.

4.4.3 Particle deposition in straight ducts with developing turbulent flow

Measured dimensionless deposition velocities to all panels of test ducts 3 and 4 in the steel system are presented in Tables 4.5 and 4.6, respectively. Tables 4.7 and 4.8 respectively present dimensionless deposition velocities to all panels of test ducts 3 and 4 in the insulated system. Figure 4.15 is an example of a plot of enhancement factors versus panel number ceiling panels in duct 4 of the steel system at an air speed of 9.0 m/s. Figures 4.16 and 4.17 display all enhancement factors measured in the steel system in test ducts 3 and 4, respectively. In these figures, plots in the left column display data collected at different duct surfaces at an air speed of 2.2 m/s; those in the center and right columns display data collected at 5.3 and 9.0 m/s, respectively. The top, middle and

bottom rows of plots display data collected at the duct ceiling, wall and floor, respectively. Data were not collected at an air speed of 2.2 m/s in the steel system for 1 and 3 μm particles. All panels in these figures have the same vertical scale except for that depicting data at the wall for the lowest air speed in Figure 4.16 which is shifted one logarithmic decade lower than the others. This was done to enable the display of enhancement factors for 9 and 16 μm particles that were less than 0.1. This was the only circumstance where enhancement factors were significantly less than one. Figures 4.18 and 4.19 respectively display all enhancement factors measured in the insulated system in test ducts 3 and 4.

4.5 Discussion

4.5.1 Particle deposition at S-connectors

Dimensionless deposition velocities to S-connectors in Figures 4.1-4.3 increased with values of τ^+ for all air speeds and for S-connectors located on all duct surfaces. In most cases, measured deposition rates to S-connectors at all three surfaces were within the same order of magnitude for the same airspeed and particle size. Measured deposition velocities to the wall S-connectors were generally lower than those measured to S-connectors on the floor and ceiling; this trend is most visible at the lowest air speed (Figure 4.1) where data for the wall S-connectors lie about an order of magnitude lower than the other data for most particle sizes. There is no clear explanation for the lower deposition rates to wall S-connectors relative to floor and ceiling S-connectors.

Measured deposition rates to ceiling and wall S-connectors were higher than those measured to the corresponding steel duct surface to which the S-connector was attached. A comparison of the data in Table 4.1 with that in Table 3.5 reveals that deposition to ceiling S-connectors was greater than deposition to the steel duct ceiling by factors of 30-520. Deposition to wall S-connectors was greater than deposition to the steel duct wall by factors in the range 1.5-48. Measured deposition rates to S-connectors on the floor were about the same as those measured to the steel duct floor.

That measured deposition rates to S-connectors on both the floor and ceiling had similar values is an indication that gravitational settling was not dominant for deposition to these surfaces. It was observed during rinsing that most of the particle mass on S-connectors was deposited at the leading edge presented to the airstream, especially for larger particles. These two observations suggest that impaction on the leading edge is the mechanism by which most particles deposited to S-connectors.

The data in Figure 4.4 exhibit scatter, but follow the same trends as other particle deposition processes known to be dominated by impaction, such as deposition to a single fiber. For connector Stokes numbers less than 0.1, deposition fractions were very close to zero. Deposition fractions increased gradually as the Stokes number increased from 0.1 to 1, and then increased more dramatically as the Stokes number increased above 1.

4.5.2 Particle deposition in duct bends

The data in Figure 4.5 show that, in general, penetration through bend 5 decreased with an increase in particle size or air speed. These trends are most clear in the data collected in the steel system. There is reasonable agreement among data collected in the steel and insulated systems and the same trends are observed in both data sets. The same trends of a decrease in penetration with an increase in particle size or air speed are observed in penetration data for bend 6 in Figure 4.6. Compared to measured penetrations through bend 5, those measured through bend 6 were generally higher and less scattered. Bend 6 had more floor surface area than bend 5 and therefore, in contrast to observations, might have been expected to yield lower values for particle penetration. The likely cause of the higher penetration values through bend 6 is the difference in inlet conditions between the two bends. The flow at the inlet of bend 6 was relatively undisturbed, but bend 5 was preceded by a duct branch and another bend, both of which were likely to increase the degree of turbulence in the flow. This higher degree of turbulence may lead to higher particle deposition in bend 5 and, therefore, lower particle penetration.

In Figures 4.7 and 4.8, particles with Stokes numbers less than 0.01 have values for penetration through both bends nearly equal to one. Bend penetrations begin to decrease for larger values of St, and this decrease is more dramatic in bend 5 than in bend 6. That the data for bend penetration are fairly well correlated by the particle Stokes number suggests that particle inertia is an important factor in determining deposition in bends. Turbulent eddies that impinge on duct surfaces are likely to be much more common in bends, where the mean flow direction is changing, than in straight ducts. Particles

associated with these impinging eddies may deposit to surfaces by impaction if they have sufficient inertia. The relatively strong secondary flows established within bends are likely to offer additional opportunities for deposition of particles by inertial impaction.

In Figures 4.9-4.11 comparing average dimensionless deposition velocities within bend 5 to the equivalent surface-area-weighted dimensionless deposition velocities to straight steel ducts, the deposition rates in the bend are greater than in the straight ducts for all particle sizes and air speeds. The increase in deposition rates in bend 5 over deposition rates in the straight ducts was greatest at the highest air speeds, where the increase for most particle sizes was one to two orders of magnitude. Increases in dimensionless deposition velocities in bend 6 over equivalent surface-area-weighted values to straight steel ducts were less dramatic than in bend 5 as can be seen in Figures 4.12-4.14. At the lowest air speed, deposition rates in bend 6 were about equal to those in straight ducts. At the higher air speeds, deposition rates in bend 6 were greater than rates in straight steel ducts by factors that were always less than 4.

4.5.3 Particle deposition in straight ducts with developing turbulent flow

Figure 4.15 displays enhancement factors at ceiling panels of test duct 4 at an air speed of 9.0 m/s. The increase in deposition rates at this location relative to the case of deposition from flow with a fully developed flow profile is apparent. Enhancement factors are expressed relative to the deposition rate of the same sized particle to the same surface and at the same velocity in a duct with fully developed turbulent flow. Thus, for example, at an air speed of 9.0 m/s, 5 μm particles were observed to deposit to ceiling panel 1 of duct

4 at a rate 72 times higher than they deposited to ceiling panels in ducts 1 and 2. The other prominent feature of this figure is the decrease in the enhancement factor from upstream locations to downstream locations along the test duct for all particle sizes. This trend is weakest at the largest particle size.

The primary trend visible in the data in Figure 4.16 is that enhancement factors at test duct 3 in the steel system increase with increasing air speed. Enhancement factors were larger for the ceiling and wall surfaces than for the floor, especially at the higher air speeds. An anomaly in the data occurs at the wall at an air speed of 2.2 m/s. The low enhancement factors observed here ($EF \sim 0.01$-1) were likely the result of a flow contraction (vena contracta) after the duct inlet. Such a flow contraction would establish zones of recirculating flow adjacent to the duct surfaces that would prevent particles from being presented to these surface. That enhancement factors were not observed at the duct ceiling at this velocity suggests that the flow contraction was asymmetrical in this case. Such a recirculating flow region would not affect particle deposition to the floor as readily because of the influence of gravitational settling. The reason that this phenomenon was not observed on the ceiling of duct 3 at the low velocity is unknown. Deposition trends similar to those observed in test duct 3 were observed in test duct 4, as seen in Figure 4.17: enhancement factors increased with increasing air speed and were larger for the ceiling and wall surfaces than for the floor. In fact, essentially no enhancement was observed at the floor of test duct 4 for all air speeds and one can conclude that gravitational settling dominated deposition at this location. The large enhancement factors at the ceiling of test duct 4 were likely attributable to the vertically

oriented bend immediately upstream of this test duct. Air flowing through this bend may have impinged on the ceiling surface of test duct 4, giving entrained particles the opportunity to deposit by impaction more readily than in a flow with a symmetrical velocity profile. In most cases, enhancement factors at panel 4 are near one, indicating that deposition rates relax to about the same values as in ducts with fully developed turbulence, even within one duct length ($< 10D_h$) of a flow disturbance.

As seen in Figures 4.18 and 4.19, enhancement factors in the insulated system were generally smaller than those measured in the steel system for both ducts 3 and 4. In Figure 4.18, the relatively large enhancement factors for 13 μm particles at air speeds of 5.3 and 8.8 m/s contradict the trends established by the rest of the data. It is believed that the 13 μm particles may reflect uncertainty associated with projecting concentrations of particles with high deposition velocities throughout the duct. Indeed, had the composite deposition velocity for 13 μm particles measured in test ducts 1 and 2 been only 30% greater at these air speeds, the enhancement factors of these particles would be in accord with the other data.

For the insulated system there is no apparent trend of increased enhancement factor with increasing air speed in Figures 4.18 and 4.19 as was observed in the steel system. The small enhancement factors in test ducts 3 and 4 in the insulated system were probably a result of the high deposition rates to insulated duct surfaces where the turbulent flow profile was fully developed. In the steel system, enhancement factors for duct walls and ceilings were clearly larger than those for duct floors. In the insulated system, wall and

ceiling enhancement factors are only clearly larger than floor enhancement factors in test duct 4 (Figure 4.19). In Figure 4.18, enhancement factors for all surfaces of test duct 3 are of comparable size in most cases. Another difference between the data collected in the steel and insulated systems can be seen in results at the wall of test duct 3 at the lowest air speed. In the insulated system enhancement factors greater than one were measured at this location, while in the steel system, values for these enhancement factors were far below one in some cases.

4.6 Conclusions

Experiments were conducted that used fluorescent techniques to quantify particle deposition directly on the surfaces of a laboratory duct system constructed of materials typical of HVAC systems in real buildings. Experiments covered particle sizes in the range 1-16 μm and air speeds in the range 2.2-9.0 m/s in a steel and an internally insulated duct system. These experiments indicate that particle deposition rates to surfaces in a ventilation duct system vary depending on the specific location. Measured deposition rates to S-connectors, in duct bends and in ducts where the turbulent flow profile was not fully developed were generally greater than rates to equivalent surfaces in ducts with a fully developed turbulent flow profile.

S-connectors were found to be sites of relatively high particle deposition owing to impaction on their leading edges. Deposition rates to S-connectors were dependent on both particle size and air speed, but were relatively independent of orientation.

Deposition rates to S-connectors located on duct walls and ceilings were higher than deposition rates to duct surfaces of the same orientation.

Particle penetration through steel 90° duct bends was found to decrease with increases in particle size or air speed. Penetration through bends was dependent on the airflow conditions at the bend inlet: penetration was lower where the inlet airflow was disturbed and higher when the inlet airflow was undisturbed. In general, particle deposition rates in bends were greater than deposition rates in straight ducts.

In the steel duct system, particle deposition rates in a duct immediately after a bend and in a duct immediately after an inlet, locations where the turbulent profile was not fully developed, were generally greater than deposition rates in ducts with fully developed turbulence. Deposition rates in these ducts were measured to decrease with distance downstream. The degree to which deposition rates were enhanced in these ducts relative to ducts with fully developed turbulence increased with air speed in the duct. In the insulated system, similar trends were observed, but the degree of enhancement was less.

These experiments quantify particle deposition in ventilation ducts at locations that have not previously been studied. The results suggest that there are many locations within duct systems where particle deposition rates are significantly greater than deposition rates to ducts with fully developed turbulence. These experimental findings imply that models for predicting deposition rates within ventilation duct systems should account for sites with enhanced deposition.

Table 4.1 Projected airborne concentrations at test duct 4 for selected experiments.

Run # (-)	**Projected value of C_4 as a multiple of C_2** (-)
1	$1.0C_2$
9	$1.0C_2$
16	$1.8C_2$
17	$1.0C_2$
24	$1.8C_2$
31	$5.3C_2$

Table 4.2 Dimensionless deposition velocities to S-connectors in the steel system.

Run # (-)	U_{ave} (m s^{-1})	d_{mm} (μm)	τ^+ (-)	$V^+_{d,c,S}$ (-)	$V^+_{d,w,S}$ (-)	$V^+_{d,f,S}$ (-)
1	2.2	1.0	4.6×10^{-3}	1.0×10^{-3}	8.1×10^{-5}	8.5×10^{-4}
				1.0×10^{-3}		6.9×10^{-4}
2	2.2	2.8	0.028	3.7×10^{-3}	2.2×10^{-4}	2.7×10^{-3}
				5.0×10^{-3}		2.7×10^{-3}
3	2.1	5.2	0.098	0.010	4.6×10^{-4}	0.010
				5.9×10^{-3}		4.9×10^{-3}
4	2.2	9.1	0.27	0.011	3.7×10^{-3}	0.012
				0.012		0.015
5	2.2	16	0.72	0.025	0.035	0.043
				0.025		0.042
6	5.3	1.0	0.023	6.2×10^{-4}	1.5×10^{-4}	5.6×10^{-4}
				5.7×10^{-4}		5.5×10^{-4}
7	5.2	1.0	0.022	5.8×10^{-4}	3.4×10^{-4}	6.6×10^{-4}
				7.6×10^{-4}		6.5×10^{-4}
8	5.2	3.1	0.16	3.0×10^{-3}	1.5×10^{-3}	3.7×10^{-3}
				2.4×10^{-3}		4.1×10^{-3}
9	5.4	5.2	0.48	0.023	0.016	0.025
				0.025		0.023
10	5.3	9.8	1.5	0.035	0.010	0.028
				0.028		0.018
11	5.3	16	3.6	0.085	0.11	0.15
				0.089		0.11
12	9.0	1.0	0.062	5.0×10^{-4}	3.9×10^{-4}	7.3×10^{-4}
				5.4×10^{-4}		6.2×10^{-4}
13	9.0	3.1	0.42	5.0×10^{-3}	3.4×10^{-3}	4.2×10^{-3}
				4.0×10^{-3}		5.3×10^{-3}
14	8.8	5.4	1.4	0.021	0.013	0.022
				0.018		0.033
15	9.2	8.7	3.2	0.036	0.010	0.016
				0.019		0.028
16	9.1	15	8.8	0.11	0.068	0.11
				0.17		0.060

Table 4.3 Bend penetrations for experiments in the steel system.

Run # (-)	U_{ave} (m s^{-1})	d_{mm} (μm)	St (-)	P_{bend5} (-)	P_{bend6} (-)
1	2.2	1.0	-	-	-
2	2.2	2.8	-	-	-
3	2.1	5.2	2.9×10^{-3}	0.999	0.999
4	2.2	9.1	7.5×10^{-3}	0.995	0.997
5	2.2	16	0.020	0.977	0.990
6	5.3	1.0	-	-	-
7	5.2	1.0	3.2×10^{-4}	1.00	1.00
8	5.2	3.1	2.4×10^{-3}	0.999	1.00
9	5.4	5.2	7.3×10^{-3}	0.982	0.998
10	5.3	9.8	0.021	0.967	0.997
11	5.3	16	0.051	0.952	0.986
12	9.0	1.0	5.8×10^{-4}	1.00	1.00
13	9.0	3.1	4.3×10^{-3}	0.995	1.00
14	8.8	5.4	0.013	0.923	0.993
15	9.2	8.7	0.029	0.941	0.992
16	9.1	15	0.081	0.873	0.974

Table 4.4 Bend penetrations for experiments in the insulated system.

Run # (-)	U_{ave} (m s^{-1})	d_{mm} (μm)	St (-)	P_{bend5} (-)	P_{bend6} (-)
17	2.2	1.0	1.3×10^{-4}	1.00	1.00
18	2.2	3.0	9.4×10^{-4}	1.00	1.00
19	2.2	5.3	3.0×10^{-3}	0.999	0.998
20	2.2	8.4	6.7×10^{-3}	0.992	0.996
21	2.2	13	0.014	0.964	0.988
22	5.3	1.0	3.3×10^{-4}	0.999	1.00
23	5.2	2.9	2.1×10^{-3}	0.999	1.00
24	5.2	4.9	6.1×10^{-3}	0.994	0.998
25	5.3	8.2	0.016	0.967	0.991
26	5.3	13	0.034	0.970	0.983
27	8.9	1.0	5.4×10^{-4}	1.00	1.00
28	8.7	2.8	3.4×10^{-3}	0.997	0.999
29	8.9	5.0	0.011	0.971	0.996
30	8.9	8.4	0.027	0.975	0.985
31	8.9	13	0.055	0.959	0.976

Table 4.5 Dimensionless deposition velocities for all panels in test duct 3 in the steel system.

Run #	U_{ave} (m/s)	d_{mm} (μm)	Ceiling, $V_{d,c}^{+}$ (-)				Wall, $V_{d,w}^{+}$(-)				Floor, $V_{d,f}^{+}$ (-)			
			Panel 1	Panel 2	Panel 3	Panel 4	Panel 1	Panel 2	Panel 3	Panel 4	Panel 1	Panel 2	Panel 3	Panel 4
1	2.2	1.0	-	-	-	-	-	-	-	-	-	-	-	-
2	2.2	2.8	-	-	-	-	-	-	-	-	-	-	-	-
3	2.1	5.2	1.3×10^{-4}	1.2×10^{-4}	1.0×10^{-4}	9.9×10^{-5}	3.1×10^{-4}	2.2×10^{-4}	2.2×10^{-4}	1.8×10^{-4}	0.013	0.012	0.011	0.012
4	2.2	9.1	1.8×10^{-4}	1.8×10^{-4}	1.5×10^{-4}	1.3×10^{-4}	3.8×10^{-5}	3.8×10^{-5}	3.5×10^{-5}	4.5×10^{-5}	0.027	0.025	0.023	0.024
5	2.2	16	2.1×10^{-4}	1.7×10^{-4}	1.7×10^{-4}	1.9×10^{-4}	2.5×10^{-5}	3.2×10^{-5}	3.5×10^{-4}	5.7×10^{-4}	0.093	0.082	0.074	0.073
6	5.3	1.0	-	-	-	-	-	-	-	-	-	-	-	-
7	5.2	1.0	1.6×10^{-5}	1.8×10^{-5}	9.8×10^{-6}	7.8×10^{-6}	4.5×10^{-5}	3.4×10^{-5}	3.2×10^{-5}	2.8×10^{-5}	2.6×10^{-4}	2.4×10^{-4}	2.1×10^{-4}	2.3×10^{-4}
8	5.2	3.1	4.1×10^{-5}	3.4×10^{-5}	2.7×10^{-5}	2.7×10^{-5}	1.6×10^{-4}	7.1×10^{-5}	3.9×10^{-5}	3.5×10^{-5}	2.1×10^{-3}	1.7×10^{-3}	1.7×10^{-3}	1.6×10^{-3}
9	5.4	5.2	8.5×10^{-5}	8.9×10^{-5}	1.7×10^{-4}	1.4×10^{-4}	8.3×10^{-4}	4.7×10^{-4}	3.2×10^{-4}	2.9×10^{-4}	0.012	0.011	9.4×10^{-3}	9.1×10^{-3}
10	5.3	9.8	3.4×10^{-4}	1.4×10^{-4}	1.1×10^{-4}	1.1×10^{-4}	2.4×10^{-3}	1.1×10^{-3}	7.7×10^{-4}	6.6×10^{-4}	0.040	0.026	0.025	0.024
11	5.3	16	8.0×10^{-4}	5.6×10^{-4}	4.2×10^{-4}	3.6×10^{-4}	0.028	0.021	0.018	0.016	0.14	0.11	0.10	0.10
12	9.0	1.0	4.7×10^{-5}	3.7×10^{-5}	3.3×10^{-5}	2.7×10^{-5}	4.2×10^{-5}	3.7×10^{-5}	3.2×10^{-5}	3.1×10^{-5}	2.1×10^{-4}	2.0×10^{-4}	1.8×10^{-4}	1.8×10^{-4}
13	9.0	3.1	2.0×10^{-4}	1.0×10^{-4}	6.4×10^{-4}	5.2×10^{-4}	5.3×10^{-4}	2.5×10^{-4}	1.8×10^{-4}	1.5×10^{-4}	2.4×10^{-3}	1.8×10^{-3}	1.5×10^{-3}	1.5×10^{-3}
14	8.8	5.4	2.2×10^{-3}	8.3×10^{-4}	5.8×10^{-4}	4.2×10^{-4}	9.5×10^{-3}	4.5×10^{-3}	2.5×10^{-3}	1.8×10^{-3}	0.045	0.026	0.018	0.016
15	9.2	8.7	0.010	4.9×10^{-3}	2.8×10^{-3}	1.9×10^{-3}	0.023	9.7×10^{-3}	5.2×10^{-3}	4.5×10^{-3}	0.092	0.050	0.041	0.038
16	9.1	16	8.7×10^{-3}	6.8×10^{-3}	5.0×10^{-3}	6.0×10^{-3}	0.056	0.041	0.031	0.028	0.23	0.18	0.16	0.14

Table 4.6 Dimensionless deposition velocities for all panels in test duct 4 in the steel system

Run #	U_{ave} (m/s)	d_{mm} (μm)	Ceiling, $V_{d,c}^{+}$ (-)				Wall, $V_{d,w}^{+}$(-)				Floor, $V_{d,f}^{+}$ (-)			
			Panel 1	Panel 2	Panel 3	Panel 4	Panel 1	Panel 2	Panel 3	Panel 4	Panel 1	Panel 2	Panel 3	Panel 4
1	2.2	1.0	-	-	-	-	-	-	-	-	-	-	-	-
2	2.2	2.8	-	-	-	-	-	-	-	-	-	-	-	-
3	2.1	5.2	1.9×10^{-5}	2.4×10^{-5}	2.8×10^{-5}	2.6×10^{-5}	7.7×10^{-4}	5.8×10^{-4}	4.9×10^{-4}	3.4×10^{-4}	0.011	0.010	0.011	0.011
4	2.2	9.1	4.7×10^{-5}	4.0×10^{-5}	2.9×10^{-5}	2.6×10^{-5}	6.3×10^{-4}	1.1×10^{-3}	1.0×10^{-3}	1.0×10^{-3}	0.029	0.029	0.031	0.031
5	2.2	16	1.3×10^{-4}	8.3×10^{-5}	8.7×10^{-5}	4.0×10^{-5}	0.017	0.012	8.9×10^{-3}	5.0×10^{-3}	0.063	0.063	0.067	0.060
6	5.3	1.0	-	-	-	-	-	-	-	-	-	-	-	-
7	5.2	1.0	1.7×10^{-5}	1.2×10^{-5}	1.2×10^{-5}	1.0×10^{-5}	5.5×10^{-5}	4.2×10^{-5}	4.0×10^{-5}	3.7×10^{-5}	2.3×10^{-4}	2.3×10^{-4}	2.2×10^{-4}	2.0×10^{-4}
8	5.2	3.1	2.3×10^{-5}	1.4×10^{-5}	1.1×10^{-5}	1.1×10^{-5}	1.5×10^{-4}	1.1×10^{-4}	1.0×10^{-4}	9.3×10^{-5}	1.6×10^{-3}	1.6×10^{-3}	1.6×10^{-3}	1.6×10^{-3}
9	5.4	5.2	2.3×10^{-4}	8.8×10^{-5}	9.2×10^{-5}	5.7×10^{-5}	2.9×10^{-3}	1.7×10^{-3}	9.4×10^{-4}	5.9×10^{-4}	8.8×10^{-3}	8.5×10^{-3}	8.7×10^{-3}	8.9×10^{-3}
10	5.3	9.8	1.8×10^{-3}	7.4×10^{-4}	2.8×10^{-4}	1.2×10^{-4}	9.0×10^{-3}	5.0×10^{-3}	2.3×10^{-3}	8.8×10^{-4}	0.019	0.021	0.021	0.021
11	5.3	16	0.017	7.4×10^{-3}	3.7×10^{-3}	1.6×10^{-3}	0.092	0.080	0.050	0.022	0.075	0.062	0.081	0.070
12	9.0	1.0	8.0×10^{-5}	4.5×10^{-5}	3.1×10^{-5}	2.4×10^{-5}	9.6×10^{-5}	3.7×10^{-5}	6.3×10^{-5}	5.6×10^{-5}	2.5×10^{-4}	2.3×10^{-4}	2.6×10^{-4}	2.9×10^{-4}
13	9.0	3.1	5.8×10^{-4}	2.0×10^{-4}	1.0×10^{-4}	5.9×10^{-5}	8.1×10^{-4}	4.4×10^{-4}	2.7×10^{-4}	1.9×10^{-4}	1.3×10^{-3}	1.3×10^{-3}	1.3×10^{-3}	1.3×10^{-3}
14	8.8	5.4	0.011	5.5×10^{-3}	2.8×10^{-3}	1.4×10^{-3}	0.012	6.5×10^{-3}	4.0×10^{-3}	2.8×10^{-3}	0.014	0.014	0.015	0.015
15	9.2	8.7	0.026	0.011	6.7×10^{-3}	3.9×10^{-3}	0.016	0.011	9.1×10^{-3}	6.5×10^{-3}	0.028	0.029	0.033	0.035
16	9.1	16	0.020	0.021	0.019	0.015	0.043	0.040	0.038	0.040	0.10	0.10	0.10	0.11

Table 4.7 Dimensionless deposition velocities for all panels in test duct 3 in the insulated system

Run #	U_{ave} (m/s)	d_{mm} (μm)	Ceiling, $V_{d,c}^{+}$ (-)				Wall, $V_{d,w}^{+}$(-)				Floor, $V_{d,f}^{+}$ (-)			
			Panel 1	**Panel 2**	**Panel 3**	**Panel 4**	**Panel 1**	**Panel 2**	**Panel 3**	**Panel 4**	**Panel 1**	**Panel 2**	**Panel 3**	**Panel 4**
17	2.2	1.0	7.2×10^{-4}	5.3×10^{-4}	5.9×10^{-4}	3.2×10^{-4}	6.1×10^{-4}	4.0×10^{-4}	3.8×10^{-4}	3.6×10^{-4}	6.5×10^{-4}	4.9×10^{-4}	9.3×10^{-4}	6.1×10^{-4}
18	2.2	3.0	1.7×10^{-3}	1.4×10^{-3}	1.1×10^{-3}	7.7×10^{-4}	1.9×10^{-3}	1.6×10^{-3}	1.7×10^{-3}	1.5×10^{-3}	2.9×10^{-3}	3.0×10^{-3}	3.1×10^{-3}	1.6×10^{-3}
19	2.2	5.3	0.018	7.7×10^{-3}	5.2×10^{-3}	3.4×10^{-3}	0.021	9.1×10^{-3}	4.2×10^{-3}	4.9×10^{-3}	0.014	0.011	8.5×10^{-3}	9.6×10^{-3}
20	2.2	8.4	0.020	7.5×10^{-3}	5.2×10^{-3}	3.3×10^{-3}	0.021	8.3×10^{-3}	6.2×10^{-3}	3.1×10^{-3}	0.024	0.020	0.014	0.017
21	2.2	13	0.033	0.011	7.2×10^{-3}	4.6×10^{-3}	0.046	0.021	0.020	0.020	0.092	0.064	0.062	0.058
22	5.3	1.0	2.3×10^{-3}	2.1×10^{-3}	1.2×10^{-3}	9.9×10^{-4}	2.7×10^{-3}	2.4×10^{-3}	1.1×10^{-3}	9.4×10^{-4}	2.3×10^{-3}	2.1×10^{-3}	1.4×10^{-3}	1.1×10^{-3}
23	5.2	2.9	0.010	9.5×10^{-3}	8.3×10^{-3}	8.2×10^{-3}	8.8×10^{-3}	8.3×10^{-3}	7.1×10^{-3}	6.6×10^{-3}	9.8×10^{-3}	7.2×10^{-3}	8.3×10^{-3}	6.8×10^{-3}
24	5.2	4.9	0.048	0.040	0.026	0.030	0.056	0.036	0.029	0.025	0.035	0.026	0.029	0.025
25	5.3	8.2	0.089	0.054	0.035	0.035	0.099	0.055	0.034	0.037	0.080	0.046	0.046	0.044
26	5.3	13	0.31	0.18	0.12	0.088	0.28	0.16	0.13	0.094	0.27	0.18	0.15	0.13
27	8.9	1.0	4.6×10^{-3}	2.9×10^{-3}	2.3×10^{-3}	2.5×10^{-3}	3.8×10^{-3}	3.7×10^{-3}	2.4×10^{-3}	3.1×10^{-3}	5.4×10^{-3}	3.2×10^{-3}	2.7×10^{-3}	2.9×10^{-3}
28	8.7	2.8	0.044	0.030	0.024	0.018	0.038	0.025	0.023	0.020	0.033	0.023	0.023	0.020
29	8.9	5.0	0.086	0.059	0.043	0.038	0.078	0.052	0.048	0.041	0.083	0.064	0.057	0.047
30	8.9	8.4	0.12	0.075	0.061	0.059	0.14	0.083	0.059	0.056	0.12	0.083	0.066	0.057
31	8.9	13	0.40	0.22	0.16	0.13	0.33	0.17	0.13	0.091	0.27	0.19	0.16	0.13

Table 4.8 Dimensionless deposition velocities for all panels in test duct 4 in the insulated system

Run #	U_{ave} (m/s)	d_{mm} (μm)	Ceiling, $V_{d,c}^{+}$ (-)				Wall, $V_{d,w}^{+}$(-)				Floor, $V_{d,f}^{+}$ (-)			
			Panel 1	Panel 2	Panel 3	Panel 4	Panel 1	Panel 2	Panel 3	Panel 4	Panel 1	Panel 2	Panel 3	Panel 4
17	2.2	1.0	1.9×10^{-3}	9.9×10^{-4}	8.3×10^{-4}	7.2×10^{-4}	1.3×10^{-3}	8.9×10^{-4}	7.6×10^{-4}	4.7×10^{-4}	5.8×10^{-4}	5.2×10^{-4}	5.0×10^{-4}	5.2×10^{-4}
18	2.2	3.0	6.4×10^{-3}	3.4×10^{-3}	2.3×10^{-3}	2.7×10^{-3}	4.7×10^{-3}	2.7×10^{-3}	2.5×10^{-3}	1.7×10^{-3}	2.3×10^{-3}	2.2×10^{-3}	2.3×10^{-3}	2.1×10^{-3}
19	2.2	5.3	0.018	9.0×10^{-3}	4.7×10^{-3}	3.9×10^{-3}	7.0×10^{-3}	6.4×10^{-3}	6.2×10^{-3}	4.1×10^{-3}	5.9×10^{-3}	5.8×10^{-3}	5.9×10^{-3}	5.9×10^{-3}
20	2.2	8.4	0.026	0.010	5.9×10^{-3}	3.9×10^{-3}	0.023	0.018	0.014	7.3×10^{-3}	0.021	0.018	0.020	0.018
21	2.2	13	0.065	0.038	0.013	7.6×10^{-3}	0.056	0.038	0.022	8.6×10^{-3}	0.062	0.058	0.061	0.055
22	5.3	1.0	4.9×10^{-3}	2.6×10^{-3}	2.1×10^{-3}	2.0×10^{-3}	2.6×10^{-3}	2.4×10^{-3}	2.4×10^{-3}	2.2×10^{-3}	1.7×10^{-3}	1.6×10^{-3}	1.7×10^{-3}	1.9×10^{-3}
23	5.2	2.9	0.028	0.020	0.012	8.1×10^{-3}	0.016	0.013	9.4×10^{-3}	7.6×10^{-3}	6.0×10^{-3}	6.8×10^{-3}	8.2×10^{-3}	8.2×10^{-3}
24	5.2	4.9	0.066	0.038	0.031	0.017	0.048	0.034	0.029	0.022	0.016	0.018	0.022	0.024
25	5.3	8.2	0.12	0.065	0.047	0.029	0.074	0.050	0.036	0.031	0.034	0.040	0.041	0.037
26	5.3	13	0.23	0.11	0.079	0.067	0.11	0.10	0.097	0.083	0.079	0.073	0.075	0.079
27	8.9	1.0	5.2×10^{-3}	4.1×10^{-3}	3.6×10^{-3}	2.5×10^{-3}	4.0×10^{-3}	3.8×10^{-3}	4.4×10^{-3}	3.5×10^{-3}	2.4×10^{-3}	2.1×10^{-3}	2.8×10^{-3}	2.6×10^{-3}
28	8.7	2.8	0.053	0.028	0.025	0.021	0.029	0.025	0.023	0.019	0.013	0.018	0.018	0.020
29	8.9	5.0	0.14	0.071	0.053	0.045	0.072	0.065	0.047	0.047	0.027	0.033	0.042	0.042
30	8.9	8.4	0.16	0.093	0.073	0.063	0.11	0.090	0.079	0.063	0.061	0.057	0.061	0.053
31	8.9	13	0.092	0.076	0.046	0.040	0.084	0.056	0.053	0.045	0.044	0.048	0.046	0.042

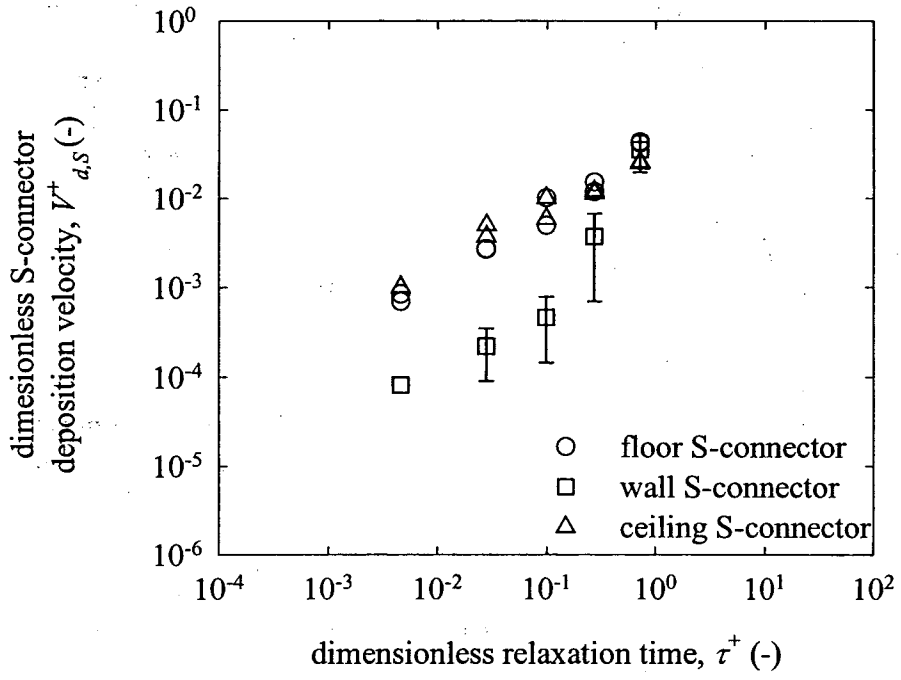

Figure 4.1 Dimensionless deposition velocities to S-connectors on the ceiling, wall and floor at an air speed of 2.2 m/s.

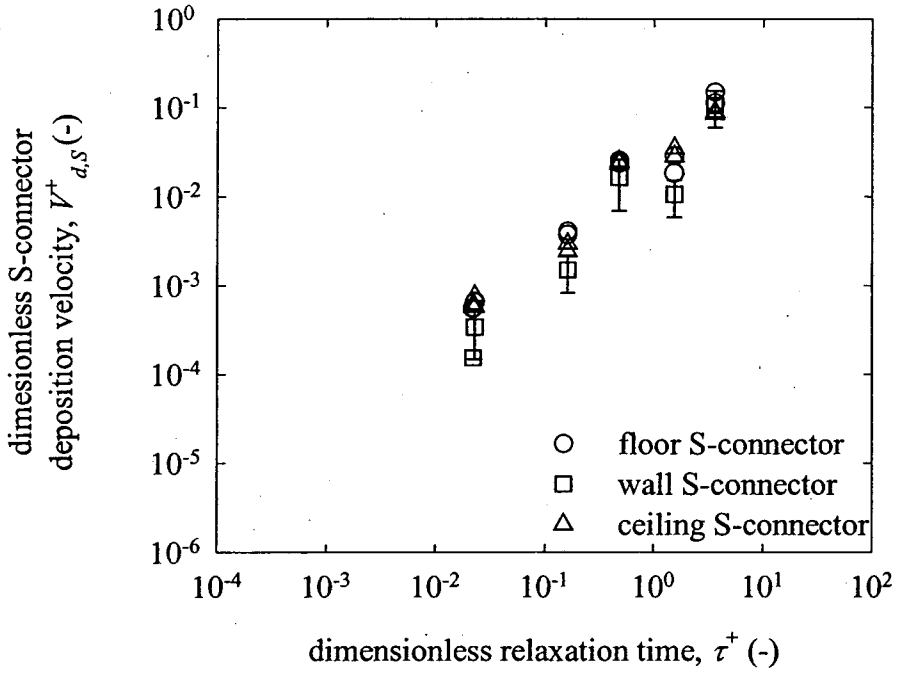

Figure 4.2 Dimensionless deposition velocities to S-connectors on the ceiling, wall and floor at an air speed of 5.3 m/s.

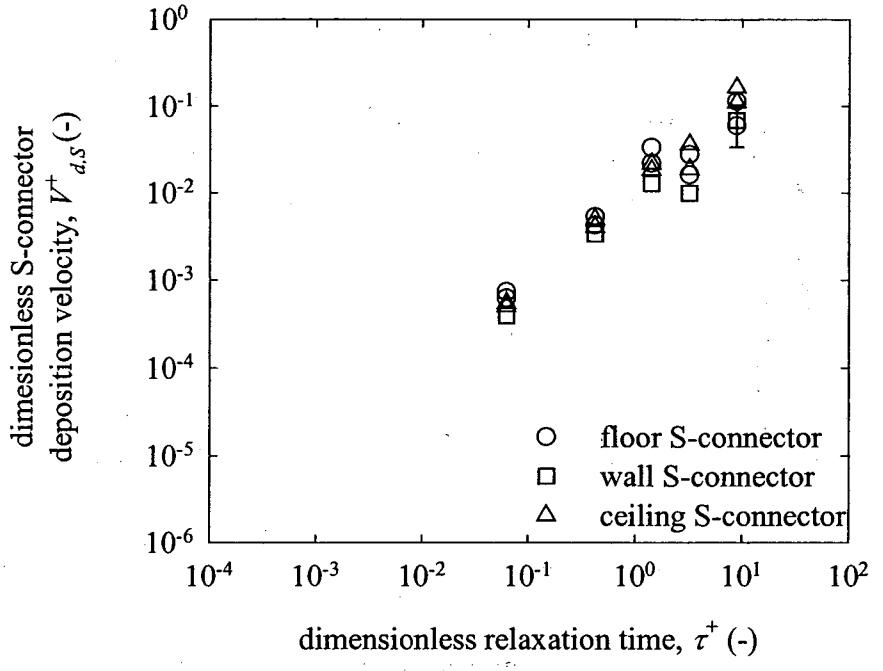

Figure 4.3 Dimensionless deposition velocities to S-connectors on the ceiling, wall and floor at an air speed of 9.0 m/s.

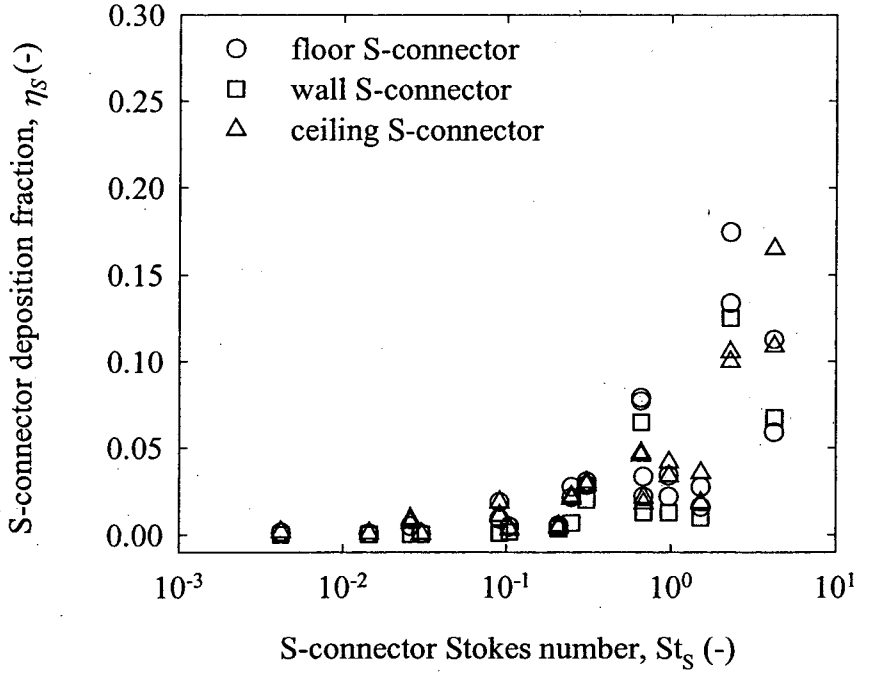

Figure 4.4 S-connector deposition fraction versus connector Stokes number for S-connectors on the ceiling, wall and floor at the three nominal air speeds.

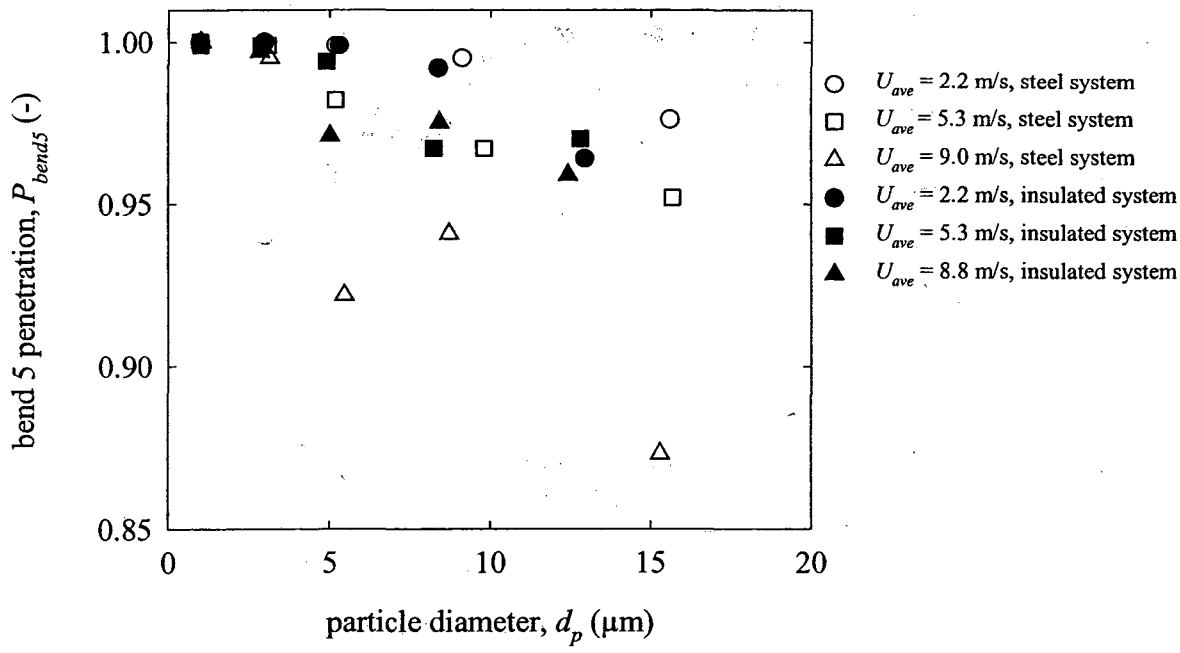

Figure 4.5 Penetration through bend 5 versus particle diameter for different air speeds in both the steel and insulated systems.

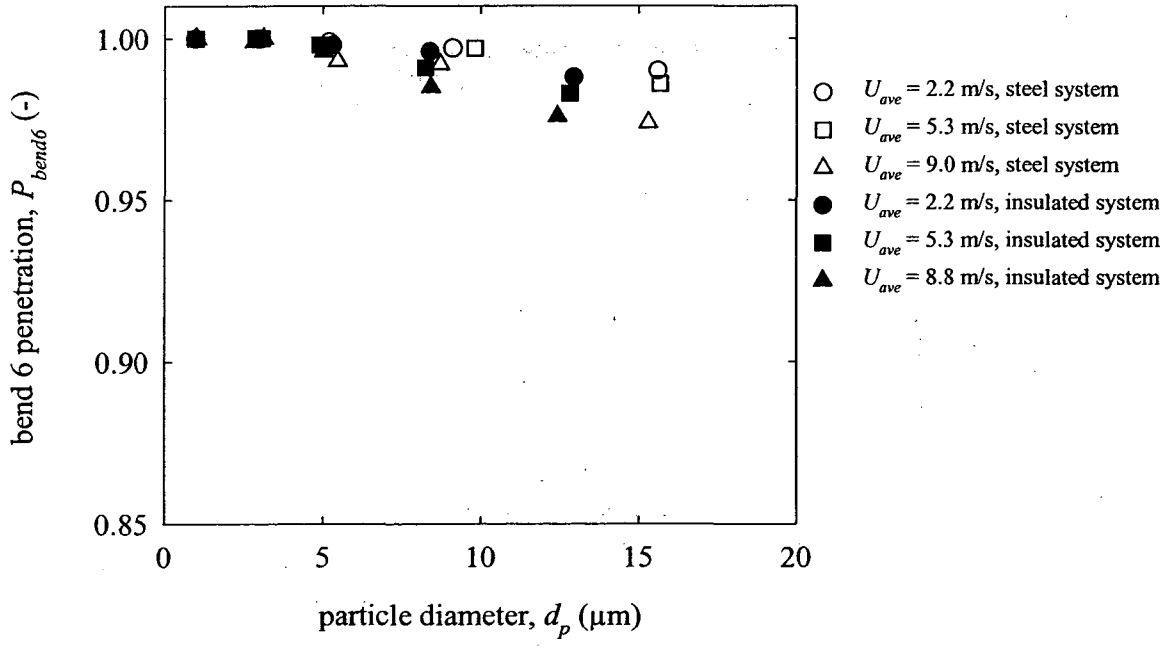

Figure 4.6 Penetration through bend 6 versus particle diameter for different air speeds in both the steel and insulated systems.

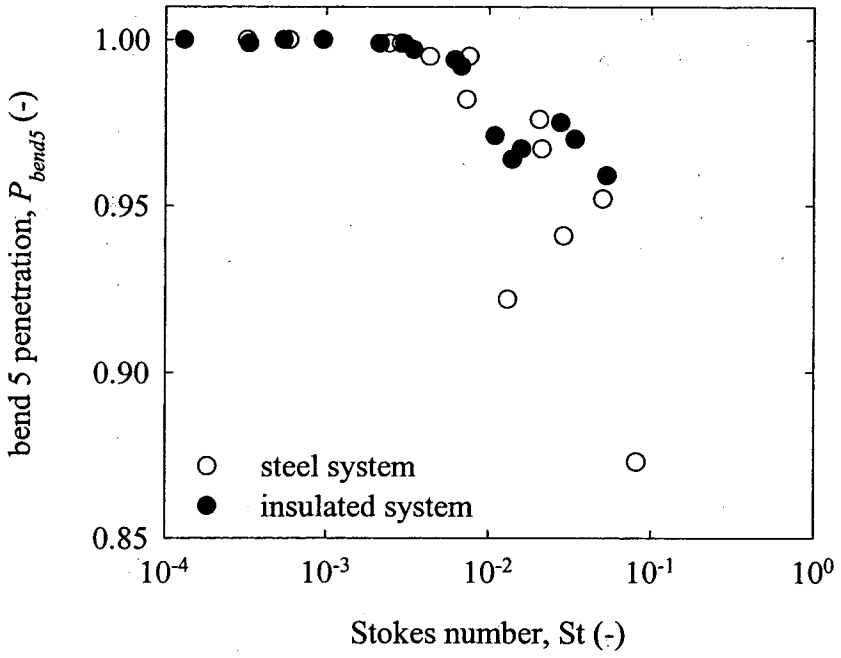

Figure 4.7 Penetration through bend 5 versus bend Stokes number for different air speeds in both the steel and insulated systems.

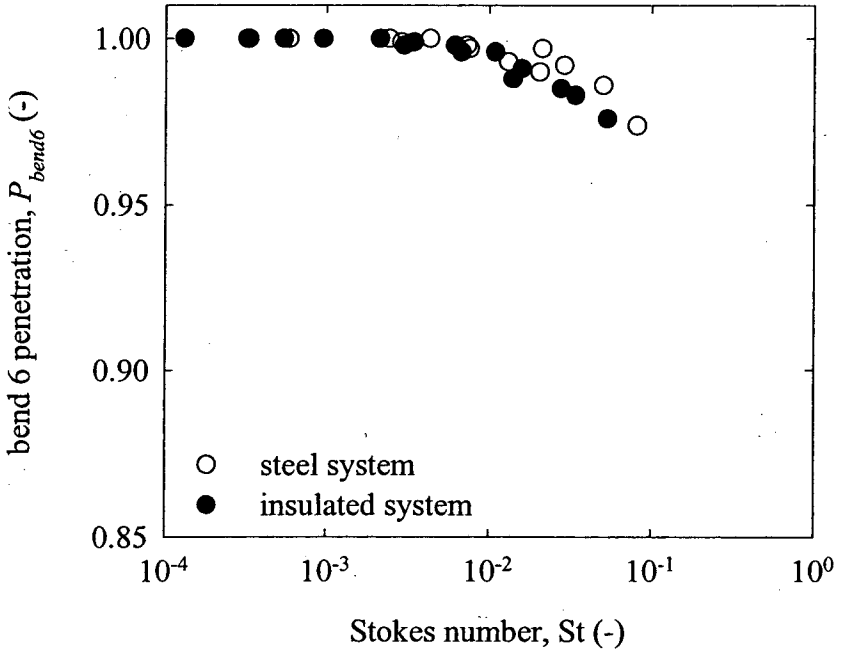

Figure 4.8 Penetration through bend 6 versus bend Stokes number for different air speeds in both the steel and insulated systems.

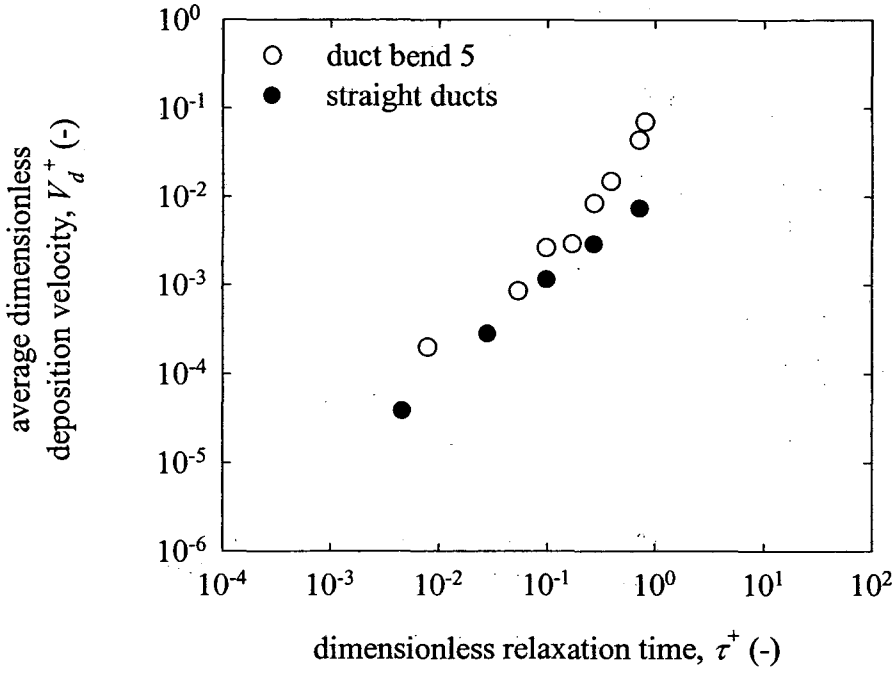

Figure 4.9 Composite dimensionless deposition velocities in bend 5 and in test ducts 1 and 2 versus dimensionless relaxation time at an air speed of 2.2 m/s.

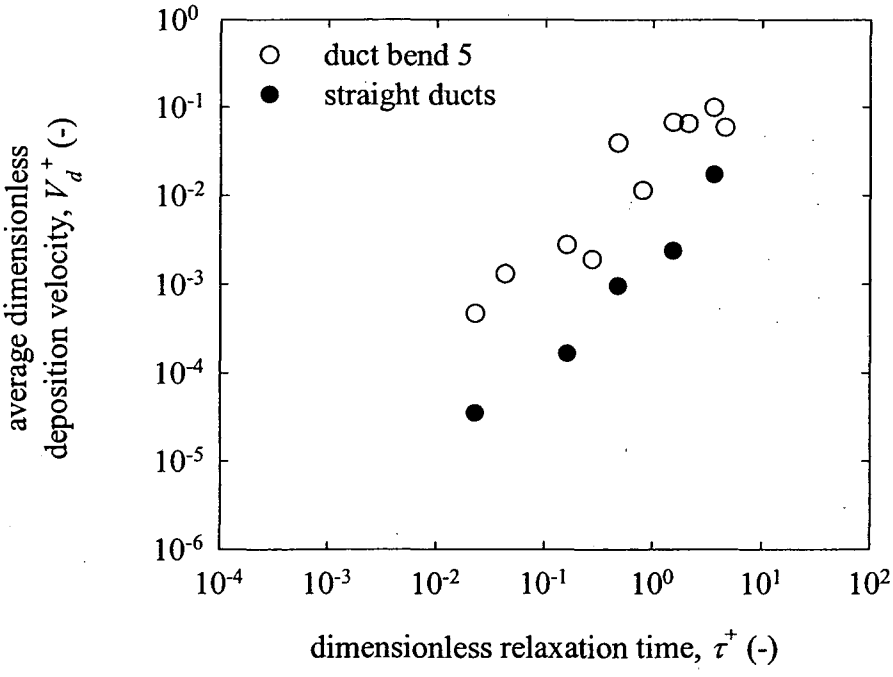

Figure 4.10 Composite dimensionless deposition velocities in bend 5 and in test ducts 1 and 2 versus dimensionless relaxation time at an air speed of 5.3 m/s.

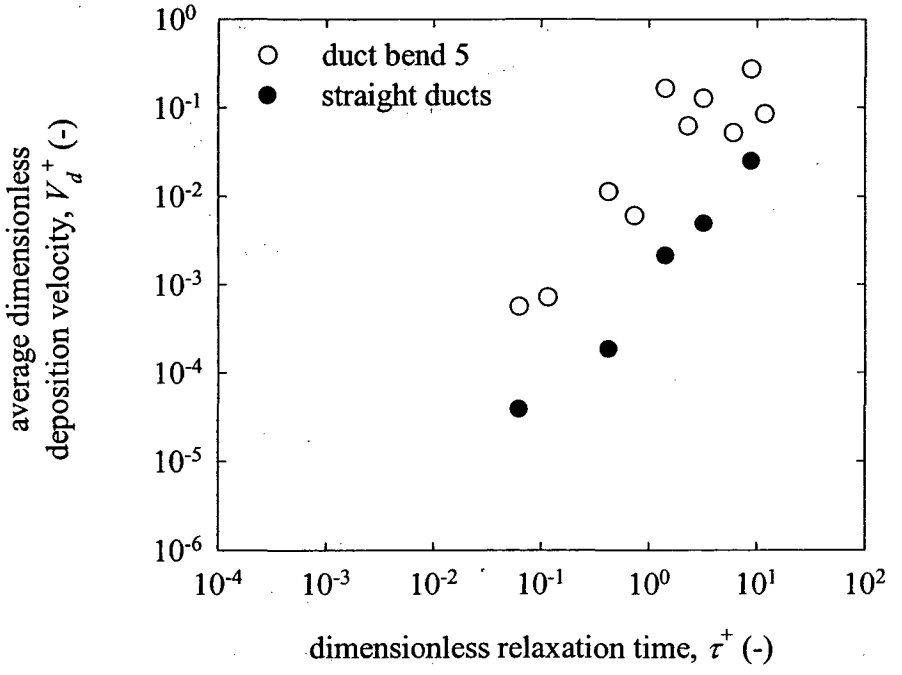

Figure 4.11 Composite dimensionless deposition velocities in bend 5 and in test ducts 1 and 2 versus dimensionless relaxation time at an air speed of 9.0 m/s.

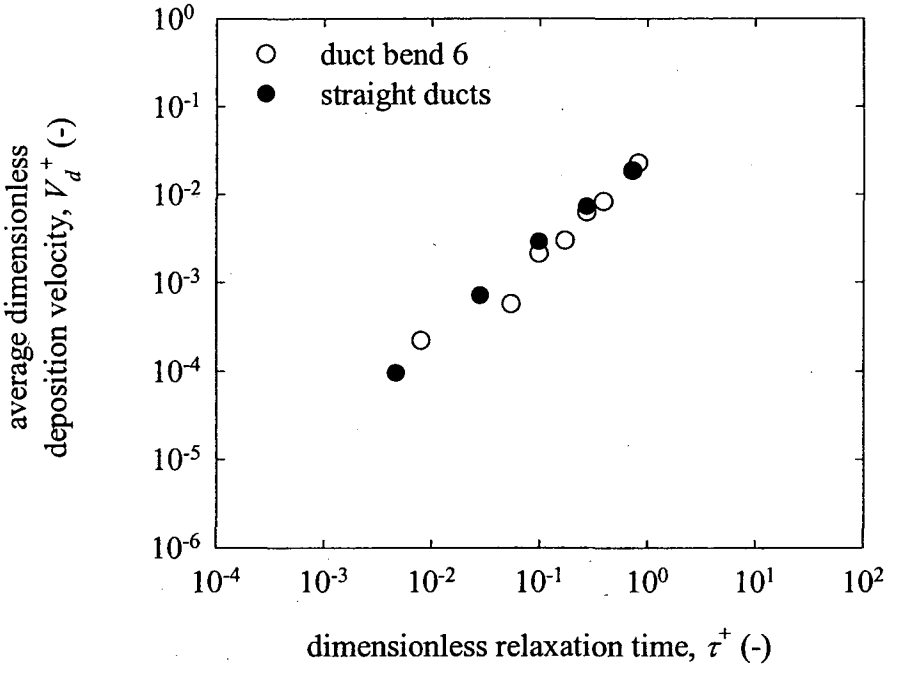

Figure 4.12 Composite dimensionless deposition velocities in bend 6 and in test ducts 1 and 2 versus dimensionless relaxation time at an air speed of 2.2 m/s.

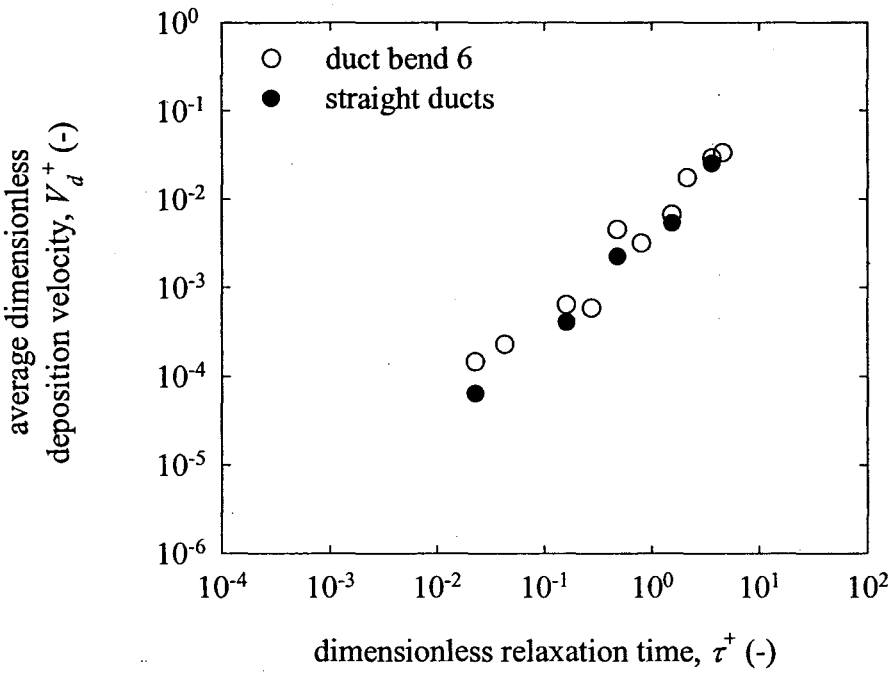

Figure 4.13 Composite dimensionless deposition velocities in bend 6 and in test ducts 1 and 2 versus dimensionless relaxation time at an air speed of 5.3 m/s.

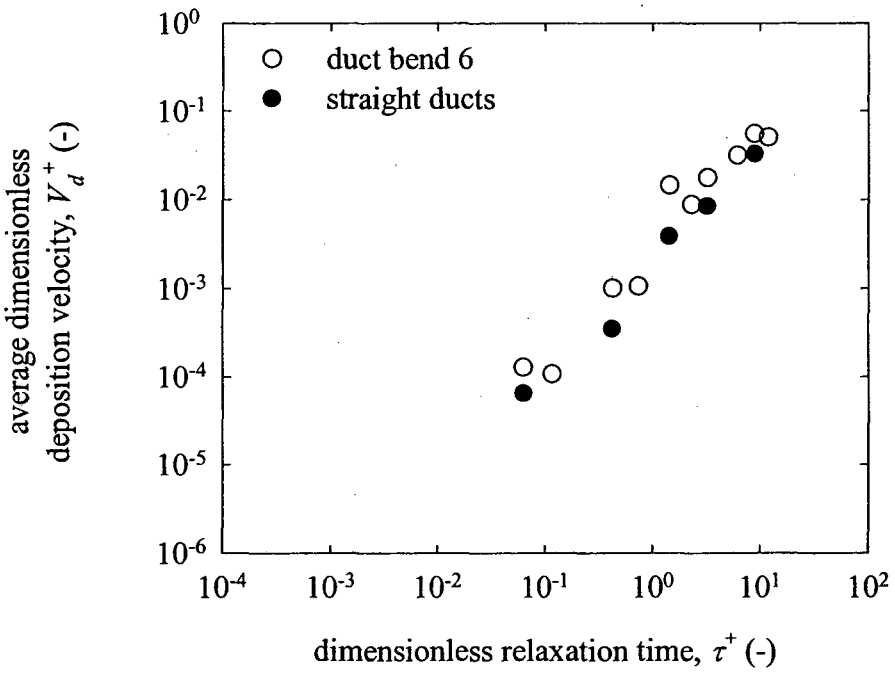

Figure 4.14 Composite dimensionless deposition velocities in bend 6 and in test ducts 1 and 2 versus dimensionless relaxation time at an air speed of 9.0 m/s.

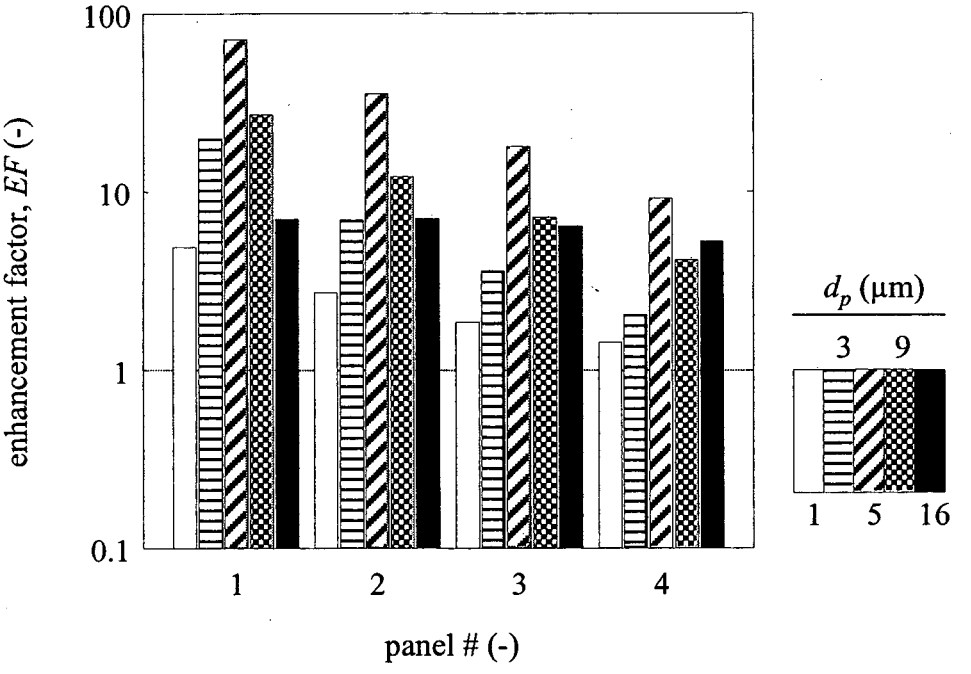

Figure 4.15 Enhancement factors versus ceiling panel number in duct 4 of the steel system at 9.0 m/s.

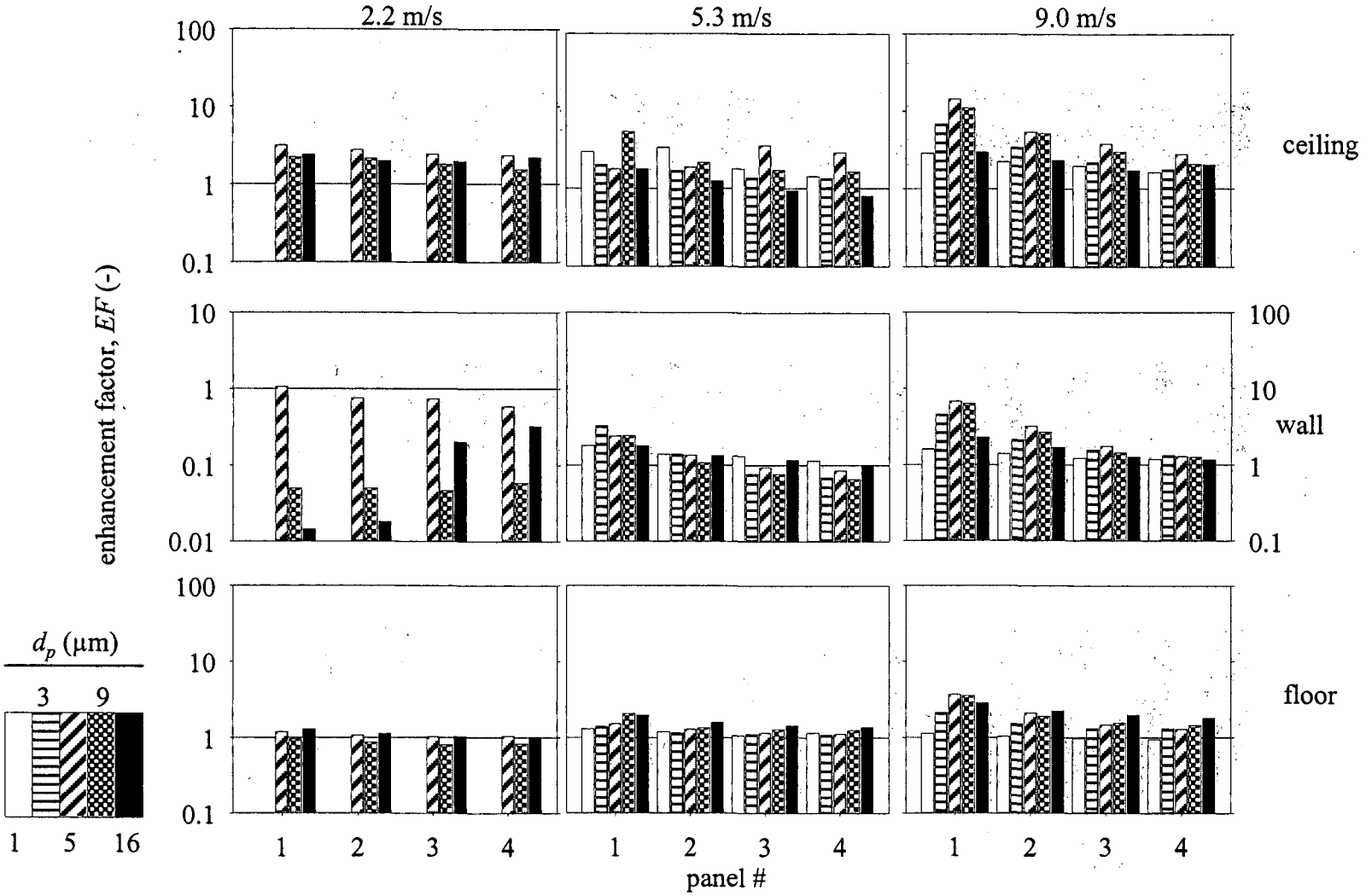

Figure 4.16 Enhancement factors at the ceiling, wall and floor at panels in duct 3 in the steel system at three air speeds.

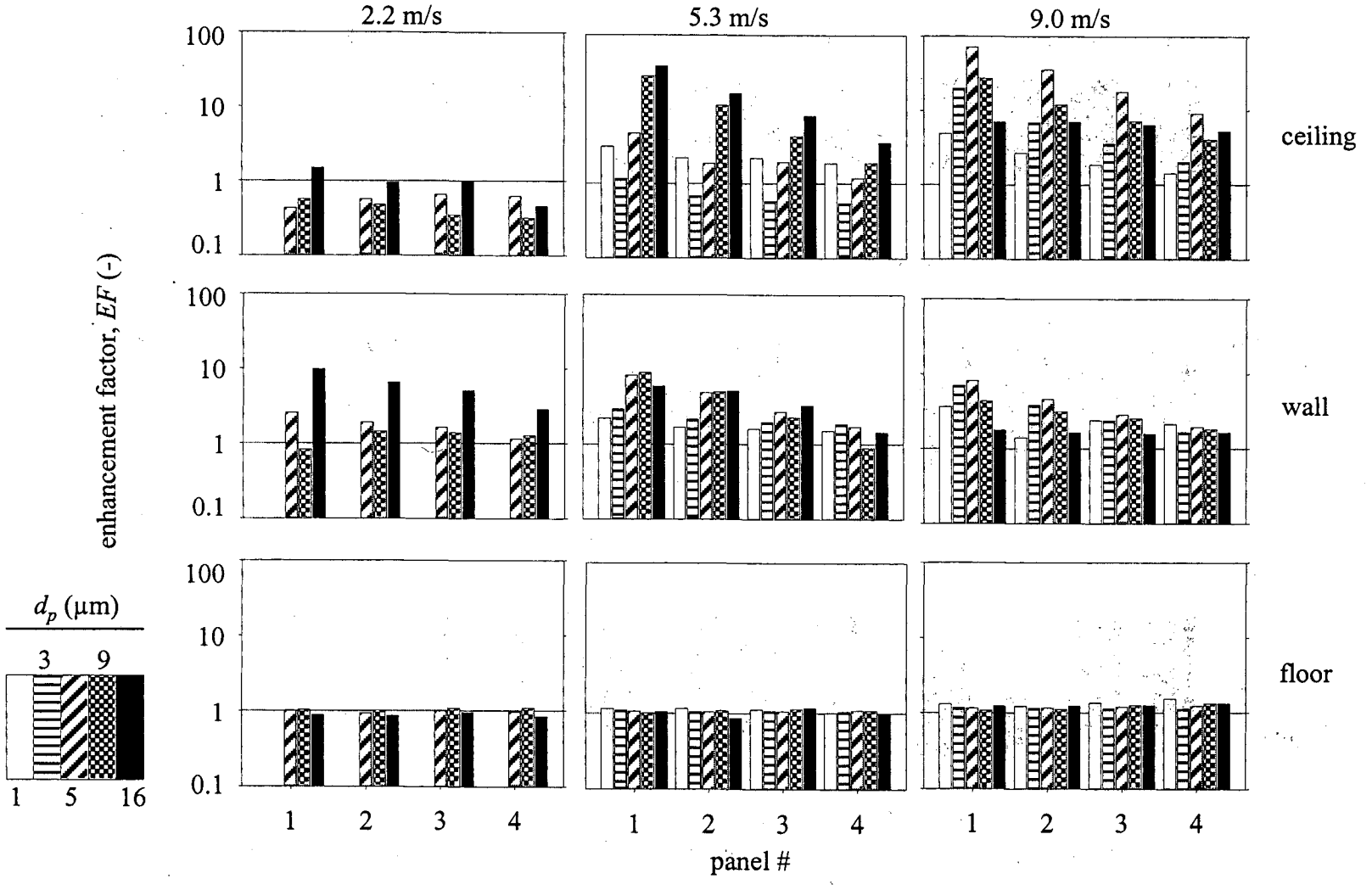

Figure 4.17 Enhancement factors at the ceiling, wall and floor at panels in duct 4 in the steel system at three air speeds.

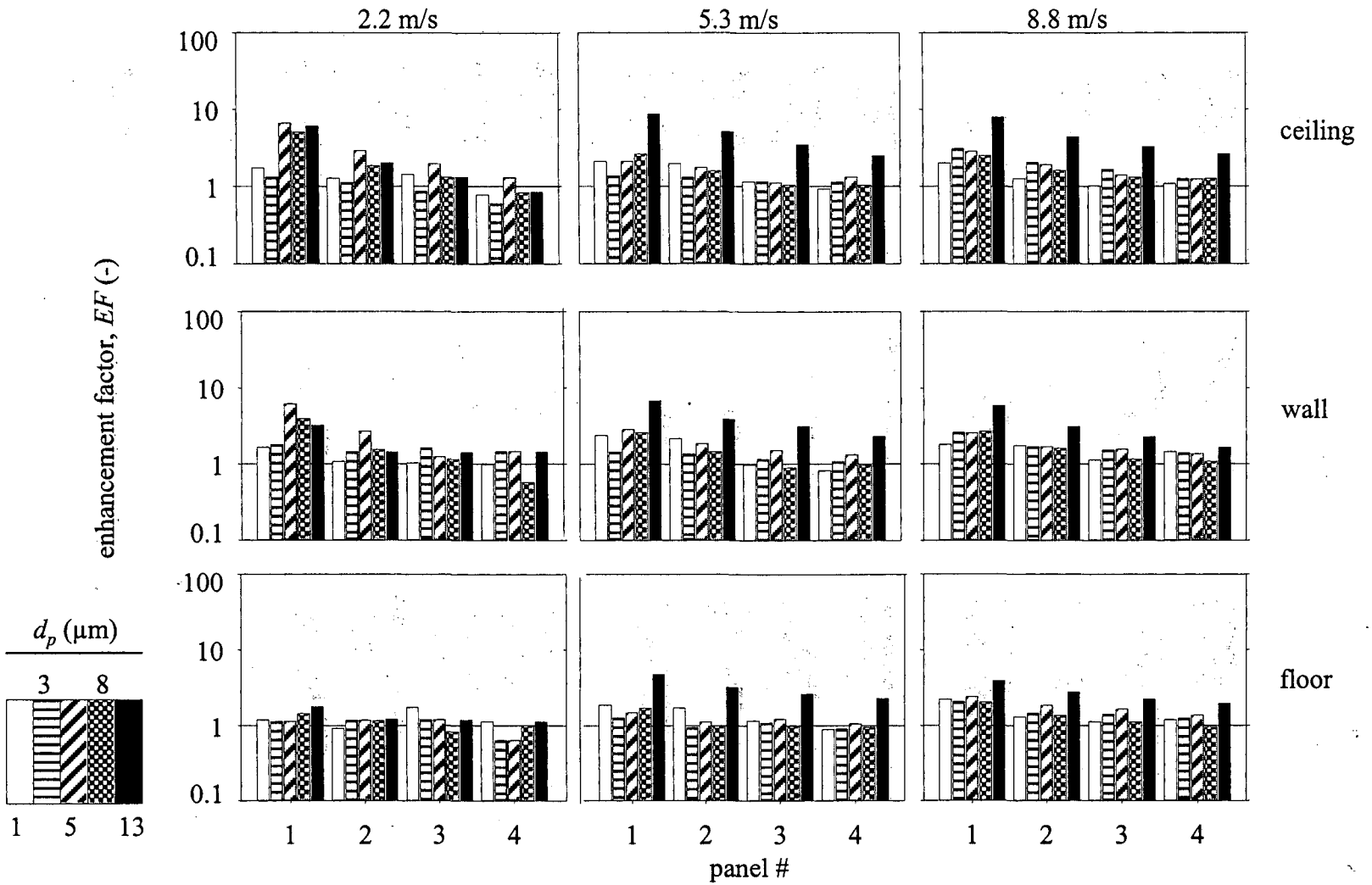

Figure 4.18 Enhancement factors at the ceiling, wall and floor at panels in duct 3 in the insulated system at three air speeds.

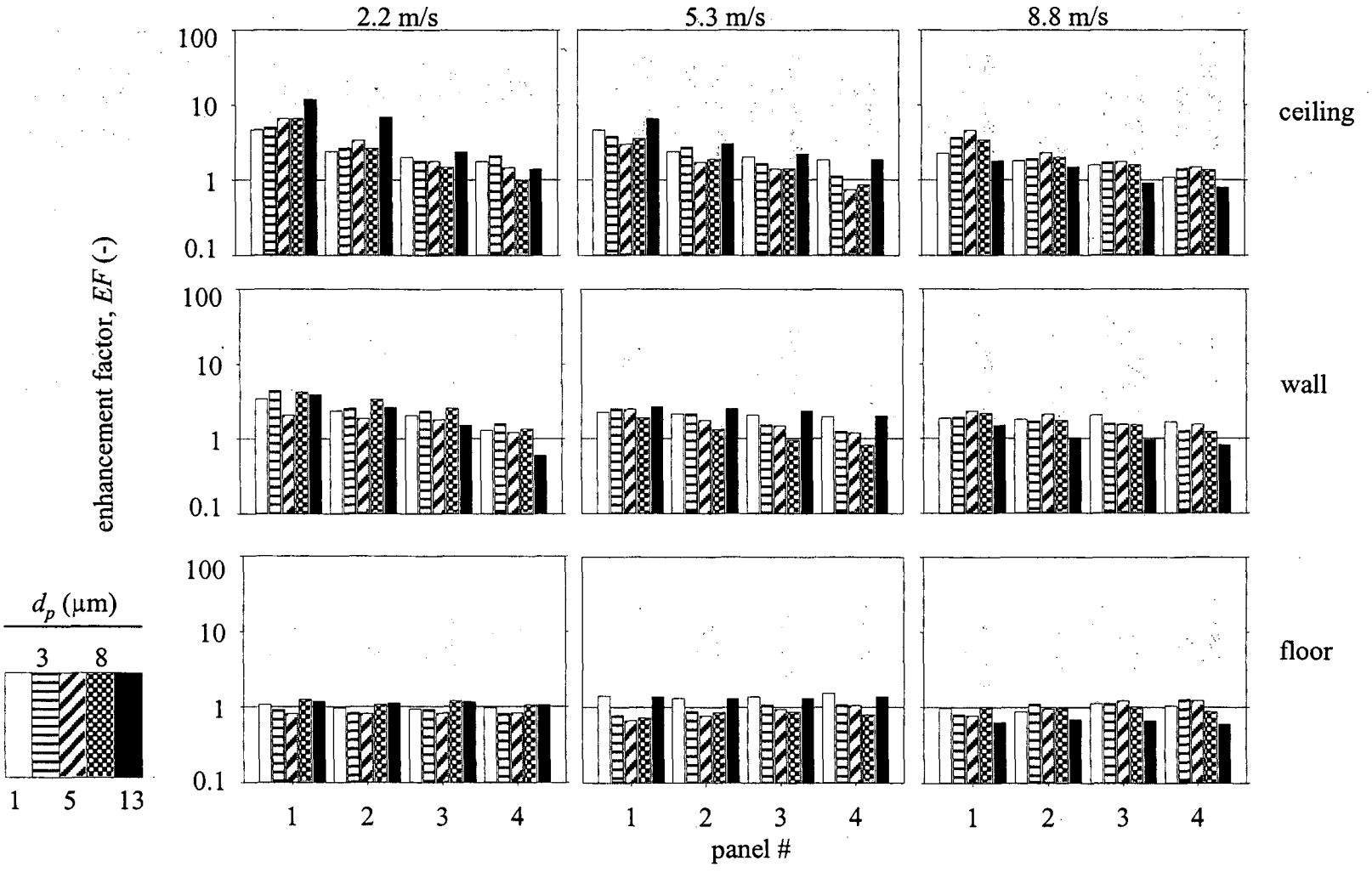

Figure 4.19 Enhancement factors at the ceiling, wall and floor at panels in duct 4 in the insulated system at three air speeds.

CHAPTER 5

Model-Measurement Comparison and Development of an Empirical Model for Predicting Deposition in Ventilation Ducts

5.0 Abstract

In this chapter, empirical equations and theoretical models for predicting particle deposition rates are compared to measurements made in an experimental ventilation duct system. Comparisons are made between models and measurements in straight galvanized steel and internally insulated ducts and at duct bends. In straight steel ducts, models generally underpredict measured deposition rates, especially to vertical duct walls and duct ceilings. In straight insulated ducts, most models give predictions that are of a similar magnitude as the experimental data when applied with surface roughness values in the range 30-180 μm, but no model when applied with a single roughness value compares favorably to the data over the entire range of particle sizes. Empirical equations for particle penetration through duct bends are found to give predictions similar to those measured in the current experiments. When predicting deposition rates in straight steel or insulated ducts, the model of Guha (1997) is found to give the best overall predictions; however, the accuracy of this model was often inadequate for predicting deposition in HVAC ducts. It is only recommended for predicting deposition rates to the floors of steel ducts. For predicting particle penetration through duct bends, the model of McFarland *et al.* (1997) is recommended.

Factors influencing particle deposition (surface roughness, temperature gradients, electrical forces, turbulence gradients) were considered individually in model applications to evaluate potential reasons for the observed model-measurement disagreement. It was found that a combination of these factors has the potential to explain model-measurement disagreement at the duct wall, but no explanation could be found for deposition rates measured at the duct ceiling that were much larger than model predictions.

Because no model was found to adequately represent the experimental deposition data, new empirical equations were developed for predicting deposition rates of particles to steel and insulated duct surfaces. For steel and insulated ducts, equations were determined for deposition to the duct wall and ceiling at each experimental air speed using power-law fits to the data. Deposition to floors of insulated ducts is best predicted by addition of a gravitational settling component to the empirical equation developed for insulated duct walls. An empirical equation was also developed to predict S-connector deposition fractions at S-connectors located at duct junctions. These empirical equations, along with a specified interpolation scheme to broaden their applicability, are recommended for predicting particle deposition rates in real ventilation ducts. These new empirical equations have the advantages of agreeing with the experimental data. They are based on high quality experiments with real HVAC materials and allow for deposition predictions to the distinct surfaces of horizontal ducts. However, they are unable to account for subtle changes in surface roughness or other potentially important factors.

5.1 Introduction

Indoor exposures are a large fraction of total particulate exposures for most people. An uncertain aspect of modeling human exposures to particles in indoor environments is the behavior of particles in building ventilation systems. Better methods of predicting particle deposition rates in ventilation ducts can reduce uncertainties in exposure modeling. Accurate predictions of deposition rates in ventilation systems will improve understanding of the fates of particles that are drawn into, or generated within a building.

Measurements in a variety of flows have frequently demonstrated higher particle deposition rates than could be explained by theory (Papavergos & Hedley, 1984; Thatcher *et al.*, 1996; Thatcher *et al.*, 2002). These model-measurement disagreements in even the simplest flows illustrate that the current understanding of particle deposition is far from complete.

A variety of empirical equations, Eulerian models and Lagrangian simulations have been developed to predict particle deposition rates from turbulent flows in tubes, pipes and ducts. Chapter 2 provides an extensive review of these methods and considers their usefulness for predicting deposition rates in ventilation systems. Most methods have been developed for the idealized case of deposition to smooth vertical surfaces from a flow with a fully developed turbulent flow profile. In ventilation systems, a variety of both horizontal and vertical surfaces are normally present. Owing to the frequent occurrence of branches and bends, fully developed turbulent flow is not present in a large fraction of the length of most ventilation duct runs. Most deposition models have been developed for flows in pipes with round cross sections;

the influence of secondary flows established in bends or in ducts with rectangular cross sections has not been considered in theoretical deposition models. Additionally, ventilation ducts commonly have internal ridges at duct junctions that can influence turbulent flows and offer sites for particle impaction. These flow and surface irregularities distinguish real ventilation ducts from the idealized world of most deposition models. The effects of these irregularities on particle deposition have not been completely explored. It is not clear which method offers the best means of predicting deposition rates in ventilation ducts. Considering the complexity of ventilation duct flows and the difficulties experienced when predicting deposition rates from simple flows, empiricism may be the most appropriate means where sufficient experimental data are available.

This chapter compares the experimental measurements presented in Chapters 3 and 4 to published equations and models. Potential sources of disagreement between the models and the measurements are explored. A method of predicting particle deposition rates in ventilation ducts based on empirical fits to the experimental data is proposed. These equations are applicable to straight steel and insulated ducts with fully developed turbulent flow profiles. Empirical equations for predicting deposition rates in straight duct sections with developing turbulence were not developed because the experimental data are insufficient to address the broad range of these types of ducts in real ventilation systems.

5.2 Methods

5.2.1 Published particle deposition models

Models published in the literature for predicting particle deposition rates from turbulent flow were compared to the deposition measurements made in straight ventilation ducts and in duct bends described in Chapters 3 and 4. When possible, models were compared to deposition rates measured at the ceilings, walls and floors of both steel and insulated ducts with fully developed turbulent flow (data collected in test ducts 1 and 2). For data collected in straight ducts, model-measurement comparisons are presented in this chapter only for experimental data collected at an air speed of 5.3 m/s; similar observations were made when comparing the models to data collected at lower (2.2 m/s) and higher (8.8 & 9.0 m/s) air speeds.

Models that are compared to data collected in straight ducts with fully developed turbulent flow are empirical equations (2.71)-(2.74), the free-flight model of El-Shobokshy & Ismail (1980), the turbophoretic model of Guha (1997) and the sublayer model of Fan & Ahmadi (1993). The relative advantages and disadvantages of the different models types are discussed at length in Chapter 2. Free-flight and sublayer models are strictly applicable only to vertical walls. It has been suggested that these models could be applied to horizontal surfaces by simple addition or subtraction of a gravitational settling velocity to the predicted deposition velocity to a vertical surface (Li & Ahmadi, 1993b). When applied to horizontal surfaces in this manner, these models lead to predictions similar to those observed when applying the empirical equations (2.71)-(2.74). Except for the empirical equations (2.71)-(2.74), all of these models are capable of predicting deposition rates to both smooth and rough surfaces. When predicting deposition rates to insulated duct surfaces, three roughness levels of

30, 90 and 180 μm were used as model inputs. These values were chosen because they yield deposition predictions that span the experimentally measured values in most cases. These roughness levels are substantially lower than the 1-2 mm roughness of the insulation estimated by direct measurement in Appendix A.

In addition to the above models, the free-flight model of Gutfinger & Friedlander (1985) for deposition to fibrous surfaces is compared to experimental data collected in insulated ducts. Gutfinger & Friedlander modified the theory of Friedlander & Johnstone (1957) by assuming that particle deposition is a two-step process consisting of free-flight and filtration by surface fibers. Deposition by surface-fiber filtration was calculated based on a model of single-fiber removal efficiency, which requires the surface-fiber diameter and the surface-fiber-bed solidity as additional input parameters. To apply this model to insulated ducts, a surface-fiber diameter of 20 μm and a solidity of 0.2 were estimated based on the images of the insulation surface presented in Appendix A.

The empirical models of Pui *et al.* (1987) and McFarland *et al.* (1997) were compared to the experimental particle penetration data collected in duct bends. No published models were found in the literature for predicting deposition to ridges like the S-connector pieces found at duct joints. In addition, there are no published models for predicting particle deposition rates in straight ducts where the flow has a developing turbulent flow profile.

5.2.2 Model-measurement disagreement and the turbophoretic model

The turbophoretic model of Guha (1997) was used to explore factors that could lead to model-measurement disagreement when considering deposition in straight steel ducts with fully developed turbulent flow profiles. Changes in deposition predictions with changes in deposition surface roughness, air-surface temperature difference and particle charge were explored. The potential influence on particle deposition of changes in the near-wall turbulence gradient caused by changes in surface roughness rates was also considered.

Deposition rates to steel ducts were modeled assuming microscale roughness levels of 0, 1 and 5 μm. The 1 and 5 μm roughness levels were chosen to represent the average and the maximum microscale roughness from the measurements presented in Appendix A. The turbophoretic model was also applied to predict deposition velocities in steel ducts with air-surface temperature differences of 0, 0.2 and 0.4 °C. The air-surface temperature difference of 0.2 °C is a best estimate from the measurements presented in Appendix C and the value of 0.4 °C represents a bounding maximum value. Because the deposition experiments were conducted using steel ducts, significant electric fields were not expected to be present; however, the image force component of the electrostatic force may influence deposition rates to a conducting surface even in the absence of an electric field. To evaluate the importance of the image force in determining deposition rates to steel ducts, it was assumed that each particle was charged with ten excess electrons. In the experiments, most particles had fewer than ten excess electrons because the aerosol was neutralized to impart a Boltzmann charge distribution. With a Boltzmann charge distribution,

only a small fraction of particles with sizes used in these experiments would have an excess of ten or more electrons.

The gradient of the root-mean-square of the wall-normal fluctuating velocity component, v'_{rms}, is a determining factor of particle turbophoretic transport towards a surface. The near-wall profile of v'^{+}_{rms} versus y^{+} recommended by Guha (1997) for use in calculating particle transport towards a smooth wall by turbophoresis is

$$v'^{+}_{rms} = \frac{0.005 y^{+2}}{1 + 0.002923 y^{+2.128}} \tag{5.1}$$

This profile comes from Kallio & Reeks (1989) and is shown in Figure 5.1. It is a fit to experimental data collected near smooth surfaces by Laufer (1954) (see Figure 2.11) and other researchers. Equation (5.1) predicts that v'^{+}_{rms} is proportional to y^{+2} very close to the wall, as expected from theoretical considerations (Chapman & Kuhn, 1986). Grass (1971) and Krogstad & Antonia (1999) both observed that peaks in the fluctuating velocity profile occurred at positions closer to rough surfaces than to smooth surfaces. No detailed measurements of the v'^{+}_{rms} versus y^{+} profile near rough walls are known. To evaluate the influence of changes in this profile on particle deposition, I developed two equations describing v'^{+}_{rms} versus y^{+} profiles near rough walls for use in the turbophoretic model. These equations are shown in Figure 5.1 and are as follows:

$$v'^{+}_{rms} = \frac{0.011 y^{+2}}{1 + 0.006927 y^{+2.128}} \tag{5.2}$$

$$v'^{+}_{rms} = \frac{0.02 y^{+2}}{1 + 0.01278 y^{+2.128}} \tag{5.3}$$

These equations preserve the same basic shape for the profile of v'^{+}_{rms} versus y^{+} as equation (5.1) but shift the peak closer to the wall. Equations (5.2) and (5.3) have peaks in the profile that are respectively 33% and 50% closer to the wall than equation (5.1). The magnitudes of these shifts were chosen based on the sparse experimental observations. Equation (5.2) was used to represent a potential shift in the profile of v'^{+}_{rms} versus y^{+} owing to the presence of S-connectors and beading ridges in steel ducts. Equation (5.3) was used to represent a potential shift in the profile of v'^{+}_{rms} versus y^{+} resulting from the presence of internal duct insulation. When equations (5.2) and (5.3) are used instead of equation (5.1) in the turbophoretic model, they lead to an increase in turbophoretic transport towards surfaces owing to the steeper near-wall gradient in v'^{+}_{rms}.

5.2.3 New empirical equations for predicting deposition in ventilation ducts

Empirical equations for predicting deposition rates to surfaces in straight ducts and to S-connectors at duct junctions were developed based on the experimental data presented in Chapters 3 and 4. Equations similar in form to equations (2.71)-(2.74) are proposed for both steel and insulated duct surfaces. The general form of the equations for duct ceiling and wall surfaces are as follows:

$$V_d^{+} = k_1 \mathrm{Sc}^{-2/3} + k_4 \tau^{+k_5} \qquad \text{if} \quad k_1 \mathrm{Sc}^{-2/3} + k_4 \tau^{+k_5} \le k_3 \tag{5.4}$$

$$V_d^{+} = k_3 \qquad \text{if} \quad k_1 \mathrm{Sc}^{-2/3} + k_4 \tau^{+k_5} > k_3 \tag{5.5}$$

In these equations, k_1 and k_3 are the same constants discussed in reference to equations (2.71)-(2.74). The constants k_4 and k_5 are the constants that were adjusted to fit the new experimental data. The first term on the right side of equation (5.4) accounts for particle deposition by pure turbulent diffusion and is most important for small particles in the diffusive regime. The second term accounts for deposition owing to particle inertia and is most important for particles in the diffusion-impaction regime. The limit established by equation (5.5) is the deposition rate of particles in the inertia-moderated regime. The value for k_1 can be calculated by

$$k_1 = \sqrt{\frac{f}{2}} \tag{5.6}$$

which comes from Colburn's j-factor approach for determining the deposition rate of a diffusive species from turbulent flow (Kay & Nedderman, 1990). For k_3, a value of 0.13 was selected from Table 2.11 because the current experimental data suggest a value at this level or lower.

Values of k_4 and k_5 were determined by power-law regressions of the experimental data at each surface and air speed. Regressions were performed on deposition data at the wall and ceiling of both steel and insulated ducts at each experimental air speed. These values are summarized for steel surfaces in Table 5.1 and for insulated surfaces in Table 5.2. In Table 5.1, values determined for k_4 at steel duct walls are somewhat higher than the values of k_2 in Table 2.10 recommended for use in equations (2.71) and (2.73). Values of k_5 are less than the value of 2 assumed in previous empirical equations. In insulated ducts at an air speed of either 5.3 or 8.8 m/s, measured deposition rates at duct walls and ceilings were nearly the same. Consequently, for these air speeds in insulated ducts, a single regression was performed on deposition

data collected at the duct wall and ceiling. This is the reason that k_4 and k_5 are the same for both duct walls and ceilings at air speeds of 5.3 and 8.8 m/s in Table 5.2.

For predicting deposition rates to the floors of steel and insulated ducts, the following equation is recommended

$$V_{d,f}^{+} = V_{d,w}^{+} + g^{+}\tau^{+} \tag{5.7}$$

where $V_{d,w}^{+}$ is the deposition rate to an insulated wall determined by equations (5.4) and (5.5). Equation (5.7) is analogous to equation (2.73) recommended by previous researchers for calculating deposition rates to a horizontal floor surface. Equation (5.7) was found to represent the measured deposition rates to insulated duct floor better than any other model. In the case of deposition to the floors of steel ducts, the turbophoretic model of Guha (1997) was found to perform somewhat better than equation (5.7), but the turbophoretic model is also much more burdensome to apply. Equation (5.7) is presented for steel duct floors so that the new empirical equations may be applied to the full range of surfaces present in a typical ventilation duct run.

Equations (5.4)-(5.7) are strictly applicable only in flows with friction velocities equal to those that were present in the experiments. An interpolation scheme was developed so that the equations could be used to predict deposition rates for a broader range of conditions. Application of these equations to a general turbulent duct flow involves determining the friction velocity of the flow, determining the bounding deposition rates from equations (5.4)-(5.7) and interpolating to the actual friction velocity. This method is outlined in the following discussion.

Given the duct dimensions and air speed, the friction velocity can be calculated by use of equation (2.6). For clean steel ducts, the friction factor, f, can be calculated by equation (2.8). For the internally insulated ducts used in the experiments reported in this dissertation, the data presented in Appendix A shows that the equation from White (1986) (see Table 2.1) yielded good estimates of the friction factor if a roughness of 1700 μm was used. This is a limited case; the appropriate roughness value for determining the friction factor in an insulated duct is likely to depend on the specific characteristics of the insulation. Until better information is available, the equation from White applied with a roughness value of 1700 μm is recommended to calculate f in insulated ducts.

Once the friction velocity is known, the dimensionless relaxation time for a given particle size can be calculated by equation (2.17). Then, values of the dimensionless deposition velocity at the three experimental friction velocities, u_1^*, u_2^* and u_3^*, can be calculated by equations (5.4)-(5.7). For steel ducts, the friction velocities u_1^*, u_2^* and u_3^* correspond to 12, 27 and 45 cm/s and for insulated ducts, they are 16, 37 and 62 cm/s, respectively. Values of k_4 and k_5 for use in the equations are selected from Table 5.1 for steel ducts and Table 5.2 for insulated ducts. Once dimensionless deposition velocities have been calculated at u_1^*, u_2^* and u_3^*, the dimensionless deposition velocity of the particle at the actual friction velocity can be calculated by logarithmic interpolation. The appropriate interpolation equations are

$$V_d^+ = \text{antilog}\left[\log\left(V_d^+(u_2^*)\right) - \frac{\left(u_2^* - u^*\right)\log\left(V_d^+(u_2^*)/V_d^+(u_1^*)\right)}{\left(u_2^* - u_1^*\right)}\right] \qquad u^* \le u_2^* \qquad (5.8)$$

$$V_d^+ = \text{antilog}\left[\log\left(V_d^+(u_2^*)\right) + \frac{\left(u^* - u_2^*\right)\log\left(V_d^+(u_3^*)/V_d^+(u_2^*)\right)}{\left(u_3^* - u_2^*\right)}\right] \qquad u^* > u_2^* \qquad (5.9)$$

The interpolation equations (5.8) and (5.9) allow equations (5.4)-(5.7), which were developed only for the specific experimental friction velocities, u_1^*, u_2^* and u_3^*, to be applied over a range of friction velocities.

No equations were found in the literature for predicting deposition rates at a ridge like that presented by an S-connector at the junction between two duct sections. An equation for predicting the S-connector deposition fraction of the following form was fit to the experimental data:

$$\eta_S = 1 - 10^{-k_6 \mathrm{St_S}} \qquad (5.10)$$

The form of this equation is similar to the equation proposed by Pui *et al.* (1987) for particle penetration through a small-diameter bend with turbulent flow. It was chosen for its simplicity and because deposition at S-connectors, like deposition in a small-diameter bend, is expected to be dominated by impaction. The equation was fit to the data by a least-squares adjustment of the Stokes number coefficient, k_6, which was determined to equal 0.012. This equation represents a fit to deposition data collected at S-connectors located at the duct floor, wall and ceiling at all experimental air speeds.

5.3 Results and Discussion

5.3.1 Published particle deposition models for straight ducts

Figure 5.2 compares the predictions of empirical equations (2.71)-(2.74) with experimental data collected in straight steel ducts at an air speed of 5.3 m/s. Figure

5.3 compares the same equations to similar data collected in insulated ducts. The equations were applied with $k_1 = 0.051$, $k_2 = 6\times10^{-4}$ and $k_3 = 0.13$. In Figure 5.2, reasonable agreement among the predictions and the measurements are observed at the duct floor and duct wall. Measurements at the duct floor are slightly underpredicted at large relaxation times. The empirical equations predict no deposition to the duct ceiling in the particle size range where the measurements were made. In Figure 5.3, the predictions lie significantly below the data for all three duct surfaces. These empirical equations include no means of accounting for variations in the character of the deposition surface; the small differences among the model predictions in Figures 5.2 and 5.3 only result from the slightly higher friction velocity in the insulated ducts. The inability of these empirical equations to account for surface roughness is a clear disadvantage when predicting deposition rates to insulated ducts.

Figures 5.4 and 5.5 compare the free-flight model of El-Shobokshy & Ismail (1980) to deposition data collected in steel and insulated ducts, respectively. In Figure 5.4, good model-measurement agreement is observed for deposition to the duct wall; predictions were not made for other duct surfaces because free-flight models are strictly applicable only to vertical walls. In Figure 5.5, the free-flight model applied with surface roughness levels of 30, 90 and 180 μm is compared to the experimental data collected in insulated ducts. This range of roughness values lead to model predictions of the same magnitude as the experimental data, but no single roughness value gave model predictions that matched the data across the range of particle sizes that were studied. The influence of roughness due to insulation at the duct floor and ceiling could not be evaluated with this free-flight model.

The free-flight model of Gutfinger & Friedlander (1985) for calculating deposition rates to fibrous surfaces is compared to data collected in the insulated duct in Figure 5.6. The model was applied with surface-fiber lengths of 30, 90 and 180 μm. The predictions with the three different fiber lengths span the experimental data, but no single modeling scenario was found that accurately describes the data. When the model agrees with data collected at large particle sizes, it overpredicts measured deposition rates of small particles. When the model agrees best with measured small particle deposition rates, it underpredicts data collected at larger particle sizes.

Figure 5.7 compares the turbophoretic model of Guha (1997) to experimental data collected in steel ducts and Figures 5.8-5.10 compares the same model to data collected in insulated ducts. In Figure 5.7, model-measurement agreement is good for data at the duct floor; this model does not underpredict floor deposition rates of larger particles as the empirical model did. Turbophoresis appears to be a plausible explanation for measured deposition velocities to duct floors that were significantly higher than gravitational settling velocities. This is a potentially important improvement because particle losses in ventilation ducts are dominated by high deposition rates. Thus, to accurately predict particle penetration or losses in ducts it is most important to accurately predict deposition rates at locations where they are the highest. Although the model matches the data at steel duct floors, it substantially underpredicts measurements at the duct wall and drastically underpredicts measurements at the duct ceiling.

In Figures 5.8-5.10, the turbophoretic model is applied with surface roughness values of 30, 90 and 180 μm, respectively, and compared to data collected in the insulated ducts. In Figure 5.8, when the model is applied with a roughness of 30 μm, it underpredicts most of the experimental data. The model is applied with a roughness of 90 μm in Figure 5.9. Here, the model predictions for the different duct surfaces are more closely bunched and suggestive of the nearly uniform deposition observed experimentally. Most of the data is underpredicted in Figure 5.9. In Figure 5.10, the model is applied with a roughness of 180 μm and the model predicts nearly uniform deposition to duct floors, walls and ceilings. At this high roughness level, the model exhibits reasonable estimates of the magnitude and trends observed in the data; however, it significantly overpredicts deposition rates of the smallest (1 μm) particles. These observations are similar to those made when comparing the free-flight models to data collected at the wall of insulated ducts in Figures 5.5 and 5.6.

The sublayer model of Fan and Ahmadi (1993) is compared to the experimental data in Figure 5.11. This model is applicable only to vertical walls and is applied with and without the lift force. When the lift force is included in the calculations, it is calculated as if the flow were in the downward direction with the difference in the axial particle and fluid velocities being equal to the gravitational settling velocity of the particle. This method of accounting for the lift force probably overestimates its magnitude for the horizontal flow arrangement in the experiments. When the lift force is included, even though it is likely overestimated, the model still underpredicts the data; however, both the magnitude and the slope of the model predictions are in better accord with experimental observations.

The sublayer model is compared to data collected in insulated ducts in Figure 5.12. None of the model lines represent the data particularly well. Similar observations can be made here as have been made in comparisons of these data with other models. When the model agrees best with the trends and magnitudes of larger particle deposition, it overpredicts deposition of smaller particles. The model agrees with measured deposition rates of small particles when the roughness is smaller and it agrees with the large-particle data when the roughness is larger.

5.3.2 Published particle penetration models for bends

The two empirical equations that have been proposed to predict particle penetration through bends with turbulent flow are compared to the experimental data collected at all three air speeds in Figures 5.13 and 5.14. Figure 5.13 displays data collected at bend 5. This bend had a disturbed flow at its inlet because it was immediately downstream of a duct branch and bend in the experimental configuration. In this figure, the model of McFarland *et al.* (1997) agrees with the data better than the model of Pui *et al.* (1987) for Stokes numbers less than 0.01. At larger Stokes numbers, the model of McFarland *et al.* overpredicts penetration (underpredicts deposition) relative to the experimental data while the model of Pui *et al.* shows relatively good agreement with the data.

Figure 5.14 shows data collected in bend 6 which had an undisturbed flow inlet because it was downstream of an 18.3 m (60.0 ft) length of straight duct. In this figure, both models predict penetrations that are lower than measured experimentally. The model of Pui *et al.* lies well below most of the data. The model of McFarland *et*

al. does agree with much of the data and lies only marginally below the data for the steel system at the largest Stokes numbers.

The range of flow conditions at bend inlets in real ventilation ducts is likely to include both disturbed and undisturbed conditions. The bends in these experiments represent extreme cases of inlet flow conditions. Bend 5 had a duct branch and bend immediately upstream of its inlet and it represents a bend with highly disturbed inlet flow conditions. Bend 6 was preceded by 120 diameters in length of straight duct and represents a bend with a very well-developed inlet flow condition. Most bends in real duct systems have inlet conditions somewhere in the range between the limits established by bends 5 and 6 in the experimental system. Consequently, it is argued that penetrations through bends in real ventilation ducts are likely to fall within the range of penetrations measured in these experiments. The model of McFarland *et al.*, which gives predictions of bend penetrations near the middle of the range of the current measurements, was chosen as the best model for estimating penetrations through bends in real HVAC systems.

5.3.3 Model-measurement disagreement and the turbophoretic model

The turbophoretic model was used to explore potential reasons for discrepancies between models and measurements of deposition at the wall and ceiling of steel ducts. Figure 5.15 compares the turbophoretic model of Guha (1997) applied with surface roughness levels of 0, 1 and 5 μm to the experimental data collected in steel ducts. Three lines are shown for each deposition surface; in all cases the lowest line is for the smooth wall, the middle line is for 1 μm roughness and the uppermost line is for 5 μm roughness. These roughness levels have only a modest effect on model

predictions. There is almost no effect predicted for deposition to the duct floor, and these roughness levels alone do not explain the high deposition rates measured at the duct wall and ceiling.

In Figure 5.16, the turbophoretic model is applied with three different air-surface temperature differences to evaluate the potential importance of thermal forces in affecting the experimental deposition rates. In the figure, three model lines are shown for each surface. The lower, middle and upper lines for each surface refer to air-surface temperature differences of 0, 0.2 and 0.4 °C, respectively. As observed when varying the surface roughness in the model application, changing the air-surface temperature difference had the greatest impact on predictions of deposition rates to the duct wall. These modeling results suggest that thermal forces were potentially important when deposition rates were low, but thermal forces do not fully explain the model-measurement disagreement at the duct wall. In these model applications, the thermophoretic velocity was small compared to the gravitational settling velocity, and thermal forces were expected to play a nearly negligible role in determining deposition rates to horizontal surfaces.

Figure 5.17 shows the predictions of the turbophoretic model when applied with and without the image force. For predictions at each surface, the upper line for a given surface is the prediction with the image force and the lower line corresponds to the prediction without the image force. Even with the large net charge of ten excess electrons per particle in the model application, the image force was predicted to enhance deposition by a very small amount and it is unlikely to account for the model-measurement discrepancy.

No measurements of near-wall turbulence gradients were made in these experiments, but the effect of potential changes in the near-wall turbulence gradient on particle deposition was explored by means of the turbophoretic model. Figure 5.1 shows three profiles of the dimensionless root-mean-square of the wall-normal fluctuating velocity component, v'^{+}_{rms}, one for smooth surfaces and two for rough surfaces. In Figure 5.18, the turbophoretic model is applied using either equation (5.1) or (5.2). Use of equation (5.1) in the turbophoretic model leads to the lower lines in the figure, and use of equation (5.2) leads to the upper lines. The greater turbophoretic force when equation (5.2) is used leads to an increase in the predicted deposition velocities to both the floor and wall for particles in the diffusion-impaction regime. The increase improves model-measurement agreement at the wall, and leads to a modest overprediction of the data at the floor. Using equation (5.2) has very little effect on predicted deposition velocities at the duct ceiling.

Figure 5.19 compares experimental data collected in insulated ducts to the turbophoretic model applied with a roughness level of 60 μm and using equation (5.3) for the profile of v'^{+}_{rms} versus y^{+}. Using equation (5.3) in the turbophoretic model leads to good model-measurement agreement over the entire range of particle sizes studied, especially at the duct wall and floor. This result contrasts with all other model comparisons with the data collected in insulated ducts. In previous comparisons, models were either in agreement with large-particle data but overpredicted small-particle data or underpredicted large-particle data when they were in agreement with small-particle data. While it is recognized that this agreement is facilitated by somewhat arbitrarily adjusting model input parameters, these model

predictions do suggest that an increase in the turbophoretic force owing to a change in the structure of near-wall turbulence near a rough wall is potentially important in determining particle deposition rates to roughened surfaces. Measurements or simulations directly associating changes in the near-wall profile of v'^{+}_{rms} versus y^{+} to changes in the wall roughness would improve the ability to evaluate this effect. While this phenomenon provides a potentially satisfying explanation for the shape of the deposition curves on insulated surfaces and on steel duct walls, it does not explain the measured deposition rates on the ceilings of steel ducts.

Figure 5.20 shows predicted deposition rates to the steel duct surfaces under the combined influences of a temperature gradient and surface roughness when using equation (5.2) for the v'^{+}_{rms} versus y^{+} profile. In this model application the air-surface temperature difference was 0.2 °C, the best estimate from measurements and the surface roughness was 5 μm, the maximum roughness height from measurements. The model applied in this manner shows reasonably good agreement with the experimental data at the wall and the floor, but there is still a wide disagreement between the model and the measurements at the duct ceiling.

5.3.4 New empirical equations for predicting deposition in ventilation ducts

Because no theoretical model adequately represents all the experimental data, the new empirical equations (5.4)-(5.7) were developed as the most practical means of estimating deposition rates in straight ventilation ducts. An example of the application of these empirical equations is given in Figure 5.21 for steel ducts and Figure 5.22 for insulated ducts. Predicted deposition rates from these equations do not perfectly follow the trends established by the experimental data, but they do give

good estimates of the measured deposition rates in all cases. The data upon which these equations are based were collected with high quality methods using real HVAC materials. These equations are likely to give good predictions of particle deposition rates in both steel and insulated ventilation ducts, especially for particles in the diffusion-impaction regime where the experiments were conducted. The empirical expression for the deposition rate of small particles by diffusion is well supported by theoretical and experimental evidence. These equations have the drawback that they cannot account for changes in the microscale roughness character of the ducts.

Measured deposition fractions at duct S-connectors are shown in Figure 5.23 along with the empirical equation (5.10) that is a fit to these data. The data in this figure were collected at all three nominal velocities in the steel system. When the data for S-connector deposition are expressed as a plot of dimensionless deposition velocity versus dimensionless relaxation time, as in Figure 5.24, the empirical equation (5.10) shows good agreement with the experiments. This equation is easy to apply, gives good estimates of deposition rates at these S-connectors and is the only known method for predicting deposition rates at such ridges in turbulent flow.

5.4 Conclusions

Several empirical and theoretical models have been compared to particle deposition rates measured in an experimental ventilation duct system. In straight steel ducts, models generally predicted lower deposition rates than were measured. Most models underpredicted measurements to vertical duct walls. Models that are capable of predicting deposition rates to horizontal surfaces drastically underpredicted measured deposition to duct ceilings. The empirical model predicted slightly lower deposition

rates than were measured at duct floors. The turbophoretic model showed good agreement with measured deposition rates at the duct floor; this was the only case where a model agreed well with measurements without empirical tuning or arbitrary assumptions.

In straight insulated ducts, model predictions were found to be strongly influenced by the assumed roughness level of the insulation. The empirical model has no means of accounting for surface roughness and substantially underpredicts measured deposition rates to insulated duct surfaces. Other models gave predictions that were of a similar magnitude as the experiments when applied with surface roughness values in the range 30-180 μm, but no model compared favorably to the data over the entire range of particle sizes. This range of roughness values was applied as empirical fitting parameters rather than as a physical parameter that was independently determined. The only model developed explicitly for particle deposition to fibrous surfaces, that of Gutfinger & Friedlander (1985), gave predictions that compared neither more nor less favorably to measurements than other models. The model that seemed to follow the trends of the data most closely was the turbophoretic model of Guha (1997). The large difference in surface roughness between steel and insulated ducts is the best explanation for the large difference in deposition rates to these surfaces.

Published empirical equations for particle penetration through duct bends were found to give predictions similar to those measured in the current experiments. The model of McFarland *et al.* (1997) is recommended as the model most likely to give the best predictions of particle penetration through bends in real ventilation ducts.

The turbophoretic model of Guha (1997) was used to explore the influence of microscale roughness, temperature gradients, image forces from electrical charges and near-wall turbulence gradients on particle deposition rates in the steel duct experiments. These phenomena were determined to have a very small effect on deposition rates to duct floors and ceilings and a more substantial, though still modest effect on deposition rates to duct walls. A steepening of the near-wall turbulence gradient caused by surface roughness yielded appreciable differences in deposition predictions. Modeled deposition rates to rough surfaces increased owing to greater particle transport by turbophoresis near rough surfaces. Relatively modest shifts in turbulence gradients cause increases in predicted deposition rates for intermediate sized particles to both the duct wall and the floor. A shift in the near-wall turbulence gradient also yields better model-measurement agreement when considering the shape of the deposition curve to insulated ducts. While it seems that small changes in surface roughness, near-wall temperature gradient and near-wall turbulence gradient may partially explain differences between model predictions and measurements at duct walls, none of these phenomena could explain the magnitude of the deposition rates measured at duct ceilings. The particle transport mechanisms leading to higher than modeled deposition on the ceilings of ducts is unclear.

New empirical equations (5.4)-(5.7) were developed for predicting deposition rates of particles to steel and insulated duct surfaces. The constants k_4 and k_5 for determining the inertial contribution to particle deposition rates were determined by power-law fits to experimental data and are summarized in Tables 5.1 and 5.2. An interpolation scheme is recommended to permit application of these equations over a broad range of straight duct flows. These equations are easy to use, give good estimates of

deposition rates and are based on experiments with real HVAC materials. They also yield predictions for the distinct surfaces of horizontal ducts. However, they offer little insight into deposition mechanisms and are unable to account for subtle changes in surface roughness or temperature gradients. An empirical equation (5.10) to predict deposition rates at S-connectors located at duct junctions is also presented. Because deposition at S-connectors appears to be an impaction dominated process, this equation should give reasonable estimates of deposition rates to S-connectors at duct floors, walls or ceilings. It may also be an appropriate approach for estimating deposition to certain other flow obstructions in ducts; however, further experiments would be required to test this inference.

Table 5.1 Values of k_4 and k_5 for use in equations (5.4) and (5.5) for the three experimental friction velocities in steel ducts.

		Duct ceiling		Duct wall	
Air speed, U_{ave} (m/s)	**Friction velocity (cm/s)**	**k_4 (-)**	**k_5 (-)**	**k_4 (-)**	**k_5 (-)**
2.2	$u_1^* = 12$	1.2×10^{-4}	0.64	2.6×10^{-3}	1.01
5.3	$u_2^* = 27$	7.7×10^{-5}	0.74	1.1×10^{-3}	1.13
9.0	$u_3^* = 45$	1.8×10^{-4}	1.10	8.1×10^{-4}	1.40

Table 5.2 Values of k_4 and k_5 for use in equations (5.4) and (5.5) for the three experimental friction velocities in insulated ducts.

		Duct ceiling		Duct wall	
Air speed, U_{ave} (m/s)	**Friction velocity (cm/s)**	**k_4 (-)**	**k_5 (-)**	**k_4 (-)**	**k_5 (-)**
2.2	$u_1^* = 16$	6.7×10^{-3}	0.57	2.6×10^{-3}	0.77
5.3	$u_2^* = 37$	0.019	0.74	0.019	0.74
8.8	$u_3^* = 62$	0.014	0.71	0.014	0.71

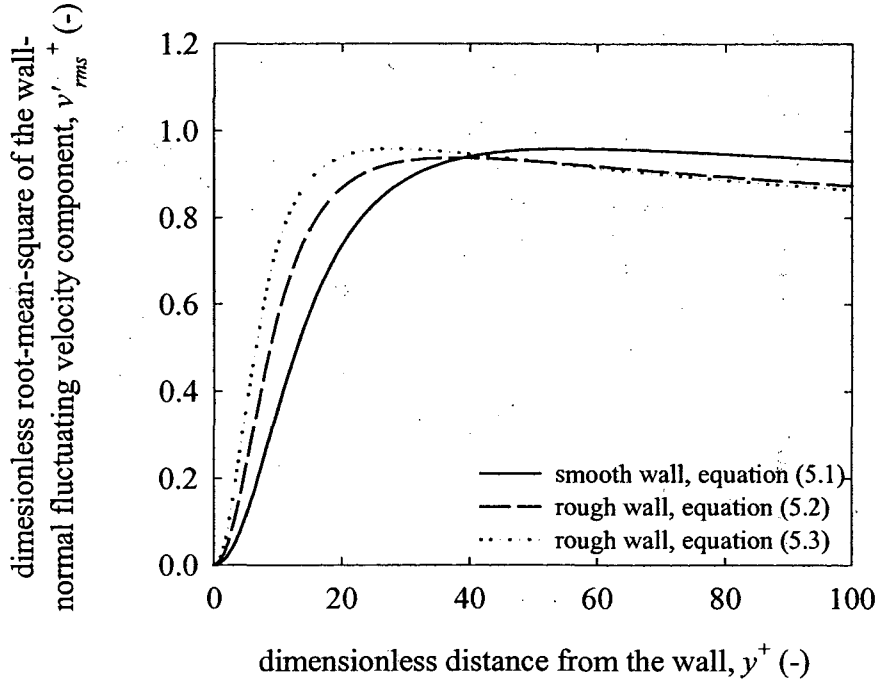

Figure 5.1 Profile of v'^{+}_{rms} versus y^{+} used to evaluate turbophoretic transport in the turbophoretic model of Guha (1997).

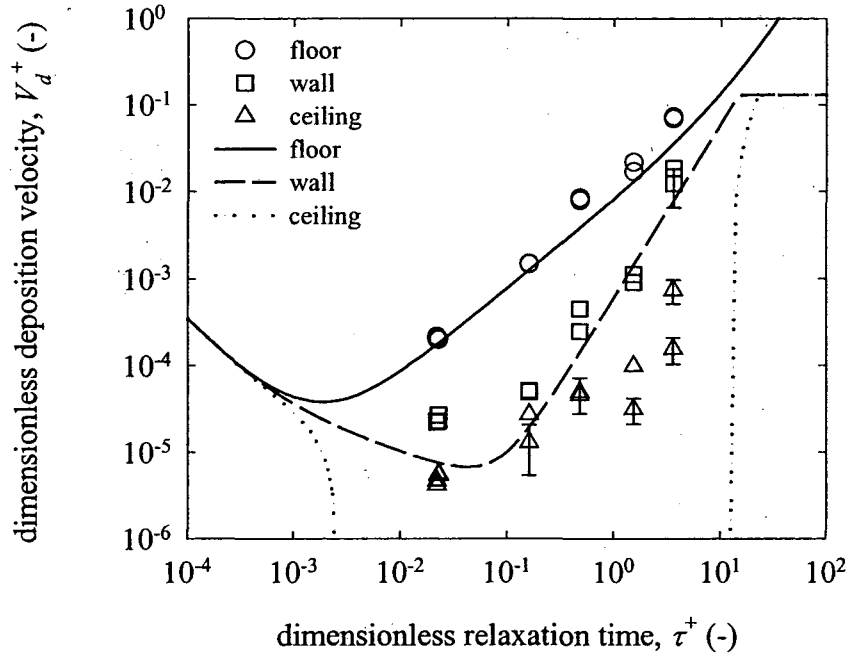

Figure 5.2 Comparison of empirical equations (2.71)-(2.74) with $k_1 = 0.051$, $k_2 = 6\times10^{-4}$ and $k_3 = 0.13$ to data collected in straight steel ducts with $U_{ave} = 5.3$ m/s.

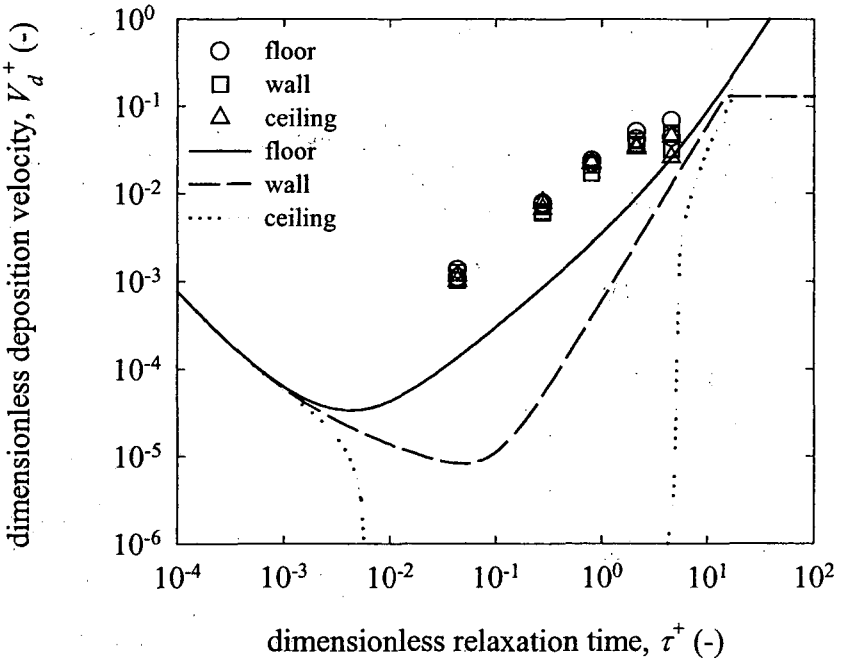

Figure 5.3 Comparison of empirical equations (2.71)-(2.74) with $k_1 = 0.051$, $k_2 = 6\times10^{-4}$ and $k_3 = 0.13$ to data collected in straight insulated ducts with $U_{ave} = 5.3$ m/s.

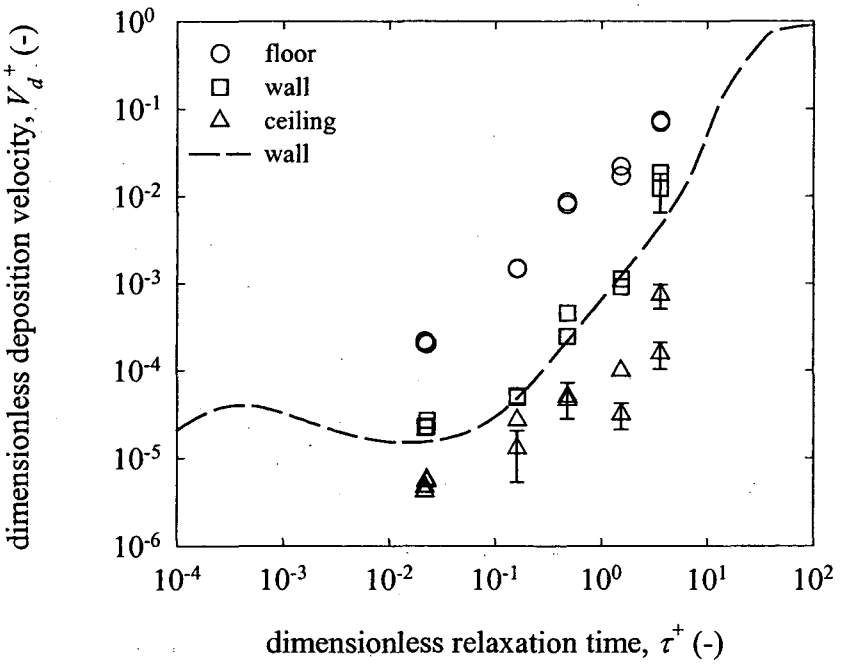

Figure 5.4 Comparison of the free-flight model of El-Shobokshy & Ismail (1980) to data collected in straight steel ducts with $U_{ave} = 5.3$ m/s.

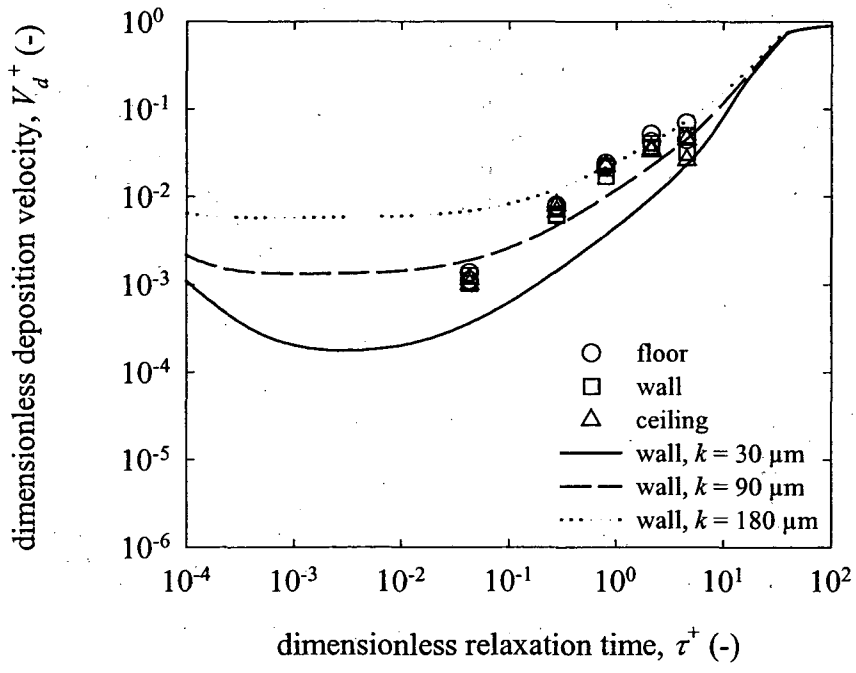

Figure 5.5 Comparison of the free-flight model of El-Shobokshy & Ismail (1980) with three roughness levels, k, to data collected in straight insulated ducts with U_{ave} = 5.3 m/s.

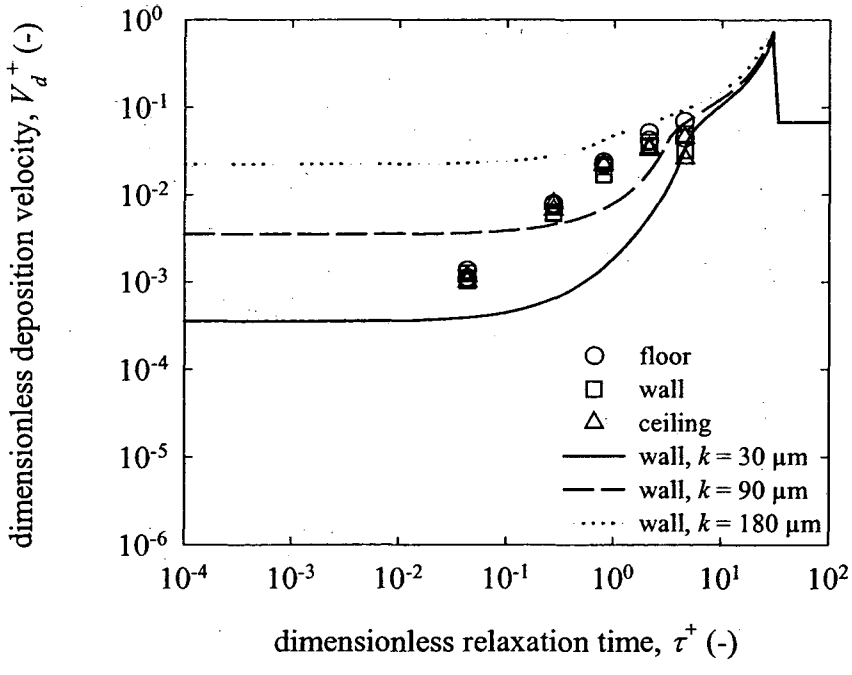

Figure 5.6 Comparison of the free-flight model of Gutfinger & Friedlander (1985) with three roughness levels, k, to data collected in straight insulated ducts with U_{ave} = 5.3 m/s.

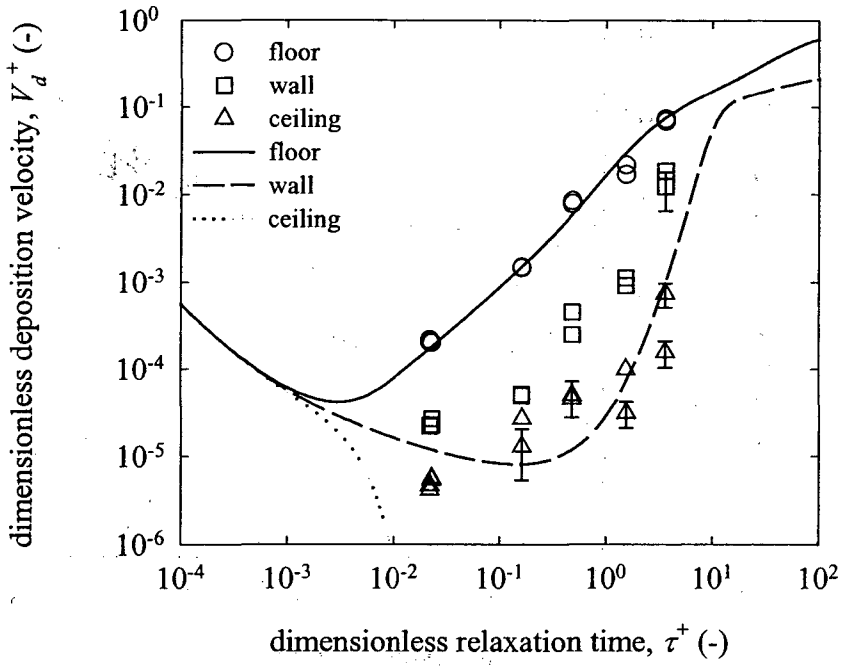

Figure 5.7 Comparison of the turbophoretic model of Guha (1997) to data collected in straight steel ducts with U_{ave} = 5.3 m/s.

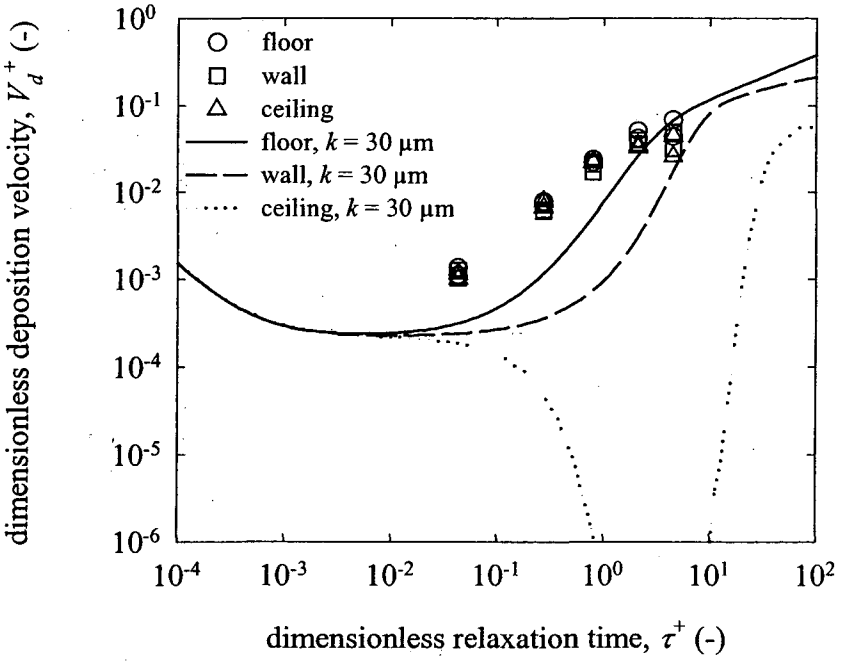

Figure 5.8 Comparison of the turbophoretic model of Guha (1997) with a surface roughness of 30 μm to data collected in straight insulated ducts with U_{ave} = 5.3 m/s.

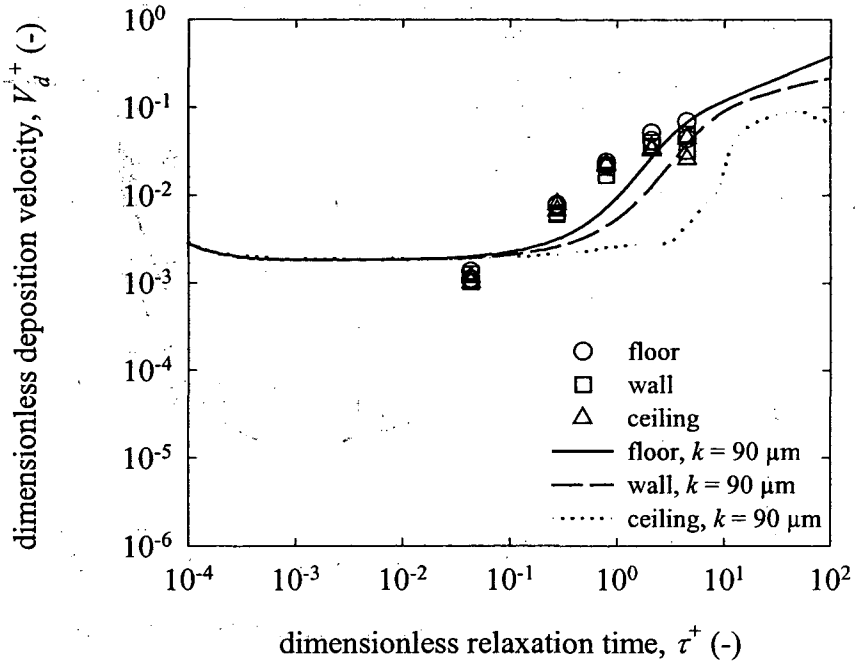

Figure 5.9 Comparison of the turbophoretic model of Guha (1997) with a surface roughness of 90 μm to data collected in straight insulated ducts with U_{ave} = 5.3 m/s.

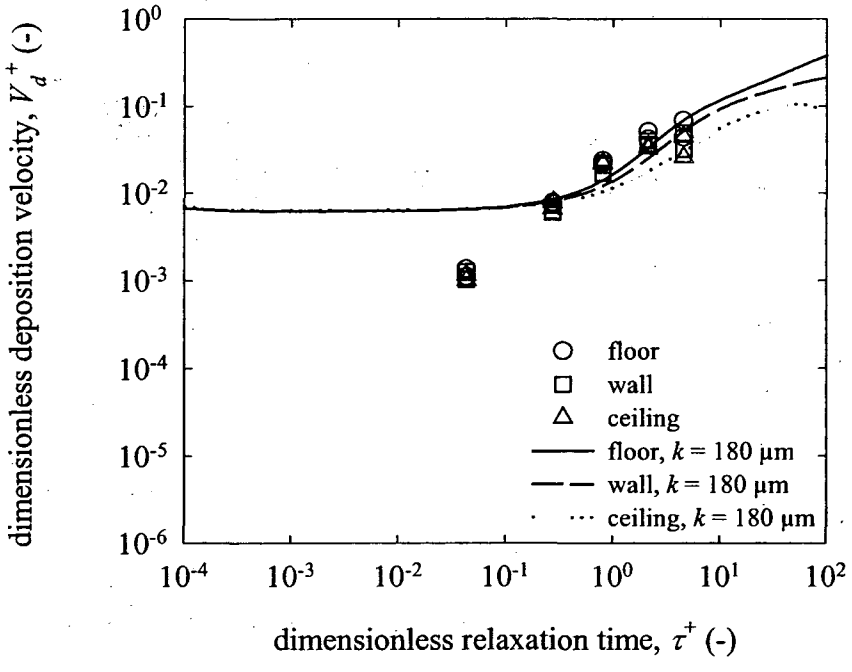

Figure 5.10 Comparison of the turbophoretic model of Guha (1997) with a surface roughness of 180 μm to data collected in straight insulated ducts with U_{ave} = 5.3 m/s.

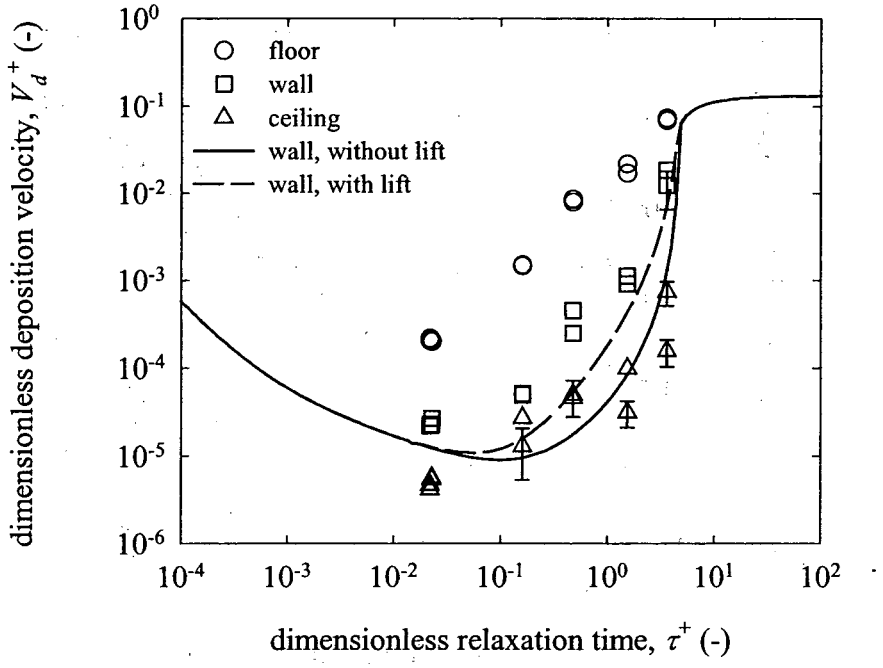

Figure 5.11 Comparison of the sublayer model of Fan & Ahmadi (1993) with and without the lift force to data collected in straight steel ducts with U_{ave} = 5.3 m/s.

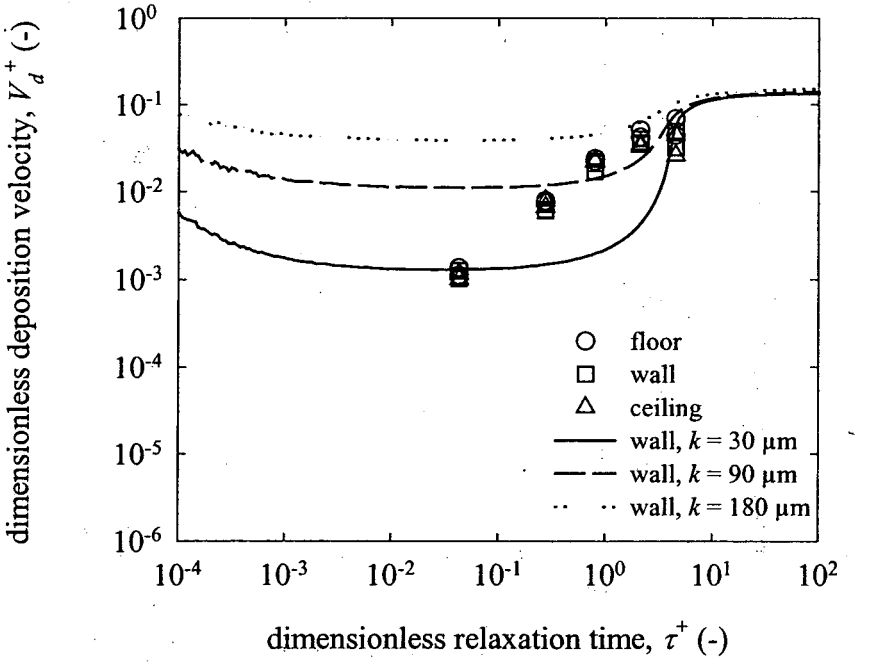

Figure 5.12 Comparison of the sublayer model of Fan & Ahmadi (1993) with three roughness levels, k, to data collected in straight insulated ducts with U_{ave} = 5.3 m/s.

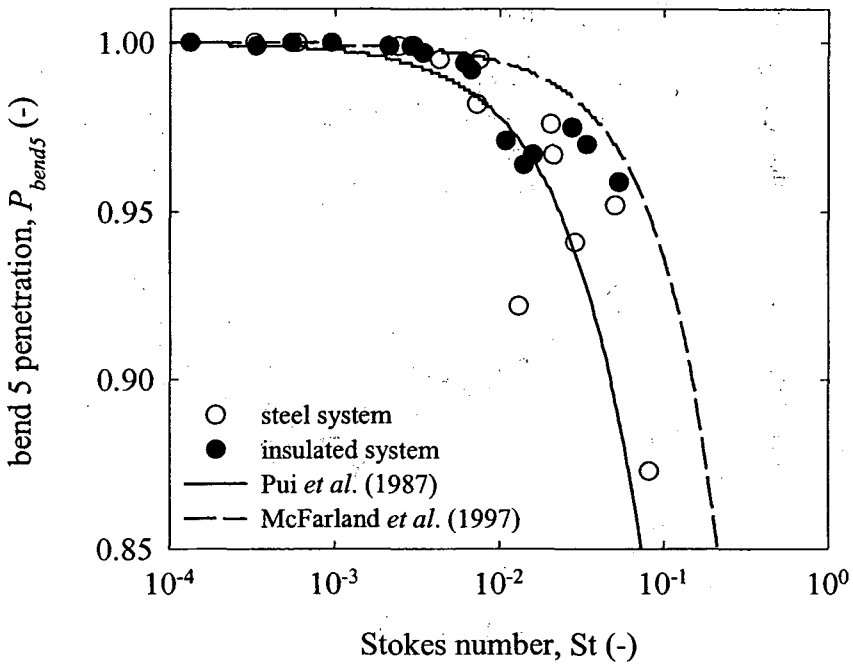

Figure 5.13 Comparison of the empirical models for bend penetration to data collected in steel bend 5 at air speeds of 2.2, 5.3 and 8.8 & 9.0 m/s.

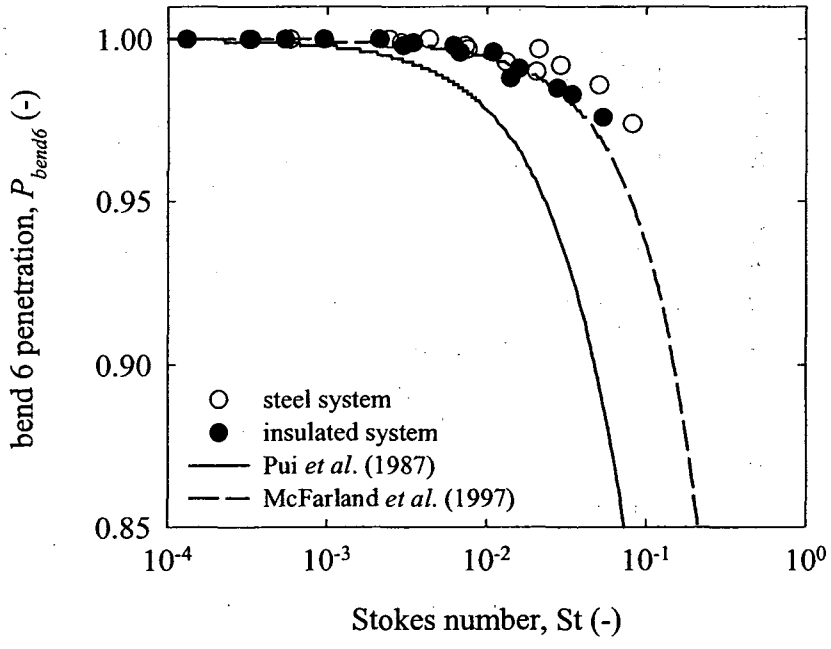

Figure 5.14 Comparison of the empirical models for bend penetration to data collected in steel bend 6 at air speeds of 2.2, 5.3 and 8.8 & 9.0 m/s.

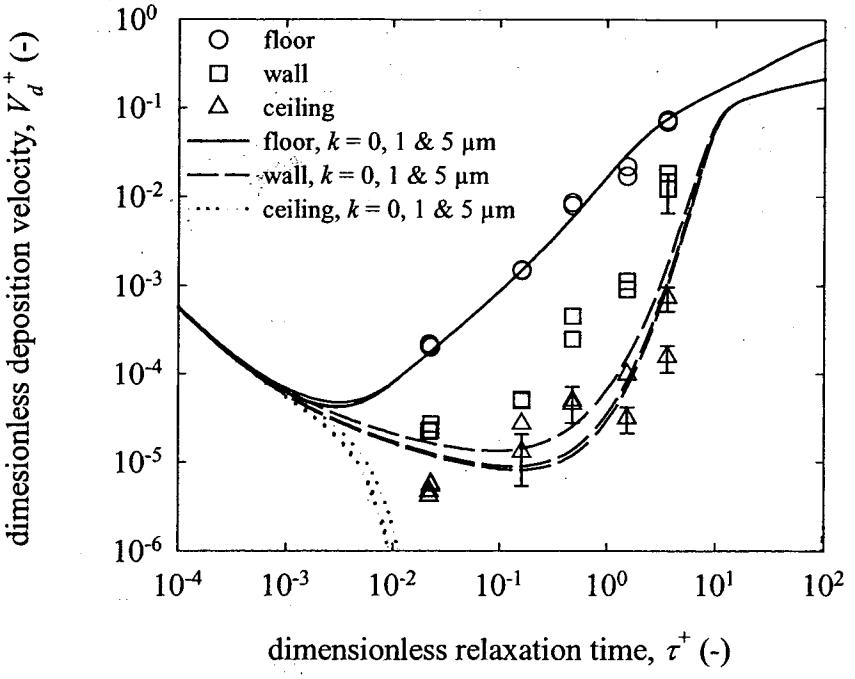

Figure 5.15 Comparison of turbophoretic model of Guha (1997) with different values for the surface roughness, k, to data collected in straight steel ducts with U_{ave} = 5.3 m/s.

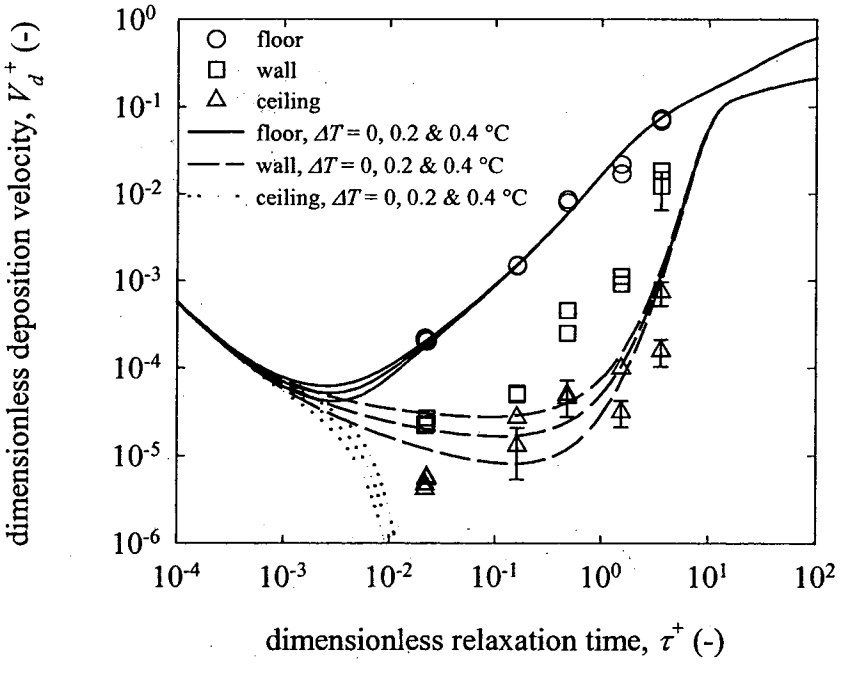

Figure 5.16 Comparison of turbophoretic model of Guha (1997) with different air-wall temperature differences, ΔT, to data collected in straight steel ducts with U_{ave} = 5.3 m/s.

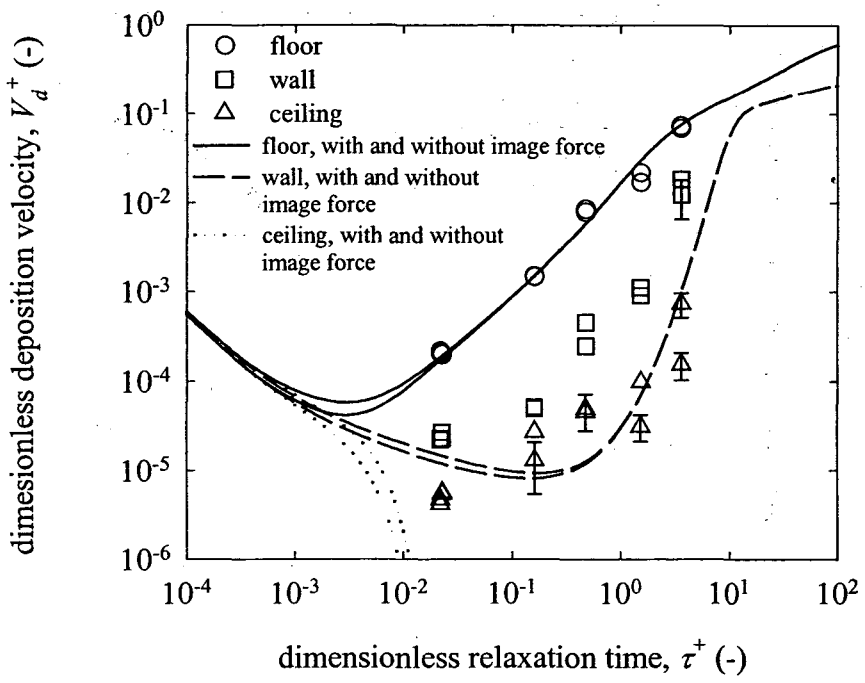

Figure 5.17 Comparison of turbophoretic model of Guha (1997) with and without the image force to data collected in straight steel ducts with U_{ave} = 5.3 m/s.

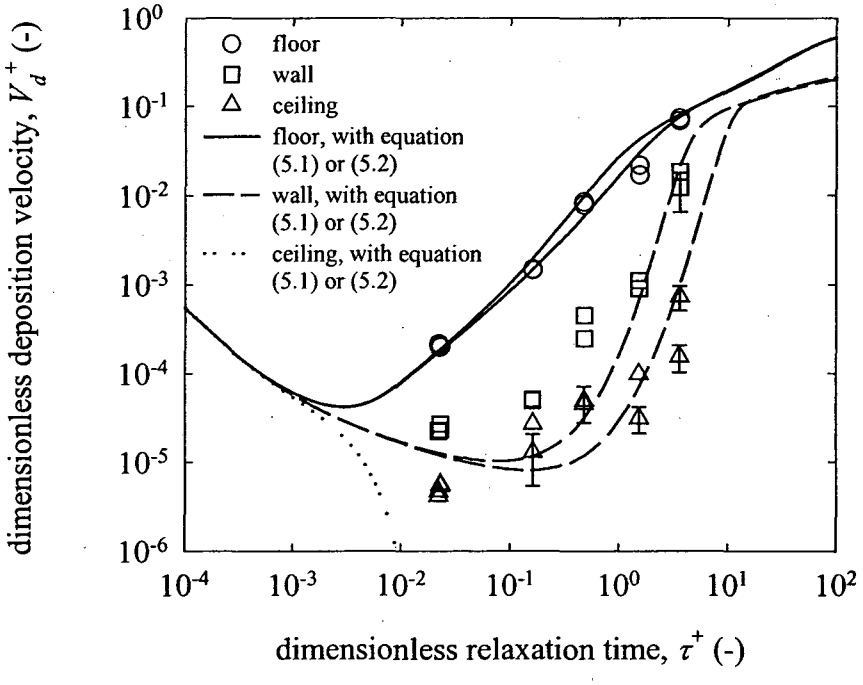

Figure 5.18 Comparison of the model of Guha (1997) when using either equation (5.1) or (5.2) for the profile of v'^+_{rms} versus y^+ to data collected in straight steel ducts.

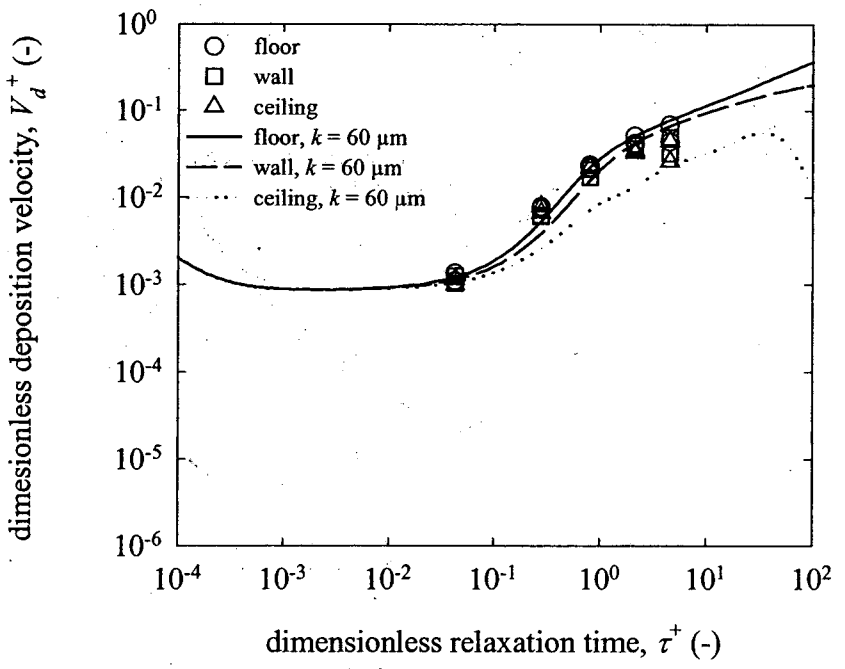

Figure 5.19 Comparison of the turbophoretic model of Guha (1997) with a roughness of 60 μm and equation (5.3) for v'^+_{rms} to data collected in insulated ducts with U_{ave} = 5.3 m/s.

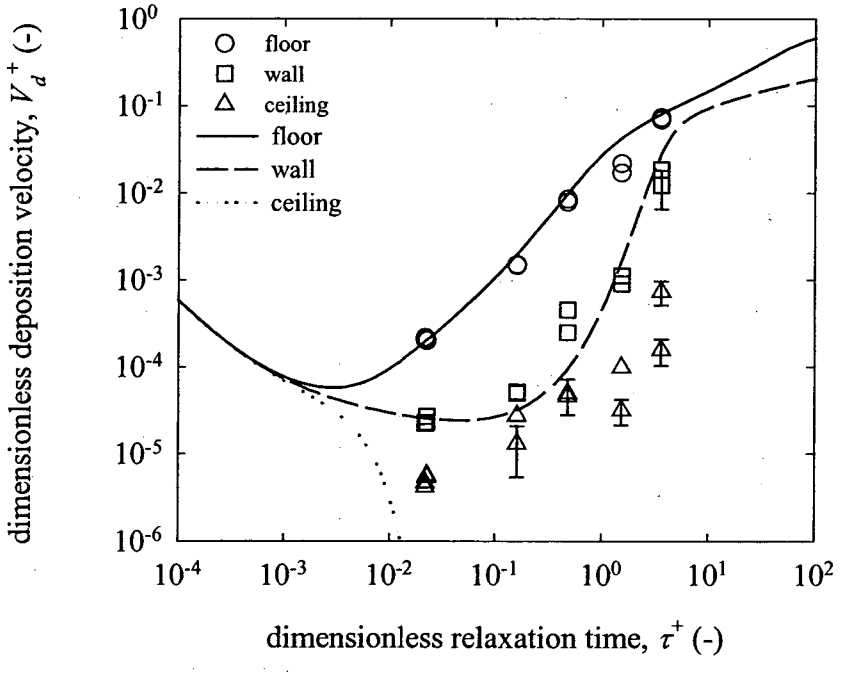

Figure 5.20 Comparison of the turbophoretic model of Guha (1997) with a roughness of 5 μm, an air-wall ΔT of 0.2 °C and equation (5.2) for v'^+_{rms} to data collected in steel ducts.

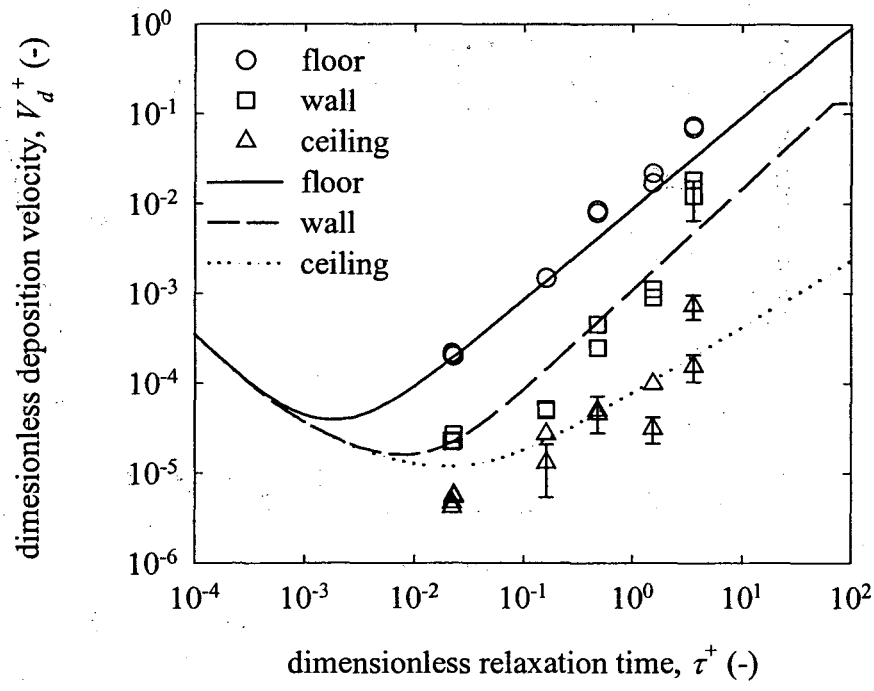

Figure 5.21 Comparison of the new empirical model to data collected in straight steel ducts with U_{ave} = 5.3 m/s.

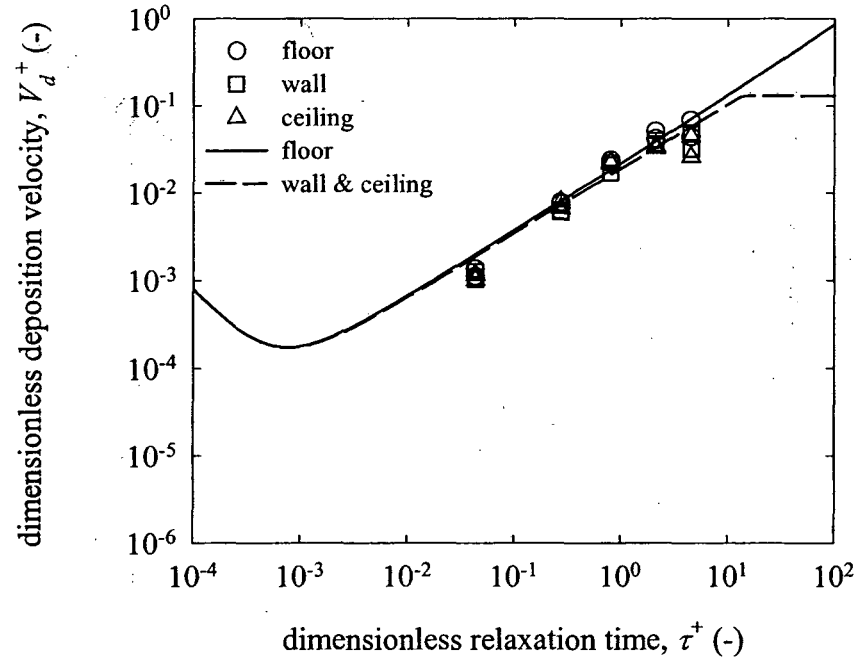

Figure 5.22 Comparison of the new empirical model to data collected in straight insulated ducts with U_{ave} = 5.3 m/s.

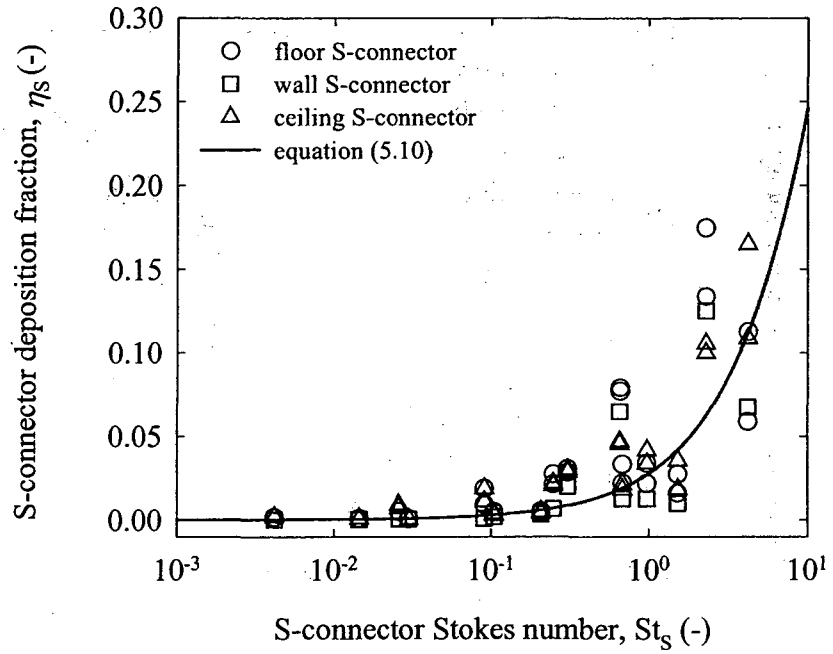

Figure 5.23 Comparison of equation (5.10) to data collected at S-connectors in the steel system at air speeds of 2.2, 5.3 and 9.0 m/s.

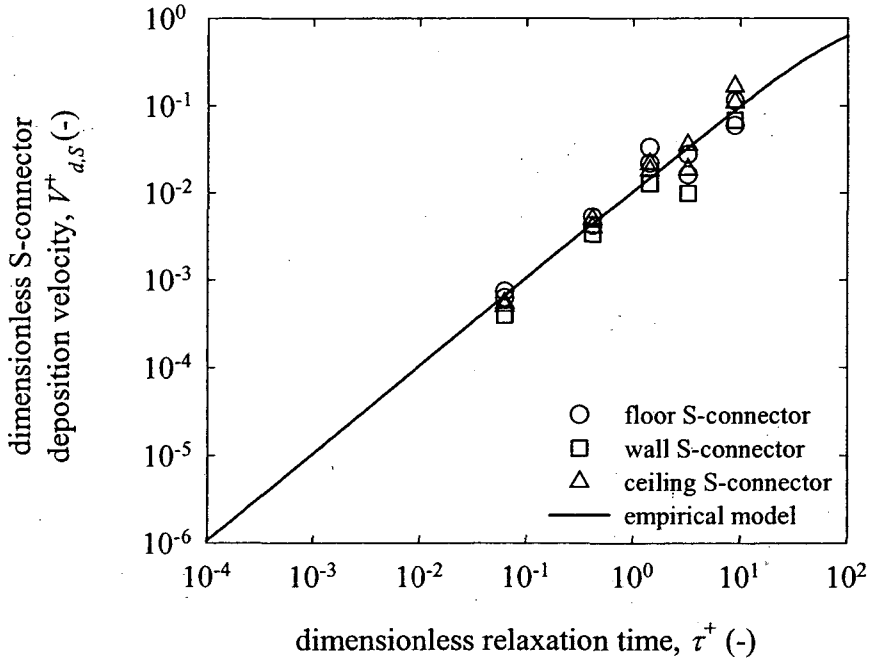

Figure 5.24 Comparison of dimensionless deposition velocities predicted by equation (5.10) to data collected at S-connectors in the steel system at an air speed of 5.3 m/s.

CHAPTER 6

Modeling Particle Losses in Ventilation Ducts

6.0 Abstract

In this chapter, empirical equations are applied to predict losses of 0.01-100 μm airborne particles making a single pass through 120 different ventilation duct runs typical of those found in mid-sized office buildings. For all duct runs, losses were negligible for submicron particles and nearly complete for 50 μm particles. The 50th percentile cut-point diameters were 15.2 μm in supply duct runs and 24.9 μm in return duct runs. Losses in supply duct runs were higher than in return duct runs, mostly because internal insulation was present in portions of supply duct runs, but completely absent from return duct runs. When insulation is not present, losses of particles larger than 1 μm are controlled by deposition to duct floors, especially in small ducts. When a significant fraction of a duct run is internally insulated, deposition to the insulated surfaces is predicted to dominate overall particle losses.

Single-pass particle losses in duct runs were combined with models for predicting HVAC filtration efficiency and particle deposition to indoor surfaces to evaluate the fates of particles in an archetypal mechanically ventilated building. The fates of particle drawn into an HVAC system from outdoors and of particles generated indoors were modeled. Ventilation ducts with either high particle losses or low particle losses were considered under different HVAC filtration scenarios. When considered in the context of an entire building, modeling results suggest that losses in ventilation ducts are only modestly important for determining indoor particle concentrations for most

particle sizes. For the duct runs considered and building considered, losses in ventilation ducts were of a comparable magnitude to losses to indoor surfaces for most particle sizes. When considering outdoor particles drawn into an unfiltered HVAC system, the model predicts that most smaller than 1 μm are exhausted from the building before depositing and that most larger particles deposit within the building, mostly in supply ducts or to indoor surfaces. When filters are present and all supply air is filtered, modeling suggests that most particles are either filtered or exhausted; only a small fraction of particles are expected to deposit to ducts or indoor surfaces.

The model predicts that the fates of particles generated indoors follow similar general trends as particles drawn into the building from outdoors with some key differences. For particles generated indoors, deposition in return ducts is predicted to be a more significant fate than for outdoor particles. In the presence of filtration, the fates of indoor-generated and outdoor particles are similar for particle sizes smaller than 4 μm, but differ for larger particle sizes. Most large outdoor particles are filtered, while large indoor particles deposit in the building, mostly to indoor surfaces, but also in return ducts.

6.1 Introduction

Knowledge of depositional losses in ventilation ducts can be useful for evaluating human exposures to particles within buildings and for predicting particle accumulation rates in ducts. Ventilation ducts are likely to influence indoor concentrations of outdoor particles as air is drawn through the HVAC system and delivered to the building. Concentrations of particles generated indoors are also influenced by deposition in ventilation ducts as indoor air is recirculated through the

HVAC system. The magnitude of these depositional losses is uncertain and has not been the subject of previous investigations.

Building remediation may be necessary following the release of a hazardous aerosol near, or within a building. Deposition to HVAC system surfaces may be the ultimate fate for a significant fraction of some hazardous aerosols, but these surfaces are often not easily accessible for remediation. Duct surfaces, unlike fans and cooling coils, are usually not designed to be easily cleaned. The ability to predict the locations within ventilation ducts where hazardous aerosols deposit can improve the effectiveness of remediation and reduce the associated costs.

Models for predicting particle penetration through a series of straight tubes and bends have been proposed (Anand & McFarland, 1993; Brockman, 2001). These were developed to predict penetration through aerosol sampling lines that are similar to ventilation duct runs, but that also have several important differences. Aerosol sampling lines are generally much simpler than ventilation duct runs, with fewer components, flow obstructions and surface irregularities. Furthermore, sampling lines usually have round cross sections with constant tube diameters, while ventilation duct runs commonly have rectangular cross sections and have duct sections with a variety of dimensions. The previously proposed models have generally used a combination of free-flight or empirical approaches for predicting deposition in straight tubes and empirical approaches for predicting deposition in bends. The shortcomings of the methods upon which these aerosol sampling line deposition models are based when applied to ventilation ducts have been discussed in previous chapters of this dissertation.

Wallin (1994) applied a model to predict accumulation rates of particle deposits in ventilation ducts. This model combined the free-flight method of El-Shobokshy & Ismail (1980) for predicting deposition in straight ducts with the empirical equation of Diu & Yu (1980) for predicting bend penetration. The free-flight method was modified to account for gravitational settling in horizontal tubes using the approach described by Anand & McFarland (1989). The model is applicable only to round ventilation ducts and cannot be reliably applied to ducts with rectangular cross sections. The equation proposed by Diu & Yu (1980) was developed for laminar flow, which is rarely the case in ventilation ducts. Wallin (1994) applied this method to predict accumulation rates of 10 μm particles in small ventilation ducts; a range of particle sizes was not considered.

In this chapter, the empirical equations developed to predict particle deposition rates in HVAC ducts (Chapter 5) are applied to predict particle losses in several supply and return ventilation duct runs selected from mid-sized office buildings. Advantages of using these equations are that they may be applied to ducts of rectangular cross section and that they should provide good estimates of deposition rates to both steel and insulated duct surfaces. More detailed information regarding the location of particle losses is accessible through application of these empirical equations compared to through the application of models developed for deposition in round tubes. Particle losses resulting from a single pass of an aerosol through these duct runs are determined and the locations within the duct runs where losses occur are evaluated for the size range 0.01-100 μm. These single pass duct losses are combined with predictions of HVAC filtration efficiencies and indoor particle loss rates to evaluate

the fates of particles in an archetypal mechanically ventilated building. The fates of particles drawn into the building's HVAC system from outdoors and of particles generated indoors are evaluated under different HVAC filtration scenarios.

6.2 Methods

6.2.1 Particle losses in a single pass through duct runs

Empirical equations were applied to determine fractional particle losses resulting from a single pass of an aerosol through 120 different duct runs, comprising 60 supply runs and 60 duct runs. These modeled duct runs were based on real duct runs chosen from four university buildings that housed a combination of offices, classrooms and laboratories. The characteristics of the buildings are summarized in Table 6.1. To determine model inputs, duct lengths, dimensions and airflow rates were read from as-built mechanical system drawings and confirmed by observation. Supply duct runs were defined to begin immediately after a supply fan and to end at a supply register within the building. Return duct runs began at a return air register and ended at the plenum where return air was either exhausted or returned to the supply side of the ventilation system. General characteristics of the modeled duct runs are summarized in Table 6.2. All of the ducts in these buildings had rectangular cross-sections. All supply duct runs had some length that was internally insulated, and no return duct runs had any internal insulation. Usually, vertical supply ducts were completely insulated and portions of the horizontal supply ducts were insulated. On average, supply duct runs were slightly longer and had more bends than the return duct runs.

Supply ducts runs generally begin with a large duct generation that branches into a series of successively smaller duct generations. Return duct runs begin with small

duct generations that combine into successively larger generations. Penetration of particles in the size range 0.01-100 μm through each duct generation was calculated independently. A new duct generation was defined to occur whenever one of the following characteristics changed along the length of a duct run: duct width, duct height, air speed, insulation status or orientation. Air speeds were assumed to be constant in each duct generation. Duct generations are commonly joined by duct bends. Particle penetration through each duct bend was calculated independently by means of an empirical model.

Particle deposition at variable-air volume boxes and heating and cooling coils was ignored. Deposition in straight duct sections near flow disturbances was calculated as if the turbulent flow profile were fully developed. Thus, particle losses are potentially underpredicted by the model.

Particle penetration through the entire duct run, P_{total}, was calculated by multiplying the calculated penetrations for all duct generations and bends in the duct run as follows:

$$P_{total} = \prod_{i=1}^{n_d} P_{duct,i} \prod_{j=1}^{n_b} P_{bend,j} \tag{6.1}$$

Here n_d is the total number of straight duct generations in the duct run and n_b is the total number of duct bends.

Empirical equations were applied to each of the 120 duct runs to determine particle penetrations and fractional losses for the size range 0.01-100 μm. Equations (5.4)-(5.9) were used to predict deposition velocities to duct surfaces in straight duct

generations. Equation (5.10) was used to predict deposition fractions at the S-connectors present at duct junctions. For a given particle size, penetration through a straight duct generation was calculated by

$$P_{duct,i} = P_{ceiling,i} P_{wall,i} P_{floor,i} P_{S,i} \tag{6.2}$$

Here, $P_{ceiling,i}$, $P_{wall,i}$, $P_{floor,i}$ and $P_{S,i}$ are the penetrations through a straight duct generation owing to deposition that occurs only at either the duct ceiling, wall, floor or S-connectors, respectively. Penetration through bends was calculated by the model of McFarland *et al.* (1997), as described in equations (2.122)-(2.126).

For a straight horizontal generation, the single-surface penetrations were calculated by

$$P_{ceiling,i} = exp\left(\frac{-LV_{d,c}}{HU_{ave}}\right) \tag{6.3}$$

$$P_{wall,i} = exp\left(\frac{-2LV_{d,w}}{WU_{ave}}\right) \tag{6.4}$$

$$P_{floor,i} = exp\left(\frac{-LV_{d,f}}{HU_{ave}}\right) \tag{6.5}$$

$$P_{S,i} = \left(1 - \frac{\eta_S h_S L_S u_S}{HWU_{ave}}\right)^{N_S} \tag{6.6}$$

Here, W is the duct width, H is the duct height and N_S is the number of S-connectors in the duct section. For an insulated generation, N_S is equal to zero and $P_{S,i}$ is one. To determine N_S in a steel generation, it was assumed that two S-connectors were located at each duct junction. Duct junctions occur at bend inlets and outlets and at every 1.5 m (5.0 ft) of straight duct. For a vertical duct generation, all four duct surfaces were treated as duct walls so that the single-surface penetrations were

$$P_{ceiling,i} = P_{floor,i} = 1 \tag{6.7}$$

$$P_{wall,i} = exp\left(\frac{-4LV_{d,w}}{D_h U_{ave}}\right) \tag{6.8}$$

Equation (6.6) was used to calculate $P_{S,i}$.

The total fraction of particles lost in a straight duct generation was

$$l_{duct,i} = \left(1 - P_{duct,i}\right)P_t \tag{6.9}$$

Here, P_t is the total particle penetration through the duct run up to the inlet of the duct generation under consideration. Equation (6.9) calculates the fraction of particle lost in a duct generation based on the total number of particles entering the duct run, not based on the particles entering that generation.

The fraction of particles lost to a given surface in a straight duct generation was calculated by multiplying the total fraction of particles lost in the duct generation by the ratio of the single-surface loss rate to the total loss rate in that duct generation. Single-surface loss rates for the ceiling, wall, floor and S-connectors in a horizontal duct were respectively calculated by

$$r_{ceiling} = LWV_{d,c} \tag{6.10}$$

$$r_{wall} = 2LHV_{d,w} \tag{6.11}$$

$$r_{floor} = LWV_{d,f} \tag{6.12}$$

$$r_S = N_S \eta_S L_S h_S u_S \tag{6.13}$$

For a vertical duct generation, the single-surface loss rates were

$$r_{ceiling} = r_{floor} = 0 \tag{6.14}$$

$$r_{wall} = 2L(W + H)V_{d,w} \tag{6.15}$$

and equation (6.13) was used to calculate r_S. It was assumed that S-connectors were located on the floor and ceiling of horizontal ducts and on the walls with the larger dimension in vertical ducts. Thus, the transverse length of the S-connector, L_S in equation (6.13), was set equal to the duct width, W, in all cases.

The total loss rate in a straight duct generation is the sum of the losses to the distinct surfaces within that duct and was calculated by

$$r_{duct,i} = r_{ceiling,i} + r_{wall,i} + r_{floor,i} + r_{S,i} \tag{6.16}$$

Thus, the fraction of particles entering a duct run lost to single surfaces within a straight duct generation were

$$l_{ceiling,i} = \frac{r_{ceiling}}{r_{duct}} l_{duct,i} \tag{6.17}$$

$$l_{wall,i} = \frac{r_{wall}}{r_{duct}} l_{duct,i} \tag{6.18}$$

$$l_{floor,i} = \frac{r_{floor}}{r_{duct}} l_{duct,i} \tag{6.19}$$

$$l_{S,i} = \frac{r_S}{r_{duct}} l_{duct,i} \tag{6.20}$$

Particle penetrations through bends in a duct run were calculated by the model of McFarland *et al.* (1997). To apply this model, the particle Stokes number was calculated using the duct dimension (width or height) in the plane of the bend for D_h in equation (2.19). This choice makes this calculation consistent with other

assessments of deposition due to impaction. For example, when considering particles depositing on an impaction plate, it is the diameter of the inlet air jet that is the appropriate dimension for determining the Stokes number. The bend ratio, R_o, that appears in the model of McFarland *et al.* was difficult to determine for all modeled duct bends; however, for the dimensions of ducts considered, the model was not sensitive to the value of R_o in the range 1-5. The range of bend ratios for nearly all ventilation duct bends is within this range; a value of 3 was used for all bend penetration calculations.

The fraction of particles entering a duct run that are lost in a bend was calculated by

$$l_{bend,j} = \left(1 - P_{bend,j}\right) P_t \tag{6.21}$$

Equation (6.21) is analogous to equation (6.9) for straight duct generations. In this case, P_t is the total particle penetration through the entire duct run up to the bend inlet.

The total fraction of particles lost in a duct run, l_{total}, could be found by adding the fraction lost in all straight duct generations and in all duct bends. Alternatively, the total particle fraction lost in a duct run could be calculated by

$$l_{total} = 1 - P_{total} \tag{6.22}$$

Because losses to each duct surface were calculated independently, the fraction of the total losses attributable to deposition on any given surface could be easily calculated. The fractions of total losses in an entire duct run owing to deposition on duct ceilings, duct walls, duct floors, duct bends and S-connectors at duct junctions were determined in each single-pass particle loss calculation. Similarly, the fraction of the total losses owing to deposition in different classes of duct generations were

calculated for the range of particle sizes. Duct generation classes depended on the duct size, orientation and insulation status of the duct. Thus, eight classes of straight duct generations were considered: small-horizontal-steel, small-vertical-steel, small-horizontal-insulated, small-vertical-insulated, large-horizontal-steel, large-vertical-steel, large-horizontal-insulated and large-vertical-insulated. When considering duct size, ducts with a hydraulic diameter smaller than 0.4 m were classified as small ducts and those with larger hydraulic diameters were classified as large ducts. Duct bends were classified as either large bends or small bends, according to whether the bend dimension was larger or smaller than 0.4 m.

It was found that fractional losses for a single pass through most duct runs were negligible for submicron particles and close to one for particle larger than about 50 μm. For the size range 1-50 μm, the fraction of particles lost increased dramatically from near zero to one for a given duct run. The cut-point particle diameter for a duct run was defined as the diameter for which half of the particles were lost (and half penetrated) in a single pass. Supply duct runs were ranked by decreasing cut-point diameter. The ten supply duct runs with the smallest cut-point diameters were characterized as high-loss supply ducts and the ten with the largest cut-point diameters were characterized as low-loss supply ducts. The fraction of the total losses onto different surfaces was determined as an average for all the high-loss supply ducts. Similarly, the fraction of total losses resulting from deposition within each of the ten duct generation classes (eight straight duct classes and two bend classes) was calculated as an average for all high-loss supply ducts. The same calculations were carried out for low-loss supply ducts to determine the fraction of total losses occurring at deposition to different duct surfaces and different duct classes.

The same ranking scheme was applied to return duct runs to determine ten high-loss and ten low-loss return ducts. Average fractional losses in the high-loss and low-loss return duct runs were determined using the same methods as for supply duct runs. Because no return duct runs had any internal insulation, deposition in only four straight duct generation classes (rather than eight) could contribute to particle losses in return duct runs.

6.2.2 Particle fates in a building

Single-pass particle losses in duct runs were combined with empirical models for HVAC filtration and deposition to indoor surfaces to evaluate the fates of particles in an archetypal mechanically ventilated building. Outdoor particles drawn into a building through the HVAC system and particles generated indoors were considered separately. A schematic of the model used to predict particle fates in the archetypal building is shown in Figure 6.1. The indoor volume, V, was treated as a well-mixed space. Air was assumed to enter the building only through the HVAC system's outdoor air intake and exit only at the HVAC system exhaust. In the figure, airflows are shown as block arrows and the small, squiggly arrows represent depositional losses. Flow rates are labeled in relation to the total flow rate of air supplied to the building, Q_s. The fraction of return air from the building that is recirculated is R. Bypass of air around filters was accommodated and the fraction of supplied air bypassing filtration is F_b. Five particle fates were considered in the model: deposition to HVAC filters, deposition to supply ducts surfaces, deposition to indoor surfaces, deposition to return duct surfaces and leaving the building in exhaust air. Isothermal

conditions were assumed and particle resuspension, coagulation and phase change were ignored. The total air exchange rate, λ_s, is defined by

$$\lambda_s = \frac{Q_s}{V} \tag{6.23}$$

The outdoor air exchange rate, λ_o, was calculated by

$$\lambda_o = (1 - R)\lambda_s \tag{6.24}$$

For all model applications presented in this chapter, λ_s was set equal to 5 h^{-1} and R was set equal to 0.8, giving an outdoor air exchange rate of 1 h^{-1}. These are typical values for an occupied mechanically ventilated building.

Two types of filters common in commercial HVAC systems were considered, one with a 40% ASHRAE dust spot average efficiency and the other with an 85% ASHRAE duct spot average efficiency. The filtration efficiency, η_f, versus particle size of these two filters are shown in Figure 6.2. These filtration efficiency curves were generated by a combination of theory and fitting to experimental data by the method described in Riley *et al.* (2002). To determine filtration efficiencies for particle sizes smaller than 2.4 μm, linear interpolation between the measured data of Hanley *et al.* (1994) was used and filtration theory was used for larger particle sizes.

Deposition to indoor surfaces can be characterized by an indoor loss-rate coefficient, β, with dimensions of inverse time. The indoor loss-rate coefficient is related to the particle deposition velocity and is a strong function of particle size. The loss rate of particles to indoor surfaces is quantified by

$$r_{indoor} = \beta V C_{indoor} \tag{6.25}$$

where C_{indoor} is the indoor particle concentration. Indoor loss-rate coefficients were modeled using the method described by Riley *et al.* (2002) which combines theory and empiricism. In brief, the model of Lai & Nazaroff (2000) was applied with an indoor surface area to volume ratio of 3.0 m^{-1} and an indoor friction velocity of 3.0 cm/s to calculate β for particle sizes smaller than 0.06 μm. Because this model predicts lower loss-rate coefficients than have been observed experimentally at larger particle sizes, an empirical fit to the experimental data was used for particles larger than 0.06 μm.

Using this combination of models, the fates of two types of particles were evaluated: those drawn in through the outdoor air intake and those generated indoors. Examples with high-loss and low-loss ducts are presented to illustrate the expected range of importance of deposition in ventilation ducts. When considering high-loss duct runs, the single-pass losses that were used as model inputs were those with the 90th percentile cut-point diameter for both the supply and return ducts. For low-loss duct modeling scenarios, supply and return losses in duct runs were set equal to the losses of duct runs with the 10th percentile cut-point diameter.

6.2.2.a Outdoor particles

Using the stated methods for determining HVAC filtration, losses in supply and return ducts and losses to indoor surfaces, the fraction of outdoor particles remaining suspended indoors for a given particle size can be estimated by a steady-state material balance:

$$\frac{C_{indoor}}{C_{outdoor}} = \frac{\lambda_s (1-R)(1-l_s)\left[F_b + (1-\eta_f)(1-F_b)\right]}{\lambda_s + \beta - \lambda_s R(1-l_r)(1-l_s)\left[F_b + (1-\eta_f)(1-F_b)\right]} \tag{6.26}$$

In this equation, l_s and l_r are the fractional losses in supply and return duct runs, respectively, determined by equation (6.22). The fractions of outdoor particles drawn into the building that deposit on the filter, f_f, deposit in supply ducts, f_s, deposit on indoor surfaces, f_i, deposit in return ducts, f_r, and are exhausted from the building, f_e, are determined as follows:

$$f_f = \frac{\eta_f(1-F_b)}{(1-R)}\left[(1-R)+R(1-l_r)\frac{C_{indoor}}{C_{outdoor}}\right] \tag{6.27}$$

$$f_s = \frac{l_s}{(1-R)}\left[F_b+(1-F_b)(1-\eta_f)\right]\left[(1-R)+R(1-l_r)\frac{C_{indoor}}{C_{outdoor}}\right] \tag{6.28}$$

$$f_i = \frac{\beta}{\lambda_s(1-R)}\frac{C_{indoor}}{C_{outdoor}} \tag{6.29}$$

$$f_r = \frac{l_r}{(1-R)}\frac{C_{indoor}}{C_{outdoor}} \tag{6.30}$$

$$f_e = (1-l_r)\frac{C_{indoor}}{C_{outdoor}} \tag{6.31}$$

Fractional fates were determined for a variety of modeling scenarios. HVAC systems with no filters, 40% ASHRAE filters and 85% ASHRAE filters were considered, each with either low-loss or high-loss duct runs. Fractional fates of outdoor particles were also modeled for cases when 15% of the supplied air was allowed to bypass the HVAC filters ($F_b = 0.15$). The fraction of outdoor particles remaining suspended in indoor air was also evaluated for similar HVAC system configurations.

6.2.2.b Indoor particle emissions

When the fractional fates of particles generated indoors was considered, an arbitrary particle emissions profile was assumed and the generated aerosol was assumed to be

instantaneously mixed into the indoor space. An unsteady state mass balance leads to the following equation for the indoor concentration of particles:

$$\frac{dC_{indoor}}{dt} = \frac{E_{indoor}(t)}{V} + k_d C_{indoor} \tag{6.32}$$

Here, E_{indoor} is the arbitrary indoor particle emissions profile as a function of time and k_d is overall indoor particle decay constant calculated by the following equation:

$$k_d = \lambda_s + \beta - R\lambda_s(1-l_s)(1-l_r)\left[F_b + (1-\eta_f)(1-F_b)\right] \tag{6.33}$$

If equation (6.32) is integrated over a sufficiently long time, t_{end}, so that the indoor concentration has decayed to zero ($C_{indoor}(t_{end}) = 0$), then the time-averaged indoor particle concentration over that time period is

$$\overline{C_{indoor}} = \frac{M}{k_d V t_{end}} \tag{6.34}$$

where M is the total particle mass released indoors. This total mass is equal to

$$M = \int_{t=0}^{t_{end}} E(t)dt \tag{6.35}$$

The fractional fates of indoor-released particles were calculated by:

$$f_f = R\lambda_s(1-l_r)\eta_f(1-F_b)\frac{1}{k_d} \tag{6.36}$$

$$f_s = R\lambda_s l_s(1-l_r)\left[F_b + (1-\eta_f)(1-F_b)\right]\frac{1}{k_d} \tag{6.37}$$

$$f_i = \beta\frac{1}{k_d} \tag{6.38}$$

$$f_r = l_r\lambda_s\frac{1}{k_d} \tag{6.39}$$

$$f_e = \lambda_s (1-R)(1-l_r)\frac{1}{k_d} \tag{6.40}$$

The fates of particles released indoors were modeled under six different HVAC system scenarios. HVAC systems with no filters, with ASHRAE 40% filters and with ASHRAE 85% filters were considered for both low-loss and high-loss ducts.

6.3 Results

6.3.1 Particle losses in a single pass through supply and return ducts

The 10^{th}, 50^{th} and 90^{th} percentile cut-point diameters for return and supply duct runs are summarized in Table 6.3. Figures 6.3 and 6.4 show predicted single-pass particle losses for the modeled return and supply duct runs, respectively. Losses are shown for the duct runs with the 10^{th}, 50^{th} and 90^{th} percentile cut-point diameters. Figure 6.5 illustrates differences in the predicted fractional losses of a duct run when duct bends, internal insulation, or both, are ignored.

The average characteristics of the ten low-loss and ten high-loss return and supply duct runs are summarized in Tables 6.4 and 6.5, respectively. For particles that deposit in a duct run, deposition fates considered by the single-pass model are deposition to vertical duct walls, to horizontal duct floors, to horizontal duct ceilings, to duct bends or to S-connectors at duct junctions. Figure 6.6 shows the fraction of total losses resulting from deposition at each of these locations for particle sizes in the range 0.01-100 μm. The two panels in this figure show the average for the ten low-loss (top) and high-loss (bottom) return duct runs. In these plots, the fraction of the total losses for a certain particle size attributable to a given surface is indicated by the distance between the line for that surface and the next lowest line. The values in

parentheses in the figures provide the percentages of the total straight duct surface area associated with each surface type. Figure 6.7 shows the fraction of the total losses occurring in different classes of return ducts. The three straight duct classifications are large-horizontal ducts, small-horizontal ducts and large-vertical ducts; bends are classified as either small bends or large bends. The value in parenthesis after each straight duct label is the percentage of the total straight duct surface area associated with that duct class. The value after each bend label is the percentage of the total number of bends belonging to that bend class. No vertical return duct had a hydraulic diameter smaller than 0.4 m; consequently, there were no small-vertical ducts.

The fractions of total losses resulting from deposition to duct walls, duct floors, duct ceilings, duct bends and S-connectors in both low-loss and high-loss supply ducts are illustrated in Figure 6.8. This figure is analogous to Figure 6.6 for return ducts. Figure 6.9 shows the fraction of total particle losses occurring in different duct classes. All vertical supply ducts had hydraulic diameters greater than 0.4 m and were internally insulated. Thus, small-vertical-steel, small-vertical-insulated and large-vertical-steel ducts were not considered when classifying supply duct generations. In the top panel of Figure 6.9, considering low-loss supply ducts, there is no contribution to particle loss from deposition in small-horizontal-insulated ducts because there were no ducts of this type in these duct runs. Similarly, there were no large-horizontal-steel duct generations in the high-loss supply duct runs shown in the bottom panel of Figure 6.9.

6.3.2 Particle fates in a building: Outdoor particles

For particles drawn into the building via the outdoor air intake, the modeled fates of particles in the size range 0.01-100 μm are shown in Figure 6.10 for the case when the HVAC system has no filtration. The top panel of this figure is for the model scenario with low-loss supply and return ducts and the bottom panel shows the case with high-loss supply and return ducts. The fates considered are deposition in supply ducts, deposition to indoor surfaces, deposition in return ducts and exiting the building by exhaust. Figures 6.11 and 6.12 are similar to Figure 6.10 and show predicted fates of particles drawn into an HVAC system with either ASHRAE 40% filters (Figure 6.11) or ASHRAE 85% filters (Figure 6.12). In these figures, the fates considered are deposition to the filters, deposition in supply and return ducts, deposition to indoor surfaces and exhaust from the building. Deposition in supply and return ducts were combined in these figures to make the contribution of duct deposition to the total more visible. Figure 6.13 shows fates of outdoor particle when 15% of the supplied air bypasses the HVAC filters for high-loss ducts. The top panel shows results for the modeled building with ASHRAE 40% filters and the bottom panel shows results for the building with ASHRAE 85% filters.

Figure 6.14 shows the fraction of outdoor particles that remain suspended in indoor air for several modeling scenarios. Figure 6.15 shows how this fraction of outdoor particles indoors changes when 15% of the supplied air bypasses the HVAC filters.

6.3.3 Particle fates in a building: Indoor particle emissions

The modeled fractional fates of particles released indoors are illustrated in Figures 6.16-6.18. Figure 6.16 shows the fractional fates of particles released in the modeled

building with an unfiltered HVAC system with low-loss and high-loss ducts. Figures 6.17 and 6.18 show fractional fates of particle released indoors in buildings with either AHSRAE 40% filters (Figure 6.17) or ASHRAE 85% filters (Figure 6.18).

6.4 Discussion

6.4.1 Particle losses in a single pass through supply and return ducts

As shown in Figure 6.3, particle losses resulting from a single pass through return ducts are predicted to be negligible for particles less than 1 μm and nearly complete for particles larger than 50 μm. Predicted particle losses in supply duct runs (Figure 6.4) show a similar shape as for return duct runs, but losses are generally higher in the supply duct runs for particle sizes in the range 1-50 μm. Differences in duct runs are most important for determining losses of particles in the size range 1-50 μm. For example, 58% of 10 μm particles traveling through the supply duct run with the 90^{th} percentile cut-point diameter are predicted to deposit in the duct run, but only 12% are expected to deposit in the duct run with the 10^{th} percentile cut-point diameter. Less than 0.2% of 0.1 μm particles are predicted to deposit regardless of whether the duct run has the 10^{th} or 90^{th} percentile cut-point diameter. Factors contributing to higher losses in supply duct runs include the presence of internal insulation, more bends and longer duct runs.

In Table 6.4, duct runs with high particle losses are seen to have longer lengths, longer residence times, more bends and more total surface area than the average duct run, as expected. Conversely, the low-loss return duct runs, on average, have shorter lengths, shorter residence times, fewer bends and less surface area than the average duct run. Low-loss ducts also had less horizontal floor surface area and less surface

area associated with small ducts than the average return duct. Horizontal floor surface area is important for determining particle losses because deposition rates to duct floors are high. Small ducts are potentially important in determining particle losses because they have higher surface-area-to-volume ratios than larger ducts. The same trends can be seen in low-loss and high-loss supply ducts in Table 6.5. An additional trend apparent in Table 6.5 is that of increasing particle loss with increasing insulation surface area.

In Figure 6.5, single-pass particle losses are illustrated for the supply duct run with the 50^{th} percentile cut-point diameter under four modeling scenarios: without bends or insulation, with bends and without insulation, without bends and with insulation, and with both bends and insulation. The cut-point diameter when insulation and bends are ignored is 20.4 μm; when bends and insulation are included, the cut-point diameter is 15.2 μm. For particles smaller than 20 μm, the model lines for the case when both bends and insulation were considered and the case when only insulation was considered are nearly coincident, suggesting that internal insulation is much more important than bends in determining losses of these particles in this duct run.

Figure 6.6 illustrates that there is little difference among loss locations between the low-loss and high-loss return ducts for the range of particle sizes considered. For very small particles, losses to all three duct surface orientations contribute significantly to the total. For these small particles, diffusion controls deposition rates and deposition velocities to duct floors, ceilings and walls are equal. Only 14% of the total surface area in the low-loss return ducts was horizontal ceiling surface, but 27% of small particles that deposit by diffusion deposit to duct ceilings. This is because

losses are higher in small ducts which are usually horizontally oriented and have a higher percentage of ceiling surface than the average duct generation. Losses to S-connectors constitute a small fraction of total losses for all particle sizes. Although deposition rates to S-connectors are high relative to other duct surfaces, losses to S-connectors are low because they constitute only a small fraction of the total duct surface area. As seen in Figure 6.4, losses for particles smaller than 1 μm are very low in all supply ducts. When considering locations within duct runs where particles deposit, an important particle size range to consider is 1-30 μm. This size range encompasses a variety of biological particles that are of concern and losses of particles of this size in ducts are expected to be significant. In return ducts, losses of 1-30 μm particles result mainly from deposition to duct floors. Deposition in duct bends and deposition to vertical duct walls both make a significant contribution to particle losses. Duct bends are slightly more important in determining losses in low-loss duct runs compared to high-loss duct runs, even though these runs had, on average, fewer bends. The bends are more important in low-loss ducts because other surfaces play a less significant role in determining losses relative to high-loss ducts.

The importance of horizontal duct losses in determining total losses in return ducts is illustrated in Figure 6.7. Horizontal duct generations are predicted to dominate losses for all but the largest particles in both low-loss and high-loss ducts. The importance of small horizontal ducts increases in importance from low-loss to high-loss ducts. In the high-loss return ducts, 64% of the 10 μm particles that deposit do so to surfaces in small ducts even though these surfaces constitute only 15% of the total surface area in the duct runs. Deposition in small duct bends is predicted to contribute more to total losses in bends than deposition in large bends, especially in high-loss ducts. Part of

the reason for this is that smaller bend dimensions lead to higher particle Stokes numbers and higher deposition rates in bends. Another reason that small ducts and bends dominate losses at large particle sizes is that return duct runs begin with small ducts that increase in size as they join with other ducts. Thus, ducts and bends with smaller dimensions are encountered first in a single pass through a return duct run. When particles are lost in these smaller ducts and bends, there are fewer particles left in the airstream to deposit downstream where dimensions are larger.

Losses in small ducts are the most likely to lead to deposits that may disrupt duct airflows. Accumulated particle deposits in ducts with small flow areas will occupy a greater fraction of the flow area than deposits in large ducts. Return duct runs commonly begin with a small duct drawing in unfiltered indoor air with a broad particle size distribution. These two considerations suggest that small return ducts are the ducts most likely to have airflows influenced by accumulated particle deposits.

Figure 6.8 shows that, for most particle sizes, losses to all duct surfaces were important in both low-loss and high-loss supply duct runs, where duct insulation was present. For very small particles, the patterns of fractional losses in Figure 6.8 are similar to those for return duct runs seen in Figure 6.6. For larger particles, duct walls and ceilings played a more prominent role in determining losses in the insulated supply duct runs than in the return duct runs with no insulation. Deposition to duct floors and bends made a smaller contribution to the total loss in supply ducts. This is mainly the result of the large increase in predicted deposition velocities to insulated duct walls and ceilings compared to steel walls and ceilings.

In Figure 6.9, losses to insulated ducts are seen to be the major contributor to total losses for most particle sizes in supply duct runs. This was especially true in the high-loss supply duct runs where only a small fraction of the total deposit occurred at steel surfaces for particles larger than 0.5 μm. When losses are highest, in high-loss supply ducts, losses are mostly attributable to deposition in insulated duct generations. That approximately 14% of 1 μm particles that are lost deposit to small-horizontal-insulated duct surfaces which represent only 2% of the total duct surface area is another indication of the importance of insulation and small duct size in determining particle losses. Vertical ducts play a larger role in determining particle losses when they are insulated, as in the supply ducts in Figure 6.9, compared to when they are not insulated, as in the return ducts of Figure 6.7. In the top panel of Figure 6.9, deposition in insulated ducts leads to only 18% of total losses for small particles, but this fraction increases to 80% for 0.7 μm particles. For particles larger than 0.7 μm, the fraction of total losses due to deposition in insulated ducts decreases as the fraction of losses in steel ducts and in bends increases. Most small ducts at the ends of supply duct runs are steel and horizontal. Deposition to floors in these ducts is likely to account for the increase in losses in steel ducts for particles larger than 1 μm. In ducts with high losses, losses in bends are predicted to be a very small fraction of the total particle loss for particles smaller than 10 μm. Of note, however, is that when the same calculations were performed using the model of Pui *et al.* (1987) instead of that of McFarland *et al.* (1997) to calculate penetrations through bends, the fraction of total losses in bends increased significantly.

The information in Figures 6.6-6.9 could be useful in targeting remediation efforts if a hazardous aerosol is suspected to have entered an HVAC system. If resources for

remediation are limited or time consuming, activities could be focused on duct generations and locations expected to be the sites of greatest contamination. Because remediation techniques may differ for steel and insulated duct surfaces, prior knowledge of contamination sites may be useful in devising HVAC system remediation schemes.

Because particles deposited in ducts can degrade indoor air quality by contributing to biological growth, emitting of VOCs or by other interactions, deposition is generally undesirable. The potential for reducing particle accumulation in ventilation ducts, especially in the size range 1-30 μm, exists at the HVAC system design stage. Particle losses in duct are expected to be substantially reduced by minimizing both the usage of internal insulation and the length of horizontal ducts. External duct insulation is likely to be as thermally effective and durable as internal insulation. Closer attention to the sizing of ducts and balancing of airflows in the initial HVAC system design can reduce noise that creates the need for acoustic insulation in ducts. The use of external duct insulation and more careful design can reduce the usage of internal duct insulation, leading to reduced particle losses in ducts and potentially improved indoor air quality.

6.4.2 Particle fates in a building: Outdoor particles

Consider the fates of outdoor particles drawn into a building via an unfiltered HVAC system. Figure 6.10 illustrates that the majority of submicron particles are exhausted from the building. Most particles larger than 1 μm are predicted to deposit within the building. In the top panel of this figure, showing results for a building with low-loss ducts, a large fraction of super-micron particles are predicted to deposit to indoor

surfaces. In the modeled building with low-loss ducts, deposition in supply ducts is an important fate only for particles larger than 5 μm. The maximum percentage of particles depositing in low-loss return ducts is 3% for 12 μm particles. If ducts have high losses, deposition in supply ducts is expected to be a significant fate for particles as small as 1 μm. If losses in ducts are high, the fraction of 1-30 μm particles depositing to indoor surfaces is significantly reduced compared to a case in which losses in ducts are low.

For a case in which 40% ASHRAE filters are installed in the HVAC system supply ducts, Figure 6.11 shows a large decrease in indoor surface deposition and duct deposition as a particle fate compared to the unfiltered case. With filters installed, most particles are expected to be either filtered or exhausted. Particles larger than 4 μm are efficiently removed by filtration. In the case with high-loss ducts, deposition to duct surfaces is a fate comparable to deposition to indoor surfaces for most particle sizes. Duct deposition achieves maximum importance in this case for 1.8 μm particles, 14% of which are predicted to deposit in ducts. If the quality of filtration is improved to 85% ASHRAE filters, nearly all particles are either filtered or exhausted from the building, as shown in Figure 6.12. Particles that penetrate an 85% ASHRAE filter also penetrate duct runs and remain suspended in indoor air.

If 15% of the air supplied to the modeled building bypasses filtration, Figure 6.13 shows that it is the fates of super-micron particle that are affected the most. Comparing the top panel of Figure 6.13 to the bottom panel of Figure 6.11, a filter bypass fraction of 0.15 is predicted to have negligible influence on the fates of particles smaller than 2 μm when ASHRAE 40% filters are installed. Most larger

particles entrained in air that bypasses filtration are expected to deposit in ducts. Similar results were observed when ASHRAE 85% filters were considered with a filter bypass fraction of 0.15, as shown in the bottom panel of Figure 6.13. Filter bypass is a likely explanation for the observed accumulation of large particles and debris in supply ducts of HVAC systems with even high quality filtration.

Figure 6.14 illustrates the impact of duct deposition and HVAC filtration on the fraction of outdoor particles remaining suspended in indoor air, as predicted by the model. In a building with no filtration, there is an appreciable difference between the predictions with low-loss and high-loss ducts. For 1-10 μm particles, the fraction in the high-loss duct case is less than in the low-loss duct case by an amount in the range 0.07-0.15. As filtration is improved by adding ASHRAE 40% or 85% filters, differences in the concentration ratio between the low-loss duct and high-loss duct cases diminishes. Variations in filtration are predicted to play a much larger role in determining the fraction of outdoor particles indoors than variations in ventilation duct runs. Figure 6.15 shows the change in the predicted fraction of outdoor particles remaining indoors when 15% of the supply air bypasses filtration. Filter bypass increases the predicted concentration fraction to a small degree for all particles smaller than 10 μm. Filter bypass has a stronger effect on this concentration fraction when higher efficiency filters are implemented.

6.4.3 Particle fates in a building: Indoor particle emissions

For particles released inside a building with an unfiltered HVAC system, Figure 6.16 shows that their predicted fates follow the same general trends as the outdoor particles considered in Figure 6.10. Most submicron particles are expected to be exhausted

from the building before depositing and most larger particles are expected to deposit within the building. The main differences between the fates of outdoor particles and the fates of particles generated indoors are the deposition locations of larger particles. A greater fraction of indoor-released particles are predicted to deposit in return ducts. Most very large particles released indoors are expected to deposit to indoor surfaces, not in ventilation ducts as predicted for outdoor particles.

Figure 6.17 shows the expected fates of particles released in a building with 40% ASHRAE filters. In this case, deposition to indoor surfaces and ducts remains an important fate for large particles, and even for particles as small as 1 μm. For particles smaller than 4 μm deposition in high-loss ducts is a fate comparable in magnitude to deposition to indoor surfaces. For 1-30 μm particles, deposition in ducts may be an important fate. For 13 μm particles released indoors, 25% are predicted to deposit in high-loss ducts. Comparing Figure 6.18, where a building with 85% ASHRAE filters is modeled, to Figure 6.17, it can be seen that improving filtration does little to influence the ultimate fate of particles larger than 4 μm. Most large particles deposit to indoor surfaces or in the return ventilation duct before reaching the HVAC filters.

6.5 Conclusions

Empirical models for predicting deposition rates were applied to predict particle losses during the single pass of an aerosol through 120 duct runs. The modeled duct runs were 60 supply runs and 60 return runs chosen from four university buildings. Supply duct runs were a combination of steel duct generations and internally insulated surfaces; return duct runs included only steel generations. For nearly all modeled duct

runs, losses were negligible for particles smaller than 1 μm and complete for particles larger than 50 μm. Variations in the characteristics of duct runs were most important for determining the losses of 1-50 μm particles. Table 6.3 summarizes the range of cut-point diameters predicted for the modeled duct runs. Depositional losses were generally higher in supply duct runs than in return duct runs, mostly because of the presence of insulation in supply ducts. On average, losses were higher in duct runs with greater value of one or more of these attributes: length, total surface area, insulated surface area, small-duct surface area and number of bends.

Considering the particle diameter range 1-30 μm, losses in return ducts are predicted to be dominated by losses to the floors of horizontal ducts. When losses are highest in return ducts, a large fraction of the losses result from deposition to ducts that are small and horizontally oriented, even though these ducts constitute a small fraction of the total duct surface area. Losses in vertical ducts are very small compared to losses in horizontal ducts in the absence of insulation. When insulation is present, as in supply duct runs, losses to vertical surfaces are a more significant contributor to total particle losses, but losses in horizontal duct generations remain the most important for determining losses. The presence of insulation is the most important factor for determining particle losses in a duct run.

Empirical equations for predicting HVAC filtration efficiencies and particle losses to indoor surfaces were combined with loss predictions in supply and return ducts to evaluate the fates of particles in an archetypal mechanically ventilated building. Losses in ducts were predicted to play a small role in influencing exposures of building occupants to outdoor particles. The concentration of outdoor particles

remaining in indoor air changed by a maximum of 15 % (for 2 μm particles) when considering low-loss and high-loss ducts in the absence of filtration. The importance of duct losses as a fate of outdoor particles is diminished when HVAC filtration is present. With ASHRAE 40% filters, deposition in ducts with high losses is predicted to be a fate comparable to indoor surface deposition for particles smaller than 4 μm; larger particles are efficiently removed by filtration. If a fraction of supply air bypasses the HVAC filters, most large outdoor particles that would otherwise be filtered are expected to deposit in ducts rather than to penetrate to the indoor environment.

For 1-30 μm particles generated in a building with no filtration, a significant fraction may deposit in both supply and return ducts. When released within a building with ASHRAE 40% HVAC filters, a larger fraction of particles larger than 1 μm are predicted to deposit in ventilation ducts compared to particles drawn in from outdoors. Deposition in return ducts is a more important fate of particles released indoors than for outdoor particles. A significant percentage (up to 25%) of 1-30 μm particles generated indoors may deposit in ventilation ducts, even when relatively efficient ASHRAE 85% filters are installed. In addition to providing information useful for evaluating particle exposures, the modeling results have implications for HVAC system design and maintenance and for building remediation after the release of a hazardous aerosol.

Table 6.1 Characteristics of modeled buildings.

Building	Floors	Footprint area (m^2)	HVAC type[a]	Year built
A	7	1970	CAV	1961
B	7	1750	CAV	1966
C	7	1550	VAV	1993
D	7	1300	CAV	1957

[a] CAV = continuous air volume; VAV = variable air volume

Table 6.2 Characteristics of modeled duct runs. Reported values are averages for 60 supply or 60 return duct runs with the range in parentheses.

Parameter	Return duct runs	Supply duct runs
length (m)	48 (22-94)	55 (25-106)
residence time (sec)	9.7 (4-18)	10.7 (4-20)
insulated length (%)	0	52 (20-90)
number of bends (-)	5.1 (3-9)	6.2 (4-12)

Table 6.3 Values for the 10^{th}, 50^{th} and 90^{th} percentile cut-point diameters for a single pass through supply and return duct runs.

Rank	Cut-point diameter in return ducts (μm)	Cut-point diameter in supply ducts (μm)
10^{th} percentile	37.1	25.0
50^{th} percentile	24.9	15.2
90^{th} percentile	17.2	8.7

Table 6.4 Characteristics of low-loss and high-loss return duct runs compared to the average of all return duct runs.

Parameter	Average of 10 low-loss duct runs	Average of all 60 return duct runs	Average of 10 high-loss duct runs
length (m)	29	48	63
residence time (s)	5.6	9.7	14.1
number of bends (-)	3.6	5.1	5.8
total surface area (m^2)	97	169	199
wall surface area (%)	72	62	62
floor surface area (%)	14	19	19
ceiling surface area (%)	14	19	19
insulated area (%)	0	0	0
steel area (%)	100	100	100
large duct area[a] (%)	94	89	85
small duct area[a] (%)	6	11	15

[a] = for small ducts, $D_h \leq 0.4$ m; for large ducts, $D_h > 0.4$ m.

Table 6.5 Characteristics of low-loss and high-loss supply duct runs compared to the average of all supply duct runs.

Parameter	Average of 10 low-loss duct runs	Average of all 60 supply duct runs	Average of 10 high-loss duct runs
length (m)	38	55	70
residence time (s)	7.7	10.7	12.0
number of bends (-)	4.4	6.2	8.0
total surface area (m^2)	152	211	315
wall surface area (%)	60	60	58
floor surface area (%)	20	20	21
ceiling surface area (%)	20	20	21
insulated area (%)	66	73	89
steel area (%)	34	27	11
large duct area[a] (%)	94	89	87
small duct area[a] (%)	6	11	13

[a] = for small ducts, $D_h \leq 0.4$ m; for large ducts, $D_h > 0.4$ m.

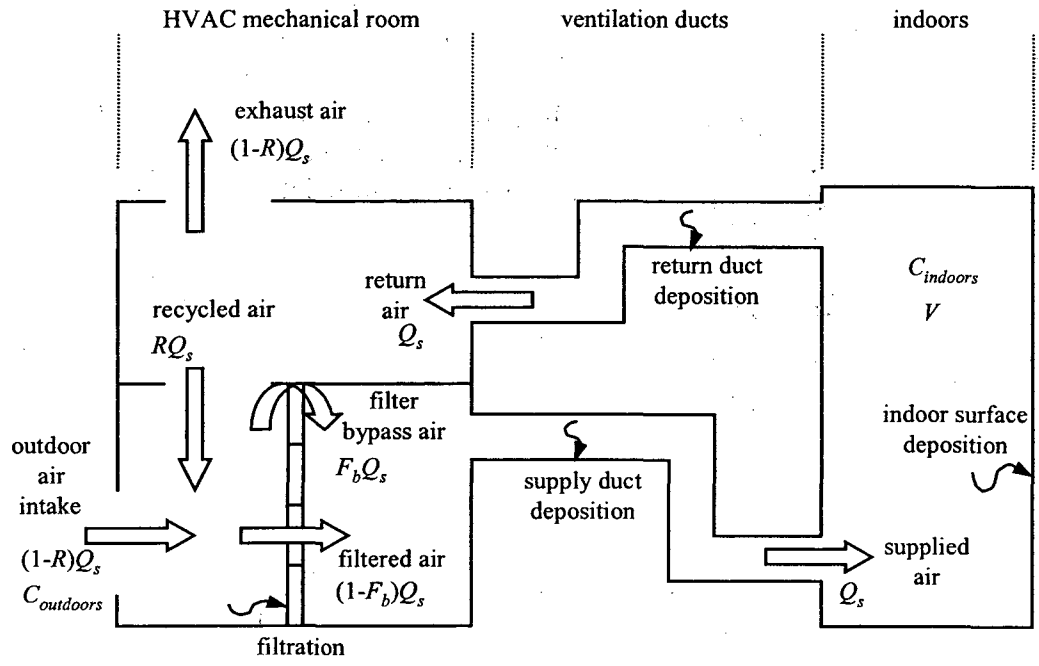

Figure 6.1 Schematic diagram showing airflow and potential particle fates when modeling particle fates in buildings.

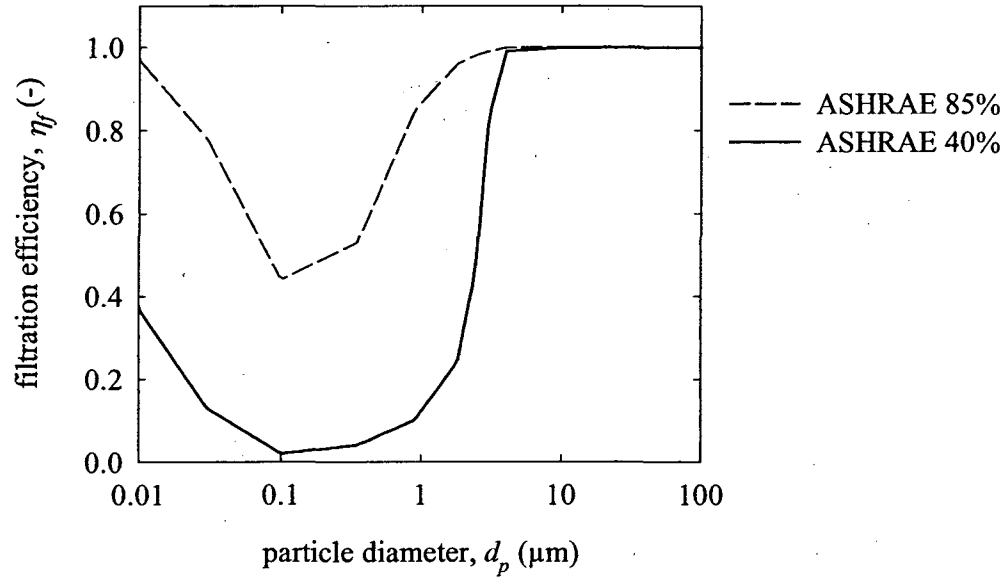

Figure 6.2 Filtration efficiency of ASHRAE 40% and ASHRAE 85% filters.

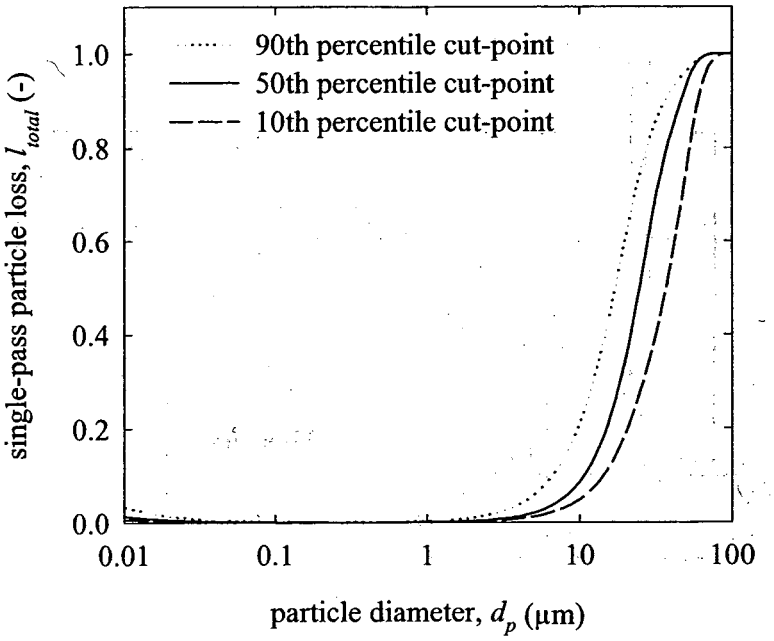

Figure 6.3 Predicted fractional losses for a single pass through return duct runs.

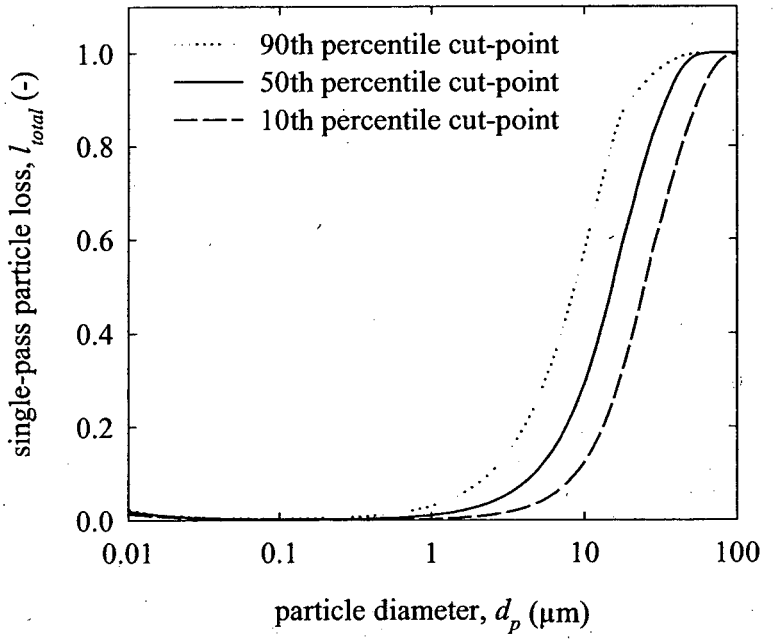

Figure 6.4 Predicted fractional losses for a single pass through supply duct runs.

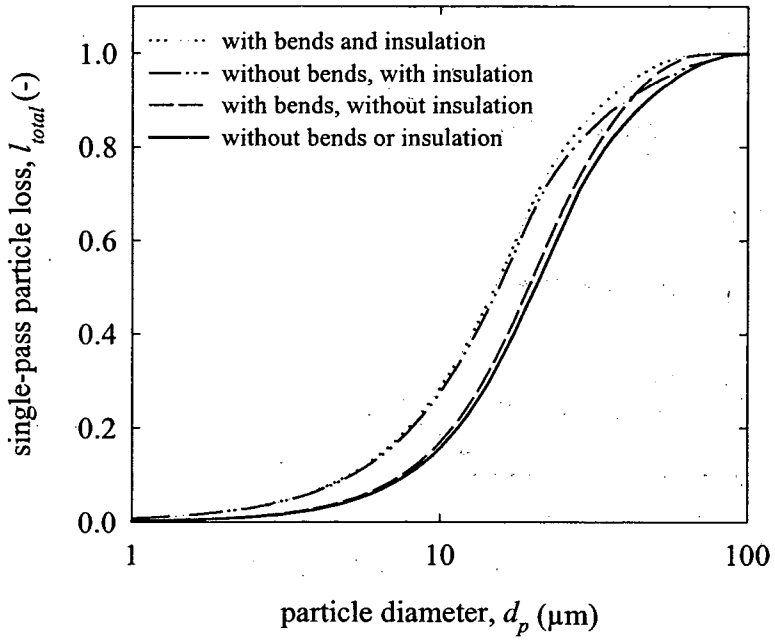

Figure 6.5 Predicted fractional losses in a medium-loss duct run considering the influence of duct bends and interior insulation.

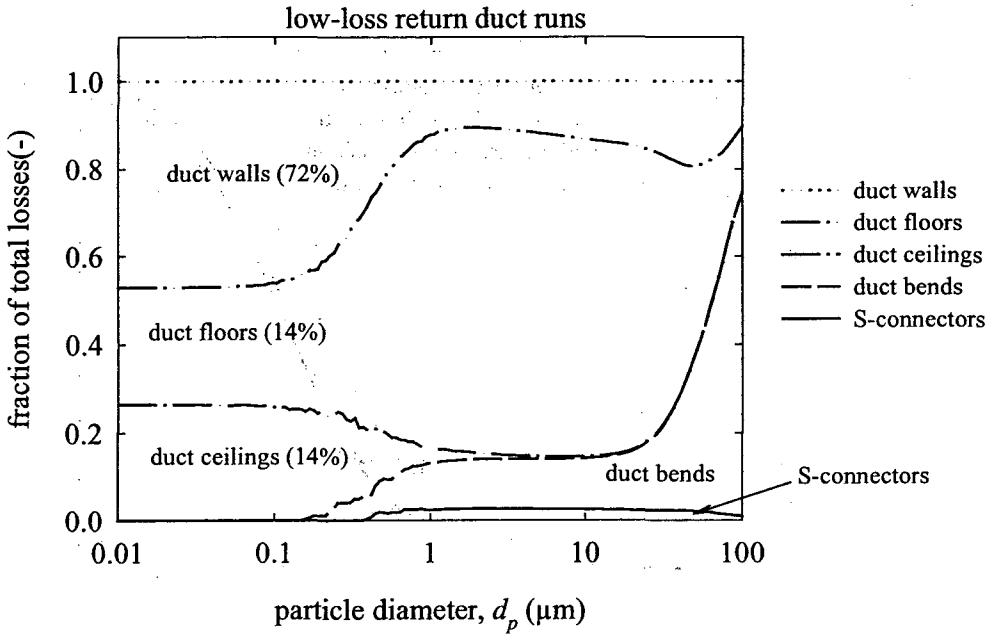

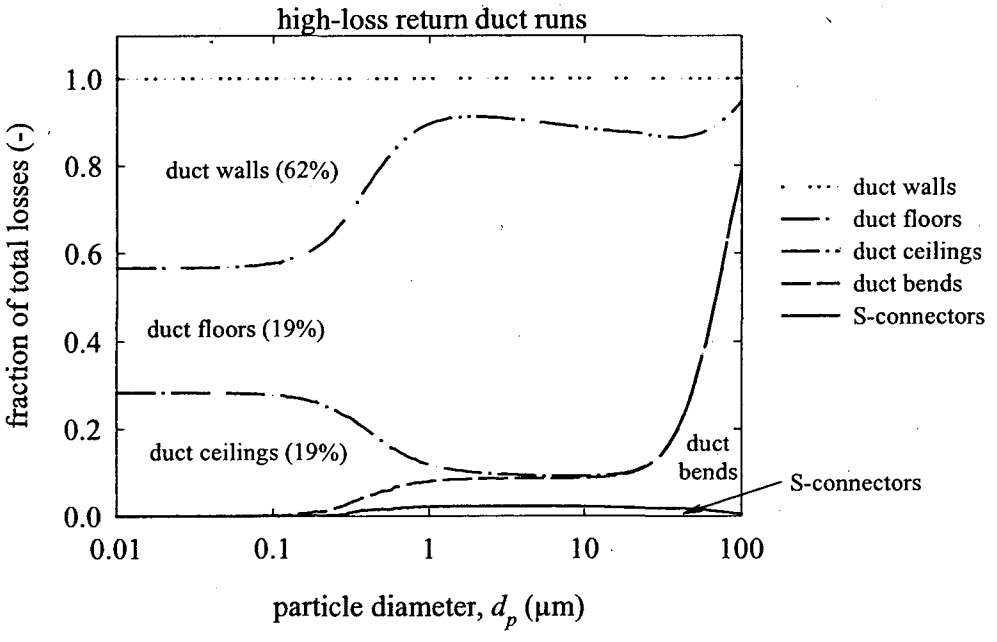

6.6 Fraction of total losses occurring at different duct surfaces for low-loss and high-loss return ducts.

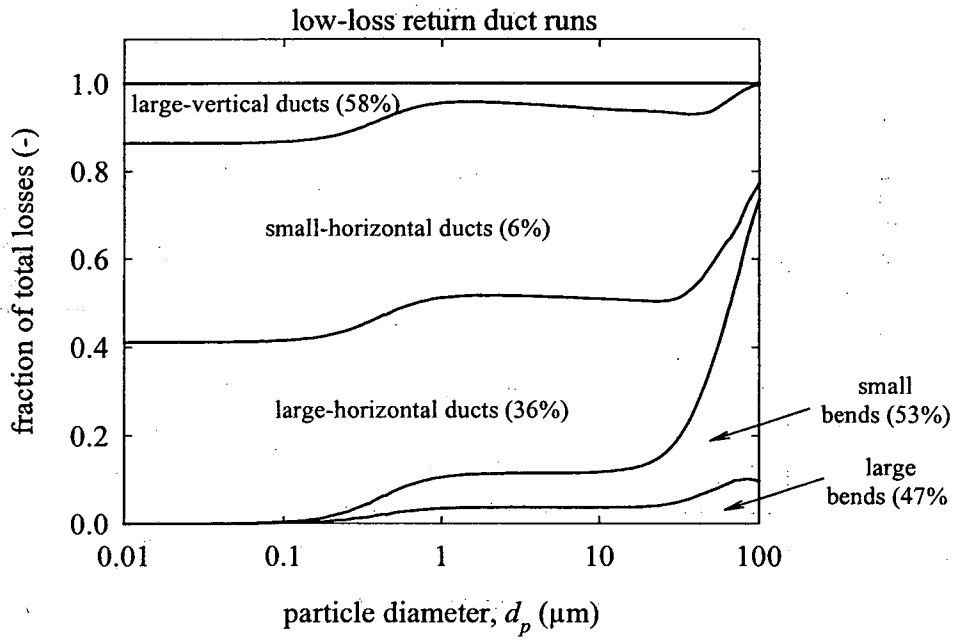

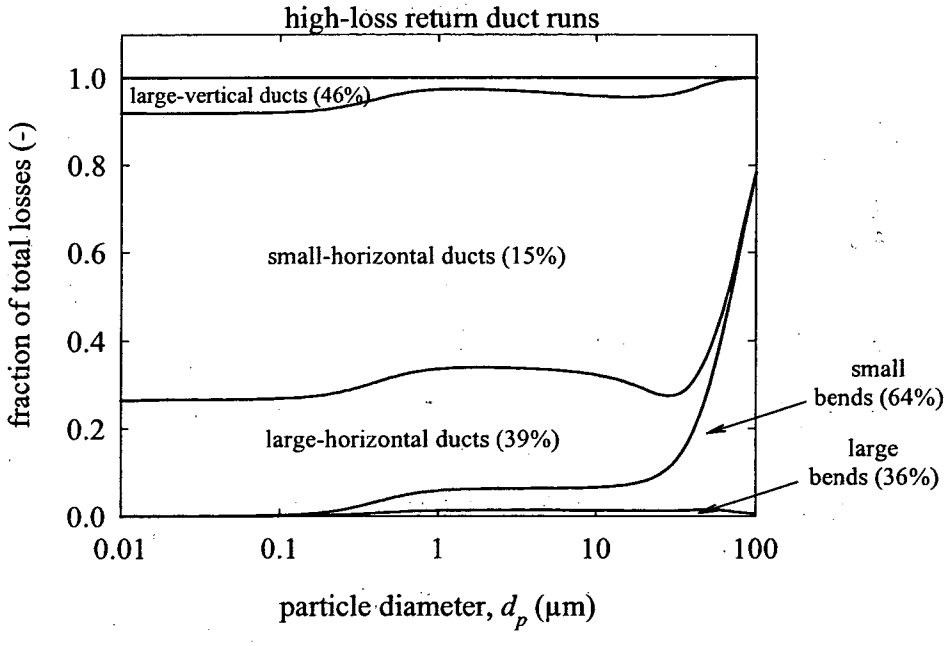

6.7 Fraction of total losses occurring in different duct generation classes for low-loss and high-loss return duct runs.

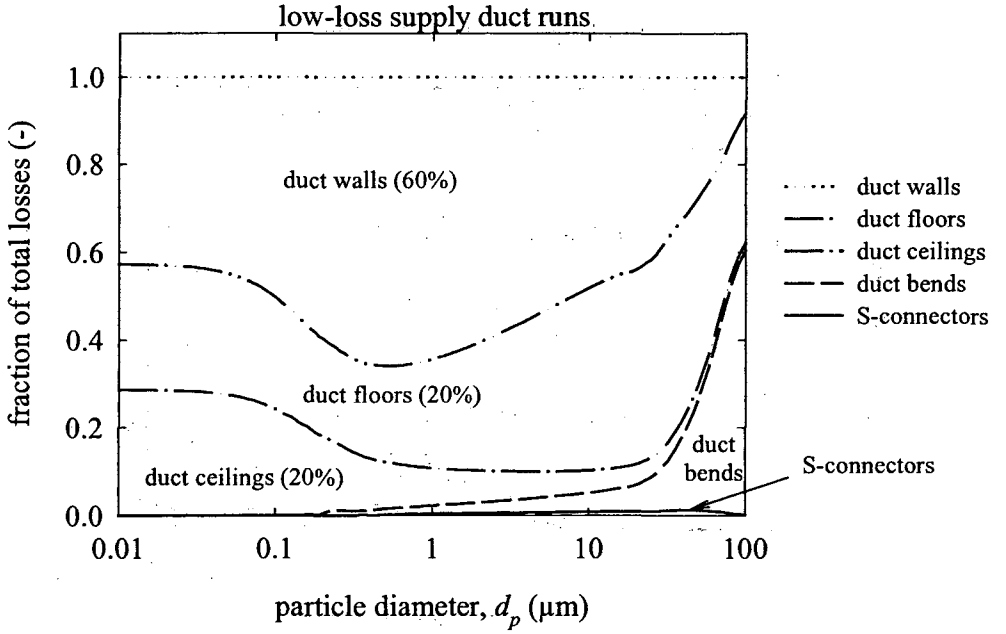

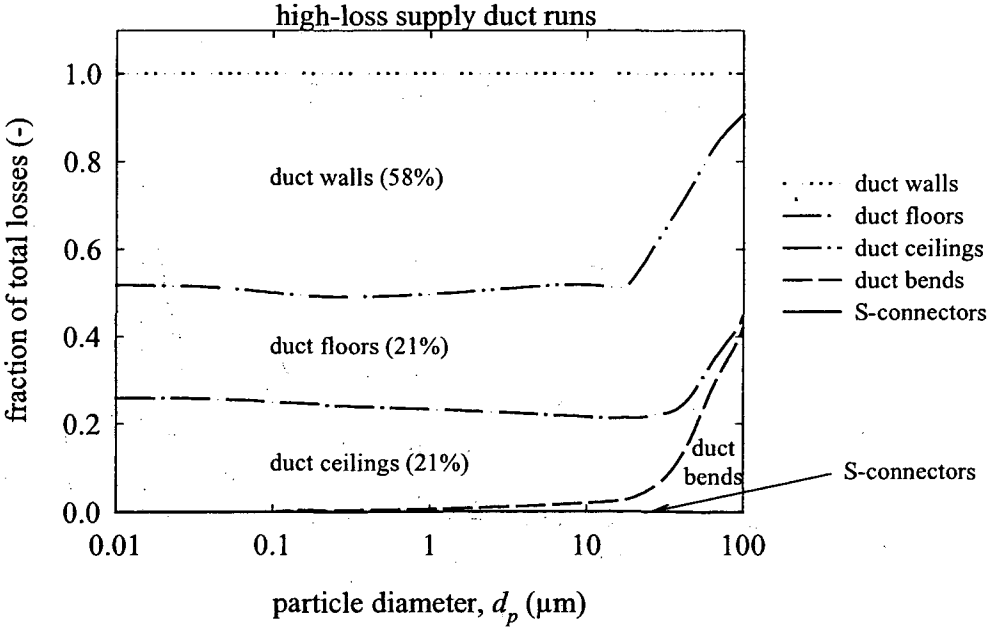

6.8 Fraction of total losses occurring at different duct surfaces for low-loss and high-loss supply duct runs.

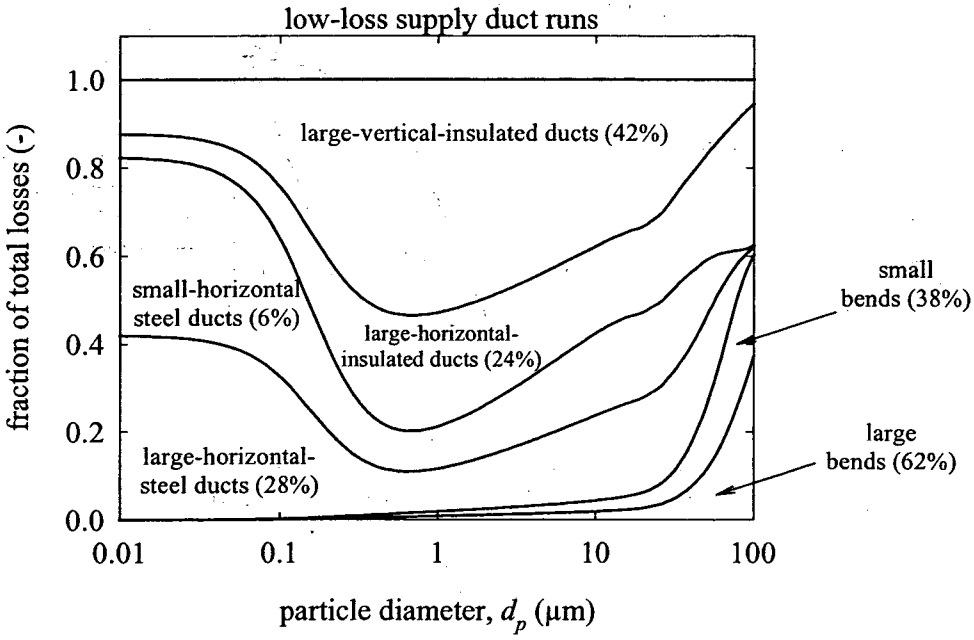

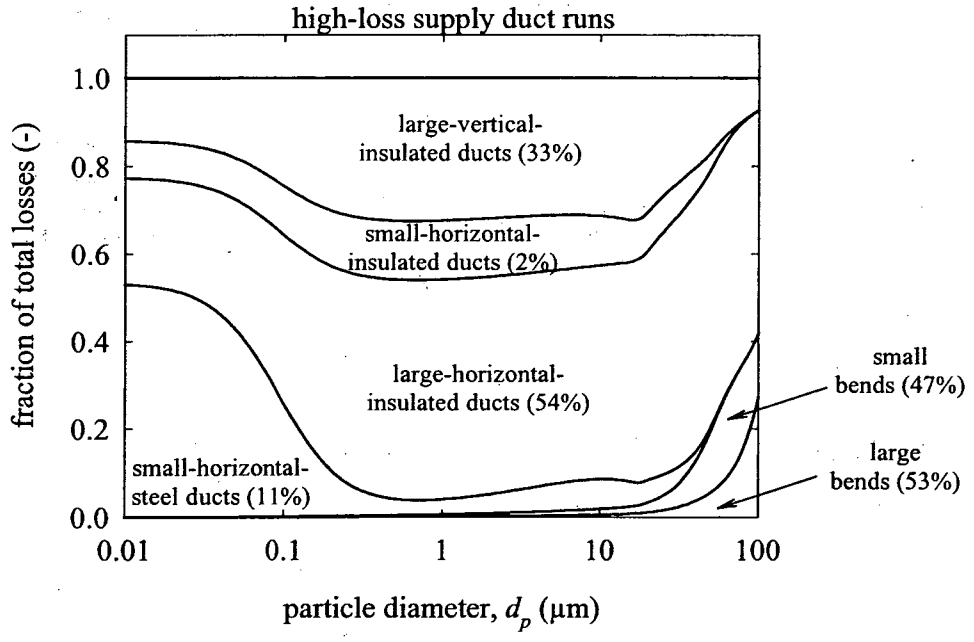

6.9 Fraction of total losses occurring in different duct generation classes for low-loss and high-loss supply duct runs.

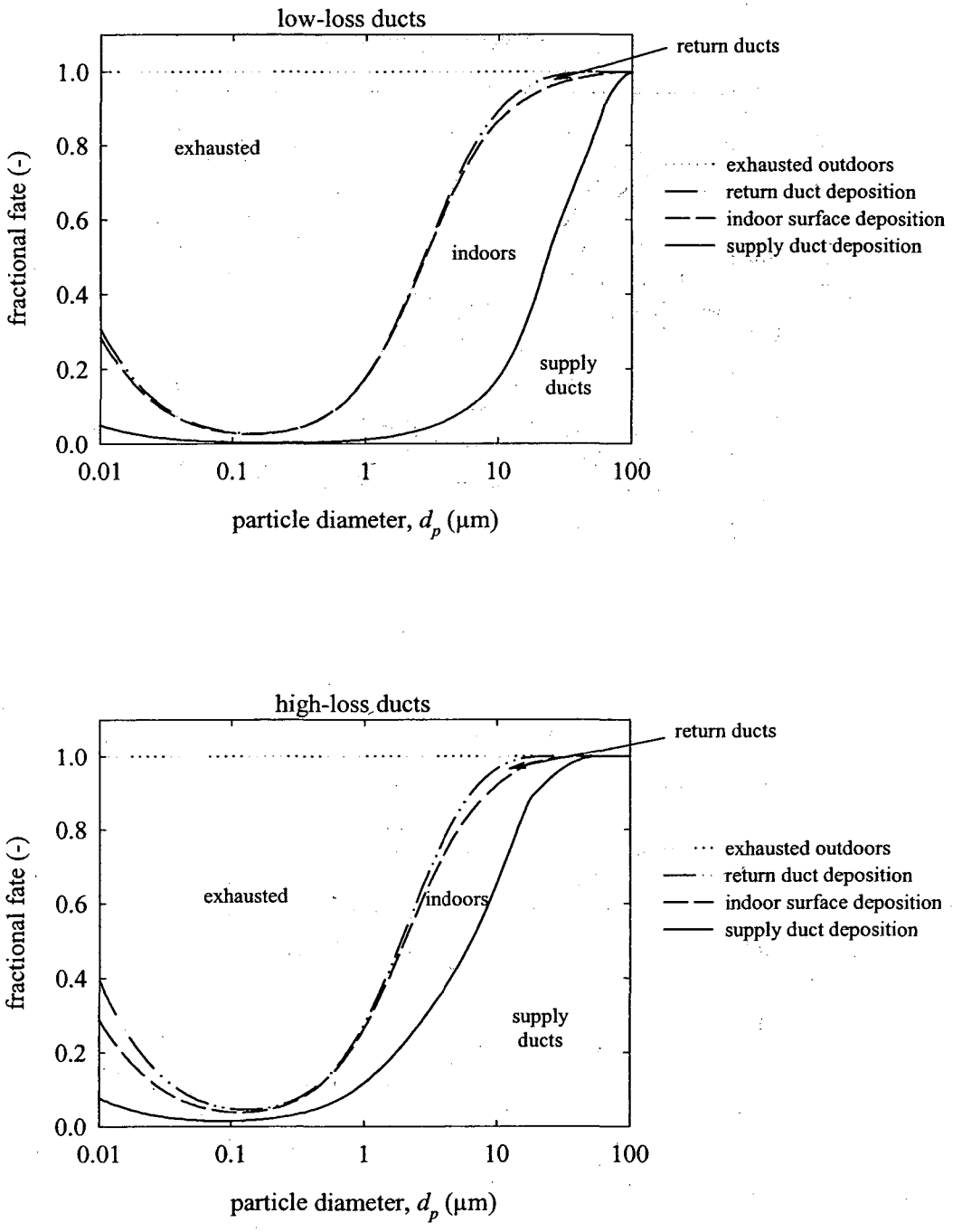

Figure 6.10 Predicted fractional fates of outdoor particles drawn into an unfiltered air intake for low-loss and high-loss ducts.

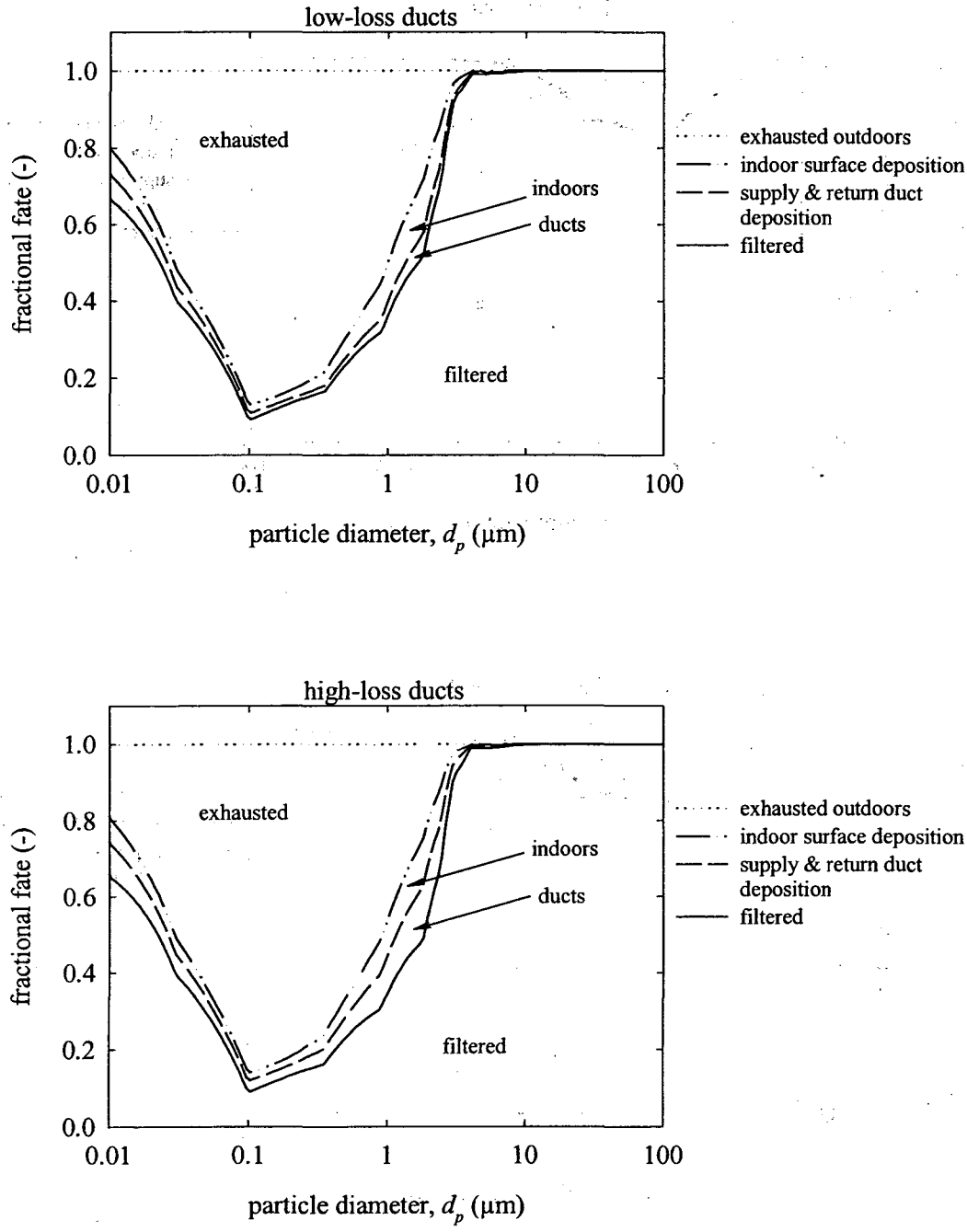

Figure 6.11 Predicted fractional fates of outdoor particles drawn into an air intake with ASHRAE 40% efficient filters for low-loss and high-loss ducts.

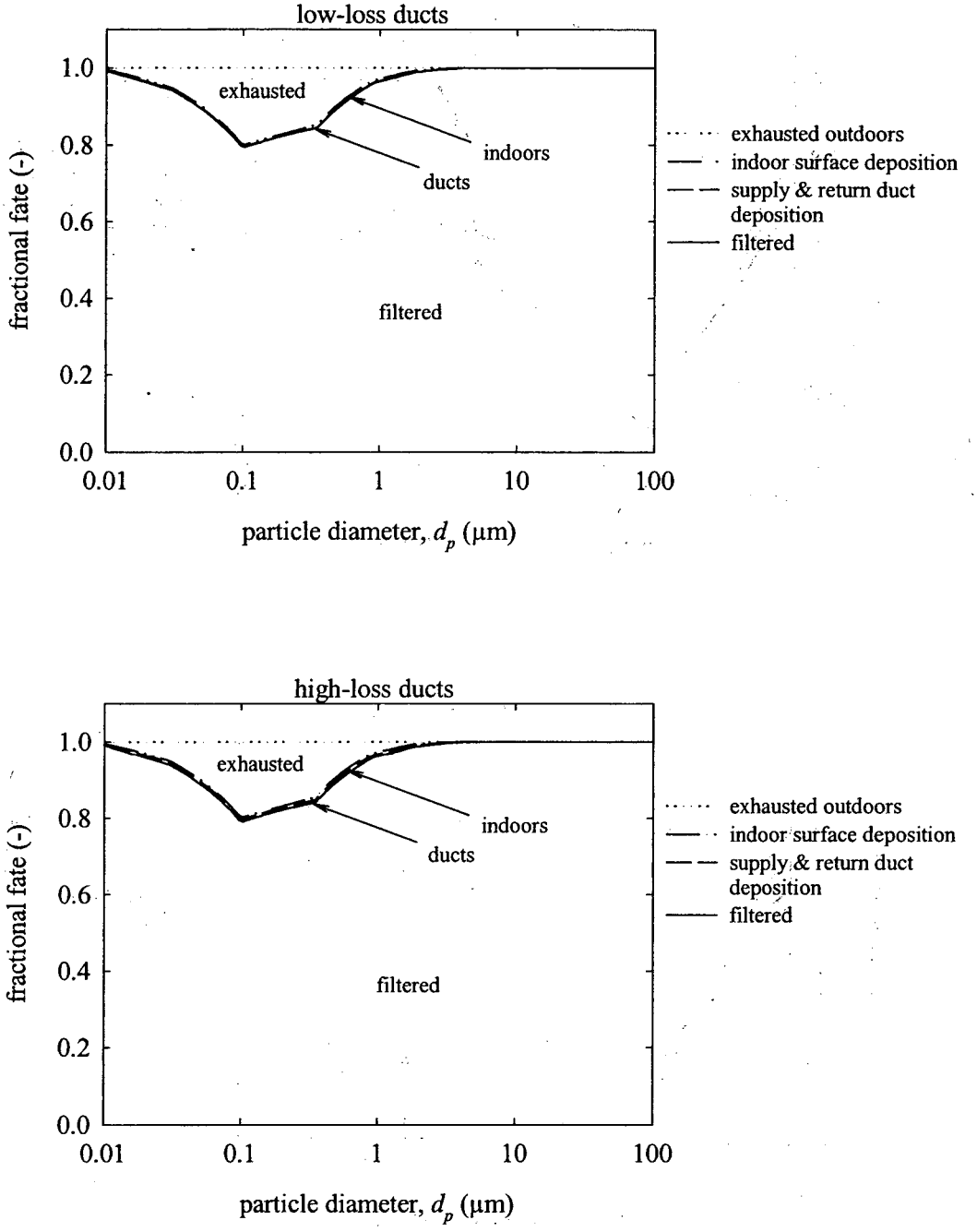

Figure 6.12 Predicted fractional fates of outdoor particles drawn into an air intake with ASHRAE 85% efficient filters for low-loss and high-loss ducts.

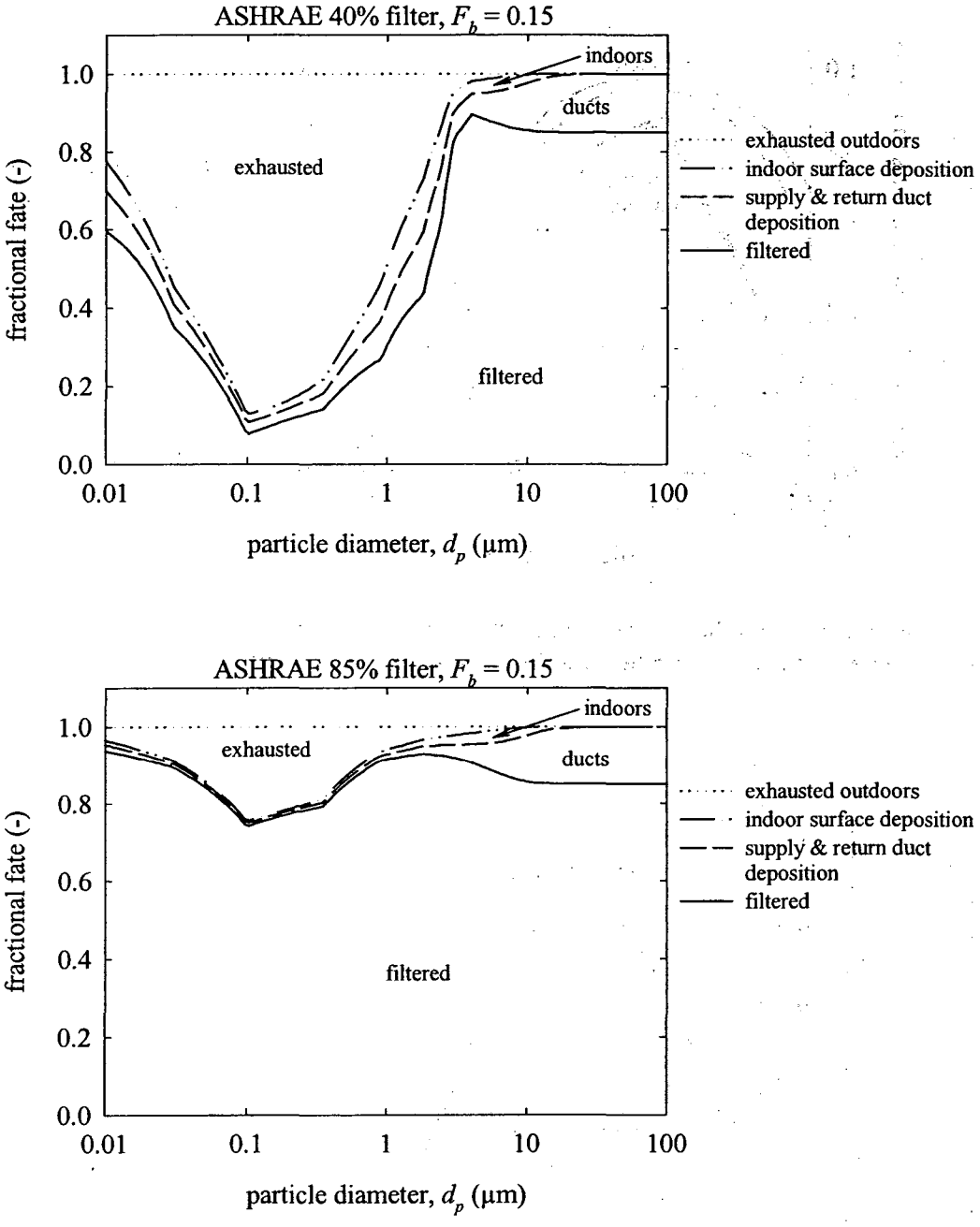

Figure 6.13 Predicted fractional fates of outdoor particles drawn into air intakes with either ASHRAE 40% or ASHRAE 85% efficient filters and a filter bypass fraction, F_b, of 0.15 for high-loss ducts.

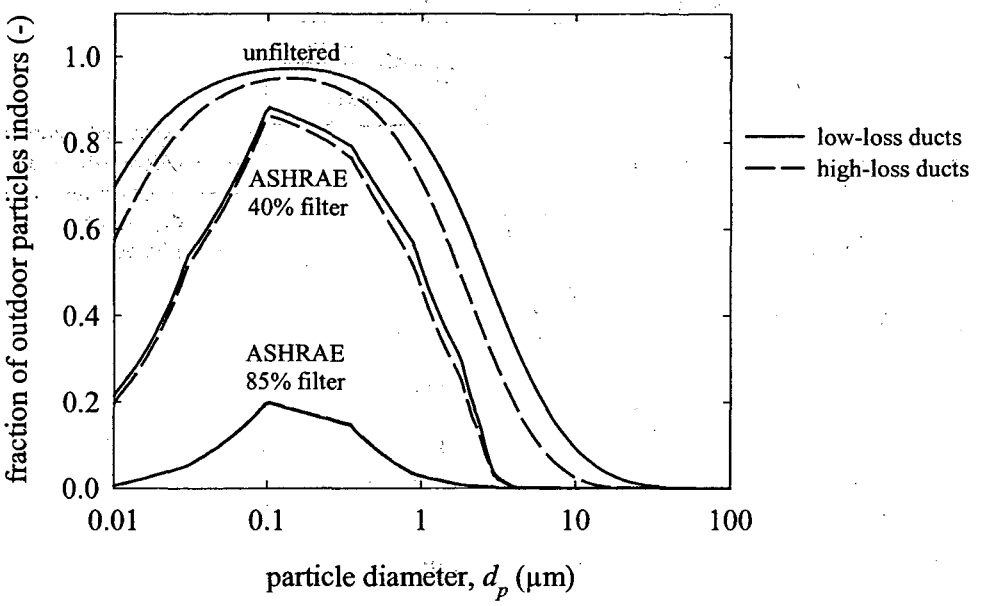

Figure 6.14 Predicted fraction of outdoor particles remaining indoors with different degrees of HVAC filtration and low-loss or high-loss ventilation ducts.

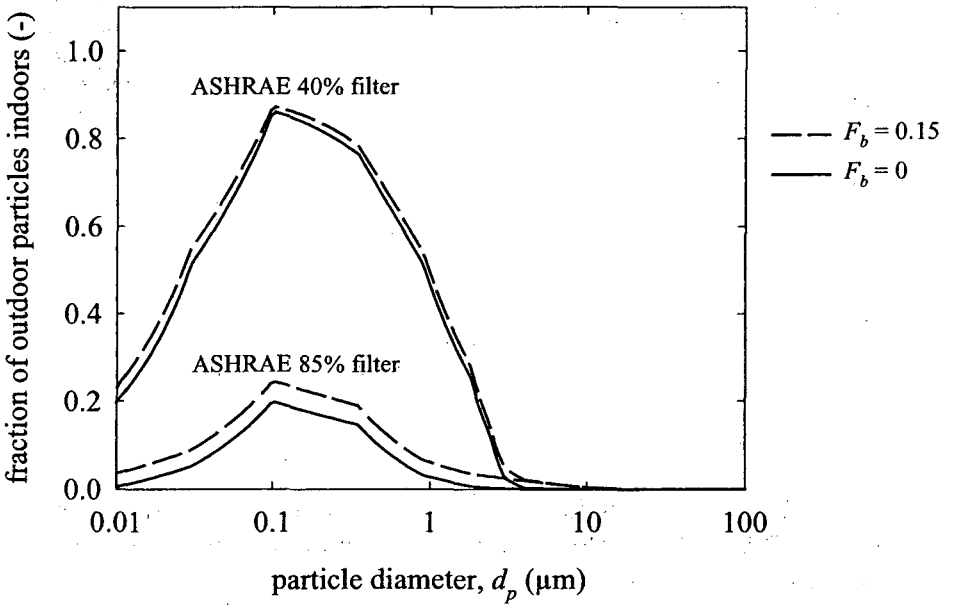

Figure 6.15 Predicted fraction of outdoor particles remaining indoors for particles drawn into an air intake with ASHRAE 40% filters and a bypass fraction, F_b, of zero or 0.15 for ducts with average losses.

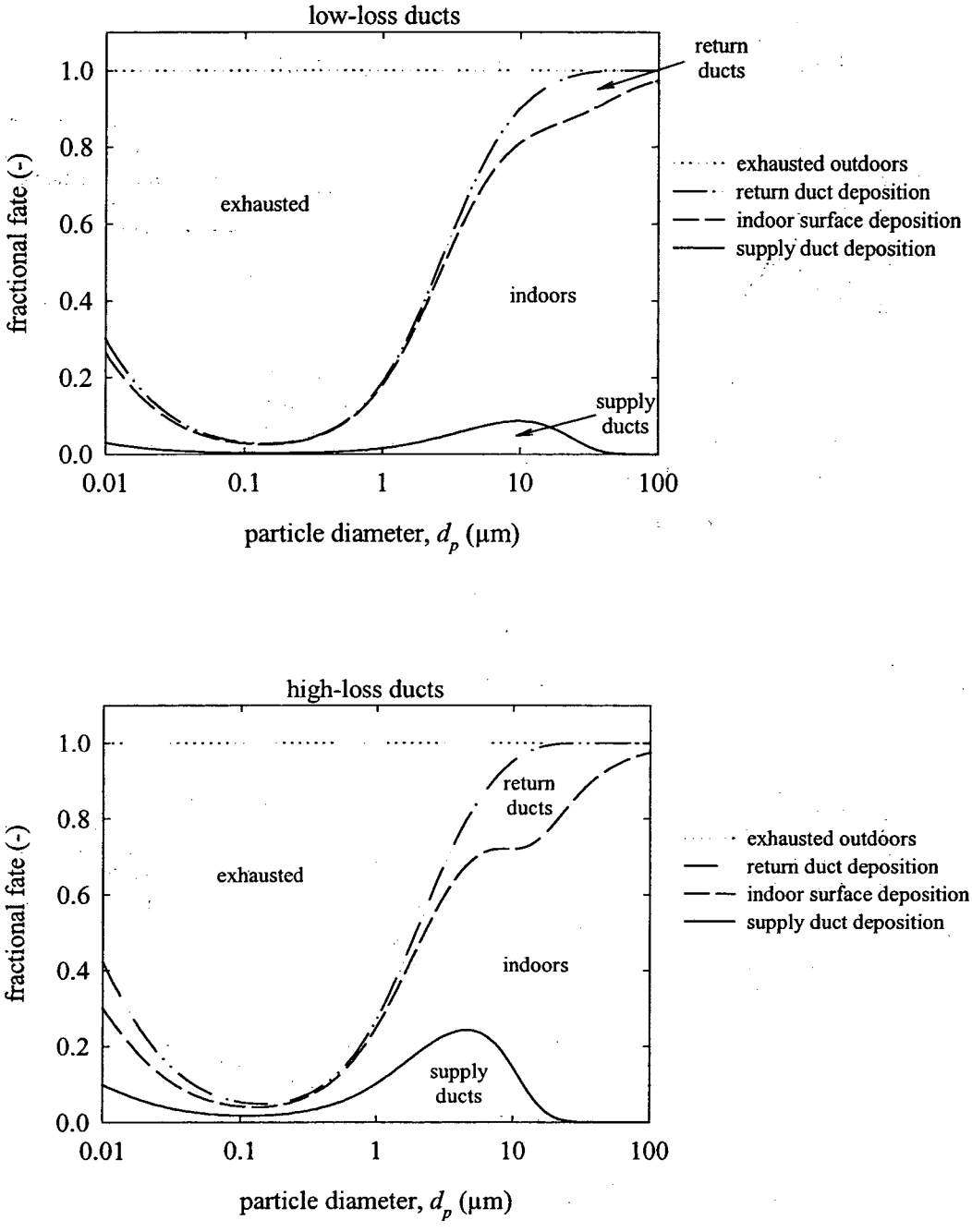

Figure 6.16 Predicted fractional fates of particles released in a building with an unfiltered ventilation system for both low-loss and high-loss ducts.

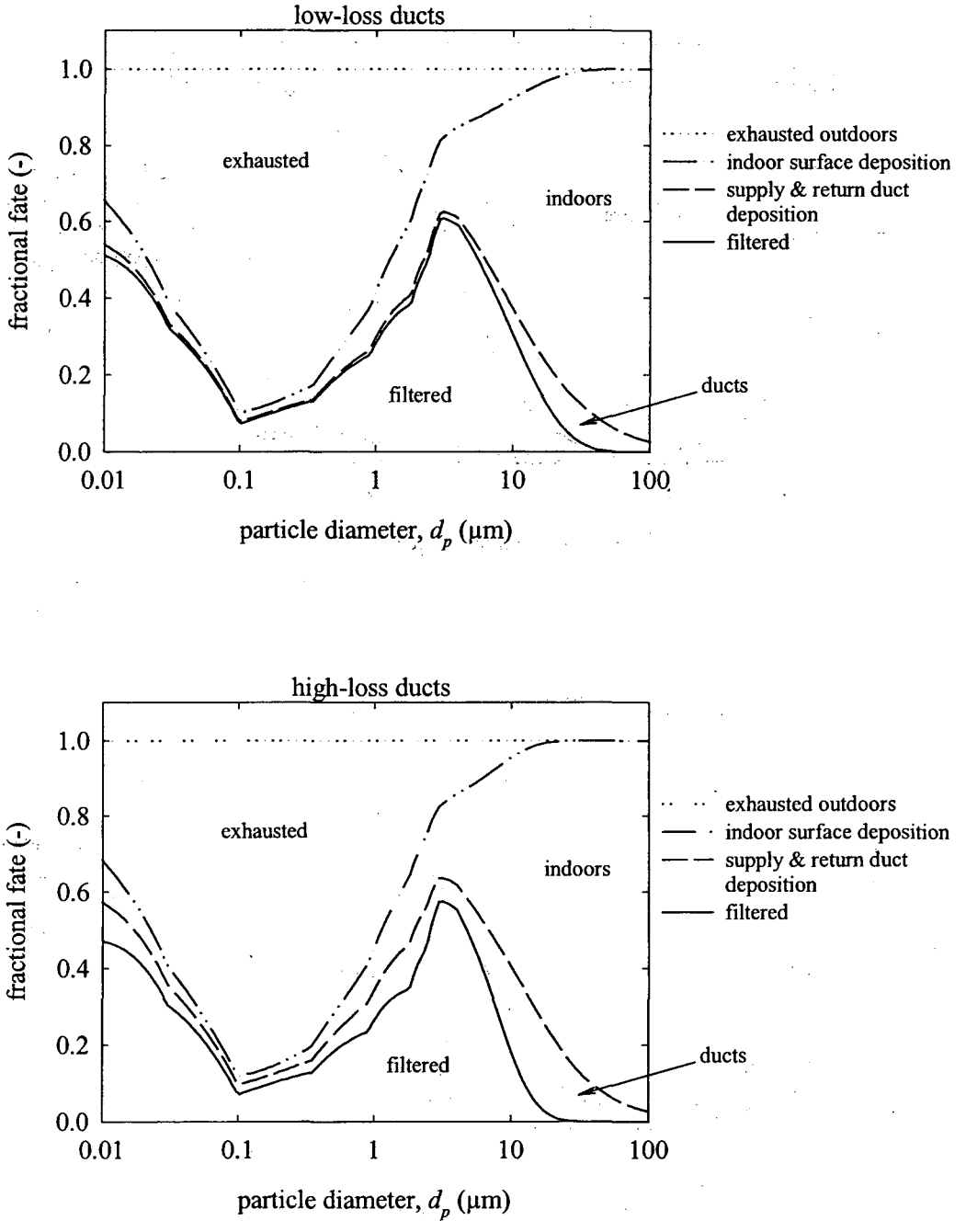

Figure 6.17 Predicted fractional fates of particles released in a building with ASHRAE 40% efficient filters for both low-loss and high-loss ducts.

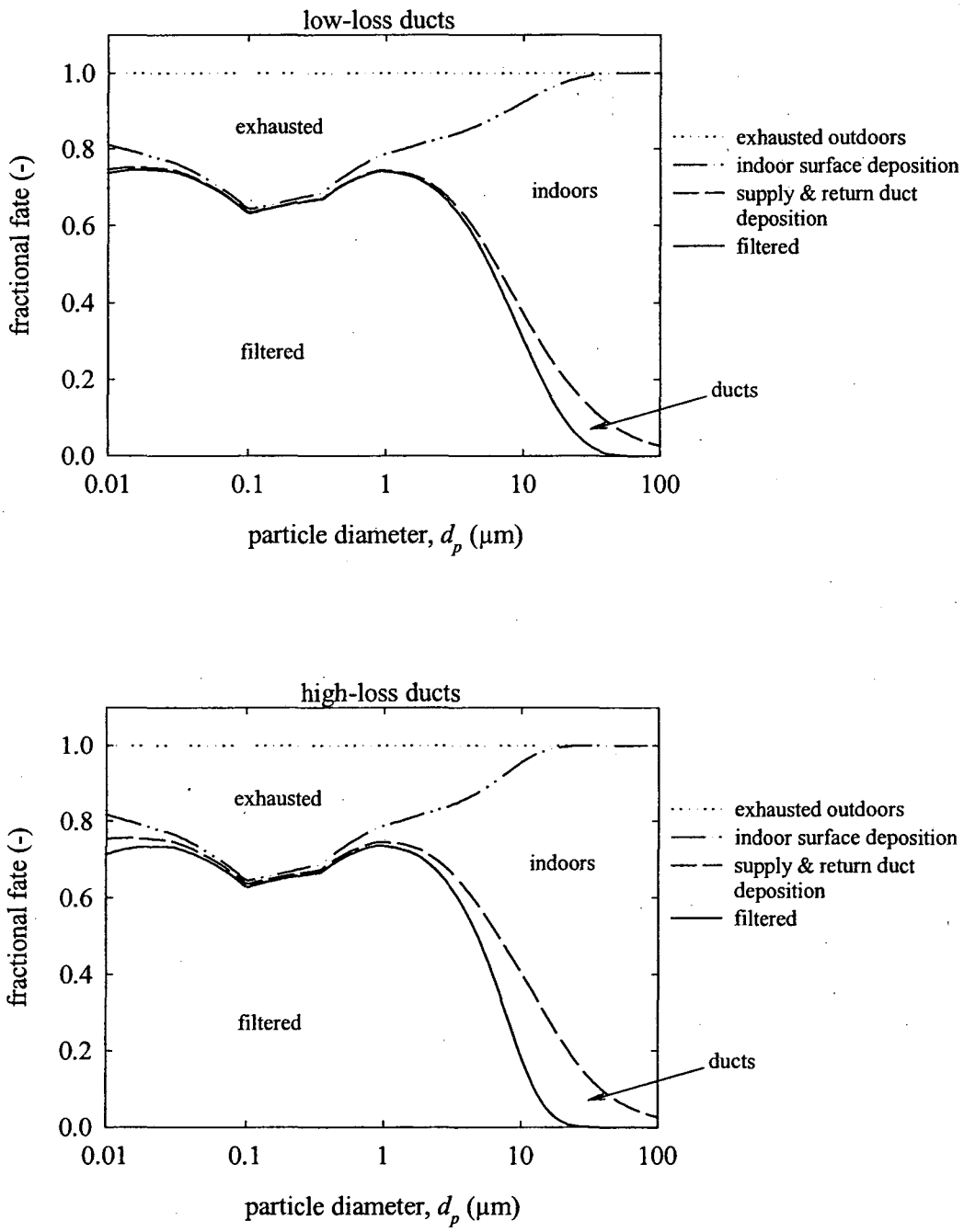

Figure 6.18 Predicted fractional fates of particles released in a building with ASHRAE 85% efficient filters for both low-loss and high-loss ducts.

CHAPTER 7

Summary and Recommendations for Future Research

7.1 Summary of Results

Particle deposition in ventilation ducts has been explored with experiments and models. Experiments were conducted to evaluate how air speed, particle size, duct surface orientation, duct material and proximity to flow disturbances influence deposition rates. The experiments provide high quality data that helps to fill gaps in the current knowledge of particle deposition in ventilation ducts. Empirical models were applied to evaluate magnitudes and locations of particle losses for an aerosol traveling through a range of ventilation duct runs. Modeling was also used to investigate the importance of deposition to ventilation ducts as a final fate of particles in an archetypal mechanically ventilated building.

7.1.1 Experiments

Experiments were performed in a laboratory to quantify particle deposition rates in horizontal, square ventilation ducts using real HVAC materials. The experiments were conducted in steel and internally insulated ducts over a range of particle sizes (1-16 μm) and air speeds (2-9 m/s) of concern in building ventilation systems. These experiments showed that in straight steel ducts with fully developed turbulence, deposition rates were highest at duct floors, intermediate at duct walls, and lowest at duct ceilings. In steel and insulated ducts, deposition rates to a given duct surface increased with an increase in either particle size or air speed. Deposition was much higher in insulated ducts than in uninsulated steel ducts, especially for vertical wall

and horizontal ceiling surfaces. For a given particle size and air speed in insulated ducts, deposition rates were nearly the same to the duct floor, wall and ceiling. The rough, fibrous character of the airstream side of the internal insulation appeared to be the strongest factor controlling deposition in the insulated ducts.

These experiments also indicated that particle deposition rates to surfaces in a ventilation duct run vary with position along its length. In most cases, deposition rates at and near flow disturbances were higher than in straight ducts with fully developed turbulence. Measured deposition rates in duct bends, at S-connectors found at duct junctions, and in straight ducts immediately after a bend or flow inlet were usually higher than rates in a straight duct with fully developed turbulence for the same particle diameter and air speed. Deposition in duct bends was strongly influenced by the airflow conditions at the bend inlet: deposition rates were higher where the inlet airflow was disturbed and lower when the inlet airflow was undisturbed. Measured deposition rates at S-connectors at duct junctions were nearly independent of the orientation of the S-connector. Deposition rates in straight ducts after flow disturbances were generally highest immediately after the disturbance, and were measured to relax to the same rates observed in straight ducts with fully developed flow within a distance of 10 hydraulic duct diameters in most cases.

Reasonably good correlations between the measured deposition rates at these locations and the particle Stokes number suggest that an inertial mechanism is important for determining the rates. Impaction is hypothesized as the mechanism contributing to the increase in deposition rates observed at all of the flow disturbances. The strong secondary flows within bends and in ducts with developing

turbulent flow profiles lead to strong air motions toward duct walls. The abrupt ridge associated with S-connectors is expected to lead to sharp changes in the direction of nearby airflows. Inertial particles in airflows directed at these surfaces will deposit if they cannot change direction as rapidly as the airflow. The experimental results suggest that the effects of flow disturbances on deposition should be considered when modeling particle deposition in ventilation ducts.

7.1.2 Models

Several models were compared to the deposition measurements made in straight galvanized steel and internally insulated ducts and in duct bends. In straight steel ducts, most models underpredicted observations at vertical duct walls and drastically underpredicted those at duct ceilings. In straight insulated ducts, model predictions were very sensitive to the assumed roughness level of the insulation. When roughness was used to empirically fit models to the data in insulated ducts, roughness values in the range 30-180 μm gave predictions that were of a similar magnitude as the experimental data; however, model-measurement agreement was generally poor. Published models for particle penetration through bends were found to be in general agreement with the experimental results in duct bends.

Modeling suggests that uncertainties in temperature gradients, turbulence gradients and duct surface roughness may explain differences between model predictions and measurements when considering deposition to a vertical steel wall. However, no explanation could be found for the deposition rates at the ceilings of steel ducts that were measured to be orders of magnitude higher than any model prediction. This model-measurement discrepancy suggests a fundamental lack in current approaches to

modeling particle interactions with turbulent airflows. One possible reason for the low model predictions is the use in models of average properties to represent turbulence structures that are variable and exhibit a distribution of properties. If deposition rates are more strongly influenced by turbulence events that are at the extreme of these distributions, the use of average turbulence properties may lead to significant underestimation of those rates. Another potential explanation for low model predictions are that secondary flows are not considered in any deposition model. Current models have been developed to predict deposition to flat plates or in round tubes. Secondary flows towards the walls of rectangular ducts would be expected to bring particles into closer proximity of these walls than in the walls of a round duct. Neither of these hypotheses has been explored quantitatively, but both seem plausible.

New empirical equations were developed for predicting deposition rates of particles to steel and insulated surfaces in ducts with fully developed turbulent flow. These equations, along with a published empirical equation for predicting bend penetration, were applied to evaluate particle losses in 60 supply and 60 return duct runs. Results suggest that duct losses are negligible for particle sizes less than 1 μm and complete for particle sizes greater than 50 μm. The 50^{th} percentile cut-point diameters were 15.2 μm in supply duct runs and 24.9 μm in return duct runs. Losses in supply duct runs were higher than in return duct runs, mostly because of the presence of internal insulation in supply ducts. In the absence of insulation, losses of particles larger than 1 μm were controlled by deposition to the floors of horizontal ducts and to duct bends. The presence or absence of a significant amount of insulation appears to be the most important factor for determining particle losses in a duct run.

A model considering HVAC filtration, deposition to indoor surfaces and deposition to ventilation ducts was applied to an archetypal mechanically ventilated building to evaluate the fates of particles in the building. The modeling results suggest that ventilation ducts play only a small role in determining indoor particle concentrations, especially when HVAC filtration is present. For the duct runs considered, losses in ventilation ducts were generally of a comparable magnitude to losses to indoor surfaces for most particle sizes. When filters are present and all supply air is filtered, modeling suggests that most particles are either filtered or exhausted; only a small fraction of particles are expected to deposit to ducts or indoor surfaces. However, in the case of a hazardous aerosol, even this small fraction may be important in terms of building remediation. The concentration of outdoor particles remaining in indoor air was modeled to be a maximum of 15% lower (for 2 μm particles) when particle losses in duct runs are high compared to when they are low. The importance of duct losses as a fate of outdoor particles is diminished with improved HVAC filtration.

7.2 Recommendations for Future Research

The experiments in this dissertation have shown that particle deposition in ventilation ducts depends on many factors. For a more complete understanding of particle deposition in ventilation systems, additional experimental evidence using real HVAC materials is still needed. Deposition to ducts with rough surfaces (different insulation types, flexible duct) and deposition within duct bends are two cases where deposition rates are known to be high enough to lead to significant particle losses, but still have relatively large associated uncertainties.

Duct surfaces vary widely. Because insulation in ducts was found to influence deposition and loss rates to such a strong degree, it is important to have a broader understanding of its effects. While the insulation used in these experiments is common in buildings, it represents only a single brand of a single type of duct insulation. Experiments similar to those reported in this dissertation (particle size resolved with direct measurement of deposition fluxes) investigating deposition to a range of duct insulation types would clarify the role of insulation in determining deposition rates. Also, experiments investigating deposition rates in flexible Mylar and aluminum ducts would provide needed empirical evidence and could allow for predictions of particle loss to be made in a wider range of buildings than can currently be considered. Additional information regarding the general prevalence of internal duct insulation would also be helpful to broaden the spectrum of buildings in which particle losses in ducts could be evaluated.

The current experimental data for penetration rates through duct bends exhibited scatter. Modeling suggested that this range of scatter is important in determining losses in ventilation ducts. Further experiments focusing on deposition within duct bends and in straight duct sections after bends would help reduce current uncertainties evaluating losses in duct runs. Ninety degree duct bends are generally present in five different orientations in HVAC systems. It is currently unclear what role, if any, bend orientation plays in particle deposition. For particle sizes larger than 1 μm, where deposition in bends is most important, it seems likely that changes in bend orientation are likely to influence deposition rates within bends owing to the interaction between gravitational acceleration and impaction. Deposition rates in straight duct sections after bends are likely to differ depending on the bend orientation as well. For

example, deposition to vertical duct walls after a right turn in a bend is likely to be larger than to duct walls after a bend that changes the flow direction from vertically downward to horizontal owing to the flow's greater tendency to impinge on the vertical wall in the former case. As a result of these multiple permutations, deposition rates in most straight ducts with developing turbulent flows downstream of bends are not readily predicted by empiricism using the current experimental data set.

The current range of experimental evidence is limited to 1-16 μm particles in the diffusion-impaction regime. Extending this range to include smaller particles in the diffusion regime and larger particles in the inertia-moderated regime would provide new information to either confirm or refute the current empirical model results in regimes where model applicability is less certain. Measurement of particle deposition over a wide range of sizes is important for a complete understanding of particle behavior. An understanding of small particles is important because they are more closely regulated as air pollutants; large particles are of concern because they could contribute significantly to total mass accumulations in ducts.

To advance understanding of the mechanisms leading to enhanced deposition to rough surfaces, a valuable contribution would be experiments that combine high quality deposition measurements and high quality measurements of the near-surface turbulent flow characteristics. Specifically, the profile of the dimensionless wall-normal fluctuating velocity component, v'^{+}_{rms}, near a wall is important for evaluating the contribution of turbophoresis to particle transport. Measurements quantifying changes in this profile with surface roughness, combined with measurements

quantifying changes in particle deposition rates with surface roughness, would help to better evaluate the role turbophoresis plays in determining deposition rates.

While particle deposition to duct ceiling surfaces is unlikely to be important for determining particle losses in ventilation ducts, it presents an interesting problem from a modeling standpoint. That deposition occurs at duct ceilings and cannot be explained by current mechanistic models suggests that these models miss an important aspect of the interaction between particles and air turbulence. The hypothesis that using average values to represent variable turbulence parameters fails to capture important aspects of the deposition process should be investigated using a detailed modeling approach.

Resuspension of particles from duct surfaces will influence the ultimate fates of particles in buildings. Resuspension was observed, but not quantified, in the current experiments. Resuspension has been the subject of some investigations, but it has long defied simple explanation and will almost certainly continue to do so. Focused experimental studies of particle resuspension from ventilation duct surfaces will help evaluate long term particle accumulation rates in ducts.

Finally, field measurements of particle size resolved deposition rates in, and penetration through, the ventilation ducts of real buildings would be another important contribution to the subject of this dissertation. Concentrations of ambient particles in duct runs may be measured by means of the shrouded probe and APS method developed and reported here. Such concentration measurements could be employed to evaluate particle penetrations through duct runs. Field measurements of deposition

velocities of ambient particles in ducts could be made through the use of filter samples and deposition plates made of HVAC materials. If microscopy were used to evaluate particle number counts on the filters and deposition plates, particle size-resolved deposition velocities could be evaluated. While microscopic analysis would be tedious and error-prone if performed manually, automated microscopic techniques could make this method a practical one. Field investigations of particle deposition in the ducts of buildings for a range of particle sizes would establish an important connection between particle behaviors in real ventilation ducts and those observed in laboratory experiments and models.

REFERENCES

Adam, N., Everitt, P. and Riffat, S.B. (1996) Aerosol deposition in ventilation ducts. *International Journal of Energy Research*, **20**: 1095-1101.

Alexander, L.G. and Coldren, C.L. (1951) Droplet transfer from suspending air to duct walls. *Industrial and Engineering Chemistry*, **43**: 1325-1331.

Altshul, A.D. (1970) *Hydraulic Resistance.* Moscow: Nedra Press, as cited in Idelchik (1986).

Anand, N. K. and McFarland, A. R. (1989) Particle deposition in aerosol sampling lines caused by turbulent diffusion and gravitational settling. *American Industrial Hygiene Association Journal*, **50**: 307-312.

Anand, N. K., McFarland, A. R., Wong, F. S., and Kocmoud, C.J. (1993) DEPOSITION: Software to calculate particle penetration through aerosol transport systems. *NUREG/GR-0006*, , Washington DC: Nuclear Regulatory Commission.

ASHRAE (1989a) ASHRAE Guideline 1-1989, Guideline for commissioning of HVAC systems. Atlanta: American Society of Heating, Refrigeration and Air-Conditioning Engineers.

ASHRAE (1989b) ANSI/ASHRAE Standard 62-1989, Ventilation for acceptable indoor air quality. Atlanta: American Society of Heating, Refrigeration and Air-Conditioning Engineers.

ASHRAE (1992) ANSI/ASHRAE Standard 55-1992, Thermal environmental conditions for human occupancy. Atlanta: American Society of Heating, Refrigeration and Air-Conditioning Engineers.

ASHRAE (1995) *ASHRAE Handbook: HVAC Applications*. Atlanta: American Society of Heating, Refrigeration and Air-Conditioning Engineers.

Batterman, S.A. and Burge, H. (1995) HVAC systems as emission sources affecting indoor air quality: A critical review. *HVAC&R Research*, **1**: 61-80.

Beal, S.K. (1970) Deposition of particles in turbulent flow on channel or pipe walls. *Nuclear Science and Engineering*, **40**: 1-11.

Belyaev, S.P. and Levin, L.M. (1972) Investigation of aerosol aspiration by photographing particle tracks under flash illumination. *Aerosol Science*, **3**: 127-140.

Bennet, C.O. and Meyers, J.E. (1962) *Momentum, Heat and Mass Transfer*. New York: McGraw-Hill.

Björkroth, M.K. (1999) Cleanliness of a ventilation system, how clean is clean enough? *Proceedings of Indoor Air '99*, Edinburgh, Scotland, Vol. 3, pp. 80-85.

Boersma, B.J. and Nieuwstadt, F.T.M. (1996) Large-eddy simulation of turbulent flow in a curved pipe. *Journal of Fluids Engineering*, **118**: 248-254.

Brockman, J.E. (1999) Aerosol sampling and transport: A tutorial. *1999 AAAR Conference Tutorial Notes*, Tacoma, Washington.

Brockman, J.E. (2001) Sampling and transport of aerosols. In *Aerosol Measurement: Principles, Techniques and Applications,* 2nd edition, edited by Baron, P.A. and Willeke, K., New York: John Wiley and Sons.

Brodkey, R.S. and Hershey, H.C. (1988) *Transport Phenomena: A Unified Approach*. New York: McGraw-Hill.

Brooke, J.W., Kontomaris, K., Hanratty, T.J. and McLaughlin, J.B. (1992) Turbulent deposition and trapping of aerosols at a wall. *Physics of Fluids A*, **4**: 825-834.

Brooke, J.W., Hanratty, T.J. and McLaughlin, J.B. (1994) Free-flight mixing and deposition of aerosols. *Physics of Fluids A*, **6**: 3404-3415.

Browne, L.W.B. (1974) Deposition of particles on rough surfaces during turbulent gas-flow in a pipe. *Atmospheric Environment*, **8**: 801-816.

Cantwell, B.J. (1981) Organized motion in turbulent flow. *Annual Review of Fluid Mechanics*, **13**: 457-515.

Caporaloni, M., Tampieri, F., Trombetti, F. and Vittori, O. (1975) Transfer of particles in nonisotropic air turbulence. *Journal of the Atmospheric Sciences*, **32**: 565-568.

Cebeci, T. and Smith, A.M.O. (1974) *Analysis of Turbulent Boundary Layers*. New York: Academic Press.

Chamberlain, A.C. (1966) Transport of gases to and from grass and grass-like surfaces. *Proceedings of the Royal Society of London Series A*, **290**: 236-265.

Chamberlain, A.C. (1967) Transport of lycopodium spores and other small particles to rough surfaces. *Proceedings of the Royal Society of London Series A*, **296**: 45-70.

Chamberlain, A.C., Garland, J.A. and Wells, A.C. (1984) Transport of gases and particles to surfaces with widely spaced roughness elements. *Boundary Layer Meteorology*, **29**: 343-360.

Chandra, S. and McFarland, A.R. (1996) Comparison of aerosol sampling with shrouded and unshrouded probes. *American Industrial Hygiene Association Journal*, **56**: 459-466.

Chapman, D.R. and Kuhn, G.D. (1986) The limiting behavior of turbulence near a wall. *Journal of Fluid Mechanics*, **170**: 265-292.

Chen, M. and McLaughlin, J.B. (1995) A new correlation for the aerosol deposition rate in vertical ducts. *Journal of Colloid and Interface Science*, **169**: 437-455.

Chen, Q. and Ahmadi, G. (1997) Deposition of particles in a turbulent pipe flow. *Journal of Aerosol Science*, **28**: 789-796.

Cheong, K.W. (1997) Deposition of aerosol particles in ductwork. *Applied Energy*, **57**: 253-261.

Cherukat, P. and McLaughlin, J.B. (1994) The inertial lift on a rigid sphere in a linear shear flow field near a flat wall. *Journal of Fluid Mechanics*, **263**: 1-18.

Choi, H., Moin, P. and Kim, J. (1993) Direct numerical simulation of turbulent flow over riblets. *Journal of Fluid Mechanics*, **255**: 503-539.

Cleaver, J.W. and Yates, B. (1975) A sub layer model for the deposition of particles from a turbulent flow. *Chemical Engineering Science*, **30**: 983-992.

Colebrook, F. (1939) Turbulent flow in pipes with particular reference to the transition region between the smooth and rough pipe laws. *Journal of the Institution of Civil Engineering*, **4**: 14-25, as cited in Idelchik (1986).

Collet, C.W., Nathanson, T., Scott, J.A., Baer, K. and Waddington, J. (1999) The impact of HVAC system cleaning on levels of surface dust and viable fungi in ductwork. *Proceedings of Indoor Air '99*, Edinburgh, Scotland, Vol. 3, pp. 56-61.

Corino, E.R. and Brodkey, R.S. (1969) A visual investigation of the wall region in turbulent flow. *Journal of Fluid Mechanics*, **37**: 1-30.

Crandall, M.S. and Sieber, W.K. (1996) The National Institute for Occupational Safety and Health indoor environmental evaluation experience, Part I: Building

environmental evaluations. *Applied Occupational and Environmental Hygiene*, **11**: 533-539.

Davies, C.N. (1966a) Deposition of aerosols from turbulent flow through pipes. *Proceedings of the Royal Society of London Series A*, **289**: 235-246.

Davies, C.N. (1966b) Brownian deposition of aerosol particles from turbulent flow through pipes. *Proceedings of the Royal Society of London Series A*, **290**: 557-562.

Davies, J.T. (1983) A new theory of aerosol deposition from turbulent fluids. *Chemical Engineering Science*, **38**: 135-139.

Delp, W.W., Matson, N.E., Tschudy, E., Modera, M.P. and Diamond, R.C. (1997) Field investigation of duct system performance in California light commercial buildings. *Report LBNL-40102*, Berkeley, California: Lawrence Berkeley National Laboratory.

Demare, S., Labraga, L. and Tournier, C. (1999) Comparison and scaling of the bursting period in rough and smooth walls channel flows. *Journal of Fluids Engineering*, **121**: 735-746.

Diu, C.K. and Yu, C.P. (1980) Deposition from charged aerosol flows through a pipe bend. *Journal of Aerosol Science*, **11**: 397-402.

Durst, F., Milojevic, D. and Schönung, B. (1984) Eulerian and Lagrangian predictions of particulate two-phase flows: A numerical study. *Applied Mathematical Modeling*, **8**: 101-115.

Durst, F., Jovanović, J. and Sender, J. (1995) LDA measurements in the near-wall region of a turbulent pipe flow. *Journal of Fluid Mechanics*, **295**: 305-335.

El-Shobokshy, M.S. and Ismail, I.A. (1980) Deposition of aerosol particles from turbulent flow onto rough pipe wall. *Atmospheric Environment*, **14**: 297-304.

El-Shobokshy, M.S. (1983) Experimental measurements of aerosol deposition to smooth and rough surfaces. *Atmospheric Environment*, **17**: 639-644.

Erhart, D.L. (1986) Turbulent aerosol deposition and reentrainment. Ph.D. Dissertation, University of California, Berkeley, California.

Fan, F-G. and Ahmadi, G. (1993) A sublayer model for turbulent deposition of particles in vertical ducts with smooth and rough surfaces. *Journal of Aerosol Science*, **24**: 45-64.

Fan, F-G. and Ahmadi, G. (1994) On the sublayer model for turbulent deposition of aerosol particles in the presence of gravity and electric fields. *Aerosol Science and Technology*, **21**: 49-71.

Fan, F-G. and Ahmadi, G. (1995) A sublayer model for wall deposition of ellipsoidal particles in turbulent streams. *Journal of Aerosol Science*, **26**: 813-840.

Fichman, M., Gutfinger, C. and Pnueli, D. (1988) A model for turbulent deposition of aerosols. *Journal of Aerosol Science*, **19**: 123-136.

Fisk, W.J., Delp, W., Diamond, R., Dickerhoff, D., Levinson, R., Modera, M., Nematollahi, M. and Wang, D. (1999) Duct systems in large commercial buildings: Physical characterization, air leakage and heat conduction gains. *Report LBNL-42339*, Berkeley, California: Lawrence Berkeley National Laboratory.

Forney, L.J. and Spielman, L.A. (1974) Deposition of coarse aerosols from turbulent flow. *Aerosol Science*, **5**: 257-271.

Fransson, J.I. (1996) Particle deposition in ventilation air supply ducts. *Proceedings of Indoor Air '96*, Nagoya, Japan, Vol. 2, pp. 717-722.

Friedlander, S.K. and Johnstone, H.F. (1957) Deposition of suspended particles from turbulent gas streams. *Industrial and Engineering Chemistry*, **49**: 1151-1156.

Friedlander, S.K. (1977) *Smoke, Dust and Haze: Fundamentals of Aerosol Behavior.* New York: John Wiley & Sons.

Friedrich, R., Hüttl, T.J., Manhart, M. and Wagner, C. (2001) Direct numerical simulation of incompressible turbulent flows. *Computers and Fluids*, **30**: 555-579.

Gavrilakis, S. (1992) Numerical simulation of low-Reynolds-number turbulent flow through a straight square duct. *Journal of Fluid Mechanics*, **244**: 101-129.

Gieseke, J.A., Lee, K.W. and Goldenberg, M.A. (1980) Measurement of aerosol deposition rate in turbulent flows. *NUREG/CR-1262, BMI-2041*, as cited in Erhart (1986).

Gong, H., Chandra, S., McFarland, A.R. and Anand, N.K. (1996) A predictive model for aerosol transmission through a shrouded probe. *Environmental Science and Technology*, **30**: 3192-3198.

Gormley, P.G. and Kennedy, M. (1949) Diffusion from a stream flowing through a cylindrical tube. *Proceedings of the Royal Irish Academy*, **52**: 163-169.

Gouesbet, G. and Berlemont, A. (1999) Eulerian and Lagrangian approaches for predicting the behavior of discrete particles in turbulent flows. *Progress in Energy and Combustion Science*, **25**: 133-159.

Grass, A.J. (1971) Structural features of turbulent flow over smooth and rough boundaries, *Journal of Fluid Mechanics*, **50**: 238-255.

Grass, A.J., Stuart, R.J. and Mansour-Tehrani, M. (1993) Common vortical structure of turbulent flows over smooth and rough boundaries. *AIAA Journal*, **31**: 837-847.

Guha, A. (1997) A unified Eulerian theory of turbulent deposition to smooth and rough surfaces. *Journal of Aerosol Science*, **28**: 1517-1537.

Gutfinger, C. and Friedlander, S.K. (1985) Enhanced deposition of suspended particles to fibrous surfaces from turbulent gas streams. *Aerosol Science and Technology*, **4**: 1-10.

Hahn L.A., Stukel, J.J., Leong, K.H. and Hopke, P.K. (1985) Turbulent deposition of submicron particles on rough walls. *Journal of Aerosol Science*, **16**: 81-86.

Hangal, S. and Willeke, K. (1990) Overall efficiency of tubular inlets sampling at 0-90 degrees from horizontal aerosol flows. *Atmospheric Environment*, **24**: 2379-2386.

Hanley, J.T., Ensor, D.S., Smith, D.D. and Sparks, L.E. (1994) Fractional aerosol filtration efficiency of in-duct ventilation air cleaners. *Indoor Air*, **4**: 169-178.

He, C. and Ahmadi, G. (1998) Particle deposition with thermophoresis in laminar and turbulent duct flows. *Aerosol Science and Technology*, **29**: 525-546.

Heyder, J. and Gebhart, J. (1977) Gravitational deposition of particles from laminar aerosol flow through inclined circular tubes. *Aerosol Science*, **8**: 289-295.

Hinze, J.O. (1975) *Turbulence*, 2nd Edition. New York: McGraw-Hill.

Holopainen, R., Palonen, J. and Seppänen, O. (1999) Measuring methods for determining the level of dust in the air duct. *Proceedings of Indoor Air '99*, Edinburgh, Scotland, Vol. 3, pp. 103-108.

Huser, A. and Biringen, S. (1993) Direct numerical simulation of turbulent flow in a square duct. *Journal of Fluid Mechanics*, **257**: 65-95.

Hutchinson P., Hewitt, G.F. and Dukler, A.E. (1971) Distribution of liquid or solid dispersions from turbulent gas streams: A stochastic model. *Chemical Engineering Science*, **26**: 419-439.

Idelchik, I.E. (1986) *Handbook of Hydraulic Resistance,* 2nd Edition. New York: Hemisphere Publishing.

Ilori, T.A. (1971) Turbulent deposition of aerosol particles inside pipes. Ph.D. Dissertation, University of Minnesota, Minneapolis, Minnesota.

Im, K.H. and Ahluwalia, R.K. (1989) Turbulent eddy deposition of particles on smooth and rough surfaces. *Journal of Aerosol Science*, **20**: 431-436.

Ishikawa, K., Iwata, T., Kumagai, K., Kimura, K. and Yoshizawa, S. (1999) Field investigation on the effects of duct cleaning on indoor air quality with measured results of TVOC and perceived air quality. *Proceedings of Indoor Air '96*, Nagoya, Japan, Vol. 2, pp. 809-814.

Johansen, S.T. (1991) The deposition of particles on vertical walls. *International Journal of Multiphase Flow*, **17**: 355-376.

Kallio, G.A. and Reeks, M.W. (1989) A numerical simulation of particle deposition in turbulent boundary layers. *International Journal of Multiphase Flow*, **15**: 433-446.

Kay, J.M. and Nedderman, R.M. (1990) *Fluid Mechanics and Transfer Processes*, New York: Cambridge University Press.

Kim, J., Moin, P. and Moser, R. (1987) Turbulence statistics in fully developed channel flow at low Reynolds number. *Journal of Fluid Mechanics*, **177**: 133-166.

Kline, S.J., Reynolds, W.C., Schraub, F.A. and Runstadler, P.W. (1967) The structure of turbulent boundary layers. *Journal of Fluid Mechanics*, **30**: 741-773.

Kneen, T. and Strauss, W. (1969) Deposition of dust from turbulent gas streams. *Atmospheric Environment*, **3**: 55-67.

Krogstad, P-Å., Antonia, R.A. and Browne, L.W.B. (1992) Comparison between rough- and smooth-wall turbulent boundary layers. *Journal of Fluid Mechanics*, **245**: 599-617.

Krogstad, P-Å. and Antonia, R.A. (1999) Surface roughness effects in turbulent boundary layers. *Experiments in Fluids*, **27**: 450-460.

Kvasnak, W., Ahmadi, G., Bayer, R. and Gaynes, M. (1993) Experimental investigation of dust particle deposition in a turbulent channel flow. *Journal of Aerosol Science*, **24**: 795-815.

Kvasnak, W. and Ahmadi, G. (1996) Deposition of ellipsoidal particles in turbulent duct flows. *Chemical Engineering Science*, **51**: 5137-5148.

Laatikainen, T., Pasanen, P., Korhonen, L., Nevalainen, A. and Ruuskanen, J. (1991) Methods for evaluating dust accumulation in ventilation ducts. *Proceedings of Healthy Buildings 1991*, Washington DC, pp. 379-382.

Labraga, L., Mazouz, A., Demare, S. and Tournier, C. (1997) Effect of roughness aspect ratio on the "bursting" period in a fully turbulent channel flow. *Journal of Fluids Engineering*, **119**: 469-471.

Lai, C.K. (1997) An experimental study of the deposition of aerosol on rough surfaces and the implications for indoor air quality control. Ph.D. Dissertation, Imperial College, London, England.

Lai, A.C.K. and Nazaroff, W.W. (2000) Modeling indoor particle deposition from turbulent flow onto smooth surfaces. *Journal of Aerosol Science*, **31**: 463-476.

Laufer, J. (1954) The structure of turbulence in fully developed pipe flow. *NACA Technical Note 1174*, pp. 417-434.

Lee, K.W. and Gieseke, J.A. (1994) Deposition of particles in turbulent pipe flows. *Journal of Aerosol Science*, **25**: 699-709.

Levinson, R., Delp, W., Dickerhoff, D., Fisk, W., Nematollahi, M., Stordahl, I., Torre, C., Wang, D., Diamond, R. and Modera, M. (1997) Commercial thermal distribution systems: Final report for California Institute for Energy Efficiency. *Report LBNL-41045*, Berkeley, California: Lawrence Berkeley National Laboratory.

Li, A. and Ahmadi, G. (1993a) Deposition of aerosols on surfaces in a turbulent channel flow. *International Journal of Engineering Science*, **31**: 435-451.

Li, A. and Ahmadi, G. (1993b) Computer simulation of deposition of aerosols in a turbulent channel flow with rough walls. *Aerosol Science and Technology*, **18**: 11-24.

Li, A. and Ahmadi, G. (1993c) Aerosol particle deposition with electrostatic attraction in a turbulent channel flow. *Journal of Colloid and Interface Science*, **158**: 476-482.

Li, A., Ahmadi, G., Bayer, R.G. and Gaynes, M.A. (1994) Aerosol particle deposition in an obstructed turbulent duct flow. *Journal of Aerosol Science*, **25**: 91-112.

Lin, C.S., Moulton, R.W. and Putnam, G.L. (1953) Mass transfer between solid wall and fluid streams: Mechanism and eddy distribution relationships in turbulent flow. *Industrial and Engineering Chemistry*, **45**: 636-640.

Liu, B.Y.H. and Agarwal, J.K. (1974) Experimental observation of aerosol deposition in turbulent flow. *Aerosol Science*, **5**: 145-155.

Liu, B.Y.H. and Ilori, T.A. (1974) Aerosol deposition in turbulent pipe flow. *Environmental Science and Technology*, **8**: 351-356.

Liu, B.Y.H., Zhang, Z.Q. and Kuehn, T.H. (1989) A numerical study of errors in anisokinetic sampling. *Journal of Aerosol Science*, **20**: 367-380.

Luoma, M., Pasanen, P. and Ikäheimo, M. (1999) The effect of duct cleaning on indoor air quality in office buildings. *Proceedings of Indoor Air '99*, Edinburgh, Scotland, Vol. 3, pp. 91-96.

Maxey, M.R. and Riley, J.R. (1983) Equation of motion for a small rigid sphere in a nonuniform flow. *Physics of Fluids*, **26**: 883-889.

Mazouz, A., Labraga, L. and Tournier, C. (1998) Anisotropy invariants of Reynolds stress tensor in a duct flow and turbulent boundary layer. *Journal of Fluids Engineering*, **120**: 280-284.

McCoy, D.D. and Hanratty, T.J. (1977) Rate of deposition of droplets in annular two-phase flow. *International Journal of Multiphase Flow*, **3**: 319-331.

McFarland, A.R., Ortiz, C.A., Moore, M.E., DeOtte, R.E., and Somasundarum, S. (1989) A shrouded aerosol sampling probe. *Environmental Science and Technology*, **23**: 1487-1492.

McFarland, A.R., Gong, H., Muyshondt, A., Wente, W.B. and Anand, N.K. (1997) Aerosol deposition in bends with turbulent flow. *Environmental Science and Technology*, **31**: 3371-3377.

McLaughlin, J.B. (1989) Aerosol particle deposition in numerically simulated channel flow. *Physics of Fluids A*, **1**: 1211-1224.

McLaughlin, J.B. (1991) Inertial migration of a small sphere in linear shear flows. *Journal of Fluid Mechanics*, **224**: 261-274.

McLaughlin, J.B. (1993) The lift on a small sphere in wall-bounded linear shear flows. *Journal of Fluid Mechanics*, **246**: 249-265.

Miyake, Y., Tsujimoto, K. and Agata, Y. (2000) A DNS of a turbulent flow in a rough-wall channel using roughness elements model. *JSME International Journal Series B – Fluids and Thermal Engineering*, **43**: 233-242.

Moin, P. and Mahesh, K. (1998) Direct numerical simulation: A tool in turbulence research. *Annual Review of Fluid Mechanics*, **30**: 539-578.

Montgomery, T.L. and Corn, M. (1970) Aerosol deposition in a pipe with turbulent airflow. *Aerosol Science*, **1**: 185-213.

Morrison, G.C., Nazaroff, W.W., Cano-Ruiz, J.A., Hodgson, A.T. and Modera, M.P. (1998) Indoor air quality impacts of ventilation ducts: Ozone removal and emissions of volatile organic compounds. *Journal of the Air and Waste Management Association*, **48**: 941-952.

Moser, R.D., Kim, J. and Mansour, N.N. (1999) Direct numerical simulation of turbulent channel flow up to Re_τ=590. *Physics of Fluids*, **11**: 943-945.

Muyshondt, A., Anand, N.K. and McFarland, A.R. (1996) Turbulent deposition of aerosol particles in large transport tubes. Aerosol Science and Technology, **24**: 107-116.

NADCA (1992) NADCA 1992-01, Mechanical cleaning of non-porous air conveyance system components. Washington, DC: National Air Duct Cleaners Association.

Nikuradse, I. (1936) Laws governing turbulent flow in smooth tubes. In *Probl. Turnulentnosti*, Edited by Velikanov, M.I. and Shveikovsky, N.G., Moscow: ONTI Press, pp. 75-150, as cited in Idelchik (1986).

Oron, A. and Gutfinger, C. (1986) On turbulent deposition of particles to rough surfaces. *Journal of Aerosol Science,* **17**: 903-920.

Ostro, B. and Chestnut, L. (1998) Assessing the health benefits of reducing particulate matter air pollution in the United States. *Environmental Research*, **76**: 94-106.

Ottney, T.C. (1993) Particle management for HVAC Systems. *ASHRAE Journal*, **35 (7)**: 26-34.

Ounis, H., Ahmadi, G. and McLaughlin, J.B. (1991) Dispersion and deposition of Brownian particles from point sources in a simulated turbulent channel flow. *Journal of Colloid and* Interface *Science*, **147**: 233-250.

Ounis, H., Ahmadi, G. and McLaughlin, J.B. (1993) Brownian particle deposition in a directly simulated turbulent channel flow. *Physics of Fluids A – Fluid Dynamics*, **5**: 1427-1432.

Owen, P.R. (1960) Dust deposition from a turbulent airstream. *International Journal of Air Pollution*, **3**: 8-25.

Owen, P.R. (1969) Pneumatic transport. *Journal of Fluid Mechanics*, **39**: 407-432.

Papavergos, P.G. and Hedley, A.B. (1984) Particle deposition behaviour from turbulent flows. *Chemical Engineering Research and Design*, **62**: 275-295.

Parker, D.S., Sherwin, J.R., and Raustad, R.A. (1997) Impact of evaporator airflow in residential air-conditioning systems. *ASHRAE Transactions*, **103**: 395-405.

Pasanen, P., Nevalainen, A., Ruuskanen, J. and Kalliokoski, P. (1992) The composition and location of dust settled in supply air ducts. *Proceedings of the 13th AIVC Conference on Ventilation for Energy Efficiency and Optimum Air Quality*, Nice, France, pp. 481-488.

Pasanen, P. (1994) Impurities in ventilation ducts. *Proceedings of IAQ '94: Engineering Indoor Environments*, Atlanta: American Society of Heating, Refrigerating and Air-Conditioning Engineers, pp. 149-153.

Pasanen, P.O., Pasanen, A-L. and Kalliokoski, P. (1995) Hygienic aspects of processing oil residues in ventilation ducts. *Indoor Air*, **5**: 62-68.

Pasanen, P., Salo, J., Hyttinen, M., Vartiainen, M. and Kalliokoski, P. (2000) Ozone reduction in supply air filters. *Proceedings of Healthy Buildings 2000*, Helsinki, Finland, Vol. 2, pp. 263-268.

Pearce, D. and Crowards, T. (1996) Particulate matter and human health in the United Kingdom. *Energy Policy*, **24**: 609-619.

Pope, C.A. and Dockery, D.W. (1999) Epidemiology of particle effects. In *Air Pollution and Health*, edited by Holgate, S.T., Samet, J.M., Koren, H.S. and Maynard, R.L., London: Academic Press, pp. 673-705.

Pope, C.A. (2000) Review: Epidemiological basis for particulate air pollution health standards. *Aerosol Science and Technology*, **32**: 4-14.

Postma, A.K. and Schwendiman, L.C. (1960) Studies in micrometrics: I. Particle deposition in conduits as a source of error in aerosol sampling. *Report HW-65308*, Richland, Washington: Hanford Laboratory.

Pui, D.Y.H., Romay-Novas, F. and Liu, B.Y.H. (1987) Experimental study of particle deposition in bends of circular cross section. *Aerosol Science and Technology*, **7**: 301-315.

Ram, M., Cain, S.A. and Taulbee, D.B. (1995) Design of a shrouded probe for airborne aerosol sampling in a high velocity airstream. *Journal of Aerosol Science*, **26**: 945-962.

Reeks, M.W. and Skyrme, G. (1976) The dependence of particle deposition velocity on particle inertia in turbulent pipe flow. *Journal of Aerosol Science*, **7**: 485-495.

Reeks, M.W. (1983) The transport of discrete particles in inhomogeneous turbulence. *Journal of Aerosol Science*, **14**: 729-739.

Riley, W.J., McKone, T.E., Lai, A.C.K. and Nazaroff, W.W. (2002) Indoor particulate matter of outdoor origin: Importance of size dependent removal mechanisms. *Environmental Science and Technology*, **36**: 200-207.

Rodgers, J.C., Fairchild, C.I., Wood, G.O., Ortiz, C.A., Muyshondt, A. and McFarland, A.R. (1996) Single point aerosol sampling: Evaluation of mixing and probe performance in a nuclear stack. *Health Physics*, **70**: 25-35.

Rouhiainen, P.O. and Stachiewicz, J.W. (1970) On the deposition of small particles from turbulent streams. *Journal of Heat Transfer*, **92**: 169-177.

Sabot, J., Saleh, I. and Comte-Bellot, G. (1977) Effects of roughness on the intermittent maintenance of Reynolds shear stress in pipe flow. *Physics of Fluids*, **20**: S150-S155.

Saffman, P.G. (1965) The lift on a small sphere in a slow shear flow. *Journal of Fluid Mechanics*, **22**: 385-400.

Saffman, P.G. (1968) Corrigendum to 'The lift on a small sphere in a slow shear flow.' *Journal of Fluid Mechanics*, **31**: 624.

Schlichting, H. (1979) *Boundary-Layer Theory*, 7th Edition. New York: McGraw-Hill.

Schwartz J., Dockery D.W. and Neas, L.M. (1996) Is daily mortality associated specifically with fine particles? *Journal of the Air and Waste Management Association*, **46**: 927-939.

Sehmel, G.A. (1968) Aerosol deposition from turbulent airstreams in vertical conduits. *Report BNWL-578*, Richland, Washington: Pacific Northwest Laboratory.

Sehmel, G.A. (1970a) Turbulent deposition of monodisperse particles on simulated grass. In *Assessment of Airborne Particles: Fundamentals, Applications, and Implications to Inhalation Toxicity*, edited by Mercer, T.T., Morrow, P.E. and Stöber, W., Springfield, Illinois: Charles C. Thomas.

Sehmel, G.A. (1970b) Particle deposition from turbulent air flow. *Journal of Geophysical Research*, **75**: 1766-1781.

Sehmel, G.A. (1973) Particle eddy diffusivities and deposition velocities for isothermal flow and smooth surfaces. *Aerosol Science*, **4**: 125-138.

Sehmel, G.A. (1980) Particle and gas dry deposition: A review. *Atmospheric Environment*, **14**: 983-1011.

Shaw, D.A. and Hanratty, T.J. (1977) Turbulent mass transfer rates to a wall for large Schmidt numbers. *AIChE Journal*, **23**: 28-37.

Shimada, M., Okuyama, K. and Asai, M. (1993) Deposition of submicron aerosol particles in turbulent and transitional flow. *AIChE Journal*, **39**: 17-26.

Siegel, J.A. (2002) Particulate fouling of HVAC heat exchangers. Ph.D. Dissertation, University of California, Berkeley, California.

Skoog, D.A., West, D.M. and Holler, F.J. (1996) *Fundamentals of Analytical Chemistry*, 7th Edition. New York: Harcourt Brace College Publishers.

Stavropoulos, N. (1957) Deposition of particles from turbulent gas streams. M.Sc. Thesis, Columbia University, New York.

Ström, L. (1972) Transmission efficiency of aerosol sampling lines. *Atmospheric Environment*, **6**: 133-142.

Talbot, L., Cheng, R.K., Schefer, R.W. and Willis, D.R. (1980) Thermophoresis of particles in a heated boundary layer. *Journal of Fluid Mechanics*, **101**: 737-758.

Thatcher, T.L., Fairchild, W.A. and Nazaroff, W.W. (1996) Particle deposition from natural convection enclosure flow onto smooth surfaces. *Aerosol Science and Technology*, **25**: 359-374.

Thatcher, T.L., Lai, A.C.K., Moreno-Jackson, R., Sextro, R.G. and Nazaroff, W.W. (2002) Effects of room furnishings and air speed on particle deposition rates indoors. *Atmospheric Environment*, **36**: 1811-1819.

Townsend, A.A. (1956) *The Structure of Turbulent Shear Flow*. Cambridge, England: Cambridge University Press.

Uijttewaal, W.S.J. and Oliemans, R.V.A. (1996) Particle dispersion and deposition in direct numerical and large eddy simulations of vertical pipe flows. *Physics of Fluids*, **8**: 2590-2604.

U.S. EPA (1993) *40CFR60, Appendix A, Method 1, Code of Federal Regulations*. Washington DC: U.S. Government Printing Agency.

Valbjørn, O., Nielsen, J.B., Gravesen, S. and Mølhave, L. (1990) Dust in ventilation ducts. *Proceedings of Indoor Air '90*, Toronto, Canada, Vol. 3, pp. 361-364.

Vincent, J.H., Emmet, P.C., Mark, D., Marshall, M. and Smith, T.A. (1986) On the aspiration characteristics of large-diameter thin-walled aerosol sampling probes at yaw orientations with respect to the wind. *Journal of Aerosol Science*, **17**: 211-214.

Wagner, C. and Friedrich, R. (1998) On the turbulence structure in solid and permeable pipes. *International Journal of Heat and Fluid Flow*, **19**: 459-469.

Wallace, L. (2000) Correlations of personal exposure to particles with outdoor air measurements: A review of recent studies. *Aerosol Science and Technology*, **32**: 15-25.

Wallin, O. (1994) Computer simulation of particle deposition in ventilating duct systems. Ph.D. Dissertation, Royal Institute of Technology, Stockholm, Sweden.

Wang, Q. and Squires, K.D. (1996a) Large eddy simulation of particle-laden turbulent channel flow. *Physics of Fluids*, **8**: 1207-1223.

Wang, Q. and Squires, K.D. (1996b) Large eddy simulation of particle deposition in a vertical turbulent channel flow. *International Journal of Multiphase Flow*, **22**: 667-683.

Wang, Q., Squires, K.D., Chen, M. and McLaughlin, J.B. (1997) On the role of the lift force in turbulence simulations of particle deposition. *International Journal of Multiphase Flow*, **23**: 749-763.

Wargocki, P., Wyon, D.P., Sundell, J., Clausen, G. and Fanger, P.O. (2000) The effects of outdoor air supply rate in an office on perceived air quality, Sick Building Syndrome (SBS) symptoms and productivity. *Indoor Air*, **10**: 222-236.

Wasan, D.T. and Wilke, C.R. (1964) Turbulent exchange of momentum, mass and heat between fluid streams and pipe wall. *International Journal of Heat and Mass Transfer*, **7**: 87-94.

Wasan, D.T., Sood, S.K., Davies, R. and Lieberman, A. (1973) Aerosol transport: Particle charge and re-entrainment effects. *Journal of Colloid and Interface Science*, **43**: 144-149.

Wells, A.C. and Chamberlain, A.C. (1967) Transport of small particles to vertical surfaces. *British Journal of Applied Physics*, **18**: 1793-1799.

White, F.M. (1986) *Fluid Mechanics*, 2nd Edition. New York: McGraw-Hill.

Wood, N.B. (1981a) A simple method for the calculation of turbulent deposition to smooth and rough surfaces. *Journal of Aerosol Science*, **12**: 275-290.

Wood, N.B. (1981b) The mass transfer of particles and acid vapour to cooled surfaces. *Journal* of *the Institute of Energy*, **76**: 76-93.

Yoder, J.D. and Silverman, L. (1967) Influence of turbulence on aerosol agglomeration and deposition in a pipe. *Paper No. 67-33, 60th Annual Air Pollution Control Association Meeting*, Cleveland, Ohio.

Young, J. and Leeming, A. (1997) A theory of particle deposition in turbulent pipe flow. *Journal of Fluid Mechanics*, **340**: 129-159.

Yudine, M.I. (1959) Physical considerations on heavy-particle diffusion. *Advances in Geophysics*, **6**: 185-191.

Zhang, H. and Ahmadi, G. (2000) Aerosol particle transport and deposition in vertical and horizontal turbulent duct flows. *Journal of Fluid Mechanics*, **406**: 55-80.

Zhang, Z., Kleinstreuer, C. and Kim, C.S. (2001) Effects of curved inlet tubes on air flow and particle deposition in bifurcating lung models. *Journal of Biomechanics*, **34**: 659-669.

APPENDIX A

Surface Roughness of the Experimental Ducts

A.1 Introduction

The roughness of a deposition surface can be an important factor in determining particle deposition rates to that surface. Roughness may be characterized as macroscale, with roughness elements on the scale of 1 mm and larger, or microscale, with roughness elements much smaller than 1 mm. Small scale surface irregularities determine the microscale roughness level of a clean surface. Macroscale roughness may be attributable to the nature of a surface or the presence of foreign objects on the surface. Surface roughness has rarely been characterized or systematically analyzed in particle deposition experiments. Various techniques were used to characterize and quantify the roughness of the steel ducts and the internal insulation used as particle deposition surfaces in the experiments described in Chapters 3 and 4. This appendix describes these techniques and presents results for the best estimates of the roughness scales of the steel ducts and the internal insulation.

A.2 Methods

To better understand the microscale roughness characteristics of the experimental ducts, duct surface samples were analyzed using an optical microscope, a scanning electron microscope (SEM), an atomic force microscope (AFM) and a profilometer. The surfaces analyzed were the galvanized steel duct and the top black composite layer of the duct

insulation. Macroscale roughness elements were measured with a ruler. The hydraulic roughnesses of the ducts were also estimated from measurements of the pressure drop as air flowed through the ducts during experiments.

A.2.1 Microscale roughness analysis by microscopy

Ten samples were cut from experimental steel ducts and from the top layer of the insulation so that the surfaces could be investigated by microscopy. An optical microscope outfitted with a digital camera was used to photograph magnified images of the steel duct samples. Adequate images of the top layer of the insulation could not be obtained with an optical microscope because the depth of focus of the microscope was much narrower than the depth over which fibers were spread. An SEM was used to capture images of both the steel and insulation surfaces. Only steel surfaces were analyzed by the AFM; the roughness of the insulation was too large to be measured by the AFM.

A.2.2 Profilometer measurements of microscale roughness

Surface roughnesses of experimental steel ducts were quantified with a profilometer (Alphastep, AS200). The profilometer measures surface roughness by periodically recording the vertical displacement of a stylus as it traverses the surface. The radius of the stylus tip was 5 μm and the scan length was 2 mm for each measurement.

A single scan yields three values useful for quantifying surface roughness: the average profile height, the arithmetic average roughness and the maximum roughness. The

average profile height of a scan, h_{ave}, is a simple average of vertical displacements measured relative to the lowest point in the scan. It is calculated by

$$h_{ave} = \frac{\sum_{i=1}^{N} h_i}{N_p} \tag{A.1}$$

where h is a discrete vertical displacement measured by the profilometer referenced to the lowest position and N_p is the number of displacements measured in a single scan. Several discrete vertical displacements and the average profile height are shown in Figure A.1 using the surface height profile of a steel surface generated by the AFM. Note that each profilometer scan was 2 mm in length, much longer than the 50 μm represented in this figure.

The arithmetic average roughness, R_{ave}, is defined by

$$R_{ave} = \frac{\sum_{i=1}^{N} |h_i - h_{ave}|}{N_p} \tag{A.2}$$

The maximum roughness, h_{max}, is simply the largest vertical displacement measured relative to the lowest point in the scan. Scans were automatically corrected to account for any tilting of the sample during the stylus traverse.

A total of seventeen profilometer scans were performed on samples from the steel experimental ducts. So that these measurements could be compared to values used ventilation ducts, four scans were performed on samples from steel ventilation ducts that had served a movie theater in a coastal city for several years. These theater ducts were

free of visible corrosion and large debris, but were soiled. Because of the nonrigid nature of the insulation, its roughness could not be measured by the profilometer. Measurement of large scale roughness elements associated with the insulation was accomplished with a ruler with millimeter graduations.

A.2.3 Macroscale roughness measurement

S-connectors and beading indentations in steel ducts were measured at several locations with a ruler with millimeter graduations. Visual inspection of the top layer of insulation revealed that it was not flat; regular bumps and waves were present. These roughness elements were measured with a ruler for several samples.

A.2.4 Estimation of hydraulic roughness scales

Estimates of the hydraulic roughness of the experimental ducts were obtained from measured pressure drops along the duct length during experiments. The methods for making the static pressure measurements used to calculate pressure drops are described in Chapter 3. Examples of profiles of measured pressure drops versus time at different air speeds in the steel and insulated duct systems are presented in Appendix C. Pressure drop measurements were used to calculate friction factors by equation (2.7). In most cases, five experiments were run at each nominal air speed in both the steel and insulated duct systems; six were run at 5.3 m/s in the steel system. All friction factors measured at a single air speed were averaged to give one value for the measured friction factor at each air speed in each duct system. These friction factors were then compared to empirical friction factor relationships like the Blasius equation for smooth surfaces and the

equations from Table 2.1 for rough surfaces. The hydraulic roughness of the experimental ducts could be evaluated by matching empirical equations to the measured friction factor data by adjusting the roughness value in the empirical equations.

A.3 Results

A.3.1 Microscopy

Figure A.2 shows two images of the surface of an experimental galvanized steel duct as seen through an optical microscope at different magnification levels. Figure A.3 shows images of the surface of a steel duct at two magnification levels generated by SEM. A contour plot of a 50×50 μm square surface of a steel duct generated by the AFM is displayed in Figure A.4. The different colors on this plot correspond to different surface heights. A side view of the section demarked by the pointers is shown in the lower panel of Figure A.4. The surface height is exaggerated relative to the lateral distances in this side view plot to make the depression more visible. Figure A.5 shows the same surface as in Figure A.4 as a three-dimensional contour plot from the AFM. The vertical scale in this figure is amplified relative to the horizontal scale. Two images of the top layer of the insulation at different levels of magnification from the SEM are displayed in Figure A.6.

A.3.2 Profilometer measurements

A summary of arithmetic average roughness values and maximum roughness values from profilometer measurements of the steel experimental ducts and the steel theater ducts is given in Table A.1.

A.3.3 Macroscale roughness measurement

In the steel ducts, the depth of the beading indentations was measured to be 1.0 mm; the height that S-connectors projected into the flow was measured to be 2.0 mm. There was very little variability in both of these measured values for several samples. Macroscopic bumps on the top layer of insulation were 1-2 mm tall and waviness associated with this surface was on the scale of 1-5 mm.

A.3.4 Hydraulic roughness estimates

Measured friction factors for both the steel and insulated systems are compared to empirical friction factor equations in Figure A.7. Each data point represents the average of (usually five) measurements made at each air speed. The Blasius equation is equation (2.8) and the Colebrook equation is that reported in Table 2.1.

A.4 Discussion

The most striking feature in the optical microscope images of steel duct surfaces in Figure A.2 are the vein-like structures that stretch across most of the steel surface. Most of these structures were comprised of a long vein with several shorter veins the branching off of the main vein. Typical vein widths were observed to be in the range 10-25 μm from the optical microscope images.

In the SEM images of steel duct surfaces in Figure A.3, the vein-like structures seen in Figure A.2 are faintly visible in the top panel. Also visible in this image are what appear to be thin cracks in the steel surface that are widely spaced. The lower panel of Figure

A.3 shows a close-up view of one of these cracks. These cracks were more widely spaced over the steel surface than the veins; they also appear to be narrower and of greater depth than the veins described earlier.

A branching section of the veins described earlier is visible in the AFM contour plot shown in Figure A.4. This figure reveals the veins to be surface depressions, a series of connected shallow valleys. Most valleys on the steel surface observed with the AFM had dimensions similar to the example in Figure A.4: widths were about 20 μm and depths were about 1-3 μm. The valleys are also visible in Figure A.5. Notable from the AFM contour plots is the smooth character of the steel surface at scales smaller than the valleys. The microscale surface roughness of these experimental steel ducts appears to be dominated by widely-spaced, vein-like valleys and occasional surface cracks. The branching valleys are possibly formed during cooling after the galvanization process.

In the SEM images of the top layer of insulation in Figure A.6, the fibrous nature of the layer is apparent in the upper panel. The lower panel, at a greater magnification, shows many ambient particles deposited on the fibers. Upon close inspection of this figure, the adhesive material that binds this top layer of the insulation is visible. From SEM images, fiber diameters were estimated to be in the range 3-30 μm, but the roughness height of these fibers was difficult quantify.

The data from the profilometer measurements of the steel experimental ducts in Table A.1 are in accord with values expected from the AFM scans. The mean average

arithmetic roughness and the mean maximum roughness of the steel ducts from the movie theater are both greater than the corresponding values for the experimental duct, possibly because of material accumulation on the surface of the used movie theater ducts.

Figure A.7 illustrates that measured friction factors in the steel duct system agree well with the predictions of the Blasius equation, indicating that the steel duct is hydraulically smooth. This means that the roughness elements on the steel duct surface, including protrusions by S-connectors and beading indentations, do not increase the pressure drop for a flow in the duct relative to a similar flow in a duct with perfectly smooth walls.

In Figure A.7, measured friction factors in the insulated duct are much greater than those predicted by the Blasius equation, indicating that the roughness of the internal insulation does influence the pressure drop of the flow. The Colebrook equation for the friction factor of a rough-wall flow agrees well with the measured friction factors in the insulated system when applied with a roughness height of $k = 1570$ μm. Other empirical friction factor equations from Table 2.1 were matched to the data in the same way to determine a hydraulic roughness values associated with the interior insulation. Hydraulic roughness values of 1720, 2720 and 1750 μm were respectively found for the equations of Bennet & Meyers (1962), Altshul (1970) and White (1986). These hydraulic roughness values are in accordance with the measured physical roughness scales of the insulation.

Based on analyses by the profilometer and by microscopy, the best estimate of the microscale roughness of the steel ducts is 2 μm. This roughness scale is associated with

well-spaced, shallow valleys, not a closely packed sand-grain type roughness. This level of roughness is much less then the macroscale roughness associated with the beading indentations (1 mm) or the S-connectors (2 mm). If a value of 2 μm is used for the roughness of the steel experimental duct, values of the dimensionless roughness, k^+, for the air speeds of 2.2, 5.3 and 9.0 m/s are 0.02, 0.04 and 0.06, respectively. These values are well within the hydraulically smooth roughness regime. The widely spaced valley-like roughness elements are likely to be less important for influencing particle deposition than closely packed protrusions of the same dimensions. The dimensionless roughness values of the S-connectors at air speeds of 2.2, 5.3 and 9.0 m/s are 20, 40 and 60. These elements are widely spaced and do not affect the hydraulic roughness even though their heights place them in the transitional roughness regime.

SEM images of the outer insulation layer suggest that it has a fibrous structure with individual fiber widths in the range 3-30 μm. Larger roughness elements associated with the insulation were measured to be 1-5 mm in height. Beading indentations and S-connectors did not contribute to any macroscale roughness in insulated ducts because they were buried beneath the insulation. Estimates of the hydraulic roughness yielded values in the range 1.5-2.7 mm. If a value of 2 mm is used for the roughness of the insulated experimental duct, values of the dimensionless roughness, k^+, for the air speeds of 2.2, 5.3 and 8.8 m/s are 20, 50 and 80, respectively. This suggests that roughness from the insulation is in the transition roughness regime or in the completely rough regime.

Table A.1 Roughnesses of duct surfaces measured by profilometer.

Sample	Arithmetic average roughness, R_{ave} (μm)	Maximum roughness, h_{max} (μm)
steel experimental duct	1.1 ± 0.5	4.8 ± 2.0
steel movie theater duct	2.5 ± 0.4	18 ± 3.0

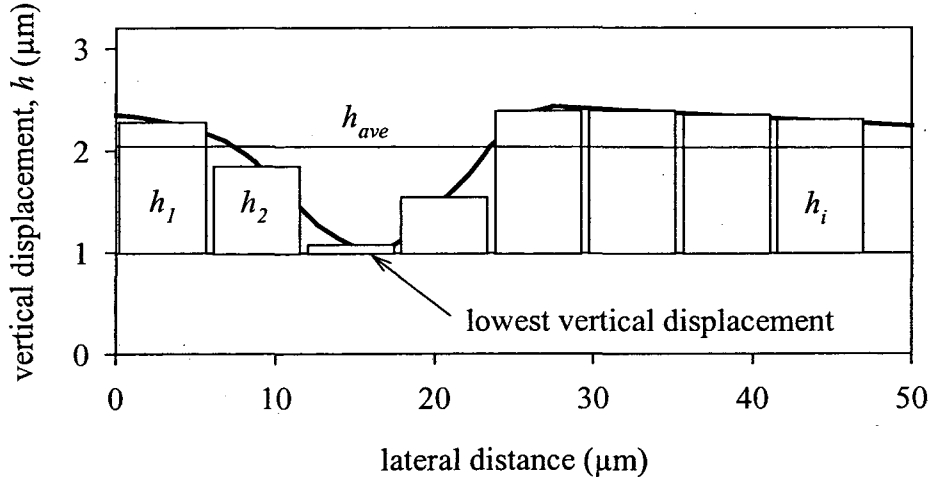

Figure A.1 Example of discrete measurements of vertical displacement that may be measured by a profilometer for a sample surface height profile.

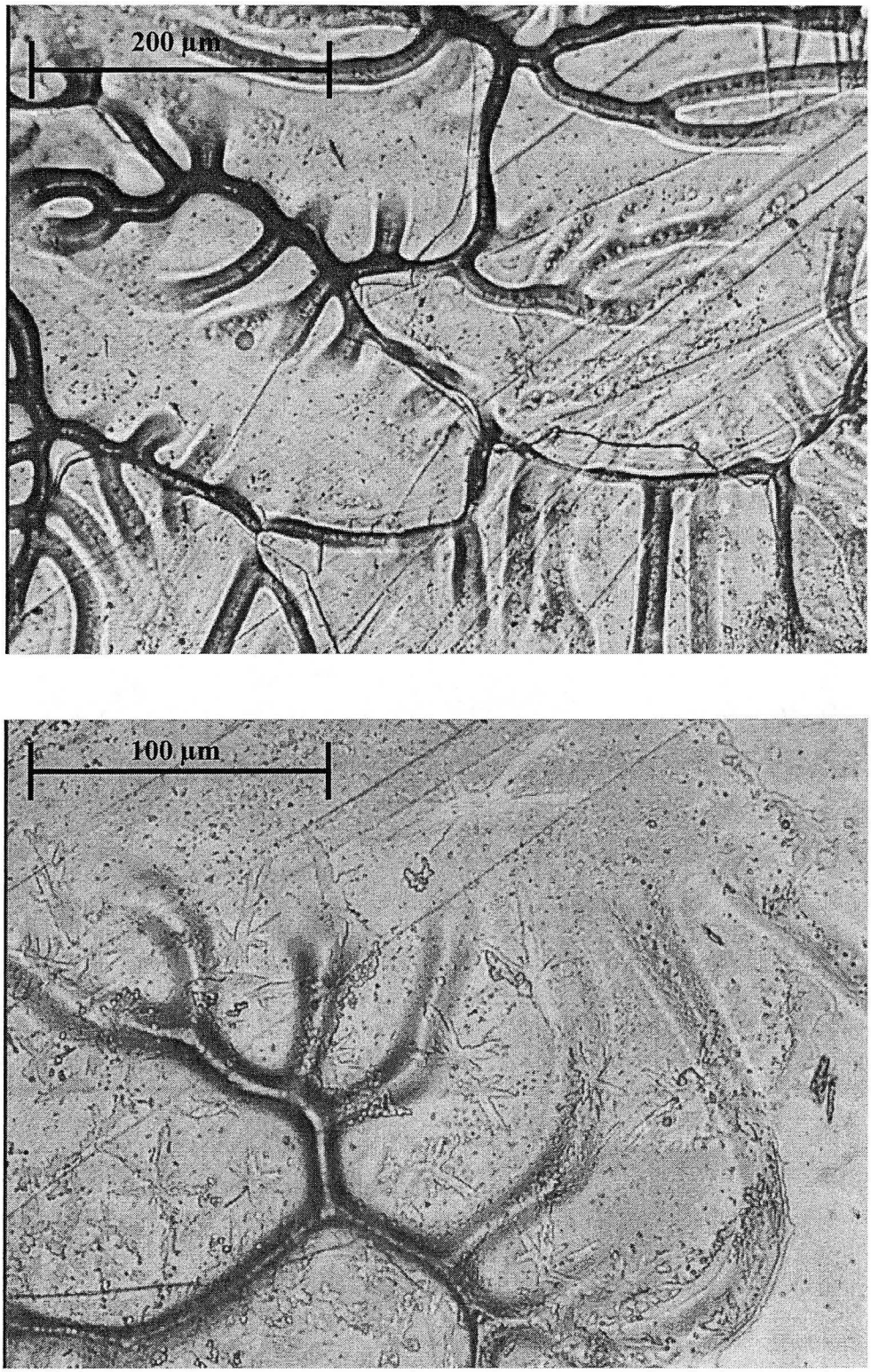

Figure A.2 The surface of a steel experimental duct as seen through an optical microscope at two different levels of magnification.

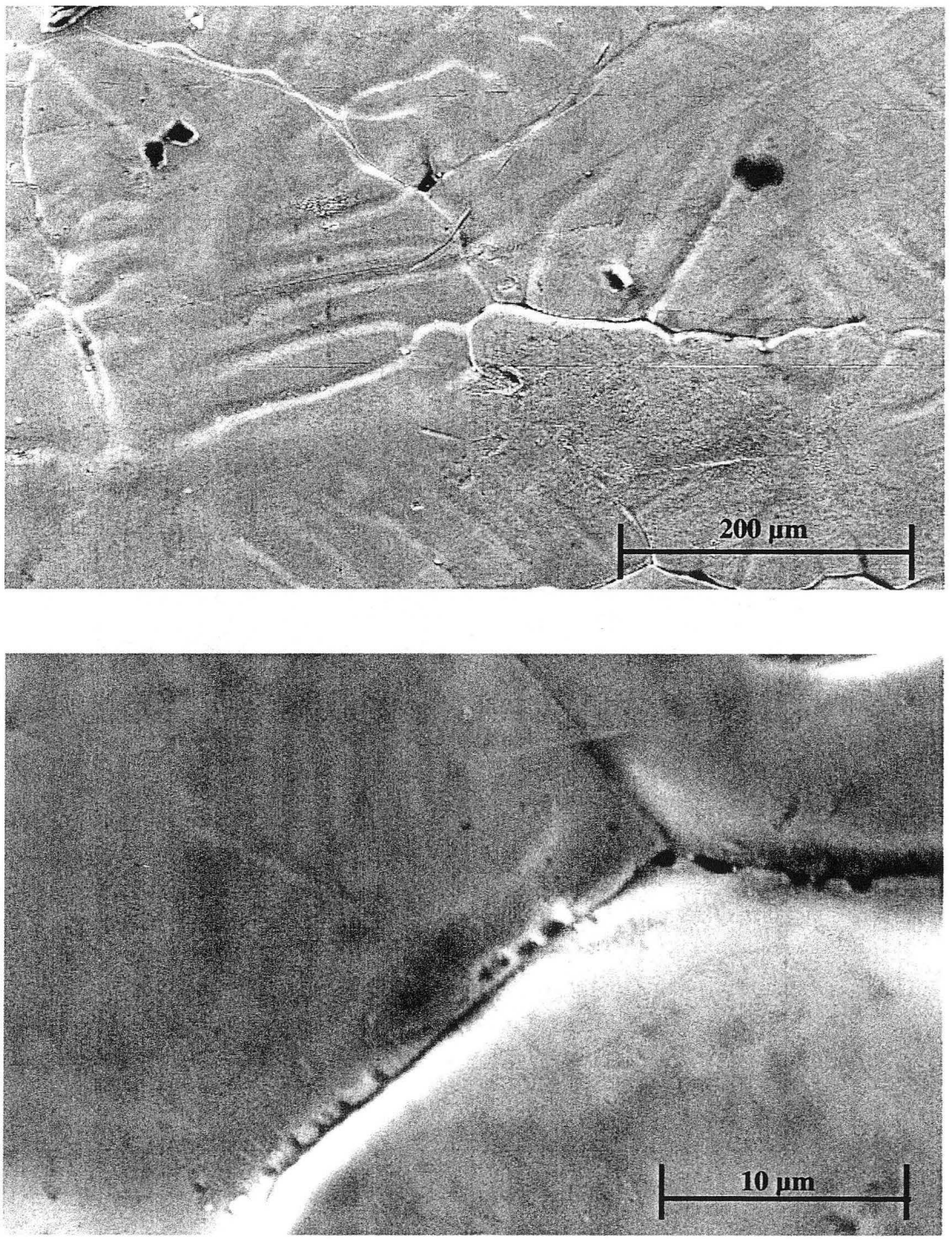

Figure A.3 Images of the surface of a steel experimental duct generated by a scanning electron microscope at two different levels of magnification.

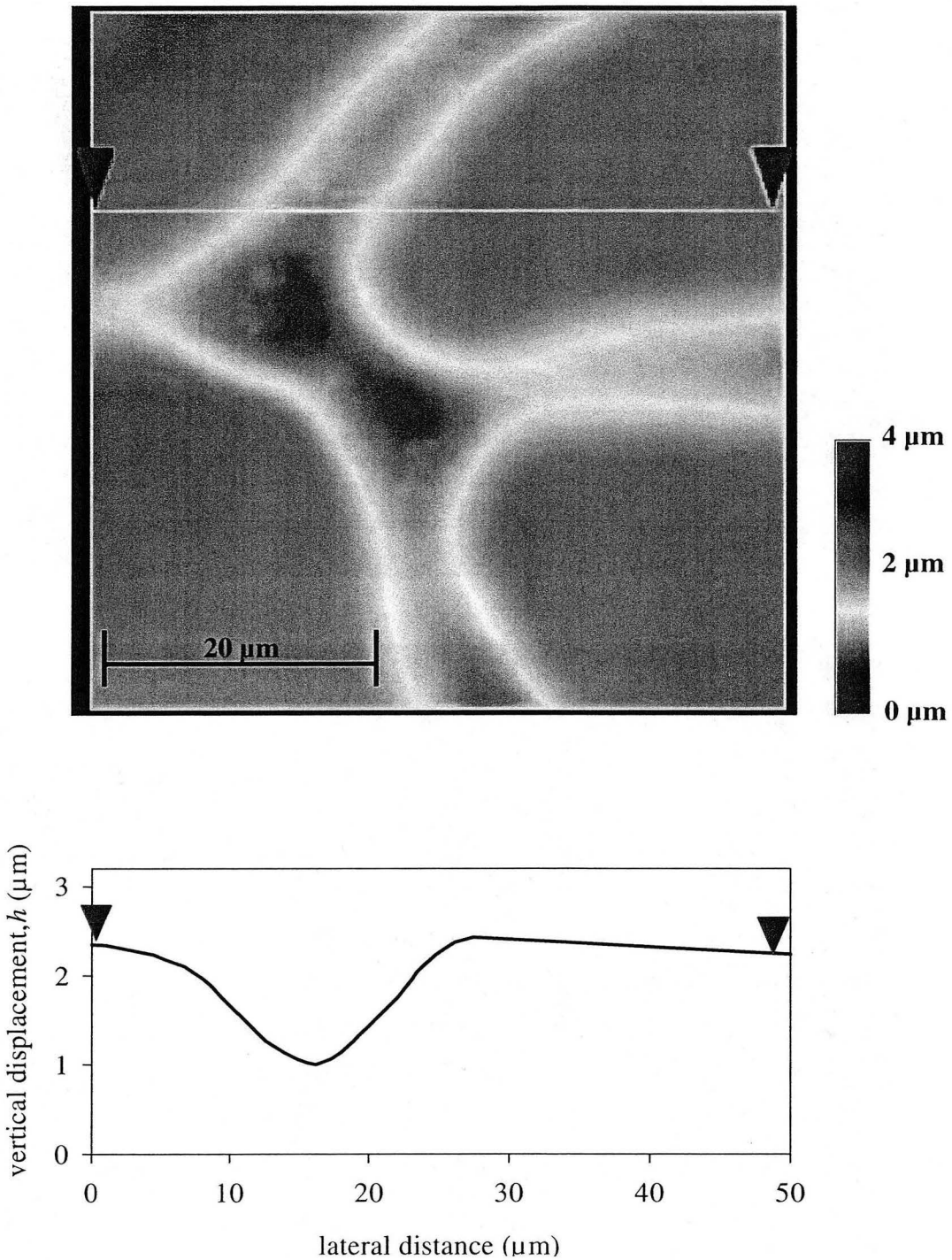

Figure A.4 Two-dimensional contour plot of the surface of a steel experimental duct from an atomic force microscope. The lower panel displays a plot of the surface height versus the lateral distance for the section through the surface demarked by the pointers.

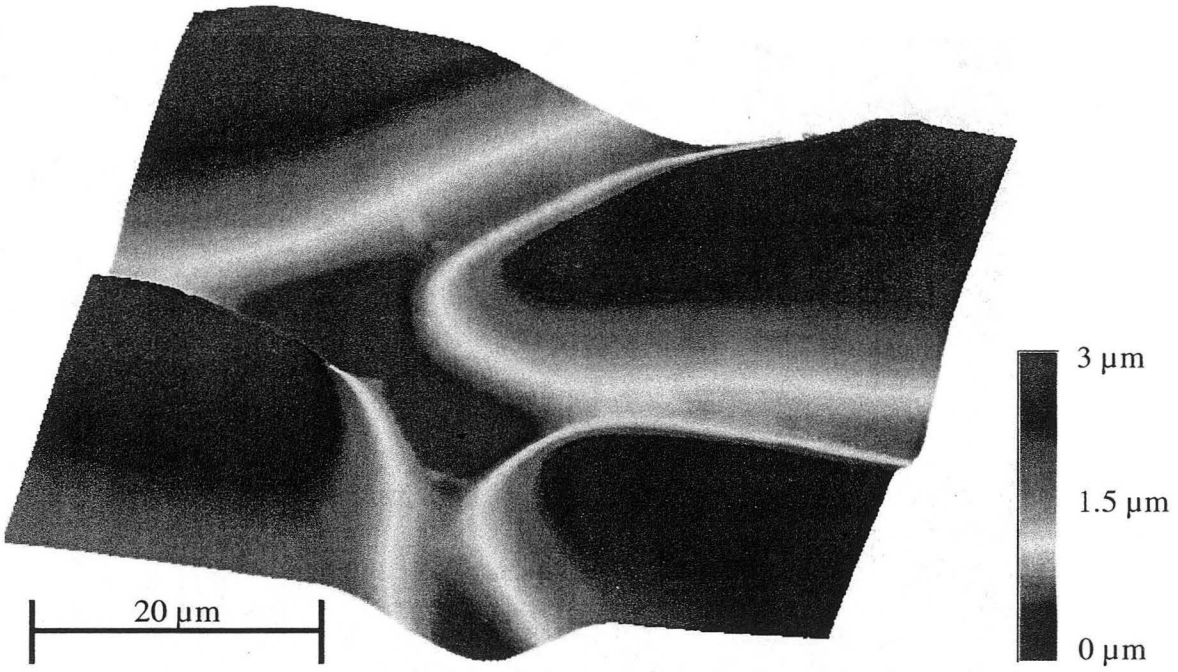

Figure A.5 Three-dimensional contour plot of the same steel experimental duct surface as in Figure A.4, generated by an atomic force microscope.

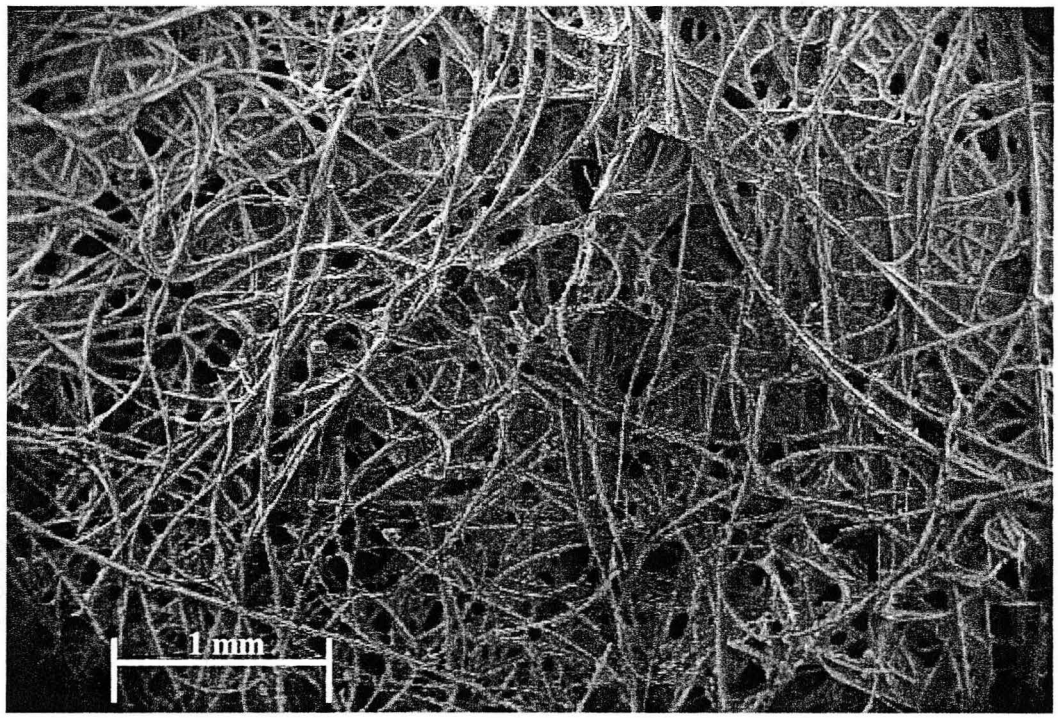

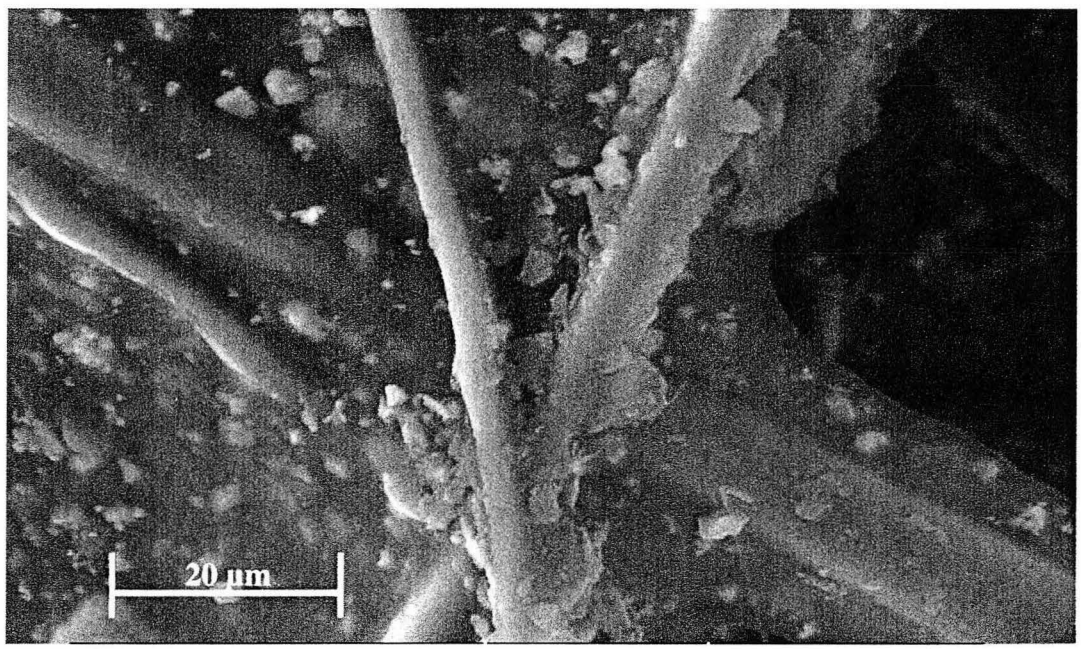

Figure A.6 Images of the top layer of insulation from an insulated experimental duct generated by a scanning electron microscope at two different levels of magnification.

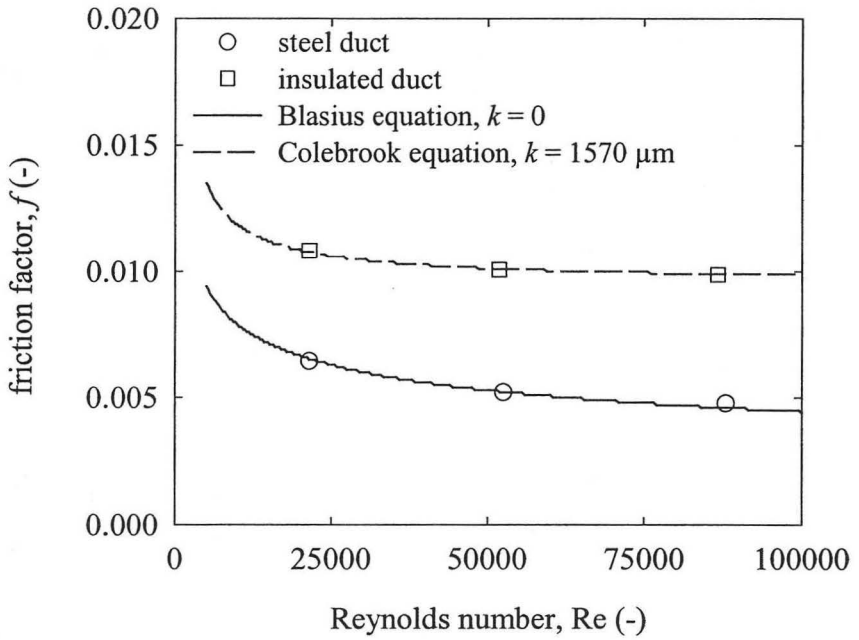

Figure A.7 Comparison of friction velocities measured in the steel and insulated systems with friction velocities predicted by empirical equations.

APPENDIX B

Aerosol Sampling from Turbulent Duct Flow with Isokinetic Nozzles and Shrouded Anisokinetic Nozzles

B.0 Abstract

A shrouded anisokinetic nozzle for sampling aerosols from a ventilation duct to an Aerodynamic Particle Sizer (APS) has been designed and built. The shrouded nozzle was intended to deliver a larger fraction of particles to the APS than a comparable unshrouded isokinetic nozzle. To use this shrouded nozzle with an APS to measure ambient particles in a real duct, its performance with regard to aspiration efficiency and transport efficiency must be understood. During the particle deposition experiments in the insulated duct system described in Chapter 3, a shrouded nozzle sampled the fluorescent experimental particles to a filter so that its aspiration and transport efficiencies could be evaluated. Aspiration and transport efficiency measurements were made for five particle sizes in the range 1-13 μm at each of three air velocities in the range 2.2-8.8 m/s and the results of these measurements are presented. Measured particle transport efficiencies through isokinetic nozzles during experiments in both the steel and insulated duct system are also presented. Measured transport and aspiration efficiencies are compared to the predictions of a combination of empirical models.

Measured transport efficiencies through the shrouded nozzle were generally higher and more predictable than those through the isokinetic nozzles. Model-measurement

agreement for transport efficiencies through isokinetic nozzles was good for all particle sizes at the 2.2 m/s air speed, but the model underpredicted these measurements for particles larger than 3 μm at air speeds higher than 2.2 m/s. Resuspension of deposited particles within the nozzle is suspected to be the cause of the model-measurement discrepancy at the high air speeds. Measured transport efficiencies through the shrouded nozzle were near one for all particle sizes at the lowest air speed of 2.2 m/s and decreased gradually with increases in both particle size and duct air speed. Shrouded nozzle aspiration efficiencies were near one for all particle sizes at the lowest air speed. Measured aspiration efficiencies increased with increases in both particle size and duct air speed. Good predictions of the transport and aspiration efficiencies in the shrouded nozzle could be made with empirical models. The shrouded nozzle could be used with an APS to reliably measure concentrations in most ventilation ducts for particles in the size range 0.5-16 μm.

B.1 Introduction: Aspiration and Transport Efficiencies and Isokinetic Sampling

To determine the airborne particle concentration in an airstream, a sample of the aerosol often must be delivered to a filter or particle detection device. Ideally, a delivered sample should have the same particle size distribution as the air in the original environment and be unaffected by the sampling process. Sampling systems generally consist of a sampling inlet, transport lines and a filter or particle detection device. Particle behavior at the sampling inlet and in the transport lines influence the degree to which the delivered aerosol is representative of the environmental aerosol. Under certain circumstances, particles may not enter the sampling inlet in a representative manner. Additionally,

particles may deposit on the walls of sampling transport lines before reaching the filter or particle detection device.

A bias in the concentration of particles entering the inlet is quantified by the aspiration efficiency, η_a, defined by

$$\eta_a = \frac{C_{inlet}}{C_{bulk}} \tag{B.1}$$

where C_{inlet} is the particle concentration just inside the sampling inlet and C_{bulk} is the concentration in the bulk flow. An aspiration efficiency equal to one means that a representative aerosol has entered the inlet.

Deposition to the walls of the transport line is quantified by the transport efficiency, η_t, defined by

$$\eta_t = \frac{C_{outlet}}{C_{inlet}} \tag{B.2}$$

where C_{outlet} is the particle concentration at the outlet of the transport line, where the filter or particle detection device is located.

Aspiration at the inlet and deposition in the transport lines are the two factors most likely to influence the degree to which a sampled aerosol represents an environmental aerosol. Losses in transport lines are inevitable, but can be minimized by keeping lines short, by using larger diameter lines and by avoiding sharp bends. The total transmission, T_{total},

through a sampling system is a measure of how representative a delivered aerosol is of the environmental aerosol. It can be calculated by

$$T_{total} = \frac{C_{outlet}}{C_{bulk}} = \eta_a \eta_t \tag{B.3}$$

Figure B.1 shows schematics of sampling inlets with air streamlines and hypothetical particle trajectories under three sampling conditions: isokinetic, sub-isokinetic and super-isokinetic. Sampling is isokinetic when the average air velocity at the inlet, u_{inlet}, is equal to the local air velocity in the free stream, u_o. Isokinetic sampling leads to aspiration efficiencies equal to one for all particle sizes. Sub-isokinetic sampling, when $u_{inlet} < u_o$, causes air streamlines to decelerate and diverge as the sampling inlet is approached. Because of their inertia, particles often cannot follow air streamlines exactly. Sub-isokinetic sampling can lead to aspiration efficiencies greater than one when particles enter sampling inlets from air streamlines that do not flow into the inlet. Similarly, super-isokinetic sampling, when $u_{inlet} > u_o$, can lead to aspiration efficiencies less than one when air streamlines flow into the inlet, but particles associated with those streamlines fail to follow the same path into the inlet owing to their inertia.

When sampling from a turbulent airstream, as in a ventilation duct, one can not always sample at the isokinetic velocity because of the rapid and random velocity fluctuations of the turbulent flow. When attempting to sample isokinetically from a turbulent flow, the best that can be achieved is to sample with the nozzle velocity equal to the local mean velocity. The mean velocity in a ventilation duct may change as demand for air flow changes within the building, further complicating the process of isokinetic sampling in

real HVAC ducts. If one is sampling at a constant flow rate, as may be required for certain particle measuring instruments, isokinetic sampling from airstreams with different air speeds requires isokinetic nozzle inlets with different diameters. For example, an Aerodynamic Particle Sizer (APS) samples at a constant rate of 5.0 L/min. To meet this requirement and also match an arbitrary mean airstream velocity in a duct, u_o, the isokinetic nozzle inlet must have a uniquely specified diameter.

Previous investigators have reported on the advantages of shrouded anisokinetic nozzles compared to unshrouded isokinetic nozzles when sampling at a constant flow rate from turbulent airstreams with variable air speeds (McFarland *et al.*, 1989; Ram *et al.*, 1995). These advantages include the delivery of a greater number of large particles to the particle detection device (higher total transmission) and a greater ease of use. Shrouded nozzles achieve higher total transmission rates than isokinetic nozzles operating at the same flow rate because of their decreased transport line losses and their higher aspiration efficiencies.

B.2 Methods

B.2.1 Description of isokinetic nozzles and shrouded nozzle

Measurements of particle transmission and aspiration efficiencies through sampling nozzles reported in this appendix were made during the experiments described in Chapter 3. In these experiments, two types of nozzles were used to sample the experimental aerosol in the ventilation duct: unshrouded isokinetic nozzles and shrouded anisokinetic nozzles. Isokinetic nozzles sampled to filters to measure airborne concentrations at four

locations in the duct system. These nozzles sampled air isokinetically via pumps with adjustable flow rates. A shrouded nozzle was used to deliver experimental particles to the APS for particle sizing in all experiments. For experiments in the insulated duct system, a second shrouded nozzle sampled to a filter. The shrouded nozzles did not sample isokinetically; they sampled air at a constant flow rate of 5.0 L/min regardless of the air speed in the duct. The interior portions of nozzles and filter holders, along with filters, were subjected to fluorometric analysis after each experiment to evaluate the particle transport efficiencies through the nozzles. Isokinetic nozzles were assumed to have an aspiration efficiency of one. Aspiration efficiencies of the shrouded nozzle were evaluated by comparing the concentrations measured by the isokinetic nozzles to those measured by the shrouded nozzles.

Figure B.2 is a photograph of an isokinetic nozzle and Teflon filter holder used in these experiments. Nozzles were inserted through a hole in the duct floor and secured in place with the mounting assembly on the shaft. The total length of the nozzles from inlet to filter holder was 22.2 cm. The measured inlet diameters of the eight isokinetic nozzles used in the experiments are summarized in Table B.1. Nozzles 1-4, with nominal inlet diameters of 0.180 in, were used in experiments with nominal air speeds of 2.2 and 5.3 m/s, and nozzles 5-8, with nominal diameters of 0.120 in, were used at nominal air speeds of 8.8 and 9.0 m/s. Sample flow rates through isokinetic nozzles were maintained at isokinetic sampling rates so that expected aspiration efficiencies were always one. These isokinetic flow rates were typically in the range 2-6 L/min, comparable to the constant 5.0 L/min sample flow rates for the shrouded nozzles. Nozzles 5-8 were used at

the highest air speeds because not enough pumping capacity was available to achieve isokinetic sampling velocities with nozzles 1-4.

A photograph of a shrouded nozzle is shown in Figure B.3. The shrouded nozzle comprised of three different parts: the shrouded inlet piece, the elbow and the shaft with mounting assembly. The nozzle inlet was mounted coaxially within the shroud. A schematic of a side view of a section through the centerline of the shrouded inlet piece is shown in Figure B.4. An end view schematic of this inlet piece is also shown in this figure, which is not drawn to scale. Parameters for describing the shrouded inlet piece are defined in the figure and the associated dimensions are given. The elbow and shaft pieces had inner diameters of 17 mm, equal to the inner diameter of the shrouded inlet piece at its outlet. The three pieces were constructed to give a smooth internal fit at the joints. The shaft length was 13.5 cm and the centerline flow path through the 90° elbow piece was 9.5 cm. The total length of the shrouded nozzle from inlet to outlet was 28.9 cm. In the end view schematic, the three supports attaching the nozzle inlet to the shroud are visible. The waist of the shrouded nozzle, the narrowest open area between the nozzle and the shroud can be seen in the end view as well. Altering the waist area is the means by which the total airflow rate through the shroud is adjusted in shrouded nozzle design.

Shrouded nozzles have been previously designed to facilitate aerosol sampling from airstreams with varying air speeds when using a constant flow pump (McFarland *et al.*, 1989; Rodgers *et al.*, 1996). At typical duct air speeds, most air entering the shroud exits

through the waist and a small fraction enters the nozzle inlet. Because of the flow constriction at the waist, air entering the shroud inlet is decelerated. For a given sample flow rate and air speed, this deceleration allows for the use of a larger nozzle inlet than in the case of an unshrouded nozzle if isokinetic sampling is desired. The larger nozzle inlet leads to smaller particle losses at the inlet of the nozzle. The gradual expansion of the nozzle inner diameter immediately after the inlet allows for larger diameter transport lines which leads to less wall deposition and higher transport efficiencies. In addition to these benefits, the shroud reduces the turbulence intensity at the nozzle inlet and helps reduce sampling errors when the nozzle is not precisely aligned with the mean flow-direction.

The shrouded nozzle described here is a scaled down version of the previous designs of McFarland *et al.* (1989), Ram *et al.* (1995) and Chandra & McFarland (1996). This shrouded nozzle was specifically designed for sampling from ventilation duct flow with an Aerodynamic Particle Sizer (APS). The APS measures concentrations for particle sizes in the range 0.5-20 μm. It samples at a constant flow rate of 5.0 L/min through an inlet with a 19 mm outside diameter. Ventilation duct air velocities considered in the shrouded nozzle design were in the range 1-20 m/s. To sample isokinetically from such duct velocities at the APS flow rate would require several isokinetic nozzle inlets with diameters in the range 1-7 mm. Because of wall losses, such small diameter nozzles and transport lines would be unlikely to reliably deliver particles larger than 3 μm to the APS. A shrouded probe with a larger nozzle inlet and transport line diameter is more likely to

deliver these 0.5-20 μm particles from the duct flow to the APS. A shrouded nozzle also eliminates the need for many different isokinetic nozzles.

B.2.2 Models for predicting transport efficiencies through nozzles

Predictions of particle transport efficiencies through isokinetic nozzles and shrouded nozzles were made using a combination of empirical equations presented by Brockman (1999). Deposition in transport lines by gravitational settling in nonvertical segments, Brownian diffusion and inertial deposition in bends were taken into account. Brockman also presents equations for transport efficiencies through nozzle inlets when sampling velocities are not isokinetic. Turbulent diffusion was not included in the transport efficiency calculations because all transport line flows were laminar.

Wall-deposition losses at inlets owing to sampling at nonisokinetic velocities were calculated by empirical equations. When sampling was sub-isokinetic, the transport efficiency through a short length just inside the nozzle inlet, η_{inlet}, was calculated by the following expression from Liu *et al.* (1989):

$$\eta_{inlet} = \frac{1+\left(\frac{u_o}{u_{inlet}}-1\right)\Big/\left(1+\frac{2.66}{\mathrm{St}_{\mathrm{inlet}}^{2/3}}\right)}{1+\left(\frac{u_o}{u_{inlet}}-1\right)\Big/\left(1+\frac{0.418}{\mathrm{St}_{\mathrm{inlet}}}\right)} \qquad \text{(B.4)}$$

$$\text{for } 0.01 \le \mathrm{St}_{\mathrm{inlet}} \le 100 \text{ and } 1 \le \frac{u_o}{u_{inlet}} \le 5$$

Here, $\mathrm{St}_{\mathrm{inlet}}$ is the particle Stokes number at the inlet calculated with the local airstream velocity and the nozzle inlet diameter:

$$\mathrm{St}_{\mathrm{inlet}} = \frac{\tau_p u_o}{d_{inlet}} \tag{B.5}$$

Hangal & Willeke (1990) present the following equation for η_{inlet} when sampling is super-isokinetic:

$$\eta_{inlet} = \exp\left[-0.61\left(\frac{\mathrm{St}_{\mathrm{inlet}}\left(u_{inlet} - u_o\right)}{u_o}\right)^{0.6}\right] \tag{B.6}$$

$$\text{for } 0.02 \le \mathrm{St}_{\mathrm{inlet}} \le 4 \text{ and } 0.25 \le \frac{u_o}{u_{inlet}} \le 1$$

The equation of Heyder & Gebhart (1977) was used to determine the transport efficiency resulting from gravitational settling, η_g, from laminar flow in a circular tube:

$$\eta_g = 1 - \frac{2}{\pi}\left[2\kappa\sqrt{1-\kappa^{2/3}} - \kappa^{1/3}\sqrt{1-\kappa^{2/3}} + \arcsin\left(\kappa^{1/3}\right)\right] \tag{B.7}$$

$$\kappa = \frac{3L_{t,nv}v_g}{d_t u_t}\cos(\beta_t) \tag{B.8}$$

$$\text{for } v_g \sin(\beta_t) << u_t$$

where $L_{t,nv,}$ is the length of a nonvertical segment of the transport line, d_t is the transport line diameter, u_t is the velocity in the transport line and β_t is the angle of the axis of the transport line segment measured from the horizontal plane.

The transport efficiency through the transport line owing to Brownian diffusion, η_B, was calculated by means of the analytical solution of Gormley & Kennedy (1949):

$$\eta_B = 1 - 2.56\zeta^{2/3} + 1.2\zeta + 0.77\zeta^{4/3} \qquad \text{for } \zeta < 0.02 \tag{B.9}$$

$$\eta_B = 0.818\exp(-3.657\zeta) + 0.097\exp(-22.3\zeta) + 0.032\exp(-57\zeta) \tag{B.10}$$

for $\zeta \geq 0.02$

$$\zeta = \frac{4 D_B L_{t,total}}{u_t d_t^2} \tag{B.11}$$

Here, ζ is the diffusional deposition parameter and $L_{t,total}$ is the total transport line length.

An equation for the transport efficiency owing to deposition in a bend, η_{bend}, in laminar flow was developed by Brockman (1999). This equation is a fit to the experimental data collected by Pui *et al.* (1987):

$$\eta_{bend} = \left[1 + \left(\frac{\mathrm{St}_t}{0.171}\right)^{2.64\mathrm{St}_t + 2.242}\right]^{-\frac{2}{\pi}\phi} \tag{B.12}$$

Here, ϕ is the bend angle in radians and St_t is the particle Stokes number in the transport line calculated using the air velocity in the transport line and the transport line diameter

$$\mathrm{St}_t = \frac{\tau_p u_t}{d_t} \tag{B.13}$$

To complete the model for transport efficiency through transport lines, inlet deposition, gravitational settling, Brownian diffusion and bend deposition were assumed to act independently; thus, the overall transport efficiency for a given particle size could be calculated by

$$\eta_t = \eta_{inlet} \eta_g \eta_B \eta_{bend} \tag{B.14}$$

B.2.3 Models for predicting aspiration efficiency at sampling inlets

Two empirical equations were used to predict aspiration efficiencies of the shrouded anisokinetic nozzle, one by Belyaev & Levin (1972) and another by Vincent *et al.* (1986). The equation from Belyaev & Levin is

$$\eta_a = 1 + \left(\frac{u_o}{u_{inlet}} - 1\right)\left[1 - \left[1 + \mathrm{St}_{\mathrm{inlet}}\left(2 + \frac{0.617 u_{inlet}}{u_o}\right)\right]^{-1}\right] \tag{B.15}$$

$$\text{for } 0.005 \le \mathrm{St}_{\mathrm{inlet}} \le 10 \text{ and } 0.2 \le \frac{u_o}{u_{inlet}} \le 5$$

The equation for aspiration efficiency presented by Vincent *et al.* is

$$\eta_a = 1 + \left(\frac{u_o}{u_{inlet}} - 1\right)\frac{1.05\mathrm{St}_{\mathrm{inlet}}}{\left(1 + 1.05\mathrm{St}_{\mathrm{inlet}}\right)} \tag{B.16}$$

With the shrouded nozzle, neither the shroud nor the inlet nozzle sample air isokinetically under most conditions. Aspiration efficiencies can be defined for both the shroud and the inlet nozzle. The aspiration efficiency of the shroud is

$$\eta_{a,shroud} = \frac{C_{shroud}}{C_{bulk}} \tag{B.17}$$

where C_{shroud} is the average concentration within the shroud immediately before the nozzle inlet. The aspiration efficiency of the inlet nozzle is defined by

$$\eta_{a,inlet} = \frac{C_{inlet}}{C_{shroud,c}} \tag{B.18}$$

where $C_{shroud,c}$ is the concentration in the shroud immediately upstream of the nozzle inlet and near the shroud centerline.

The total aspiration efficiency for the shrouded nozzle is defined, as in equation (B.1) by

$$\eta_{a,total} = \frac{C_{inlet}}{C_{bulk}} \tag{B.19}$$

Predictions of $\eta_{a,shroud}$ and $\eta_{a,inlet}$ can be made by equations (B.15) or (B.16). When predicting $\eta_{a,shroud}$ by these equations, u_o is the local velocity of the airstream and u_{inlet} should be set equal to the average velocity within the shroud upstream of the inlet, u_{shroud}. To predict $\eta_{a,inlet}$, u_o is equal to u_{shroud} and u_{inlet} is the average velocity at the nozzle inlet. It is not necessarily true that $\eta_{a,total}$ can not be predicted by multiplying $\eta_{a,shroud}$ by $\eta_{a,inlet}$ because of the difference between C_{shroud} and $C_{shroud,c}$. The shroud is expected to decelerate the flow to 30-40% of the free stream velocity (McFarland *et al.*, 1989; Chandra & McFarland, 1996). Therefore, it samples sub-isokinetically leading to an enrichment of large particles within the shroud. This enrichment is not uniform within the shroud; it is expected to be greater near the walls of the shroud where fluid streamlines diverge more than those near the shroud centerline. Most of the flow with higher particle concentrations is expected to flow out through the waist while the inlet nozzle samples the relatively unbiased aerosol at the shroud centerline. Values of C_{shroud} are expected to be greater than those of $C_{shroud,c}$ because C_{shroud} includes the flow regions near the shroud walls, where concentrations are higher.

Gong *et al.* (1996) developed a correlation for the ratio of $C_{shroud,c}$ to C_{shroud} based on the results of numerical simulations. They expressed this ratio, F, as

$$F = \frac{C_{shroud,c}}{C_{shroud}} = 1 - \left(\frac{u_o}{u_{shroud}} - 1\right) \frac{0.861 \mathrm{St}_{\mathrm{shroud}}}{\mathrm{St}_{\mathrm{shroud}}\left[2.34 + 0.939\left(\frac{u_o}{u_{shroud}} - 1\right)\right] + 1} \quad \text{(B.20)}$$

$\mathrm{St}_{\mathrm{shroud}}$ is the Stokes number based on the shroud diameter and the local air velocity

$$\mathrm{St}_{\mathrm{shroud}} = \frac{\tau_p u_o}{d_{shroud}} \quad \text{(B.21)}$$

Gong *et al.* recommend predicting the total aspiration efficiency of a shrouded probe by

$$\eta_{a,total} = F \eta_{a,shroud} \eta_{a,inlet} \quad \text{(B.22)}$$

where $\eta_{a,shroud}$ and $\eta_{a,inlet}$ can both be predicted by equation (B.15) or (B.16). In these model applications the air velocity through the shroud waist was taken to be $0.9u_o$ so that average velocities in the shroud were 36-40% of u_o.

B.2.4 Procedures for calculating measured transport and aspiration efficiencies

After each experiment, the fluorescent particle mass deposited on filters, m_f, and on the interiors of nozzles, m_n, and filter holders, m_{fh}, were measured as described in section 3.2.3.f. From these measurements, transport efficiencies through isokinetic nozzles could be determined by

$$\eta_t = \frac{m_f + m_{fh}}{m_n + m_f + m_{fh}} \quad \text{(B.23)}$$

The transport efficiency of the shrouded nozzle was calculated by

$$\eta_t = \frac{m_f + m_{fh}}{m_{inlet} + m_{elbow} + m_{shaft} + m_f + m_{fh}} \quad \text{(B.24)}$$

where m_{inlet}, m_{elbow} and m_{shaft} are respectively the measured fluorescent particle mass on the interior surface of the shrouded inlet piece, the elbow and the shaft.

The total aspiration efficiency of the shrouded nozzle was evaluated by comparing the particle concentration measured by the shrouded nozzle to the expected concentration at the shrouded nozzle location. The expected concentration was estimated by projecting the average concentration measured by the isokinetic filter samples surrounding test duct 1, C_1, to the shrouded nozzle location. Because the isokinetic nozzles had a known aspiration efficiency of one, concentrations measured by these nozzles and their filters were expected to be representative of actual concentrations in the duct. The bulk concentration in the duct at the location of the shrouded nozzle, C_o, was projected following the same method described in section 4.3.1 to give:

$$C_o = \frac{C_1}{exp\left(\frac{-4LV_{d,comp}}{D_h U_{ave}}\right)} \tag{B.25}$$

where L, the distance between the isokinetic nozzles and shrouded nozzle, was 4.1 m.

The concentration measured by the shrouded nozzle and filter is equivalent to C_{inlet} in equation (B.18). This experimentally measured concentration was calculated by

$$C_{inlet} = \frac{m_{inlet} + m_{bend} + m_{shaft} + m_f + m_{fh}}{m_{f/p} Q_{pump} t} \tag{B.26}$$

The experimentally measured total aspiration efficiency of the shrouded nozzle could be calculated by means of equation (B.19), substituting C_o from equation (B.25) for C_{bulk}.

B.3 Results

B.3.1 Transport efficiencies in isokinetic nozzles

Measured isokinetic nozzle transport efficiencies versus particle diameter are presented for all three nominal air speeds in both the steel and insulated systems in Figure B.5. Predicted transport efficiencies from the empirical model described in section B.2.2 are also shown. Because the nozzle inlets were located at the duct centerline, the air velocity at the inlets were higher than the average air speed. For similar nominal air speeds, centerline air velocities were slightly larger in the insulated system compared to the steel system. The model was applied using the slower inlet velocities in the steel system.

In most cases, data points represent the average of the transport efficiencies measured through the four nozzles in a given experiment. Error bars indicate the variability among the four measurements and are only included when they are significantly larger than the data points. For two experiments in the insulated system, run 25 with 8 μm particles at 5.3 m/s and run 31 with 13 μm particles at 8.8 m/s, two data points are shown instead of a single point. For each of these two experiments, the transport efficiencies measured in nozzles near test duct 1 agreed with each other, and those measured in nozzles near test duct 2 were in agreement, but there was poor agreement between data collected at the two different locations. The two data points respectively represent the average transport efficiencies in the two nozzles near test duct 1 and test duct 2.

B.3.2 Transport and aspiration efficiencies in the shrouded nozzle

Measured transport efficiencies through the shrouded nozzle versus particle size at the three nominal air speeds of 2.2, 5.3 and 8.8 m/s are shown in Figure B.6. In the plots in this figure, as with all plots regarding transport and aspiration efficiencies in the shrouded nozzle, each data point represents a single measurement. Predictions of transport efficiencies from the model are also included.

Plots of the measured total aspiration efficiency of the shrouded nozzle versus particle diameter for the three nominal air speeds are shown in Figure B.7. Total aspiration efficiencies predicted by equations (B.15) (Belyaev & Levin, 1972) and (B.16) (Vincent *et al.*,1986) are included. The model predictions were calculated using equation (B.22) with equation (B.20) for the factor F. In Figure B.8, the same data for total aspiration efficiencies as in Figure B.7 are presented with predictions from equations (B.15) and (B.16). In this figure, model predictions were calculated by equation (B.22) assuming $F = 1$. The measured total transmission efficiencies through the shrouded probe, T_{tot}, are presented in Figure B.9 along with model predictions. The model includes predictions by the empirical transport efficiency model and by equations (B.15) and (B.22), with $F = 1$ as in Figure B.8, for total aspiration efficiencies.

B.4 Discussion

B.4.1 Transport efficiencies in the isokinetic nozzles and the shrouded nozzle

In the top panel of Figure B.5, measured isokinetic nozzle transport efficiencies at the lowest nominal air speed are observed to be near one for the smallest particles and to

decrease to near zero for the largest particles. Measured values are in reasonable agreement with the empirical model for all particle sizes. In the middle panel, at the intermediate nominal air speed, measured transport efficiencies are again near one for the smallest particles; however, they are not close to zero for the larger particle sizes as observed at the lower air speed and as predicted by the model. This same trend was observed in the measured transport efficiencies at the highest nominal air speed in the bottom panel. There is a perceptible dip in the measured transport efficiencies at particle sizes between 3 and 9 μm at the two highest air speeds. At the two highest air speeds, the measurements do not agree with the model, which predicts transport efficiencies to be near zero for larger particle sizes.

A possible explanation for the trends in the measured data is that large particles deposited within the nozzle at the higher air speeds, but then resuspended into the nozzle airstream and were carried onto the filter at the nozzle outlet. Another possible explanation is that large particles bounced upon striking the nozzle wall and never deposited. That the experimental data and the empirical model show good agreement at the lowest air speed, where resuspension and bounce are less likely, is an indication that the model can give reasonable predictions. The model predicts that most of the deposition in the standard isokinetic nozzles occurs in the bends. That the transmission efficiency of 13 and 16 μm particles through these nozzles would increase as the air velocity through the nozzles increases is counterintuitive and resuspension and bounce are possible causes of this result. The combinations of particle sizes and air speeds that were observed to lead to resuspension of particles in the steel duct system are the same conditions observed to lead

to model-measurement disagreement here. Particles that are 5 μm and larger seem to be resuspended at the nominal air speeds of 5.3, 8.8 and 9.0 m/s. For particles smaller than 5 μm and for air velocities lower than 5.3 m/s, the model predictions are in good agreement with the measurements.

For the shrouded probe, agreement between the measured data and the transport efficiency model in Figure B.6 is reasonable at all air speeds. At the lowest air speed, measured transport efficiencies through the shrouded nozzle are about one for the 1 μm particles and gently decrease with increasing particle size. The same trends are seen at the higher air speeds, but the measured transport efficiencies decrease more rapidly with an increase in particle size at the higher velocities. The good model-measurement agreement for transmission through the shrouded probe contrasts with the case of the isokinetic nozzles, where model-measurement agreement for transport efficiencies was often poor.

For the isokinetic nozzles, where average velocities inside the transport lines were equal to the centerline duct velocities (up to 10.8 m/s), it was argued that resuspension or bounce of particles that were deposited on the nozzle interior could have been the cause of the model-measurement discrepancy. In the shrouded nozzle, the velocity inside the transport lines was 0.37 m/s for all experiments. Resuspension is much less likely to occur at this low velocity compared to the velocities in the isokinetic nozzles. High transport efficiencies through the isokinetic nozzles for large particles at high velocities may have been the result of resuspension of particles deposited within the transport line.

High transport efficiencies through the shrouded nozzle in these cases were probably due to particles traveling through the transport lines without depositing. Because the resuspension of particles is a poorly understood phenomena, the high transport efficiencies through the shrouded nozzle are much more predictable and repeatable than those in the standard nozzles.

B.4.2 Aspiration efficiencies in the shrouded nozzle

As shown in Figure B.7, measured total aspiration efficiencies are near one for all particle sizes at the lowest air speed. At the two higher air speeds, measured total aspiration efficiencies increase with increasing particle size. This increase in aspiration efficiency with increasing particle size was greatest at the highest air speed of 8.8 m/s. This trend is expected because the velocity at the inlet of the shrouded nozzle is 1.7 m/s. As the free stream velocity increases above 5 m/s, the shrouded inlet samples at a rate that is more sub-isokinetic causing large particles to be oversampled. Both of the empirical aspiration efficiency equations follow the same trends as the measured data, but both underpredict the measured aspiration efficiencies.

The same experimental data are presented in Figure B.8 as in Figure B.7, but the models are applied with $F = 1$ instead of using equation (B.20) to calculate F. This is equivalent to a simple cascade application of the aspiration efficiency equations to the shroud and to the nozzle inlet. In Figure B.8, equation (B.15) from Belyaev & Levin (1972) agrees well with the experimental data, while equation (B.16) from Vincent *et al.* (1986) underpredicts the data significantly. That model-measurement agreement is improved in

Figure B.8 compared to Figure B.7 suggests that the air within the shroud is relatively well-mixed and that the factor F accounting for the unequal distribution of particles within the shroud is unnecessary. The best model for the total aspiration efficiency of the shrouded probe is equation (B.22) using equation (B.15) to calculate $\eta_{a,shroud}$ and $\eta_{a,inlet}$ and assuming $F = 1$.

For all air speeds and particle sizes studied, the measured total transmission efficiencies in the shrouded nozzle were appreciable as seen in Figure B.9. High total transmission efficiencies of large particles at high air speeds were a result of both high aspiration efficiencies and high transport efficiencies through the transport lines of the shrouded nozzle. High total transmission efficiencies are important in the case of monitoring ambient particles in ventilation ducts with an APS. Ambient particles cannot be rinsed from nozzle interiors and quantified as fluorescent experimental particles can be. The relatively low concentrations of large particles in ventilation ducts makes it important that these large particles are delivered with a high transmission efficiency to the APS. Figure B.9 suggests that good estimates of the total transmission efficiency through the shrouded probe can be made for most particle sizes and air speeds of concern by the presented models. High transmission efficiencies may be achieved at high air speeds with the isokinetic nozzles, but these high values may result from resuspension of particles after deposition within the nozzle. The process of resuspension is difficult to quantify and prediction of transmission efficiencies through the isokinetic nozzles in these high-air-speed cases is much less certain than for the shrouded nozzle.

The shrouded nozzle could be used to reliably deliver an aerosol with particles in the range 0.5-16 μm from most ventilation ducts to an APS sampling at a constant rate of 5.0 L/min. The concentration measured by the APS at the outlet of the shrouded nozzle could be corrected to give the bulk concentration in a ventilation duct using the models presented in this appendix with good confidence.

B.5 Conclusions

Measurements suggest that the shrouded nozzle described here could be used with an APS to reliably measure concentrations in most ventilation ducts for particles in the size range 0.5-16 μm. Anisokinetic sampling with a shrouded nozzle has advantages over sampling with isokinetic nozzles when sampling particles from duct flow with an APS that samples at a constant flow rate of 5.0 L/min. These advantages include a higher total transmission efficiency for most particles, a more predictable total transmission efficiency for most particles and a greater ease of use.

Measured total transmission rates through the shrouded anisokinetic nozzles were greater than or equal to those through the isokinetic nozzles for all particle sizes and air speeds studied. The higher total transmission rates through the shrouded nozzle resulted from both higher transport efficiencies and higher aspiration efficiencies. Furthermore, total transmission rates through the shrouded nozzle could be more reliably predicted by the presented empirical models. There is evidence to suggest that transmission rates through the isokinetic nozzles are difficult to predict because the high air speeds within the nozzles may lead to resuspension of deposited particles.

When sampling at a constant rate from a real ventilation duct, where air flow rates may change owing to changing demand within the building, an anisokinetic shrouded nozzle is easier to use than isokinetic nozzles. Because isokinetic nozzles come in discrete sizes and air speeds in ventilation ducts cover a continuous range, isokinetic nozzles would frequently sample at an anisokinetic rate if the sampling flow rate is fixed. The shrouded nozzle can be used to sample over the continuous range of air speeds and the presented correlations can be applied with good confidence to adjust measured concentrations to actual concentrations in the duct.

Table B.1 Measured inlet diameters of isokinetic nozzles.

Nozzle #	**Measurement location (-)**	**Nominal inlet diameter (in)**	**Measured inlet diameter, d_{inlet} (mm)**
1	$C_{1,up}$	0.180	4.57
2	$C_{1,down}$	0.180	4.65
3	$C_{2,up}$	0.180	4.44
4	$C_{2,down}$	0.180	4.42
5	$C_{1,up}$	0.120	3.10
6	$C_{1,down}$	0.120	3.10
7	$C_{2,up}$	0.120	3.10
8	$C_{2,down}$	0.120	3.10

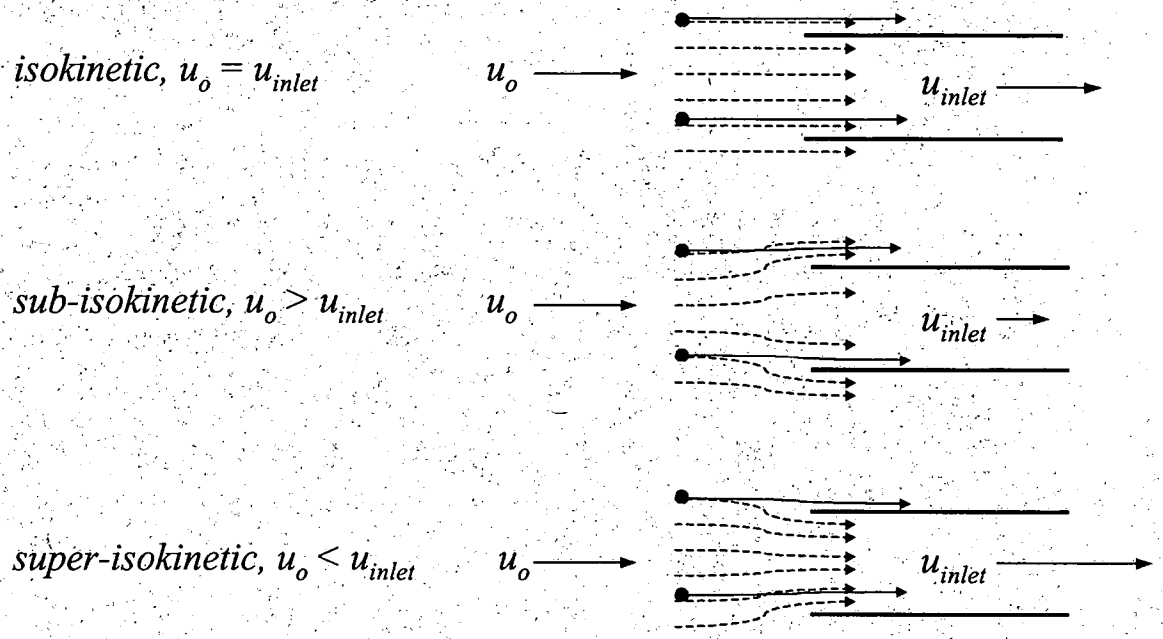

Figure B.1 Sampling inlets with air streamlines and hypothetical particle trajectories under three sampling conditions: isokinetic, sub-isokinetic and super-isokinetic.

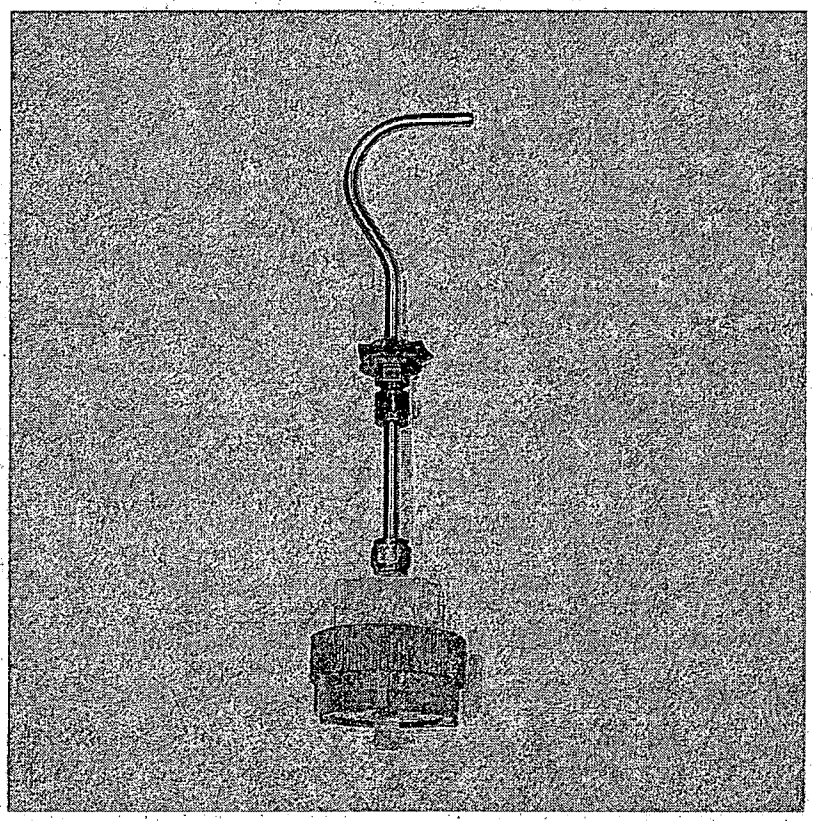

Figure B.2 Photograph of a stainless steel isokinetic nozzle with a mounting assembly on the shaft. The nozzle is attached to a 47 mm Teflon filter holder.

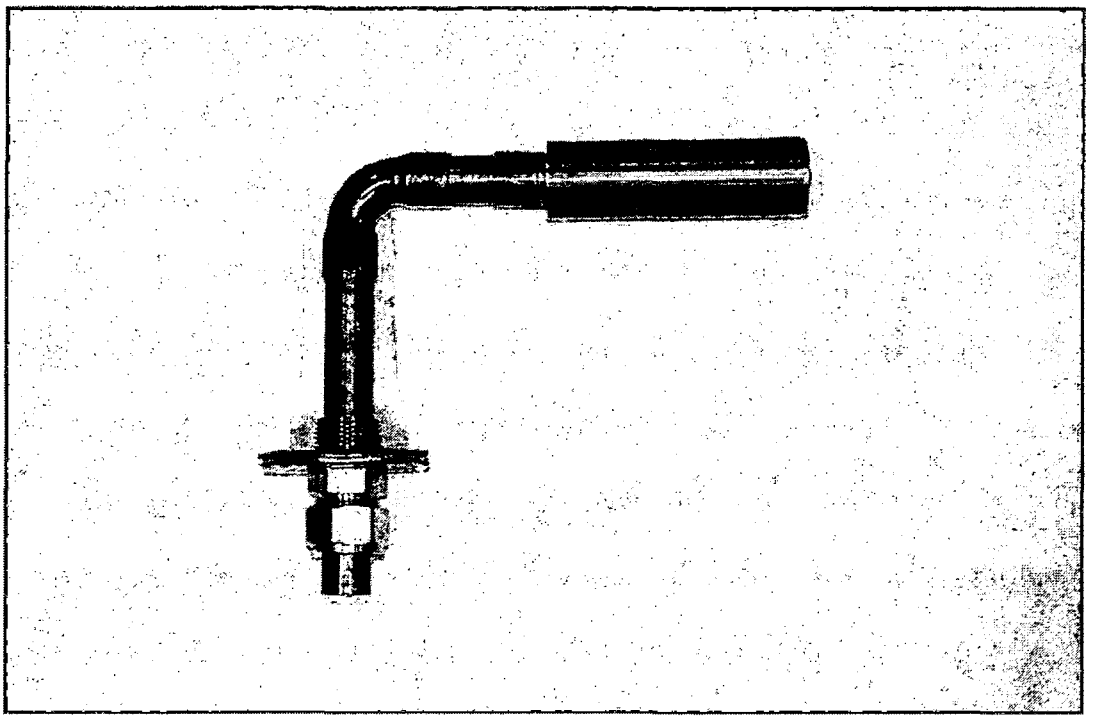

Figure B.3 Photograph of a shrouded nozzle showing the shrouded inlet piece, the elbow and the shaft with the mounting assembly.

length of shroud:	L_{shroud}	=	100 mm
length of nozzle inlet piece:	L_{inlet}	=	75 mm
length between shroud inlet and nozzle inlet:	L_{offset}	=	45 mm
inner diameter of nozzle at inlet:	d_{inlet}	=	8 mm
inner diameter of nozzle at outlet:	d_t	=	17 mm
outer diameter of nozzle at outlet:	od_{inlet}	=	21 mm
inner diameter of shroud:	d_{shroud}	=	28 mm

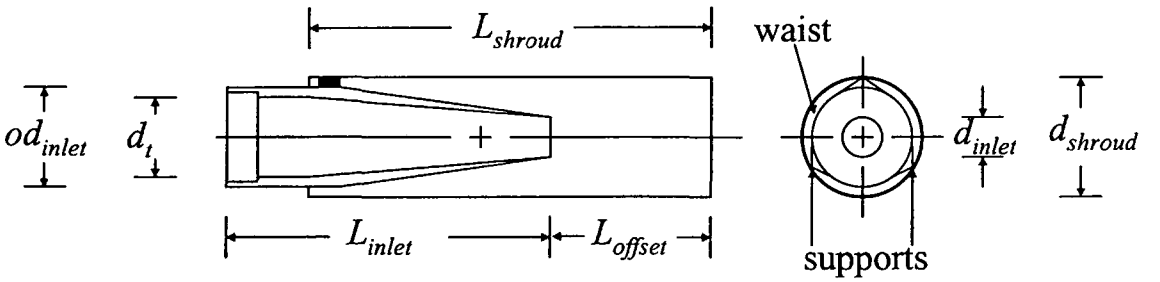

Figure B.4 Schematics of a side view of a section through the centerline of the shrouded inlet and of an end view of the inlet. Dimensions of defined parameters are also given.

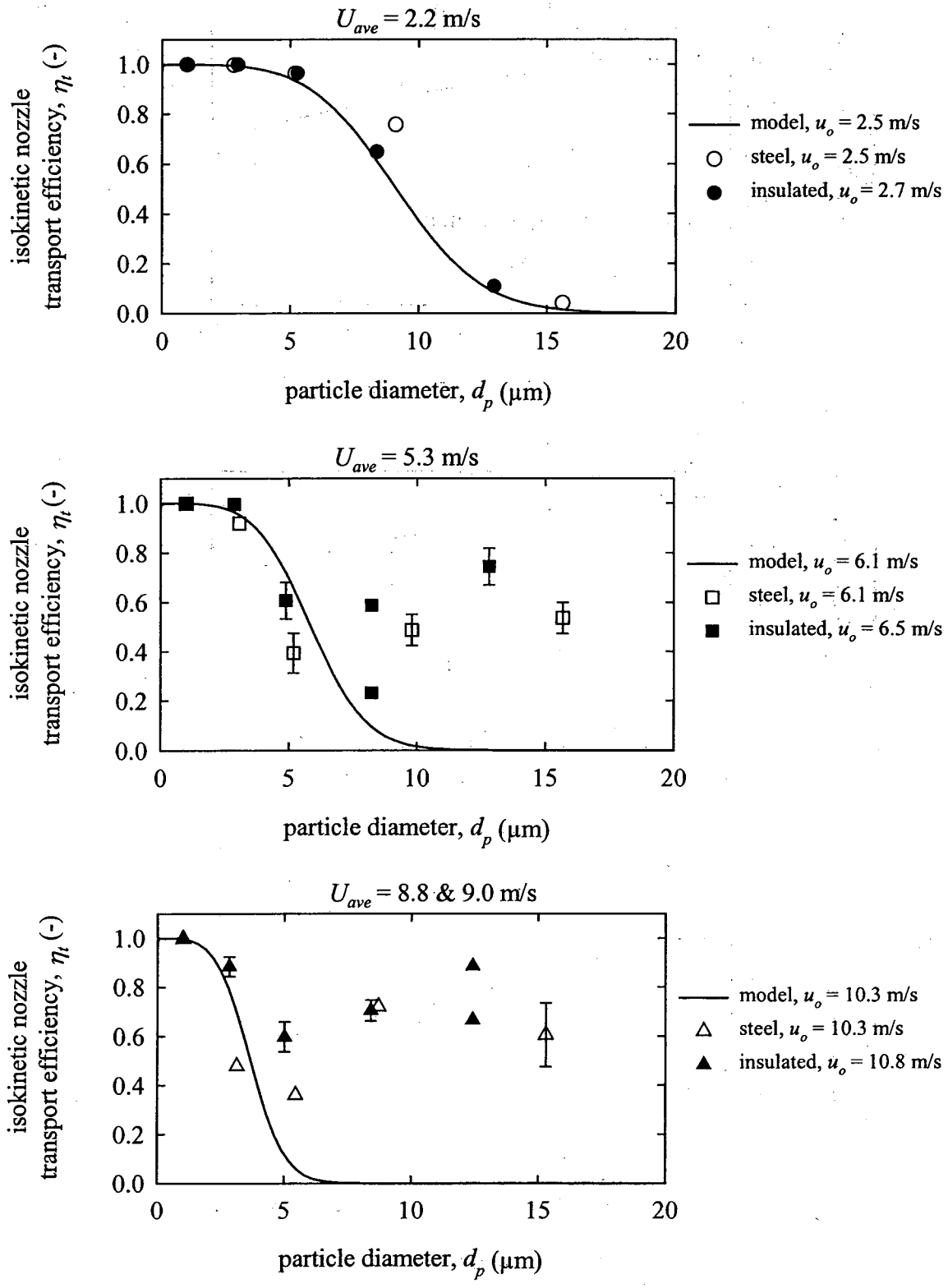

Figure B.5 Isokinetic nozzle transport efficiencies versus particle diameter for the nominal air speeds of 2.2, 5.3 and 8.8 & 9.0 m/s.

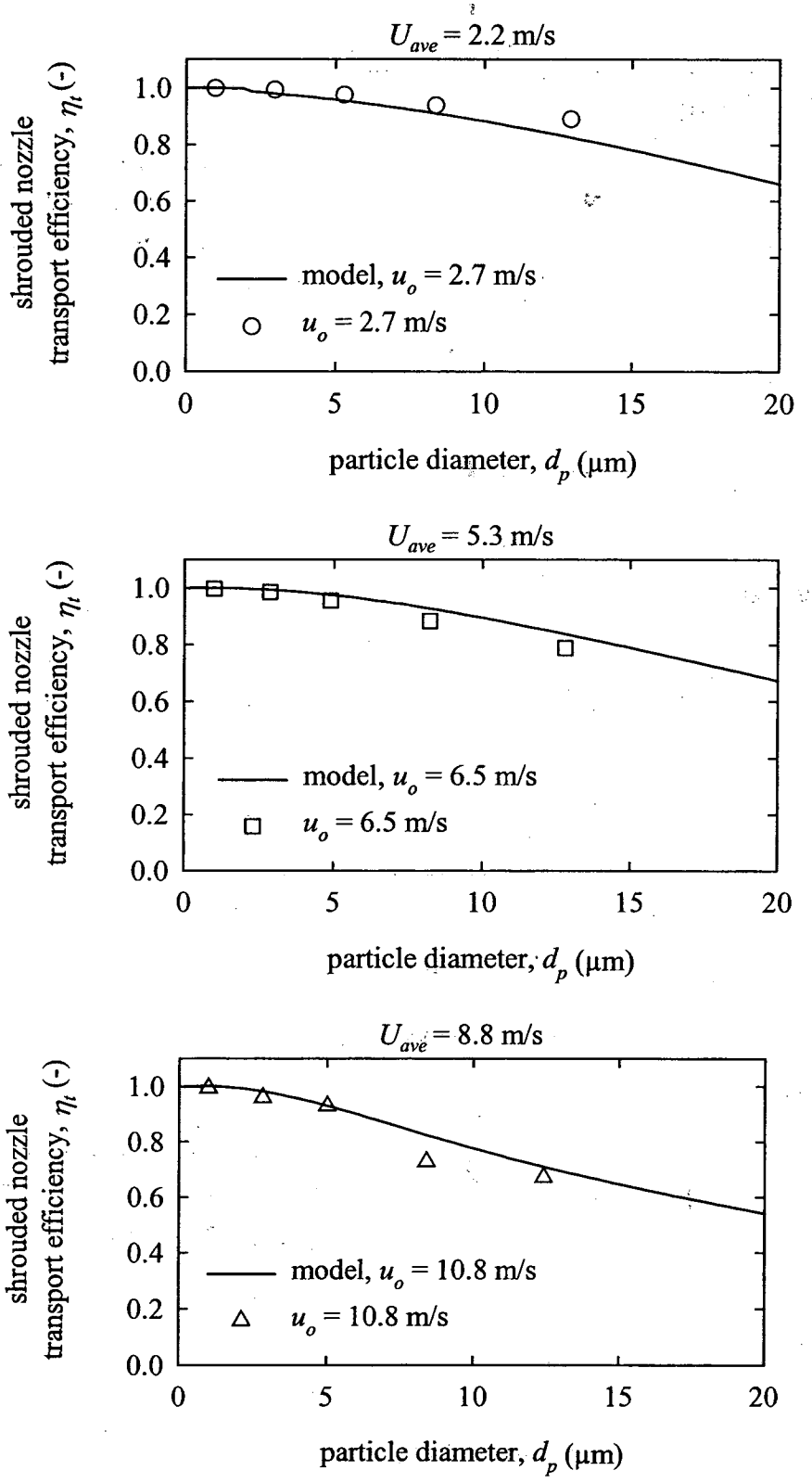

Figure B.6 Shrouded nozzle transport efficiencies versus particle diameter for the nominal air speeds of 2.2, 5.3 and 8.8 m/s.

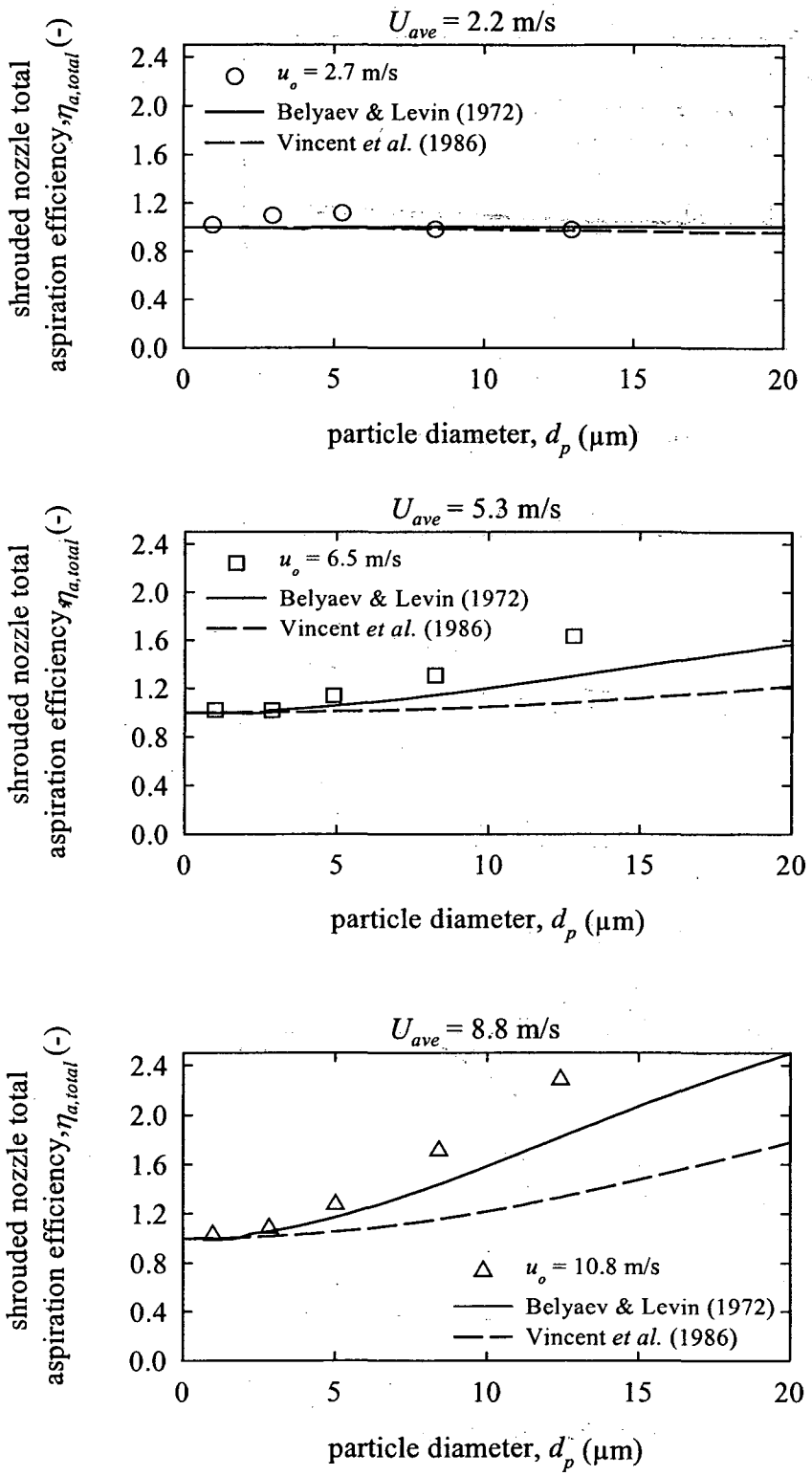

Figure B.7 Total aspiration efficiencies for the shrouded nozzle versus particle diameter for the nominal air speeds of 2.2, 5.3 and 8.8 m/s. The models are applied using equation (B.22) and equation (B.20) from Gong *et al.* for the factor *F*.

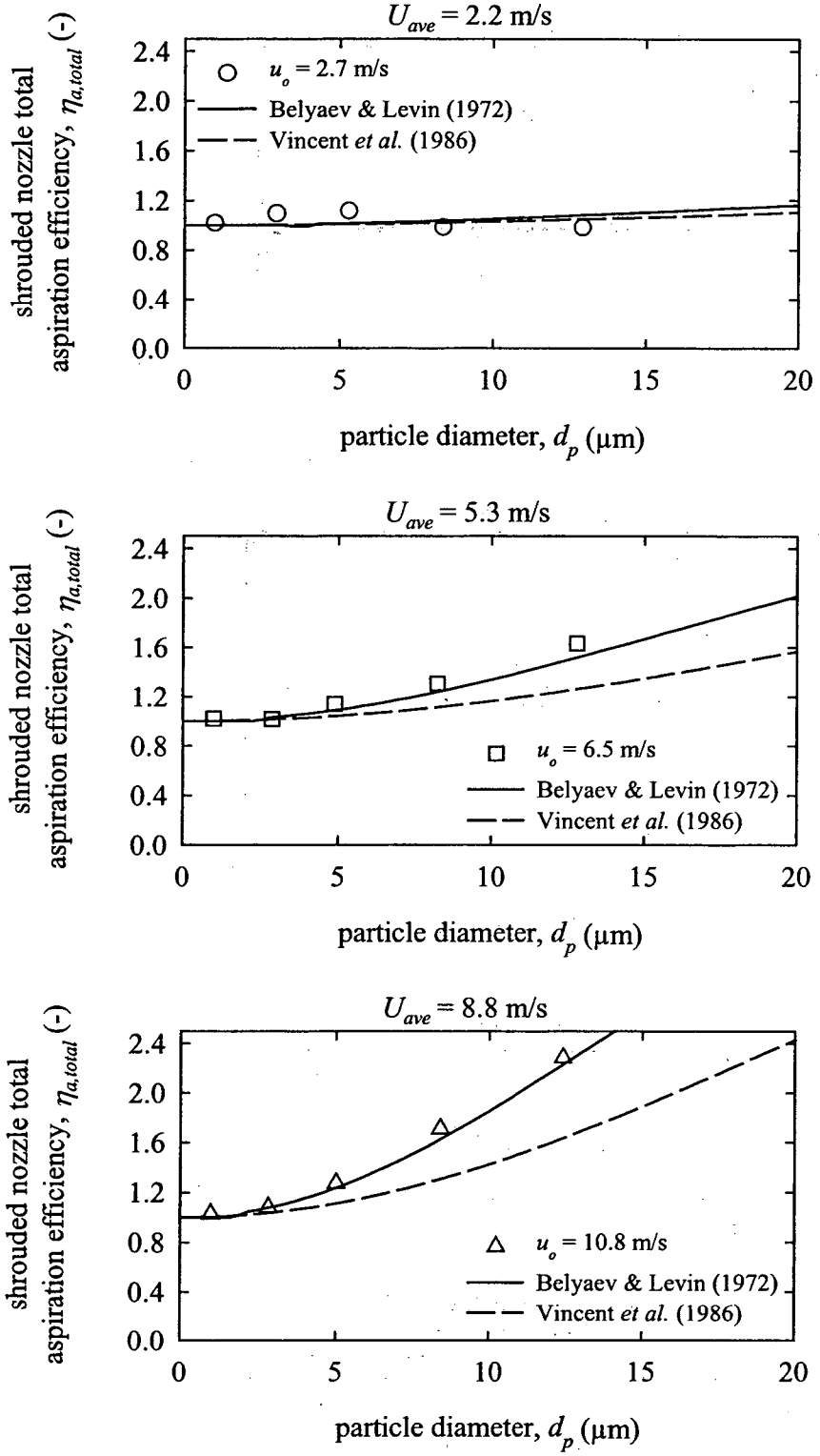

Figure B.8 Total aspiration efficiencies for the shrouded nozzle versus particle diameter for the nominal air speeds of 2.2, 5.3 and 8.8 m/s. The models are applied using equation (B.22) with $F = 1$.

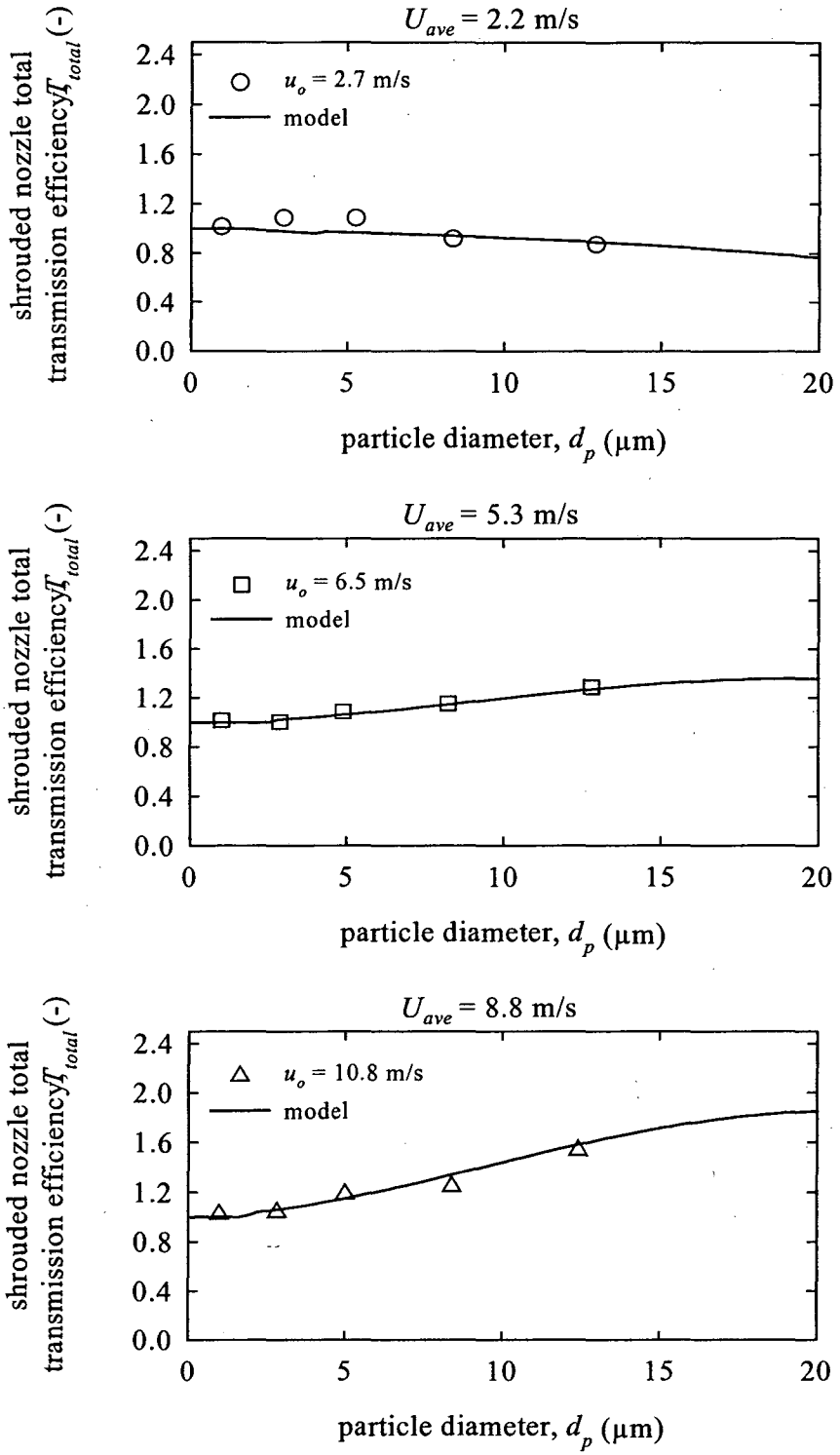

Figure B.9 Total transmission efficiencies for the shrouded nozzle versus particle diameter for the nominal air speeds of 2.2, 5.3 and 8.8 m/s. The model includes the empirical model for transport efficiencies and equations (B.15) and (B.22) with $F = 1$ for total aspiration efficiencies.

APPENDIX C

Pressure Gradient, Temperature and Relative Humidity Measurements and An Evaluation of Thermophoretic Deposition Rates

C.1 Introduction

When performing experiments to investigate particle deposition from turbulent duct flows, it is useful if the flow can be well characterized. Two parameters that are important for understanding particle deposition are the friction velocity of a turbulent flow and the near-wall temperature gradient. The friction velocity indicates the level of turbulence in the flow and the degree to which particles may be transported and deposited to walls by turbulent fluctuations. The near-wall temperature gradient can be used to evaluate the importance of thermal forces in depositing particles to duct walls.

This appendix presents measurements of pressure drop, air temperature and relative humidity made in the steel and insulated ducts during the particle deposition experiments described in Chapter 3. Measurements of duct surface temperatures made during an auxiliary experiment in the steel duct system are also presented. Pressure drop measurements were used to calculate friction velocities in each experiment. Equations for estimating near-wall temperature gradients from air and surface temperature measurements are introduced. Particle deposition rates owing to thermophoresis are estimated and compared to the measured particle deposition rates in the steel system.

C.2 Methods

Measurements of pressure gradient, air temperature and relative humidity were made in the experimental duct during each experiment. The ambient air temperature was also. An auxiliary experiment was conducted without particles to evaluate the interior and exterior surface temperatures of the steel ducts at the three nominal air speeds of 2.2, 5.3 and 9.0 m/s.

The air temperature, relative humidity and pressure drop measurements made during these experiments are described in section 3.2 and essential details are repeated here. Air temperature measurements were made at the duct centerline at locations A and B in Figure 3.1. Location A was 1.8 m downstream of the mixing box in the lower duct and location B was immediately downstream of test duct 2 in the upper duct. Relative humidity measurements were made at the duct centerline at location A. Static pressures in the lower duct were measured at locations A and C and were used to calculate pressure gradients using equation (3.4). Location C was positioned 13.1 m downstream of location A. Temperatures, relative humidities and static pressures were measured and recorded once every 1-10 minutes during the course of an experiment, with the time interval between measurements depending on the total length of the experiment.

An auxiliary experiment was conducted to evaluate interior and exterior duct surface temperatures at the three nominal air speeds in the steel system. Duct surface temperature measurements were made close to the position of the air temperature measurements at locations A and B. Thermistors for measuring surface temperature were

securely fastened to the appropriate surface and heavily insulated. In this trial, the fan was turned on to circulate air through the duct system at a speed of 9.0 m/s for about two hours, then the fan speed was decreased to achieve an air speed of 5.3 m/s for two hours. After that, the fan speed was again decreased to yield an air speed of 2.2 m/s for a period of about two hours before the fan was turned off. Surface temperature measurements could not be made at the internal (insulated) surface of insulated ducts because of the nonconductive nature of the insulation.

Pressure drops were used to calculate friction factors for flows by equation (2.7). These friction factors were then used to determine friction velocities by equation (2.6). Air temperatures and duct surface temperatures were used to evaluate the magnitude of thermal forces that may influence particle transport. Relative humidity and temperature measurements were used to calculate the air density at the prevailing pressure of one atmosphere.

To estimate the deposition velocity of a particle attributable to thermophoresis, the temperature gradient adjacent to the wall must be evaluated. For a turbulent flow, the local air temperature in a duct, $T(y^+)$ can be estimated by the following equations (Kay & Nedderman, 1990):

$$T(y^+) = T_w + \mathrm{Pr} y^+ \frac{\Delta T}{\Delta T_{200}^+} \qquad \text{for } y^+ < 5 \qquad \text{(C.1)}$$

$$T(y^+) = T_w + \left[5\mathrm{Pr} + 5ln\left(0.2\mathrm{Pr}y^+ + 1 - \mathrm{Pr}\right)\right]\frac{\Delta T}{\Delta T_{200}^+} \qquad \text{for } 5 \le y^+ \le 30 \qquad \text{(C.2)}$$

$$T(y^+) = T_w + \left[5\mathrm{Pr} + 5\ln(1+5\mathrm{Pr}) + 2.5\ln\left(\frac{y^+}{30}\right) \right] \frac{\Delta T}{\Delta T_{200}^+} \qquad \text{for } 30 < y^+ < 200 \quad \text{(C.3)}$$

Here, T_w is the surface temperature of the duct wall, Pr is the Prandtl number of air, equal to about 0.7, ΔT is the difference in temperature between $y^+ = 200$ and the duct wall and ΔT_{200}^+ is defined by

$$\Delta T_{200}^+ = 5\mathrm{Pr} + 5\ln(1+5\mathrm{Pr}) + 2.5\ln(200/30) \quad \text{(C.4)}$$

It was assumed that the measured centerline duct temperature, T_o, was equal to the temperature at $y^+ = 200$ so that

$$\Delta T = T_o - T_w \quad \text{(C.5)}$$

The near-wall temperature gradient can be found by converting equation (C.1) to dimensional form and taking the derivative with respect to the distance from the wall, y:

$$\left(\frac{\partial T}{\partial y}\right)_{wall} = \frac{\mathrm{Pr} u^*}{\nu} \frac{\Delta T}{\Delta T_{200}^+} \quad \text{(C.6)}$$

Alternatively, the following expression has been proposed for the temperature gradient at a duct wall if the centerline and surface temperatures are known (Wood, 1981b):

$$\left(\frac{\partial T}{\partial y}\right)_{wall} = \frac{u^{*2}(T_o - T_w)}{\nu(U_{ave} - 5u^*)} \quad \text{(C.7)}$$

Near-wall temperature gradients at locations A and B were calculated based on the air and surface temperature measurements at each location. Near-wall temperature gradients at locations A and B were calculated by both equations (C.6) and (C.7); the best estimate of the gradient at each location was taken to be the average of these two determinations.

Because location B was very close to test duct 2, the near-wall temperature gradient at test duct 2 was set equal to the best estimate at location B. Test duct 1 was about half way between locations A and B; the near-wall temperature gradient at test duct 1 was taken to be the average of the best estimates at locations A and B.

These near-wall temperature gradients at test ducts 1 and 2 could then be used to predict particle velocities toward the duct walls owing to thermophoresis, v_{th}, using equation (2.42). The thermal conductivity of air, k_a, was taken to be 0.026 W m^{-1} K^{-1}. The thermal conductivities of oleic acid and fluorescein are 0.23 and 0.43 W m^{-1} K^{-1}, respectively. The value for the thermal conductivity of the experimental particles was taken to be 0.31 W m^{-1} K^{-1} based on a volume weighted average of conductivities of oleic acid and fluorescein for 9 μm particles. Thermophoretic velocities were nondimensionalized by dividing by the friction velocity:

$$v_{th}^{+} = \frac{v_{th}}{u^{*}} \tag{C.8}$$

C.3 Results

Figure C.1 displays plots of the measured pressure gradient, air temperature and relative humidity versus experimental time for run 4 conducted at an air speed of 2.2 m/s in the steel system. Figures C.2 and C.3 show similar plots for runs 10 and 16 conducted in the steel system at air speeds of 5.3 and 9.1 m/s, respectively. Measurements made during these three experiments were typical of other measurements made in the steel system for

the same nominal air speeds. The horizontal axes on these plots include time before the fan was started and after the fan was turned off.

Figures C.4-C.6 show plots of the measured pressure gradient, air temperature, and relative humidity versus experimental time for representative experiments conducted in the insulated system at the three nominal air speeds of 2.2, 5.3 and 8.8 m/s.

Table C.1 summarizes the average differences between the air temperature at locations A and B and the ambient air temperature during experiments in both the steel and insulated systems at the three nominal air speeds.

Interior and exterior duct surface temperatures, along with centerline air temperatures, measured at locations A and B during the auxiliary experiment are shown in Figure C.7. The different regimes of fan operation are delineated by vertical dotted lines. Measured differences between the centerline air temperature and the interior duct wall temperature at locations A and B are summarized in Table C.2, along with near-wall temperature gradients at locations A and B calculated using equations (C.6) and (C.7).

Figures C.8-C.10 present the same experimental data as are presented in Figures 3.12-3.14 for particles depositing to the duct floor, wall and ceiling in the steel system at 2.2, 5.3 and 9.0 m/s, respectively. Included in these figures are dimensionless near-wall thermophoretic velocities at test ducts 1 and 2 predicted by equations (2.42) and (C.8).

C.4 Discussion

In the top panel of Figure C.1, that the fan was turned on at a time of about 1.5 hours can be seen by the small rise in measured pressure gradient from zero to about 0.5 Pa/m. Turning the fan off at a time of about 22.5 hours corresponds to the return of the measured pressure drop to zero. In run 4, particles were injected during the time between 4 and 22 hours on this time scale. The middle panel of Figure C.1 shows little variation in air temperature measurements during the course of run 4. Measured air temperatures at locations A and B are about the same as the measured ambient air temperature, 22.2 °C. Relative humidity measurements during run 4, shown in the bottom panel of Figure C.1, show some fluctuation, but were mostly constant at 46% during the experiment.

From the pressure gradient measurements made during run 10 in the top panel of Figure C.2, it can be seen that the fan was turned on at 0.8 hours and turned off at 12 hours. Particles were injected during times between 2.5 and 11.5 hours on this time scale. The measured pressure gradient during this time was nearly constant at about 2.6 Pa/m. Air temperature measurements were mostly constant and were different depending on the location of the measurement. The average ambient air temperature was 22.2 °C, significantly lower than air temperatures at locations A and B, which averaged 23.2 °C and 22.9 °C, respectively. The higher air temperatures inside the duct were the result of energy being added to the circulating duct air by the fan. Air temperatures within the duct increased when the fan was turned on and relaxed back to the ambient temperature after the fan was turned off. This temperature increase within the duct was observed during every experiment with nominal air speeds of 5.3 or 9.0 m/s; at air speeds of 2.2

m/s, there was no measured increase in the air temperature within the duct. Air temperatures at location A, nearest to the fan, were always highest. Air temperatures at location B were lower than at location A because of energy losses through the duct walls to the surroundings as air flowed from location A to location B. In the bottom panel of Figure C.2, relative humidity measurements were observed to be nearly constant during the experiment. Changes in relative humidity associated with turning the fan on and off are visible. For a given water content of the air, increasing air temperature decreases the relative humidity. This leads to the abrupt (but small) changes in relative humidity when the fan is turned on and off.

From the graphs in Figure C.3, it can be seen that the fan was turned on for run 16 at 1 hour and turned off at 11.5 hours; particles were injected during times from about 2.5 to 11 hours on this time scale. The measured pressure gradient for run 16 was larger than in the two previous figures owing to the higher air speed. Once steady-state conditions were achieved, the average temperature at location A was 3.7 °C greater than the ambient temperature. At location B, the average difference between the air temperature and the ambient temperature was 2.6 °C. The relative humidity profile shows a relatively constant value during the experiment, with the changes expected from turning the fan on and off.

In Figures C.4-C.6, respectively displaying data collected during runs 21, 23 and 31 in the insulated system, the same trends seen in measurements in the steel system are observed in the insulated system. Measured pressure gradients increased with increasing

air speed, as expected. For a given air speed, measured pressure gradients in the insulated system were higher than those the steel system. As shown in the middle panel of Figure C.4, the air temperature inside the duct was measured to be about the same as the ambient temperature for run 21 at the lowest air speed. In runs 23 and 31 at the higher air speeds, the measured temperatures inside the duct were higher than the ambient temperature, and the temperature at location A was higher than at location B. As in the steel system, the temperature increase inside the duct was greatest for the highest air speed.

Changes in the air and surface temperatures at locations A and B with changes in the air speed are clear in Figure C.7. The air temperature inside the duct was higher than the interior duct surface temperature at all air speeds, indicating that heat was transferred from the airstream through the duct walls to the ambient air. The measured internal and external duct surface temperatures were almost equal, suggesting that most of the resistance to heat transfer rested in convection at the air-surface interface, rather than in conduction through the steel duct wall. It is surprising that a difference in centerline air temperature and duct surface temperature was measured at the 2.2 m/s air speed at location A in this experiment. Air temperatures within the duct did not increase significantly above the ambient temperature during the particle deposition experiments with particles at this lowest air speed; however, in the top panel of Figure C.7, there is a clear relaxation of measured temperatures at location A to a lower temperature after the fan is turned off. The reason for the difference among experiments at the low air speed is unclear; the difference between the ambient temperature and the centerline duct

temperature at location A at the two higher speeds in this experiment were comparable to those measured in experiments with particles.

The near-wall temperature gradients at locations A and B calculated by equations (C.6) and (C.7) and presented in Table C.2 show that the gradients sharply increase as the air speed increases. Equation (C.7) yields estimates of temperature gradients that are 46-73% greater than those obtained from equation (C.6).

Because the duct walls were at a lower temperature than the airstream, particles may deposit on the walls because of thermophoresis. In Figure C.8, the estimated near-wall dimensionless velocity owing to thermophoresis, v_{th}^{+}, at test duct 1 is approximately 10^{-5} for all particle sizes at an air speed of 2.2 m/s. No estimate of this velocity was made at test duct 2 for this air speed because the measured air-surface temperature difference was zero. Values of v_{th}^{+} are negligible compared to most of the experimental data, but they are of comparable magnitude to some deposition data collected for small particles depositing to duct ceiling and wall surfaces. Similar observations can be made regarding Figures C.9 and C.10 which compare estimated thermophoretic deposition rates to experimental data collected at air speeds of 5.3 and 9.0 m/s, respectively. Owing to the different temperature gradients at the two locations, estimated values of v_{th}^{+} are about 50% higher in test duct 1 than in test duct 2 at the higher air speeds.

Values of v_{th}^{+} should represent a theoretical minimum dimensionless deposition velocity to vertical walls in these experiments. Measured deposition rates to the duct ceiling may

be less than the estimated thermophoretic velocity owing to the counteracting influence of gravity. At air speeds of 2.2 and 5.3 m/s, measured wall deposition rates are equal to or greater than v_{th}^{+}; however, at the highest air speed, the wall deposition rates measured for 1 μm particles are significantly lower than the estimated thermophoretic velocity. This suggests either an overestimation of v_{th}^{+} or experimental measurements that do not accurately reflect actual deposition rates at these low values.

Except for occasional discrepancies, the measured deposition rates in test ducts 1 and 2 are in agreement for all duct surfaces at all air speeds. This indicates that the higher air-surface temperature differences at test duct 1 did not lead to a measurable increase in particle deposition rates due to thermophoresis compared to rates in test duct 2. The uncertainty analysis in Appendix D suggests that the experimental techniques were sensitive enough to detect such differences in deposition rates when the deposition velocity is comparable to the thermophoretic velocity.

C.5 Conclusions

Measured static pressure gradients and air temperatures were stable during the course of all experiments. Measured pressure gradients increased with air speed in the duct; for a given air speed, the pressure gradient was greater in the insulated system than in the steel system.

Measured air temperatures at the duct centerline were the same as the ambient air temperature in both systems at a nominal air speed of 2.2 m/s. At higher air speeds, the

temperature inside the duct was greater than the ambient temperature because of energy input from the fan. The air temperature increase above the ambient temperature was highest for the highest air speed in both systems. The internal surface temperature of the steel ducts was cooler than the air temperature in the ducts for air speeds of 5.3 and 9.0 m/s. The estimated near-wall temperature gradient was greatest for the highest air speed.

Estimates of thermophoretic particle deposition velocities owing to the near-wall temperature gradient suggest that thermophoresis were small in most experiments; however, thermophoresis may have influenced measured deposition rates to duct walls and ceilings in the experiments in the steel system with the smallest (1 μm) particles studied..

Table C.1 Differences between the centerline air temperature and the ambient temperature at locations A and B averaged for the three nominal air speeds in both the steel and insulated systems.

	Steel system		Insulated system	
air speed, U_{ave} (m/s)	Difference between air temperature at location A and ambient temperature (°C)	Difference between air temperature at location B and ambient temperature (°C)	Difference between air temperature at location A and ambient temperature (°C)	Difference between air temperature at location B and ambient temperature (°C)
2.2	0.0	0.0	0.0	0.0
5.3	0.9	0.6	1.1	0.8
8.8 & 9.0	3.6	2.8	4.1	3.4

Table C.2 Differences between the centerline air temperature and the duct surface temperature at locations A and B for the three nominal air speeds in the steel system and predicted near-wall temperature gradients.

air speed, U_{ave} (m/s)	air-surface temperature difference at location A, ΔT (°C)	near-wall temperature gradient at location A from equation (C.6), $(dT/dy)_{wall}$ (K/m)	near-wall temperature gradient at location A from equation (C.7), $(dT/dy)_{wall}$ (K/m)	air-surface temperature difference at location B, ΔT (°C)	near-wall temperature gradient at location B from equation (C.6), $(dT/dy)_{wall}$ (K/m)	near-wall temperature gradient at location B from equation (C.7), $(dT/dy)_{wall}$ (K/m)
2.2	0.2	69	120	0.0	0	0
5.3	0.4	320	520	0.2	160	260
9.0	1.0	1300	1900	0.6	770	1200

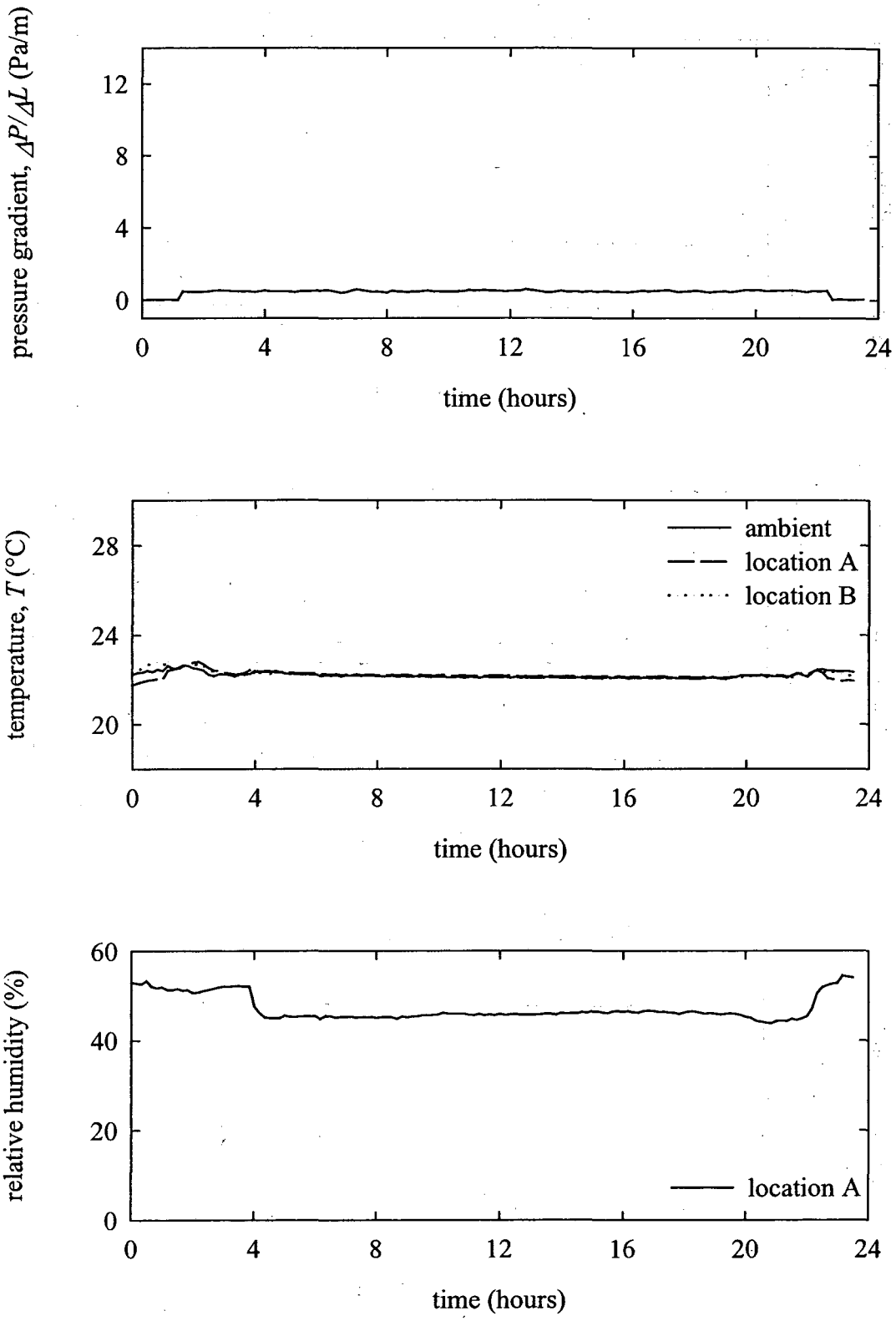

Figure C.1 Pressure gradient, temperature and relative humidity profiles for run 4 in the steel duct with an air speed of 2.2 m/s.

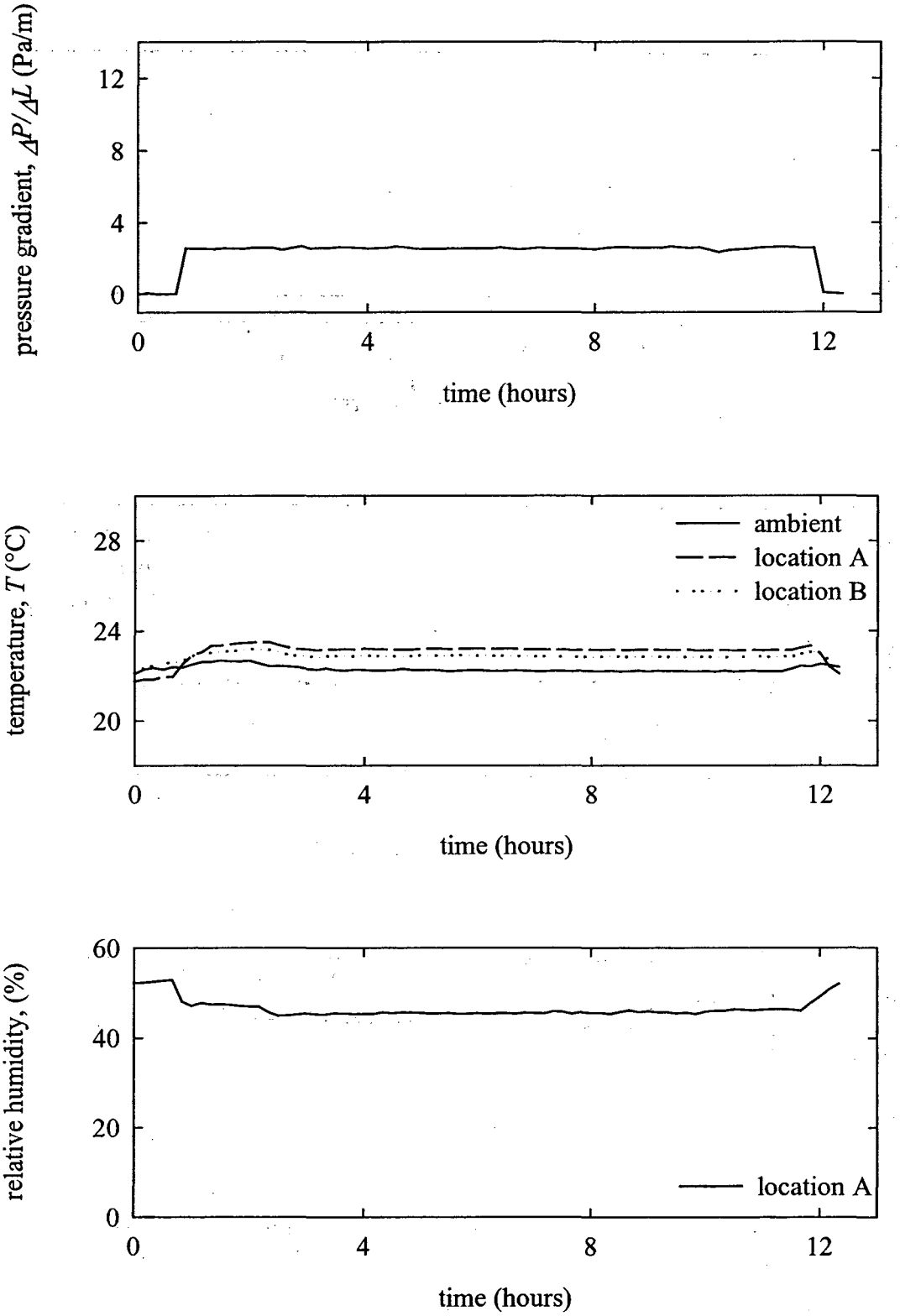

Figure C.2 Pressure gradient, temperature and relative humidity profiles for run 10 in the steel duct with an air speed of 5.3 m/s.

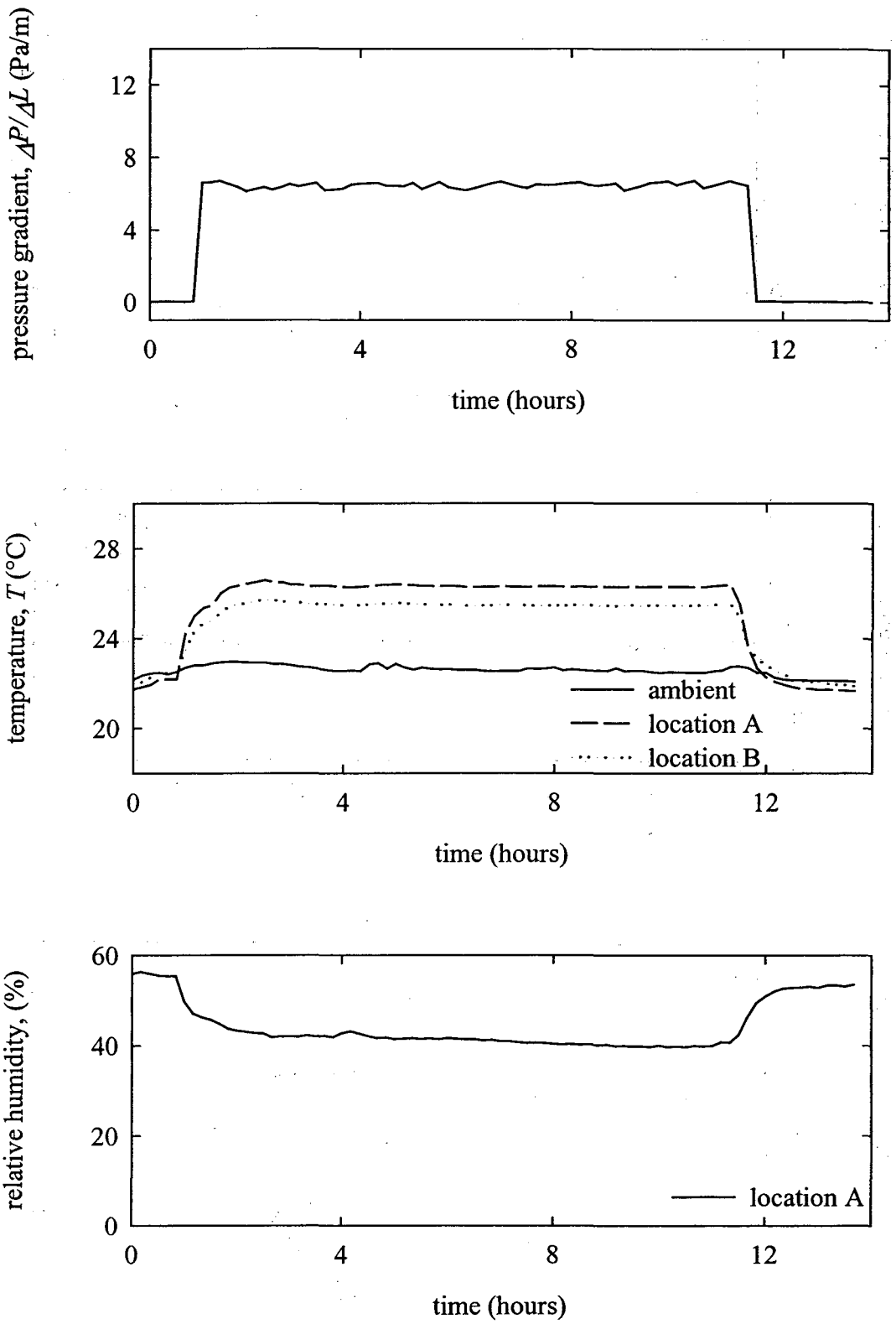

Figure C.3 Pressure gradient, temperature and relative humidity profiles for run 16 in the steel duct with an air speed of 9.1 m/s.

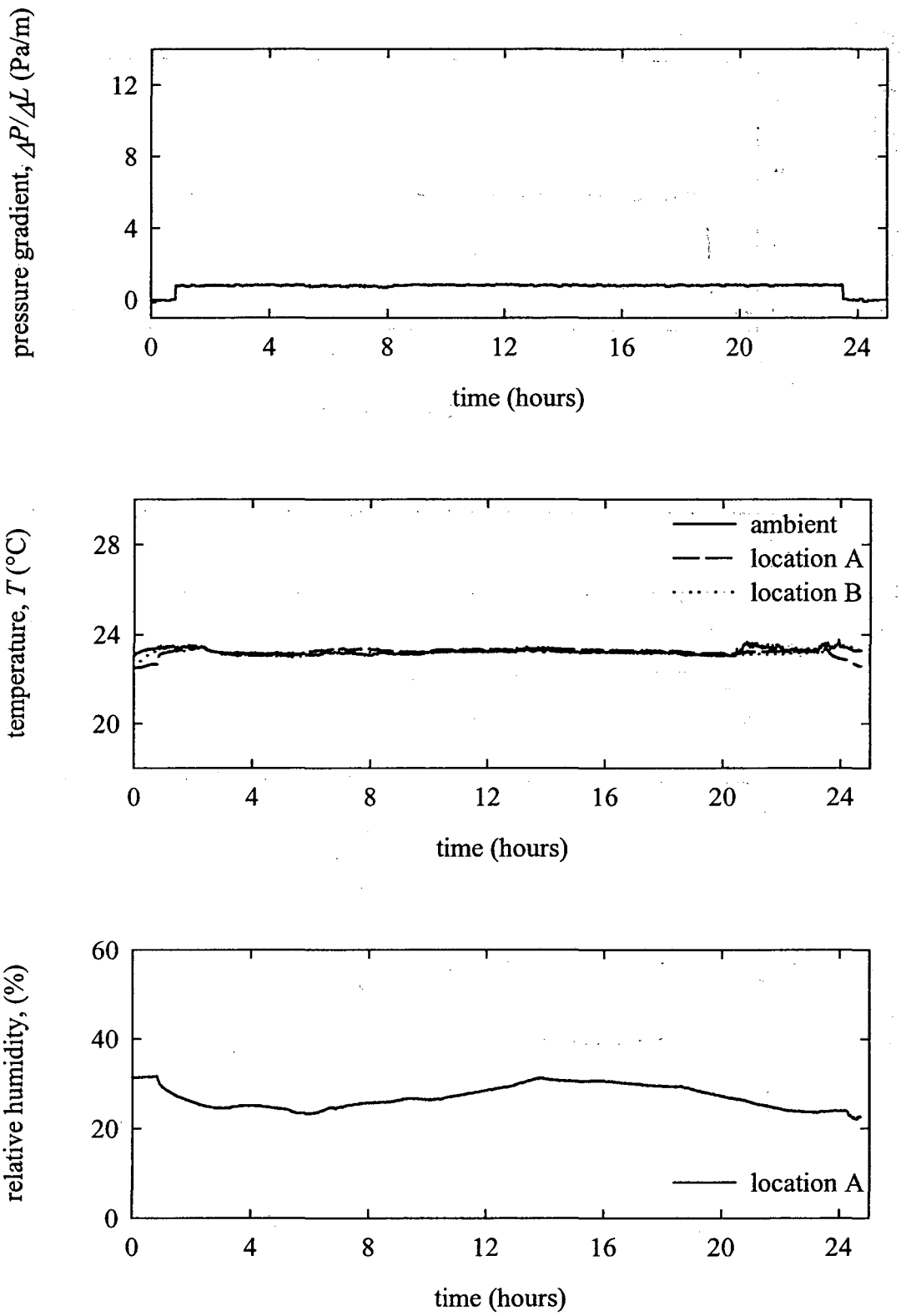

Figure C.4 Pressure gradient, temperature and relative humidity profiles for run 21 in the insulated duct with an air speed of 2.2 m/s.

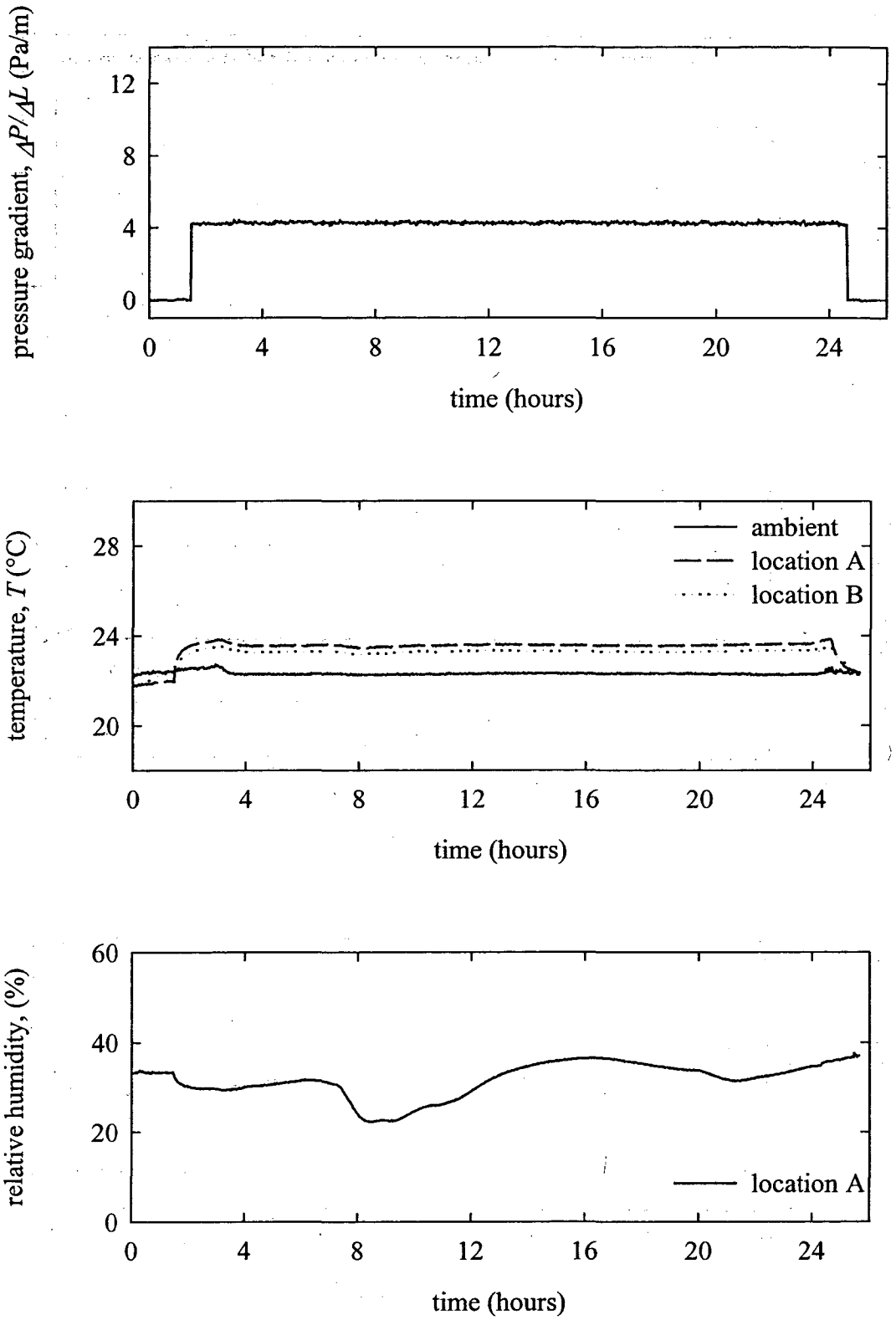

Figure C.5 Pressure gradient, temperature and relative humidity profiles for run 23 in the insulated duct with an air speed of 5.2 m/s.

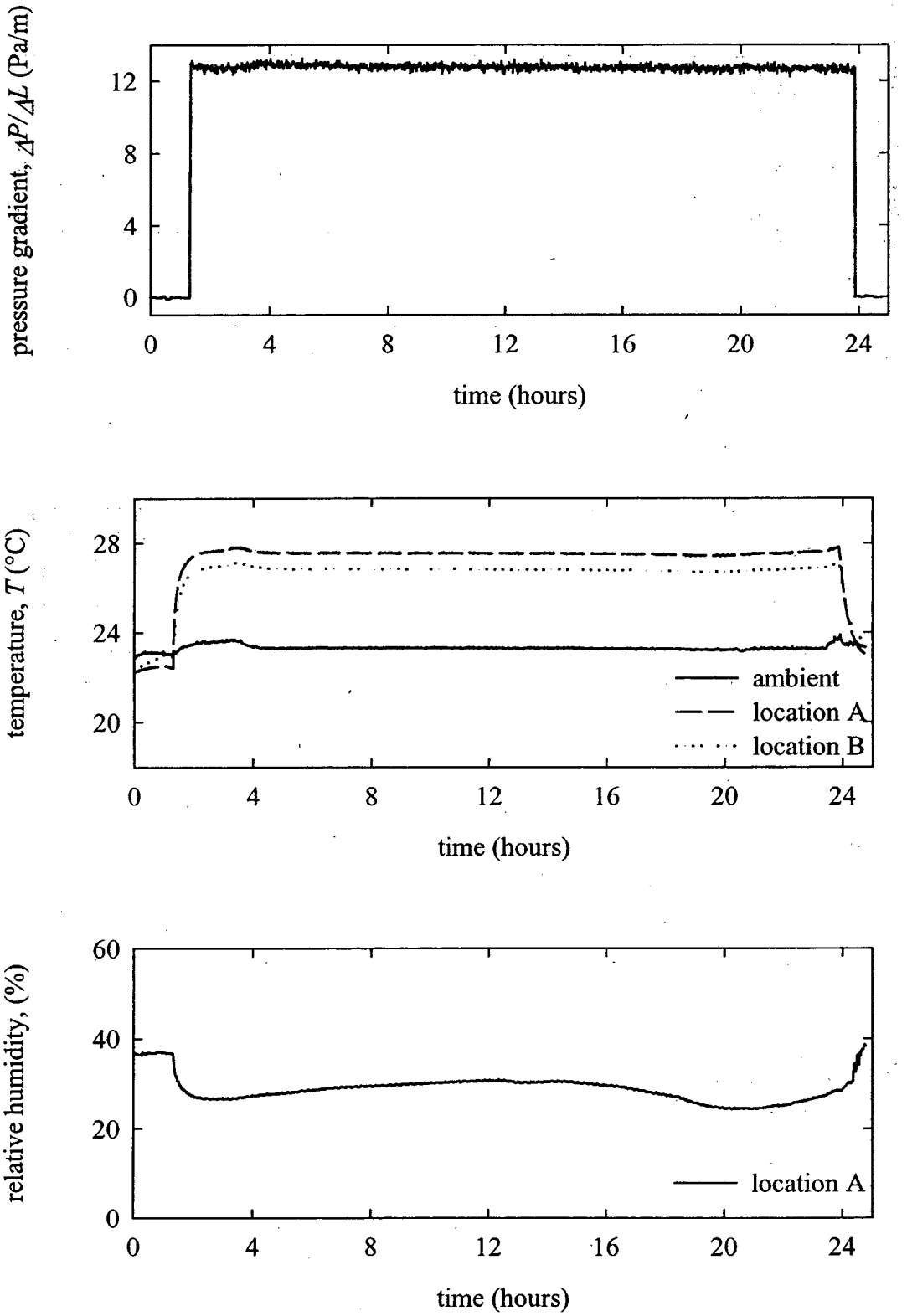

Figure C.6 Pressure gradient, temperature and relative humidity profiles for run 31 in the insulated duct with an air speed of 8.9 m/s.

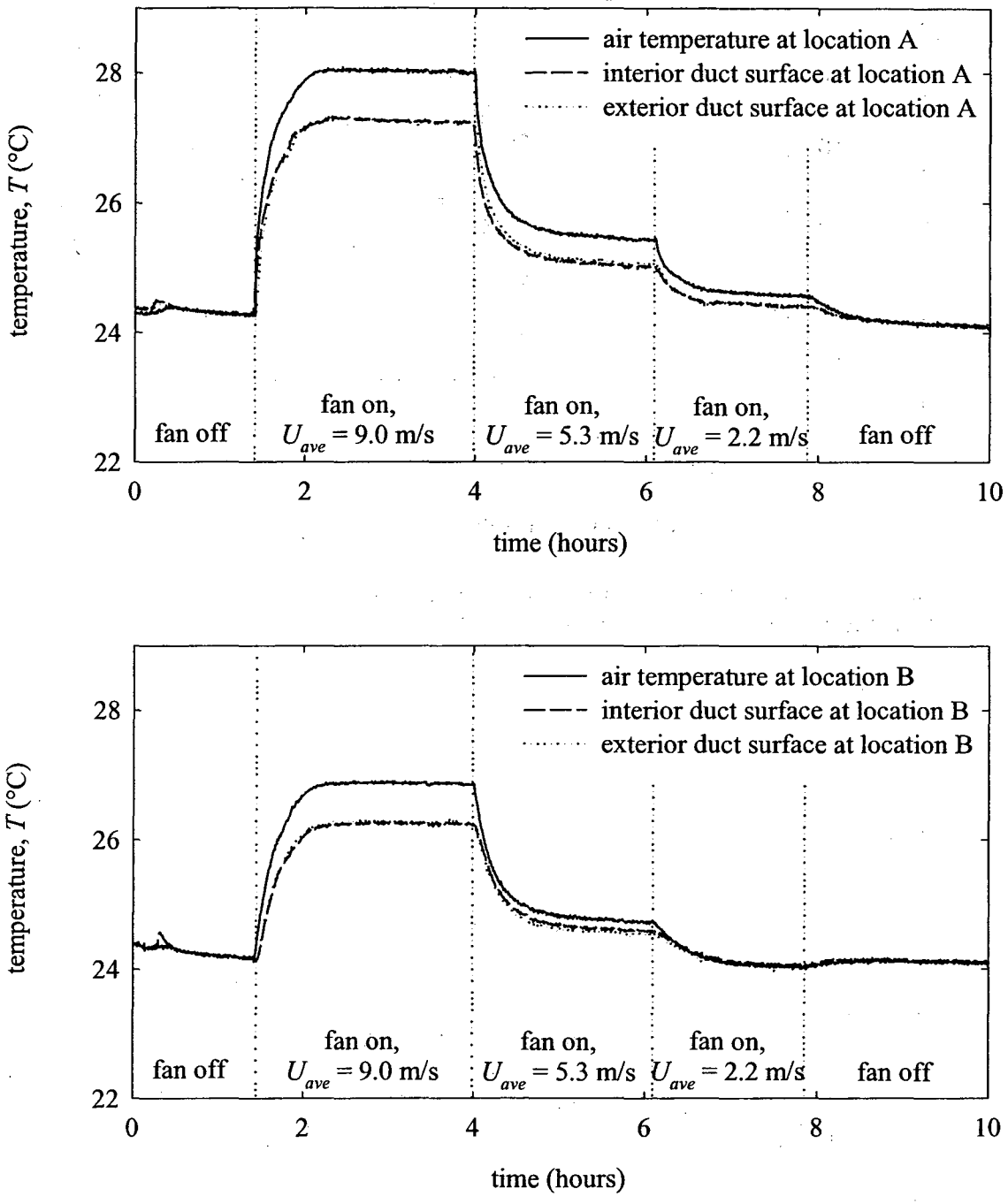

Figure C.7 Interior and exterior duct surface temperatures and centerline air temperatures measured at locations A and B in the auxiliary surface temperature experiment.

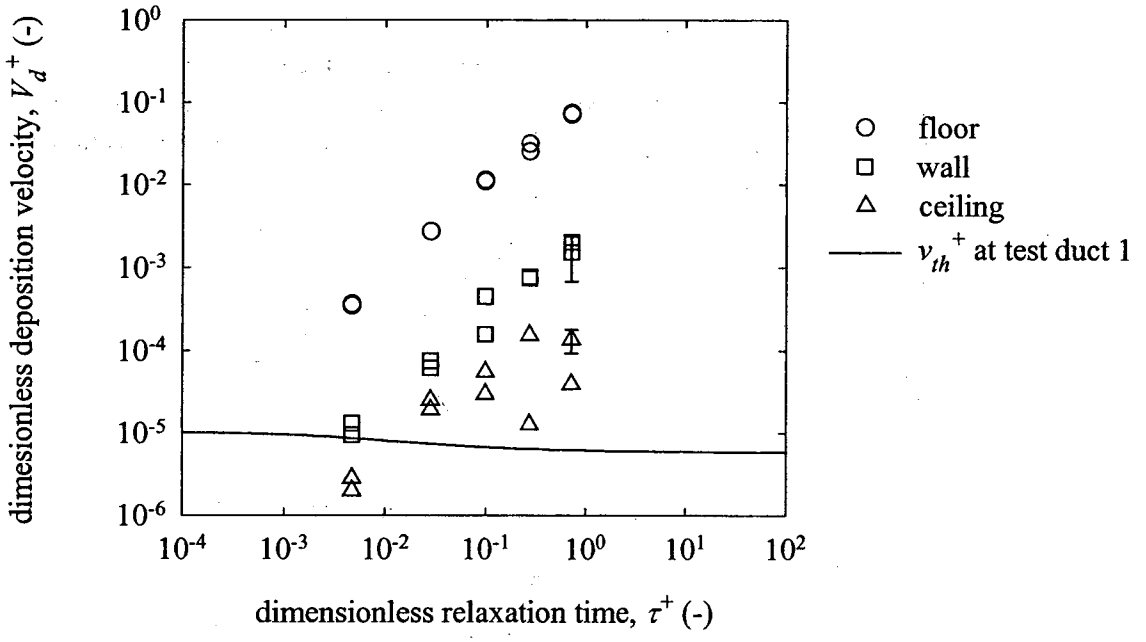

Figure C.8 Comparison of estimated thermophoretic deposition velocities, v_{th}^+, to measured dimensionless deposition velocities in the steel system at an air speed of 2.2 m/s.

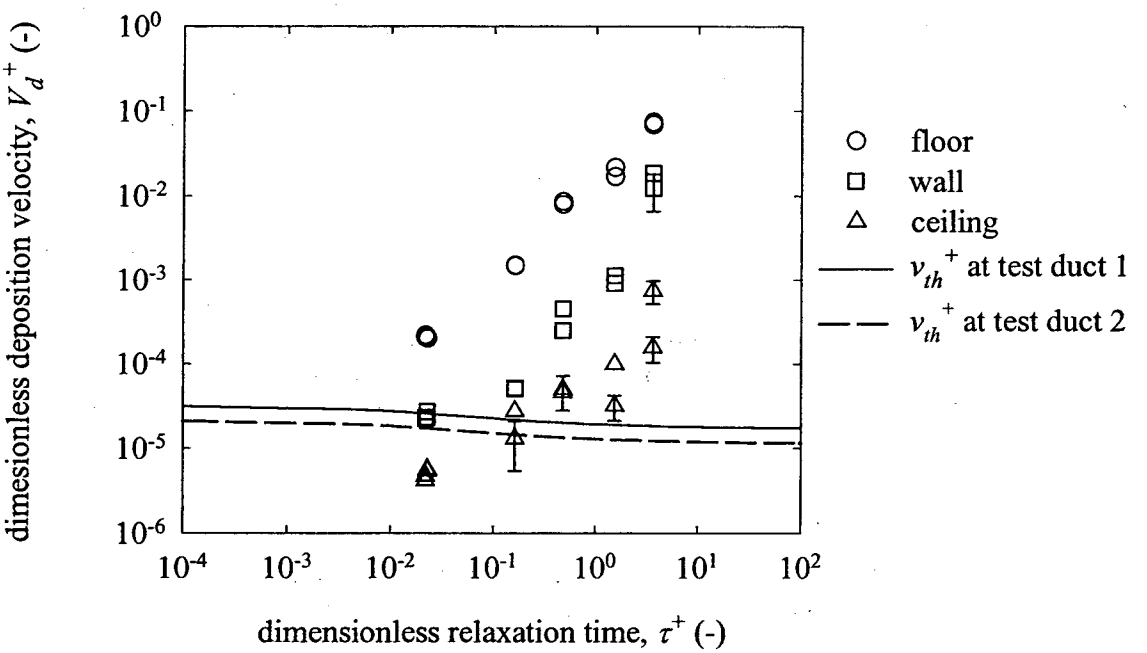

Figure C.9 Comparison of estimated thermophoretic deposition velocities, v_{th}^+, to measured dimensionless deposition velocities in the steel system at an air speed of 5.3 m/s.

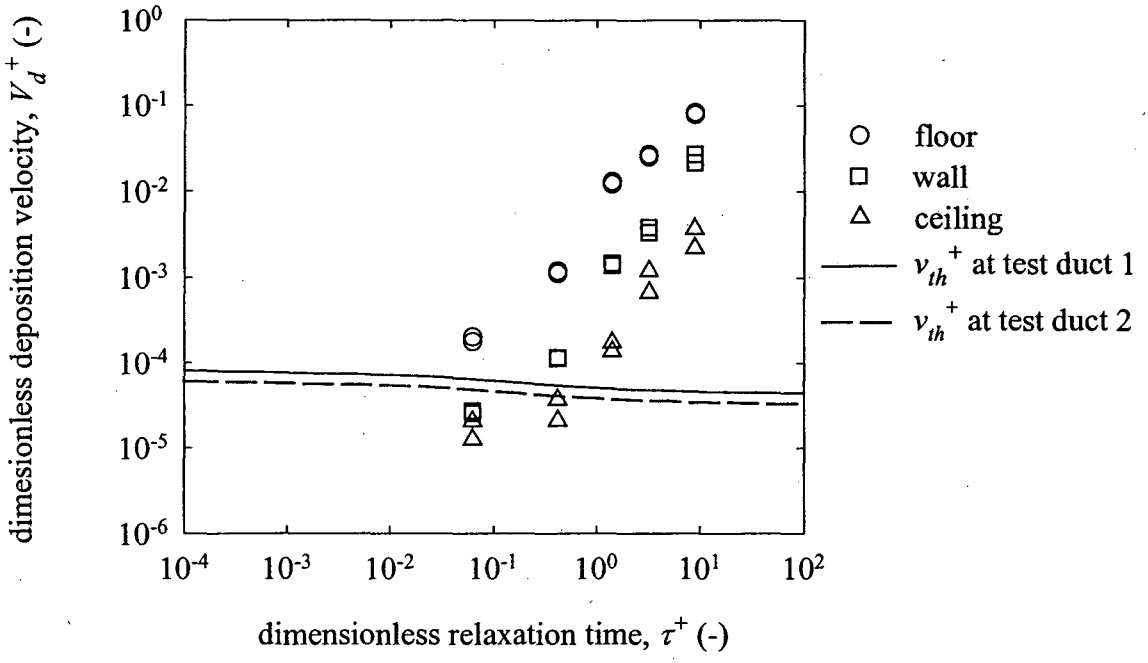

Figure C.10 Comparison of estimated thermophoretic deposition velocities, v_{th}^+, to measured dimensionless deposition velocities in the steel system at an air speed of 9.0 m/s.

APPENDIX D

Experimental Uncertainty

D.0 Abstract

Estimates of uncertainties in reported experimental measurements were made by propagation of random errors and by calculating 95% confidence limits for parameters that were subjected to repeated measurements. The propagation of errors analysis suggested that, in most cases, random errors in fundamental measurements led to errors of 10% or less in reported parameters. The magnitude of the estimated errors was only significant for interpreting the data for particle penetration through duct bends. The levels of error in other parameters, such as deposition velocities, dimensionless relaxation times and enhancement factors, were estimated to be small enough so that they would not significantly limit data interpretation. Calculated 95% confidence limits were small and are an indication that measured values are accurate. Overall, the experimental data are expected to be of good quality and to have a reasonably low level of uncertainty.

D.1 Introduction

Every measurement has an associated uncertainty resulting from uncontrollable random errors. Knowledge of the magnitude of these uncertainties is valuable for characterizing the quality of experimental data and estimating how near measured values are likely to be to their true values.

In experiments, calculated results of a single parameter are usually based on many different fundamental measurements. If random errors in fundamental measurements are known, the random error in calculated results can be estimated by propagation of errors through the equations. Consider the general equation

$$x_o = f(a_x, b_x, c_x \ldots) \tag{D.1}$$

where x_o is a calculated result depending on the experimental variables a_x, b_x and c_x, etc. The random error in x_o, s_{x_o}, resulting from random errors in the measured experimental variables can be calculated by the following equation (Skoog *et al.*, 1996):

$$s_{x_o}^2 = \left(\frac{\partial x_o}{\partial a_x}\right)^2 s_{a_x}^2 + \left(\frac{\partial x_o}{\partial b_x}\right)^2 s_{b_x}^2 + \left(\frac{\partial x_o}{\partial c_x}\right)^2 s_{c_x}^2 \ldots \tag{D.2}$$

Here, s_{a_x}, s_{b_x} and s_{c_x} are the magnitudes of the random errors associated with a_x, b_x and c_x, respectively. Thus, when the calculated value results from addition and subtraction processes, as in

$$x_o = a_x + b_x - c_x \tag{D.3}$$

the random error in the result is obtained from addition in quadrature:

$$s_{x_o} = \sqrt{s_{a_x}^2 + s_{b_x}^2 + s_{c_x}^2} \tag{D.4}$$

When the calculated value results from only multiplication and division, as in

$$x_o = \frac{a_x b_x}{c_x} \tag{D.5}$$

the random error in the result is estimated as follows

$$s_{x_o} = x_o \sqrt{\left(\frac{s_{a_x}}{a_x}\right)^2 + \left(\frac{s_{b_x}}{b_x}\right)^2 + \left(\frac{s_{c_x}}{c_x}\right)^2} \tag{D.6}$$

Thus, when a parameter is measured only once, an estimate of the random error associated with the measurement can be made by propagation of errors. This random error gives an estimate of how widely scattered repeated measurements of the parameter are likely to be. The relative error, defined here by

$$E_r = \frac{s_{x_o}}{x_o} \times 100\% \tag{D.7}$$

is useful for reporting the magnitudes of random errors.

In cases where a parameter is measured several times, random errors lead to measured values that are scattered about the true value. The spread of data about the average is characterized by its standard deviation. Given a parameter x_o which has been measured multiple times, the standard deviation of the measurements, σ_{x_o}, is estimated by

$$\sigma_{x_o} = \sqrt{\frac{\sum_{i=1}^{N_m} \left(\bar{x}_o - x_{o,i}\right)^2}{N_m - 1}} \tag{D.8}$$

where $\bar{x}_o$ is the average of the measurements and N_m is the number of measurements. In the absence of systematic errors, it is expected that the average of the measurements approaches the true value as the number of measurements increases. The probability that the true value lies within a range about the average can be characterized by confidence limits. When $N_m = 4$, the 95% confidence limits can be calculated by

$$CL_{x_o} = \bar{x}_o \pm \frac{3.18\sigma_{x_o}}{\sqrt{N_m}} \tag{D.9}$$

The limits expressed by equation (D.9) define a range in which the true value has a 95% probability of existing. Confidence limits can only be determined when a standard deviation can be calculated from multiple data points. For the purposes of this discussion, a relative confidence interval was defined as

$$CL_{rel} = \frac{3.18\sigma_{x_o}}{x_o\sqrt{N_m}} \times 100\% \tag{D.10}$$

D.2 Methods

Uncertainties in all reported values in these particle deposition experiments were estimated by propagation of errors through calculations. In cases where repeated measurements of a single value were made, 95% confidence limits based on the standard deviation of the repeated measurements were also calculated. In these experiments, estimates of measurement errors were based on instrument specifications and observed variability in equipment performance.

D.2.1 95% Confidence limits

Three parameters were subjected to multiple measurements in each experiment: the deposition velocity in test ducts 1 and 2, the deposition velocity at wall S-connectors and the transport efficiency through isokinetic nozzles (reported in Appendix B). Four measurements were made of each parameter in every experiment. Standard deviations and confidence limits could be calculated for these parameters using equations (D.8) and (D.9).

Other parameters were measured only once in each experiment. These parameters were the penetration through bends 5 and 6, the aspiration efficiency and transport efficiency in the shrouded nozzle, the deposition velocity in test ducts 3 and 4 and the deposition velocity at floor and ceiling S-connectors. Because deposition rates were not expected to be constant in test ducts 3 and 4, measurements of deposition velocities and enhancement factors in these ducts at each panel were considered unique and not averaged. Duplicate measurements were made of deposition to floor and ceiling S-connectors, but calculating confidence limits based on the standard deviation of only two measurements was considered unreliable. Thus, averages, standard deviations and confidence limits were not calculated for these parameters.

D.2.2 Estimates of random errors in fundamental measurements

Table D.1 summarizes estimated errors for all fundamental experimental measurements or input parameters. These are the errors used for the error propagation calculations. Error estimates are believed to be conservative, meaning that the true error is probably not larger than the indicated error estimate.

Errors associated with values of the kinematic viscosity and air density were estimated based on the ranges of temperature and relative humidity measurements in the duct. Local velocity pressures were measured with a pitot tube and a digital manometer. The accuracy of the digital manometer was expected to be ±0.1 Pa, but measurement errors were assumed to be larger for two reasons. First, there are errors associated with positioning the pitot tube in the flow. Second, the variability of measured velocity pressures was often greater than ±0.1 Pa because of the velocity fluctuations inherent in turbulent flow. These fluctuations increased with air speed;

thus, errors were larger at higher air speeds. Velocity pressure errors were assumed to be 0.2, 0.5 and 1.0 Pa for air speeds of 2.2, 5.3 and 9.0 m/s, respectively.

Static pressures measured by Setra pressure sensors attached to the digital data acquisition board were used to calculate pressure drops along the duct by equation (3.4). These static pressures were the average of hundreds of measurements; consequently, random errors were estimated as the standard deviation of these multiple measurements. The estimated error was 0.5 Pa.

The error in the length measurement between the two pressure sensors, made with a tape measure, was estimated to be 0.1 m. The error in the hydraulic duct diameter measurement was estimated at 3.0 mm to account for the observed variations in the duct dimensions. Errors in the length and width measurement of rinsed duct panels, made with a ruler with millimeter graduations, were estimated to be 2.0 mm.

A particle density error of 50 kg m^{-3} was assumed to apply for all particle sizes and densities. Errors in the measurement of liquid volumes in the wet-chemistry analysis were assumed equal to the errors printed on the glassware used for measuring the volumes. Errors in fluorescein concentration measurements were taken to be 0.3 ng/mL, higher than the expected fluorometer accuracy of 0.1 ng/mL. The higher error value was assumed to account for variations in the efficacy of rinsing, for incomplete mixing of the rinsing solution and for inconsistencies in the fluorometer calibration. This error value was associated with fluorescein mass determinations for all pieces: duct panels, S-connectors, filters, nozzle interiors and filter holder interiors. There

was assumed to be no error associated with the determination of the background fluorescein concentration, $C_{f,b}$.

Experimental times were measured with a digital clock; an error value of 5 minutes was assumed. Pump flow rates were measured with an electronic bubble flow meter with an accuracy of better than 0.01 L/min. The pumps drew air at a nearly constant flow rate; however, fluctuations over the course of an experiment were usually greater than the ±0.01 L/min error in measurement. To account for variations in the pump flow rate, the error was taken to be 0.05 L/min.

The error in the measurement of the particle size was taken to be the standard deviation of the particle size data from the APS, calculated by

$$s_{d_p} = \sigma_{d_{mm}} = \left[\frac{\sum_{i=1}^{51} N_i \left(d_{p,i} - d_{mm} \right)^2}{\left(\sum_{i=1}^{51} N_i \right) - 1} \right]^{1/2} \tag{D.11}$$

where N is the number count of particles in the APS size bin defined by d_p. Values of $\sigma_{d_{mm}}$ were typically less than 8% of the measured particle diameter.

D.2.3 Propagation of random errors

Equation (D.2) was used to propagate the estimated random errors summarized in Table D.1 to final values reported as experimental results. Table D.2 shows equations that were used for the propagation of errors through the calculation of the dimensionless relaxation time, τ^+. All propagation of error equations in Table D.2 are derived from equation (D.2). A similar series of equations was used for propagation

of random errors to other parameters. Relative errors based on the propagated errors were calculated using equation (D.7)

D.3 Results and Discussion

D.3.1 Propagation of random errors

Relative errors were estimated by propagation of errors for each reported result in every experiment. The ranges of relative errors for each parameter are summarized in Table D.3. Relative errors varied among experiments because of variations in aerosol polydispersity, air speed, total deposited particle mass, wet-chemistry techniques and a variety of other factors. In most cases, relative errors of all parameters were estimated to be less than 10%. This magnitude of relative error is acceptable for parameters that varied over many orders of magnitude. For example, if error bars were included on Figures 3.08-3.10 and 3.18-3.20 to express the magnitude of errors on V_d and U_{ave}, they would be equal in size or smaller than the data points themselves. The same can be said for the estimated errors associated with τ^+ and V_d^+ in Figures 3.12-3.17 and 3.22-3.25; a 10% change on a logarithmic scale that spans six decades is hardly noticeable. Estimated errors associated with the shrouded nozzle variables η_t, η_a and T_{total} are also too small to be noticed if included in Figures B.6-B.9.

Cases where the estimated magnitude of the relative error is significant occurred for penetration through bends and for the transport efficiency through isokinetic nozzles. If relative errors in the measurement of bend penetrations were as large as expressed in Table D.3, it would be difficult to distinguish among the data presented in Figures 4.6-4.9. Most of the error in the bend penetration measurements is expected to result from errors in the calculation of the total particle mass passing through the bend

during an experiment. For larger particle sizes, errors in airborne concentration projections were the dominant factor contributing to the error because these projections are very sensitive to errors in the deposition velocity when the deposition velocity is high. For smaller particles, errors in the evaluation of the hydraulic diameter were most important for determining the error in the bend penetration measurement. When estimating the errors associated with determining isokinetic nozzle transport efficiencies, relative errors were usually on the order of 1% as observed for the shrouded nozzle. In cases where the measured transport efficiencies were low, the magnitude of the estimated errors were about the same as in other cases, but the relative errors were greater (sometimes on the order of 10%) because of the normalization by a small number. The estimated level of the absolute errors are low in all cases and of acceptable magnitude.

Relative errors in enhancement factors were greater than 10% on occasion. In summary, by the propagation of error analysis, the relative random errors associated with most reported values in these experiments are expected to be less than about 10%. This level of expected error is acceptable in most cases, but may be problematic when interpreting the results of the bend penetration measurements. This error analysis suggests that the quality of the bend penetration measurements could have been improved by measurement of the airborne particle concentration directly at the bends. However, there could be significant errors associated with measuring particle concentrations near bends where air velocity and particle concentrations are nonuniform. Furthermore, measurement of bend penetration was found to be sensitive to variations in the duct dimensions, which could not be readily controlled. These variations alone could lead to relative errors of 2-3% for bend penetrations, a

level of error high enough to confound interpretation of the current results. Thus, it is not clear that there is an easy method for improving upon the methods used in these experiments.

D.3.2 95% Confidence limits

Confidence limits were calculated for deposition velocities in test ducts 1 and 2, deposition velocities at wall S-connectors and transport efficiencies through isokinetic nozzles. The 95% confidence limits for dimensionless deposition velocities in test ducts 1 and 2 are expressed by the error bars in Figures 3.12-3.17 and Figures 3.22-3.25. In these figures, error bars are only included when the relative confidence interval is greater than 40%. In general confidence limits were narrower for data from insulated ducts than for data from steel ducts. There was only one case when the relative confidence interval exceeded 40% in insulated ducts. In steel ducts, measured deposition velocities to duct floors had relative confidence intervals that were always less than 15%. Relative confidence intervals for deposition data at steel duct walls and ceilings were mostly in the range 10-30% and 15-40% respectively.

The 95% confidence limits for dimensionless deposition velocities at wall S-connectors are expressed by the error bars in Figures 4.1-4.3. As previously, error bars are only included when the relative confidence interval exceeds 40%. Relative confidence intervals for these data were usually in the range 25-40% and this level of uncertainty appears acceptable considering that the measured deposition rates vary by nearly three orders of magnitude.

The 95% confidence limits for transport efficiencies through the isokinetic nozzles are expressed by the error bars in Figure B.5. Because the plots in this figure involve linear axes, absolute confidence intervals are more useful than relative confidence intervals. Error bars are excluded from Figure B.5 if the confidence interval is 0.04 or less. Most confidence intervals associated with these data were less than 0.02.

For the three cases in which confidence limits were calculated in these experiments, they were relatively small compared to the magnitudes of the parameters being measured. The small confidence limits suggest that the data reported are accurate representations of the true value that is being quantified.

D.4 Conclusions

Uncertainties in reported data from the particle deposition experiments were evaluated by estimating probable random errors through propagation of errors and by calculating 95% confidence limits when possible. The propagation of errors analysis suggested that, in most cases, random errors in fundamental measurements lead to relative errors of 10% or less in reported parameters. For most reported data, this level of estimated error is acceptable, but it would limit the interpretation of the data for particle penetration through duct bends. When 95% confidence limits were calculated, they were small and indicate accurate measurements. The low levels of propagated random errors and the small confidence intervals indicate that the methods used in these experiments were of good quality.

Table D.1 Typical values and estimated errors associated with fundamental measurements or input parameters.

Measured or input parameter	Typical values	Estimated error
kinematic viscosity of air, ν	1.53×10^{-5}-1.57×10^{-5} m^2 s^{-1}	2×10^{-7} m^2 s^{-1}
air density, ρ_a	1.17-1.19 kg m^{-3}	0.015 kg m^{-3}
velocity pressure, P_v	2-4 Pa (U_{ave} = 2.2 m/s) 12-24 Pa (U_{ave} = 5.3 m/s) 35-65 Pa (U_{ave} = 9.0 m/s)	0.2 Pa 0.5 Pa 1.0 Pa
static pressure, P_A and P_C	10-300 Pa	0.5 Pa
length of duct, L or ΔL	3.8-14.1 m	0.1 m
hydraulic diameter of duct, D_h	0.152 m	0.003 m
length of duct panel, L_p	0.1-0.22 m	0.002 m
width of duct panel, W_p	0.08-0.12 m	0.002 m
particle density, ρ_p	950-1350 kg m^{-3}	50 kg m^{-3}
volume of buffer for rinsing, V_r	10-500 mL	0.1-0.3 mL
fluorescein concentration measured by fluorometer, C_f	2-120 ng/mL	0.3 ng/mL
experimental time, t	300-8000 min	5 min
sampling pump flow rate, Q_{pump}	2.3-6.3 L/min	0.05 L/min
internal surface area of a bend, A_{bend}	0.218 m^2	0.005 m^2

Table D.2 Equations for error propagation in calculated values of the dimensionless relaxation time.

Parameter	Error propagation equation
$\mu = \rho_a \nu$	$s_\mu = \mu \sqrt{\left(\frac{s_{\rho_a}}{\rho_a}\right)^2 + \left(\frac{s_\nu}{\nu}\right)^2}$
$u = \sqrt{\frac{2P_v}{\rho_a}}$	$s_u = u \sqrt{\frac{1}{4}\left(\frac{s_{P_v}}{P_v}\right)^2 + \frac{1}{4}\left(\frac{s_{\rho_a}}{\rho_a}\right)^2}$
$U_{ave} = \frac{\sum_{i=1}^{16} u_i}{16}$	$s_{U_{ave}} = \sqrt{\sum_{i=1}^{16}\left(\frac{s_{u_i}}{16}\right)^2}$
$\Delta P = P_A - P_C$	$s_{\Delta P} = \sqrt{s_{P_A}^2 + s_{P_C}^2}$
$\frac{\Delta P}{\Delta L} = \frac{\Delta P}{\Delta L}$	$s_{\Delta P/\Delta L} = \frac{\Delta P}{\Delta L}\sqrt{\left(\frac{s_{\Delta P}}{\Delta P}\right)^2 + \left(\frac{s_{\Delta L}}{\Delta L}\right)^2}$
$f = \frac{\Delta P}{\Delta L}\frac{D_h}{2\rho_a U_{ave}^2}$	$s_f = f\sqrt{\left(\frac{s_{\Delta P/\Delta L}}{\Delta P/\Delta L}\right)^2 + \left(\frac{s_{D_h}}{D_h}\right)^2 + \left(\frac{s_{\rho_a}}{\rho_a}\right)^2 + 4\left(\frac{s_{U_{ave}}}{U_{ave}}\right)^2}$
$u^* = U_{ave}\sqrt{f/2}$	$s_{u^*} = u^*\sqrt{\left(\frac{s_{U_{ave}}}{U_{ave}}\right)^2 + \frac{1}{4}\left(\frac{s_f}{f}\right)^2}$
$\mathrm{Kn} = \frac{2\lambda}{d_p}$	$s_{\mathrm{Kn}} = \mathrm{Kn}\sqrt{\left(\frac{s_{d_p}}{d_p}\right)^2 + \left(\frac{s_\lambda}{\lambda}\right)^2}$
$C_c = 1 + \mathrm{Kn}\left[1.257 + 0.4\,exp\left(-\frac{1.1}{\mathrm{Kn}}\right)\right]$	$s_{C_c} = C_c\sqrt{s_{Kn}^2\left[1.257 + 0.4\,exp\left(\frac{-1.1}{Kn}\right) + \frac{0.44}{Kn}exp\left(\frac{-1.1}{Kn}\right)\right]^2}$
$\tau^+ = \frac{C_c \rho_p d_p^2 u^{*2}}{18\mu\nu}$	$s_{\tau^+} = \tau^+\sqrt{\left(\frac{s_{C_c}}{C_c}\right)^2 + \left(\frac{s_{\rho_p}}{\rho_p}\right)^2 + 4\left(\frac{s_{d_p}}{d_p}\right)^2 + 4\left(\frac{s_{u^*}}{u^*}\right)^2 + \left(\frac{s_\mu}{\mu}\right)^2 + \left(\frac{s_\nu}{\nu}\right)^2}$

Table D.3 Ranges of relative errors of reported parameters based on propagation of random errors.

Calculated parameter	Relative error (%)
average air speed, U_{ave}	0.3-1
friction velocity, u^*	1-4
mass-mean particle diameter, d_{mm}	4-8
dimensionless relaxation time, τ^+	8-13
deposition velocity, V_d	3-11
dimensionless deposition velocity, V_d^+	2-5
dimensionless S-connector deposition velocity, $V_{d,S}^+$	3-9
Stokes number, St	8-14
bend penetration, P_{bend}	4-11
average bend dimensionless deposition velocity, V_d^+	6-12
enhancement factor, EF	5-15
transport efficiency for isokinetic nozzle, η_t	0.5-13
transport efficiency for shrouded nozzle, η_t	0.5-1
total aspiration efficiency for shrouded nozzle, $\eta_{a,total}$	1-3
transmission efficiency for shrouded nozzle, T_{tot}	1-3

Ernest Orlando Lawrence Berkeley National Laboratory
One Cyclotron Road | Berkeley, California 94720

Prepared for the U.S. Department of Energy under Contract No. DE-AC03-76SF00098